

Durham E-Theses

The structural setting of the Canaã dos Carajás region and Sossego-Sequeirinho deposits, Carajás – Brazil

DOMINGOS, FABIO

How to cite:

DOMINGOS, FABIO (2009) *The structural setting of the Canaã dos Carajás region and Sossego-Sequeirinho deposits, Carajás – Brazil*, Durham theses, Durham University. Available at Durham E-Theses Online: <http://etheses.dur.ac.uk/144/>

Use policy

The full-text may be used and/or reproduced, and given to third parties in any format or medium, without prior permission or charge, for personal research or study, educational, or not-for-profit purposes provided that:

- a full bibliographic reference is made to the original source
- a [link](#) is made to the metadata record in Durham E-Theses
- the full-text is not changed in any way

The full-text must not be sold in any format or medium without the formal permission of the copyright holders.

Please consult the [full Durham E-Theses policy](#) for further details.

**The structural setting of the Canaã dos Carajás region
and Sossego-Sequeirinho deposits, Carajás – Brazil**

Fábio Henrique Garcia Domingos

Department of Earth Sciences

University of Durham

A thesis submitted for the degree of

Doctor of Philosophy

November 27, 2009

DECLARATION

No part of this thesis has previously been submitted for a degree at this or any other university. The work described in this thesis is entirely that of the author, except where reference is made to previously published or unpublished work.

Fábio Henrique Garcia Domingos
University of Durham
Department of Earth Sciences
November 2009

Copyright © by Fabio H.G. Domingos

The copyright of this thesis rest with the author. No quotation from it should be published without their prior written consent and information from it should be acknowledged.

To mum and dad

Aos meus pais Ilis e Marcia

"Os soldados saíram de Roma a 2000 anos. Chegando na península ibérica, latinizaram os íberos. Ficam dormindo 1500 anos lá. Depois saltaram o mar, o oceano, e vieram pra cá. Falando a língua dos romanos! E aqui, essa língua dos romanos se expandiu por esse povo que é de 180 milhões. É o maior dos povos latinos! É mais que França somada com Itália, com Portugal, com Espanha, com Romênia! Quem mais representa como massa humana a Latinidade somos nós, os mestiços Brasileiros. (...)

Nesse sentido, nós somos a Nova Roma, uma Roma que o mundo vai ver, espantado, no momento em que realizarmos nossa potencialidade - tantas! - no momento em que resolvermos problemas elementares: que todo mundo coma todo dia, que toda criança tenha uma escola, que se faça aquelas reformas urbanas e rurais para que a terra seja acessível para quem trabalha, para que as cidades sejam a morada dos homens cordiais. Nesse dia, vai florescer no mundo uma civilização diferente, que nunca ninguém viu.

(...)Ao lado dos eslavos - milhões de eslavos -, ao lado dos neo-britânicos - milhões -, ao lado dos chineses - milhões -, dos árabes - milhões -, de outros - milhões-, existirá essa face morena."

Darcy Ribeiro – O Povo Brasileiro

Acknowledgements

I would like to thank kindly CAPES Foundation for funding this PhD project through the full time doctoral scholarship scheme. Field work and analysis were funded by CNPq through the CT Mineral Fund for the project “*Estudo das Relações entre a Deformação das Rochas e os Depósitos Minerais na Região Sudeste da Serra dos Carajás - PA, com base na Aquisição Geoespacial, Visualização e Análise de Dados Geoestruturais.*”

I would like to extend my thanks to Bob Holdsworth and Ken McCaffrey for accepting to supervise me and for their guidance, suggestions and comments throughout the project development.

I am especially thankful to Vale Mining Company and the geologist Benevides Aires (GALOY) for granting access to the Sossego and Sequeirinho Mines and drill-cores, as well as providing logistical support and accomodation in the field. Additionally I would like to say thank you to other staff at Vale for their priceless support, discussion, help and company during fieldwork (names in alphabetical order): Alene Fernandes; Ana Claudia (Tesouro); Claudionor Silva; Cleive; Defferson Oliveira; Ediney Duarte; Isidoro Costa; Jose Garbelloto; Luiz Antonio; Marceley Neves; Marcio Soares; Mauricio and Rafael Ajub.

Thanks to KLM logistics staff for helping with those hundreds of core-samples boxes, for my sample boxes and a vast suply of geladinho and cuzcuz (Amarelinho, Cachorro, Soja, Novo, Cartilho...).

Thanks to Prof. Jonas Klein and Jana Neubert from Friedrich-Schiller-Universität for the valuable time, company and discussions in the field.

A big thank you goes to people from UFPA-Geology Institute who are the funniest guys to do fieldwork with: Carlo Alberto, Geane Cavalcante, Luiz Gustavo and Roberto Barbalho.

Thanks to the Earth Sciences Department staff at Durham for helping with all sorts of problems: Janice Oakes, Karen Atkinson, Alan Carr, Garry Wilkinson, Dave Stevenson, Maria Arkless, Dave Sales, Semone Macintyre, Carole Blair.

My departmental colleagues deserve a big thank you for providing me with the common things of a normal life: Sarah Bradley, Cole-My Boy, Nicola Marsh, Mike Mawby, Adam Pugh, Jen Waters, Alex Finlay, Steve Smith, Rich Walker, David

Moy, Khalifa Abdunaser, Richard Jones, Jonny Imber, Dave Sagi, Dave the Shark, Max the bike master, Jen Martin, Ekaterina Vsemirnova.

Thanks to the Bradley family (Sarah, Brian, Shirley, Gdad Larry) for making me feel part of a family environment during my time in the UK. Specially to Rosebaaaaa for sharing her very nice house and happy moments with me. To mum, dad and brother for the long distance support.

The biggest and most special thank you is saved for the last. It goes to my mentor, the one known in the dark world of geology as the structure's master: Roberto Vizeu. I have no words to express my sincere gratitude for having him as an undergraduate teacher, master's supervisor, present working colleague and friend. Without Vizeu's support, example and encouragment I would never have made it.

Abstract

The Carajás Terrane in the Amazon Craton hosts Precambrian Cu-Au deposits with resources larger than 100 million tonnes of ore (e.g. Igarapé Bahia-Alemão, Cristalino, Sossego, 118 and Salobo). This thesis examines at a local scale, structural aspects of the Sossego and Sequeirinho deposits, located in the Archaean granite-gneiss basement of the Canaã dos Carajás region, the boundary between the Carajás and Rio Maria Granite Greenstone Terranes.

The study focuses on the understanding of the processes, controls and styles of two regionally representative Archaean IOCG examples and also investigates the tectonic framework and structural evolution of the Canaã dos Carajás region. Primary data comprises traditional methods of field mapping and structural analysis, microscopic investigation, combined with modern digital mapping, lineament and particles size analysis. The principal aims of the study include: (1) identification of crustal scale regional lineaments and their relationship with mineral deposits; (2) a new tectonic framework and structural model for the Canaã dos Carajás region; and (3) description and interpretation of the structural framework of the Sossego and Sequeirinho mines.

The most prominent crustal scale lineaments in the Carajás Terrane comprise early WNW-ESE sets that configure the regional structural trend and mark the basement-cover assemblage contact, and relatively late NE-SW lineaments. Higher lineament frequencies and density were observed in the cover assemblage domain and coincide with numerous lineament intersections. Mineral occurrences and deposits are clustered and spatially associated with domains of higher lineaments density and areas where major lineaments intersect. Then, there is a spatial relationship between major lineaments and the occurrence of mineral deposits.

The Canaã dos Carajás region comprises Archaean TTG gneisses, lens shaped amphibolite bodies, 2.7 Ga. syn-tectonic alkali granitoids and 1.88 Ga. isotropic granites. These rocks display widespread heterogeneous, anastomosing WNW-ESE and NE-SW foliation sets, related steeply dipping ductile shear zones associated with steep-to-moderately plunging mineral lineations. The nature and geometry of the ductile fabrics are compatible with a bulk pure-shear dominated transpression with partitioning of strain intensity with shortening and extensional

directions oriented at approximately near horizontal ($\sim 020^\circ$ Az) and near vertical respectively. Microstructures in quartz and feldspar indicate deformation at metamorphic conditions compatible with middle to upper amphibolite facies (~ 650 - 700°C), overprinted by deformation at middle to upper greenschist facies conditions (~ 400 - 500°C). The Canaã dos Carajás region represents part of an original granite-greenstone terrane that has undergone substantial reworking during a late sinistral transpressional deformation. The reworking took place at c.a. 2.7 Ga, coeval with syn-tectonic sub-alkaline magmatism. The basement comprises intensely deformed rocks uplifted from the lower-to-middle crust, deformed under high amphibolite facies conditions and later affected by localised deformation at greenschist facies conditions.

The structural framework of the Sossego and Sequeirinho deposits comprises regional WNW-ESE structures (foliations and shear zones) offset by NE-SW sinistral faults. Sequeirinho is hosted along a NE-SW sinistral fault, associated with a positive magnetic anomaly. It comprises an “S” shaped tabular orebody whose tips are hosted by sub-vertical WNW-ESE sheared and foliated granitoids and schists. These are linked by a NE-SW sinistral fault zone containing mineralized breccias. Sossego comprises a sub-circular, vertical, pipe-like orebody with a central breccia body surrounded by a stockwork array of sulphide veins, faults and shear zones. Tensile and shear veins show single or composite mineral fillings consistent with episodic vein opening, with a progressive change in hydrothermal fluid composition during time. The Sossego breccias show high clast angularity, characteristic of immature explosion breccias, whilst the Sequeirinho breccias display rounded fragments with low angularity, typical of mature breccias whose particle fragmentation was dominated by wear and attrition during subsequent slip along a fault zone. Microstructures in quartz and feldspar indicate that the deformation at Sossego and Sequeirinho initially took place under low-to-middle (300 - 400°C) and middle-to-upper (400 - 500°C) greenschist facies, respectively. Latter overprinted by brittle-ductile structures and veins containing lower-temperature minerals formed between 170 - 250°C . The rocks in the area of the mines record deformational processes that initially took place under the viscous regime ($>15\text{km}$), represented by mylonites and ultramylonites. Progressive exhumation, possibly synchronous with regional transpressional thickening led to conditions compatible with the frictional-viscous transition with intense fluid activity, with mineralization.

Contents

Chapter 1

1.1 – Introduction.....	1
1.2 - Thesis Outline.....	4

Chapter 2

A synthesis of the geological aspects of the South American Platform, Amazon Craton and Carajás Province

2.1 - The South American Platform.....	7
2.2 - Regional Geotectonic Events.....	10
2.3- Regional Structural Provinces.....	12
2.4- The Amazonian Craton.....	17
2.5- The Carajás Region - A Summary of The Previous Work.....	21
2.5.1- Lithostratigraphy.....	23
2.5.1.1 - Rio Maria Granite-Greenstone Terrane.....	26
2.5.1.1.1- TTG Suite.....	27
2.5.1.1.2- The Andorinhas Supergroup - Greenstone-Belts...29	
2.5.1.1.3 - Other rock units.....	31
2.5.1.2- The Carajás Terrane.....	31
2.5.1.2.1- High Grade Granite-Gneiss Terrain.....	34
2.5.1.2.2- The Low Grade Supracrustal Volcanic and Sedimentary Sequences.....	39
2.5.1.2.3- Mafic-Ultramafic Intrusions.....	44
2.5.1.2.4- Anorogenic Granites.....	45
2.6- Previous Tectonic Models.....	47
2.7- Metamorphism.....	54

2.8- Geochronology.....	55
-------------------------	----

Chapter 3

Investigating ore-lineament relationships using multi-scale lineament analysis and magnetometry in the Carajás Region, Amazon Craton-Brazil

3.1 Introduction.....	63
3.2 Regional Geological Setting.....	65
3.3 Dataset and Methods.....	68
3.3.1 Imagery acquisition and processing.....	69
3.3.2 Lineament Extraction.....	70
3.3.3 Lineament treatment/correction.....	71
3.3.4 Lineament Analysis.....	72
3.3.5 Geophysics – Magnetic Lineaments.....	73
3.4 Results – Lineament Characterization.....	73
3.4.1 Length Analysis.....	74
3.4.2 Orientation Analysis.....	75
3.4.3 Lineament Length vs. Azimuth.....	77
3.4.4 Lineament Density.....	77
3.4.5 Lineament Intersections.....	78
3.4.6 Spatial Analysis of Orientations.....	78
3.4.7 Lineaments and Geology.....	79
3.4.8 Magnetic Lineaments.....	80
3.4.9 Lineaments and Mineral Deposits – Spatial Relationships.....	81
3.5 Discussion.....	82
3.5.1 General Aspects.....	82
3.5.2 Lineaments length distribution.....	83
3.5.3 Lineaments density and intersections.....	84

3.5.4 Lineaments and geology.....	85
3.6 Implications for Mineral Exploration.....	86
3.7 Conclusions.....	86

Chapter 4

The geological and structural aspects of the “Canaã dos Carajás” region, limit between the Carajás and Rio Maria Granite Greenstone terranes

4.1 Introduction.....	115
4.2 Datasets and Methods.....	117
4.2.1 Regional scale methods.....	117
4.2.2 Field logistics and Outcrop scale methods.....	118
4.2.3 Microscopic scale methods.....	120
4.3 Geological Setting.....	120
4.3.1 Regional geology.....	121
4.3.1.1 Carajás Terrane.....	121
4.3.1.2 Rio Maria terrane.....	123
4.3.2 Local geology.....	125
4.3.2.1 The Xingu Complex.....	125
4.3.2.2 The Plaque suite.....	126
4.3.2.3 Palaeoproterozoic (anorogenic) granites.....	127
4.3.2.4 Dykes.....	127
4.3.2.5 East of Canaã dos Carajás Village.....	128
4.3.2.6 Serra Dourada area.....	129
4.3.3 Geochronology.....	131
4.4 Results.....	133
4.4.1 Regional scale interpretation.....	133
4.4.1.1 Aeromagnetic characteristics.....	134

4.4.1.2 Aeromagnetic Patterns.....	134
4.4.1.3 Gamma Spectrometric datasets.....	136
4.4.1.4 Gamma Spectrometric Patterns.....	136
4.4.1.5 Summary.....	138
4.4.2 Outcrop Data.....	139
4.4.2.1 General lithologies.....	139
5.4.2.1.1 Old Basic rocks.....	139
4.4.2.1.2 TTG Gneisses.....	141
4.4.2.1.3 Mylonites.....	142
4.4.2.1.4 Granitoids.....	142
4.4.2.1.5 Dykes.....	144
4.4.2.1.6 Contact relationships.....	144
4.4.2.2 Structural Geometries and Kinematics.....	146
4.4.2.2.1 Foliation.....	146
4.4.2.2.2 Lineation.....	149
4.4.2.2.3 Folds.....	150
4.4.2.2.4 Mylonitic Zones.....	152
4.4.2.2.5 Brittle Structures.....	154
4.4.2.2.6 Summary of the field observations.....	157
4.4.3 Microstructural observations.....	158
4.4.3.1 Isotropic Granitoids.....	158
4.4.3.2 Basalt & Gabbro Dykes.....	159
4.4.3.3 Amphibolites.....	160
4.4.3.4 Deformed Granitoids.....	163
4.4.3.5 Mylonites.....	166
4.4.3.6 Granitic gneisses.....	169
4.5 Tectonic History and Structural Model.....	173

4.6 Comparison with Other Archaean Cratons.....	177
4.7 Regional Issues.....	177
4.8 Conclusions.....	179

CHAPTER 5

The role of tectonic structures in the development of Archaean IOCG deposits: examples from the Sossego and Sequeirinho deposits, Carajás, Brazil

5.1 Introduction.....	228
5.2 Tectonic Setting.....	230
5.3 Regional Geology of the Carajás Terrane.....	230
5.3.1 Lithostratigraphy.....	230
5.3.2 Structure.....	233
5.3.3 Metamorphism.....	233
5.4 The Sossego Deposit.....	234
5.4.1 History.....	235
5.4.2 Geology.....	235
5.4.3 Hydrothermal Alteration.....	238
5.4.4 Fluids Sources and Temperature.....	238
5.4.5 Geochronology.....	239
5.5 Field Logistics and Methods.....	240
5.6 Lineament Analysis.....	242
5.6.1 Regional Structural Framework – summary and implications of lineament analysis.....	244
5.7 Structures and Mineralization Controls.....	246
5.7.1 Sossego orebody.....	246
5.7.1.1 Foliation.....	247
5.7.1.2 Ductile Shear Zones.....	248
5.7.1.3 Faults.....	250

5.7.1.4 Veins.....	252
5.7.2 Interpretations of the structures at Sossego.....	254
5.7.3 Sequeirinho Orebody.....	256
5.7.3.1 Foliation.....	257
5.7.3.2 Shear Zones.....	260
5.7.3.3 Faults.....	262
5.7.3.4 Veins.....	264
5.7.4 Interpretations of the structures at Sequeirinho.....	265
5.7.5 Rio Branco Granite.....	268
5.7.6 Interpretation of the faults in the Rio Branco Granite.....	269
5.8 Breccia Classification and Characterization.....	270
5.8.1 Textural characterization.....	272
5.8.2 Textural analysis.....	273
5.8.3 Interpretation of the clasts size analysis.....	274
5.9 Microstructures.....	276
5.9.1 Sequeirinho.....	276
5.9.2 Sossego.....	285
5.9.3 Interpretation of the microstructural observations.....	288
5.9.3.1 Ductile Features.....	288
5.9.3.2 Kinematic Indicators & Porphyroclasts.....	289
5.9.3.3 Brittle Features.....	290
5.9.3.4 Veins and temperature.....	291
5.9.3.5 Faults & Fault Zones.....	292
5.10 Tectonic Interpretation.....	293
5.11 Fragmentation Mechanisms.....	296
5.12 Implications for Exploration.....	297
5.13 Conclusions.....	298

Chapter 6

Conclusions summary and suggestions for future work

6.1 – Regional Lineaments.....	375
6.2 – The Canaã dos Carajás Region.....	376
6.3 – The IOCG Sossego and Sequeirinho Deposits.....	379
6.4 - Timing of the Major Crust Forming Events and Global Implications.....	382
6.5 - Regional Issues.....	384
6.5 Future Work.....	385

Appendix	388
-----------------	-----

References	459
-------------------	-----

List of Figures

Chapter 2

Figure 2.1.....	9
Figure 2.2.....	12
Figure 2.3.....	14
Figure 2.4.....	15
Figure 2.5.....	16
Figure 2.6.....	19
Figure 2.7.....	21
Figure 2.8.....	25
Figure 2.9.....	26
Figure 2.10.....	33
Figure 2.11.....	35
Figure- 2.12.....	49
Figure 2.13.....	53
Figure 2.14.....	62

Chapter 3

Figure 3.1.....	88
Figure 3.2.....	89
Figure 3.3.....	90
Figure 3.4.....	93
Figure 3.5.....	94
Figure 3.6.....	95
Figure 3.7.....	96
Figure 3.8.....	97
Figure 3.9.....	98
Figure 3.10.....	99
Figure 3.11.....	100
Figure 3.12.....	101
Figure 3.13.....	102
Figure 3.14.....	103

Figure 3.15.....	104
Figure 3.16.....	105
Figure 3.17.....	106
Figure 3.18.....	107
Figure 3.19.....	108
Figure 3.20.....	109
Figure 3.21.....	111
Figure 3.22.....	112
Figure 3.23.....	113
Figure 3.24.....	114

Chapter 4

Figure 4.1.....	181
Figure 4.2.....	182
Figure 4.3.....	183
Figure 4.3 (cont).....	183
Figure 4.4.....	186
Figure 4.5.....	187
Figure 4.6.....	188
Figure 4.7.....	189
Figure 4.8.....	190
Figure 4.9.....	191
Figure 4.10.....	192
Figure 4.11.....	193
Figure 4.11 (cont)	194
Figure 4.12.....	195
Figure 4.13.....	196
Figure 4.14.....	197
Figure 4.15.....	198
Figure 4.16.....	199
Figure 4.17.....	200
Figure 4.18.....	201
Figure 4.19.....	202
Figure 4.19 (cont)	203
Figure 4.20.....	204

Figure 4.21.....	205
Figure 4.22.....	206
Figure 4.23.....	207
Figure 4.24.....	208
Figure 4.25.....	209
Figure 4.26.....	210
Figure 4.27.....	211
Figure 4.28.....	212
Figure 4.29.....	213
Figure 4.30.....	214
Figure 4.31.....	215
Figure 4.32.....	216
Figure 4.33.....	217
Figure 4.34.....	218
Figure 4.35.....	219
Figure 4.36.....	220
Figure 4.37.....	222
Figure 4.38.....	224
Figure 4.39.....	226
Figure 4.40.....	227

Chapter 5

Figure 5.1.....	302
Figure 5.2.....	303
Figure 5.3.....	306
Figure 5.4.....	307
Figure 5.5.....	308
Figure 5.6.....	309
Figure 5.7.....	311
Figure 5.8.....	312
Figure 5.9.....	313
Figure 5.10.....	314
Figure 5.11.....	315
Figure 5.11 cont.....	316
Figure 5.12.....	317

Figure 5.13.....	318
Figure 5.14.....	319
Figure 5.15.....	320
Figure 5.16.....	321
Figure 5.17.....	322
Figure 5.18.....	323
Figure 5.19.....	324
Figure 5.20.....	325
Figure 5.21.....	326
Figure 5.22.....	327
Figure 5.23.....	328
Figure 5.23 cont.....	329
Figure 5.24.....	330
Figure 5.25.....	331
Figure 5.26.....	332
Figure 5.27.....	333
Figure 5.28.....	334
Figure 5.29.....	335
Figure 5.30.....	336
Figure 5.31.....	337
Figure 5.32.....	338
Figure 5.33.....	339
Figure 5.34.....	340
Figure 5.35.....	341
Figure 5.36.....	342
Figure 5.37.....	343
Figure 5.38.....	344
Figure 5.39.....	345
Figure 5.40.....	346
Figure 5.41.....	347
Figure 5.42.....	348
Figure 5.43.....	349
Figure 5.44.....	350
Figure 5.45.....	351
Figure 5.46.....	352

Figure 5.47.....	353
Figure 5.48.....	355
Figure 5.49.....	356
Figure 5.50.....	357
Figure 5.51.....	358
Figure 5.52.....	359
Figure 5.53.....	360
Figure 5.54.....	361
Figure 5.55.....	362
Figure 5.56.....	363
Figure 5.57.....	364
Figure 5.58.....	365
Figure 5.59.....	366
Figure 5.60.....	368
Figure 5.61.....	369
Figure 5.62.....	370
Figure 5.63.....	371
Figure 5.64.....	372
Figure 5.65.....	374

Chapter 6

Figure. 6.1.....	375
------------------	-----

List of Tables

Chapter 2

Table 2.1.....	8
Table 2.2.....	11
Table 2.3.....	58
Table 2.4.....	61

Chapter 3

Table 3.1.....	91
Table 3.2.....	92

Chapter 4

Table 4.1.....	185
----------------	-----

Chapter 5

Table 5.1.....	304
Table 5.2.....	305
Table 5.3.....	310
Table 5.4.....	354
Table 5.5.....	367
Table 5.6.....	373

Chapter 6

Table 6.....	365
--------------	-----

Chapter 1

1.1 - Introduction

Iron-Oxide-Copper-Gold (IOCG) mineral deposits comprise an unusual group of economic geological features because of their unusually wide variations in age, size, mineralogy, geochemical signatures, host rock lithologies and tectonic setting (Hitzman et al. 1992; Haynes 2000). The size and grade of the larger examples, together with their geological diversity has drawn considerable attention from exploration companies and academic researchers in the last decade (Pollard 2006).

IOCG deposits are recognized in all continents, ranging in age of formation from the Late Archaean to the Early Tertiary; a majority have an age between 2.55 and 1.5 Ga. Tectonically, they are considered to have formed in intracratonic or continental margin environments and, in many cases, show spatial and temporal controls associated with extensional tectonics (Hitzman et al. 1992). The sources of the hydrothermal mineralizing fluids are controversial, and are thought to result from either magmatic (Pollard 2001; Sillitoe 2003; Mark et al. 2005) or non-magmatic (Barton 2000; Haynes 2000) processes. In the former case, this deduction is based upon the temporal and spatial association between magmatic intrusions, the fluids that formed the Cu-Au mineralization and regional alteration patterns (Barton 1996; Oliver et al. 2004).

The Carajás Terrane hosts Precambrian Cu-Au deposits with resources larger than 100 million tonnes of ore. Examples include the Igarapé Bahia-Alemão, Cristalino, Sossego, 118 (or 118 Target) and the world class Salobo deposits. Research on these deposits has generally focussed on petrological, metallogenetic, geochemical and geochronological aspects, with structural characteristics and possible controls being very poorly documented in most cases. This thesis examines at a local scale, structural aspects of the Sossego and Sequeirinho deposits to: (i) improve the understanding of the processes, controls and styles of the Archaean IOCG examples; and (ii) reduce the degree of uncertainty when comparing the settings of these deposits to those formed by modern plate tectonic processes during the Phanerozoic.

Additionally, this research investigates at a broader scale, the tectonic framework of the granitic-gneissic basement, in the region close to the boundary between the Carajás and Rio Maria Granite Greenstone Terranes, known as the Canaã dos Carajás region, hosting the Sossego-Sequeirinho deposits. A knowledge of the tectonic framework and structural evolution here is crucial in order to better understand what sort of Archaean processes shaped the region as a whole, including the adjacent terranes located to the north and south.

Finally, this study investigates geophysical and topographic lineaments in the Carajás Terrane, an area where several high economic value Cu-Au deposits have already been identified, and where prospecting campaigns are still in development. Some of the deposits are structurally controlled and display a close association with large scale faults or shear zones. Multi-scale observation and interpretation of lineaments can show how these may be related to underlying, geological controls and the development of ore deposits. They also have the potential to help develop

better ways to more accurately predict and locate other IOCG deposits elsewhere in the world.

Motivated by the need to advance the understanding of the enigmatic IOCG deposit class and its Archaean structural setting, the purpose of this study is to examine two regionally-representative IOCG orebodies and their surrounding region in the Carajás Terrane, Amazon Craton. Primary data comprises traditional methods of field mapping and structural analysis, microscopic investigation, combined with modern digital mapping, lineament and particle size analysis. The principal aims of the study include:

- The identification of crustal scale regional lineaments and investigation of their relationship to the mineral deposits and known occurrences in the Carajás Terrane.
- To develop a new tectonic framework and structural evolution for the Canaã dos Carajás region, and shed new light on the nature of the enigmatic boundary between the Carajás and Rio Maria Granite Greenstone Terranes.
- To describe and interpret the structural framework of the Sossego and Sequeirinho mines by investigating the character and structural controls on their mineralization.
- To provide new data to be used as geological-structural criteria in the future prospection of mineral deposits in the Amazon Craton and equivalent geological regions worldwide.

1.2 - Thesis outline

This section presents the structure of the thesis and a summary of each chapter's content. Each of the core chapters (3-4-5) deals with a specific issue and they are presented from regional (chapter 3) to local (chapter 5) scales. Chapters 3-5 were written as individual manuscripts, which can potentially be submitted to a scientific journal in the future. Consequently, each chapter includes a separate introduction and methods section, and distinct sections describing geological setting, geochronology, discussion of data and conclusions. Unavoidably, there is some overlap in the content of chapters 3-5, especially in the geological setting topics. Lastly, the appendix section contains: (1) a published paper to which I contributed with during the first year of my research when learning about and testing digital mapping methods; and (2) the vertical structural sections constructed in the Sossego and Sequeirinho mines described in chapter 5.

Chapter 2

This chapter describes the regional geological setting of the study region. Key geological aspects of the Carajás and Rio Maria Granite Greenstone Terranes are summarized, including: stratigraphic, lithological, geochronological, tectonic and metamorphic information. This summary is particularly important in order to demonstrate the variety and the evolution of the geological knowledge in the region.

Chapter 3

This chapter presents a regional, 2D multi-scale lineament analysis carried out using topographic (LANDSAT and digital elevation model) and airborne

magnetic surveys. The geometric (i.e. length, orientation and intersection) and spatial (i.e. density, and spacing) attributes of lineaments were quantified and compared within the Basement and Cover Assemblage domains. Finally, the spatial relationship between lineaments and mineral occurrences in the region was investigated to test the hypothesis that lineaments can act as potential sites for the preferential development of ore deposits.

Chapter 4

This chapter describes structural aspects of the Canaã dos Carajás region, the transitional domain between the Carajás and the Rio Maria Granite-Greenstone terranes. The proposed structural framework and tectonic history for the region are constructed using combined studies of: (a) detailed aeromagnetic and gamma-radiometric surveys; (b) field observations and measurements of planar and linear structural fabrics from rock outcrops; and (3) microstructural observations. Importantly, the microstructural results have implications for evaluating the exhumation history of the area. The integrated dataset is used to underpin a structural model that explains the dominant character and evolution of the tectonics in the region. Additionally, the observations and conclusions presented in this chapter are used as a framework for the more local mine studies presented in chapter 5.

Chapter 5

This chapter focuses on two specific copper and gold orebodies currently exposed in two open cast mines. The structural framework and controls of the mineralization in the Sossego and Sequeirinho deposits are investigated by: (1) interpretation of aeromagnetic survey; (2) field observations and structural mapping

of exposed mine benches; and (3) structural logging of drill-cores from mineralized and barren zones. Complementary studies of particle size and shape analysis were carried out to characterize the brecciation processes and their intensity in both orebodies. Finally, the dominant deformation mechanisms and their respective temperature and pressure conditions were characterized using microstructural analysis of samples from mine benches and drill-cores.

Chapter 6

Presents a summary of the key findings and general conclusions of the study with suggestions for future research.

Chapter 2

A synthesis of the geological aspects of the South American Platform, Amazon Craton and Carajás Province

2.1 - The South American Platform

The South American Platform can be conveniently subdivided into two main types of Precambrian geotectonic units (Table 2.1): (1) cratonic blocks, comprising high-grade Archaean granitic-gneissic complexes (shields & cratons); and (2) a surrounding and anastomosing array of lower-grade collisional suture zones which typically act as persistent zones of reactivation and apparent tectonic weakness (mobile or fold belts) all through the regional geologic evolution (Almeida et al. 1981; Almeida et al. 1984). During the Precambrian, the mobility along these sutures through successive rifting and orogenic processes resulted in the development of high-grade (up to granulite facies) shear zone belts, and highly folded and metamorphosed volcanoclastic sequences that correspond to reworked rift basins (Saadi et al. 2002).

Shields	Cratons	Massifs	Mobile Belts	Sedimentary Covers
Guyana	Amazonian	Goiás Central	Uruaçu & Espinhaço	Amazonas
Central Brazilian	São Luiz	Pernambuco Alagoas	Paraguai Araguaia	Parnaíba
Atlantic	São Francisco	Guaxupé	Brasília	Paraná
	Rio de La Plata		Araçui	Costal and Continental Margin

Table 2.1- Main geological units within the South American Platform. Maps in Fig. 2.1 show the location of the shields, cratons and sedimentary covers.

The South American Platform basement is typically composed of igneous and metamorphic rocks, which are subdivided into three large shields separated by Phanerozoic basins (**Fig. 2.1 A**): (1) the *Guyanas Shield* in the north; (2) the *Central Brazilian Shield* south of the Amazon River; and (3) the *Atlantic Shield* along the coastline region of the modern Atlantic Ocean (Almeida et al. 1981; Almeida et al. 2000).

Archaean lithologies are mainly preserved in cratons that were assembled during the Neoproterozoic. These include: (1) the Amazonian Craton; (2) the São Francisco Craton; (3) the São Luiz Craton; (4) the Rio de La Plata Craton (Almeida et al. 2000) (**Fig. 2.1 B**). There are also a number of more minor massifs (not labelled in Fig. 2.1), including: (1) the *Goiás Central Massif*; (2) the *Pernambuco-Alagoas Massif*; (3) the *Guaxupe Massif* (Almeida et al. 1981; Almeida et al. 2000).

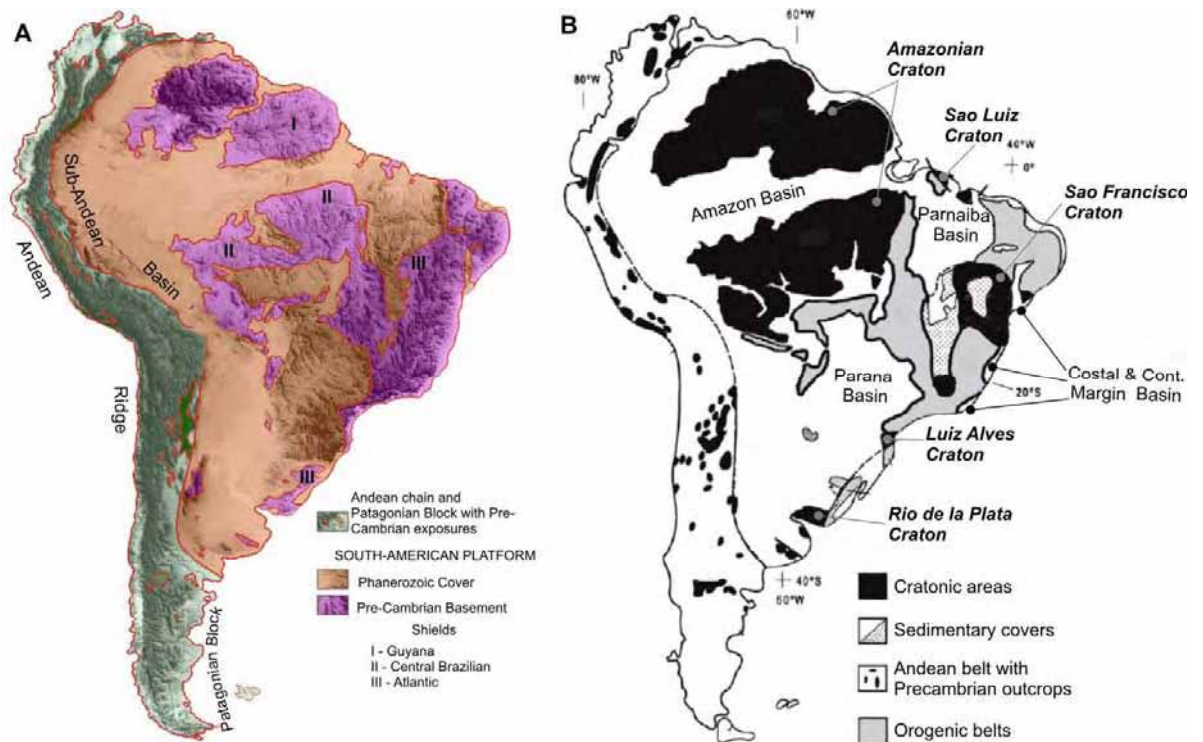


Figure 2.1 – A – The continental area of the South-American plate showing the Andean Ridge, the Phanerozoic cover and the Pre-Cambrian basement (modified from Almeida et al., 1976); B – Crustal provinces of the South American Platform including: (1) Cratons; (2) Major Sedimentary basins; (3) the Andean Belt; and (4) unlabeled orogenic belts (modified from Cordani & Sato, 1999 and Cordani et al., 2000).

The most important mobile belts, surrounding the cratons are: (1) the *Paraguai-Araguaia*; (2) the *Brasilia*, (3) the *Araçui* and (4) the *Uruaçú-Espinhaço* (Cordani et al. 2000).

From the Early Silurian onwards, these basement units were covered to varying extents by large sedimentary basins (see **Fig. 2.1 B**), such as the *Amazonas*, the *Parnaiba* and the *Paraná* basins. The *Coastal & Continental Margin* sedimentary sequences accumulated in coastal graben and half graben of Cretaceous to Cenozoic age (Almeida et al. 1981). These intracratonic basins were established in the Palaeozoic and are bordered by marginal faulted regions that ultimately led to the

development of seaways between the basins (Petri et al. 1983) and the opening of the Modern Atlantic Ocean.

2.2 - Regional Geotectonic Events

The numerous geochronological ages obtained for the geological units that make up the South American Platform (excluding the Andean region) allow the definition of several geotectonic events on a continental scale (Table 2). In Brazil, the following orogenic cycles are generally recognised (Wernick 1981): Guriense (> 3.0 Ga); Jequié (2.7 ± 0.1 Ga); Transamazonico (2.0 ± 0.2 Ga) and Brasiliano (1.0–0.52 Ga).

Chapter 2

	Age Ga.		
Neo-Proterozoic	Cambrian	0.54-0.50	Brasiliano Collage* Orogenic events of the Brasiliano collage. These are diachronous from one structural province to another. The last interval 0.54–0.50 Ga. is characterized by escape tectonics and dyking magmatism.
		0.58-0.54	
		0.65-0.60	
		0.80-0.75	
Meso-Proterozoic		0.90-0.85	
		0.97	Cariris Velhos Orogeny Suansas-Aguapei Belts Sunsas–Aguapei belt, southwestern part of the Amazonian region (Brazil–Bolivia), with low-grade volcano-sedimentary assemblages. - Cariris Velhos orogenic event (Wilsonian Cycle) along the central part of the Borborema Province.
		1.10	
		1.30	Espinhaco/ Uruacuano evens* Rondonian/ San Ignacio Belts* Orogenic events in the southwestern part of the Amazonian region: - Guapore/Rondonian/San Ignacio (1.45–1.30 Ga) - Putative orogenic events in the southwestern part of the Central Goias Massif (“Uruacuano Belt”, high-grade rocks) and along the Espinhaco range (Central Bahia and Minas Gerais, low-grade assemblages)
	1.40		
Paleo-Proterozoic		1.80-1.60	Statherian Taphrog. Rio Negro - Jurena Orogenes Widespread events of extensional tectonics (Statherian Taphrogenesis) - The Rio Negro–Juruena Orogenesis (arc plutonism) in the central-western Amazonian region
		1.8-1.55	
		2.0-1.90	Trans-Amazonian Orogenes* Trans-Amazonian Orogeneses: main deformational events of the Paleoproterozoic mobile belts. Granitic plutonism
		2.15	
		2.35	
Archean		2.50	Local occurrences of metamorphic events and granite plutonism
		2.8-2.7	Rio das Velhas Event* (Jequie Cycle) High diversity of rock assemblages: orthogneisses (Trondhjemitites, tonalites, granodiorites, monzogranite and granites, TTG suites), gneissic granulites (of both igneous and sedimentary origins), mafic–ultramafic complexes, noritic dikes; volcano-sedimentary rocks (Grao-Para Group), greenstone belt associations, etc
		3.1	Guriense Cycle* Widespread occurrences of high-grade terranes, mainly orthogneisses, and the oldest known occurrences of granite-greenstone (LTG) assemblages
		3.2	
		3.5-3.4	Sparse high-grade complexes

Table 2.2 – The main tectonic events recorded in the basement of the South America Platform (Modified from Almeida et al., 2000).

* indicates the important events recorded in Brazil.

2.3- Regional Structural Provinces

The structural provinces of Brazil and their significance have been debated for many years, with many different models proposed based on either geochronological or tectonic evidence.

Traditionally, ten Brazilian Structural Provinces (**Fig. 2.2**), each with an individual geological history, were defined based on the nature of the crystalline basement rocks and the sedimentary cover (Almeida et al. 1981; Wernick 1981).

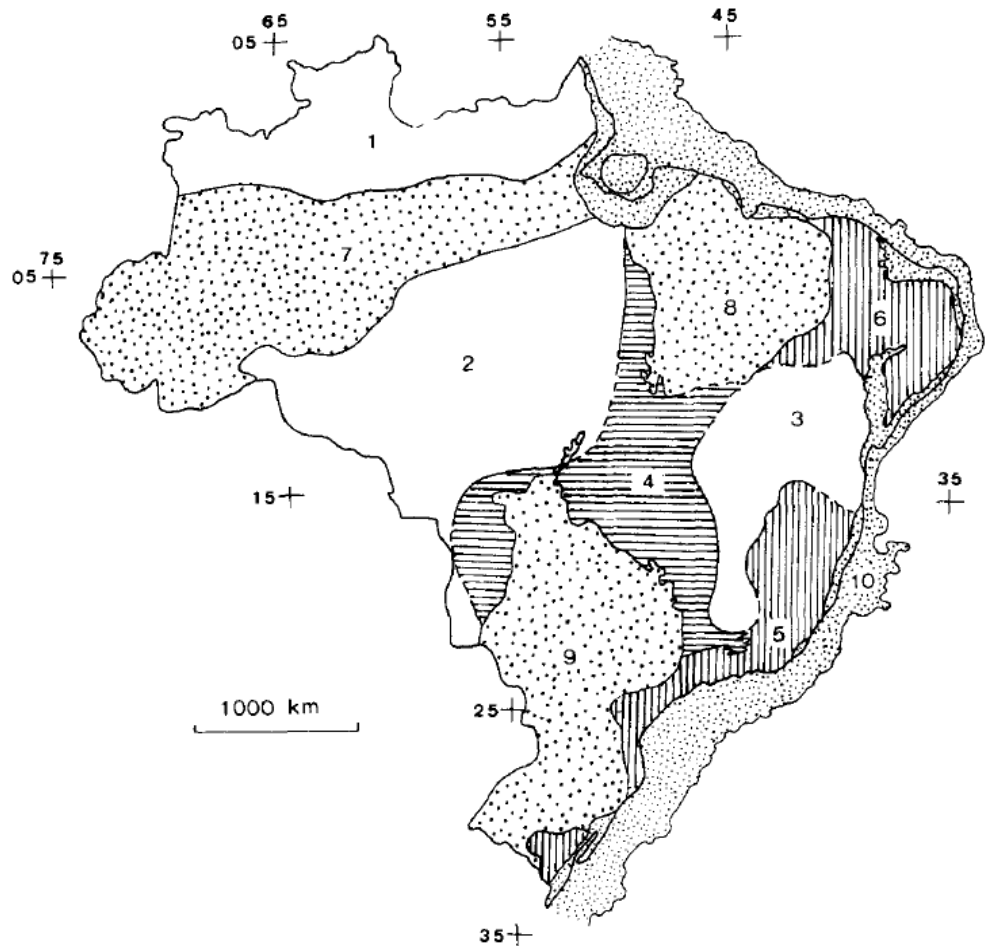


Figure 2.2 – The structural Provinces of Brazil. Legend: 1- Rio Branco; 2- Tapajós; 3- São Francisco; 4- Tocantins; 5- Mantiqueira; 6- Borborema; 7- Amazonian; 8- Parnaíba; 9- Paraná; 10- Costal and Continental. (Almeida et al., 1981).

(Cordani 1979; Cordani et al. 1982) and (Cordani et al. 1988) proposed a new model for the Brazilian structural domains, using Sm-Nd and Rb-Sr data from more than 10,000 isotopic ages obtained from samples collected all over Brazil. They suggested that 45% of the present continental crust in the shields had formed by the end of the Archaean and that about 80% had formed by the end of the Palaeoproterozoic. They divided the Brazilian shield into 14 structural domains (**Fig. 2.3**).



Figure 2.3 – Structural domains of the Brazilians shield. 1: Sao Francisco Craton (E-Eastern, C-Central, W-Western), 2: Amazonian Craton (CA- Central Amazonian, MI- Maroni Itacaiúnas, RNJ- Rio Negro Jurena, RO/S –Rondonian/Sunsas), 3: Rio de la Plata and Luiz Alvez cratonic fragments, 4: Sao Luiz Craton, 5- Rio Apa cratonic fragment, 6- Central Goias Complex, 7: Borborema Province (E-East, W-West, C-Central, Including NE Goias State), 8: Curitiba crustal fragment, including Sao Roque Belt, 9: Araxa, Alto Rio Grande belts, including Amparo complex, 10: Paraguay-Araguaia/Tocantins belts, 11: Dom Feliciano Belt, 12: Brasilia Belt, 13: Jequitinhonha Belt (Cordani et al., 1988).

However (Hasui et al. 1984) called attention to the limitations of the Cordani's model because the geochronological data used was substantially based on previously published K-Ar and Rb-Sr isotopic ages, some of them obtained from poorly defined isochrons of uncertain significance. Further, (Macambira et al. 1994)

also brought into question the reliability of these ages, and suggested that more robust radiometric dating techniques should be used (e.g. U-Pb, Pb-Pb and Sm-Nd), which led to the re-evaluation of the Cordani model. Fourteen major crustal blocks (Fig. 2.4) were therefore identified in Brazil based on this new isotopic data combined with gravimetric and magnetic surveys integrated with geological data (Costa et al. 1991; Hasui et al. 1992). The nuclei of the crustal blocks comprise granite-gneiss complexes and greenstone belt sequences bounded by high grade shear zone belts associated with sub-parallel volcano sedimentary sequences (Costa et al. 1992).



Figure 2.4 – Major crustal blocks identified in Brazil by integrated interpretation of geological and geophysical data (Hasui et al., 1992).

The most recent proposal by (Schobbenhaus et al. 2003) combines both geochronological and tectonic approaches. They identified fifteen distinct chrono-tectonic provinces (Fig. 2.5) defined as “regions with discrete stratigraphic, tectonic, magmatic, metamorphic and geomorphic features that are distinctive of those from the confining units”. The limits for the Provinces are either well-defined geological features (faults and shear zones, metamorphic fronts, hinterland terrains, erosion limits of sedimentary areas) or are poorly defined (arbitrary or transitional limits assumed in view of an inadequate knowledge base) (Schobbenhaus et al. 2003).

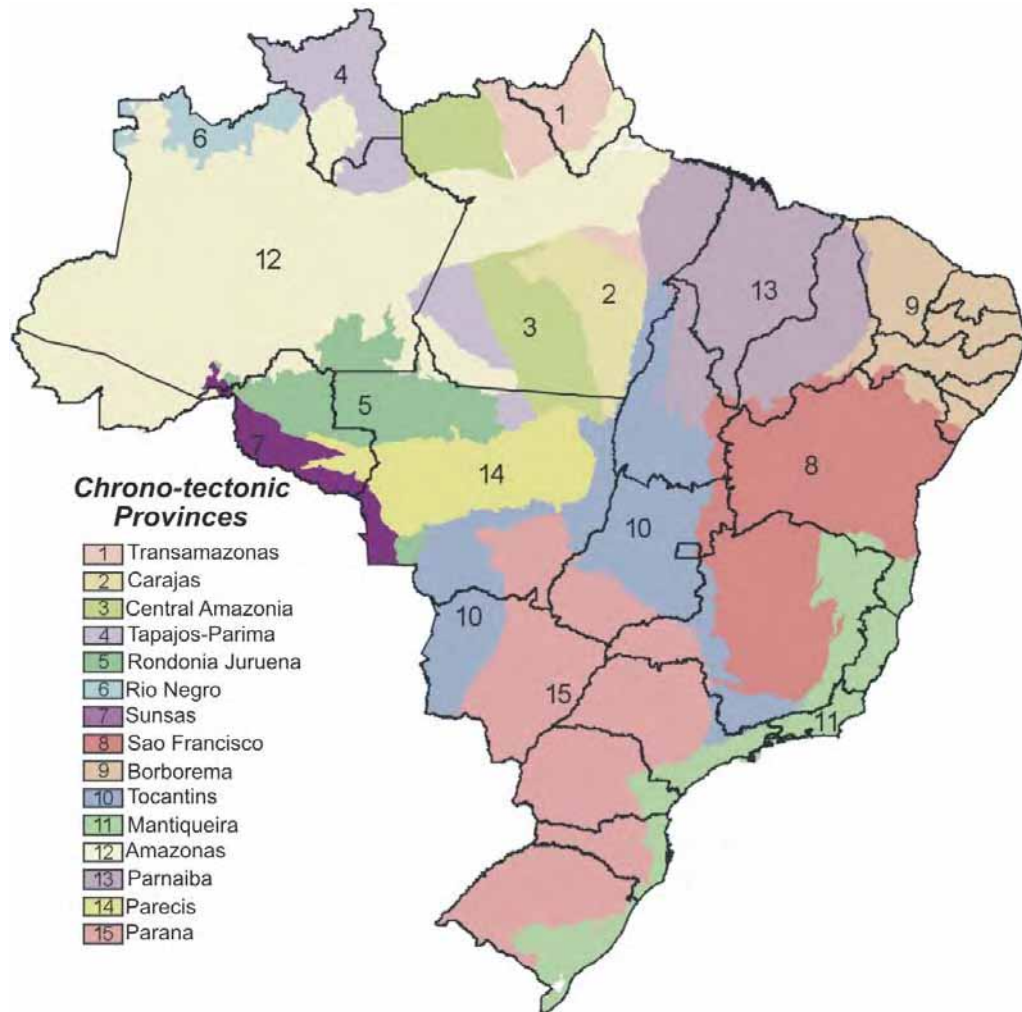


Figure 2.5 – Chrono-tectonic Brazilian provinces from Schobbenhaus & Neves, 2003.

2.4- The Amazonian Craton

The Amazonian Craton (**Figs. 2.1 B and 2.6**) is one of the largest cratonic areas in the world. It occurs in the northern part of South America, covering an area of about $4.3 \times 10^5 \text{ km}^2$ and stabilized towards the end of the Mesoproterozoic (Almeida 1976; Cordani et al. 1988). The craton is geographically divided into two Shields separated by the sedimentary sequences of the Palaeozoic Amazonas basin (see **Fig. 2.1 A and B**): the Guiana Shield to the north and the Central Brazilian Shield to the south (Cordani et al. 2000).

The geological subdivision proposed for the Amazonian Craton follows two main thematic streams: (1) *the geochronological model*; and (2) *the structural-geophysical model*.

The first geochronological model was introduced by (Amaral 1974), who divided the Amazon Craton into three Archaean units based on sparse Rb-Sr data (**Fig. 2.6-1**). The model was improved and adapted by various authors as new additional data based on more robust analytical methods (Sm-Nd, U-Pb, Pb-Pb), became available. (Cordani 1979) improved Amaral (1974)'s model, by adopting a 'mobilistic' approach and introducing the Rondinian Province (**Fig. 2.6-2**). The craton was redefined as an Archaean/Palaeoproterozoic old nuclei (Central Amazonian Province) surrounded by mobile belts formed during the Proterozoic. (Teixeira et al. 1989) proposed a new geochronological model for the region (**Fig. 2.6-3**), modifying boundaries and adding the Sunsas province. Again, the geographical boundaries were adjusted by (Tassinari et al. 1996), who additionally reclassified the age intervals for the provinces and introduced the Rio Negro-Juruena Province (**Fig. 2.6-4**). The most recent geochronological model for the region was proposed by (Santos et al. 2000), using new U-Pb and Sm-Nd ages combined with

systematic mapping projects across the region. This model suggests a sevenfold division into provinces for the craton (**Fig. 2.6-5**) with the introduction of the Carajás Province.

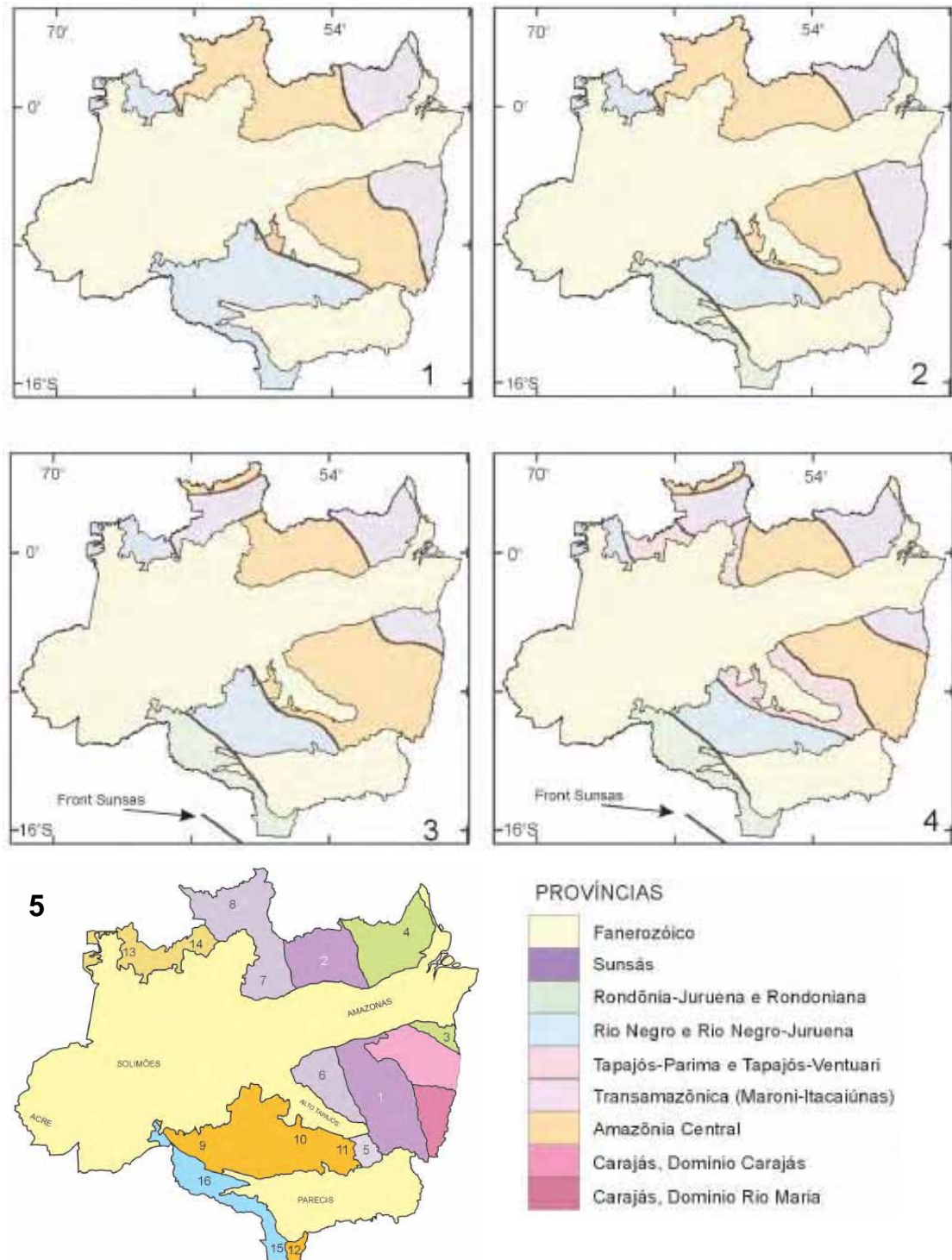


Figure 2.6– The evolution of the models proposing the geotectonic-geochronological provinces for the Amazon Craton. Models: 1- Amaral (1974); 2- Cordani et al., (1979); 3- Teixeira et al., (1989); 4- Tassinari et al., (1996) ; 5- Santos et al., 2000. –note the repeated changes to province borders.

The fact that the geochronological models were heavily reliant on Rb-Sr data (even those with some Sm-Nd and U-Pb data) and the well known limitations of this isotopic method when used to study high grade polydeformed terrains, encouraged some authors (Hasui et al. 1984; Santos et al. 1984; Schobbenhaus et al. 1984; Costa et al. 1997) to limit the conclusions that could be based upon such isotopic information when proposing alternative models (Santos 2003).

The structural-geophysical model is based on a combination of gravimetry-magnetometry, geochronological data and structural geology (Hasui et al. 1984; Costa et al. 1997). Under this scheme, the Amazonian craton was divided into twelve Archaean blocks (**Fig. 2.7**) comprising granite-gneiss and/or greenstone terrains (Hasui et al. 1984). The boundaries of these blocks were taken to be nineteen Archaean collisional/shear belts (**Fig. 2.7**) many of which have experienced reactivation during the Phanerozoic (Costa et al. 1997). The model relies on an analogy with modern day “Himalayan” collisional processes to explain the initial formation and evolution of the craton.

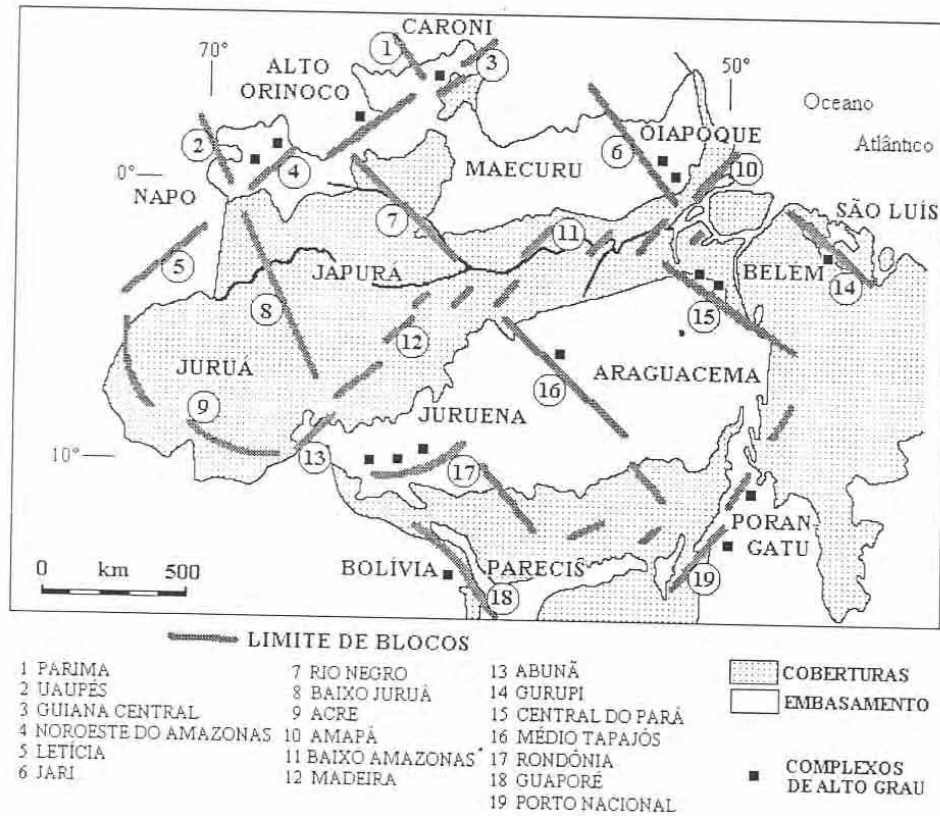


Figure 2.7 – The main crustal blocks and its limits for the Amazon region in Brazil. (Hasui et al., 1984).

2.5- The Carajás Region - A summary of the previous work

The current understanding of the Carajás region has developed over the last three decades, and has advanced significantly since the pioneering work of the Vale do Rio Doce's exploration of the region in 1968, and research by the Brazilian Geological Survey (CPRM) and universities.

Initial research during the 1960's was aimed mainly at new prospective mining interests, describing lithological aspects, ore deposit genesis, stratigraphy, geochronology, and structural geology (Moraes Rego 1933; Barbosa et al. 1966; Almeida 1967; Ramos et al. 1983).

During the 1970's, regional studies were given prominent importance, with a special focus on lithological descriptions and the establishment and correlation of stratigraphic sequences (Knup 1971; Puty et al. 1972; Beisiegel et al. 1973; Silva et al. 1974; McCandles et al. 1975; Issler 1977). The first attempts to model the main ore deposits in the region were proposed by (Resende et al. 1972; Suszczyński 1972; Anderson et al. 1974) and (Beisiegel et al. 1978). Additionally, some authors have tried to establish the main geological events using geochronological data (Amaral 1974; Basei 1974; Amaral et al. 1975; Gomes et al. 1975).

In the 1980's a significant amount of research was carried out to determine petrogenetic and geochronological characteristics, and some descriptive studies of mineral deposits were also carried out (Almeida 1980; DOCEGEO 1981; Lindenmayer 1981; Hirata et al. 1982; Figueiras et al. 1984; Montalvão et al. 1984; Gibbs et al. 1986; Wirth et al. 1986; Huhn et al. 1988). Additional studies related to the regional framework were also presented, particularly those produced by: (Santos 1980; Bernardelli et al. 1982; Cordani et al. 1982; Dall'Agnol 1982; Tassinari et al. 1982).

By the end of the 1980's, DOCEGEO presented the first fully defined litho-stratigraphic column for the Carajás Geochronological Province, based on a substantial volume of compiled geological data available for the region. An updated tectonostratigraphic framework for the Carajás Terrane was presented by (Araújo et al. 1991).

More recent studies into the regional geology were developed by (Lindenmayer 1990; Barros 1991; Costa et al. 1995; Barros 1997; Pinheiro 1997) and have further improved the understanding of the geological framework in the region. There have also been a number of more localised tectonic and structural

studies that have mostly concentrated on specific mines and localities (Siqueira 1990; Marçal 1991; Lab 1992; Pinheiro et al. 1997b; Domingos 2004).

Since the end of the 1990's, most of the published research focused mainly on the geological evolution, petrology, metalogenesis, regional geology and geochronology of the Carajás Geochronological Province. The most notable studies are work by (Pinheiro et al. 1997a; Althoff et al. 2000; Barros et al. 2001; Leite 2001; Villas et al. 2001; Macambira et al. 2003).

In the Rabo Ridge region, work carried out by (Lima 2002; Oliveira 2002) and (Sardinha 2002; Sardinha et al. 2006) have contributed to a finer-scale detailed characterization of the lithology and tectonic structures in the area.

2.5.1- Lithostratigraphy

The Carajás Geochronological Province lies within the southern portion of the Amazon Craton, part of the Central Brazil Shield (**Fig. 2.8**). It is limited to the east by the Neoproterozoic Araguaia Belt and to the west by the Iriri-Xingu Domain. It represents an important metallogenic province with several iron, copper, gold, manganese and tin deposits and contains some of the oldest and best preserved sequences of rocks in the craton.

The Carajás Geochronological Province was formed and stabilized during the Archaean and was later affected by extensive Palaeoproterozoic magmatism characterized by anorogenic granitic intrusions and the intrusion of mafic and felsic dikes e.g., (Macambira et al. 1995). It is typically divided into two major tectonic domains (**Fig. 2.9**): (1) the **Rio Maria Granite–Greenstone Terrane** (3.05 to 2.86 Ga) in the south, and (2) the **Carajás Terrane** also described as **Itacaiúnas Shear**

Belt or (2.76 to 2.55 Ga) in the north (DOCEGEO 1988; Machado et al. 1991; Macambira et al. 1995; Dall'Agnol et al. 1997). The ages indicate the period when the tectonic domains were formed. Both domains exhibit distinctive lithological, tectonic, stratigraphic and geochronological characteristics, but their exact boundary remains undefined. The existence of the Itacaiúnas Belt is disputed by (Barros et al. 2001) who suggest that the north of the Carajás Geochronological Province could be a distinct and separate plutono-metamorphic belt instead of a shear zone belt.

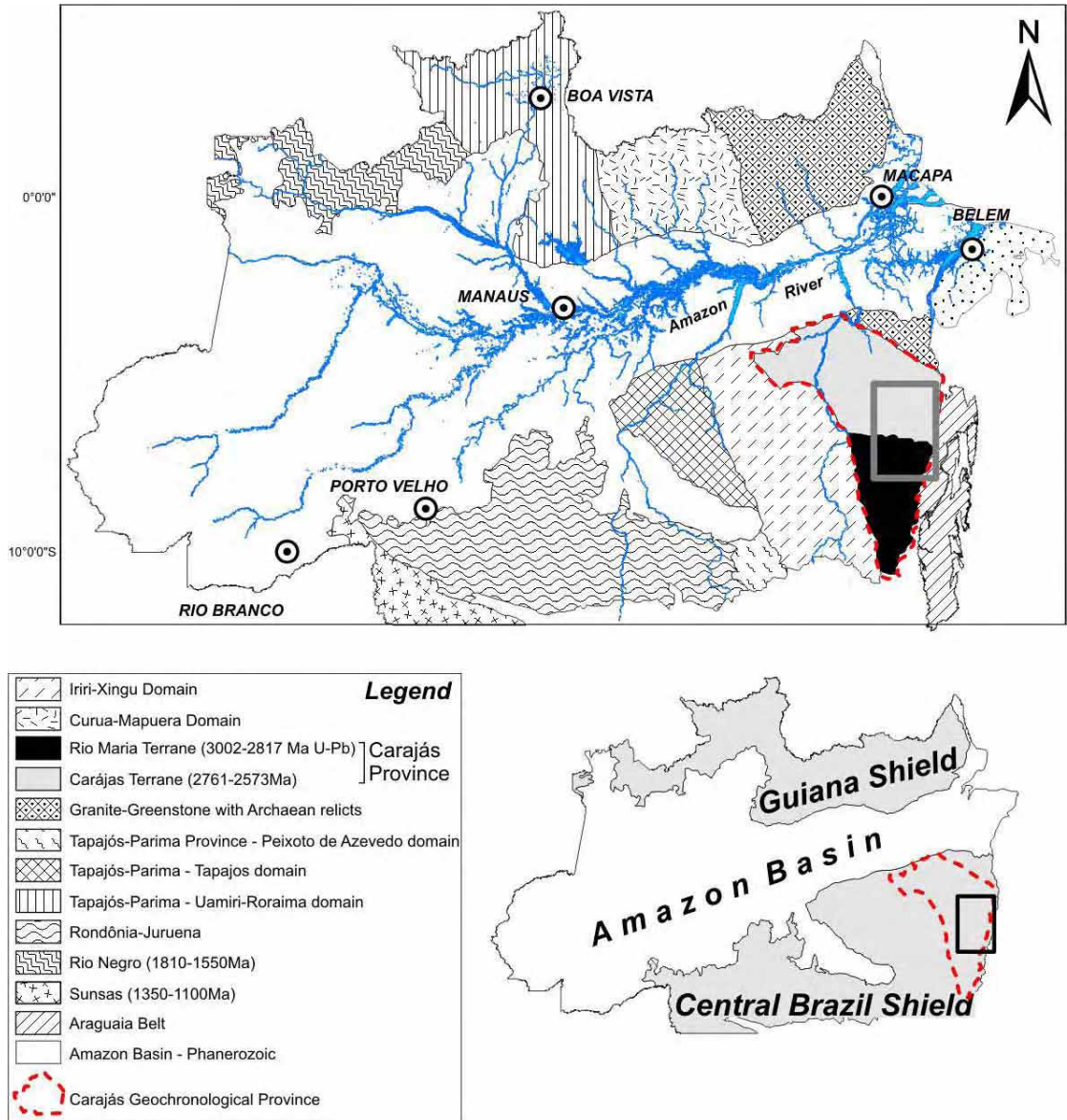


Figure 2.8 – Location of the Carajás Geochronological Province (red dashed line) in the Amazon Craton according to Santos, 2000; the highlighted rectangles indicate the location of the map presented in Figure 2.9. Note the location of the Carajás (grey) and Rio Maria (black) Terranes limited to the east by the Araguaia Belt and to the west by the Irixi-Xingu Domain.

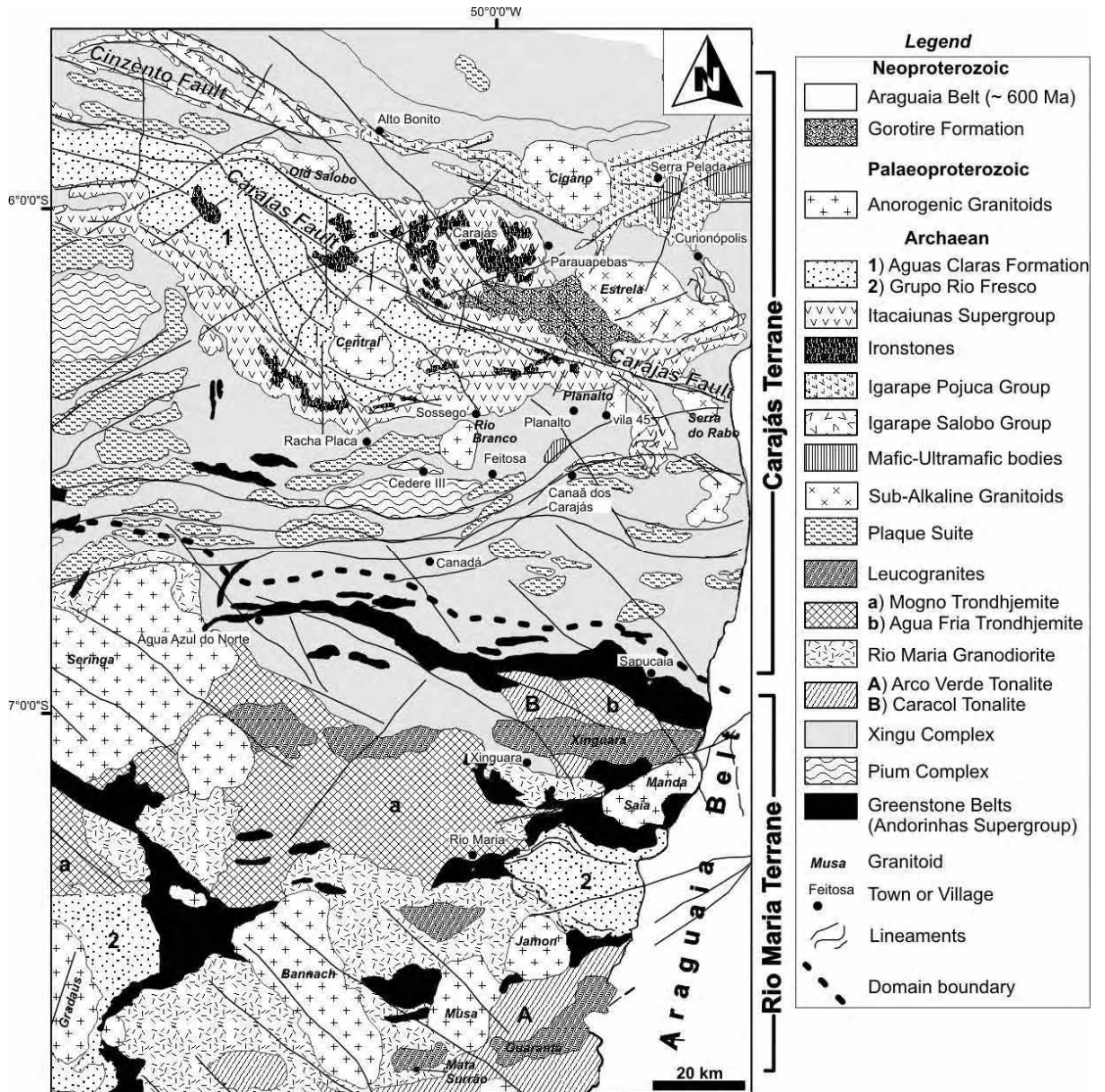


Figure 2.9 – Geological map of the Carajás Geochronological Province and its division into the Carajás Terrane and Rio Maria Granite-Greenstone Terrane (after Villas & Santos, 2001)

2.5.1.1 - Rio Maria Granite-Greenstone Terrane

The term ‘Rio Maria Granite Greenstone Terrane’ is used to describe the group of Archaean rocks located mainly in the south-eastern part of the Amazon

Craton limited to the north by the High Grade Granite-Gneiss Terrain (Xingu Complex). It is characterized by belts of metamorphosed volcano-sedimentary sequences (“greenstone” belts) surrounded by large regions of high-grade infracrustal rocks (granites and gneisses) ranging in age from ca. 2.96 to 2.87 Ga (Huhn et al. 1988). The contacts between the granitoids and the greenstones are typically steeply-dipping shear zones trending E-W, NW-SE, and NE-SW. These structures are thought to represent transpressive duplexes linked by dextral E-W strike-slip segments (Costa et al. 1995).

The Rio Maria Granite-Greenstone Terrane (**Fig. 2.9**) is represented by a series of granitoids (the **TTG Suite**) and by a group of greenstone terrains (the **Andorinhas Supergroup**).

2.5.1.1.1- TTG Suite

The oldest basement units are the **Arco Verde Tonalites** (Althoff et al. 1993) dated at $2,957 \pm 21$ Ma (U-Pb zircon; (Macambira et al. 1991; Macambira et al. 1992)) and the **Caracol Tonalitic Complex** (Leite 2001) dated at $2,948 \pm 5$ Ma. (Pb-Pb zircon; (Leite et al. 2004)). These are intruded by Archaean granitoids including the **Mogno Trondhjemite** (2,871 Ma, U-Pb titanite; (Pimentel et al. 1994)), the **Rio Maria Granodiorite** (2,874 \pm 9/-10 Ma, U-Pb zircon, (Macambira et al. 1991; Macambira et al. 1992); 2,872 \pm 5 Ma, U-Pb zircon, (Pimentel et al. 1994), the **Mata Surrão Granite** (2,872 \pm 10 Ma, Pb-Pb whole rock; (Rodrigues et al. 1992; Lafon et al. 1994a); and 2,871 \pm 7 Ma Pb–Pb zircon; (Althoff et al. 1998), and the **Parazônia Tonalite** (not shown in Fig. 2.9) (2,858 Ma, U/Pb titanite; (Pimentel et al. 1994)). These syn-tectonic granitoids were generated and emplaced during the closure of the

greenstone belt marginal basins during the final stages of evolution of the Rio Maria Granite-Greenstone Terrane (Souza et al. 1997).

The *Arco Verde Tonalite* is the oldest unit in the TTG suite and consists of grey, equigranular, medium-grained (locally fine-grained) tonalites and trondhjemites with igneous isotropic to strongly foliated textures. Widespread compositional banding is defined by layers of distinct modal compositions, likely indicating a mingling of crystal-rich magmas with distinct proportions of biotite and feldspars (Althoff et al. 2000). Quartz-dioritic microgranular enclaves are common and conformable or cross-cutting veins of aplite and pegmatite are widespread.

Solid state deformation of the Arco Verde tonalites is heterogeneous with low strain domains (well-preserved magmatic banding and textures) and orthogneissic domains. These display an E–W trend with mainly subvertical foliations, associated with horizontal lineations, upright folds and subvertical shear zones (Althoff et al. 2000).

The *Caracol Tonalitic Complex* was initially included in the Xingu Complex, but (Leite 2001) identified it as a new unit based on geochronological and structural data. The Complex occurs as three main domains. In the NW, it is characterized by a slightly wavy, sub-vertical N-S banding cross-cut by NE-SW dextral, ductile shear zones. The SW domain is oriented NW-SE, displaying rocks with prominent foliations and a sub-horizontal mineral lineation dipping to NW. Several NW-SE shear zones dipping ca. 20° to SW cross-cut this domain. The southern domain exhibit either NW-SE or WNW-ESE banding (Leite et al. 2004).

The *Mogno Trondhjemite* is a large batholith composed mainly of coarse grained plagioclase, quartz, subordinate biotite, hornblende and accessories.

Granodioritic and metabasaltic xenoliths present in the trondhjemite indicate an intrusive relation with the rocks of the Andorinhas Supergroup (DOCEGEO 1988).

The *Rio Maria Granodiorite* is intruded into the greenstone sequences (Dall'Agnol et al. 1999). It is characterized by granodiorites and tonalites formed by oligoclase, microcline, quartz, biotite, clinozoisite, allanite, zircon, and apatite (Araújo et al. 1991). The granitic body shows an elongate geometry aligned parallel to the structural grain in the adjacent supracrustal sequences (Costa et al. 1995).

The *Mata Surrão Granite* is intruded into the Arco Verde Tonalite, is weakly deformed and consists of medium-grained equigranular grey granite with crosscutting veins of granite, pegmatite, and diorite (Althoff et al. 2000).

The *Parazonia Tonalite* is represented by tonalitic stocks and sills mainly composed of plagioclase, quartz, and chloritized biotite (DOCEGEO 1988). It is a deformed pluton intruded into the Rio Maria Granodiorite and in the Mogno Trondhjemite (Pimentel et al. 1994).

2.5.1.1.2- The Andorinhas Supergroup - Greenstone-Belts

The **Andorinhas Supergroup** is a typical greenstone sequence, stratigraphically divided into the basal **Babaçu Group** and the upper **Lagoa Seca Group** (DOCEGEO 1988).

The main rock types of the *Babaçu Group* include metamorphosed komatiitic flows (dunites, peridotites, pyroxenites) and metabasalts intercalated with banded iron formations, schists, and metachert. The overlying *Lagoa Seca Group* consists of clastic (greywakes, siltstones) and chemical (banded iron formation)

metasedimentary rocks intercalated with ultramafic to felsic metavolcanic rocks (andesites, dacites, and riodacites) (DOCEGEO 1988).

U–Pb dating of zircons in the Lagoa Seca group volcanic rocks yields ages of 2.970 ± 7 Ma which have been interpreted as the crystallization age of the original magma (Pimentel et al. 1994).

Other individual greenstone belts (**Sapucaia Group**, **Inajá Group**, **Identidade Group**, **Gradaus Group** and **Tucumã Group** – these two are not shown in Fig. 2.9) are also included in the Andorinhas Supergroup (DOCEGEO 1988).

The *Identidade Group* (metagabbros, metabasalts, and metadacite) is thought to be correlative with the Lagoa Seca Group, with a Sm-Nd whole-rock age of $3,046 \pm 74$ Ma interpreted as representing the emplacement age of the magmas (Souza et al. 2001).

The *Inajá Group* is composed of meta-ultramafic, metamafic (basalts and gabbros) rocks, and banded iron formations (Neves et al. 1999). (Rolando et al. 2003) obtained a precise age of 2.988 ± 4 Ga (U-Pb zircon) which is thought to date the age of magmatism.

The *Tucuma and Gradaus Groups* are considered to be product of the second cycle of greenstone belts generation (2.87-2.85) that is characterized by the relatively higher content of metasediments (greywakes, turbidites) and BIFs in comparison to the early supracrustal rocks, e.g. to correlate with the Lagoa Seca Group (Santos 2003).

2.5.1.1.3 - Other rock units

Other lithostratigraphic units in the region include mafic-ultramafic layered rocks (the **Serra Azul Complex**) and extensive sequence of clastic platform sedimentary rocks (the **Rio Fresco Formation**).

The *Serra Azul Complex* (dunites cumulates, serpentinized pyroxenites, peridotites, gabbros and anorthosites) intrude the Andorinhas greenstones belts in the Rio Maria region (DOCEGEO 1988), crystallizing at $2,970 \pm 97$ Ma (U–Pb zircon; (Pimentel et al. 1994)).

The *Rio Fresco Formation* is a laterally variable, 2000m thick, low- to very low-grade metasedimentary sequence, which unconformably overlies the granitoid and greenstone assemblages. In the sequence, basal fluvial clastic sediments grade upwards into lagoonal to shallow marine carbonaceous, clastic and chemical sediments (Cunha et al. 1984; Meireles et al. 1984; Ramos et al. 1984; DOCEGEO 1988). (Araújo et al. 1988) referred to the Rio Fresco Formation as Águas Claras Formation in the central Carajás area. Detrital zircons analyzed from this formation show ages ranging from 3.67 to 2.76 Ga (Macambira et al. 1991; Macambira et al. 1998), which establish the maximum age for its deposition as Neoproterozoic.

2.5.1.2- The Carajás Terrane

There are three main stratigraphical schemes proposed for the Carajás Terrane (**Fig. 2.10**): (i) (DOCEGEO 1988); (ii) (Araújo et al. 1991) and (iii) (Pinheiro 1997) published in (Pinheiro et al. 1997a).

(i) DOCEGEO (1988)'s proposal is based on lithological mapping, particularly within mines, and focuses on the lithostratigraphic and geochronological aspects of the Archaean and Proterozoic rocks. This proposal lacks much structural geological information and tries to establish a rather complex terminology.

(ii) Araújo and Maia (1991) make the first attempt to organize the rocks in the region using tectonostratigraphic criteria. This proposal resulted from a regional mapping project with attention to the tectonic aspects of the area.

(iii) Pinheiro (1997) proposed a new tectono-structural subdivision and evolution for the region based on detailed structural studies developed in key localities around Carajás. This proposal groups the rocks into two major groups: the *Basement Assemblage*, and the *Cover Assemblage* utilizing tectono-structural criteria. The stratigraphical proposal of Pinheiro & Holdsworth (1997a) was used as reference for the studies developed in this thesis.

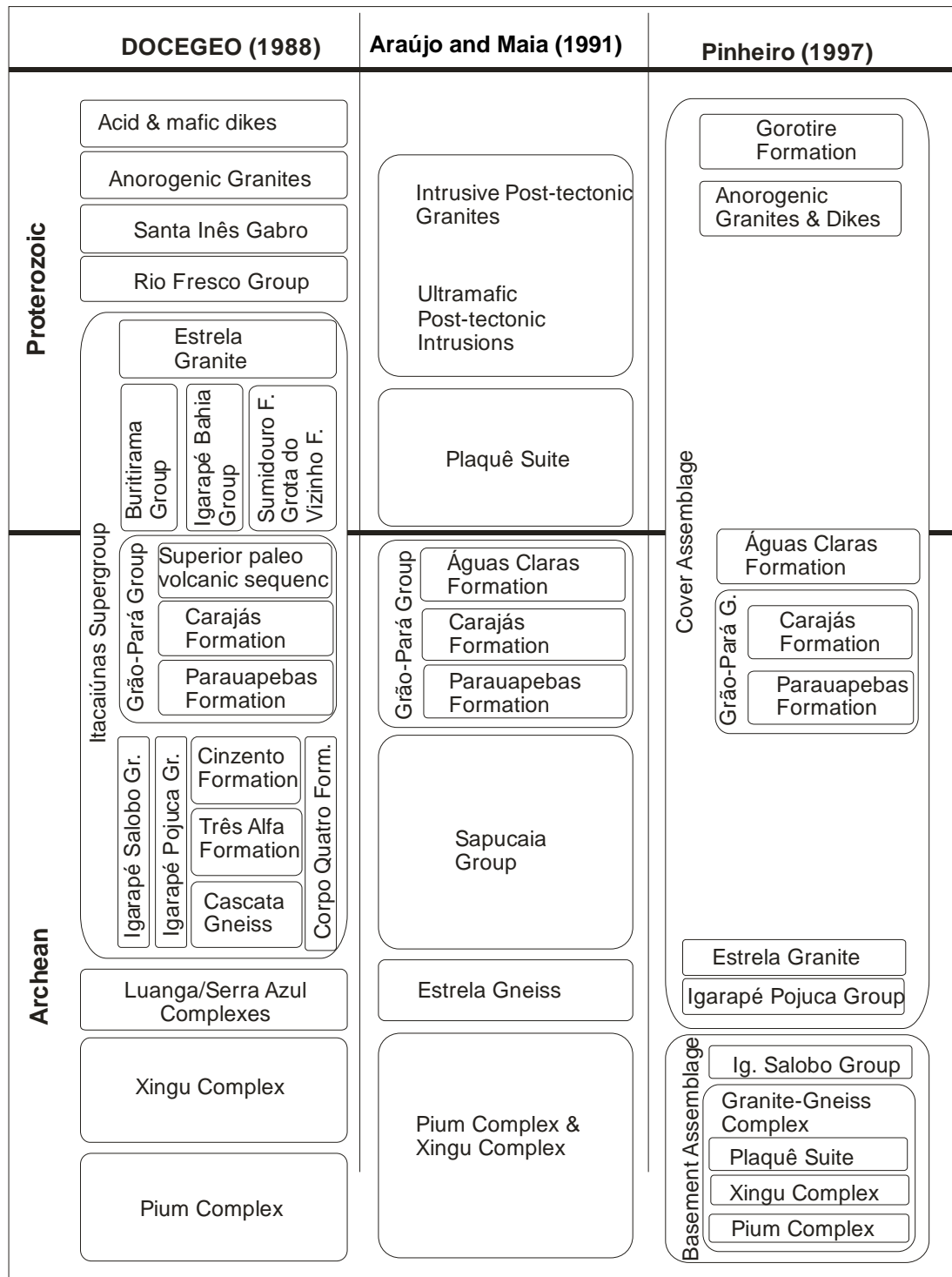


Figure 2.10 – Stratigraphical proposals for the Carajás Terrane.

It is now generally agreed that two main Archaean and Proterozoic domains present in the area: (1) a **High Grade Granite-Gneiss Terrain** corresponding to the *Basement Assemblage* of (Pinheiro 1997); and (2) the **Low Grade Supracrustal Volcano-Sedimentary Sequences** corresponding to the *Cover Assemblage* (Araújo et al. 1991; Pinheiro 1997).

2.5.1.2.1- High Grade Granite-Gneiss Terrain

The High Grade Granite-Gneiss Terrain situated in the north of the Carajás Terrane is represented by the **Xingu Complex** (Silva et al. 1974), **Pium Complex** (Hirata et al. 1982), and several **syn-tectonic Archean Granitoids** – including the **Plaque Suite** (Araújo et al. 1988), and isolated small mafic-ultramafic intrusive bodies (**Fig. 2.11**).

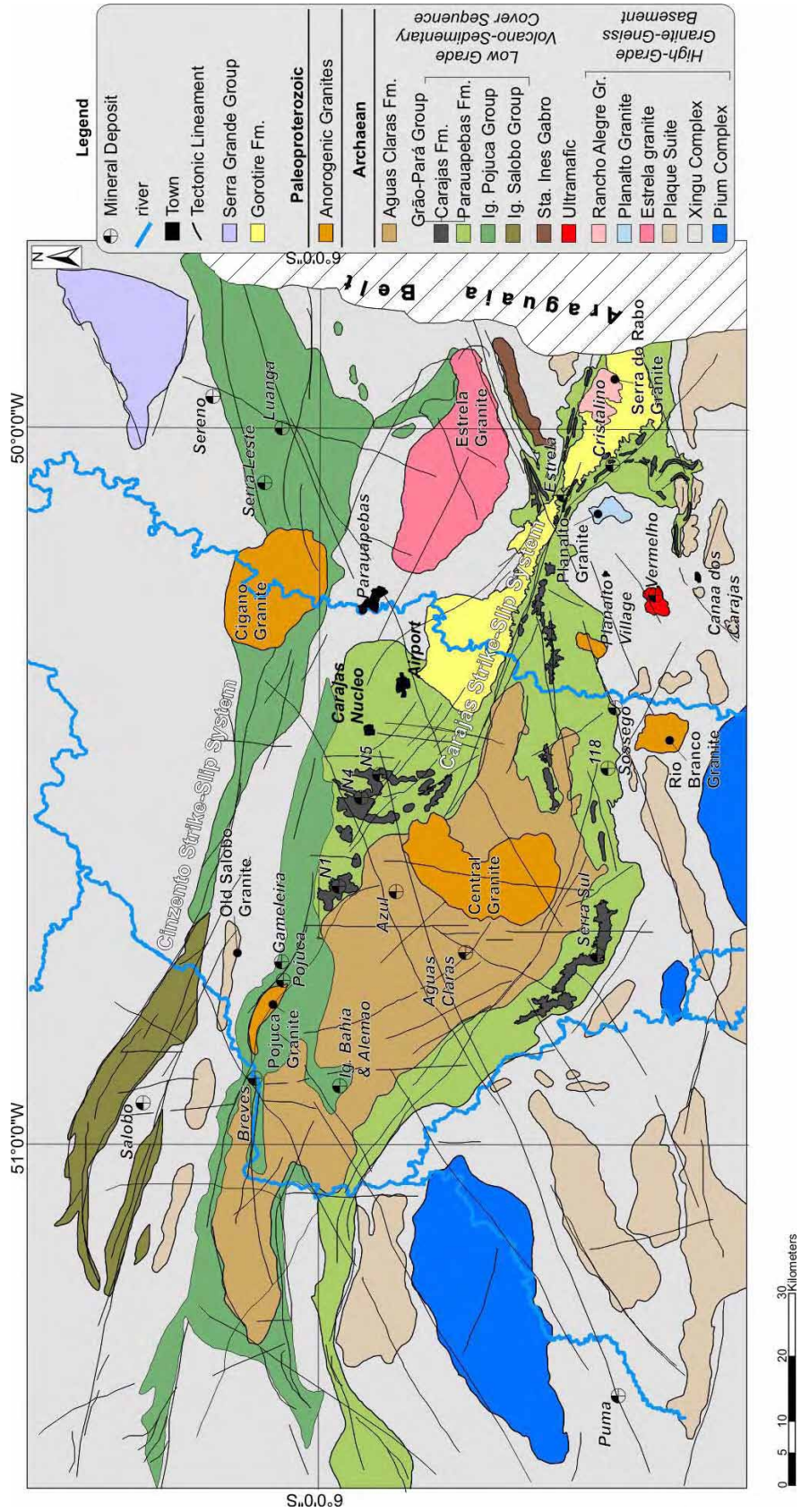


Figure 2.11 – Geological map of the Carajás Terrane highlighting the Carajás and Cinzento Strike-Slip Systems, major lineaments and ore deposits (after Pinheiro, 1997).

The *Pium Complex* was initially considered to be an integral part of the Xingu Complex (Hirata et al. 1982; DOCEGEO 1988). (Araújo et al. 1988) re-evaluated this interpretation, and identified it as a separate originally igneous rock unit, presently interleaved by strike-slip shear zones with rocks of the Xingu formation. It is typically composed of lenticular shaped stratiform basic and ultrabasic rocks (Hirata et al. 1982), with an E-W orientation. Its type locality lies near to the southern boundary of the Carajás Strike-Slip System, within the Xingu Complex. This unit corresponds to a heterogeneously deformed assemblage of granulite-facies rocks of varied composition (orthogneisses – charnokite/enderbites/mangerites; and para-gneisses – kinzigitic gneisses; (Costa et al. 1997; Pidgeon et al. 2000)). The contacts between these rocks and those of the Xingu Complex is marked by shear zones (Araújo et al. 1991). (Rodrigues et al. 1992) dated the Pium Complex as $3,050 \pm 114$ Ma (Pb-Pb whole rock) whilst (Pidgeon et al. 2000) used U-Pb (SHRIMP) methods to date crystallisation of the parent rock at $3,002 \pm 14$ Ma and the granulite facies metamorphism at $2,859 \pm 9$ Ma.

The term *Xingu Complex* was originally proposed by (Silva et al. 1974) to define the “infracrustal” rocks present throughout much of the Amazon Craton. It is typically composed of tonalitic gneisses, granodiorites, monzogranites, amphibolites and minor occurrences migmatites (Araújo et al. 1991). The rocks are metamorphosed at amphibolite facies and may be associated with migmatization. Preserved minor structures and fabrics strongly suggest superimposed polyphase deformation (Araújo et al. 1988; Araújo et al. 1991). Some amphibolites and migmatites in this unit may be derived from intensely reworked parts of the granite-greenstone terrains (Araújo et al. 1988; Costa et al. 1995). Isotopic ages for the

Xingu Complex indicate that the last episode of migmatization took place at ca. $2,851 \pm 4$ Ma (U-Pb zircon; (Machado et al. 1988)) with later tectono-thermal events at $2,519 \pm 04$ Ma (Machado et al. 1991).

The *Plaque Suite*, defined by (Araújo et al. 1988), corresponds to a group of small lenticular deformed granitoids aligned in an E-W trend (see **Fig. 2.11**). They are restricted to the southern portion of the Carajás Terrane and the uppermost part of the Rio Maria Granite-Greenstone Terrane.

These granitoids are syntectonically emplaced within the Xingu Complex during a major tectono-thermal event that caused partial melting of the crust associated with ductile shearing (Araújo et al. 1988; Araújo et al. 1991). Isotopic ages (Pb-Pb whole rock) for the emplacement of the granitoids are: $2,727 \pm 29$ Ma (Avelar 1996); and $2,792 \pm 29$ Ma (Avelar et al. 1999). The Planalto Granite ($2,747 \pm 2$ Ma, Pb/Pb zircon; (Huhn et al. 1999)) exposed in the Rabo Ridge is belongs to this group of granites.

Younger Syntectonic Granitoids

A number of deformed granitoids were identified during the nineties in the Carajás Terrane. Many were initially thought to be part of the Xingu Complex but new mapping and geochronological data were obtained revealing their intrusive nature into the older rocks of the Xingu Complex.

A range of Neoproterozoic granitoids are present within the basement rocks of the *High Grade Granite-Gneiss Terrain*. These include:

- 1- the **Old Salobo Granite** located in the Igarapé Salobo region (Lindenmayer et al. 1991; Lindenmayer et al. 1994) dated at $2,573\pm 3$ Ma (U-Pb zircon; (Machado et al. 1991);
- 2- the **Itacaiúnas Granite** (not shown in **Fig. 2.11**) – $2,560\pm 3$ Ma (U-Pb zircon; (Souza et al. 1996);
- 3- the **Rancho Alegre Granite (Serra do Rabo)** – $2,743\pm 2$ Ma (U-Pb zircon; (Sardinha et al. 2006);
- 4- the **Granitic Stock Geladinho** (not shown in **Fig. 2.11**) – $2,688\pm 11$ Ma (Pb-Pb zircon; (Barbosa et al. 2001);
- 5- the **Planalto Granite** – $2,747\pm 2$ Ma (Pb-Pb zircon; (Huhn et al. 1999);
- 6- the **Cristalino Diorite** (not shown in **Fig. 2.11**) – $2,738\pm 6$ Ma (Pb-Pb zircon; (Huhn et al. 1999); and
- 7- the **Estrela Granitic Complex** (Barros 1997) situated in the east of the Carajás Region, dated at $2,527\pm 34$ Ma (Rb-Sr whole rock; (Barros et al. 1997), and more recently at $2,763\pm 7$ Ma (Pb-Pb zircon; (Barros et al. 2001).

These foliated granitoid bodies are typically elongated parallel to the strike of the regional WNW-ESE foliation. They are intrusive into both the Xingu Complex and the Low-Grade Supracrustal Volcano Sedimentary Sequence (Holdsworth et al. 2000; Barros et al. 2001; Sardinha et al. 2006). The granitoids are separated into two major groups: (1) an older (2.76-2.73 Ga) set, including the Plaque, Estrela, Planalto and Serra do Rabo granitoids, with monzogranitic compositions and intrusive relationships within the supracrustal rocks; and (2) a younger (2.5-2.6 Ga) set of calc-alkaline granitoids, that are rather poorly exposed and include the Geladinho, Old Salobo and Itacaiúnas granites (Sardinha 2002; Santos 2003; Tallarico et al. 2005).

2.5.1.2.2- The Low Grade Supracrustal Volcanic and Sedimentary Sequences

The Low Grade Volcanic and Sedimentary Sequences are mainly located in the inner portions of the Carajás Terrane (see **Fig. 2.11**). They comprise the rocks of the **Itacaiúnas Supergroup** (DOCEGEO 1988), overlain by the sedimentary cover sequences of **Águas Claras Formation** (Nogueira et al. 1995) and **Gorotire Formation** (Lima et al. 2001).

The Itacaiúnas Supergroup forms continuous E-W elongated zones, linked to major tectonic lineaments and strike-slip fault zones. It is primarily composed of metavolcanics and metasedimentary rocks (Costa et al. 1995). These include: (1) the **Igarapé Salobo Group**; (2) the **Igarapé Pojuca Group**; (3) the **Igarapé Bahia Group**; (4) the **Grão-Pará Group**; and (5) the **Buritirama Group** (not shown in **Fig. 2.11**).

The ***Igarapé Salobo Group*** is divided into three major units, oriented WNW-ESE with sub-vertical dips and contains deposits of copper, gold, molybdenum and silver. The contact of this unit with the Xingu Complex is generally marked by shear zones (Oliveira et al. 1994). From the base of the unit upwards, the stratigraphy is divided into: the **Cascata Gneiss**, composed of granitic gneiss and subordinate units of alternating amphibolites and meta-pelites; the **Three Alfa Formation** - clastic and chemical metasedimentary rocks with subordinate units of basic to intermediate volcanics; and the **Cinzento Formation** - quartzites (DOCEGEO 1988). The age of metamorphism was estimated from U-Pb dating of zircon in the foliated amphibolites as being $2,761 \pm 3$ Ma (Machado et al. 1991).

The Igarapé Pojuca Group consists of a sub-vertical, WNW-ESE-striking volcano-sedimentary sequence, composed of mafic to intermediate meta-volcanic rocks, amphibolite, biotite schist, clastic sedimentary rocks, and ironstones. The metamorphic grade varies from greenschist to amphibolite facies (DOCEGEO 1988). The *Corpo Quatro Formation* is part of the Igarapé Pojuca Group and was identified and characterized by geochemical surveying and drilling campaigns. This unit comprises banded mafic rocks and schists (quartz, amphibole, sulphides, magnetite, almandine, and biotite) alternating with discontinuous units of chert, banded iron formations and massive sulphides (DOCEGEO 1988).

The Igarapé Bahia Group is a volcano-sedimentary sequence oriented NNW and dipping on average 70° E, with occurrence limited to the area of the Bahia gold mine. It was metamorphosed under low grade conditions and contains occurrences of copper, gold, molybdenum and silver (DOCEGEO 1988). It is formed by two units: The lowermost “*Grota do Vizinho*” *Formation* – a sequence of sedimentary (siltstones, claystones, greywackes, rhythmites) and pyroclastic rocks (lapilli tuffs, laminated tuffs) with primary structures preserved, alternating with basic rocks (basalts, diabases, micro-gabbros); and the uppermost *Sumidouro Formation* – sandstones alternating with mafic volcanics (DOCEGEO 1988).

The *Grão-Pará Group* is renowned for its high economic grade, high tonnage iron ore deposits. It is composed of volcano-sedimentary sequences (mafic and felsic volcanics alternated with banded iron formations) that were originally divided into three main units: An ‘Upper Paleovolcanic’ sequence (basalts); the Carajás *Formation* (banded iron formations); and the lowermost Parauapebas

Formation sequence (basalts) (CVRD/CMM 1972). More recently, (Pinheiro 1997) divided the Grão-Pará Group into two main units: the older volcanic rocks of the Parauapebas Formation (Meireles et al. 1984); and the ironstones of the Carajás Formation (Beisiegel et al. 1973). He proposed that units of the Parauapebas Formation are interlayered or tectonically juxtaposed both above and below the Carajás Formation in the region of the N4 Plateau (Beisiegel et al. 1973; Anderson et al. 1974; Araújo et al. 1988; Pinheiro et al. 1997b).

The *Parauapebas Formation* is composed of felsic to mafic metavolcanics metamorphosed at greenschist facies under low temperatures and pressures (Araújo et al. 1991). The units are bimodal sequences of basalts, dolerites and rhyolites. The age of crystallisation has been estimated by (Wirth et al. 1986), using U-Pb dating of zircons at $2,758 \pm 39$ Ma and by (Machado et al. 1991) at $2,759 \pm 2$ Ma. Geochemical studies suggest that these volcanic rocks have a strong affinity with continental tholeites (Gibbs et al. 1990; Lindenmayer et al. 1992) that were subsequently metamorphosed and hydrothermally altered (Wirth et al. 1986; Araújo et al. 1991; Teixeira et al. 1994).

The *Carajás Formation* is represented by a thick unit of banded iron formations (jaspillites) and iron ore bodies (Pinheiro et al. 1997b). The jaspillite comprises alternating layers (2-20 mm) thick of very fine crystalline quartz and/or chert bands, with hematite, martite and pyrite (Araújo et al. 1991). The iron ore bodies are composed of different types of iron oxide with a nomenclature mostly related to its physical properties or industrial uses (Beisiegel 1982; Hoppe et al. 1987).

The *Buritirama Group* comprises a supracrustal sequence of clastic and chemical metasediments containing manganese deposits and marble layers (Oliveira et al. 1994). The stratigraphic succession begins with mica rich quartzite passing upwards into mica-schists, banded quartzite and mafic schists (DOCEGEO 1988).

The Águas Claras (Araújo et al. 1991; Nogueira et al. 1994) and Gorotire Formation (Barbosa et al. 1966; Hirata et al. 1982) are younger and have significantly contrasting lithologies compared to the other volcano-sedimentary rocks in the region. They also clearly stratigraphically overlie the Grão-Pará Group in the centre of the Carajás region (**Fig. 2.11**).

The *Águas Claras Formation* was initially identified as an upper part of the Grão-Pará Group e.g. (Araújo et al. 1991). (Nogueira 1995) combined analysis of sedimentary and stratigraphic characteristics, and structural data to redefine the unit as a 'separate formation'. The unmetamorphosed sedimentary sequence lies unconformably on the older, low-grade metamorphosed volcanic rocks of the Parauapebas Formation and ironstones of the Carajás Formation, within the Archaean Grão-Pará Group (Araújo et al. 1991; Pinheiro 1997; Holdsworth et al. 2000).

The rock formations display heterogeneous deformation where high strain zones are closely associated with strike-slip faults and locally folds. Elsewhere the deformation is exclusively brittle and weak (Nogueira 1995; Holdsworth et al. 2000). This unit has a total thickness in the region of 1,500 meters and is divided into two members: (1) a *Lower Member*, deposited in a marine platform system, composed of mudstones, siltstones and subordinate sandstones; and (2) an *Upper Member*, related

to fluvial to shallow water littoral deposits comprising mainly sandstones and locally conglomerates (Nogueira 1995).

(Nogueira et al. 1994; Nogueira et al. 1995) proposed an Archaean age for this unit and disagreed with a pull-apart basin model previously proposed by (Araújo et al. 1991). They proposed instead that the sedimentary sequence was laid down in an extensive basin, whose margins extended well beyond the limits of the present day outcrop of the Águas Claras Formation.

Isotopic analysis of detrital zircons yielded ages between 2,778 and 3,020 Ma (U-Pb zircon, (Mougeot et al. 1996)). Zircons within a sandstone derived from syndepositional volcanism were dated at $2,681 \pm 5$ Ma and this is thought to represent a minimum age for the sedimentary sequence (Trendall et al. 1998). The Águas Claras Formation is intruded by gabbro/diabase dikes and sills with a minimum age for crystallization of $2,708 \pm 37$ (U-Pb zircon, (Mougeot et al. 1996)) and $2,645 \pm 12$ Ma (Dias et al. 1996).

The *Gorotire Formation* comprises sequences of clastic, immature and little-deformed rocks (sandstones and conglomerates) outcropping predominantly around the eastern part of the Parauapebas River and in restricted areas overlying the supracrustal rocks of the Carajás Strike-Slip System. (Holdsworth et al. 2000). These rocks are believed to be deposited by debris-flow-dominated alluvial fans and braided fluvial systems, in an asymmetric graben closely linked to the later kinematic history of the Carajás Fault (Lima et al. 2001). The sandstones are purple arkosic wackes to arkoses with medium to coarse grain sizes, which are moderately- to poorly-sorted. The polymictic conglomerates are well lithified and grain-

supported with pebbles and boulders derived from a broad range of protolith compositions (Pinheiro 1997).

2.5.1.2.3- Mafic-Ultramafic Intrusions

Mafic-ultramafic plutonism is represented in the Carajás Terrane by the **Luanga Complex**, the **Vermelho Ultramafics** and the **Santa Inês Gabbro** (see location in **Fig. 2.9**). All these intrusions are thought to be related to an extensional Neoproterozoic event (Costa et al. 1995).

The **Luanga Complex** is an intrusive, mafic-ultramafic layered body formed by a basal unit of peridotites and dunites passing upwards into anorthosite gabbros (DOCEGEO 1988). The igneous mineral assemblages have been partially replaced by a metamorphic–hydrothermal assemblage formed of talc, tremolite, serpentine, albite, chlorite, epidote, and actinolite (Suita et al. 1988). An Rb–Sr age of 1,850 Ma has been interpreted as corresponding to a metamorphic–hydrothermal overprint (Suita et al. 1991), with the true age of crystallization being $2,763 \pm 6$ Ma (U–Pb zircon in an anorthosite gabbro) (Machado et al. 1991). Chromite seams and layers occur in the transition zone between pyroxenites and peridotite–dunites. The ore bodies are commonly characterized by massive to disseminated chromites cemented by olivine and orthopyroxene (Girardi et al. 2006).

The **Santa Inês Gabbro** is a tabular body about 20 km long, trending NE–SW, and formed by leucocratic and anorthositic gabbros showing ophitic to subophitic and subordinate porphyritic textures (DOCEGEO 1988). These rocks are thought to have undergone greenschist metamorphism given the presence of

widespread hornblende/andesine. The weak non-penetrative schistosity/foliation indicates some limited ductile deformational process (Araújo et al. 1991).

The *Vermelho Ultramafics* unit is located at the SW end of the *Rabo Ridge* (or Serra do Rabo), and it comprises a series of NE-SW trending basic-ultrabasic bodies and nickel deposits (Bernardelli et al. 1982). The unit contains a concentric spatial distribution of gabbros, metagabbros, norite-gabbros, pyroxenites, bronzites, serpentinites and silexites (DOCEGEO 1988). Serpentinites within the unit are interpreted as being derived from dunites and peridotites. Metapyroxenites with high diopside-tremolite are suggestive of greenschist facies metamorphism, coupled with brittle-ductile processes recorded by the development of a protomylonitic-protocataclastic deformation fabric (Araújo et al. 1991). The lack of isotopic ages for these units prevents accurately locating them in the regional stratigraphic column. However, (DOCEGEO 1988) and (Araújo et al. 1991) suggest for the Vermelho Ultramafics and Santa Ines Gabbro, Paleoproterozoic and Mesoproterozoic ages respectively.

2.5.1.2.4- Anorogenic Granites

Several Suites of Palaeo- to Mesoproterozoic (ca. 1.8-1.6 Ga) plutons intrude almost all the rocks of both basement and low-grade volcanic- sedimentary sequences in the Carajás and the Rio Maria granite-greenstone terranes (Machado et al. 1991; Dall'Agnol et al. 1999).

These post-tectonic felsic plutons are widespread but are more abundant in the south (Rio Maria). They are generally non-foliated, monzogarnitic-syenogranitic

in composition, coarse to medium grained, massive, and remarkably discordant showing sharp contacts with, and angular inclusions of the Archaean country rocks (Ramo et al. 2002; Dall'Agnol et al. 2005).

In the Carajás Terrane, the main anorogenic granites are: the **Cigano Granite** – $1,883 \pm 2$ Ma (U-Pb zircon; (Machado et al. 1991); the **Serra dos Carajás or Central Granite** – $1,880 \pm 2$ Ma (U-Pb zircon; (Machado et al. 1991); and the **Pojuca Granite** – $1,874 \pm 2$ Ma (U-Pb zircon; (Machado et al. 1991).

In the Rio Maria Granite-Greenstone Terrane, the anorogenic plutons are more abundant, with six main units: the **Jamon Granite** – $1,885 \pm 32$ Ma (Pb-Pb zircon; (Dall'Agnol et al. 1999); the **Musa Granite** – $1,883 \pm 2$ Ma (U-Pb zircon; (Machado et al. 1991); the **Banach Granite** – $1,880$ Ma (Almeida et al. 2007); the **Manda Saia Granite** (Ramo et al. 2002); the **Redenção Granite** – $1,870 \pm 68$ Ma (Pb-Pb whole-rock; (Barbosa et al. 1995); and the **Marajoara Granite** – $1,724 \pm 50$ Ma (Rb-Sr whole-rock; (Macambira 1992).

Neodymium isotopic data indicate that the Palaeoproterozoic granites were derived from Archaean sources (Dall'Agnol et al. 1999; Ramo et al. 2002; Teixeira et al. 2002). Magmatic underplating has been proposed as the heat source that formed the *Carajás* granite magmas (Dall'Agnol et al. 1994; Dall'Agnol et al. 1999). It has similarly been suggested that the *Rio Maria* granites could have been formed by processes involving thermal perturbations in the upper mantle, mafic underplating, and associated extension or transtension in the crust (Ramo et al. 2002).

2.6- Previous Tectonic Models

There are currently three main tectonic models proposed for the Carajás Terrane. Chronologically, these were proposed by: (1) (Costa et al. 1995); (2) (Araújo et al. 1991); and (3) (Pinheiro 1997) (published in (Pinheiro et al. 1997b; Pinheiro et al. 1997a) and (Holdsworth et al. 2000). Other tectono-structural models (Veneziani et al. 2004; Rosière et al. 2006) have also been proposed for the region, but have rarely been referred by other authors.

The *Araújo & Maia, 1991* model (**Fig. 2.12**) follows on from the structural subdivision of the Amazon Craton made by (Hasui et al. 1984). They consider the Itacaiúnas Shear Belt to be a major structural feature developed under an obliquely convergent (transpressional) regime. They defined two distinct structural domains: (1) an *Imbricated Domain* – extending from the southern boundary of the Carajás Terrane into a transitional region up to the granite-greenstone terrain to the south; and (2) a *Transcurrent* domain – located along the Carajás Terrane and represented by the Carajás and Cinzento Strike-Slip Systems. They proposed that both the *Imbricated* and *Transcurrent* domains were genetically related to an Archaean collisional episode involving continental blocks. This led to reworking of the granite-greenstone terrain rocks and controlled the later deposition of the supracrustal sequences along strike-slip systems. During the Proterozoic, NE-SW regional extension produced granitic and mafic-ultramafic intrusions, followed by the deposition of volcano-sedimentary sequences infilling transtensional pull-apart basins (Araújo et al. 1991).

The model of *Costa et al. (1995)* separates the tectonostratigraphic evolution of the Carajás Terrane into three main tectonothermal events during the Precambrian.

(i) The initial and longest event is marked by the nucleation and propagation of E-W oblique, south-dipping shear zones, associated with amphibolite facies metamorphism, leading to the uplift of granulites from the lower crust and reworking of the basement granitic rocks.

The Carajás and Cinzento strike-slip systems were envisaged as having formed under a transpressional regime that ultimately led to the development of several pull-apart basins that were subsequently filled with volcano-sedimentary sequences belonging to the Itacaiúnas Supergroup.

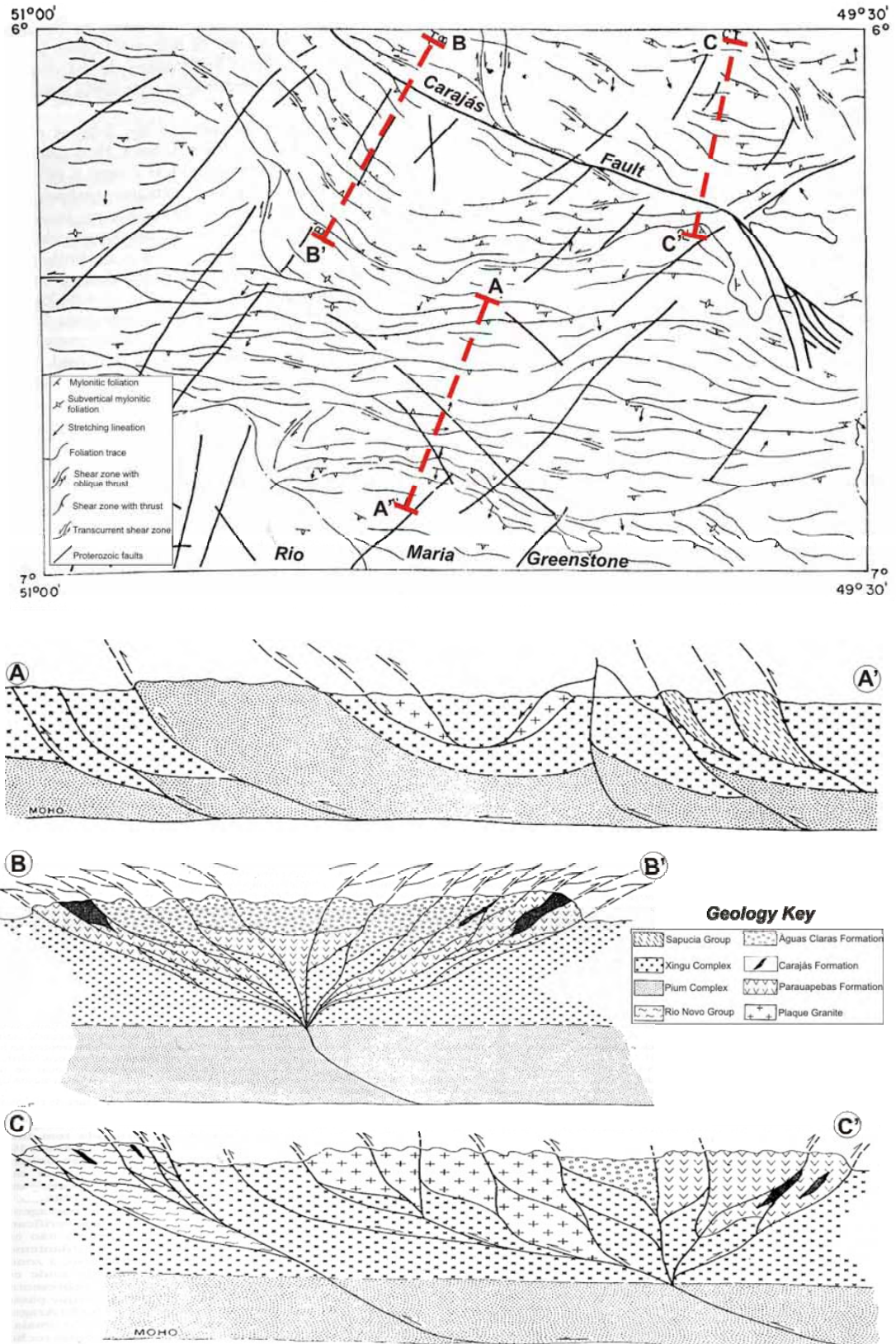


Figure- 2.12 – Geological cross sections showing geometrical interpretation for: A-A' the Imbricated Domain; B-B' the Carajás Transcurrent Domain; and C-C' the Cinzento Transcurrent Domain. Adapted from Araújo & Maia, 1991.

The pull-apart basins were then thought to be inverted under sinistral transpression accompanied with amphibolite-greenschist metamorphism along shear zones and widespread hydrothermal alteration.

Finally, discrete WNW-ESE, N-S and NE-SW strike-slip faults were thought to have formed as the result of an oblique collision between the Araguacema and Belem tectonic blocks.

(ii) During the second event, several NE-SW extensional segments developed along pre-existing faults, which were thought to be of Proterozoic age.

(iii) Finally, the third event was related to the establishment of the Araguaia Belt that lies to the east of the Carajás Terrane.

The tectonic model of (*Pinheiro 1997*) (**Fig. 2.13**) is based on a history in which subsequent brittle-ductile and brittle tectonic reactivation events were geometrically controlled by pre-existing Archaean ductile fabrics developed initially in the basement. This model proposes an alternating series of transpressional and transtensional reactivations in four main stages supported by field data:

1- Initially, the rocks of the Basement Assemblage (Pium Complex, Xingu Complex, Plaque Suite and Igarapé Salobo Group) were affected by high temperature sinistral transpression forming broad E-W trending shear belts with blastomylonitic penetrative fabrics between about 3.0 to 2.8 Ga;

2- Between 2.8 and 2.7 Ga, sinistral transpression caused folding of the basement rocks and the development of sinistral shear zones under medium to low temperature metamorphism. Later extension formed regional intracratonic basins that hosted the volcano-sedimentary sequences of the Grão-Pará Group at

approximately 2.76 Ga. These were later affected by low temperature metamorphism and hydrothermal alteration and were subsequently overlain by the rocks of the Águas Claras Formation.

3- The Carajás and Cinzento Strike-Slip Fault Systems were contemporaneously formed during dextral transtension at about 2.0-1.8 Ga. This regime down-faulted parts of the volcanic-sedimentary cover rocks within transtensional pull-apart-like features formed by the intersections of E-W transcurrent faults and NW-SE normal faults.

4- The final stage is marked by a weak sinistral transpression that led to weak inversion of the volcanic-sedimentary sequences through fault reactivation and folding, with moderate to strong amounts of deformation localised adjacent to major fault zones, especially the Carajás Fault.

Whilst there are some similarities, the (Costa et al. 1995) and (Pinheiro 1997) models are significantly different:

(i) (Costa et al. 1995) propose that the basement reactivation is related to thrusts formed due to collisional processes. By contrast, (Pinheiro 1997) suggests that the reactivation events are strongly influence by the development of an early, steeply-dipping ductile planar fabric in the basement. This, it was suggested, favoured transcurrent reactivation styles rather than thrusting.

(ii) The pull-apart basin models suggested by (Costa et al. 1995), within which the volcano-sedimentary sequences were deposited and associated dextral transcurrent systems developed, are not consistent with the stratigraphic and sedimentological features observed in the rocks of the Grão-Pará Group and Águas

Claras Formation. (Nogueira 1995) and (Pinheiro et al. 1997b; Pinheiro et al. 1997a) therefore propose that these volcanic and sedimentary cover sequences were more likely deposited in wide intracratonic basins, with depocentres possibly located outside of the present Carajás Terrane and little local fault control on sedimentation patterns.

(iii) According to (Pinheiro 1997), the regional tectonic inversion events recognised by (Costa et al. 1995) are restricted only to the rocks adjacent to major faults.

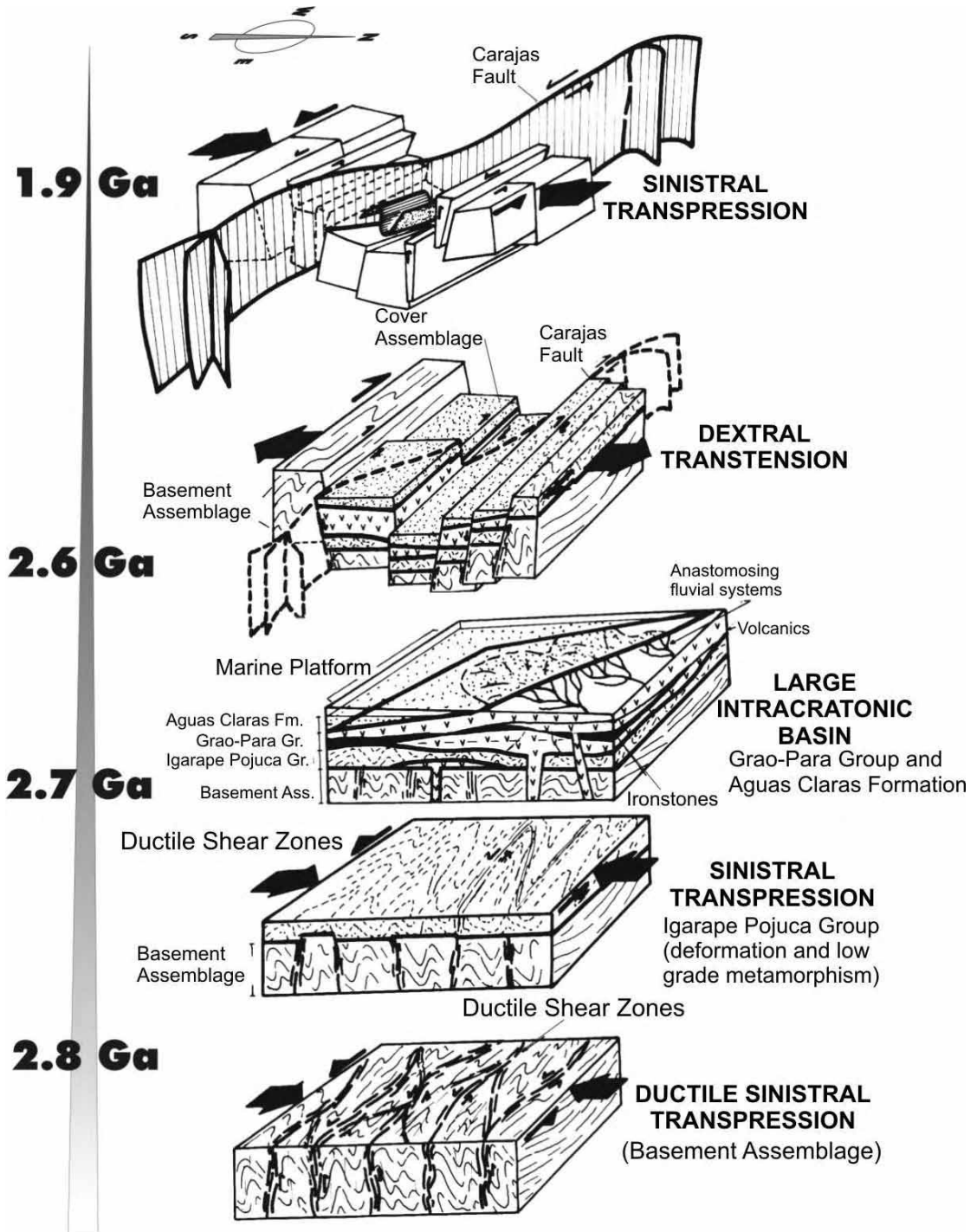


Figure 2.13 – Summary of the tectono-structural history of the Carajás Terrane (Pinheiro, 1997).

2.7- Metamorphism

High grade metamorphic rocks are present in the basement units represented by the granulites of the Pium Complex. The supracrustal sequences of the Andorinhas and Itacaiúnas Supergroups record different metamorphic grades, ranging from virtually unmetamorphosed and undeformed, through to greenschist-amphibolite-facies conditions with regional metamorphic temperatures rarely exceeding 700°C (Lindenmayer 1990).

Hydrothermal submarine metamorphism affected the Itacaiúnas Supergroup prior to the regional metamorphic events. It produced variable amounts of decalcified plagioclase, epidote, chlorite, tremolite-actinolite, white mica, quartz and carbonates in the rocks of the Grão Pará and Igarapé Bahia Groups (Villas et al. 2001).

Low grade greenschist and amphibolite and/or granulite facies metamorphism are described for the rocks of the Grão-Pará and Salobo Groups respectively (DOCEGEO 1988; Olszewski et al. 1989).

Contact metamorphism represented by granitic thermal aureoles overprints the submarine and regional metamorphic assemblages in at least two confirmed examples: as anthophyllite-cordierite-rich rocks developed in the metavolcanics of the Igarapé Pojuca Group (Winter 1995) and as pyroxene-hornfels and albite-hornblende-hornfels facies rocks developed at temperatures of 600-650 °C in the thermal aureole surrounding the Estrela Granite (Barros 1997; Barros et al. 2001).

2.8- Geochronology

A substantial number of geochronological ages are available for the rocks in the Carajás Geochronological Province. The initial published ages were based on Rb-Sr and K-Ar isotopic techniques. However, the Rb-Sr ages are systematically younger compared to data obtained from more robust methods. This led to the use of more reliable techniques, such as U-Pb zircon and U-Pb SHRIMP, or Pb-Pb ages from whole rock or zircon analyses.

However, (Machado et al. 1991) point out that some of the ambiguous geochronological results obtained for the Carajás Terrane could be due to the polymetamorphic/tectonic character of the area and the extensive alteration of many rock types.

Table 3 shows some of the geochronological data obtained from the different lithological units in the province, which can be used to correlate and group the units into well defined time intervals.

- 1) The granite-gneiss basement rocks are older than **2.8 Ga**, becoming progressively older as one moves southwards from the Carajás Terrane (*Xingu Complex 2.8 Ga*) towards the Rio Maria Granite Greenstone Terrane (*Caracol and Arco Verde Tonalites 2.9 Ga*).
- 2) The greenstone sequences of the Andorinhas Supergroup have a minimum age of **2.87 Ga** (*Tucumã Group*) and a maximum age of **2.98 Ga** (*Inajá Group*).
- 3) The ultramafic intrusive bodies are dated at **2.76 Ga** (*Luanga Complex* in the Carajás Terrane) and **2.97 Ga** (*Serra Azul Complex* in the Rio Maria Terrane),

suggesting that they correlate with the events that formed the Itacaiúnas Supergroup (~ 2.7 Ga – see below) and the Andorinhas Supergroup (~ 2.9 Ga – see above), respectively.

4) The Archaean syntectonic granitoids can be arranged into distinct groups produced by three intrusive episodes that occurred at: ~**2.87** Ga in the Rio Maria Terrane (*Rio Maria Granodiorite, Mogno Trondhjemite, Xinguara Granite, etc*); ~**2.7** and ~**2.5** Ga in the Carajás Terrane (*Estrela Granite, Planalto Granite, Plaque Suite; Itacaiúnas and Old Salobo Granites respectively*).

5) The volcanic-sedimentary sequences of the Itacaiúnas Supergroup display ages ranging from **2.73** to **2.76** Ga. The widespread correspondence and clustering of ages from widely separated localities suggests formation in the same, regionally extensive geological environment.

6) The gabbroic sill intruded into the Águas Claras Formation is dated at **2,645 ± 12** Ma, which can be regarded as a minimum age for this unit.

7) The Proterozoic anorogenic granites exhibit ages from **1.72** to **1.88** Ga (*Cigano, Carajás, Pojuca, Musa and Jamon Granites*) related to a widespread 1.8 – 2.0 regional intrusion event recorded in many parts of the Amazon Craton.

8) Many of the granitic and supracrustal units in the Carajás region also often record younger ages compared to the absolute ages of crystallization for these rocks. The younger ages (2.4, 2.5 and 2.6 Ga) are likely linked to a variety of metamorphic, hydrothermal and tectonic events widely described in the literature (see (Machado et al. 1991; Lindenmayer et al. 1994; Reis et al. 1999; Holdsworth et al. 2000; Barros et al. 2001; Requia et al. 2003; Marschik et al. 2005)).

Chapter 2

Supergroup	Group / Formation	Intrusive Rocks	Lithology	Age (Ga)	Method	Author
A - Carajas Region						
Proterozoic Granites		Cigano Granite	Granite	1.731 ± 28	W-R Rb-Sr	Gonzalez et al. (1988)
		Cigano Granite	Granite	1.883 ± 3	ZR U-Pb	Machado et al. (1991)
		Carajas Granite	Granite	1.880 ± 2	ZR U-Pb	Machado et al. (1991)
		Carajas Granite	Granite	1.820 ± ?	ZR U-Pb	Wirth et al. (1986)
		Carajas Granite	Granite	1.820 ± 49	ZR U-Pb	Olszewski et al. (1989)
		Pojuca Granite	Granite	1.874 ± 2	ZR U-Pb	Machado et al. (1991)
		Breves Granite	Episyenite	1.880 ± 9	ZR SHR MP II	Tallarico et al. (2004)
		Breves Granite	Granite	1.878 ± 8	ZR SHR MP II	Tallarico et al. (2004)
		Young Salobo Gran.	Syenite	1.88 ± 80	W-R Rb-Sr	Cordani (1981)
		Águas Claras	gabro	2.645 ± 12	ZR Pb-Pb	Dias et al. (1996)
		Grão-Pará	volcanic sill	2.751 ± 4	ZR Pb-leach	Krymsky et al. (2002)
		Grão-Pará	Rhyodacite	2.759 ± 2	ZR U-Pb	Machado et al. (1991)
		Grão-Pará	Metarhyolite	2.758 ± 39	ZR U-Pb	Olszewski et al. (1989)
		Grão-Pará	Rhyolite	2.758 ± 39	ZR U-Pb	Gibbs et al. (1986)
		Grão-Pará	Probable Tuff	2.743 ± 11	ZR SHRIMP	Trendall et al. (1998)
		Grão-Pará	Dolerite	2.740 ± 8	ZR SHRIMP	Trendall et al. (1998)
		Grão-Pará	Mylonitised Metarhyolite	2.757 ± 7	ZR SHRIMP	Trendall et al. (1998)
		Grão-Pará	Prphyritic metarhyolite	2.760 ± 11	ZR SHRIMP	Trendall et al. (1998)
		Grão-Pará	Rhyolite	2.758 ± 39	ZR U-Pb	Macambira & Lafon (1995)
	Grão-Pará	Rhyolite	2.757 ± 18	ZR Pb-Pb	Macambira et al. (1996)	
tacaiunas Group	Igarape Pojuca	Metarhyolite	2.497 ± 62	WR Rb-Sr	Olszewski et al. (1989)	
	Igarape Pojuca	Aphibolite	2.732 ± 2	ZR U-Pb	Machado et al. (1991)	
	Igarape Pojuca	Gabro	2.678 ± 107	WR Sm-Nd	Lindenmayer et al. (2001)	
	Igarape Pojuca	Metagabro	2.696 ± 109	WR Sm-Nd	Lindenmayer et al. (2001)	
	Igarape Pojuca	Andesite	2.683 ± 80	WR Sm-Nd	Lindenmayer et al. (2001)	
	Igarape Pojuca	Garnet-Biotite-Schist	2.668 ± 60	WR Sm-Nd	Lindenmayer et al. (2001)	
	Igarape Pojuca	mafic intrusive rocks	2.705 ± 2	ZR Pb-Pb	Galarza et al. (2002b)	
	Igarape Pojuca	saprolith	2.683 ± 7	ZR Pb-Pb	Galarza et al. (2002b)	
	Igarape Pojuca	metavolcanic	2.646 ± 30	WR Pb-Pb	Galarza et al. (2002b)	
	Igarape Pojuca	Meta Andesites host rock	2.719 ± 80	WR Sm-Nd	Pimentel et al. (2003)	
	Igarape Pojuca	Meta Gabro/ Andesite	2.757 ± 81	WR Sm-Nd	Pimentel et al. (2003)	
	Igarape Salobo	Rhyolite	2.740 ± ?	ZR U-Pb	Wirth et al. (1986)	
	Igarape Salobo	Aphibolite	2.761 ± 3	ZR U-Pb	Machado et al. (1991)	
	Igarape Salobo	Aphibolite	2.497 ± 5	TI U-Pb	Machado et al. (1991)	
Igarape Salobo	Gneiss	2.851 ± 4	ZR U-Pb	Machado et al. (1991)		
Igarape Salobo	B F	2.551 ± 2	Mi U-Pb	Machado et al. (1991)		
Ultramafic	Igarape Bahia	Basic granophyre	2.577 ± 144	WR Rb-Sr	Ferreira Filho (1985)	
	Igarape Bahia	Metapyroclastic	2.330 ± 120	WR Rb-Sr	Ferreira Filho (1985)	
	Igarape Bahia	metapyroclastic	2.747 ± 1	ZR Pb-Pb	Galarza et al. (2002)	
	Igarape Bahia	mafic metavolcanic	2.758 ± 75	WR Sm-Nd	Galarza et al. (2002)	
	Igarape Bahia	Metapyroclastic	2.742 ± 72	WR Pb-Pb	Santos (2002)	
	Igarape Bahia	Meta volcanic/pyroclastic	2.759 ± 24	WR Sm-Nd	Santos (2002)	
	Igarape Bahia	Metavolcanic	2.748 ± 34	ZR SHRIMP	Tallarico et al. (2005)	
	Igarape Bahia	Metavolcanic	2.624 ± 8	ZR SHRIMP	Tallarico et al. (2005)	
		Luanga Complx.	Anorthosite	2.763 ± 6	ZR U-Pb	Machado et al. (1991)
		tacaiunas Granite	Granitoid	2.480 ± 40	WR Rb-Sr	Montalvao et al. (1984)
Archean Granites	tacaiunas Granite	Granitoid	2.560 ± 37	ZR Pb-Pb	Souza et al. (1996)	
	tacaiunas Granite	Granitoid	2.525 ± 38	ZR Pb-Pb	Souza et al. (1996)	
	Old Salobo Granite	Granitoid	2.573 ± 2	ZR U-Pb	Machado et al. (1991)	
	Geladinho Granite	Granitoid	2.688 ± 11	ZR Pb-Pb	Barbosa et al. (2001)	
	Estrela Granite	Granitoid	2.527 ± 68	WR Rb-Sr	Barros et al. (1992)	
	Estrela Granite	hornblenda sienogranite	2.763 ± 7	ZR Pb-Pb	Barros et al. (2001)	
Basement Units	Xingu Complex	Gneiss	2.480 ± 30	WR Rb-Sr	Montalvao et al. (1984)	
	Xingu Complex	Granitic Leucossoma	2.859 ± 2	ZR U-Pb	Machado et al. (1991)	
	Xingu Complex	Felsic Gneiss	2.851 ± 4	ZR U-Pb	Machado et al. (1991)	
	Xingu Complex	Amphibolite	2.519 ± 5	TI U-Pb	Machado et al. (1991)	
	Pium Complex	Granulite	3.050 ± 114	WR Pb-Pb	Rodrigues et al. (1992)	
	Pium Complex	Enderbite Protolith	3.002 ± 14	ZR SHRIMP	Pidgeon et al. (2000)	
	Pium Complex	Granulite	2.859 ± 9	ZR SHRIMP	Pidgeon et al. (2000)	
B - Transitional Region						
Archean Granites	Plaque Suite	Granitoid	2.729 ± 29	ZR Pb-Pb	Avelar et al. (1999)	
	Plaque Suite	Granitoid	2.736 ± 24	ZR Pb-Pb	Avelar et al. (1999)	
	Planalto Granite	Granitoid	2.747 ± 2	ZR Pb-Pb	Huhn et al. (1999)	
	Cristalino Diorite	Diorite	2.738 ± 6	ZR Pb-Pb	Huhn et al. (1999)	
	Serra do Rabo Gran.	Granitoid	2.743 ± 1	ZR U-Pb	Sardinha et al. (2002)	
Basement Units	Rio Maria Granod.	Granitoid	2.850 ± 17	ZR Pb-Pb	Avelar et al. (1999)	
	Xingu Complx	Gneiss	2.972 ± 16	ZR Pb-Pb	Avelar et al. (1999)	

C - Rio Maria Greenstone		Terrain					
		Musa Granite	Granitoid	1 883 +5/-2	ZR U-Pb	Machado et al. (1991)	
		Jamon Granite	Granitoid	1 885 ± 32	ZR Pb-Pb	Dall'Agnol et al. (1999)	
		Jamon Granite	Granitoid	1.601±42	WR Rb-Sr	Dall'Agnol et al. (1984)	
Proterozoic Granites		Marajoara Granite	Granitoid	1.724 ± 50	WR Rb-Sr	Macambira (1992)	
		Redenção Granite	Granite	1 870 ± 68	WR Pb-Pb	Barbosa et al. (1995)	
		Rio Maria Granod.	Granodiorite	2 660 ± 40	WR Rb-Sr	Montalvaio et al. (1984)	
		Rio Maria Granod.	Granodiorite	2.874 +9/-10	ZR U-Pb	Macambira (1992)	
		Rio Maria Granod.	Granodiorite	2.872 ± 5	TI U-Pb	Pimentel & Machado (1994)	
		Rio Maria Granod.	Granodiorite	2 874 ± 10	ZR U-Pb	Macambira & Lancelot (1996)	
		Rio Maria Granod.	Granodiorite	2 850 ± 17	ZR Pb-Pb	Avelar (1996)	
		Rio Maria Granod.	Quartz-Diorite	2.878 ± 4	ZR Pb-Pb	Dall'Agnol et al. (1999)	
		Rio Maria Granod.	Granodiorite	2.877 ± 6	ZR Pb-Pb	Rolando & Macambira (2003)	
		Rio Maria Granod.	Diorite	2.880 ± 4	ZR Pb-Pb	Rolando & Macambira (2003)	
		Agua Fria Trondhjemite	banded trondhjemite	2 864 ± 21	ZR Pb-Pb	Leite et al. (2004)	
TTG		Mogno Trondhjemite	Granitoid	2.871 ± ?	TI U-Pb	Pimentel & Machado (1994)	
		Mogno Trondhjemite	Granitoid	2 87	TI U-Pb	Dall'Agnol et al. (1998)	
Granitoids		Parazonia Tonalite	Granitoid	2.858	TI U-Pb	Pimentel & Machado (1994)	
		Cumaru Granodiorite	Granitoid	2.817 ± 4	ZR Pb-Pb	Lafon et al. (1994)	
		Mata Surrao Granite	Monzogranite	2.872	ZR U-Pb	Rodrigues et al (1992)	
		Mata Surrao Granite	Leucogranite	2 872 ± 10	WR Pb-Pb	Althoff et al. (2000)	
		Mata Surrao Granite	Leucogranite	2.871 ± 7	ZR Pb-Pb	Althoff et al. (2000)	
		Mata Surrao Granite	Leucogranite	2.541	WR Rb-Sr	Duarte et al. (1991)	
		Mata Surrao Granite	Monzogranite	2.881 ± 2	ZR Pb-Pb	Rolando & Macambira (2003)	
		Mata Surrao Granite	Monzogranite	2 875 ± 11	ZR Pb-Pb	Rolando & Macambira (2003)	
		Mata Surrao Granite	Leucogranite	2.872	WR Pb-Pb	Lafon et al. (1994)	
		Guaranta Granite	Leucogranite	2 93	ZR Pb-Pb	Althoff et al. (2000)	
		Xinguara Granite	Granitoid	2.87	ZR Pb-Pb	Dall'Agnol et al. (1998)	
		Xinguara Granite	Leucogranite	2.865 ± 1	ZR Pb-Pb	Leite (2001)	
		Xinguara Granite	Leucogranite	2 875	ZR Pb-Pb	Rolando & Macambira (2002)	
		Inaja Group	Metabasalt	2.988 ± 4	ZR U-Pb	Rolando & Macambira (2003)	
		Lagoa Seca Grp.	Metagraywakes	2 971 ± 18	ZR U-Pb	Macambira (1992)	
	Andorinhas Supergroup		Lagoa Seca Grp.	Felsic Metavolcanic	2.904 +29/-22	ZR U-Pb	Macambira & Lancelot (1992)
			Lagoa Seca Grp.	Felsic Metavolcanic	2.979 ± 5	ZR U-Pb	Pimentel & Machado (1994)
		Identidade Grp.	Metadacite	2 944 ± 88	WR Pb-Pb	Souza (1994)	
	Tucumã Grp.	Metabasalt	2.868 ± 8	ZR Pb-Pb	Avelar et al. (1999)		
Ultramafic		Serra Azul Complex	peridotite	2.970 ± 7	ZR U-Pb	Pimentel & Machado (1994)	
	Caracol Ton.	Tonalite	2.948 ± 5	ZR Pb-Pb	Leite et al. (2004)		
	Caracol Ton.	Tonalite	2.936 ± 3	ZR Pb-Pb	Leite et al. (2004)		
	Caracol Ton.	Tonalite	2.942 ± 2	ZR Pb-Pb	Leite et al. (2004)		
Basement Units		Arco Verde Ton.	Tonalite	2.957 +25/-21	ZR U-Pb	Macambira (1992)	
		Arco Verde Ton.	Tonalite	2.96	ZR U-Pb	Dall'Agnol et al. (1998)	
		Arco Verde Ton.	Tonalite	2.948 ± 7	ZR Pb-Pb	Rolando & Macambira (2002)	
		Arco Verde Ton.	Tonalite	2.988 ± 5	ZR Pb-Pb	Rolando & Macambira (2003)	
		Arco Verde Ton.	Tonalite	2.981 ± 8	ZR Pb-Pb	Rolando & Macambira (2003)	

* WR- whole-rock, ZR- zircon, TI- titanite, MI- mineral

Table 2.3 – Geochronological data from the Archaean and Proterozoic stratigraphic units of the Carajás Geochronological Province separated into 3 geochronological/structural domains (from N to S): the Carajás Region, the Transitional Region and the Rio Maria Granite-Greenstone Terrane.

A considerable number of robust isotopic ages have been obtained from the mineral deposits in the Carajás Terrane. These data are important for deposits hosted in old crustal segments with long geological histories and complex structural evolution, where geochronological ages allow ore formation to be linked to specific structural or geological events.

Table 4 presents isotopical ages for the major deposits in the Carajás Terrane.

- 1) Most metallogenic deposits formed during two main time periods: an Archaean phase at **2.7-2.5 Ga** and a Proterozoic phase at **1.88 Ga**.
- 2) The world-class high tonnage Fe-oxide, Cu-Au Salobo, Igarapé-Bahia-Alemão, Cristalino and Sossego-Sequeirinho deposits are related to mineralizing events at ca. **2.7-2.5 Ga**.
- 3) The smaller to medium size Cu-Au Breves, Target 118, Gameleira, Estrela and Serra Pelada deposits were dated at **1.88 Ga**, similar age to the time of crystallizations of the 1.88 Ga isotropic granitoids in the Amazon Craton.
- 4) A small but significant number of ages are in the range **2.2 to 2.4 Ga** in the Archaean deposits. These can be linked to ore remobilization events triggered by local tectonic activity and associated hydrothermal alteration.

Age histogram plots for the lithological units and mineral deposits show a good correlation in the region as a whole. Three age maxima are observed for the regional lithological units (**Fig. 2.14 A**). They indicate major episodes of igneous (volcanic, plutonic) activity at **1.88, 2.57** and **2.76 Ga**. Two of the three maxima are in accordance with the models presented in (Condie 2000; Parman 2007), which propose that episodic growth of continental crust and supercontinents caused by superevents took place at 2.7, 1.9 and 1.2 Ga. The age interval of **2.57 Ga** can be related to either the plutonism that formed the Itacaiúnas and Old Salobo granites and/or to the tectonic episode that formed the Itacaiúnas shear belt.

The age maxima on the graph of mineral deposits (**Fig. 2.14 B**) coincide well with the regional data suggesting that the deposits are closely associated with the

magmatic activity recorded at 1.88 and 2.76 Ga in the Carajás Terrane. The mineralization dated at 2.57 Ga can be linked to hydrothermal remobilization caused by tectonic reactivation events in the 2581-2497 Ma interval, possibly associated with the latest activity of a WNW-ESE sinistral shear system (Machado et al. 1991).

MINERAL DEPOSITS					
Deposit	Lithology	Material dated	Method	Age (Ma)	Author
Fernando Mine	ore (weathering profile)	Molybdenite	Re-Os	2.592 ± 13	Marschik et al. (2005)
Fernando Mine	ore (weathering profile)	Molybdenite	Re-Os	2.602 ± 13	Marschik et al. (2005)
Serra verde	host rock - metavolcanic	Plagioclase	Pb-Pb	2.747 ± 120	Reis et al. (2000)
Serra verde	ore - massive sulfide	Chalcopyrite-Molybdenite	Pb-Pb	2.509 ± 85	Reis et al. (2000)
Serra verde	ore-cpy-moly-qtz pods inside sulfide body	cpy-moly	Pb-Pb	2.760 ± 77	Reis et al. (2000)
Serra verde	ore - massive sulfide	Apatite	U-Pb	2.362 ± 19	Reis et al. (2000)
Serra verde	ore (primary massive chalcopyrite)	Molybdenite	Re-Os	2.609 ± 13	Marschik et al. (2005)
Gameleira	Mineralized vein	Biotite + Sulfide	Sm-Nd	1700 ± 60	Lindenmayer et al. (2001)
Gameleira	vein sulphide	Whole-Rock	Pb-Pb	2.422 ± 12	Galarza (2002b)
Gameleira	vein sulphide	Whole-Rock	Pb-Pb	2.246 ± 30	Galarza (2002b)
Gameleira	ore	chalcopyrite	Pb leaching	2.218 ± 14	Galarza (2002b)
Gameleira	ore	chalcopyrite	Pb leaching	2.190 ± 42	Galarza (2002b)
Gameleira	biotite schist	Whole-Rock	Sm-Nd	1 958	Pimentel et al. (2003)
Gameleira	metagabro	Whole-Rock	Sm-Nd	2.68	Pimentel et al. (2003)
Gameleira	sienogranite	Zircon	U-Pb	1.583 +9 / -7	Pimentel et al. (2003)
Gameleira	quartz grunerite vein	Whole-Rock	Sm-Nd	1.839 ± 15	Pimentel et al. (2003)
Gameleira	meta andesite	Biotite	Ar-Ar	1.734 ± 8	Pimentel et al. (2003)
Gameleira	biotite in sulfide vein	Whole-Rock	Sm-Nd	1.700 ± 31	Pimentel et al. (2003)
Gameleira	ore (chalcopyrite + molybdenite)	Molybdenite	Re-Os	2.614 ± 14	Marschik et al. (2005)
Salobo	hydrothermal altered gneiss	whole-Rock	Rb-Sr	2.029 ± 21	Gomes et al. (1975)
Salobo	hydrothermal altered gneiss	Amphiboles	K-Ar	1.987 ± 77	Gomes et al. (1975)
Salobo	Cu-Au ore	Chalcocite	Pb leaching	2.762 ± 180	Mellito & Tassinari (1998)
Salobo	iron ore	Magnetite	Pb leaching	2.776 ± 240	Mellito & Tassinari (1998)
Salobo	ore	Chalcopyrite	Pb leaching	2.427 ± 130	Tassinari & Mellito (2001)
Salobo	ore	Magnetite	Pb leaching	2.112 ± 12	Tassinari & Mellito (2001)
Salobo	ore	Tourmaline	Pb leaching	2 587 ± 150	Tassinari & Mellito (2001)
Salobo	vein with bornite/magnetite	Molybdenite	Re-Os	2 576 ± 1	Requia et al. (2003)
Salobo	vein with bornite/magnetite	Molybdenite	Re-Os	2 561 ± 3	Requia et al. (2003)
Salobo	ore	Bornite-Chalcopyrite	Pb leaching	2.579 ± 71	Requia et al. (2003)
Salobo	ore	Magnetite	Pb-Pb	2 291 ± 220	Requia et al. (2003)
Salobo	ore	Chalcocite	Pb-Pb	2.705 ± 42	Tassinari et al. (2003)
Salobo	ore	Remobilized CPY	Pb-Pb	2.427 ± 130	Tassinari et al. (2003)
Salobo	tourmaline quartzite/veins	Tourmaline	Pb-Pb	2 587 ± 150	Tassinari et al. (2003)
Salobo	brecciated iron formation	Magnetite	Pb-Pb	2.112 ± 12	Tassinari et al. (2003)
Salobo	hydrothermal altered gneiss	Whole-Rock	Rb-Sr	2.101 ± 130	Tassinari et al. (2003)
Salobo	garnet-biotite schist	whole-Rock	Sm-Nd	2.424 ± 13	Tassinari et al. (2003)
Alemão	fluorite in carbonatic vein	Fluorite	Sm-Nd	2.313 ± 1000	Santos (2002)
Alemão	fluorite in carbonatic vein	Fluorite	Sm-Nd	2 504 ± 930	Santos (2002)
Alemão	fluorite in carbonatic vein	Fluorite	Sm-Nd	2.580 ± 79	Santos (2002)
Alemão	apatite inclusion in chalcopyrite	Apatite	U-Pb	2.700 ± 8,9	Santos (2002)
Alemão	apatite inclusion in chalcopyrite	Apatite	U-Pb	0.986 ± 2,4	Santos (2002)
Alemão	gold associated with CPY	Gold particles	Pb-Pb	2.575 ± 86	Santos (2002)
Alemão	gold associated with CPY	Gold particles	Pb-Pb	2 810 ± 230	Santos (2002)
Alemão	gold in late carbonatic vein	Gold particles	Pb-Pb	2 595 ± 200	Santos (2002)
Alemão	gold in sulphide breccia associated with cpy	Gold particles	Pb-Pb	2.204 ± 17	Santos (2002)
Alemão	gold in sulphide breccia associated with cpy	Gold particles	Pb-Pb	2 675 ± 130	Santos (2002)
Alemão	gold in sulphide breccia associated with cpy	Gold particles	Pb-Pb	2.556 ± 95	Santos (2002)
Alemão	late gold in sulphide breccias	Gold particles	Pb-Pb	2 651 ± 120	Santos (2002)
Alemão	late gold in sulphide breccias	Gold particles	Pb-Pb	2 555 ± 270	Santos (2002)
Alemão	ore - massive sulphide	chalcopyrite	Pb-Pb	2.521 ± 56	Santos (2002)

Chapter 2

Igarape Bahia	ore	Chalcopyrite	Pb-Pb	2.850 ± 65	Mougeot et al. (1996)
Igarape Bahia	ore	Chalcopyrite + Gold	Pb-Pb	2.764 ± 22	Galarza (2002)
Igarape Bahia	ore	Chalcopyrite	Pb-Pb	2.850 ± 65	Mougeot et al. (1996)
Igarape Bahia	ore (mineralized breccia)	hydrothermal monazite	SHR MP	2.575 ± 12	Tallarico et al. (2005)
Igarape Bahia	copper-gold bearing magnetite breccia	Monazite	SHR MP	2.572 ± 21	Tallarico et al. (2005)
Igarape Bahia	copper-gold bearing magnetite breccia	Monazite	SHR MP	2.592 ± 10	Tallarico et al. (2005)
Igarape Bahia	copper-gold bearing magnetite breccia	Monazite	SHR MP	2.576 ± 17	Tallarico et al. (2005)
Igarape Bahia	copper-gold bearing magnetite breccia	Monazite	SHR MP	2.555 ± 17	Tallarico et al. (2005)
Igarape Bahia	copper-gold bearing magnetite breccia	Monazite	SHR MP	2.561 ± 16	Tallarico et al. (2005)
Igarape Bahia	copper-gold bearing magnetite breccia	Monazite	SHR MP	2.564 ± 24	Tallarico et al. (2005)
Igarape Bahia	copper-gold bearing magnetite breccia	Monazite	SHR MP	2.560 ± 19	Tallarico et al. (2005)
Igarape Bahia	copper-gold bearing magnetite breccia	Monazite	SHR MP	2.557 ± 19	Tallarico et al. (2005)
Igarape Bahia	copper-gold bearing magnetite breccia	Monazite	SHR MP	2.600 ± 33	Tallarico et al. (2005)
Igarape Bahia	copper-gold bearing magnetite breccia	Monazite	SHR MP	2.580 ± 21	Tallarico et al. (2005)
Igarape Bahia	copper-gold bearing magnetite breccia	Monazite	SHR MP	2.542 ± 20	Tallarico et al. (2005)
Igarape Bahia	copper-gold bearing magnetite breccia	Monazite	SHR MP	2.519 ± 19	Tallarico et al. (2005)
Igarape Bahia	copper-gold bearing magnetite breccia	Monazite	SHR MP	2.610 ± 20	Tallarico et al. (2005)
Igarape Bahia	copper-gold bearing magnetite breccia	Monazite	SHR MP	2.554 ± 16	Tallarico et al. (2005)
Igarape Bahia	copper-gold bearing magnetite breccia	Monazite	SHR MP	2.567 ± 17	Tallarico et al. (2005)
Igarape Bahia	copper-gold bearing magnetite breccia	Monazite	SHR MP	2.552 ± 16	Tallarico et al. (2005)
Igarape Bahia	copper-gold bearing magnetite breccia	Monazite	SHR MP	2.583 ± 30	Tallarico et al. (2005)
Igarape Bahia	copper-gold bearing magnetite breccia	Monazite	SHR MP	2.279 ± 35	Tallarico et al. (2005)
Igarape Bahia	ore	Chalcopyrite + Gold	Pb-Pb	2.764 ± 22	Galarza (2002)
Igarape Bahia	ore	Chalcopyrite in gold	Pb-Pb	2.778	Galarza (2002)
Igarape Bahia	ore (hydrothermal breccia)	Chalcopyrite	Pb-Pb	2.772 ± 46	Galarza et al. (2007)
Igarape Bahia	ore (metapyroclastic rocks)	Chalcopyrite	Pb-Pb	2.754 ± 36	Galarza et al. (2007)
Igarape Bahia	ore veinlet (mafic metavolcanic)	Chalcopyrite	Pb-Pb	2.756 ± 24	Galarza et al. (2007)
Igarape Bahia	dikes	Chalcopyrite	Pb-Pb	2.777 ± 22	Galarza et al. (2007)
Igarape Bahia	ore (hydrot breccia+metavolc+gossan)	Gold particles	Pb-Pb	2.744 ± 12	Galarza et al. (2007)
Igarape Bahia	ore (hydrothermal breccia)	Chalcopyrite	Pb leaching	2 385 ± 122	Galarza et al. (2007)
Igarape Bahia	ore (hydrothermal breccia)	Chalcopyrite	Pb leaching	2.417 ± 120	Galarza et al. (2007)
Sossego	ore	Amphiboles	Ar-Ar	2 3	Marschik et al., (2003)
Breves	late to post mineralization veins	Monazite	SHRIMP II	1.875 ± 7	Tallarico et al. (2004)
Breves	late to post mineralization veins	Xenotime	SHRIMP II	1.869 ± 11	Tallarico et al. (2004)
Breves	late to post mineralization veins	Monazite/Xenotime	SHRIMP II	1.872 ± 7	Tallarico et al. (2004)
Aguas Claras	sulfide in quartz vein x cutting gabro sills	Sulphides	Pb-Pb	2.358 ± 42	Silva et al. (2001)
Aguas Claras	hydrothermal altered aguas claras qtz arenite	minerals	Rb-Sr	2.134 ± 64	Silva et al. (2001)
Cristalino	ore - main ore body	Chalcopyrite	Pb-Pb	2.700 ± 29	Soares et al. (2001)
Cristalino	ore - main ore body	Chalcopyrite	Pb-Pb	2.694 ± 19	Soares et al. (2001)
Cristalino	ore - main ore body	Chalcopyrite	Pb-Pb	2.719 ± 36	Soares et al. (2001)
Estrela	quartz-biotite-cooper stockwork vein	monazite	EPMA	1.839 ± 14	Volp et al. (2005)
Estrela	aplite	monazite	EPMA	1.886 ± 19	Volp et al. (2005)
Estrela	aplite	monazite	EPMA	1.827 ± 23	Volp et al. (2005)
Estrela	aplite	monazite	EPMA	1.716 ± 19	Volp et al. (2005)
Estrela	fluorite-sulphide secondary stockwork veins	allanite	EPMA	1.85	Volp et al. (2005)
Estrela	fluorite-sulphide secondary stockwork veins	monazite	EPMA	1.85	Volp et al. (2005)
Serra Pelada	Au ore	monazite	Pb-Th	1.861 ± 45	Grainger et al. (2007)
Serra Pelada	hydrothermal biotite+chalcopyrite+pyrrhotite	biotite	Ar-Ar	1882 ± 3	Grainger et al. (2007)
118	chalcopyrite+xenotime in qtz vein	Xenotime	SHR MP II	1 868 ± 7	Tallarico 2003
118	massive cpy ± bornite ± Fe-oxide ± xenotime	Xenotime	SHRIMP II	1 869 ± 7	Tallarico 2003

Table 2.4 – Geochronological data of the Archean and Paleoproterozoic mineral deposits in the Carajás Terrane.

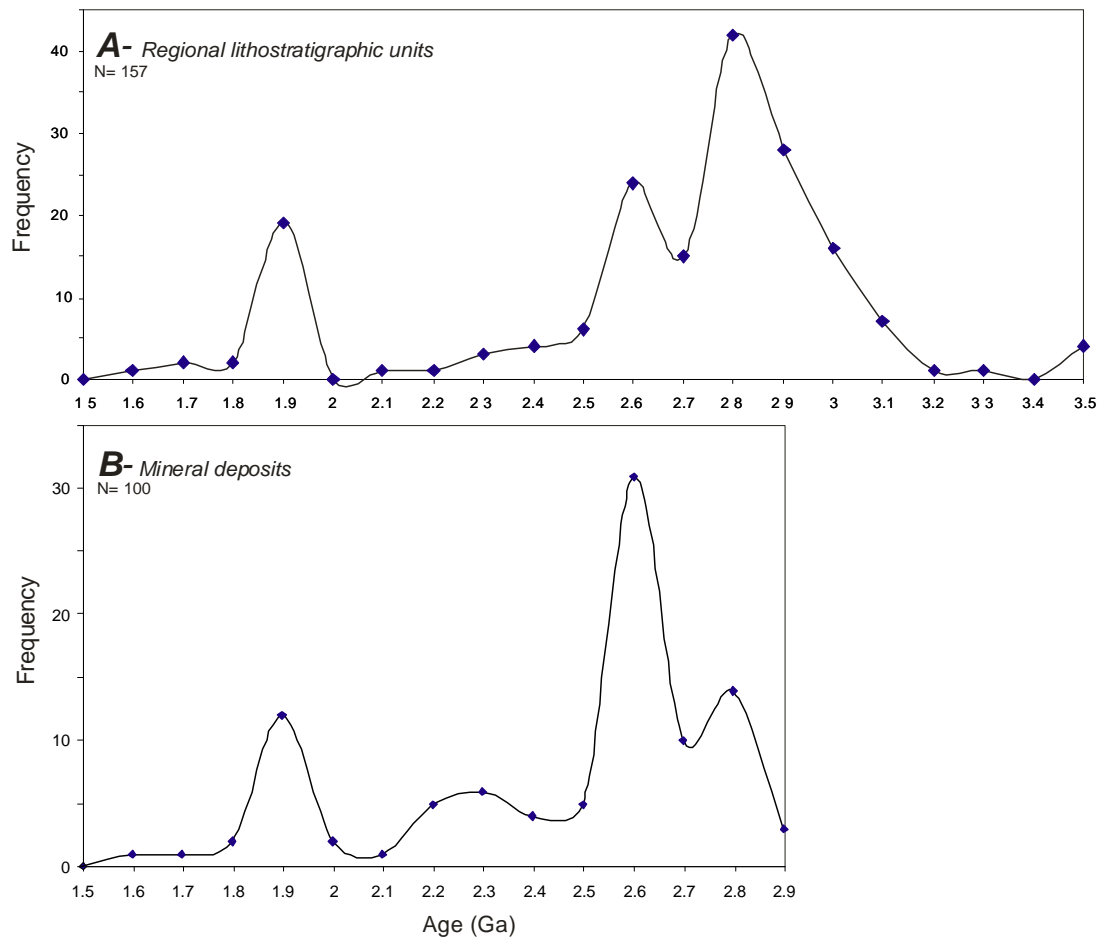


Figure 2.14 – Age histograms for the geochronological data from (A) the regional lithostratigraphic units and (B) the mineral deposits in the Carajás Terrane.

Chapter 3

Investigating ore-lineament relationships using multi-scale lineament analysis and magnetometry in the Carajás Region, Amazon Craton-Brazil

3.1 Introduction

Since the launch of the first LANDSAT satellite in 1972, remotely sensed imagery has become widely available and is used to support a range of applications in areas such as global change research, agriculture, forestry, geology, resource management, geography, mapping and oceanography. From 1984, geological mapping has undergone a dramatic transformation, entering the era of digital technology. Computer-aided mapping, multicriteria analysis, three dimensional representation and geographic information systems (GIS) have displaced conventional paper-based techniques (Scanvic et al. 1997).

This new data has been subjected in many geological studies to lineament interpretation and analysis. The technique has been applied to structural mapping (Harrys 1991; Raghavan et al. 1993); mineral and hydrocarbon prospecting (Bonham-Carter 1985; Mirsa et al. 1991; Hein 1999); studies of groundwater flow-paths and aquifer controls (Mabee et al. 1994; Ferguson et al. 1997) and the

prediction of ground control problems related to underground mining activities and structures (Kane et al. 1996).

(Sabins 1987) defines lineaments as *straight linear features, presumably expressing a sub-surface phenomenon that differs distinctly from the patterns of adjacent features*. The processes that form these lineaments may influence its properties such as size, spatial distribution pattern and trend. Spatial analysis can help to unravel and provide insights into causative geological processes and may also reveal features that assist in the testing or formulation of hypotheses about geological processes (Clark et al. 1994). It is also important to interpret lineaments at different scales because, within a single dataset, differing features become evident at differing scales. Discrete lineaments are more evident on large scale maps, whereas regional lineament clusters or corridors are more easily identified in small scale maps (Boucher 1997).

Lineaments maps and analyses have proved to be an effective, relatively quick and cost-effective tool during mineral resource exploration and were used, for example, in the discovery of many of the classical ore deposits in Australia. These include: the Olympic Dam Cu-Au-U deposit (O'Driscoll 1985; Lalor 1987); the Century Pb-Zn deposit (Woodall 1992); the Boddington, Plutonic and Kanowna Belle gold deposits (Woodall 1991); the Kambalda-St Ives nickel deposit (Odriscoll 1986); and the Broken Hill nickel and gold deposit (O'Driscoll 1983). These discoveries were associated with lineaments and illustrate that this inexpensive and straightforward technique can play an important role in prospecting especially in the initial stages of mineral exploration campaigns.

This study investigates lineaments in an area within the Carajás Terrane in the Amazon Craton, Brazil. Here, several high economic Cu-Au deposits have

already been identified, and prospecting campaigns are still in development with some successful discoveries recently made. Most of the deposits are structurally controlled and display close association with large scale faults or shear zones. These structures are typically expressed on Earth's surface as sets of lineaments and an analysis of these features helps to better characterize the regional tectonic framework in what is in reality a structurally complex area. This chapter presents an integrated study of topographic (surface) and magnetic (subsurface) lineaments extracted from LANDSAT, SRTM images and aeromagnetic surveys. The datasets were analysed using GIS tools to determine lineaments characteristics and the main tectonic features present in the area. An investigation of what can be learnt from a multi-scale observation and interpretation of lineaments is also presented and it is shown how these may be related to underlying, geological controls and the development of ore deposits.

3.2 Regional geological setting

The study area lies within the Carajás Terrane situated in the southern portion of the Amazon Craton, part of the Central Brazil Shield (see **Fig. 3.1**). It used to be part of the Central Amazonian Province (Tassinari et al. 1999), but recent studies consider it to be an independent tectonic province (Santos et al. 2000). It is bounded to the east by the Neoproterozoic Araguaia Belt and to the west is overlain by Paleoproterozoic volcano-plutonic and sedimentary rocks of the Uatumã Supergroup (Araújo et al. 1991; Macambira et al. 1995), part of the Irixi-Xingu geochronological domain (see **Fig. 3.1**). To the south it is in contact with the Achaean Rio Maria Granite-Greenstone Terrane (DOCEGEO 1988; Huhn et al. 1988), whilst to the

north, it is covered by Palaeozoic and Cenozoic sediments of the Amazon Basin (Pinheiro 1997). It represents an important metallogenic province with several major iron, copper, gold, manganese and tin deposits and contains some of the oldest and best preserved sequences of Archaean-Proterozoic rocks in the craton (Galarza et al. 2007).

The Carajás Geochronological Province was formed and stabilized during the Archaean and later affected by extensive Palaeoproterozoic magmatism characterized by anorogenic granitic intrusions and mafic and felsic dykes (Pidgeon et al. 2000). It is divided into two major geochronological domains (see **Fig. 3.2**): the *Rio Maria Granite–Greenstone Terrane* (3.05 to 2.86 Ga) to the south, and the *Carajás Terrane*, named after the prominent *Carajás Ridge* (2.76 to 2.55 Ga) to the north (DOCEGEO 1988; Machado et al. 1991; Macambira et al. 1995; Dall'Agnol et al. 1997). Both domains exhibit distinctive lithological, tectonic, stratigraphic and geochronological characteristics, but their mutual boundaries remain poorly defined (Galarza et al. 2007).

The oldest rocks present in the Carajás Province are located in the Rio Maria Granite Greenstone Terrain (Macambira et al. 1995), with granitoids (Arco Verde Tonalite, Caracol Complex, Rio Maria Granodiorite, Mogno Trondhjemite, Xinguara and Mata Surrão Granite) intruding older greenstone-belt sequences of the Andorinhas Supergroup (**Fig. 3.2**).

The Carajás Terrane (see geological map on **Fig. 3.3**) comprises two main Archaean and Proterozoic domains identified based on their markedly differing geological characteristics (Araújo et al. 1991; Pinheiro 1997).

The High Grade Granite-Gneiss Terrain or *Basement Assemblage* is represented by granulite facies orthogneisses of the Pium Complex which are

tectonically intrusive into upper amphibolite facies tonalitic gneisses, granodiorites and migmatites of the Xingu Complex (see **Table 3.1 for ages**). Subvertical, WNW-ESE-trending mylonitic fabrics formed coeval with the nucleation of the broad structure of the Carajás Terrane and are thought to have subsequently experienced several episodes of reactivation (Pinheiro 1997; Pinheiro et al. 1997a; Holdsworth et al. 2000).

Low Grade Supracrustal Volcanic and Sedimentary Sequences or the *Cover Assemblage* include the Grão-Para; Igarapé Salobo and Igarapé Pojuca groups (see **Table 3.1 for ages**). These units show a range of metamorphic grades from virtually undeformed greenschist facies in the inner part of the belt, to intensely sheared amphibolite-granulite facies in the Cinzento Strike-Slip System (DOCEGEO 1988; Lindenmayer et al. 1991; Pinheiro et al. 1997a). The Cover assemblage is composed of older metavolcanic and sedimentary ironstones and clastic sequences, overlaid by a clastic sequence of shallow-water marine to fluvial deposits of the Águas Claras Formation, which is intruded by a gabbroic sill that constrains the minimum age of the formation.

Syn-tectonic, Neoarchean, alkaline granitoids and diorites of the Plaque Suite are intruded into rocks of both the Basement and Cover assemblages. These intrusive units are typically elongate and lie parallel to the strike of the regional WNW-ESE foliation (Holdsworth et al. 2000; Barros et al. 2001; Sardinha et al. 2006).

Palaeoproterozoic plutons intrude almost all the rocks of both basement and low-grade cover sequences in the Carajás area and the Rio Maria granite-greenstone terrane (Machado et al. 1991; Dall'Agnol et al. 1999). These isotropic granitoids display monzogarnitic-syenogranitic composition, coarse to medium grained and are

markedly discordant showing sharp cross-cutting contacts with the Archaean country rocks (Ramo et al. 2002; Dall'Agnol et al. 2005).

The Carajás and Cinzento strike-slip systems (**Fig. 3.3**) are the most prominent structures within the Carajás Terrane. These fault systems were formed by at least three cycles of brittle-ductile strike-slip reactivation at low metamorphic grades, after the initial development of the terrane governed by ductile shear zones under amphibolite facies metamorphic conditions (Pinheiro 1997; Holdsworth et al. 2000). They form an E-W trending set of discontinuous, sigmoidal, anastomosing lineaments almost 200 km long with a maximum width of 80 km. The geometry of these fault zones appears to be strongly controlled by the orientation of earlier shear zone fabrics in the basement. A later set of N-S to NNE-SSW fault lineaments cross-cut the main sigmoidal structures (Pinheiro 1997; Holdsworth et al. 2000). The complex tectonic history of the Carajás region, dominated by transpressional and transtensional events is summarized in **Table 3.2**.

3.3 Dataset and Methods

The 6 major stages of data analysis employed during the study are summarised in **Fig. 3.4**, highlighting the key data manipulation and processing methods. Data were obtained from global databases that offer accessible, good quality coverage of most of the whole globe. All lineament picking and analysis were carried out using ESRI ArcMap software.

3.3.1 Imagery acquisition and processing

The remotely sensed data used in this study includes LANDSAT 7 ETM images and Shuttle Radar Topography Mission (SRTM) elevation-DEM data. The LANDSAT images were obtained from the Global Land Cover Facility (GLCF) website (<http://glcf.umiacs.umd.edu/index.shtml>), a research partnership between the University of Maryland and NASA. The two scenes utilized were acquired on 09/07/2001 (Path 224, Row 064) and 31/07/2000 (Path 223, Row 064). The final image used in this study is a coloured composition using the band 7-2-1 (RGB), blended with a band 8 panchromatic with spatial resolution of 15 m (**Fig. 3.5A**). The bands were combined using the software Global Mapper v 7.04. The LANDSAT bands were imported into the program and, by using the option Overlay Control Centre, were merged according to the parameters presented in **Figure 3.5 B**. No directional edge filters or algorithms were applied to the image.

SRTM V2 elevation data were downloaded from the NASA Jet Propulsion Laboratory website (ftp://e0srp01u.ecs.nasa.gov/srtm/version2/SRTM3/South_America/). The six SRTM, C-band radar data files (S06W050-051-052 and S07W050-051-052) have a moderate spatial resolution of 3 arc seconds or 90 m with vertical and horizontal accuracy of 12 m and 50 m respectively. Topographic features were enhanced by increasing vertical exaggeration by 15 and applying synthetic directional shading filters to produce four base hill shaded raster images (.TIFF) with directional illumination at 0°az, 45°az, 90°az and 120°az at a constant elevation angle of 2° (**Fig 3.6**).

After processing to enhance topographic features, the images were imported into a Geographic Information System (GIS) environment where lineaments were

picked (extracted). Existing lineament maps from (Lima 2002) and (Oliveira 2002), covering part of the area were georeferenced and digitized using ESRI ArcMap for semi-detailed analysis and to compare to any identified features.

3.3.2 Lineament Extraction

Lineament extraction was performed manually from satellite images by digitization of three main visually interpreted categories of linear features: (1) topographic features such as straight valleys and scarps; (2) rock or textural boundaries; and (3) sharp tonal variation boundaries. Manual extraction has the disadvantage of being time consuming, and its reliability depends on the experience and knowledge of the user; it is also prone to user bias. However, despite increasing popularity and speed, automated lineament extraction was not adopted as testing showed that it typically produced shorter, discontinuous, straight lineaments when compared to those manually extracted. The automated method therefore, is particularly useful for studies where the user requests are mainly speed and directional analysis, with geometry or length being less important parameters.

Lineaments for the regional analysis were extracted from the satellite images at four fixed scales, without zooming during extraction: (1) 1:1 000 000; (2) 1: 750 000; (3) 1:500 000; and (4) 1:250 000. The digitized lineaments maps, combined with manual extraction from the SRTM images to fill gaps on the existing dataset were used for finer scale lineament identification

3.3.3 Lineament treatment/correction

After extraction, lineaments may contain errors introduced by the interpreter during the digitizing process such as extra nodes, overlapping and/or lineament duplication. This can lead to exaggeration of lineament length, additional numbers of lineaments and cross-points and inaccuracy in the lineament density map. These errors were corrected using the script '*Lineament Analysis 20040611* for ArcView 3.1' (<http://arcscripsts.esri.com/details.asp?dbid=13579>) (Kim et al. 2004).

Two tools were utilized to reduce data inaccuracy: (i) the *Remove-Node* tool (**Fig. 3.7 A**) which reduces the number of redundant nodes contained in the interpreted lineaments, preparing the dataset for the next step; and (ii) the *Generalize* tool (**Fig. 3.7 B**) which divides a single lineament into two based on the angle formed between the intersection of the lineament's segments (Kim et al. 2004). These tools were used because of their specific development to minimize input errors inherent to the digitization process, optimizing the original digitized lineaments map data. Additionally, they have proved their efficiency in previous studies that used lineaments analysis for e.g.: (a) aid the construction of a transpressional model in a structurally complex region (Wilson et al. 2006); and (b) to examine the relations between lineament architecture and *in-situ* rocks stress on groundwater flow (Henriksen et al. 2006).

3.3.4 Lineament Analysis

The analysis was performed by studying and analysing the length and azimuth attributes of lineaments using histograms, X/Y plots, rose diagrams and density maps for lineaments and lineament intersection points.

Length and azimuth were calculated using the EasyCalculate 5.0 script (<http://arcscripsts.esri.com/details.asp?dbid=12224>). Histograms for length and azimuth together with azimuth against length plots were created using standard statistical software (Microsoft Excel and SigmaPlot 10) and directional rose diagrams were created using the EZ-ROSE computer program (Baas 2000). Lineament intersection points were generated using the tool Dist-to-cross-point in the script *Lineament Analysis 20040611* (Kim et al. 2004).

Lineament density maps were constructed to assess the frequency of lineaments per unit area by using the density analysis from the Spatial Analyst tools in ArcMap. This tool runs a circle around the centre of each grid cell using a defined search radius (**Fig. 3.8**). The sum of lineament lengths inside the circle is divided by the circle's area, giving the density value (Silverman 1986). Default values for 'search radius' and 'cell size' were used, as created within the Arc map software. These values satisfactorily delineated the resolution of density patterns across the study region. Investigations into other values for these parameters resulted in reduction in the precision of the general patterns in the data.

Lineaments were also compared and analyzed in relation to their geological character/control. This was carried out by considering their occurrence within individual geological and major tectono-stratigraphic units. This was done to investigate the role of pre-existing basement structures during the deposition and structural evolution of the Cover Assemblage and also to see if there was a spatial

control on the distribution of lineaments in particular geological units with specific ages. The spatial analysis of lineaments was carried out by overlying a square network on the lineament datasets and producing rose diagrams for each individual unit cell in the network. The procedures and methods described in this paragraph were successfully used to study lineaments in the whole Norway and in the Almazan Basin, Spain (Cortes et al. 1998; Gabrielsen et al. 2002).

3.3.5 Geophysics – Magnetic Lineaments

Aeromagnetic data was obtained from two surveys from the Brazilian National Department of Mineral Production (DNPM): (i) block 3 of the Geophysical Survey Program Brazil-Canada, 1975, total count, spacing 2 km; and (ii) Carajás Project (Area I), 1988, IGRF, spacing 2 km. Linear magnetic anomalies were visually identified and manually extracted in a GIS environment to create vector maps containing magnetic lineaments.

3.4 Results – Lineament Characterization

The lineaments extracted from the remotely sensed images are represented by five vector maps covering two study areas within the Carajás Terrane (see dashed and dotted lines in **Fig. 3.9**). On a regional scale, four maps were produced by picking lineaments at 4 different scales: 1:1 000 000; 1:750 000; 1:500 000 and 1:250 000 (**Fig. 3.10**). A smaller study region (indicated by dotted line in **Fig. 3.9**) was selected to examine the local scale features which include a copper deposit and a smaller area studied in detail and described in Chapters 4 and 5. The finer scale

lineaments datasets of (Lima 2002) and (Oliveira 2002) were adopted for the lineaments analysis of this area (**Fig. 3.11**). Additionally lineaments extracted from STRM images were used to infill areas with no or sparse data. The lineaments datasets from (Lima 2002) and (Oliveira 2002) comprise raw lineaments only and were processed using the lineaments analysis methods previously described.

3.4.1 Length Analysis

Length attributes were investigated by analysing histograms and statistical values for each of the five vector maps (**Fig. 3.12**). Lineaments extracted at larger scales are more numerous and, on average, are shorter than those picked at smaller scales. Histograms for lineament lengths at all analysed scales show log-normal distribution with an asymmetric tail towards the right (longer lengths). The plots show a consistent similarity in the style of distribution but with a notable widening of the histogram base as the scale decreases. Meaning that, the range of lineaments lengths is directly proportional to the scale of observation (i.e. the finer the scale of observation, the less variation in lineaments length is noticed). Lineament lengths analysed according to geological domain are illustrated in **Figure 3.13**. At 1: 750 000; 1:500 000 and 1:250 000 scales, lineaments are more numerous and shorter within the Cover Assemblage domain compared to the Basement Assemblage domain. However, at 1:1 000 000 and detailed scales, in the Cover Assemblage the lineaments are less numerous but longer. The ratios for numbers of lineaments in the Cover to Basement Assemblage domains from small to large scales are 2.5; 2.4; 2.25; 1.9 and 0.7, which indicates that the as the scale increases, it becomes easier to

detect lineaments within the Basement Assemblage. Therefore, the longest, crustal scale lineaments are evident in the basement rocks.

3.4.2 Orientation Analysis

Lineaments trends were studied by: (1) creating histograms of azimuth and rose diagrams to identify preferred orientations within each dataset (**Fig. 3.14**); and (2) creating maps for the lineaments separated according to the main directions recognized in the rose diagrams (**Fig. 3.15**). At a regional scale, five main lineament directions were recognized: NW-SE (I), NW-SE (II), E-W to WNW-ESE, NE-SW and N-S. The lineaments trending NW-SE were grouped into two sets (*I* – 120°-139° Az and *II* – 140°-150° Az) because: (a) the set II mainly occurs within the cover domain while the set I is widespread; and (b) the set II appears to be late, with few lineaments cross-cutting the set I. The NW-SE and N-S directions have respectively the highest and lowest statistical weight for both histograms and rose diagrams. For the most part, there is no significant change in lineament directions observed when sorting the data into geological domains, with similar patterns observed in both cover and basement rose diagrams. However, in the basement domain at 1:1 000 000 scale, there is a strong NE-SW directional component (**Fig. 3.14 A**), weakly manifested in the other data sets (**Fig. 3.14 B, C, D**).

Maps were created with lineaments separated into sets according to the five main azimuth directions identified in order to highlight the spatial distributions of the main directional sets (**Fig. 3.15**). Lineaments are generally straight to slightly curved, continuous, parallel to sub-parallel and display fairly regular spacing. It is apparent that the NW-SE I and E-W/ESE-WNW sets are numerically dominant with

1699 and 1364 lineaments respectively. Few lineaments are orientated N-S with only 284 in total.

Although the dominant lineament direction is variable, there is a distinct similarity in the mean length between all azimuth directions, apart from the NE-SW set. This set has a length two times longer than the average length of all other sets, which seems to explain the NE-SW spike in the orientation data at 1:1 000 000 (see **Fig. 3.14**). This information suggests that the NE-SW lineaments are potentially linked to major structures in the study region.

All five lineament sets are observed within both cover and basement domains in the regional area. The NW-SE I, E-W/ESE-WNW and NE-SW sets have almost equal proportions of lineaments in both geological domains (**Fig. 3.15 B, C, D**). The sets NW-SE II and N-S exhibit some preferential concentrations, with between 80-90% developed in the Cover Assemblage (**Fig. 3.15 E, F**).

The lineaments identified within the area chosen for the more detailed analysis exhibit a complex network of interconnected, straight and continuous-to-segmented lines, which occur in various directions as shown in the histograms and stereonet in **Figure 3.14 E**. A more detailed investigation of the lineament azimuths (**Fig. 3.16 A**) reveals six main directions: N-S, NE-SW I, NE-SW II, E-W, NW-SE I and NW-SE II. The spatial distribution and geometrical characteristics of these main sets are presented in **Figure 3.16**. The E-W (85°-108° Az) set is the dominant direction, with 1445 lineaments, homogeneously distributed within the area (**Fig. 3.16 E**). The NW-SE I (109°-126° Az) and NW-SE II (134°-152° Az) sets occur as spatially elongate zones with 917 and 896 counts respectively (**Fig. 3.16 F/G**). The NE-SW I (40°-53° Az), N-S (0°-10° & 173°-180° Az) and NE-SW II (58°-73° Az) sets are the least abundant directions defining elongate zones formed by

discontinuous lineaments with a regularly spacing (**Figs 3.16 B, C, D**). All the sets of lineaments show similar lengths with an average of 747 m and +/- mean length of 769m and 629 m.

3.4.3 Lineament Length vs. Azimuth

Lineament length vs. azimuth relationships at the different scales analysed are presented in **Figure 3.17**. These results indicate that WNW-ESE to NW-SE lineaments are numerically dominant in the 0-7000 m interval whilst NE-SW lineaments are dominant in the size interval 10000-20000m (**Fig. 3.17**). The length–direction relationship indicates that the mean direction vector progressively shifts from NW-SE to NE-SW as the length of the lineaments increases.

Lineaments analysed at finer scales do not show any clearly defined length–direction relationship in the interval 0-625 m. E-W sets dominate the interval 750-1500m and, as length interval increases to 3000m, the NE-SW set becomes prominent. Within the length interval 3000-5000m, E-W, NW-SE and NE-SW sets coexist in nearly equal proportions.

3.4.4 Lineament Density

Density maps for lineaments extracted at regional and finer scales (**Fig. 3.18**) show spatial distributions and cumulative concentrations of lineament lengths (meters) per square kilometre. Density values are heterogeneous across the analysed areas. At regional scales, density anomalies show elongated patterns oriented along WNW-ESE and NE-SW directions, with higher values concentrated mainly within

the Cover Assemblage domains (**Fig. 3.18 A/B/C/D**). The main density anomalies for each regional dataset are indicated by dotted ellipses (**Fig. 3.18 F**) that spatially correlate with the density map anomalies for the total combined lineaments (**Fig. 3.18 E**). At the detailed scale, the density anomalies show diffuse patterns with sub-circular shaped clusters displaying subtle alignments in an E-W direction at the centre of the map (**Fig. 3.18 G**).

3.4.5 Lineament Intersections

Intersections at regional scales are characterized by sparse clusters of dots with heterogeneous spatial distributions (**Fig. 3.19**). Numbers of intersections do not show significant variations in relation to the scale of observation. Intersections form NE-SW aligned clusters at the four regional studied scales with a predominance of points located in the Cover Assemblage and at its contacts with the underlying Basement Assemblage. Lineament intersections for the dataset extracted at finer scales are numerous and occur mainly as: (i) spatially sparse dots; (ii) sub-circular clusters with high densities of dots; and (iii) aligned dots forming trails oriented predominantly N-S, NE-SW and NW-SE (**Fig. 3.19 F**). Lineament intersections density anomalies at regional and detailed scales (**Fig. 3.19 G, H**) concur well with the lineament density anomalies previously presented.

3.4.6 Spatial Analysis of Orientations

The spatial variation of lineament orientations was investigated using a fishnet grid with cell sizes: (i) 10 km at regional scale (**Fig. 3.20 A**); and (ii) 2 km at

finer scale (**Fig. 3.20 B**). The fishnet analysis revealed six major directional domains: (1) WNW-ESE to WSW-ENE; (2) NW-SE; (3) NE-SW; (4) N-S; (5) bimodal; and (6) multidirectional. Regionally, the NE-SW directional domains are dominant in 48% of the central part of the map and in some narrow zones in the eastern and western portions. The WNW-ESE to WSW-ENE domains cover 23% of the grid as elongated clusters mainly located close to the margins of the area. NE-SW domains occur in the south of the map as two clusters composing 6% of the grid. The bimodal and multidirectional domains represent 14% and 8% of the grid while the N-S domain is not statistically representative.

The area analysed at a finer scale (**Fig. 3.20 B**) shows a heterogeneous spatial distribution for the directional domains where: (i) the WNW-ESE to WSW-ENE set has 29% coverage concentrated in the western and central parts; (ii) the NW-SE set dominates 19% of the grid, with a slightly concentration in the eastern part of the map; (iii) the NE-SW set are distributed in elongate arrays of four to five cells composing 11% of the grid; and (iv) the N-S covers 8% and is sparsely distributed. Direction cells for the bimodal and multidirectional domains correspond to 14% and 18% of the grid.

3.4.7 Lineaments and Geology

Lineaments are present in all outcropping geological units of the Carajás Region. **Figure 3.21** shows how the lineament distributions are related to the nine major geological units recognized in the area. Lineaments with azimuths in the interval 110° - 140° Az (WNW-ESE and NW-SE) occur in all geological units, showing high relative frequencies from 6 to 45%. NE-SW lineaments also show

records in all geological units, but with smaller frequencies of 2 to 25%. This set has more expression in the Basement Assemblage than in the younger geological units. The E-W set is observed in the units of both Basement and Cover Assemblage but is almost absent in the younger anorogenic granites and Gorotire Formation. N-S lineaments have a notable presence in the younger geological units and a much weaker expression within the Basement Assemblage being entirely absent in the Pium Complex. The anorogenic granites and sedimentary rocks of the Gorotire formation (relatively younger units) are preferentially cross-cut by lineaments with NW-SE and NE-SW orientations.

3.4.8 Magnetic Lineaments

Magnetic anomalies can be reliable subsurface indicators of tectonic structures e.g. (Hussein et al. 1996; Chernicoff et al. 2002; Austin et al. 2008; McLean et al. 2009), and can be considered together with topographic/geological lineaments in order to constrain surface and subsurface interpretations. The magnetic surveys analysed in this study (**Fig. 3.22 A and C**) and the interpreted lineament maps (**Fig. 3.22 B and D, Fig. 3.23 A and B**) show prominent linear NE-SW magnetic anomalies associated with – and possibly cross-cutting – sigmoidally curved WNW-ESE lineaments with an open “Z”- shaped geometry. The NE-SW lineaments are labelled *F1*, *F2* and *F3* and display a consistent 070° az, comprising a series of straight continuous segments, which can be up to 450 km long, separated by a distance of about 85 km (*F1-F2*) and 35 km (*F2-F3*). The sigmoidal geometry is best developed within the Basement Assemblage domains due to the low magnetic response in the areas of Cover Assemblage rocks. Another set of NE-SW lineaments

trending 045° Az, appears to cross-cut the WNW-ESE lineaments and may be linked to the main NE-SW set (070° Az). Some of the more prominent WNW-ESE lineaments appear to correspond to the Cinzento, Itacaiúnas, Carajás and Canaã Faults (see **Fig. 3.22 D**).

Major topographic lineaments (**Fig. 3.23 C**) were obtained by integrating all lineaments from different scales onto a single map and visually selecting the longest and most prominent segments. The comparison between the surface and magnetic lineament maps shows the following: (1) the WNW-ESE sigmoidal lineaments are clearly observed in both datasets; (2) the most prominent structures, trending NE-SW (70° Az) (F1, F2 and F3) were identified in all datasets; (3) the NE-SW (45° Az) set are present on the magnetic surveys but only one prominent trace (F4) was identified in the surface set ; and (4) the N-S and NW-SE sets detected in the surface lineament analysis are not clearly defined in the magnetic surveys.

Assuming that the NE-SW faults are strike slip faults, the geometric association with the sigmoidal features superficially suggests a sinistral sense of shear, i.e. F1-3 would correspond to regional-scale C' slip or Reidel shear surfaces (**Fig. 3.23D**) (Tchalenko 1968; Tchalenko 1970; Platt 1984).

3.4.9 Lineaments and Mineral Deposits – Spatial Relationships

The spatial association between known mineral deposits and lineaments can be assessed visually. At regional scales, five major ore deposits show a close geographical proximity to well-defined lineament density anomalies (see **Fig. 3.18 E**): Salobo, Breves, Águas Claras, Estrela and Sereno. At finer scales (**Fig 3.18 G**),

the deposits 118, Vermelho, Cristalino and Estrela are located adjacent to or within zones of maximum lineament density.

This suggests a clear association between mineral deposits and major topographic or magnetic lineaments. Ore deposits – mainly Au, Cu, Pt and Ni – occur regionally in three main clusters (indicated in **Fig. 3.24**) covering areas of 500 to 700 km². Clusters C1 and C2 are located in the eastern part of the area, adjacent to the towns of Parauapebas and Canaã dos Carajás. They include a set of major deposits (Sossego, 118, Cristalino, Serra Pelada) and minor occurrences sited along the regional-scale NE-SW lineaments F2 and F3 in areas where these features intersect major zones of prominent WNW-ESE lineaments. Cluster C3 lies in the northwest portion of the Carajás Ridge, comprising the world class Salobo and other deposits apparently associated with WNW-ESE lineaments, including the Carajás and Cinzento fault zones.

3.5 Discussion

3.5.1 General Aspects

The topographic lineaments in Carajás show four main directions (in order of importance): NW-SE, E-W to WNW-ESE, NE-SW and N-S. The recognition of these sets concurs generally with the findings of previous remote sensing studies in the region (Nunes 2002; Veneziani et al. 2004; Carneiro et al. 2006).

The lineaments in the Basement and Cover Assemblages show statistically significant differences in length, orientation and density attributes. Granitic basement typically shows numerous and longer NE-SW lineaments, with relatively lower

lineaments density, while the Cover Assemblage exhibits abundant, shorter NW-SE lineaments forming domains of higher lineaments density. Long NE-SW lineaments probably correspond to major crustal scale fault zones, which appears to affect mainly the basement and possibly cross-cut and displace early WNW-ESE structures. These fault zones apparently delimit the eastern and western outcropping boundaries of the Cover Assemblage in map view (e.g. note F1 and F3 lineaments in **Fig. 3.23**). The F2 lineament runs across the centre of the Carajás structure but is not expressed clearly at the surface as a topographic feature within the Cover Assemblage domain. If this lineament corresponds to a fault, it may indicate that this structure is older than the Grão-Para Group and Águas Claras Formation.

The Cover Assemblage displays well-developed NW-SE lineaments that may represent: (i) bedding; (ii) tectonic contacts between basement and cover assemblages; (iii) subordinate faults that propagated from major WNW-ESE faults e.g. Cinzento, Carajás and Itacaiúnas Faults; or (iv) some combination of these features. N-S lineaments occur in both Basement and Cover Assemblages and likely correspond to regionally recognised normal faults or diabase dikes e.g. (Pinheiro et al. 1997b; Pinheiro et al. 1997a; Holdsworth et al. 2000). These structures appear to truncate all the other lineaments.

3.5.2 Lineaments length distribution

Lineament lengths show log-normal distributions for all analysed scales. In most cases, differences in length distributions between sets with distinct trends are insignificant. The consistency in the type of length distribution for the five analysed scales even when comparing basement and cover may indicate that the studied

system of lineaments is scale-invariant. Log-normal distributions have been traditionally used to describe fracture length distributions and many raw fracture datasets show an apparently good fit to this distribution (Bonnet et al. 2001). However, in recent years, several studies have shown that fracture systems are scale-invariant, having fractal geometry and show that its properties (i.e. length, displacement) follow a power-law relationship e.g. (Main et al. 1990; Scholz 1990; Dawers et al. 1993). So, why do the lineaments in Carajás show a log-normal rather than power-law relation? (Segall et al. 1983; Odling 1997 and) provide a fairly good explanation for the matter. They propose that resolution effects imposed on a power law population can result in a log-normal distribution caused by a combination of sampling effects known as truncation (short trace lengths are inadequately resolved) and censoring (long traces not totally sampled). The resolution effect certainly affected the analysed lineaments dataset, which were picked at fixed scales, not permitting to zoom into the very small lineaments neither zooming out to capture the full length of the regional traces. Structures with fractal geometry imply that regardless of the scale which the system is observed, it looks the same. In the studied area, this finding has important implications for future studies on characterizing faults or shear zones networks and predicting the connectivity of vein system in the mineral deposits.

3.5.3 Lineaments density and intersections

Lineaments high density domains and intersections show clear spatial correlation, indicating that the high density anomalies were produced by intersections of non-parallel lineaments. The intersection clusters are localized especially where regional

scale NE-SW lineaments cross-cut WNW-ESE structures generating highly fractured zones. Importantly, many of these zones lie in close proximity to some of the major mineral deposits in the region.

3.5.4 Lineaments and geology

Lineament occurrence is not strongly determined by geological units. Distinct units may show a statistical abundance of certain lineament sets in relation to others, but generally, the main Basement and Cover Assemblage domains mutually record all lineaments sets identified (see **Fig. 3.21**). This may indicate that both assemblages were simultaneously affected by the processes that formed the present lineaments in the rocks. If these features correspond to faults, then it is likely that rheological contrast influenced the mechanical behaviour of the distinct units, controlling the length and frequency of the resulting lineaments. Reactivation of pre-existing structures in the granitic basement may also have affected the overlying volcanic and sedimentary sequences.

Magnetic and topographic lineaments show a good spatial agreement, implying that near surface geological and subsurface geophysical features follow systematic distribution patterns, genetically linked to specific major geological structures. This relationship is recognized in many geological settings and its main implications are concerned with crustal architecture characterization and mineral potential e.g. (Dentith et al. 1993; Hill et al. 2002; Airo et al. 2004).

3.6 Implications for mineral Exploration

The intersections of the major WNW-ESE and NE-SW lineaments show a close spatial relationship to the location of major mineral deposits and indicates that the main geological structures – likely fault zones – have an important control on the location and development of ore bodies (see **Fig. 3.24**). This could imply, for example, that these intersections may have channelled and controlled fluid flow migration through faults, acting as structural traps where fluid pressure conditions have changed, causing mineral precipitation. This hypothesis is consistent with previous models that explain how faults promote fluid migration throughout the crust during deformation, forming mineral deposits (Sibson 1996; Sanderson 1999). The scenario described in this paper is similar to the examples presented by (Odriscoll 1986) for lineament-ore relationships observed in the Precambrian cratons of Australia.

3.7 Conclusions

The combined analysis of lineaments from multi-scale surface observations and interpretations of magnetic field anomalies allows a number of major lineaments of likely geological origins to be recognised and characterised in the Carajás Region. Many of these features likely correspond to regional scale fault structures and the close link between fault/lineament intersections and the location of major ore deposits is similar to that observed in other cratonic region, e.g. Australia (Odriscoll 1986) and Abitibi Belt, Canada (Kerrich 1986b). It exemplifies a relatively common scenario where old rock sequences are cross-cut by regional structures/belts that

given the presence of suitable conditions, may facilitate and control the formation of ore deposits. The connection between ore deposits and major lineaments has important implications for mineral exploration in the area, since most current metallogenic theories tend to relate mineralization mainly to hydrothermal activity produced by magmatic events and not to fault movements.

Collectively, the major conclusions of the lineaments study include:

- The main sets of lineaments identified in the surface and sub-surface are: WNW-ESE, E-W, NE-SW, NW-SE and N-S.
- The lineaments are heterogeneously distributed in the area.
- The Cover Assemblage is characterized by short, high density NW-SE lineaments while the Basement Assemblage domain shows long, low density and dominantly NE-SW lineaments.
- The lineaments system appears to be scale independent.
- It seems likely that the outcrop geology controls lineament frequencies but not their spatial distribution.
- Mineral deposits have close spatial relationships to: (1) major WNW-ESE and NE-SW lineaments intersection zones; and (2) lineament density anomalies.

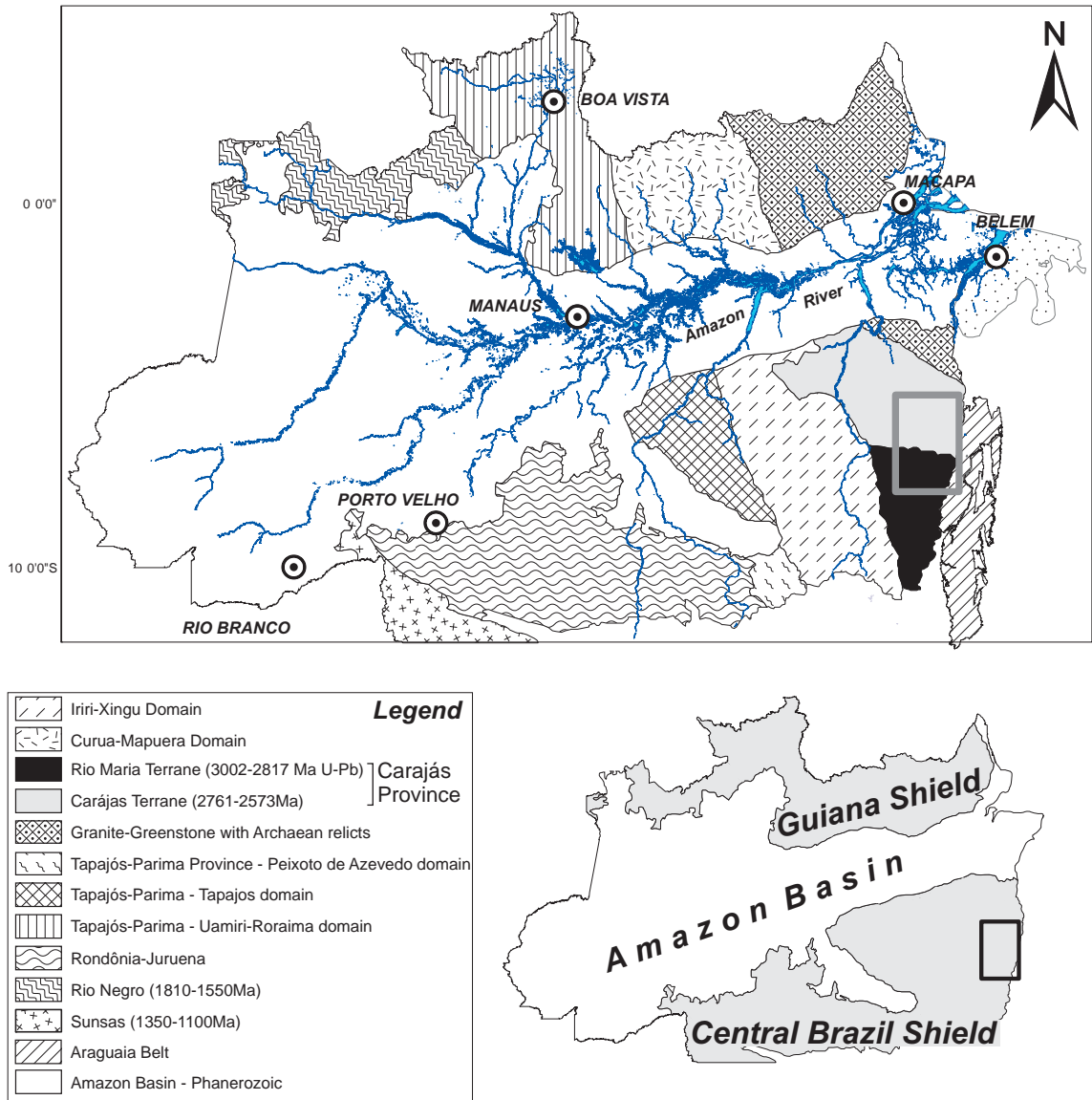


Figure 3.1- The Amazon Craton and its geochronological provinces according to Santos, 2000; the highlighted area indicates the location of the map presented in **Figure 3.2**. Note the location of the Carajás (grey) and Rio Maria (black) Terranes limited to the east by the Araguaia Belt and to the west by the Irixi Xingu Domain.

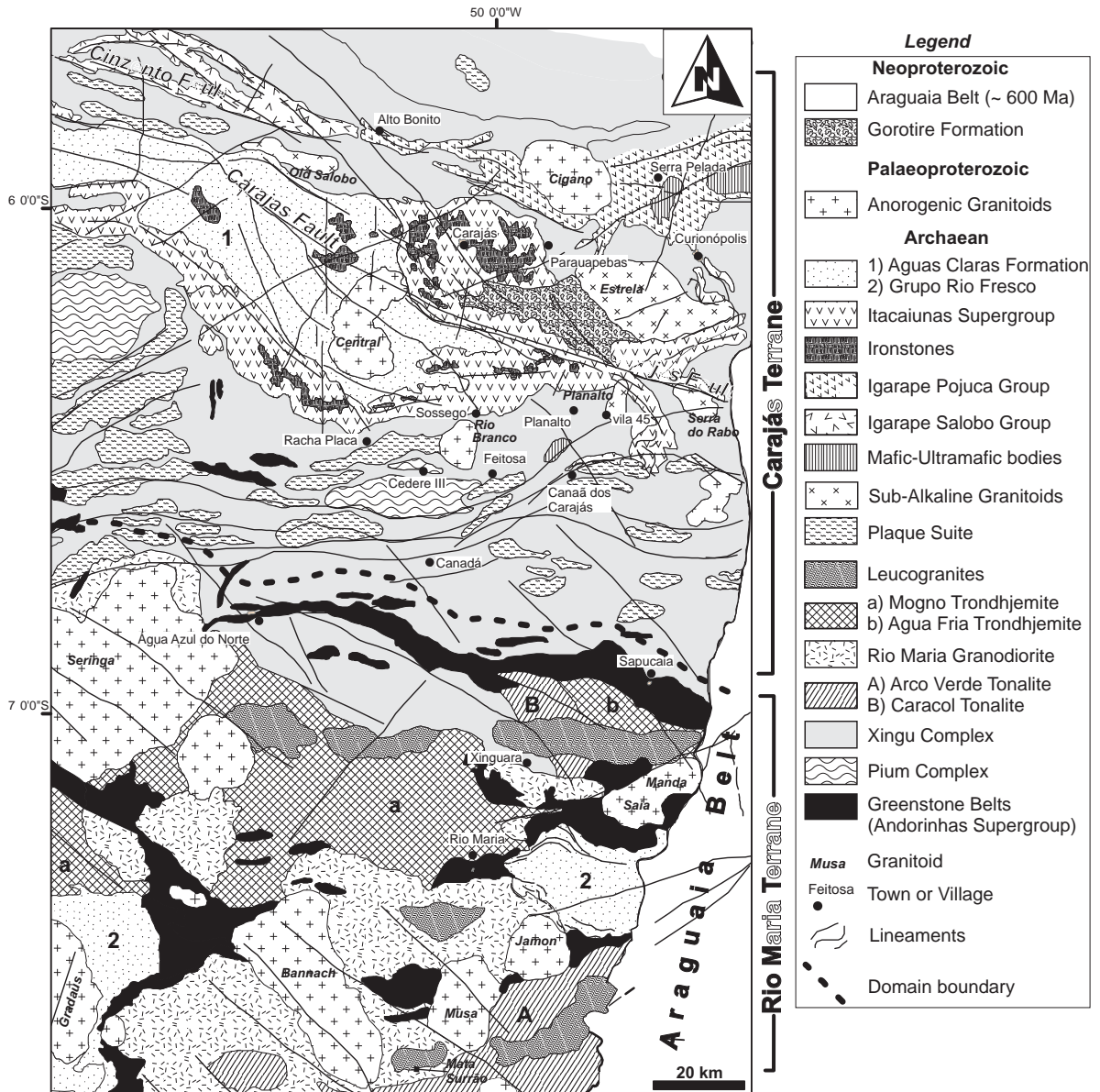


Figure 3.2- Map of the main tectono lithostratigraphic domains forming the Carajás Province: the Carajás Terrane showing NW SE elongated granitoids and portions of the volcanic and sedimentary rocks; and the Rio Maria Granite Greenstone Terrane with granitoids intruding the greenstone sequences of the Andorinhas Supergroup. Note the east limits of the province marked by the Araguaia Belt (AB).

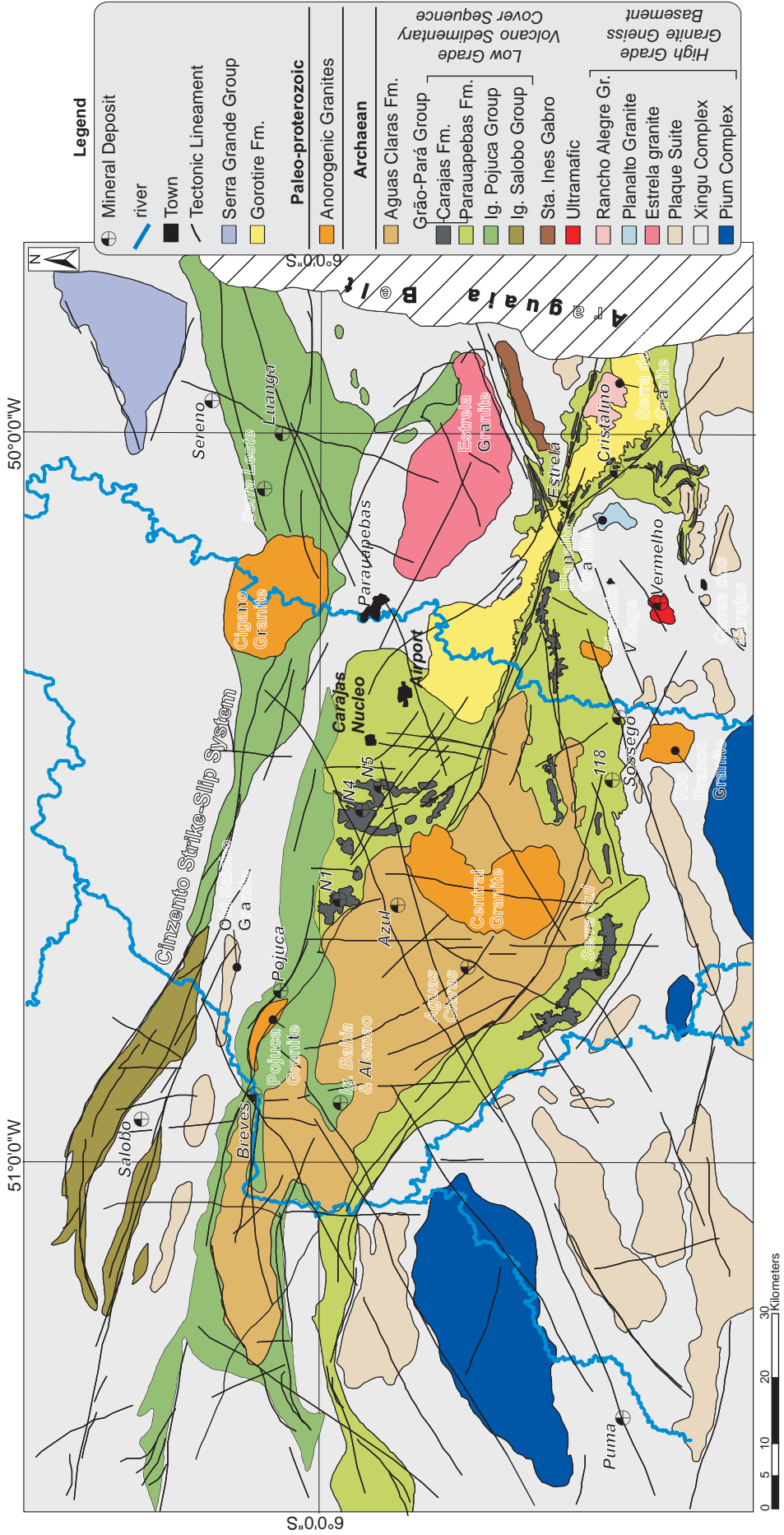


Figure 3.3- Geological map of the Carajás Terrane showing the main Archean and Proterozoic lithological domains of the the Basement and Cover assemblages, tectonic features and ore deposits. Note the two main fault zones in the region: the Carajás and Cinzento Strike-Slip Systems.

Supergroup	Group / Formation	Intrusive Rocks	Lithology	Age (Ga)	Method	Author
Proterozoic Granites		Cigano	Granite	1.883 ± 3	ZR U-Pb	Machado et al. (1991)
		Carajas	Granite	1.880 ± 2	ZR U-Pb	Machado et al. (1991)
		Pojuca	Granite	1.874 ± 2	ZR U-Pb	Machado et al. (1991)
		Breves	Episyenite	1.880 ± 9	ZR SHRIMP II	Tallarioco et al. (2004)
	Young Salobo		1.88 ± 80	W-R Rb-Sr	Cordani (1981)	
Itacaiunas Supergroup	Águas Claras	gabro	gabro	2.645 ± 12	ZR Pb-Pb	Dias et al. (1996)
	Grão-Pará		Rhyodacite	2.759 ± 2	ZR U-Pb	Machado et al. (1991)
	Grão-Pará		Rhyolite	2.758 ± 39	ZR U-Pb	Gibbs et al. (1986)
	Grão-Pará		metalyolite	2.760 ± 11	ZR SHRIMP	Trendall et al. (1998)
	Grão-Pará		Rhyolite	2.757 ± 18	ZR Pb-Pb	Macambira et al. (1996)
	Igarape Pojuca		Aphhibolite	2.732 ± 2	ZR U-Pb	Machado et al. (1991)
	Igarape Pojuca		Andesite	2.683 ± 80	WR Sm-Nd	Lindenmayer et al. (2001)
	Igarape Pojuca		mafic intrusive rocks	2.705 ± 2	ZR Pb-Pb	Galarza et al. (2002b)
	Igarape Pojuca		Meta-Andesites	2.719 ± 80	WR Sm-Nd	Pimentel et al. (2003)
	Igarape Salobo		Rhyolite	2.740 ± ?	ZR U-Pb	Wirth et al. (1986)
Cover Assemblage	Igarape Salobo		Aphhibolite	2.761 ± 3	ZR U-Pb	Machado et al. (1991)
	Igarape Bahia		meta pyroclastic	2.747 ± 1	ZR Pb-Pb	Galarza et al. (2002)
	Igarape Bahia		Meta volcanic	2.759 ± 24	WR Sm-Nd	Santos (2002)
	Igarape Bahia		Metavolcanic	2.748 ± 34	ZR SHRIMP	Tallarioco et al. (2005)
	Itacaiunas		Granitoid	2.525 ± 38	ZR Pb-Pb	Souza et al. (1996)
	Old Salobo		Granitoid	2.573 ± 2	ZR U-Pb	Machado et al. (1991)
	Geladinho		Granitoid	2.688 ± 11	ZR Pb-Pb	Barbosa et al. (2001)
	Estrela		sienogranite	2.763 ± 7	ZR Pb-Pb	Barros et al. (2001)
	Plaque Suite		Granitoid	2.736 ± 24	ZR Pb-Pb	Avelar et al. (1999)
	Planalto		Granitoid	2.747 ± 2	ZR Pb-Pb	Huhn et al. (1999)
Archean Granites	Cristalino Diorite		Diorite	2.738 ± 6	ZR Pb-Pb	Huhn et al. (1999)
	Serra do Rabo		Granitoid	2.743 ± 1	ZR U-Pb	Sardinha et al. (2002)
	Xingu Complex		Granitic Leucosoma	2.859 ± 2	ZR U-Pb	Machado et al. (1991)
	Xingu Complex		Gneiss	2.972 ± 16	ZR Pb-Pb	Avelar et al. (1999)
	Pium Complex		Enderbite Protolith	3.002 ± 14	ZR SHRIMP	Pidgeon et al. (2000)
	Pium Complex		Granulite	2.859 ± 9	ZR SHRIMP	Pidgeon et al. (2000)

Table 3.1 - Selected published isotopic ages arranged in time sequence from younger to older for the rocks present within the Itacaiunas Belt: Basement Assemblage, Archean Granites, cover assemblage and Proterozoic granites.

Chapter 3

Age (Ga)	Event	Kinematics
0.24-0.15	Reactivation of fault system recorded by recent small-scale seismicity Reactivation of fault systems during opening of the South Atlantic	Uncertain Extension
1.92-1.88	Intrusion of granite plutons and dike swarms Weak tectonic inversion by fault reactivation with moderate to strong deformation of the rocks adjacent to the Carajás Fault	Extension Sinistral transpression
2.6-2.5	Emplacement of granitic intrusions, e.g. Old Salobo Development and further reactivation of the Carajás and Cinzento strike-slip systems. Intrusion of sills and dikes and formation of the Carajás Fault	Dextral transtension
2.8-2.7	Volcanism and deposition of the Grão-Para; Igarapé Salobo, Igarapé, Igarapé Bahia and Igarapé Pojuca Groups, with the latter metamorphosed under very-low to medium temperature conditions Emplacement of syntectonic granitoids, e.g. Estrela and Plaque Formation of the Itacaiúnas Shear zone by high temperature ductile deformation	Sinistral transpression
3.1-2.9	Formation of the tonalitic Gneisses of the Xingu Complex and further intrusion of the Pium Complex	

Table 3.2- Summary of the main tectonic events, their age intervals, products and kinematics recorded in the Carajás Region. Modified from (Holdsworth and Pinheiro, 2000; Pinheiro and Holdsworth, 1997).

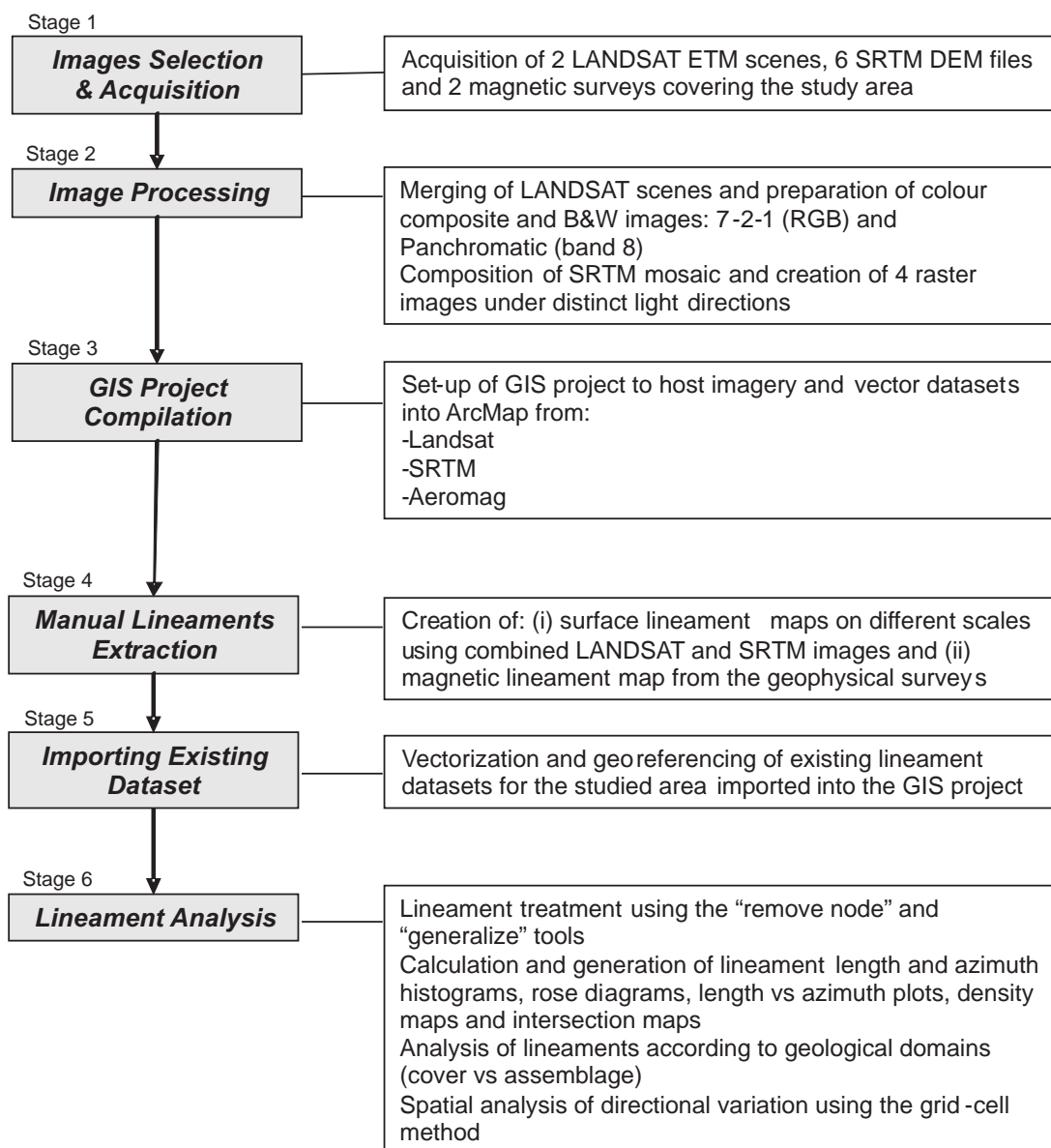


Figure 3.4- Workflow showing the main interlinked stages developed during the lineaments study for the Carajás Region. The grey boxes indicate the main tasks and the white boxes give a brief description of the activities developed within each task.

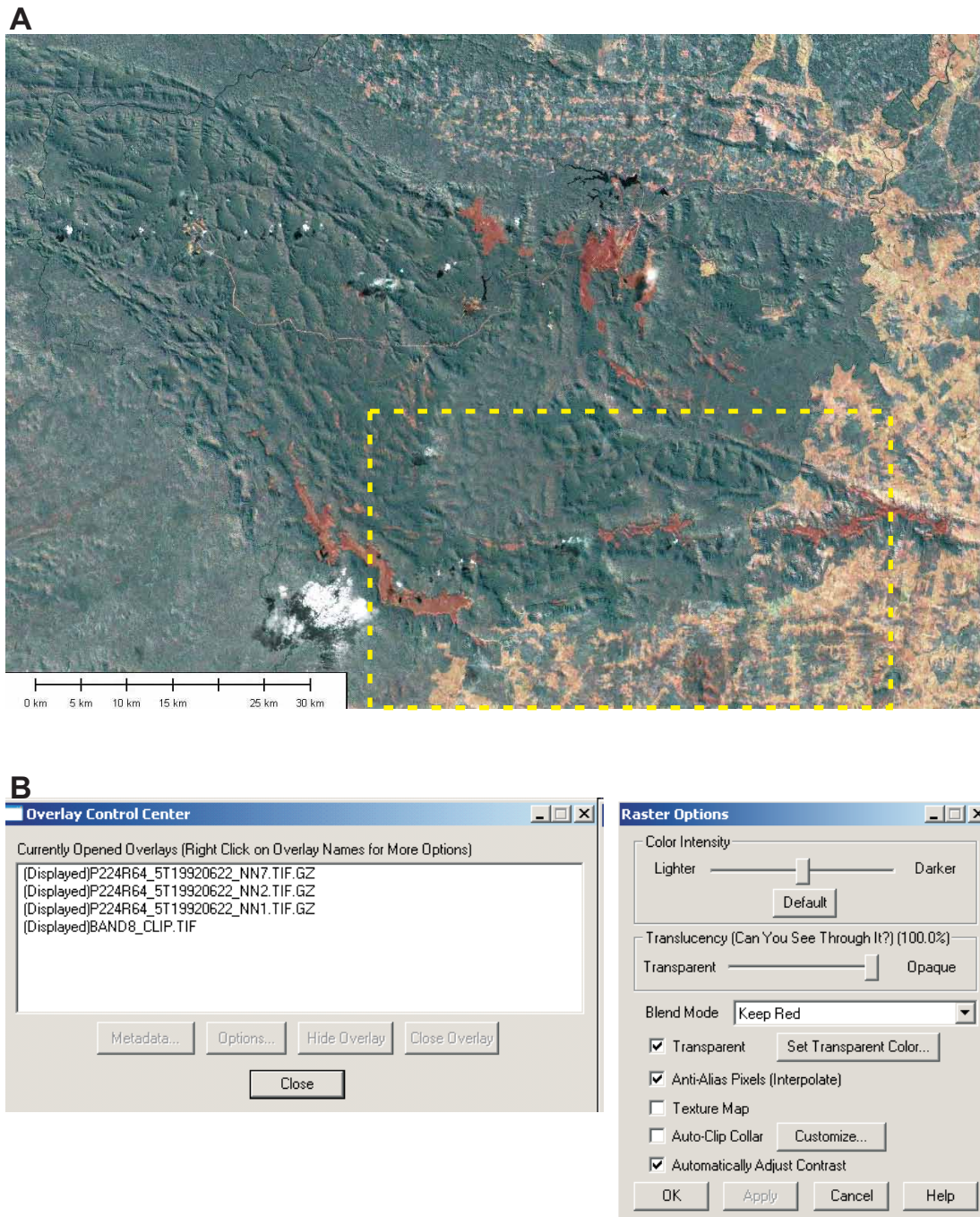


Figure 3.5 - A: a sample of the LANDSAT colour composite R7G2B1 image used for lineament extraction. The central depression corresponds to the Carajás Central Granite, reddish areas indicate ironstone plateau and yellow tones symbolise exposed soil from deforested areas. Note the prominent NW SE geometry of the Carajás Ridge with the Carajás Fault cross cutting the area obliquely. B: Control panels from Global Mapper displaying the parameters utilized to generate the LANDSAT colour composite image. The dashed yellow rectangle indicated the location of the SRTM image in Figure 3.6.

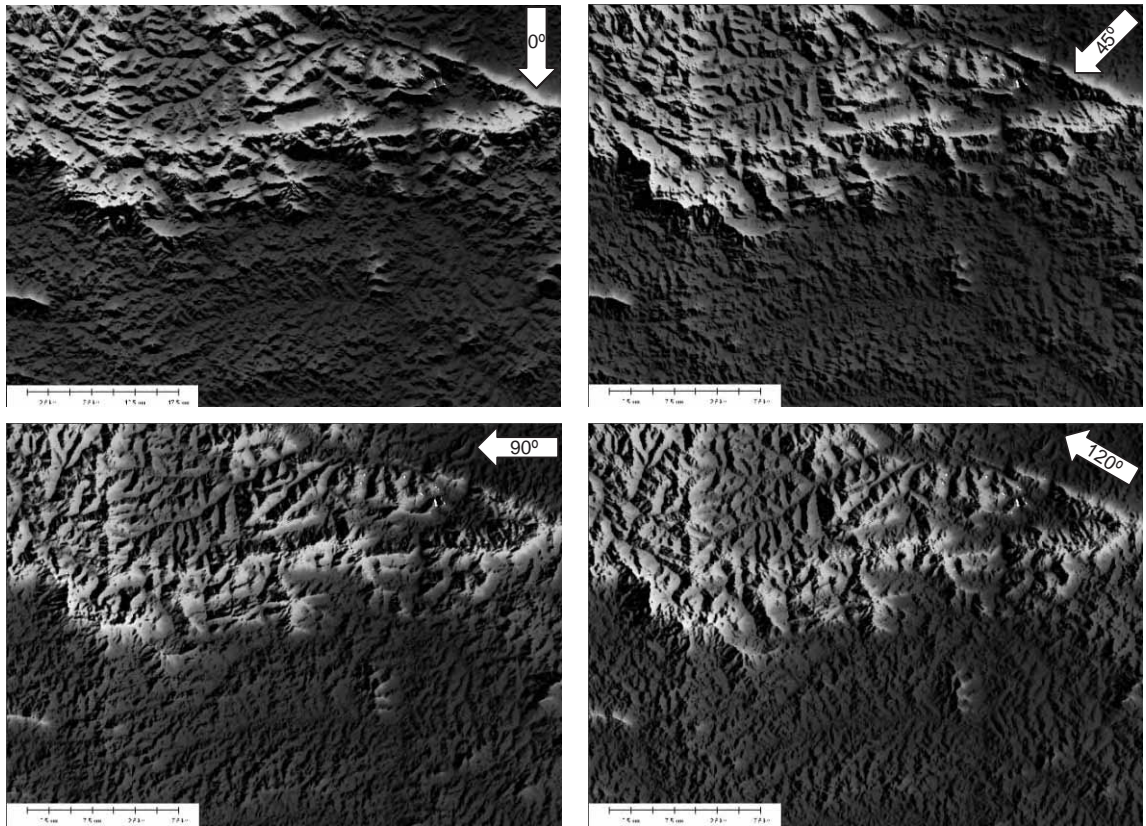
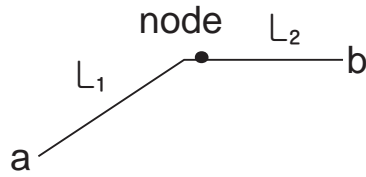
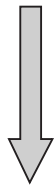


Figure 3.6 - Screen shots of the SRTM shaded relief model images (for location see Fig. 3.5) with the illumination directions indicated by the white arrows. Bright grey tones indicate areas with higher elevation, corresponding to the Carajás Ridge (720 m). Dark grey tones indicate regions of low relief (230 m) corresponding to the granitic basement for the region.

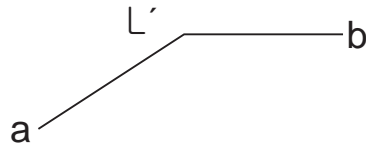
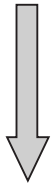
Original dataset



Two lineaments linked by a node exist
: L_1 , L_2

After "Remove-Node"

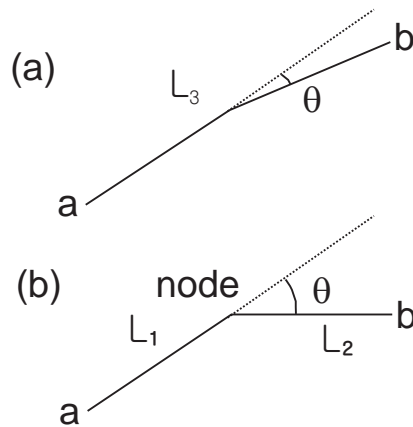
A



One lineament exists
: L_1 , $L_2 \Rightarrow L'$

After "Generalize"

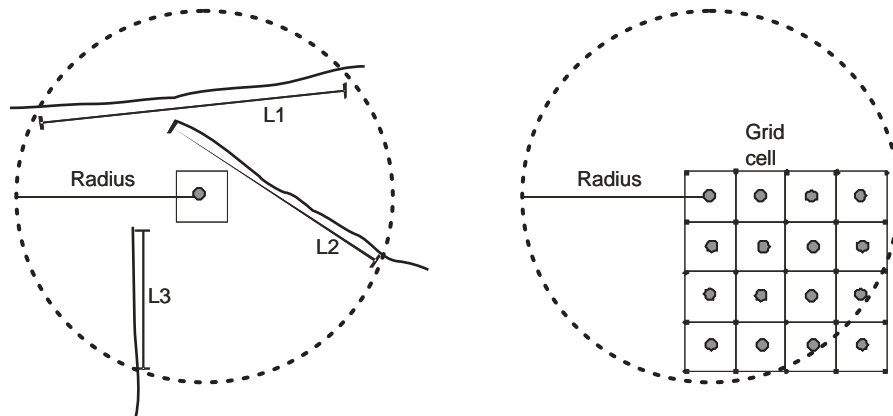
B



If θ is equal or less than 10°
Only one lineament exists.
: $L' \Rightarrow L_3$

If θ is larger than 10° ,
lineaments are split
Two lineaments exist.
: $L' \Rightarrow L_1$, L_2

Figure 3.7- Workflow of the processes utilized to treat/correct interpreted lineaments. A- lineaments after the "Remove Node" tool to eliminate redundant nodes. B- Generalize tool to split lineaments with angles between segments larger than 10 degrees (Modified from Kim et al., 2004).



$$\text{Density} = [(L1 \times V1) + (L2 \times V2) + (L3 \times V3)] / (\text{area of circle})$$

Figure 3.8 - Diagram showing the process for calculating lineament density values to generate the density maps. In A, circle radius runs around the circumference from the center of a grid cell and computes the length of each lineament within the circle. In B, the array of grid cells with the grey dots indicating the circle center where the density values from the presented equation will be assigned.

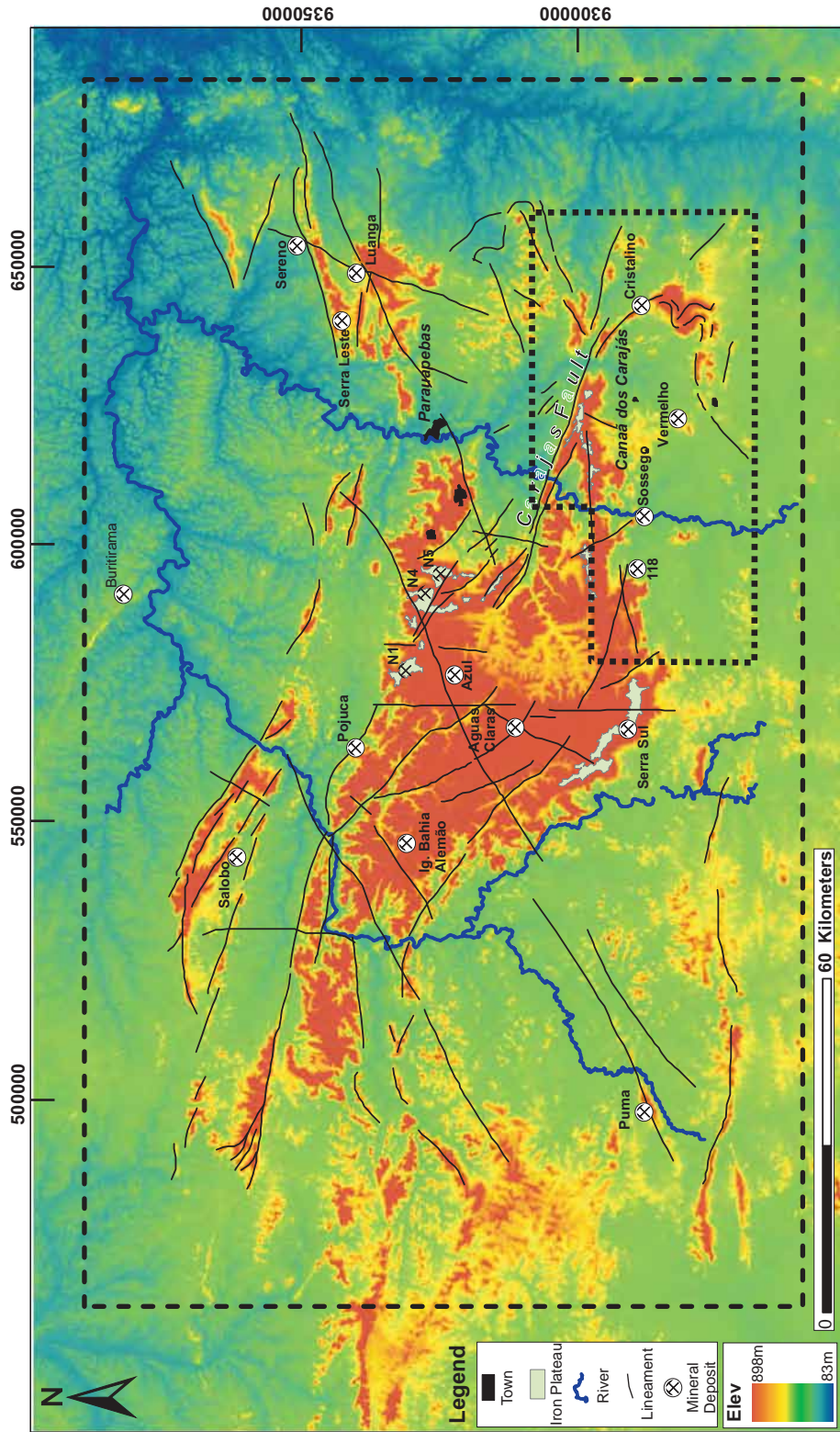


Figure 3.9 Elevation map of the Carajás region showing the major topographic lineaments and mineral deposits in the area. Polygons indicate the limits of the studied areas. The dashed polygon bounds the area for regional observations at 4 scales. The dotted polygon indicates the portion where the more detailed analysis was carried out.

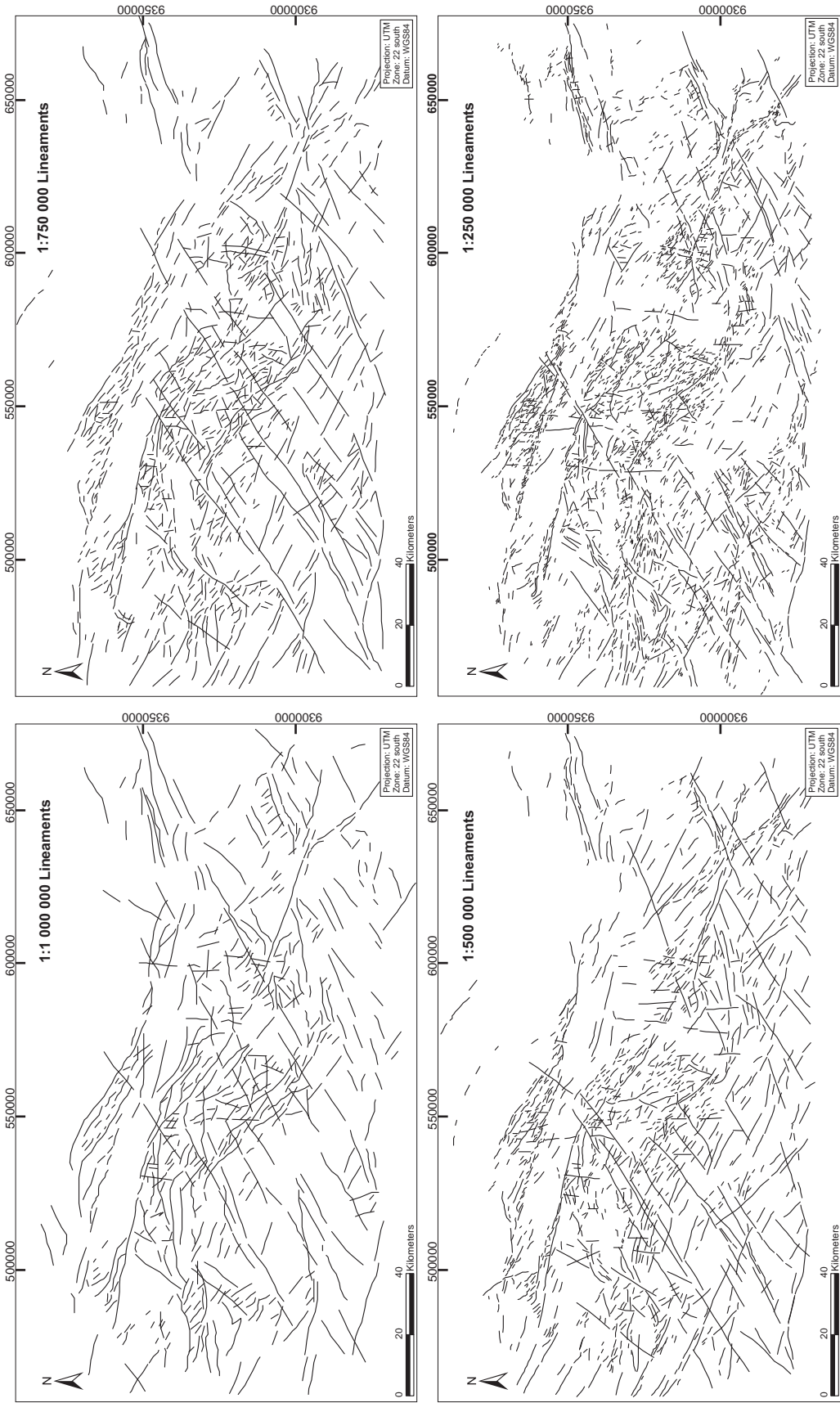


Figure 3.10 - Regional lineament maps produced by lineaments picked at 4 different scales: 1:1 000 000; 1:750 000; 1:500 000; and 1:250 000. Notice the increase in lineament length, count and level of detail as the scale at which the lineaments were extracted change from small to large. (Statistics are given in Fig. 3.12)

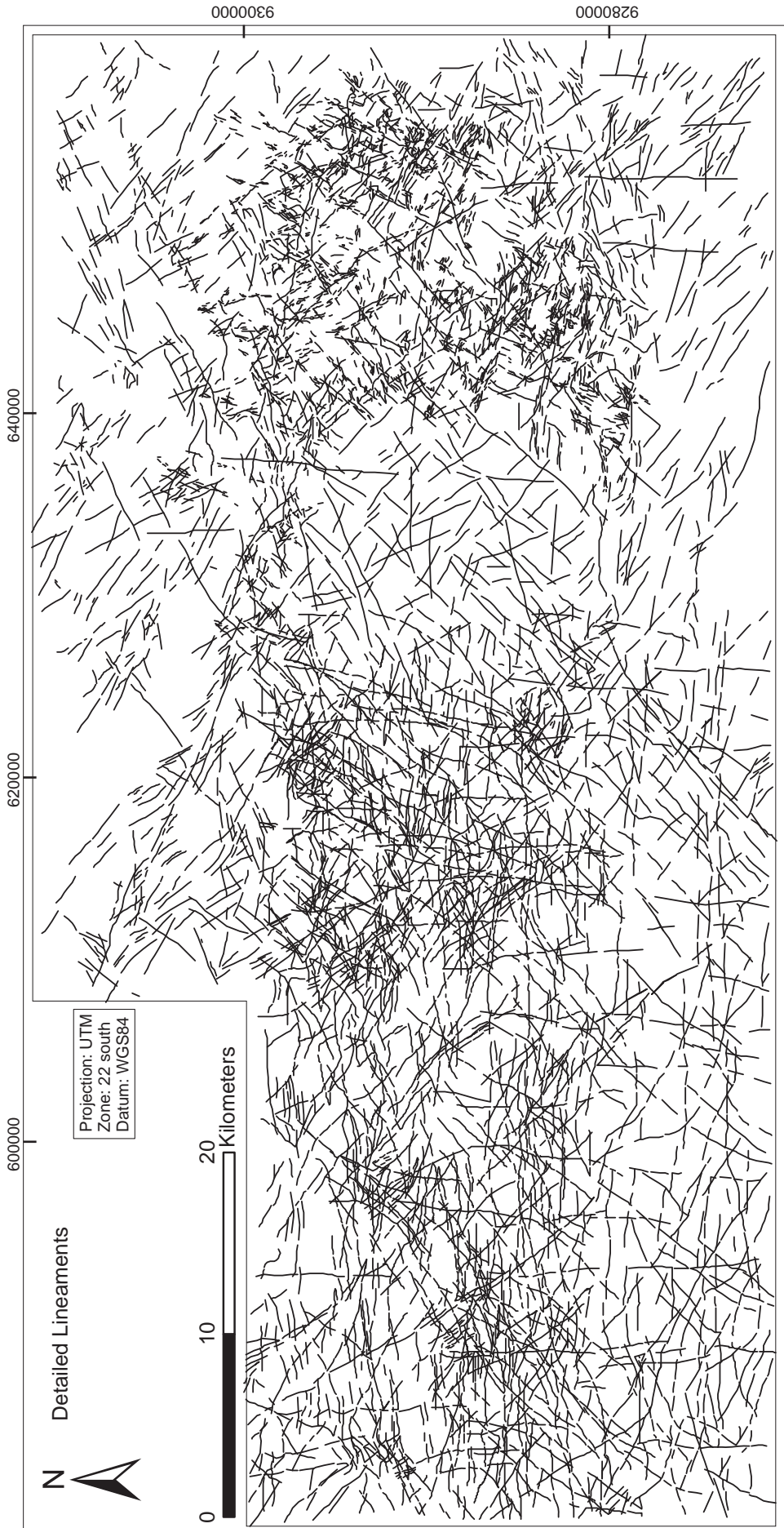


Figure 3.11- Detailed lineaments map for the southern part of the Carajás region.

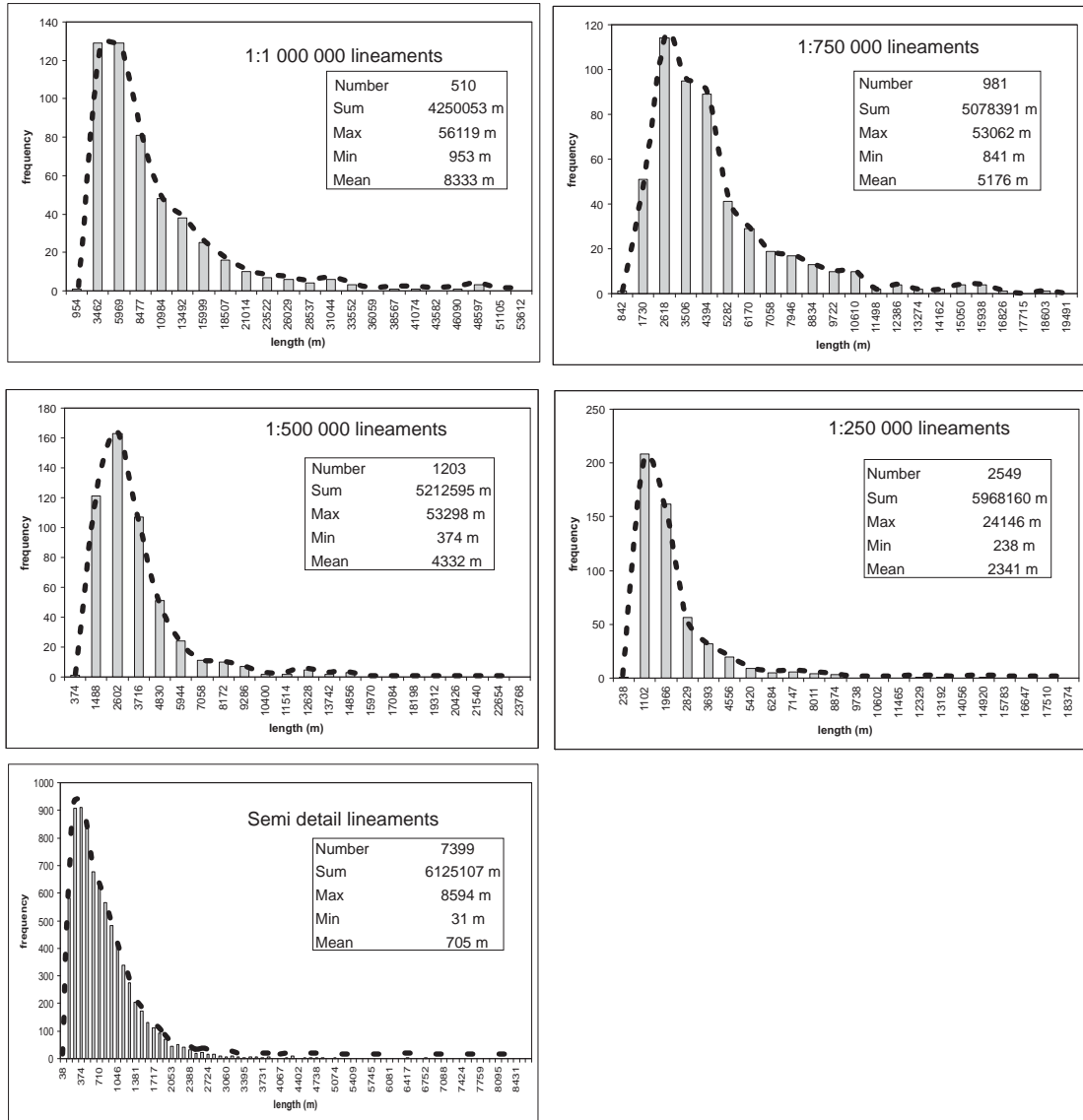


Figure 3.12- Lineament length histograms for the analysed datasets. The plots are constructed as length intervals against frequency (number of lineaments). Additional statistical figures are presented in the plots: number of lineaments, length sum, maximum length, minimum length and length mean.

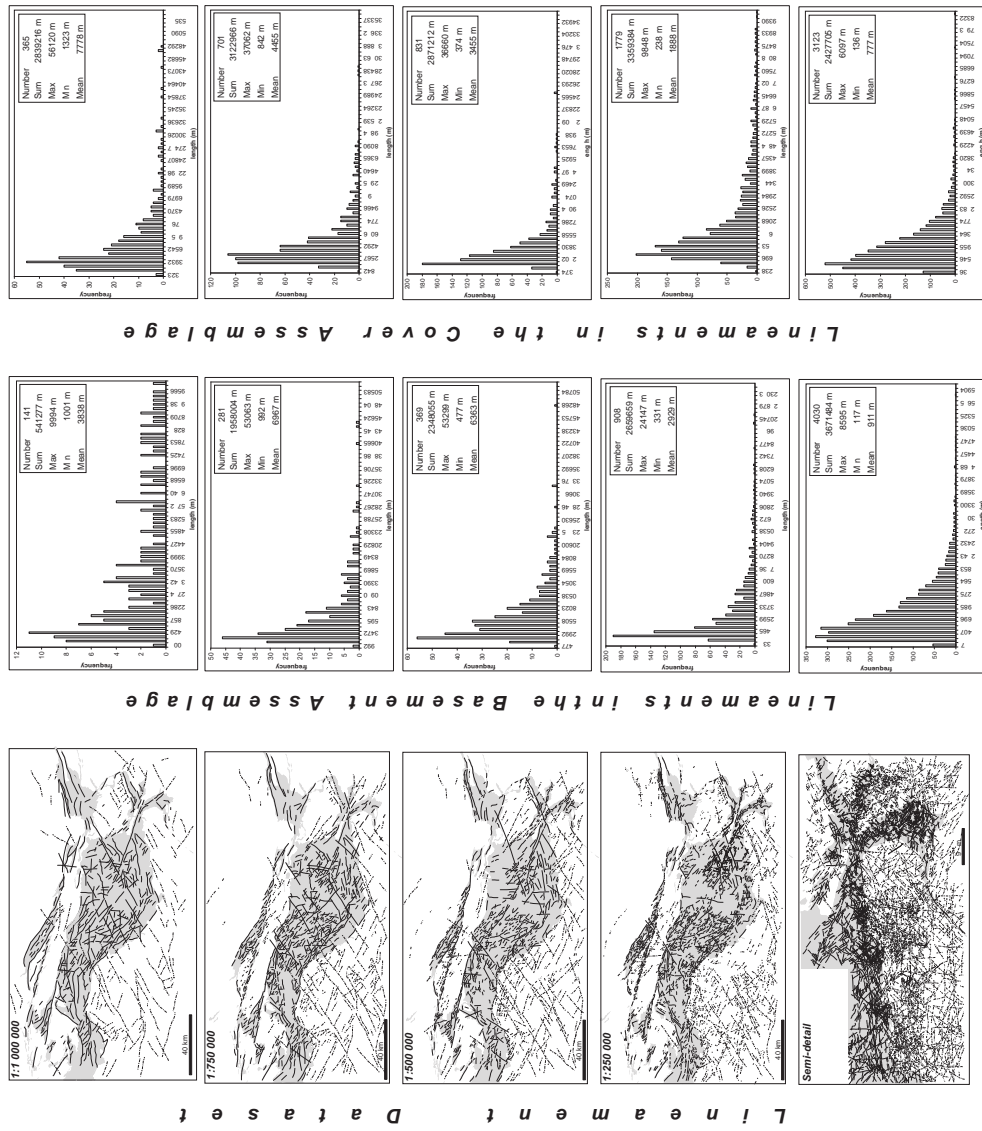


Figure 3.13 Lineament maps for the five investigated scales highlighting the Basement Assemblage domain (white) and the Cover Assemblage domains (grey). Length histograms and associated statistics values for lineaments within these domains are presented for each analysed scale.

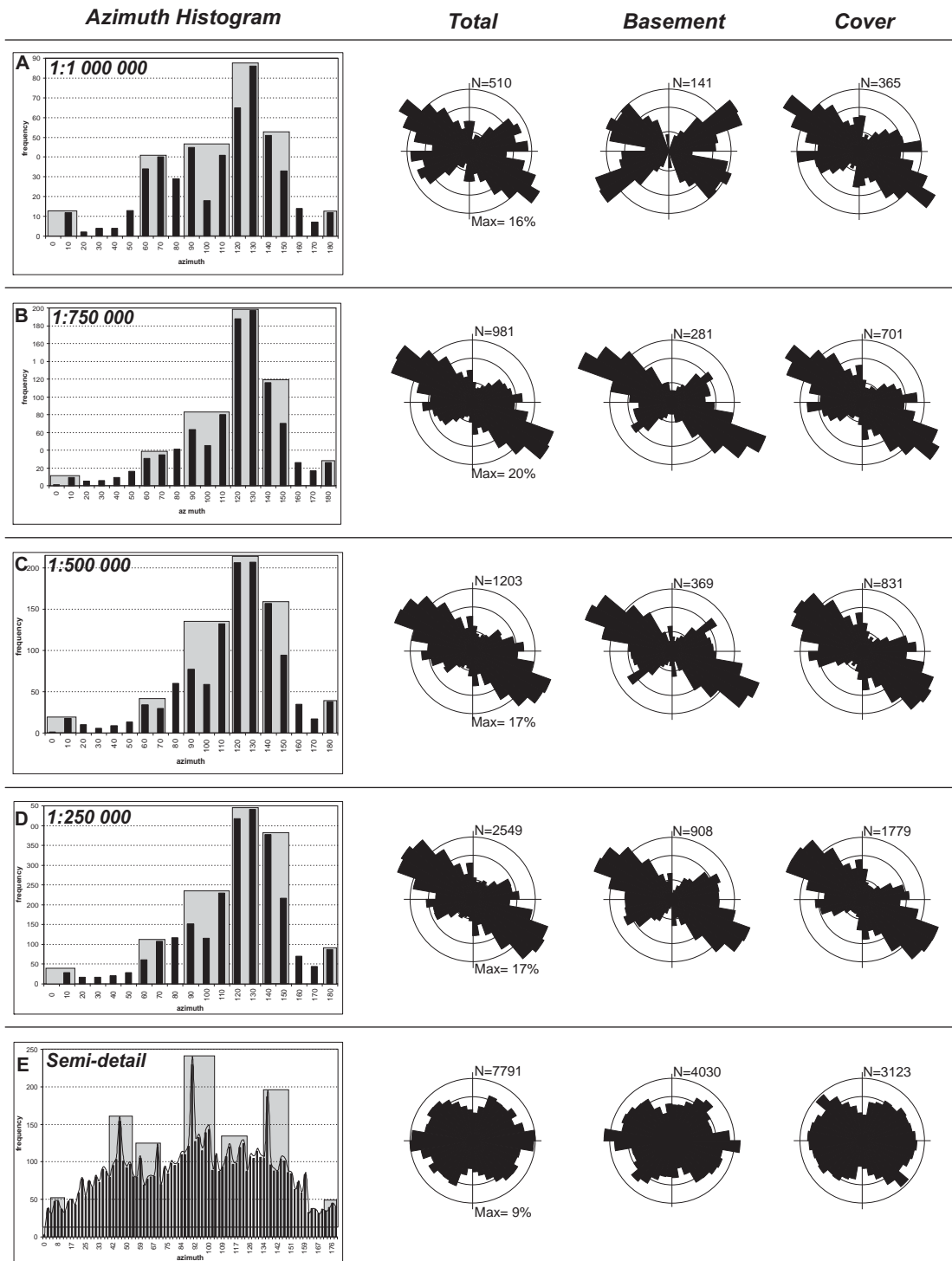


Figure 3.14 Lineament azimuth histograms and rose diagrams for the analyzed datasets. Shaded bars in the histograms indicate the main lineament directions identified. The rose diagrams show preferred directions for total lineaments and lineaments contained within the basement and cover domains.

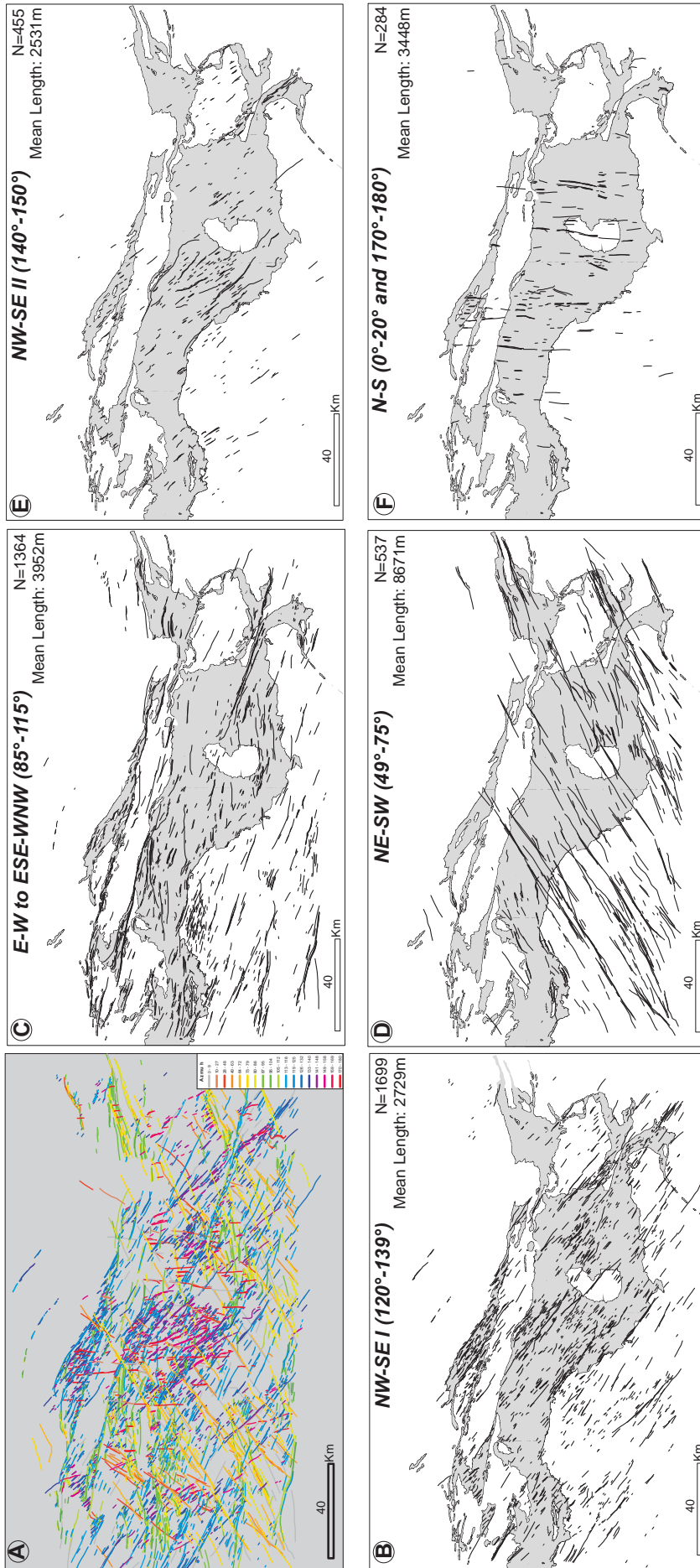


Figure 3.15 Lineament maps showing: A- all regional lineaments colour coded by azimuth intervals (see colour code chart); and B/C/D/E/F main sets of lineaments sorted according to the dominant directions indicated by the orientation analysis. The maps also show the spatial distribution of the lineament sets according to geological domain: basement (white) and cover (grey).

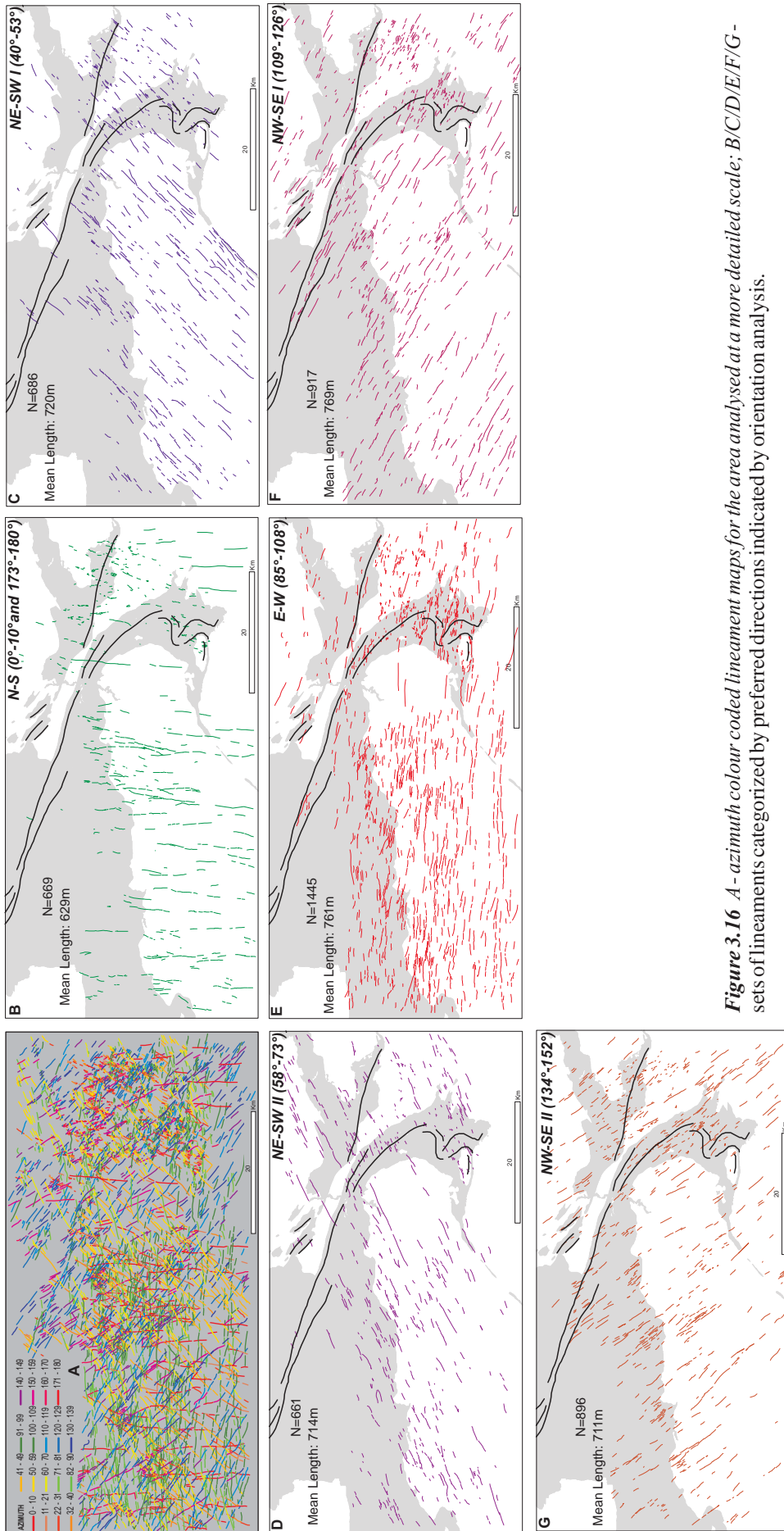


Figure 3.16 A - azimuth colour coded lineament maps for the area analysed at a more detailed scale; B/C/D/E/F/G - sets of lineaments categorized by preferred directions indicated by orientation analysis.

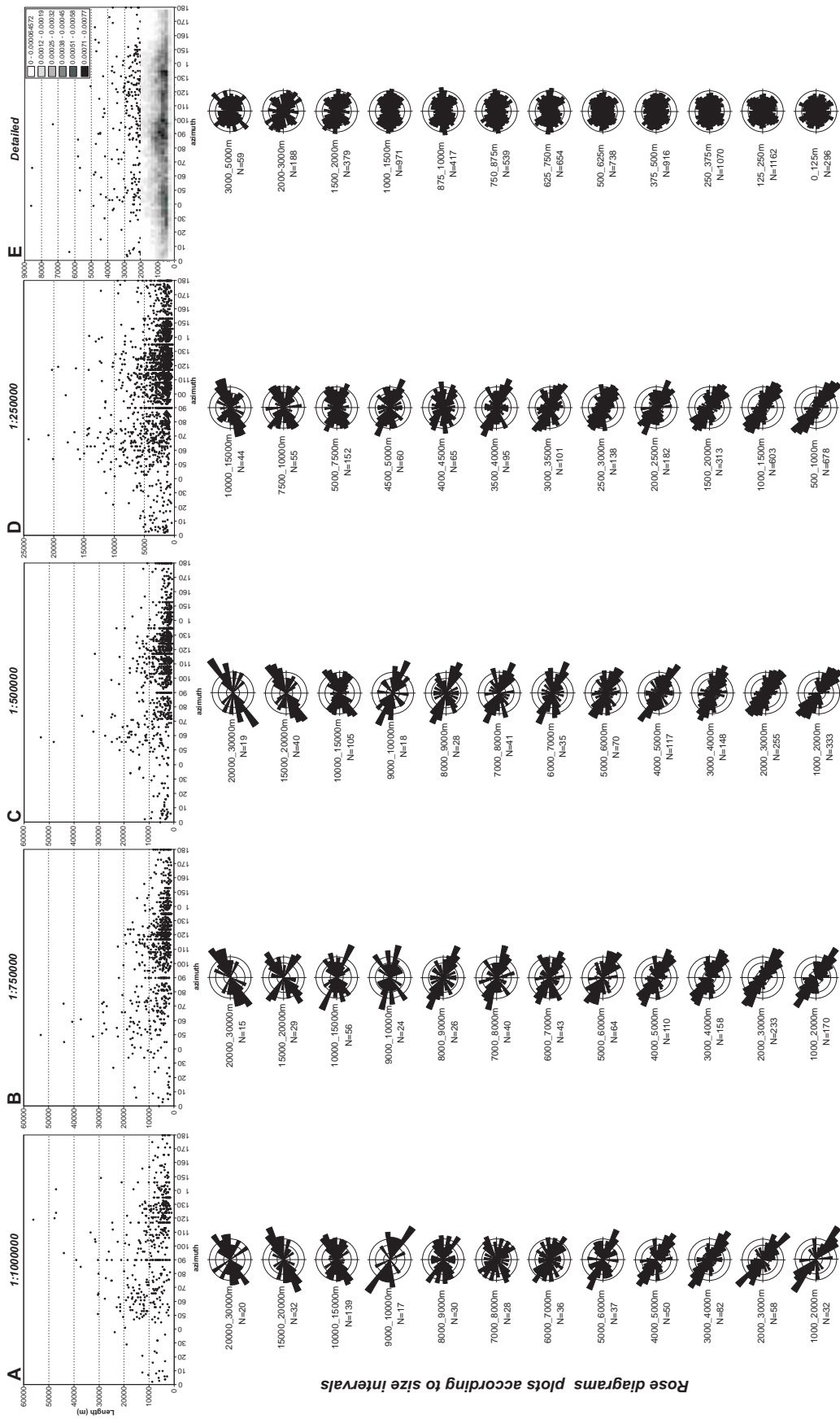
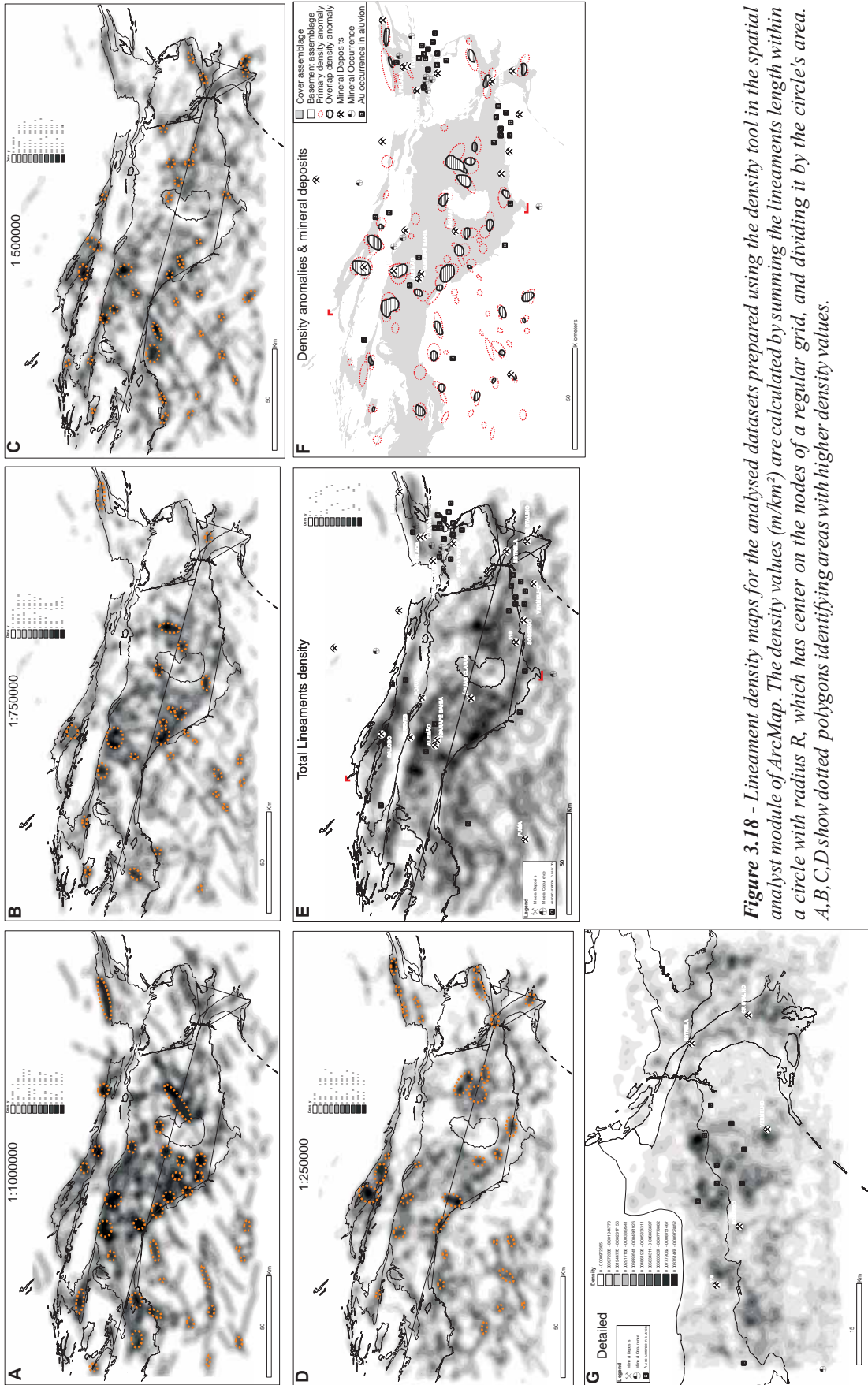


Figure 3.17- Length against azimuth plots and rose diagrams indicating the relationship between lineament lengths and their directions. Rose diagrams show the lineament orientations according to their length



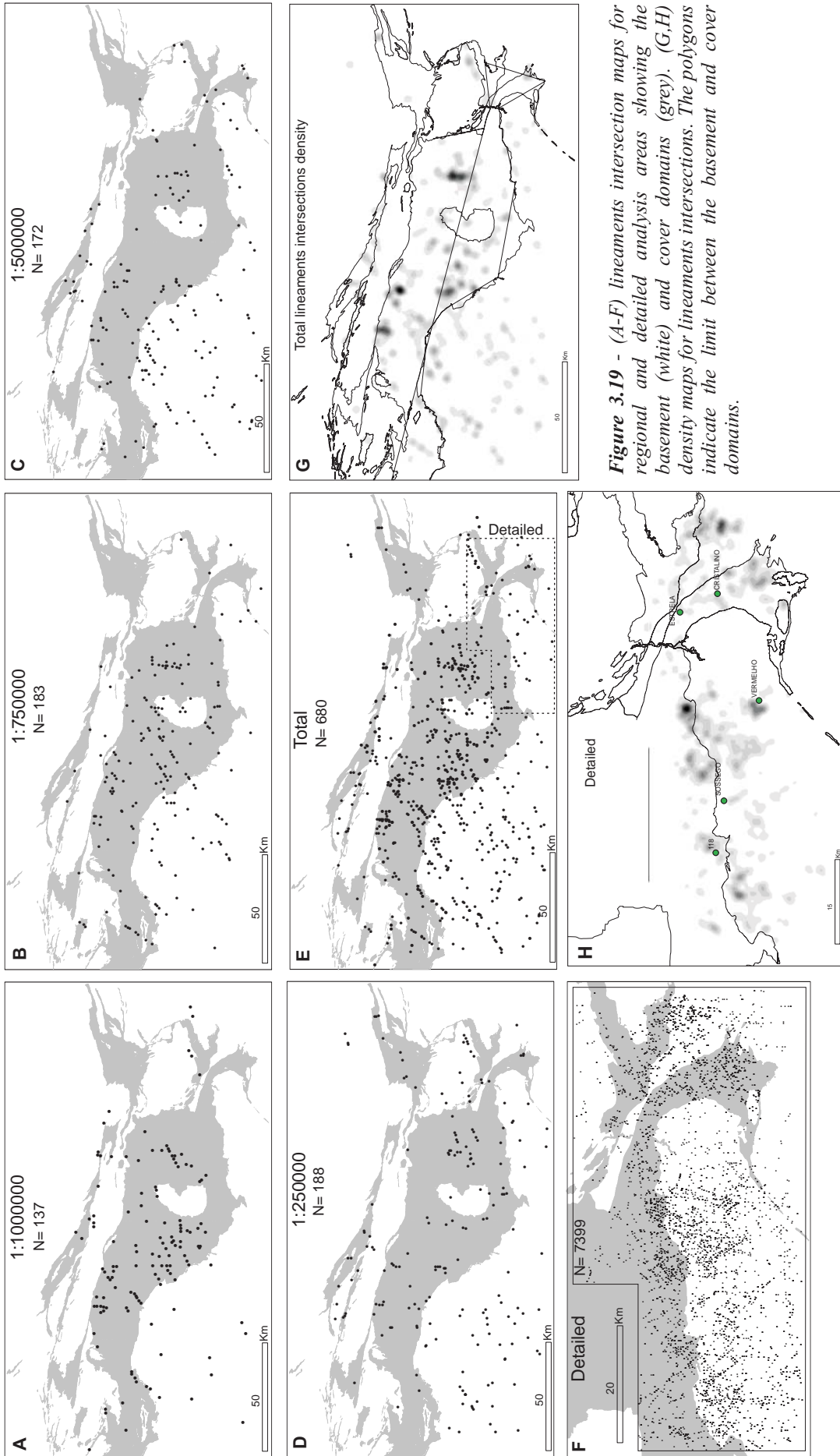


Figure 3.19 - (A-F) lineaments intersection maps for regional and detailed analysis areas showing the basement (white) and cover domains (grey). (G,H) density maps for lineaments intersections. The polygons indicate the limit between the basement and cover domains.

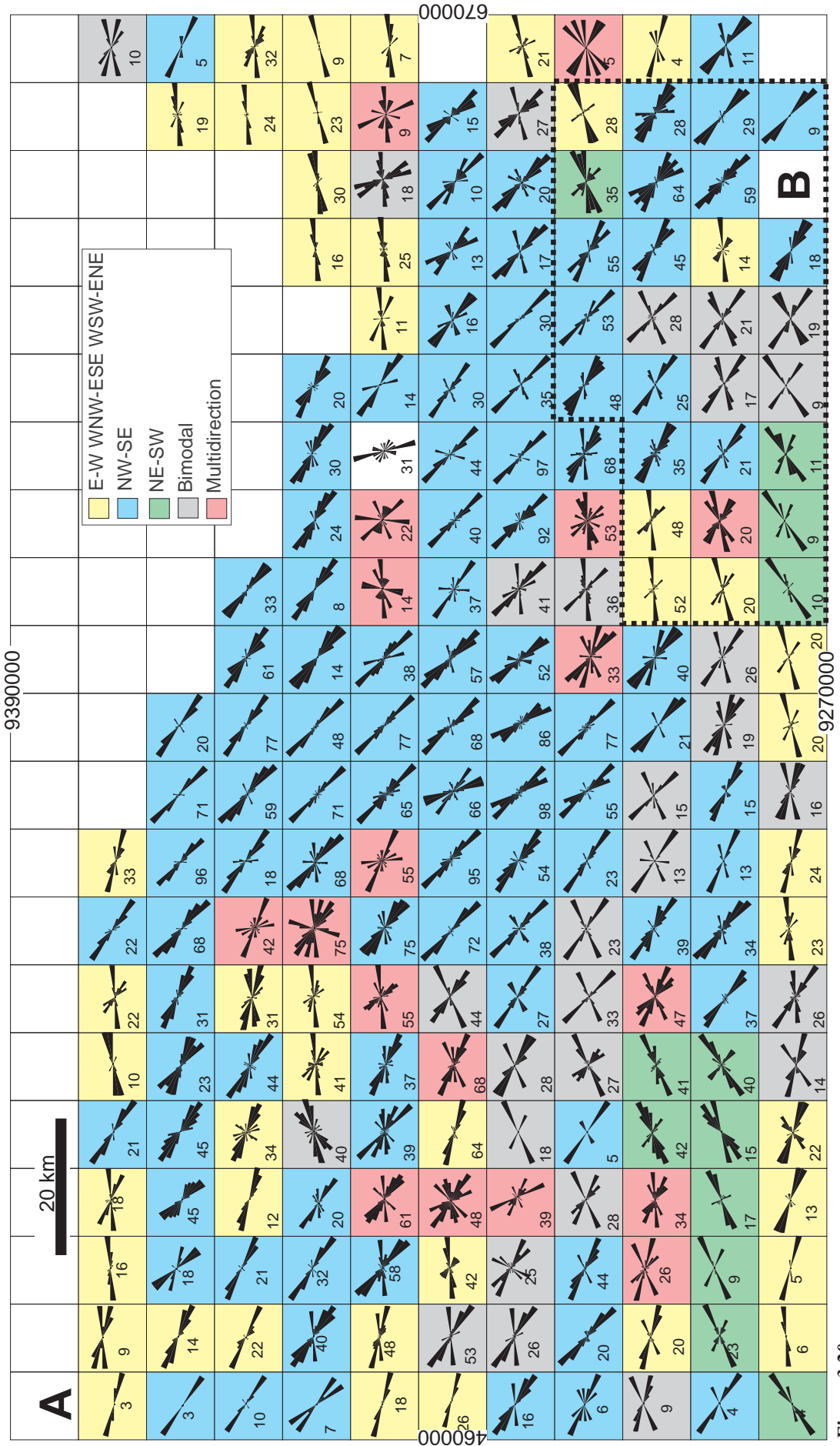


Figure 3.20-

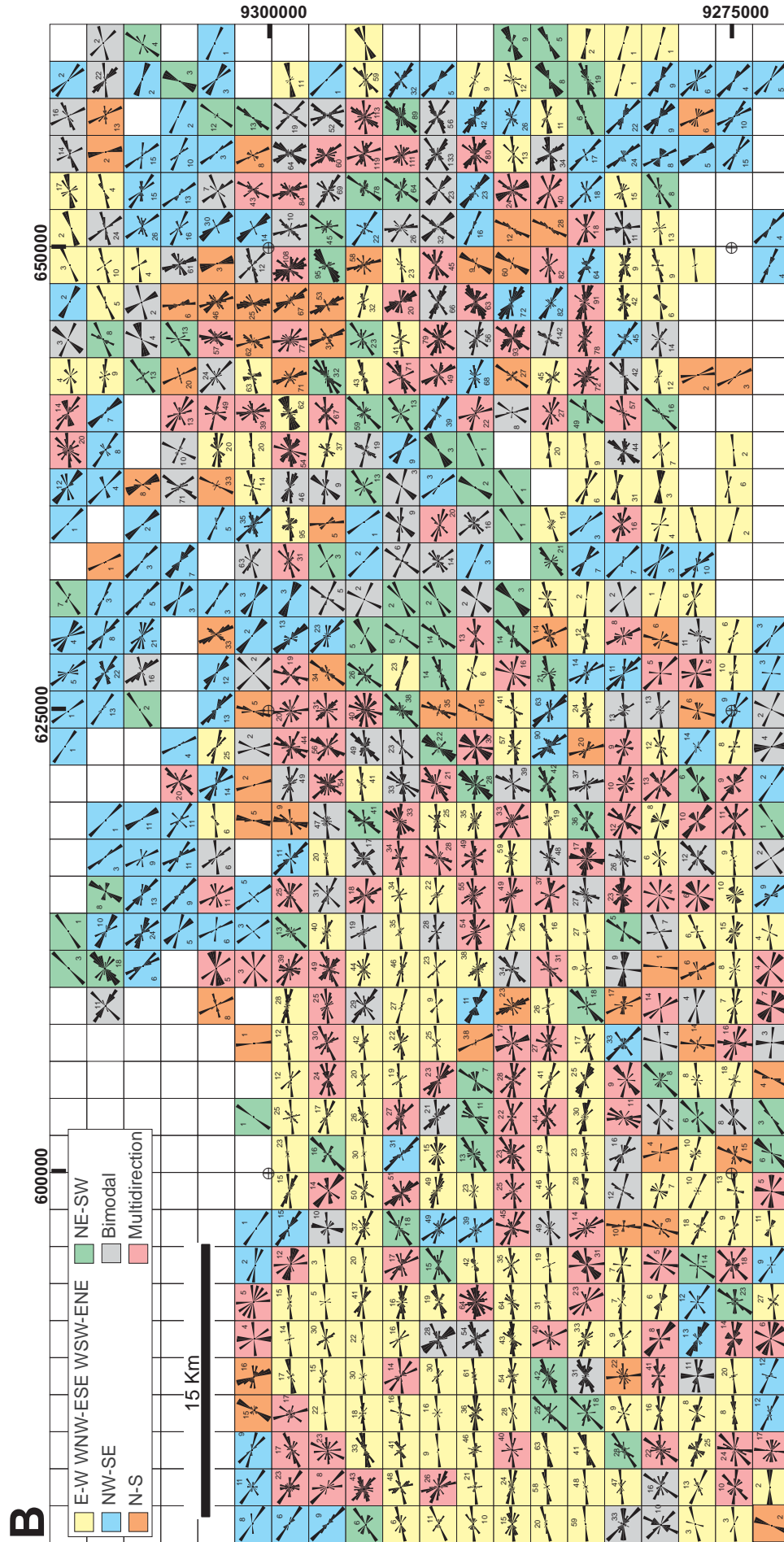


Figure 3.20 cont - Net of square grids covering the studied areas at (A) regional and (B) detailed scales, with cell sizes of 10 km and 2 km respectively. Rose diagrams for lineaments within each cell are classified into six major categories colour coded according to the rose diagram geometry (see legend). The number of lineaments composing the rose diagrams is indicate in each grid-cell.

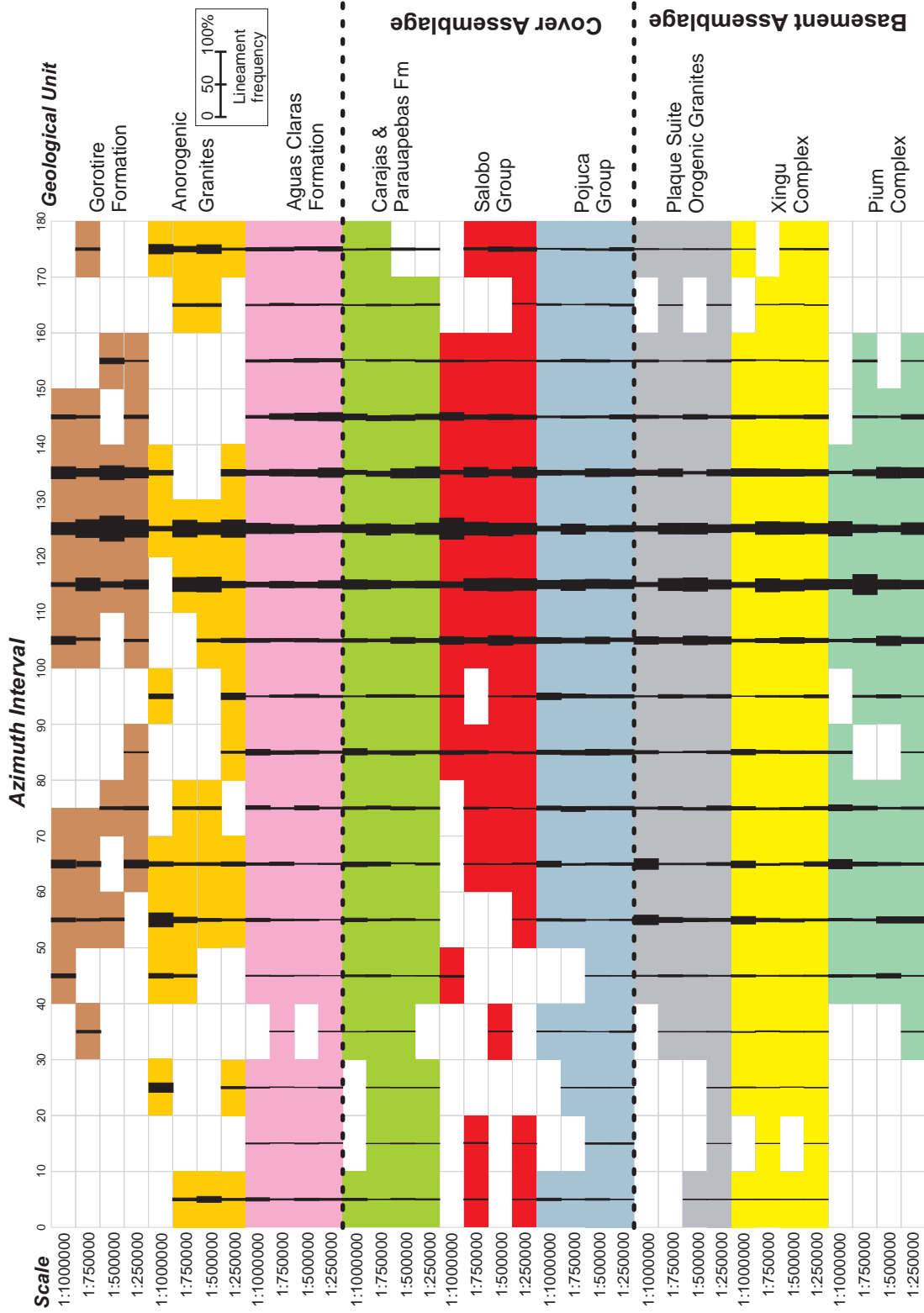


Figure 3.21 - Lineament distributions according to the geological units in the investigated area. The presence of lineaments in the units is represented by vertical lines that also indicate the relative frequency of lineaments.

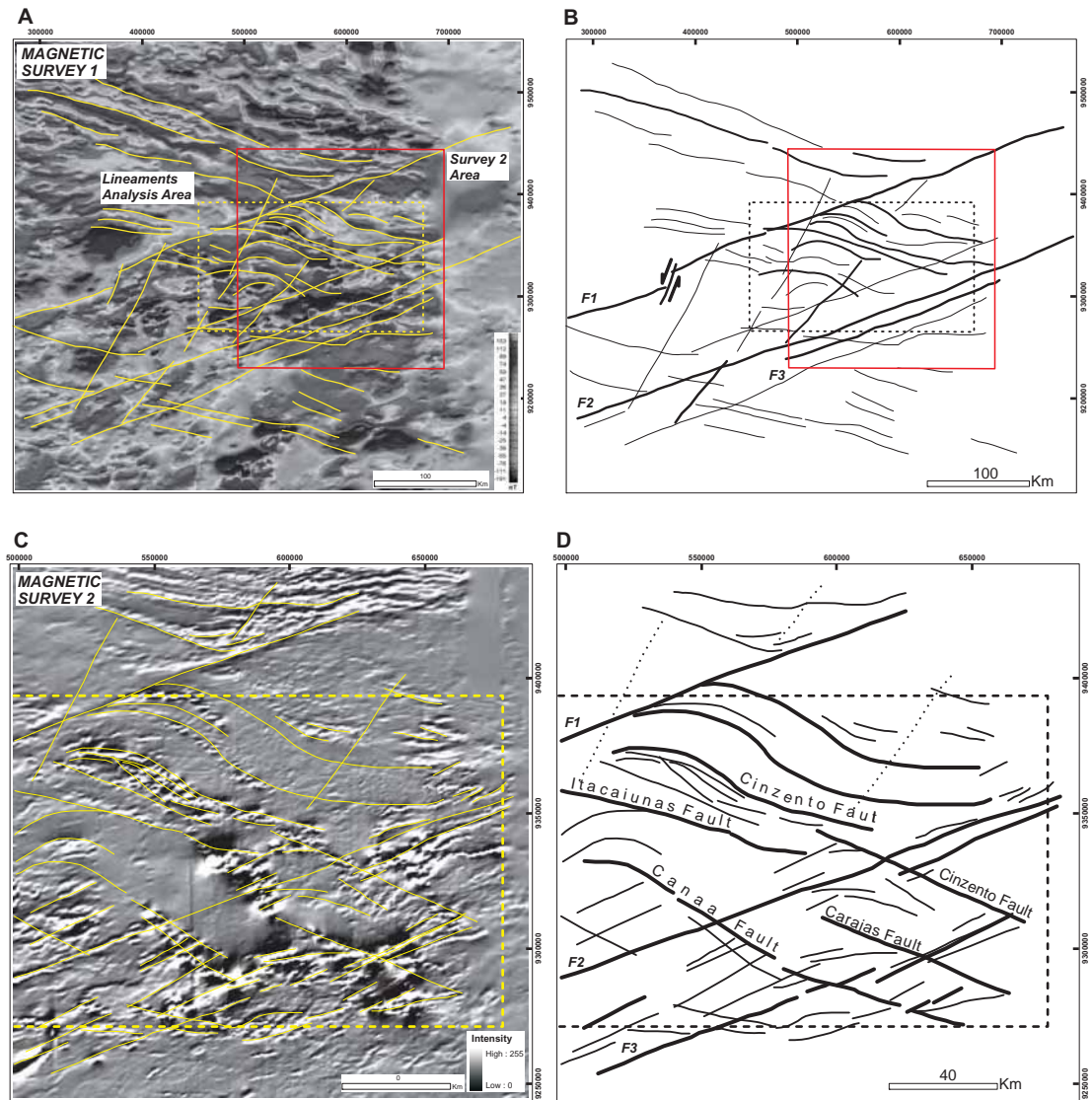


Figure 3.22 Magnetic surveys analysed (A & C) and interpreted magnetic lineaments for both surveys (B & D). Dashed rectangle on Survey 1 indicates the previously presented area analysed for surface lineaments and the square area indicates the location of Survey 2.

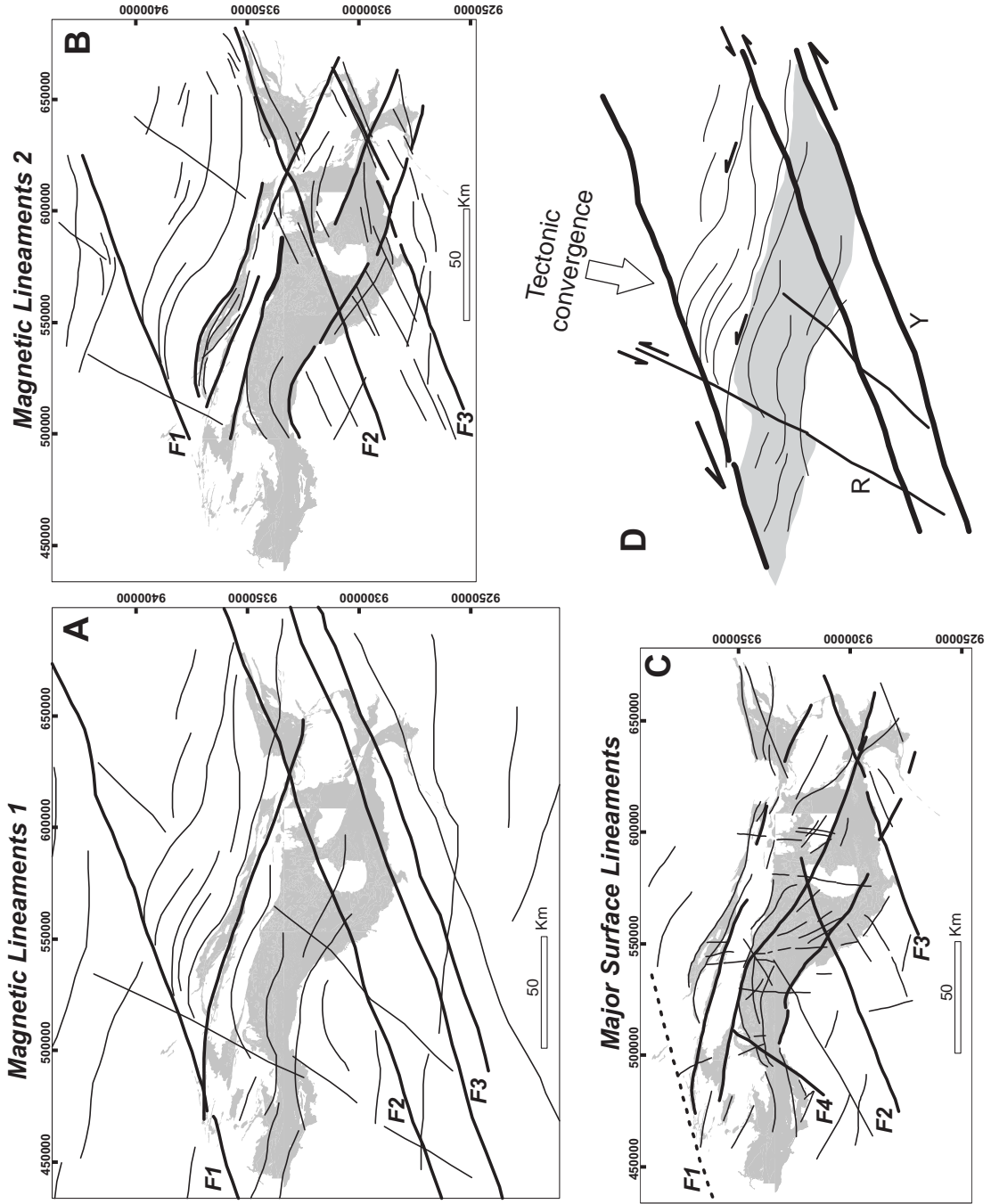


Figure 3.23 Comparison of the major lineaments identified in the magnetic surveys (A & B) and for surface features identified using satellite images analysis (C). (D) Simplified sketch relating the identified structures to Riedel's model (the sketch is based on the geometry of the models presented in Tchalenko, 1968, 1970 and Platt, 1984).

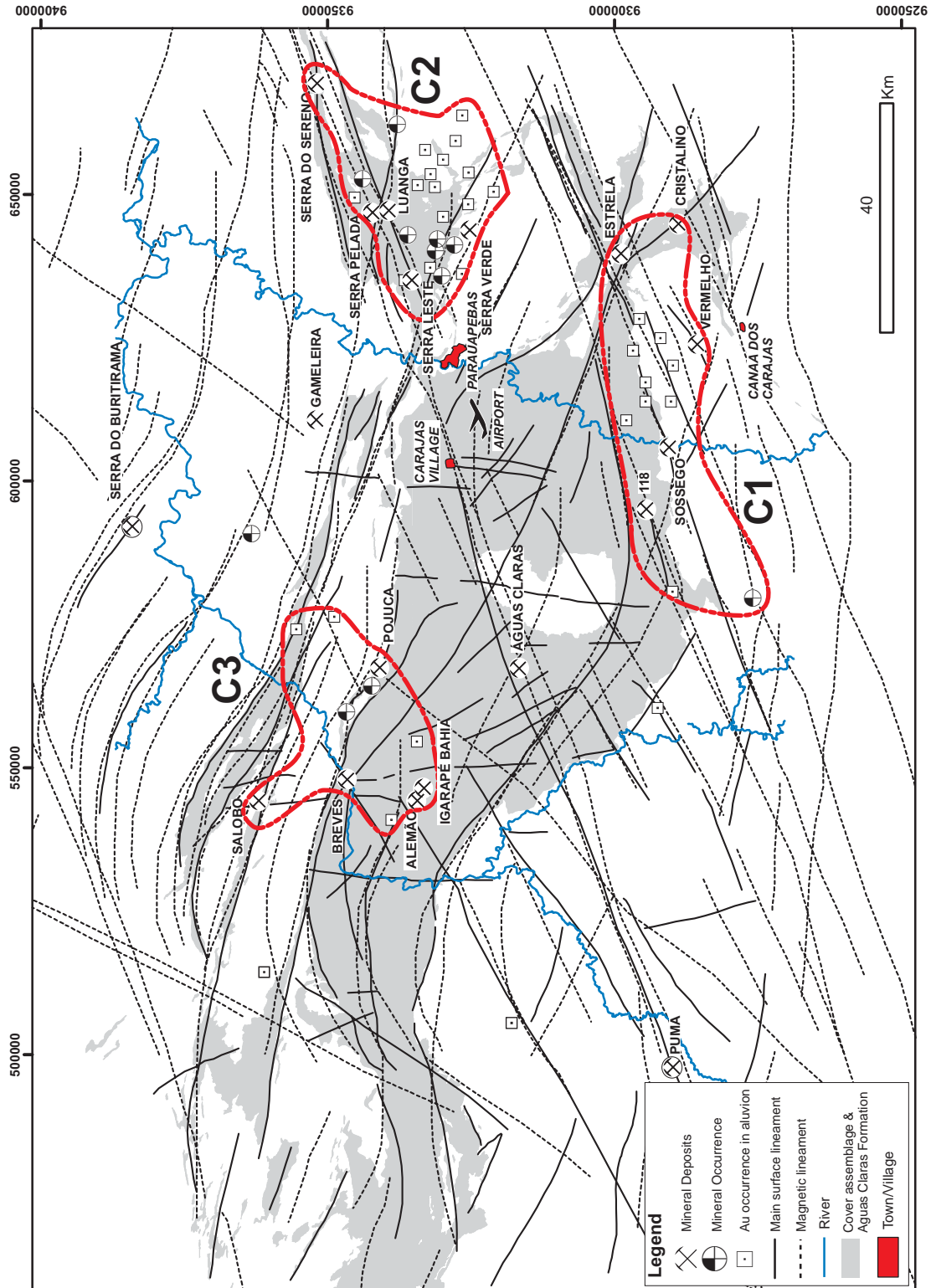


Figure 3.24 Spatial relation between the main topographic (solid) and magnetic (dashed) lineaments within the Carajás Region. Mineral deposits and occurrences are grouped into three clusters (C1, C2, C3). Lithological units of the Cover Assemblage are represented as grey areas.

Chapter 4

The geological and structural aspects of the “Canaã dos Carajás” region, limit between the Carajás and Rio Maria Granite Greenstone terranes

4.1 Introduction

Studies of the geology of Archaean terranes present opportunities to examine geological processes that operated during the earlier stages of Earth’s lithospheric evolution. However, despite decades of research and improvements in the effectiveness of geochronological and geochemical methods, one problem still remains unclear amongst geologists: whether Archaean plate tectonics operated in a manner similar to modern plate tectonics, i.e. horizontal tectonics e.g. (Bickle et al. 1980; Silvennoinen et al. 2007), or whether it was dominated by mantle plumes, i.e. vertical tectonics e.g. (Hamilton 1998; Robin et al. 2009). More recently, an alternative hypothesis has been gradually elaborated by geoscientists. It proposes that in certain regions, the Archaean crust has been shaped by temporal changes from vertical-dominated to horizontal-dominated tectonic processes e.g. (Bouhallier et al. 1993; Lin 2007; Van Kranendonk et al. 2007). Such models have helped to clarify and resolve debates about the nature of the tectonic regimes that formed, for example, the: Dharwar Craton, India (Bouhallier et al. 1993; Chardon et al. 2002);

the Superior Province, Canada (Bedard et al. 2003); and the Pilbara Craton, Australia (Hickman 2004; Van Kranendonk et al. 2004).

In the Amazon Craton, there are two important Archaean regions, both relatively well preserved, that record geological events ranging from 2.9 to 1.8 Ga: the Carajás and Rio Maria Granite Greenstone Terrane (see **Fig. 4.1**). Several studies mainly based on petrological, geochemical and geochronological data, have led to the present consensus that the regions comprise distinct terranes, formed under different tectonic settings. Specifically, it is suggested that vertical tectonics dominate in the Rio Maria Granite Greenstone terrane whilst horizontal (strike-slip) tectonics are predominant in the Carajás region. One problem with this assumption is that geochemistry alone does not allow a clear cut distinction between different tectonic settings to be made, particularly for the Archaean (Hofmann et al. 2004; Van Kranendonk 2004). Therefore, field-based observations to better constrain the interpreted tectonic history of the Archaean rocks are clearly going to be of some importance.

This chapter presents geophysical, microstructural and field-based data from the granitic-gneissic basement, in the region close to the boundary between the Carajás and Rio Maria Granite Greenstone terranes, known as the Canaã dos Carajás region (see the limits of the studied area in **Fig. 4.1B**). The ultimate aims of the study are: i) to propose a tectonic framework and structural evolution for the area and ii) to compare the findings with the geological characteristics of the adjacent terranes located to the north and south.

4.2 Datasets and methods

Datasets were collected and analysed on three main scales of observation during the present study:

- a) *Regional scale* – comprises interpreted magnetic anomalies from an airborne geophysical survey; topographic lineaments identified on digital elevation models (DEM); and interpretation of integrated structural elements mapped in the field.
- b) *Outcrop scale* – corresponds to the observations, photographic sections, sketches and structural measurements collected from outcrops at studied localities in the field area.
- c) *Microscopic scale* – microstructural features recognized in thin sections collected in the field that provide evidence to characterize the deformation mechanisms and estimate the temperatures during the main deformation episodes in the region.

4.2.1 Regional scale methods

Magnetic and radiometric airborne surveys were analysed to extract prominent features defined by positive and negative anomalies. The studied surveys cover approximately 9600 Km² (survey limits indicated by the dot-dashed rectangle in **Fig. 4.1**) and include total magnetic field (IGRF - International Geomagnetic Reference Field) and gamma spectrometry survey techniques. Initially the raw XYZ format dataset were interpolated into a regular grid utilizing the Inverse Distance Weighted (IDW) method in ArcMap v. 9. IDW interpolation involves predicting a value for

any unmeasured location, using the measured values that surround the location where the prediction is to be made. It assumes that each measured point has a local influence that diminishes with distance. Additional interpolation from the raw geophysical datasets was carried out by running the hillshade function from the “Surface Interpolation Tools” part of the Spatial Analyst module in ArcMap:

- **Hillshade:** obtains the hypothetical illumination of a surface by determining illumination values for each cell in a raster. It enhances the visualization of a surface for analysis, especially when using transparency.

Geophysical anomalies were picked for datasets viewed using a GIS platform (ESRI-ArcMap) where the diverse features interpreted from distinct datasets and maps were separated into layers. Surface (topographic) lineaments were manually picked from a 90 metres resolution DEM (digital elevation model) in ArcMap.

Regional foliation was interpreted at map scale by manually drawing lines parallel to the mapped foliation at each locality and trying to link or correlate foliation between neighbouring localities.

4.2.2 Field logistics and Outcrop scale methods

Outcrop data were collected during two campaigns that totalized 55 days of fieldwork. Rock outcrops were accessed via a reasonable network of primary and secondary unpaved roads as shown in **Fig. 4.2**. The search for outcrops in the area started along the roads and later moved to the vegetated and farming areas. Rock exposures were generally absent when traversing farming fields. Therefore, most of the studied outcrops are located near roads.

Fresh rocks exposure is relatively limited considering the total extension of the studied area. Additionally, the equatorial climate in the region has facilitated the development of a considerably thick soil layer that is extensively used for agriculture. Despite this, the 101 visited localities displayed relatively good quality outcrops with individual areas ranging from 1 up to 9275 m² and mode of 772 m². Issues that have potentially affected the studies in the area include: (1) restricted access to some roads or areas because of broken bridges or denied authorization from land owners; (2) uncertainty about the continuity of the major geological units; (3) limited exposures of the geological contacts; (4) relative lack of mineral lineation and fault slickenlines; (5) occasionally unclear or ambiguous cross cutting relations; and (6) often insignificant or null displacement in faults.

The geological map in **Fig. 4.3** was produced based on the maps of (Bizzi et al. 2002) and (Gomes 2003). The modifications incorporated into the source maps include: (1) addition of new granitoid bodies from the Plaque Suite, based on gamma spectrometry survey a and modification of geological boundaries in granitoids from the original dataset; (2) inclusion of mapped dykes; (3) incorporation of the most prominent lineaments from geophysical surveys and topography; and (4) representation of the average strikes and dips for the structures in the studied and visited localities.

The 101 studied localities were surveyed using digital mapping techniques as summarized by (Edmondo 2002; McCaffrey et al. 2005; Clegg et al. 2006; De Donatis et al. 2006) This method consists of recording the observed features and properties from the rocks into a georeferenced GIS database, using an integrated GPS-mobile GIS-PDA device with the advantage of facilitating data management, visualization and analysis. The structural aspects of planar and linear elements were

measured, collected and analyzed according to the methods published in (Passchier et al. 1990; McClay 1991; Twiss et al. 1992). Digital photo-mosaics were compiled for many outcrops and road-cuts using a tablet PC where the observations and data were annotated onto the digital photo to optimise the process of data treatment and analysis.

4.2.3 Microscopic scale methods

The description and interpretation of small-scale structures in deformed rocks were carried out using thin sections of representative samples under transmitted light microscopy. Microfabrics, textures and structures were identified and interpreted following the concepts presented in (Vernon 2004; Passchier et al. 2005). Observations of the fabric geometry and deformational characteristics of quartz and feldspars (Tullis et al. 1985; Hirth et al. 1992; Tullis 2002), were applied to understand the mechanisms of rock deformation and to estimate the metamorphic conditions under which the rocks were deformed.

4.3 Geological setting

This section presents a summary of the relevant information presented in Chapter 2, which describes the regional geology for the whole of the studied area. Additional information was included from areas where previous studies were carried out in more detailed scales: (a) the East of the Canaã dos Carajás Village; and (b) the Serra Dourada area.

4.3.1 Regional geology

The study area lies within the south-eastern portion of the Amazon Craton in the Central Brazil Shield (**Fig. 4.1 A**). It is part of the Archaean geochronological Carajás Province (Santos et al. 2000; Tassinari et al. 2004), limited to the east by the Neoproterozoic Araguaia Belt (~ 600 Ma; (Moura 1993). To the west, it is overlain by Paleoproterozoic volcano-plutonic and sedimentary rocks of the Uatumã Supergroup and to the north it is buried by Palaeozoic and Cenozoic sediments of the Amazon Basin. The Carajás geochronological province was formed and stabilized during the Archaean and was later affected by extensive Palaeoproterozoic magmatism characterized by the intrusion of anorogenic granitoids, together with mafic and felsic dykes (Pidgeon et al. 2000). It is presently divided into two tectonic domains: the northern Carajás and the southern Rio Maria Granite-Greenstone terranes (**Fig. 4.1 A**). The geological characteristics of these terranes are summarized below (refer to geological map in **Fig. 4.1 B**).

4.3.1.1 Carajás Terrane

This domain is also referred to in the literature as the **Itacaiúnas Shear Belt** or **Carajás Ridge** (DOCEGEO 1988; Machado et al. 1991). It comprises two main Archaean and Proterozoic assemblages separated according to their tectonostratigraphic characteristics and ages (Araújo et al. 1991; Pinheiro 1997):

A) Basement Assemblage comprising older mafic to felsic granulite-facies rocks of the Pium Complex (Silva et al. 1974) dated at 3050 ± 114 Ma (whole-rock Pb–Pb;

(Rodrigues et al. 1992), and undifferentiated tonalitic to granodioritic gneisses and migmatites of the Xingu Complex (Araújo et al. 1991), 2859 ± 2 Ma (zircon U–Pb data; (Machado et al. 1991). Sub-vertical, WNW-ESE-trending mylonitic fabrics were formed coeval with the development of the broad Itacaiúnas Shear Belt and experienced several episodes of reactivation (Pinheiro et al. 1997b; Pinheiro et al. 1997a; Holdsworth et al. 2000).

B) Cover Assemblage formed of lower grade supracrustal volcano-sedimentary sequences that include the Grão-Pará (2759 ± 2 Ma; zircon U–Pb; (Machado et al. 1991), Igarapé Salobo (2.761 ± 3 Ma; zircon U–Pb, (Machado et al. 1991) and Igarapé Pojuca (2.732 ± 2 , zircon U–Pb, (Machado et al. 1991) Groups. The Grão Pará Group comprises the Parauapebas and Carajás Formations, and is economically one of the most important units because of its extensive occurrence and high economic grade, high tonnage iron ore deposits. It is composed of mafic and felsic volcanics alternating with banded iron formations overlain by basic metavolcanics and metasediments. These units show a range of deformation states and metamorphic grades from virtually undeformed greenschist facies in the inner part of the belt, to intensely sheared amphibolite-granulite facies in the Cinzento Strike-Slip System (DOCEGEO 1988; Lindenmayer et al. 1991; Pinheiro et al. 1997a). The Cover Assemblage is overlain by a clastic sequence of shallow-water marine to fluvial deposits of the Águas Claras Formation. Dating of a gabbroic sill (2681 ± 5 ; zircon SHRIMP; (Trendall et al. 1998) constrains the minimum depositional age of the formation

Syn-tectonic Archaean, alkaline granitoids and diorites of the Plaque Suite (2.736 ± 24 Ma; Pb-Pb zircon; (Avelar et al. 1999) together with the Estrela (2763 ± 7 Ma; Pb-Pb zircon; (Barros et al. 2001), Planalto (2747 ± 2 Ma; Pb-Pb zircon; (Huhn et al. 1999) and Serra do Rabo (2743 ± 2 Ma; U-Pb zircon; (Sardinha et al. 2006) granites are intruded into both Basement and Cover assemblages. These units are typically elongate parallel to the strike of the regional WNW-ESE foliation (Holdsworth et al. 2000; Barbosa et al. 2001; Sardinha et al. 2006)

4.3.1.2 Rio Maria terrane

This tectonic domain comprises belts of metamorphosed greenstone sequences of the **Andorinhas Supergroup** (Souza et al. 2001) surrounded by large regions of high-grade infracrustal rocks referred to as the **TTG Suite** (Dall'Agnol et al. 2006) ranging in age from ca. 2.96 to 2.87 Ga (Huhn et al. 1988).

The **Andorinhas Supergroup** consists of the basal **Babaçu** and upper **Lagoa Seca Groups**. The former comprises metamorphosed komatiitic flows (dunites, peridotites, pyroxenites) and metabasalts intercalated with banded iron formations, schists, and metachert. The latter comprises clastics (greywakes, siltstones) and chemical (banded iron formation) metasedimentary rocks intercalated with ultramafic to felsic metavolcanic rocks (andesites, dacites, and riodacites) (Huhn et al. 1988). Felsic metavolcanics in the Lagoa Seca Group were dated at $2904\pm 29/-22$ Ma (zircon U-Pb data; (Macambira et al. 1992) and 2979 ± 5 Ma (zircon U-Pb data); (Pimentel et al. 1994).

The **TTG Suite** comprises an older basement represented by the **Arco Verde Tonalites** (Althoff et al. 1993) dated at 2957 ± 21 Ma (U-Pb zircon; (Macambira et al.

1991; Macambira 1992) and the **Caracol Tonalitic Complex** (Leite et al. 2001) dated at 2948 ± 5 Ma. (Pb-Pb zircon; (Leite et al. 2004). The basement is intruded by various calc-alkaline and potassic Archaean granitoids including: the **Mogno Trondhjemite** (2871 Ma, U-Pb titanite; (Pimentel et al. 1994), the **Rio Maria Granodiorite** (2874 \pm 9/-10 Ma, U-Pb zircon; (Macambira et al. 1991; Macambira 1992); 2872 \pm 5 Ma, U-Pb zircon, (Pimentel et al. 1994), the **Mata Surrão Granite** (2872 \pm 10 Ma, Pb-Pb whole rock; (Rodrigues et al. 1992); (Lafon et al. 1994b); and 2871 \pm 7 Ma Pb-Pb zircon; (Althoff et al. 1998), and the **Parazônia Tonalite** (2858 Ma, U/Pb titanite; (Pimentel et al. 1994), not within the limits of Fig. 4.1 B). These syn-tectonic granitoids were generated and emplaced during the closure of the greenstone belt marginal basins during the final stages of the tectonic evolution of the Rio Maria granite-greenstone terrane (Souza et al. 1997).

Paleoproterozoic plutons (ca 1.88 Ga) intrude most of the rocks of basement and low-grade volcano-sedimentary sequence in the Carajás (e.g. Cigano, Carajás Central and Rio Branco granites) and Rio Maria Granite-Greenstone terranes (e.g. Seringa, Musa, Bannach and Jamon) (Machado et al. 1991; Dall'Agnol et al. 1999). They are generally non-foliated, monzogarnitic-syenogranitic, coarse- to medium-grained, massive and highly discordant showing sharp contacts with, and angular inclusions of the Archaean country rocks (Ramo et al. 2002; Dall'Agnol et al. 2005).

4.3.2 Local geology

The geology of the Canaã dos Carajás region (see **Fig. 4.3**) and its surroundings is mainly represented by units belonging to the granitic-gneissic Basement Assemblage of (Pinheiro et al. 1997a). Oliveira (2002) and Lima (2002) described in detail the geological characteristics of the litho-stratigraphic units present in the studied region. Their key findings are summarized below:

4.3.2.1 The Xingu Complex

This unit covers most of the investigated area and comprises **granitoids** and **amphibolites**. The *granitoids* are ubiquitous and are typically migmatitic and gneissose, ranging from 2.928 ± 1 (Sardinha et al. 2004) to 2.851 ± 4 (Machado et al. 1991). They are predominantly of tonalitic composition with minor variations to granodioritic and granitic members. In the field, these rocks show various tones of grey, are coarse- to medium-grainsize with equigranular and inequigranular textures. Their mineralogical assemblage includes quartz, plagioclase, alkali-feldspar, amphibole, biotite and secondary epidote (after calcic plagioclase). Quartz and feldspars also often form porphyroclasts and lensoid fragments enveloped by a mica-rich matrix. Deformation is heterogeneous, with fabrics ranging from protomylonitic to mylonitic according to the (Sibson 1977) classification.

The *amphibolites* comprise metre wide and tens of metres long, elongated lens-like bodies spatially alternating with granitoids or occurring as enclaves with varied shapes and sizes. They have a dark-grey colour, equigranular textures with

fine- to medium-grainsizes composed essentially of amphibole, plagioclase, quartz and biotite. The only isotopic age for these rocks is 2.519 ± 5 (Machado et al. 1991).

More recent work at finer scales using detailed mapping and geochronology has progressively subdivided the rocks of the Xingu Complex into other units. The newly defined units comprise several Archaean syn-tectonic granitoid bodies (e.g. Estrela Granite, Planalto Granite and the Mogno Trondhjemite) and the deformed granitoids of the Plaque Suite. The ages of these newly defined units range from 2.763 ± 7 (Barros et al. 2001) to 2.525 ± 38 (Souza et al. 1996) (see other ages for Archaean Syn-tectonic Granites in Table 5.1) Future research in the area will potentially lead to the recognition and delineation of more new granitic bodies intruding the Xingu Complex.

4.3.2.2 The Plaque suite

This unit comprises a series of E-W elongate, alkaline granitoids, showing prominent planar fabric and geomorphologically represented by the presence of aligned and rounded ridges, 230 to 350 metres high. The rocks are dominantly biotite-granites showing pink and grey tones, coarse- to medium-grainsizes with equi and inequigranular varieties. The mineral assemblage includes K-feldspar, quartz, plagioclase, amphibole and accessory magnetite.

Granitoids from the Plaque Suite have been gradually separated into independent bodies, as more recent studies have better defined their petrological, geochemical and geochronological characteristics.

4.3.2.3 Palaeoproterozoic (anorogenic) granites

These rocks are relatively scarce in the mapped region and are represented by the Rio Branco pluton and associated bodies (**Fig. 4.3**). They comprise isotropic, alkaline granites with colours ranging from pinkish-grey to pale grey. The medium- to coarse-grained rocks typically comprise quartz, feldspars, commonly altered to epidote and clay minerals, amphibole and accessory biotite.

4.3.2.4 Dykes

Gabbroic dykes form elongate steeply-dipping intrusive sheets which intrude rocks of the Xingu Complex and the relatively younger syn-tectonic granitoids. They can be tens to hundreds of metres long and tens of metres wide, dark grey, fine- to medium-grained, equigranular, and are essentially composed of plagioclase and amphibole. These bodies are typically isotropic, but deformed varieties (weakly foliated) were also observed. They trend E-W, NW-SE, and N-S.

Two relatively small areas within the investigated region were previously studied in Masters projects, which focussed on petrological, mineralogical and hydrothermal aspects. Their results remain unpublished and the main findings are summarized below:

4.3.2.5 East of Canaã dos Carajás Village

(Gomes 2003) studied geological and geochemical aspects of the granitoids located to the east of the Canaã dos Carajás village (**Fig. 4.3 A and C**). The following rock units were identified in the area: (1) supra-crustal rocks correlated with the Itacaiúnas Supergroup; (2) basic rocks including amphibolites and gabbros; and (3) various granitoids comprising a) undifferentiated granitoids, b) leucomonzogranites (LMzG), c) hornblende-syenogranites (HbS), and d) tonalite-trondhjemites (TT).

Amphibolites occur as enclaves in the LMzG, showing fine to very fine textures characterized by alternating bands of quartz+feldspar and amphibole+biotite+pyroxene. These rocks have geochemical affinity with basalts and andesitic basalts.

The undifferentiated granitoids correspond to the Xingu Complex basement, comprising medium- to coarse-grained, grey monzogranites and tonalites with prominent ductile fabrics. Localized gneissic banding consists of alternating quartz-feldspathic and amphibole-biotite-rich layers. Mineralogically these rocks comprise plagioclase, quartz, microcline, biotite and amphibole.

The leucomonzogranites (LMzG) consist of pink or grey, medium- to coarse-grained granitoids, composed of plagioclase, quartz, microcline and biotite. These rocks are heterogeneously deformed showing E-W, sub-vertical foliations and preserve clear intrusive relationships with rocks belonging to the Xingu Complex.

Supracrustal rocks corresponding to the Itacaiúnas Supergroup comprise banded iron formations, metabasalts and talc-schists. They form isolated, E-W aligned ridges locally NE-SW oriented.

Hornblende-syenogranites are pink, medium- to coarse-grained and composed of quartz, microcline, plagioclase and hornblende + biotite. The minerals form a pervasive E-W sub-vertical foliation with localized mylonitic zones and amphibolite enclaves. (Gomes 2003) separated these bodies from the Plaque Suite as defined by (Araújo et al. 1991) and grouped them into the syn-tectonic Planalto Granite, based on petrological aspects.

The tonalite-trondhjemites are intensely deformed rocks with alternating sub-vertical layers of tonalitic and trondhjemitic composition. They exhibit grey or white colours, pervasive E-W sub-vertical foliations and equigranular, coarse textures. The mineralogy comprises quartz, plagioclase and accessory biotite. This unit was originally referred to part of the Plaque Suite (Araújo et al. 1991) and was later included in the Xingu Complex by (Lima 2002).

Gabbros occur as: (a) deformed, very fine-grained, dark grey-greenish rocks forming E-W elongated bodies; or (b) undeformed, dark coloured, coarse- to medium-grained rocks, represented by N-S dykes that cross-cut the LMzG and hornblende-syenogranites.

4.3.2.6 Serra Dourada area

(Souza 2007) studied the hydrothermal alteration in Archaean rocks in the Serra Dourada region (**Fig. 4.3 A and B**), 15 km NW of Canaã dos Carajás Village. The area comprises gabbros, diorites, dacitic dykes and ubiquitous granitoids including:

Syenogranites – pinkish grey, fine- to medium-grainsize rocks, displaying a weak 010°-trending foliation and cross-cut by quartz-feldspathic dykes oriented 070°.

Granodiorites – isotropic, pink-greyish, medium- to coarse-grained rocks, locally exhibiting migmatites and fractures filled with quartz and feldspar. The mafic-rich members preserve centimetre to metre wide, almond-shaped, tonalitic enclaves.

Tonalites – grey, medium-grained rocks in contact with albitized rocks and cross-cut by quartz-feldspathic dykes and veins.

Two groups of hydrothermally altered granitoids are also present and comprise:

A) *Scapolitized bodies*: these are typically fine- to medium-grained and isotropic where scapolite replaces primary plagioclase or occurs as veins and veinlets. The extent of scapolitization in the area gradually increases from W to E. Petrographic observations indicate that these rocks are derived from tonalites.

B) *Albitized granitoids* comprise magmatic and hydrothermal albite, k-feldspar, quartz, and chlorite-biotite-muscovite. These rocks are isotropic, inequigranular and cross-cut by metre-scale albite veins in the more altered domains. Remaining portions of the original rock show mineralogical contents similar to the syenogranites.

Gabbros form relatively small, E-W elongate bodies intruded into the granitoids. They show sub-ophitic textures and comprise amphibole, scapolite, biotite, epidote, apatite, chlorite and titanite.

Diorite dykes, trending ENE to NE are intrusive into the granitoids. The dykes show porphyritic and glomeroporphyritic textures, fine- to medium-grainsizes and mineral content including: quartz, plagioclase, microcline and minor disseminated chalcopyrite, fluorite and epidote.

4.3.3 Geochronology

A selection of representative isotopic ages for the broad area comprising the Carajás and Rio Maria Granite Greenstone terranes - and the portion separating these two terranes, known as Transitional Domain - is presented in **Table 4.1**. A brief analysis of the ages helps to define the main geochronological units in the area:

(1) The oldest ages correspond to the basement units including: (a) the Xingu Complex in the Carajás terrane and Transitional domain (2.972 ± 16 Ga); and (b) the Caracol and Arco Verde tonalites in the Rio Maria Granite-Greenstone Terrane (2.942 ± 2 and 2.981 ± 8 Ga, respectively). The basement in the Rio Maria Granite-Greenstone Terrane comprises older TTG granitoids and a number of calc-alkaline granitoids ~ 2.8 Ga old, intercalated with greenstone belts of ~ 2.9 Ga (see Andorinhas Supergroup units, **Table 4.1**).

(2) Volcano-sedimentary rocks from the Cover Assemblage with general ages of ~ 2.7 Ga (see units of the Itacaiúnas Supergroup in **Table 4.1**), that unconformably overlie the Basement Assemblage in the Carajás terrane. Syn-tectonic alkaline granitoids dated at ~ 2.7 and 2.5 Ga are intrusive into the basement in the Carajás terrane and Transitional domain (see Archaean syn-tectonic granites in **Table 4.1**). Finally, ~ 1.8 Ga Palaeo-proterozoic anorogenic granitoids are ubiquitous in all three regions, and are represent a major phase of plutonism that occurred during a major crustal extensional event recognized across the whole of the Amazon Craton (give key references).

The study area sits in the Transitional domain including the Canaã dos Carajás region where (Sardinha et al. 2004) dated granitoids at ~ 2.9 and 2.7 Ga. These authors proposed that:

(1) the oldest age (2.9 Ga) is comparable with those obtained for TTG granitoids in the Rio Maria Granite Greenstone terrane (e.g. Guaranta Granite and Caracol Tonalite), suggesting that part of the rocks forming the Transitional domain were formed synchronous with the development of the Rio Maria Greenstone terrane; and

(2) the 2.7 Ga age comes from a trondhjemite which is younger than those from the Rio Maria Granite-Greenstone Terrane, indicating that the Transitional domain also has rocks broadly equivalent in age to syn-tectonic and volcano-sedimentary rocks in the Carajás terrane. Additionally, the 2.7 Ga age from biotite-hornblende granites in Canaã dos Carajás is analogous to the age of crystallization of the closer syn-tectonic Planalto Granite (2.747 ± 2 (Huhn et al. 1999)).

The isotopic ages from (Sardinha et al. 2004) therefore suggest that a geological link exists between the three geochronological domains previously mentioned. In other words, the rocks in the Transitional domain show isotopic ages comparable with those observed in the Carajás and Rio Maria terranes. Further comparison of isotopic data (**Fig. 4.4 A**) shows a fairly good agreement between the age curves for the Carajás terrane, Transitional domain and Rio Maria Granite-Greenstone terrane.

Age histograms from the Carajás terrane (**Fig. 4.4 B,C**), Transitional domain (**Fig. 4.4 D**) and Rio Maria Granite-Greenstone terrane (**Fig. 4.4 E**) show peaks at the ages of 1.88, 2.56, 2.75, 2.84 and 2.9 Ga. corresponding to phases of mafic and granitic magmatism and latter deposition of volcano-sedimentary rocks. The ages at 2.5 and 2.7 Ga mark major events of mineralization. These peaks represent concentrations of ages at specific time periods, indicating large-scale events of crustal formation, associated with contemporaneous ore genesis. Alternatively, the

2.7 Ga ages from syn-tectonic granitoids mark an important episode of crustal shortening coeval with syn-tectonic magmatism (Holdsworth et al. 2000; Sardinha et al. 2006). Later events at 2.5 Ga have been interpreted as being related to the reactivation or nucleation of shear zones (Machado et al. 1991; Requia et al. 2003).

4.4 Results

4.4.1 Regional scale interpretation

Aeromagnetic surveys are perhaps the most common type of airborne geophysical survey. It is typically used in regional studies with applications that include: geological mapping, basement and basin tectonic studies and oil and mineral exploration e.g. (Chernicoff et al. 2002; ten Brink et al. 2007; Allek et al. 2008). Additionally, gamma spectrometry airborne survey is referred as an effective tool for geological mapping in different environments with further application in mineral exploration and structural analysis e.g. (Paradella et al. 1997; Jayawardhana et al. 2000; Debeglia et al. 2006).

Magnetometric and gamma spectrometric anomalies were manually traced onto their respective surveys aiming to characterize the geometric and directional attributes of the anomalies. Magnetic anomalies have traditionally been used to delineate regional-scale structures. The basis for this method is the fact that magnetic minerals can be concentrated or depleted in the vicinity of faults or shear zones, forming positive or negative linear anomalies. Radiometric surveys are particularly useful to determine the form, size and limits of granitic bodies when these are

intruded into a middle crustal rock assemblage with contrasting contents of K, U, and Th in mineral phases. The maps presented in this section highlight the area where field data were collected and these are then described in the following section.

4.4.1.1 Aeromagnetic characteristics

Aeromagnetic data covering an area extending from the centre of the Carajás Ridge to south of the village of Canada in the Transitional domain (for location see dashed-dotted box in **Fig. 4.1 B**) allowed imaging the geological features in terms of their magnetic responses. The resolution of the aeromagnetic data is controlled by a flight line spacing of 1 km. The raw magnetic data (in XYZ format) was interpolated into a regular grid that was subsequently processed to generate a hillshade surface.

4.4.1.2 Aeromagnetic Patterns

The magnetic survey was studied focusing on the linear geometry of the anomalies since these are generally indicative of geological features such as dykes, geological contacts, faults and/or shear zones.

Visual analysis of the interpolated raw magnetic data (see **Fig. 4.5 A**) reveals two prominent E-W-trending anomalies (shown in grey). *Anomaly One* (see **Fig. 4.5 B**) is located in the northern part of the area. It corresponds well with the location of giant iron ore bodies in the region, producing the highest intensity levels of the magnetic field observed. This anomaly also coincides with an important geological contact that separates volcano-sedimentary rocks of the Cover Assemblage (to the north) from the granitic basement (to the south) (**Figs. 4.1, 4.3, 4.5 A**).

Anomaly Two comprises a continuous and sinuous zone of high-to-intermediate magnetic intensity located in the central-southern part of the area, (see **Fig. 4.5 B**). This anomaly is spatially associated with a series of distinct lens-shaped anomalies displaying moderate to strong magnetic responses (the pink polygons shown in **Fig. 4.5 B**). These coincide in geometry and broadly in location with the position of ca. 2.7 Ga syn-tectonic granitoids in the region (e.g. Planalto and Plaque Suite granitoids, **Figs 4.1, 4.3**). The combined occurrence of long, continuous and sinuous anomalies with lenticular bodies, is consistent with the presence of a major zone of concentrated deformation, which could have acted as structural pathways for the syn-tectonic emplacement of granites.

The E-W anomalies are cross-cut by relatively narrow, straight and continuous NW-SE and NE-SW lineaments ranging in length from 10 km up to 70 km (see dashed lines in **Fig. 4.5 B**). Some of these lineaments appear to offset the E-W anomalies, suggesting that they may represent shear or fault zones.

The hillshade surface map with illumination inclined at 30° from 020° Az (**Fig. 4.6 A**) highlights well the long, straight linear anomalies. The main sets of interpreted lineaments (**Fig. 4.6 B**) include: (1) NE-SW-trending lineaments forming a 30 km wide corridor that extends from the top NE to the bottom SW corners of the map; and (2) E-W-trending anomalies comprising numerous short (~5 km) lines in the background of the image and a long and continuous zone, about 15 km wide, with its northern and southern limits located close to the Cedere III and Canada localities, respectively. NW-SE lineaments are less numerous and seem to be spatially concentrated in the northern portion of the area. They seem to correspond primarily to part of the trace of the Carajás Fault and to a contact between the

volcano-sedimentary sequences in the Carajás terrane and the underlying granite-gneiss basement.

4.4.1.3 Gamma Spectrometric datasets

Airborne radiometric data generally show the spatial distribution of natural levels of uranium, thorium and potassium, and are commonly used to assist in near surface geological mapping and mineral exploration studies. The studied gamma spectrometric survey covers the same area as magnetic survey (limits indicated by the dashed-dotted box in **Fig. 4.1 B**). The resolution of the data is determined by the 1 km spacing of the N-S flight lines. Importantly, data interpretation was made visually from a three-channel colour composite image generated by merging the signals of the U-K-Th channels into a single layer. Additionally, the resulting raster image was converted into a hillshade map where prominent anomalies were identified.

4.4.1.4 Gamma Spectrometric Patterns

The three channel (U-K-Th) radiometric composite image shows red and blue colours corresponding to low and high gamma radiation values respectively (see **Fig. 4.7 A**). The blue-green (high) anomalies occupy 17% of the studied area and seem to correspond to the locations of syn-tectonic Archaean granitoids (e.g. Plaque Suite, Estrela and Planalto) and Proterozoic anorogenic granites (e.g. Central, Cigano, Rio Branco) (compare the blue anomalies in the gamma survey with the location of the Central, Estrela and Rio Branco granites in **Figs. 4.1, 4.3 and 4.7C**). Low

radiometric values are dominant in the survey (red anomalies), and are interdispersed by subordinate blue anomalies.

The maps of interpolated radiometric values (**Fig. 4.7 A and B**) exhibit sinuous and straight linear anomalies. A prominent sinuous linear anomaly, broadly E-W-trending extends from the central-eastern to the lower south-western boundaries of the survey area (see solid lines in **Fig. 4.7 C**). The anomaly forms a 12 km wide corridor comparable to the similar feature identified in the magnetic survey (see the grey Anomaly 2 in **Fig. 4.5 B**). Above the sinuous anomaly, a straight and linear anomaly is projected from the top NE corner to the central part of the survey area (see dotted-dashed line extending from the Racha Placa to Sossego localities in **Fig. 4.7 C**). The mentioned straight and sinuous anomalies, seem to delineate the limits of a high-strain zone, associated with larger elliptical anomalies (grey) and a trail of relatively smaller sub-rounded anomalies (pink polygons). The elliptical or sub-rounded anomalies (coloured polygons in **Fig. 4.7 C**) are enclosed by curved lineaments (thin dotted lines in **Fig. 4.7 C**) that resemble aureole-like features. NW-SE-trending straight linear anomalies seem cross-cut the formerly described structures (dotted-dashed straight lines in **Fig. 4.7 B**).

Importantly, part of the gamma survey, limited by the black vertical dashed lines (see **Fig. 4.7**) has spacing between the flight lines larger than the other parts of the survey. This explains the occurrence of the obvious N-S striped pattern, which implies a relatively higher degree on uncertainty for the interpretations carried out within this zone.

Collectively, the geometry and patterns of the radiometric anomalies, suggest that: (1) the studied area is cross cut by what seems to be a prominent zone of strain accumulation; and (2) the presence of elliptical anomalies may indicate the presence

of deformed igneous bodies. The numerous high radiometric anomalies (pink polygons) appear to be spatially related with the broad deformation zone described. They are comparable with the radiometric response observed in syn-tectonic and anorogenic granites recognized in the area (e.g. Central, Estrela and Rio Branco). This suggests that the plutons and regional-scale deformation zone may be related to one another in some way.

4.4.1.5 Summary

The magnetic and radiometric surveys show good correspondence between their most prominent regional scale anomalies. Indicating that the major anomalies are more likely to correspond to real geological feature rather than being artificially produced. The features common in both datasets include:

- a) One broadly E-W trending, continuous and sinuous anomalies that may correspond to a regional scale shear zone or set of shear zones (see anomaly 2 in Fig. 4.5 and the sinuous linear anomaly in Fig. 4.7).
- b) A consistent set of sub-parallel, straight and discontinuous NE-SW-trending, and subordinate NW-SE-trending lineaments possibly corresponding to brittle faults (see widespread straight lines in **Figs. 4.5 B**; **4.6 B**; and **4.7 C**). Importantly, several of these straight and linear geophysical anomalies match quite well, topographic lineaments at regional scale presented in chapter 3.
- c) Generally elliptical features with and E-W preferred orientation of their long axes that likely correspond to the location of granitoid plutons.

The suggested geological significance of these anomalies are now investigated in the field.

4.4.2 Outcrop Data

This section describes the lithologies, spatial distribution and structure of the geological units outcropping south of the Carajás terrane in an area of approximately 1,370 Km² extending from the west near the town of Racha Placa eastwards to beyond Canaã dos Carajás and from the village of Serra Dourada in the north to Canada in the south (see the area limits in **Fig. 4.1** and **5.2**). The area comprises predominantly granite-gneissic basement rocks including highly deformed older gneisses and moderately deformed younger basic rocks (volcanics, amphibolites). The basement gneiss units are intruded by deformed medium- to coarse-grained granitoids showing varied degrees of structural anisotropy. Finally, more isotropic, less deformed late granitic plutons intrude both gneisses and basic rocks.

4.4.2.1 General lithologies

5.4.2.1.1 Old Basic rocks

This lithological group is represented by amphibolites and mafic rocks that typically occur as *in situ* outcrops or as boulders (**Fig. 4.8 A, B, C**). They often form elongated hills, 200m up to 300m long with gently rounded ridges. At map scale, these rocks represent E-W or NW-SE-trending lens-shaped domains concordant and discordant with the granitic basement. When intensely weathered, they develop dark

and compact lateritic ironstone crusts, composed of hematite and goethite, 3 to 5m thick in some cases.

Typical amphibolite mineral assemblages comprise: dark, prismatic amphiboles (hornblende and tremolite-actinolite), plagioclase and minor quartz. Grain sizes are coarser in isotropic (**Fig. 4.8 D**) and finer in sheared (**Fig. 4.8 E**) members, which display characteristic alternating feldspar- and amphibole-rich bands few millimetres up to 2-3 cm thick (**Fig. 4.8 C, F**). Deformed amphibolites are typically found: (1) associated with sub-vertical, semi-brittle, sinistral shear zones, having veins or alteration haloes consistent with fluid-related alteration during the deformation; or (2) in the sheared boundaries of amphibolites where they occur in contact with granitoids.

The mafic rocks have a dark-grey aphanitic matrix and in some members is possible to distinguish bladed plagioclase phenocrysts with the naked eye. Basalt is the dominant lithology, often showing parallel, mono or multi-directional sets of straight, 1mm thick veins apparently composed of aligned mafic minerals (**Fig. 4.8 F**).

Amphibolites also occur as xenoliths within the granitic gneisses that range in size from 10 cm up to 90 cm with geometries ranging from elliptical to sub-angular (**Fig. 4.8 G and H**). They are either isotropic or layered with alternating mafic and felsic rich mineral layers.

Collectively, amphibolites were interpreted as the oldest rocks in the study area because of their xenoliths in granitic gneisses. This relationship was not evident for the mafic rocks that have poorly exposed contacts with gneisses. At least part of the mafic rocks were observed as lens shaped bodies emplaced into the gneisses.

Characterizing a late, intrusive relationship. On the other hand, no contacts were observed in several outcrops of basic rocks.

4.4.2.1.2 TTG Gneisses

Granitic TTG gneisses form the main lithology of the Xingu Complex, which makes up at least 50% of the investigated area. However, its exposure is limited to creeks and topographically low-lying areas. The outcrops are relatively small, comprising boulders or flat platforms (**Fig. 4.9 A and B**). Gneissic banding is characterized by alternating melanocratic (grey) and leucocratic (white or pink) bands composed of biotite and amphibole and plagioclase, quartz, and k-feldspar, respectively.

The gneisses are inequigranular and comprise: (a) medium- to coarse-grained (**Fig. 4.9 C and D**) units, with relatively thick leucocratic bands (up to 3 cm wide) and low amounts of mafic minerals; and (b) medium- to fine-grained blastomylonites with a more uniform appearance, showing a streaky straight foliation defined by aligned mafic minerals and felsic minerals (**Fig. 4.9 E and F**). High temperature conditions seem to have favoured the formation of metre-scale pods and segregations of remobilized alkali-feldspar-rich material (**Fig. 4.9 G**) that lie sub-parallel to the banding in the coarse gneissic members. The finer grained, 'streaky' blastomylonites appear to be intensely deformed gneisses and contain numerous sigmoidal or lens-shaped mineral aggregates and rotated porphyroclasts.

4.4.2.1.3 Mylonites

Many gneisses and granitoids are cross-cut by networks of sub-vertical, mylonitic zones a few centimetres up to tens of m wide (**Fig. 4.10 A and B**). These are mainly composed of quartz, k-feldspar, plagioclase and biotite. The minerals form elongate aggregates or stretched crystals that define a continuous sub-vertical foliation associated with a sub-vertical mineral lineation. Grainsize reduction mechanisms have led to the development of fine-, medium- or coarse-grained varieties of mylonite (**Fig. 4.10 C, D and E**) with grey, white or reddish colours reflecting differences in the mineralogical content. K-feldspar porphyroclasts, range in size from few millimetres up to 2-3 cm across and show dominantly symmetric or less commonly, asymmetric geometries. In plan view, porphyroclasts geometry suggests clockwise, counter clockwise or null vorticity. In profile view, looking parallel to the steep foliation surfaces, porphyroclasts shapes indicate vertical displacements with top-to-SSW or top-to-NNE sense of shear and also symmetric shapes. Less common, very large k-feldspar porphyroclasts were identified in the mylonites, some of them reaching an impressive 10 cm in diameter (**Fig. 4.10 F**).

4.4.2.1.4 Granitoids

Granitoids account the majority of the exposed rocks in the study area, showing variations in their composition, grainsize and intensities of internal deformation fabrics. The petrological, petrographic and geochemical aspects of these intrusive bodies were studied in detail by (Soares 2002; Gomes 2003; Sardinha et al. 2004; Gomes et al. 2007; Souza 2007). These authors describe the occurrence of

syenogranites (**Fig. 4.11 A**), granodiorites (**Fig. 4.11 F**), tonalites (**Fig. 4.11 B, C, G** and **H**) and isotropic granites (**Fig. 4.11 E**). The granitoids typically comprise varying proportions of k-feldspar, quartz, plagioclase, mafic minerals (biotite or amphibole) and minor sulphides or oxides. Hydrothermal alteration is locally observed, characterized by albitization (**Fig. 4.11 A iii**), scapolitization and chloritization.

Structural anisotropies are widely developed in the granitoids, including foliations, lineations, shear zones and fractures/joints. Magmatic fabrics (foliations) are normally observed in coarser rocks that show a weak- or moderate-alignment of prismatic feldspar grains (see close-up photo in **Fig. 4.11 D**). Solid-state deformation fabrics are heterogeneously developed and are distinguished from magmatic foliations by the presence of deformed lensoids of quartz (see close-up in **Fig. 4.11 B** and **H**), the development of wrapped feldspar porphyroclasts, “trails” of feldspar and mica grains and the development of discrete shear zones (linear features in **Fig. 4.11 H**, not the fractures) that show either straight or curvilinear geometries.

The degree of weathering is variable in these rocks, but it is generally moderate-to-high. Plagioclase-rich granitoids in particular often display intense alteration of feldspar into fine aggregates of clay minerals that are then washed away leaving the empty mould of the original mineral grains. Iron oxide red stains are also commonly present on the outcrops probably resulting from alteration of biotite, sulphides and amphiboles in the granites.

4.4.2.1.5 Dykes

Dykes occur in the area as tabular bodies up to 50 metres wide and 400m long, forming long, straight, flat-topped ridges (see **Fig. 4.12**), trending N-S, WNW-ESE and NE-SW. The contacts between dykes and basement rocks and granitoids were not generally exposed in the field. However, observations at map scale show that the contact relations are both discordant and concordant with the main regional trend of the foliation. This is also consistent with the fact that the dykes are essentially unaffected by ductile deformation fabrics.

The dykes typically show dark grey colours, fine- to medium-grainsizes and are texturally isotropic and undeformed (**Fig. 4.12 A and B**). They are typically cross-cut by millimetre wide shears or microveins filled with chlorite (**Fig. 4.12 B and C**). The dykes are dominantly of basaltic composition with subordinate occurrences of andesitic types (**Fig. 4.12 D**).

4.4.2.1.6 Contact relationships

The previously described lithologies display two main types of contacts that are preserved in a few outcrops:

1- **Magmatic** contacts: they are typically irregular in plan view and characterized by the mixture of distinct lithologies, typically more felsic and mafic granitoid phases (see and **Fig. 4.13**) or granite and mafic volcanic (amphibolite) rocks (see **Figs. 4.14 and 4.15**). This type of contact seems to have formed by impingement see (Chen et al. 2001; Chen et al. 2004) of less competent granitic material into competent mafic domains whilst both rock types were in the magmatic state. This produces granitic

lenses or blobs (**Fig. 4.11 D, E**) with varied sizes and shapes that are interdigitated with and locally engulfed in the mafic portions. The granitic lenses normally display a preferred orientation, accompanied by the development of a sub-vertical foliation, trending E-W (solid state) or N-S (magmatic).

The nature of these contacts suggests that they are comparable with those described for the deformation of felsic and mafic magmas during the formation of Archaean greenstone belts, particularly because of the significant degree of intermingling observed (see (Condie 1981; Shackleton 1995; Windley 1995). Additionally, the development of steeply inclined to sub-vertical folds, foliations and sigmoidal-shaped lenses of mafic rocks are evidence of sub-horizontal shortening acting during the configuration of these contacts. The geometry of these structures indicates that they were formed in some areas under coaxial strains (symmetrically shaped lenses, isoclinal folds e.g. **Figs. 4.13.** and **4.15**) and in others, sinistral non-coaxial strain (asymmetric folds and sigmoidal lenses e.g. **Fig. 4.14**). This may indicate strain partitioning during bulk transpressional strain.

2- **Tectonic** contacts are characterized by regular and continuous surfaces, commonly separating granitoids from amphibolites (see examples in **Figs. 4.16** and **4.17 A**) or mafic intrusions (**Fig. 4.17 B**). The contact planes are mostly sheared, sub-vertical with straight or gently curved geometries oriented E-W, NE-SW and more rarely NW-SE. Most examples preserve smaller scale evidence of original magmatic intermingling of these lithologies (e.g. detailed images 1 and 2 in **Fig 4.16**).

4.4.2.2 Structural Geometries and Kinematics

This section describes the mesoscopic-scale planar and linear structural fabrics and kinematic indicators recorded in the studied rocks outcropping adjacent to in the Canaã dos Carajás study area.

4.4.2.2.1 Foliation

A penetrative ductile foliation was observed in gneisses, granitoids, mylonites and basic rocks. However, the degree of foliation development is extremely heterogeneous.

In the **TTG gneisses**, the foliation lies sub-parallel to the compositional banding formed by alternating mafic (biotite-amphibole-rich) and felsic (quartz-feldspar rich) layers (see examples in **Fig. 4.9 C, D and G**). The metamorphic banding corresponds to an early S_n fabric, oriented N-S, NNW-SSE and NNE-SSW with steep to sub-vertical dips ($\sim 59^\circ - 89^\circ$) towards both the E and W (**Fig. 4.19 A i and G**). The early S_n layering is folded by isoclinal folds with wavelengths ranging from few centimetres up to 30 cm. Steeply dipping to sub-vertical fold axial planes and sub-horizontal fold hinges lie parallel to the S_n banding, and are also broadly N-S oriented (see stereonets on **Figs. 4.18 C i, D i, I, J** and field photos in **Fig. 4.19 A-D and Fig. 4.28**). Migmatitic layers of medium- to coarse-grained k-feldspar often occur parallel to or cross-cutting the gneissic banding and may also form centimetre scale folds (see examples of migmatitic material in **Figs. 4.9 D, G, Fig. 4.14, Fig. 4.15 and Fig. 4.19 E, F, N**). These layers appear to be products of partial melting of

granitic gneisses under relatively high temperature conditions. It is unclear whether they were folded whilst in a partially molten state.

Shearing and transposition of the early S_n fabric produced an S_1 foliation in the gneisses. The new foliation is macroscopically classified as disjunctive, spaced and parallel. It is characterized by the preferred orientation of mafic minerals (e.g. biotite or amphibole) and elongated aggregates of medium- to fine-grained quartz and feldspars crystals (see examples in **Fig. 4.9 E, F** and **Fig. 4.19 J and N**). The S_1 foliation trends WNW-ESE and E-W with steep dips ($\sim 70^\circ$ - 89°) to the north and south (see stereonets on **Fig. 4.18 A ii** and **G**). An S_2 foliation trending NE-SW, with steep dips ($\sim 64^\circ$ - 89°) both to the NW and SE (see stereonets on **Fig. 4.18 A iii**), was observed often in association with the sinistral shear zones that cross-cut the S_n and S_1 fabrics (see examples in **Fig. 4.20** and **Fig. 4.21**). Despite the mentioned cross-cutting relations, field evidence does not make totally clear whether the S_2 foliation is older or was synchronously formed with the S_1 foliation. However the sinuous geometry of major magnetic and gamma-radiometric anomalies shows continuous linear segments that shift orientation from E-W to NE-SW and back to E-W (see **Figs. 4.5** and **4.7**). This geometrical relation suggests that S_1 and S_2 are perhaps contemporaneous.

S_n , S_1 and S_2 foliations are present in the foliated granitoids and mafic rocks (see field examples in **Fig. 4.22** and **Fig. 4.29** and stereonets in **Fig. 4.18 M** and **U**) with orientations and dip values broadly similar to those in the gneisses. This relation is consistent with a genetic and/or temporal link between the tectonic events that formed the ductile fabrics and the processes of syn-tectonic granitic emplacement and deformation.

Both the gneisses and foliated granitoids are commonly cross-cut by ductile faults, centimetres to tens of metres wide, some of them containing mylonites. These mylonitic zones are parallel to S_1 and S_2 foliation trends. Mylonites mark zones of concentrated strain accommodation, and suggest intense partitioning of the bulk strain. Further, there is no clear evidence to constrain the relative age of the mylonites relative to S_1 and S_2 but it appears that they are parts of the same anastomosing foliation. The mylonitic foliation typically comprises a prominent planar fabric formed by long and thin quartz-feldspathic layers in the matrix enveloping relatively large feldspar porphyroclasts (see examples in **Fig. 4.10**). Morphologically, the mylonitic foliation is classified as disjunctive with variations to: (1) smooth and relatively straight & continuous – in the fine- to medium-grained varieties; or (2) rough and anastomosing – in the coarser members.

The grain size in the mylonites ranges from fine (few millimetres) to coarse (up to 1 cm) in proto-mylonitic varieties. Porphyroclast shapes include lozenge, augen and spherical shapes that apparently show little rotation. The variations in textural characteristics observed in the mylonites seem to be related to an interplay between their protolith grain size and later strain intensity.

The deformed granitoids show either mylonitic (previously described) or a ductile foliation morphologically classified as disjunctive, rough or smooth and parallel (see **Fig. 4.22**). The ductile planar fabric is characterized by the preferred alignment of mafic minerals, mafic aggregates and quartz ribbons. Diffuse foliation, characterized by aligned, widely-spaced concentrations of a dominant mineral phase was subordinately recognized. The heterogeneous development of foliation in the deformed granitoids once again indicates that strain was generally partitioned and concentrated into localised high strain zones.

The foliation in the older **basic rocks** can be classified as fine, straight and continuous, and is characterized in particular by the preferred alignment of prismatic amphibole crystals. Amphibolites display foliation defined by compositional banding formed by alternating amphibole- and feldspar-rich layers (see **Fig. 4.23**). Gently wavy or folded foliation and lenses or porphyroclasts of mafic minerals aggregates are subordinate features. The ductile foliation in amphibolites include: (1) WNW-ESE ($\sim 110^\circ$ Az) dipping 69° up to 88° towards NNE and SSW; (2) N-S dipping 69° - 88° to E and W; and (3) NE-SW dipping 63° - 79° toward NW (see stereonets in **Fig. 4.18 U**).

4.4.2.2 Lineation

Mineral lineations are typically associated with foliation planes and rarely form a penetrative fabric. They are typically defined by a preferred orientation of elongate mineral grains or polycrystalline aggregates, observed in the granitic lithologies as elongate quartz crystals or quartz-feldspathic aggregates (see examples in **Fig. 4.24**). Minor L tectonites (cigar shaped grains) were observed locally in some deformed granitoids. In foliated amphibolites, the lineation is defined by aligned amphibole crystals within exposed foliation planes. Mineral lineation average plunges are steep ($\sim 62^\circ$) to sub-vertical ($\sim 88^\circ$) towards the SSE and round to the NW (see stereonet for total mineral lineation in **Fig. 4.18 B**). Further, the sub-vertical lineation is consistent both within and outside shear zones and in foliated domains with different strike directions (see stereonets **i**, **ii** and **iii** in **Fig. 4.18 B**). In gneisses and granitoids, mineral lineations plunge steeply (average of 73° in gneisses and 71° in granitoids) mainly towards SE and SSW in the gneisses and SE, SW and NW in the granitoids

(see stereonets in **Fig. 4.18 H and D**). Collectively, mineral lineation in gneisses and granitoids indicates a sub-vertical orientation for the maximum principal stretch axis.

4.4.2.2.3 Folds

These structures are characterized by the bending or flexure of the compositional banding in the TTG gneisses and deformed granitoids alternated with mafic lenses, rarely observed in amphibolites, presumably because they lack a well-defined compositional banding. Their wavelength is typically of tens of centimetres, reaching metre scales in a few examples. Folds were grouped based on their orientation and style as follows:

The early **folded gneissic banding** forms upright folds with tight to isoclinal limbs (**Fig. 4.19 A-C**). Minor similar folds were observed, showing gentle asymmetry with “long and short” limb geometries. Both fold types have axial surfaces generally oriented NNW-SSE with sub-vertical to steep dips (76° - 88°) both to the NE and SW (see stereonets in **Fig. 4.18 C and I**). Their hinge lines plunge 10° - 26° mainly to the SSE and NNW (see stereonets in **Fig. 4.18 D and J**). These folds are associated with the S_n primary gneissic banding produced during early metamorphic episodes that formed these rocks. Additionally, folds in granitoids intercalated with mafic lenses (e.g. **Fig. 4.13**) show axial planes trending NWN-SES with dips of 71° - 89° to both ENE and WSW (stereonets in **Fig. 4.18 O**) and hinge lines plunging 7° - 31° towards SSE and NNW (see stereonet in **Fig. 4.18 O**). Finally, disharmonic folds in gneisses (**Figs. 4.19 D, 4.20; 4.21; and 4.28**) display a highly heterogeneous directional pattern giving a radial aspect to the stereonet in **Fig. 4.18**

I.

Intrafolial and asymmetric “**drag folds**” folds tend to occur within and parallel to the transposed foliation (S_1 and S_2) developed in gneisses. Intrafolial folds (examples in **Figs. 4.19 I-L; Fig. 4.20; and Fig. 4.21**) appear to be produced by the transposition of the S_n foliation observed in the gneisses. The drag folds are characterized by bending of the gneissic banding, foliation or pegmatitic veins at the margins of ductile shear zones (**Figs. 4.19 M, N, P and 4.20, 4.21 and 4.29**). Collectively, these folds show sub-vertical axial surfaces trending: (1) WNW-ESE $\sim 110^\circ$ Az, dipping $\sim 88^\circ$ to NNE and SSW with hinge lines plunging gently (11° - 26°) to WNW and ESE; and (2) NE-SW $\sim 40^\circ$ Az, dipping 65° - 88° to SE or NW with hinge lines plunging 7° - 30° towards the NE and SW (see stereonets for folds axial planes and hinges in **Fig. 4.18 C, D, I, J, O, V**). Finally, subordinate folds display moderately to steeply plunging (40° - 77°) fold hinges towards the E-SE and W-SW (see stereonets in **Fig. 4.18 D and J**).

Ptygmatic folds of granitic and pegmatitic veins are locally developed with a few centimetres wavelength and asymmetric lobate geometries typically forming “S” shaped folds (**Fig. 4.19 E and F**). **Sheath folds** are represented locally by the development of elliptical concentric rings of quartz+feldspar in biotite-rich gneisses units (**Fig. 4.19 G and H**). The development of these folds seems to be consistent with the observed variations in hinge line plunges described above.

The geometrical relationships between axial surfaces and hinge lines of the folds was described by using the Fleuty diagram, (**Fig. 4.25**), where the dips of axial surfaces are plotted against the plunges of hinge lines. The majority of the studied folds fit into the categories of sub-horizontal upright and gently plunging upright. These folds correspond to the previously described early isoclinal folds, intrafolial transposed folds and “drag” folds formed by reverse shear zones.

It was not possible to determine with certainty whether large-scale folds are present in the studied area. Approximately 80% of the observed folds are upright and do not show vergence. Further, the remaining steeply inclined folds do not show a systematic change in fold vergence pattern, regionally consistent. Finally, further studies are necessary to unravel whether the mesoscopic-scale folds are linked to large-scale folds.

4.4.2.2.4 Mylonitic Zones

These features represent regions of high strain localisation, showing planar (**Fig. 4.26 A, B** and **Fig. 4.28**) or curvilinear geometries (**Fig. 4.26 C and D; Fig. 4.27**), ranging from few millimetres up to tens of metres wide at outcrop scale. Strain gradient is the most notable characteristic observed in the majority of shear zones. In general, higher strain is concentrated within the centre of the shear zone, sharply decreasing towards the walls (**Fig. 4.26 A, B, E, F** and **Fig. 4.29**). Inside the shear zones, minerals show intensely reduced grain size and strong preferred alignment of quartz ribbons and mica trails, forming a prominent planar fabric morphologically characterized by disjunctive, spaced and parallel foliation (**Fig. 4.26 E and F**; see detail B photo in **Fig. 4.27**). Additionally, a number of shear zones show evidence of fluid-rock interactions indicated by the presence of halos of hydrothermal alteration and the precipitation of minerals (e.g. clay and chlorite).

Shear zones and associated internal foliation are oriented along four main trends: (1) WNW-ESE (90° - 110° Az) with dip angles between 56° - 85° to NNE and SSW; (2) NE-SW (25° - 42° Az) dipping mainly to SE and subordinately to NW with average dips of 70° - 86° ; (3) N-S (170° - 190° Az) dipping 63° - 76° to E or W; and (4)

NW-SE sub-vertical dipping towards NE and SW (see stereonets in **Fig. 4.18 E, K** and **P**). Mineral lineation within shear zones plunge in average 72° towards SSW in gneisses and 30° to 78° towards S, SW and NW in granitoids (see stereonets in **Fig. 4.18 K** and **Q**) evidencing a dominant near vertical position for the principal stretching axis.

The directional variations in shear zone orientations appear to reflect the network geometries of these anastomosing, curvilinear and locally interconnected features (see for example **Figs. 4.26 C, D** and **Fig. 4.27**). The strikes and dips of the shear zones trending WNW-ESE, N-S and NE-SW are notably similar to the three main sets of foliation and fold axial surfaces previously described. This suggests that all these structures are genetically related to one another, although some shear zones trending NW-SE seem to cross cut and post date the other three mentioned sets.

When cross-cutting gneisses, reverse-sinistral shear zones may cause relatively small offsets or bending of the adjacent foliations or banding, forming centimetre-scale asymmetric “drag” folds (**Fig. 4.19 M, N**, **Fig. 4.20** and **Fig. 4.28**). In the foliated granitoids, shear zones modify the direction of the foliation, deflecting it from its original position to an oblique or parallel orientation in relation to the shear zone boundaries (**Fig. 4.26 G** and **H**). Observed shear sense indicators include: asymmetry in the foliation deflections, rotated porphyroclasts and more rarely “en echelon” sigmoidal veins in less common semi-brittle shear zones (see examples of kinematic indicators in **Fig. 4.30**). Shear zones show oblique kinematics with normal component showing mainly top to the S-SW kinematics and directional component comprising about 70% sinistral and 30 % of dextral examples.

4.4.2.2.5 Brittle Structures

Late brittle structures are ubiquitous in the investigated area and include faults, fractures, veins and dykes. Large scale **faults** are poorly exposed in the area. However, one example of this type of structure (see **Fig. 4.31 A**) is preserved in a road-cut between the Serra Dourada village and the Sossego Mine. It comprises a 12 metre wide, sub-vertical fault zone trending NE-SW (060° Az). The material within the fault zone comprises a predominant ultrafine grained, dark grey rock – probably a cataclasite - containing millimetric angular fragments of quartz and a few preserved lenses of granite up to a metre long and tens of centimetres thick (**Fig. 4.31 B, C, D**). Within the fault zone, a number of brittle slip surfaces occur, ornamented with slickenlines and striae indicative of both dip-slip and strike-slip motion (**Fig. 4.31 E, F**). It was not clear from the limited set of exposures whether the two sets of slip indicators were related to a single complex set of fault movements or two distinct faulting events. Minor brecciated material and mineralization (quartz, malachite and chlorite) were widely observed in the fault zone (e.g. **Fig. 4.31 C, D, G**). Displacements could not be estimated because of the absence of markers. However the substantial width of the fault zone does suggest that it is likely to have a significant displacement (tens of metres or more). The fault zone corresponds to a NE-SW topographic lineament that also coincides with a linear magnetic anomaly of the same direction. The spatial correlation between the described fault zone and topographic and magnetic lineaments is important to validate the assumption that lineaments correspond to major fault zones.

Small scale **faults** occur widely in granitoids. These structures are generally characterized by discrete, continuous and planar surfaces with displacements in gneisses ranging from few millimetres up to 10 centimetres based on observed

offsets of banding (selected examples of these structures are shown in **Fig. 4.32**). The main fault sets are oriented along the following trends, presented from early to late relative ages (see stereonet on **Fig. 4.18 F**):

- (1) **E-W** (095° Az) dipping 52°-60° to the S and **WNW-ESE** (117° Az) dipping 60°-80° to the NE;
- (2) **NE-SW** (031°-057° Az) dipping 57°-82° to the SE; and
- (3) **N-S** (173° Az) dipping 70°-84° to the W.

Gneisses record N-S and WNW-ESE fault trends (stereonet in **Fig. 4.18 K**) and granitoids are mainly cross-cut by the trends NE-SW and WNW –ESE (see stereonet in **Fig. 4.18 R**). Mafic rocks only display a negligible number of faults (stereonet in **Fig. 4.18 Y**).

Cross-cutting relations between the early E-W and WNW-ESE-trending sets were not observed, so they are grouped together. Fault slickenlines (stereonet in **Fig. 4.18 F**) indicate that oblique-slip and strike-slip movements were the dominant directions of displacement for the E-W/WNW-ESE-trending and NE-SW-trending fault sets respectively. However, senses of displacement are often ambiguous and rather poorly constrained in many cases due to lack of good 3D exposures.

Minor fault zone internal structures typically comprise interlinked sets of fault strands that wrap around angular rock fragments “cemented” by a dark clay-rich matrix. Psuedotachylytes were not observed anywhere in the area associated with faults. Fluid circulation during fault development appears to be widespread based on the frequent occurrence of: (a) hydrothermal alteration of minerals adjacent to fault planes (mainly feldspars into clay minerals); and (b) the occurrence of mineral precipitation (e.g. iron oxide, clay minerals, albite and sulphides). Additionally, the occurrence of sulphides, magnetite or malachite in some fault

planes is an important indication of the possible presence of significant copper deposits in the area. Prominent sulphide mineralization was observed in sub-vertical, NE-SW discrete fault zones, 3 to 10 cm wide crosscutting isotropic granitoids in the Serra Dourada region.

Fractures and **joints** orientations notably follow the major directional trends of faults, shear zones and foliations: N-S, E-W, WNW-ESW, and NW-SE (see stereonets in **Fig. 4.18 T**). It seems that in general, fractures tend to form parallel to pre-existing ductile fabrics that act as zones of weakness. Supporting this assumption is the much greater density of fractures observed in rocks that display intense ductile fabrics compared to those developed in isotropic lithologies. However, exceptions to this rule occur with the N-S sub-vertical fractures, as these appear to be consistently present in equal densities in almost all outcrops visited.

Most discrete fracture planes are straight and smooth with an absence of ornamentation (e.g., plumose failure structures, slickenlines). Important quantitative parameters used to characterize fractures (persistence, spacing, length and aperture) change according to lithology, although this aspect has not been studied in detail during the present work. Finally, most of the fractures show no offsets and their walls are occasionally coated by a thin film of a very fine and brown-to-red dark mineral mass of possibly hematite.

Veins were observed in granitoids and mafic rock, occurring typically as parallel to sub-parallel sets of tens of millimetres objects. They are normally sub-vertical, tabular and can range in width from few centimetres up to a metre wide. They are commonly composed of quartz, feldspar (albite) or actinolite. Vein geometry ranges from straight and tabular in undeformed veins to “S” or “Z” shaped sigmoidal tension gash veins. Granitic (fine grained) and pegmatitic (coarse grained)

veins composed of quartz, feldspar and biotite, were observed cross-cutting granitoids. In few examples, pegmatitic veins were associated with brecciated material derived from the adjacent wall rock. Most measured veins show orientations along the trends: WNW-ESE, NE-SW and N-S (see stereonet in **Fig. 4.18 T and Z**).

4.4.2.2.6 Summary of the field observations

The region south of the Carajás Ridge comprises a c.a. 2.9 Ga. granitic gneissic basement intercalated with amphibolite lenses and intruded by c.a. 2.7 Ga. alkaline syn-tectonic granitoids. These rocks display a heterogeneous, anastomosing and sub-vertical ductile regional fabric trending WNW-ESE, NE-SW and locally NNW-SSE. The regional foliation is associated with steep-to-moderately plunging mineral lineations.

The basement rocks are folded by upright isoclinal, intrafolial and asymmetric folds that show mainly sub-vertical or steeply inclined axial surfaces, and sub-horizontal or gently plunging hinge lines. These fold elements trend in the same directions observed for the foliations. Further, pygmatic and sheath folds occur associated with pegmatitic and migmatitic gneissic domains.

Mylonitic zones commonly cross-cut the basement rocks following the trends NNW-SSE, WNW-ESE, NE-SW and NW-SE.

The basement rocks are intruded by dykes and c.a. 1.88 Ga. A-type granitoids that like the oldest rocks are cut by faults, veins and joints. Discrete faults and fault zones trend from early to late relative ages: (1) E-W and WNW-ESE with respective dips of 52°-60° to the S and 60°-80° to the NE; (2) NE-SW dipping 57°-82° to the SE; and (3) N-S dipping 70°-84° to the W. Fault displacement is rarely observed and

fault slickensides indicate -slip and strike-slip dominant movements for the sets trending E-W/WNW-ESE and NE-SW.

Quartz veins and joints trend similarly along NNW-SSE, WNW-ESE and NE-SW orientations. Joints show no offset and kinematic indicators, however few show mineralization i.e. quartz, hematite and clay.

4.4.3 Microstructural observations

This section presents the results from the study of 30 thin sections of representative rocks from the investigated area. The samples were examined under a microscope using transmitted polarized light to describe and interpret the characteristics of the microstructures and fabrics observed. The interpreted data was used to try to reconstruct the metamorphic and structural history of the rocks. Finally, the microstructural observations on samples from the basement rocks is ordered from the least to the most deformed rocks

4.4.3.1 Isotropic Granitoids

These represent the least deformed members of the suite of rocks studied under the microscope. They are texturally homogeneous, with granoblastic textures, showing medium- to coarse- unimodal grain size with average grain diameters between 1900 μm and 2700 μm (**Fig. 4.33 A**). Crystal shapes are typically subhedral to anhedral and grain contacts are generally curved with the minor presence of straight contacts forming triple junctions. Graphic intergrowths were often observed (**Fig. 4.33 B**). Ductile fabrics are generally absent and fractures or micro-cracks show random

distributions, limited to individual grains of quartz. Feldspar grains are fairly well preserved, rarely fractured and occasionally show crystal zoning.

Evidence of for intracrystalline deformation in quartz in these rocks includes: (1) well-developed sweeping undulose extinction; (2) widespread presence of elongate sub-grains (**Fig. 4.33 C**) with diffuse boundaries and minor “blocky” sub-grains (**Fig. 4.33 D**); and (3) deformation lamellae (**Fig. 4.33 E**). Recrystallization of quartz is localized, restricted to aggregates of small (18 μm) sub-rounded new grains located along some grain boundaries (**Fig. 4.33 F**) and elongate zones of concentrated strain (**Fig. 4.33 G**). Microstructures in quartz are compatible with low to moderate strain. Deformation appears to be partitioned into bands where recrystallization was favoured.

4.4.3.2 Basalt & Gabbro Dykes

Basalts are composed of granular fine grained minerals with homogeneous grain size of 100 μm on average and they lack any fabrics or preferred mineral orientations (**Fig. 4.34 A**). Microcrystalline textures typically comprise randomly oriented sub-hedral to anhedral plagioclase prisms frequently showing tapering twins (**Fig. 4.34 B**). Microstructures are restricted to few long and continuous fractures/veinlets filled with ultra-fine chlorite (**Fig. 4.34 C**); ductile or brittle fabrics are absent.

The gabbros show granular textures with inequant coarse-grainsizes with crystal ranging from 105 μm up to 2995 μm in diameter (**Fig. 4.34 D**). Plagioclase occurs as tabular crystals with typical aspect ratios of 0.16, which often show zoning, undulose extinction, alteration into sericite and localized symplectites with altered k-feldspar (**Fig. 4.34 E**). Ductile fabrics and recrystallization are absent. Mineral

fracturing is widespread and represented by straight to gently curved discontinuous and multidirectional cracks, often filled with dark-brown cryptocrystalline material or chlorite (**Fig. 4.34 F**).

Despite the well preserved magmatic textures, plagioclase grains in both mafic rock types shows minor evidence of limited crystal plastic deformation including: (1) undulose extinction; (2) the presence of tapering twins; and (3) minor symplectite development. Tapering twins are formed by crystal deformation at low temperatures and their concentration may be related to local intensity of deformation (Vernon 2004). Symplectite nucleation and growth may be conditioned to low strain conditions, as evidenced by the random arrangement of delicate shapes, which could not survive in high strain environments (Hanmer 1982; Simpson et al. 1989). Collectively, these features are indicative of post-magmatic, relatively low temperature, low strain conditions.

4.4.3.3 Amphibolites

These rocks represent metamorphic and deformed products of mafic volcanic rocks from the older mafic sequence that is intruded by the granitic gneisses. Their general mineral assemblage includes: amphibole (hornblende), plagioclase (labradorite), biotite, quartz, pyroxene, k-feldspar and minor titanite. Prominent ductile fabrics can be separated into: (1) continuous foliation defined by the preferred alignment of mineral grains (**Fig. 4.35 A**); and (2) compositional banding characterized by varying concentrations of distinct mineral species with inequant grain sizes and varying degrees of preferred orientation (**Fig. 4.35 B**).

Continuous foliation in amphibolites is characterized by homogeneous mineral distributions and preferred orientation of elongated hornblende crystals, defining a grain shape preferred orientation (GSPO) (**Fig. 4.35 C**). The degree of mineral orientation varies among samples, perhaps reflecting different strain magnitudes experienced by the minerals.

The *compositional banding* observed in some amphibolites is characterized by alternating layers with distinct mineral contents or grain sizes/shapes (**Fig. 4.35 D**). Dark green bands are mainly composed of coarse grained hornblende (~950 μm) and clear bands of mixed fine grained (~100 μm) clinopyroxene, plagioclase and minor epidote. Evidence of concentrated ductile deformation promoting the development of strong GSPO in the fine grained layers, indicating that strain was partitioned and concentrated along specific layers.

The two types of foliation observed in amphibolites appear to be related to a pre-existing compositional banding that facilitated partitioning of the deformation into specific layers. Because deformation involves minerals with different competence, strain incompatibilities along boundaries between domains of difference competence can produce mechanical instabilities, favouring the accumulation of strain in certain zones (Goodwin et al. 2002; Vernon 2004)

Amphibole grain diameters ranges from 80 μm up to 500 μm with euhedral and anhedral forms. They normally show straight contacts with other minerals and occasional triple junctions. Crystal elongation is varied, but the long prismatic crystals have average aspect ratios of up to 0.25. Limited weak undulose extinction is the only evidence of crystal plastic deformation. Mechanical fragmentation of larger grains is suggested by the presence of very small (~20 μm) 'chips' of amphibole surrounding larger grains (**Fig. 4.35 E**). This leads to the development of

a feature similar to core-and-mantle texture. The partial mixture of small amphibole grains with feldspar matrix could have been produced by grain boundary sliding between the two phases. Several other studies have suggested that, at temperatures below 650-700°C, aggregates of fine-grained hornblende probably formed by fracturing rather than dynamic recrystallization (Stünitz 1993; Imon et al. 2004; Passchier et al. 2005) and that core-and-mantle structures on hornblende may also be due to fracturing (Nyman et al. 1992; Passchier et al. 2005)

Feldspars occur as polygonal aggregates of recrystallized strain-free small grains (~30 µm) and subordinate larger relict grains (~ 280 µm), showing sweeping undulose extinction, stress-induced glide-twins and multiple twinning and minor alteration to sericite (**Fig. 4.35 F**). The presence of small recrystallized grains is indicative of reasonably high grade conditions (above 600°C), compatible with climb-accommodated (regime 2) dislocation creep where both SGRR and BLG occur (Altenberger et al. 2000; Kruse et al. 2001; Tullis 2002; Passchier et al. 2005). The development of tapering twins and multiple twinning, common in plagioclase relict crystals, are favoured at lower temperatures and faster strain rates (Vernon 2004), indicating that these features may be later stage products of minor deformation during retrogression metamorphism.

Pyroxenes in amphibolites occur as granular or prismatic elongated crystals with moderate preferred orientations. The grains have euhedral and subhedral forms, ranging from 32 µm up to 366 µm diameter and occur as individual grains or polygonal aggregates with straight contacts (**Fig. 4.35 G**). Intracrystalline deformational features are absent.

Biotite occurs predominantly as thin tabular shaped crystals with lengths ranging from 40 µm up to 580 µm, oriented parallel to the foliation. Subordinated

subhedral grains with irregular shapes were also observed. Evidence of deformation is limited to sweeping undulose extinction and gentle kinking of individual grains.

Quartz forms polygonal aggregates of fine (~ 50 μm) recrystallized grains with straight boundaries (**Fig. 4.35 H**). Sub-grains are less abundant and show moderate undulose extinction with lobate and diffuse grain boundaries. LPO are absent and a localized GSPO is seen in aggregates of recrystallized quartz grains that show moderate preferred orientation. Collectively, quartz shows deformational features indicative of dynamic recrystallization under dislocation creep regimes 2 and 3 (Hirth et al. 1992) dominated mainly by GBMR and subordinately by SRR. These dislocation creep regimes and recrystallization mechanisms are compatible with temperatures of 500-700 °C, indicative of middle to upper amphibolite facies conditions (Stipp et al. 2002; Passchier et al. 2005).

4.4.3.4 Deformed Granitoids

These rocks are characterized by recrystallized minerals and foliation formed under relatively high temperature during syntectonic recrystallization. Their mineral assemblages include: quartz, plagioclase (labradorite), k-feldspar, amphibole (hornblende), minor biotite, chlorite and zircon. Foliation is heterogeneously developed with presence of weak, prominent and mylonitic varieties (see two examples in **Fig. 4.36 A**); generally classified as disjunctive, rough, parallel or anastomosing. The constitutive minerals and their deformational features are described as follows:

Feldspars, in the low strain samples, form large inequigranular (up to 11 mm), subhedral to sub-rounded relict grains surrounded by aggregates of fine (~ 20–

50 μm) recrystallized grains of uniform grain size (**Fig. 4.36 B**). The abundance of recrystallized feldspar is proportional to the strain accommodated by the rocks. In the least deformed samples, recrystallization is limited to thin mantles of recrystallized grains along the boundaries of larger crystals that show strong sweeping undulose extinction and stress-induced twins.

Intense grainsize reduction is observed in more deformed samples. Grain boundary rotation recrystallization produces relict grains with core-mantle texture and limited flattening. Fine-grained feldspar aggregates are smeared into the foliation, alternated with quartz ribbons (**Fig. 4.36 C**). Elongated recrystallized grains with a 2:1 ratio, are often oriented parallel or oblique to the foliation. They show undulose extinction, straight or lobate boundaries that can be either sharp or diffuse (**Fig. 4.36 C**).

Evidence of crystal plastic deformation in relict grains or porphyroclasts includes: patchy undulose extinction, stress-induced twins, perthites and **myrmekites** preferentially developed along grain boundaries. The presence of these features suggests that strain was localised into the recrystallized zones with the relict grains playing the role of rigid objects accumulating limited strain. Fracturing is observed locally producing angular inequant feldspar grains and local “book shelf” structures (**Fig. 4.36 D**). (Simpson et al. 1989; Tsurumi et al. 2003) propose that myrmekites are developed at stress-concentration sites during progressive deformation of high grade metamorphic and granitic rocks. Some authors suggest that they grow at temperatures of 450-500°C (Tribe et al. 1996), whilst others suggest temperatures between 500 and 670°C (Wirth et al. 1987).

Quartz is intensely recrystallized, forming elongate subhedral clusters (**Fig. 4.36 E**) or continuous ribbons with thicknesses ranging from 50 μm up to 800 μm .

The grains are strain free and show sharp, straight or gently curved boundaries normally configuring triple junction (120°). Grainsizes range from 34 μm up to 170 μm and seem to be proportional to the quartz ribbon width. The microscopic characteristics of these strain-free polygonal quartz grains suggest that they were produced by static recrystallization, dominated by grain boundary area reduction (GBAR) mechanisms. Relicts of the dynamically recrystallized grains show relatively small grain size ($\sim 25 \mu\text{m}$), interlobate contacts and undulose extinction, which indicate that, prior to the static recrystallization, quartz was dynamically recrystallized under conditions compatible with regime 3 dislocation creep (Hirth et al. 1992). Only one out of seven studied samples has partially recrystallized quartz. That shows moderately flattened grains with sweeping undulose extinction and elongated subgrains with straight and diffuse boundaries. The boundaries of relict grains are populated by very fine ($\sim 20 \mu\text{m}$) sub-grains and minor new grains, forming good core-mantle structures. Fine subgrains show interlocked or lobate, sharp or diffuse boundaries (**Fig. 4.36 F**). The preferred orientation of the flattened grains, defines an SPO and the use of a tint filter reveals a moderate LPO. These microstructural features are consistent with those described for regime 2 dislocation creep regime (Hirth et al. 1992).

Amphiboles occur as strain-free sub-hedral prismatic crystals (up to 950 μm) and more commonly as multiple needle-shaped lamellae oriented parallel to the foliation (**Fig. 4.36 G**). The amphibole “needles” seem to have formed by fracturing and were observed mixed with recrystallized quartz and feldspar, with their preferred orientation broadly parallel to the foliation.

Biotite is similar to amphibole. However, grain fracturing is practically absent and crystals are virtually strain free (**Fig. 4.36 H**). Biotite elongated grains are

oriented parallel to the foliation and show straight contacts with quartz or evidence of secondary grain growth where relatively smaller crystals are engulfed by quartz.

Titanite shows euhedral prismatic forms normally occurring associated with biotite or amphibole rich domains and shows no evidence of deformation.

Chlorite and **epidote** show no indication of deformation and represent common retrograde alteration products of biotite and feldspars respectively.

The varied foliation types and deformational features in minerals suggest that deformation was highly heterogeneous. Thus, the microstructures observed in quartz and feldspar indicate that these granitoids were initially deformed under middle to upper amphibolite facies conditions (~650-700°C) that appear to have been partially overprinted by retrograde metamorphism, with minor deformation under middle to upper greenschist facies conditions (~400-500°C).

4.4.3.5 Mylonites

These samples display a prominent mylonitic foliation defined by a regular and relatively continuous planar fabric, formed of alternating quartz- and feldspar-rich bands wrapping around rigid porphyroclasts (**Fig. 4.37 A**). The typical mineral assemblage comprises: quartz; k-feldspar (microcline); plagioclase (labradorite), biotite and accessories.

Feldspars exist as large porphyroclasts and as dominant, finely recrystallized domains produced by widespread grain size reduction of the original grains. Plagioclase and k-feldspar show similar microstructural characteristics and are described together.

Porphyroclasts form sub-rounded to elongated augen or lozenge-shaped grains 320 μm to 4700 μm in diameter (**Fig. 4.37 B**), mantled by recrystallized feldspar forming well defined core-mantle textures. Features indicative of crystal plastic deformation in porphyroclasts include: (1) moderate to strong undulose extinction, (2) deformation twins and kink bands, (3) irregularly distributed polysynthetic twins, (4) flame perthites and myrmekites mainly located along crystal edges, and (5) occasional discrete high strain zones populated with ultra fine recrystallized grains (**Fig. 4.37 B and C**). The range in their size suggests that porphyroclasts acted as mechanically rigid particles during the processes of progressive grain size reduction.

Recrystallized feldspar grains are much finer than quartz and define long and continuous bands formed of either:

A - ultra-fine aggregates of equant feldspar grains with an average size of 6 μm and the occasional presence of larger grains ($\sim 42 \mu\text{m}$) and trails of tiny biotite flakes ($\sim 8 \mu\text{m}$) (**Fig. 4.37 C**). The crystals forming aggregates show curved and sharp contacts between each other and serrated boundaries when in contact with feldspar porphyroclasts. A SPO is defined by elongated recrystallized domains oriented parallel to the foliation. **B** - Recrystallized mixed phases of feldspar ($\sim 20 \mu\text{m}$ up to $100 \mu\text{m}$), quartz ($\sim 50 \mu\text{m}$) and biotite ($\sim 100 \mu\text{m}$ long) with both straight and lobate contacts (**Fig. 4.37 D**). The grains of the mixed phase aggregates show serrated contacts with feldspar porphyroclasts and straight contacts with quartz foliae. Feldspar shows moderate to intense alteration to sericite.

The microstructural features observed in the feldspars are indicative of climb-accommodated (regime 2) dislocation creep of (Tullis et al. 1985; Tullis 2002). Porphyroclasts with sweeping undulose extinction and mantled by fine recrystallized

grains are compatible with high temperatures in upper amphibolite facies (Altenberger et al. 2000; Kruse et al. 2001). Additionally, myrmekites commonly form along high stress margins of feldspar porphyroclasts from amphibolite grade granitic rocks (Simpson et al. 1989).

Quartz occurs as aggregates of polygonal inequant grains, with very weak undulose extinction and dominant sharp and straight or minor curved boundaries. Grainsize ranges from 20 μm up to 700 μm in diameter with the common presence of elongate grains (aspect ratios of 1:2 up to 1:4) oriented parallel to the foliation. Small biotite grains engulfed by quartz suggest that temperatures during deformation were high enough to counteract “grain-boundary pinning” effects (Tullis 2002). Quartz aggregates form lenses or layers of varied thicknesses that alternate with feldspar rich folia (**Fig. 4.37 E**). The larger and dominant polygonal grains indicate static recrystallization produced by grain boundary area reduction (GBAR) mechanisms (**Fig. 4.37 F**). Subordinate smaller grains with curved or lobate boundaries, indicative of GBMR represent relicts of “early” dynamically recrystallized quartz by dislocation creep (regime 3) (Hirth et al. 1992).

Biotite comprises relatively large ($\sim 180 \mu\text{m}$ long) and very fine ($\sim 10 \mu\text{m}$ long) subhedral and tabular crystals with aspect ratios of 1:2 up to 1:5, oriented parallel to the mylonitic foliation. Larger crystals occur mainly as clusters of aligned flakes normally intergrown with quartz and feldspar subgrains (**Fig. 4.37 G**). The very fine crystals form prominent, continuous trails (10 μm to 270 μm wide) interlayered with quartz- or feldspar-rich bands or wrapping around porphyroclasts (**Fig. 4.37 H**). Biotite flakes tend to concentrate in strain shadows associated with porphyroclasts and in some examples, needle-shaped biotite grains nucleate within

feldspar porphyroclasts. Deformational features are relatively rare, limited to minor folded cleavage planes. Kinking and undulose extinction are absent.

The microstructural features observed in quartz and feldspars agree with those described for high temperature mylonites in many other shear zones (e.g. (Bell et al. 1989; Pryer 1993; Altenberger et al. 2000; Stipp et al. 2002)). The microstructures are consistent with those formed by progressive strain at middle to upper amphibolite conditions (~650-700°C) (Tullis 2002). The minerals were probably annealed after strain ceased.

4.4.3.6 Granitic gneisses

Orthogneisses corresponding to tonalites, granodiorites and subordinate monzogranites, are generally formed by varying proportions of plagioclase (labradorite), quartz, k-feldspar, biotite, minor hornblende and accessories. These rocks show prominent compositional banding, inequigranular grain sizes with larger clasts up to 8 mm in diameter set in a finer grained recrystallized matrix. The mineral assemblage is arranged typically into alternating mafic (biotite, hornblende and opaque minerals) and felsic (quartz and feldspar) bands, displaying a general granoblastic texture, with more mylonitic fabrics developed in high strain members (**Fig. 4.38 A**)

Quartz is intensely recrystallized, comprising inequant grains from 28 μm to 756 μm in diameter. Larger grains are commonly elongate and oriented sub-parallel to the gneissic banding. They show strong sweeping undulose extinction, elongated sub-grains and sharp lobate contacts with the surrounding grains. Aggregates of smaller quartz grains form ribbons, augen-shaped domains and minor porphyroclasts

tails. Grain boundaries in these aggregates can be: (i) straight, produced by GBAR and indicative of annealing; or (ii) lobate or curved, resulting from GBMR. Quartz ribbons (**Fig. 4.38 B**) occur alternating with recrystallized feldspar layers and occasionally wrap around porphyroclasts. Ribbons show inequant subhedral or elongate grains with straight or lobate boundaries. A number of grains show evidence of intracrystalline deformation including sweeping undulose extinction and subgrains with diffuse contacts and long axes generally oriented parallel to the ribbon's length.

Only one sample (P-83) shows intensely flattened quartz grains with sweeping undulatory extinction and elongate or inequant granular subgrains. Grain boundaries are decorated with aggregates of small (~ 20-30 μm) recrystallized grains with gently curved or irregular boundaries characteristic of dislocation creep recrystallization in the transition between regime 2 and regime 3 (**Fig. 4.38 C**).

Collectively, these structures are compatible with quartz having initially recrystallized by Regime 3 dislocation-creep GBMR (Hirth et al. 1992), and further annealed by GBAR that produced the polygonal "foam structures" (Passchier et al. 2005) observed in the majority of the quartz crystals.

Feldspars occur as porphyroclasts or smaller grains in the recrystallized matrix with biotite and quartz. Porphyroclasts with irregular shapes and inequant sizes represent survivors of grain size reduction processes. They display evidence of crystal plastic deformation represented by: (a) moderate to strong undulose extinction, (b) bent clasts in high strain samples, (c) kinked or lenticular (tapering) plagioclase twins, (d) stress-induced twins near to grain margins, and (e) deformation bands (**Fig. 4.38 D**). Myrmekites and perthites were observed in feldspar porphyroclasts and indicate deformation under high temperature conditions

(**Fig. 4.38 D and E**). A few clasts are cross-cut by very thin (~ 3 – 11 μm) straight or gently curved cracks filled with biotite. Porphyroclasts show lobate or curved contacts with the grains in the surrounding recrystallized matrix. They are often mantled by recrystallized feldspar grains with lobate contacts (**Fig. 4.38 F**) and average sizes smaller than grains in the matrix.

Feldspars in the recrystallized matrix comprise aggregates of intergranular and inequant grains ranging from 16 μm to 230 μm in size. Grains from the fine- to medium-grained fraction show undulose extinction and lobate boundaries. By contrast, the coarse fraction has grains with straight contacts, often forming 120° triple junctions. Partially recrystallized myrmekite aggregates were observed incorporated into the fine grained matrix.

The widespread recrystallization of feldspars is related to the operation of SGRR and GBMR processes. The minimum temperature for plagioclase recrystallization is between 500 to 550°C (Tullis et al. 2000). Additionally, k-feldspar dynamic recrystallization has been observed under amphibolite facies ~530°C (Pryer 1993) and eclogite facies conditions (Altenberger et al. 2000). Myrmekites can form at stress-concentration sites during high-grade metamorphism (Tsurumi et al. 2003), at temperatures of 450-500°C (Tribe et al. 1996) and between 500 and 670°C (Wirth et al. 1987). Finally, perthites can develop under either greenschist facies conditions (Pryer et al. 1995) or amphibolite facies at higher temperatures (Vernon 1999).

Biotite is the main mafic mineral in the gneisses and occurs as:

(a) elongate tabular flakes (**Fig. 4.38 G**) with aspect ratios ranging from 2.75 to 10.5, showing grain sizes (15 μm to 220 μm) inversely proportional to strain; or

(b) anhedral grains filling interstitial spaces between quartz-feldspathic recrystallized aggregates (**Fig. 4.38 H**).

Elongated biotite grains are normally aligned parallel to the gneissic layering, defining a mica-rich foliation in the more intensely deformed samples. The presence of continuous and discontinuous biotite trails seems to be proportional the quantity of mica available. Relatively thin and prismatic fragments are often engulfed by quartz or mark the boundaries between quartz grains giving them an elongated shape and controlling grain boundary geometry.

The collection of microstructures observed in quartz and feldspars is consistent with an initial deformation at high temperatures (amphibolite facies) that appears to have been partially overprinted by late deformation at lower temperatures (greenschist facies). Comparing the microstructural observations from the studied gneisses with a summary of the deformational characteristics for granitic rocks at different crustal levels presented by (Tullis 2002), it is deduced that: (1) the high temperature deformation took place under middle to upper amphibolite facies conditions (~650-700°C); and (2) the latter weak deformation occurred under middle to upper greenschist facies conditions (~400-500°C).

4.5 Tectonic history and structural model

The early configuration of the Archaean terrane exposed in the Transitional domain south of the Carajás terrane comprises high grade, TTG (thonalite-trondhjemite-granodiorite) gneisses, intercalated with lenses of mafic volcanics and amphibolites. These units show generally sub-vertical, complex interfingering, curvilinear contacts. The lithological associations here are clearly equivalent to the classic characteristics of granite-greenstone terranes described in North America, Southern Africa and Australia (Condie 1981).

Such granite-greenstone terranes are generally believed to have formed by vertical tectonics during processes such as diapirism with autochthonous magmatism forming dome-and-keel structures like those seen widely in the adjacent Rio Maria Granite Greenstone Terrane (Althoff et al. 2000) and similar to the structures described in other Archaean cratons, e.g. India (Chardon et al. 1996); Kaapvaal (Kisters et al. 1995); Pilbara (Collins et al. 1999); and Zimbabwe (Jelsma et al. 1993).

These early formed TTG (granitic) gneisses, occur as small preserved “islands” typified by sub-vertical N-S banding, affected by numerous small-scale, generally upright open to locally isoclinal disharmonic folds. The localized N-S structures appear to represent relicts of an early pre-2.8 Ga Archaean tectonic cycle. These early structures show notable symmetry, indicative of pure shear deformation under possibly magmatic conditions. The N-S structural trend has been recognised in parts of the Rio Maria Granite Greenstone terrane such as the Caracol Tonalite (Leite et al. 2004). The minimum age for these early structures is 2.9 Ga, the age of the oldest rocks (leuco-monzogranites) dated in the study area (Sardinha et al. 2004).

It is proposed that at approximately 2.7 Ga, the region was affected by a regional phase of sinistral transpression. This deformation has shaped much of the

present architecture of the lithological units and was accompanied by widespread coeval magmatism forming E-W elongated, foliated A-type granitoids. The ages of the syn-tectonic granitoids (see **Table 4.1**) constrain the approximate time when the transpression took place i.e. ~ 2.7-2.5 Ga.

Transpression produced a penetrative ductile fabric comprising an interlinked array of sub-vertical E-W and WNW-ESE foliation in the gneisses and syn-tectonic granitoids. Most of the strain was accommodated in shear zones oriented mainly parallel to the foliation, with the shortening direction being sub-horizontal and broadly NNE-SSW (~010-20° Az) trending. These features are responsible for the development of the prominent, continuous and sinuous E-W anomaly, ~ 15 km wide seen in the magnetic and radiometric surveys.

Microstructures indicate that during main phase of transpression, the rocks were deformed at conditions compatible with middle to upper amphibolite facies (~650-700°C). Euhedral quartz in highly deformed rocks, suggests that deformation ceased at temperatures sufficiently high to promote quartz recovery.

Discrete NE-SW shear zones with oblique-slip character seem to have formed during the latter stages of transpression. These structures cross-cut the E-W fabric and are geometrically comparable to the R, synthetic faults from the Riedel shear model, described in analogue models and natural examples of transpression presented in (Schreurs et al. 1998; Casas et al. 2001; Mattioni et al. 2007). Deformation after these later stages of transpression seems to have occurred under middle to upper greenschist facies conditions (~400-500°C) based on the microstructures that overprint the relatively high temperature fabric.

Regionally, the E-W to WNW-ESE trend is recognized both to the north in the granitic basement at the Carajás terrane (e.g., (Pinheiro et al. 1997a) and to the

south in the Rio Maria Granite Greenstone terrane (e.g. (Althoff et al. 2000). Collectively, the mineral assemblages and associated microstructures, indicate a decrease in metamorphic grade from amphibolite to sub-greenschist reflecting progressive uplift, exhumation and syn-tectonic cooling of the region. This too is recognised in adjacent terranes (refs). It appears that the early amphibolite facies fabric formed over a relatively broad area under heterogeneous strain conditions. Subsequently, at greenschist facies conditions, deformation was partitioned and concentrated into high strain zones developed along the early ductile fabric. These interpretations agree with the conceptual fault model of (Sibson 1977), which suggested that an upper crustal network of frictional faults are projected downward at depth into a viscous deformation zone. The model also suggests that, at low grade greenschist, deformation tends to be localized into discrete mylonitic zones, while amphibolite facies mylonites exist over a relatively wider region. Thus, the deformation and deformation textures recorded in the study area rocks are compatible with lower to mid crust conditions comparable to those seen in many other basement complexes worldwide, e.g. Limpopo Belt, Zimbabwe Craton (Kolb et al. 2000); Hidaka Belt, Hokkaiko – Japan (Kanagawa et al. 2008), Glastonbury gneiss, north-central Connecticut, New England (Wintsch et al. 2002).

It is proposed that during the transpression, strain was partitioned with the bulk of the simple-shear component being accommodated by the shear zones. As a result, the lower strain regions between the shear zones are in relative terms likely dominated by the pure-shear component (see cartoon in **Fig. 4.39**). The steeply-plunging mineral lineations in both pure-shear and simple-shear domains, are characteristic of heterogeneous transpression (Tikoff et al. 1997). The sub-vertical lineations preserved in the shear zones and total absence of sub-horizontal lineations

suggests a bulk pure-shear dominated transpression (Fossen et al. 1994; Tikoff et al. 1997). It seems that the partitioning of deformation may have been, at least to some degree, controlled by the rheological properties of the rocks. In general, the gneisses are more highly deformed compared to the granites and mafic rocks.

After the sinistral transpression, widespread anorogenic magmatism and faulting are the last events recorded in the area. A late magmatic event has produced A-type, sub-circular, isotropic granitoids (e.g. the Rio Branco granite) and numerous mafic and subordinated felsic dykes, trending NW-SE, NE-SW and N-S. The granitoids were emplaced at 1.88 Ga during a regional scale phase of extensional tectonism that affected the Amazon Craton (Dall'Agnol et al. 2005). The age of the dykes is not well constrained but their isotropic character suggests that they are no older than 1.88 Ga. The three statistically representative sets of faults in the studied area with their respective nature are: WNW-ESE (oblique-slip), NE-SW (strike-slip) and N-S (extensional). These structures occur throughout the area, cross-cutting early gneisses and late isotropic granitoids. A late mineral assemblage comprising epidote+chlorite+albite+quartz is widely present in deformation bands or fractures and reflects retrograde metamorphic events that occurred at relatively low temperatures, presumably synchronous with faulting.

4.6 Comparison with other Archaean Cratons

The geological setting recognized regionally and within the local study area correlates with the main stages of evolution for the Archaean crust as proposed by

(Choukroune et al. 1995). The authors used field observations and strain field analysis to develop a four stage model of crustal deformation observed in Archaean terraces (**Fig. 4.40**): Stage(1) Pilbara Craton in Australia; Stage(2) from the Dharwar craton in South India; Stage (3) the Man Shield from Ivory Coast and Stage (4) Sino-Korean craton in China.

The structural characteristics observed in the Canaã dos Carajás region correspond to those described for stages 2 and 3 in the Choukroune model. Extending the comparison to the regional scale, the northern Carajás and southern Rio Maria terranes would correspond to the Sino-Korean craton in China (stage 4) and to the Pilbara craton (stage 1). This comparison highlights the regional progressive decrease in strain from the Carajás Ridge in the north to the Rio Maria terrane in the south.

4.7 Regional issues

The rocks in the study area dominantly yield ages of between 2.9 and 2.7 Ga - ages that are also present in the rocks of the adjacent Carajás and Rio Maria Granite-Greenstone terranes. This correspondence in the isotopic ages of the three domains suggests a contemporaneous origin which casts some doubt on the validity of the current separation into different terranes.

However, it is possible that the region represents a unit of crust initially formed by a common event and then heterogeneously reworked during later events. In particular, the present study suggests that the rocks of the Transitional domain are part of the Rio Maria Granite Greenstone terrane that have experienced a much

higher degree of reworking during sinistral transpression and that this event increases in intensity northwards (**Fig. 4.39**). The same transpression also appears to dominate in the basement rocks of the Carajás terrane to the north (Pinheiro et al. 1997a; Holdsworth et al. 2000). This hypothesis would also explain the relatively young ages (2.9 and 2.7 Ga) found in the rocks of the Carajás terrane and Transitional domain. The hypothesis is still a little speculative since there are far fewer modern isotopic ages, available for the Rio Maria Granite Greenstone terrane and Transitional domain compared to the Carajás terrane.

The geophysical anomaly corresponding to the broad E-W shear zone hosting syn-tectonic granitoids in the Canaã dos Carajás region has been referred to as a tectonic discontinuity separating the Carajás and Rio Maria Granite Greenstone terranes (de Oliveira et al. 2009). This is possible, but the region also seems to mark a boundary between two domains that have suffered very different intensities of strain during a regional sinistral transpression ca 2.7Ga. The recognition of an intensely deformed granite-greenstone terrane in the region of Canaã dos Carajás has two direct regional implications:

- (1) It displaces the current geographic limit of the Rio Maria Granite-Greenstone terrane from the Sapucaia village, to the Canaã dos Carajás town, 40 km to the north.
- (2) It calls into question the currently accepted division of the Amazon Craton that establishes the Carajás and Rio Maria Granite Greenstone terranes into two distinct tectonic-geochronological domains, a proposal that is largely based on geochemical and isotopic data.

4.8 Conclusions

The Archaean rocks in the region of Canaã dos Carajás, near to the boundary between the Carajás and Rio Maria Granite-Greenstone terranes, are interpreted to represent part of an original granite-greenstone terrane that has undergone substantial reworking during a later regional transpressional deformation. This reworking records a temporal change from vertical tectonics, which formed the granite-greenstone terrane, to a more horizontal-dominated tectonics regime at c.a. 2.7 Ga. during sinistral transpression accompanied by widespread syn-tectonic sub-alkaline magmatism. The transition from vertical to horizontal tectonics is consistent – at least in this part of the Amazon Craton – with a change in global tectonic processes consistent with a non-uniformitarian theory for Earth's crustal evolution.

The Canaã dos Carajás region comprises intensely deformed rocks, uplifted from the lower-to-middle crustal levels, initially deformed under high amphibolite facies conditions and subsequently affected by more localised, down-temperature deformation at greenschist facies conditions. The widespread presence of mylonites in the region suggests that these rocks were deformed wholly within viscous deformational regime.

Finally, late brittle events formed faults, fault zones and veins, mainly observed in granitoids. Widespread hydrothermal alteration and localized occurrence of Cu mineralization in these structures, evidence the role they can play as potential sites for occurrence of ore deposits in the region. The demonstration that fault zones with evidence of mineralization correlates to major magnetic and topographic lineaments, confirms the relationship lineaments vs. mineralization investigated in Chapter 3. Further, investigation on how brittle structures can host mineralization

was carried out, and is presented in Chapter 5. This chapter describes the structural controls in the orebodies of Sossego and Sequeirinho, two IOCG deposits located within the region herein described.

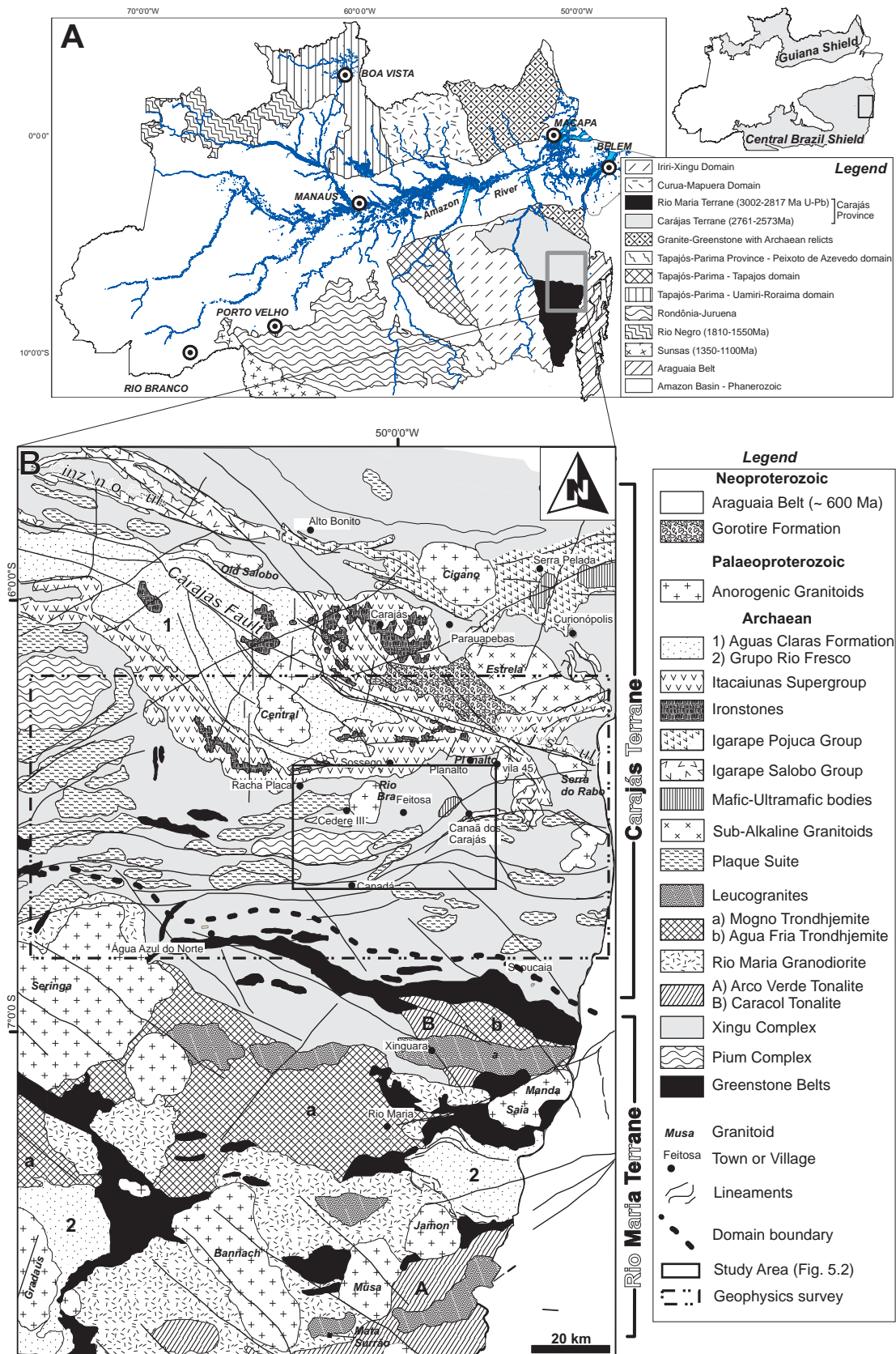


Figure 4.1 *A* The Amazon Craton and its geochronological provinces according to Santos, 2000; the highlighted square indicates the location of the studied area. *B* Geological map of parts of the Carajás and Rio Maria Terranes with the indication of the mapped area (solid line box) and the extension of the interpreted magnetic and radiometric airborne surveys (dot dashed box).

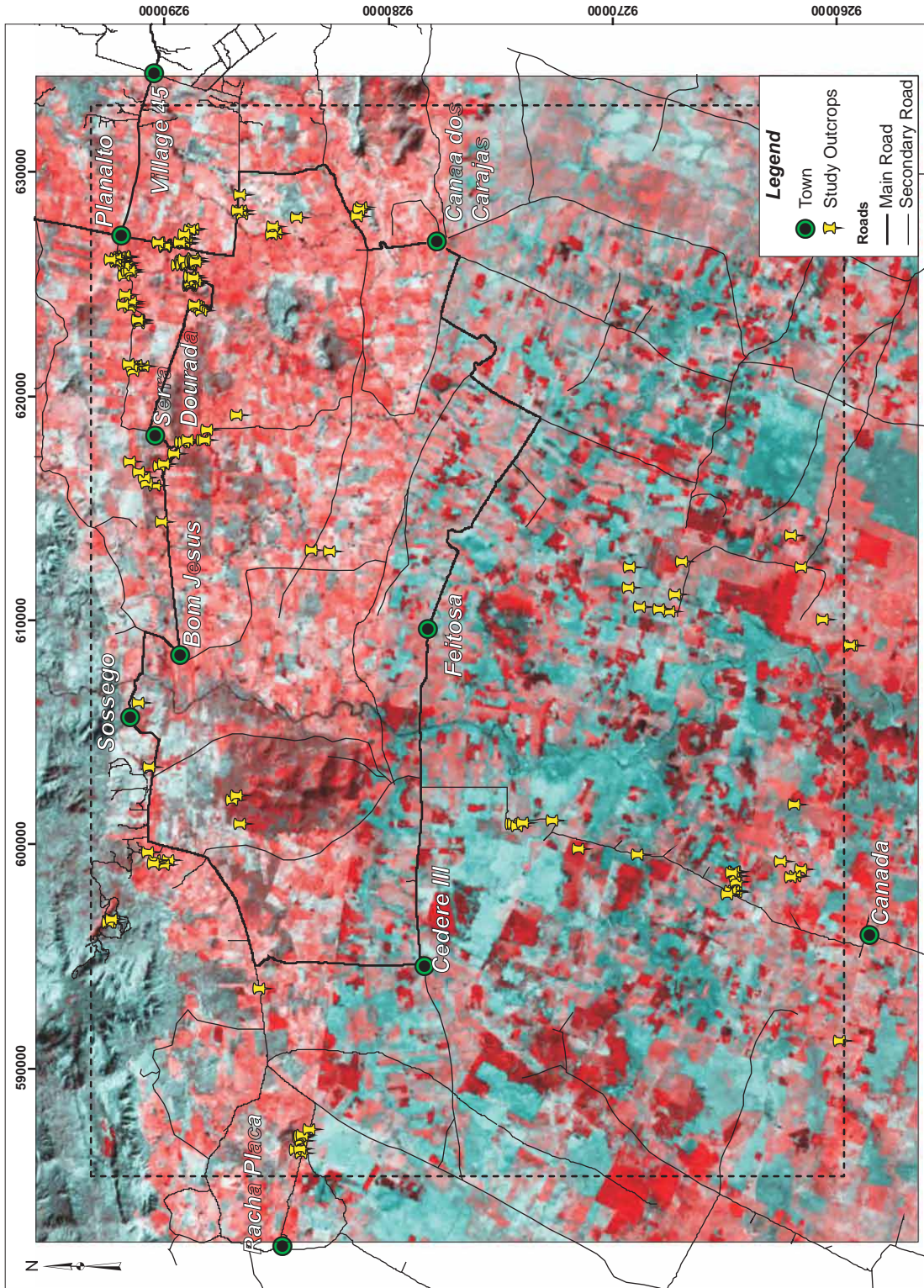


Figure 4.2 - Logistic map of the study region showing: primary and secondary roads, towns, and the studied outcrops. The background image is a false colour composition of the LANDSAT bands 4 and 5 from 2001. Red tones highlight areas of exposed soil or pastures and green tones indicate primary or secondary vegetation. The dashed line indicates the limits of the geological map in Fig. 4.3.

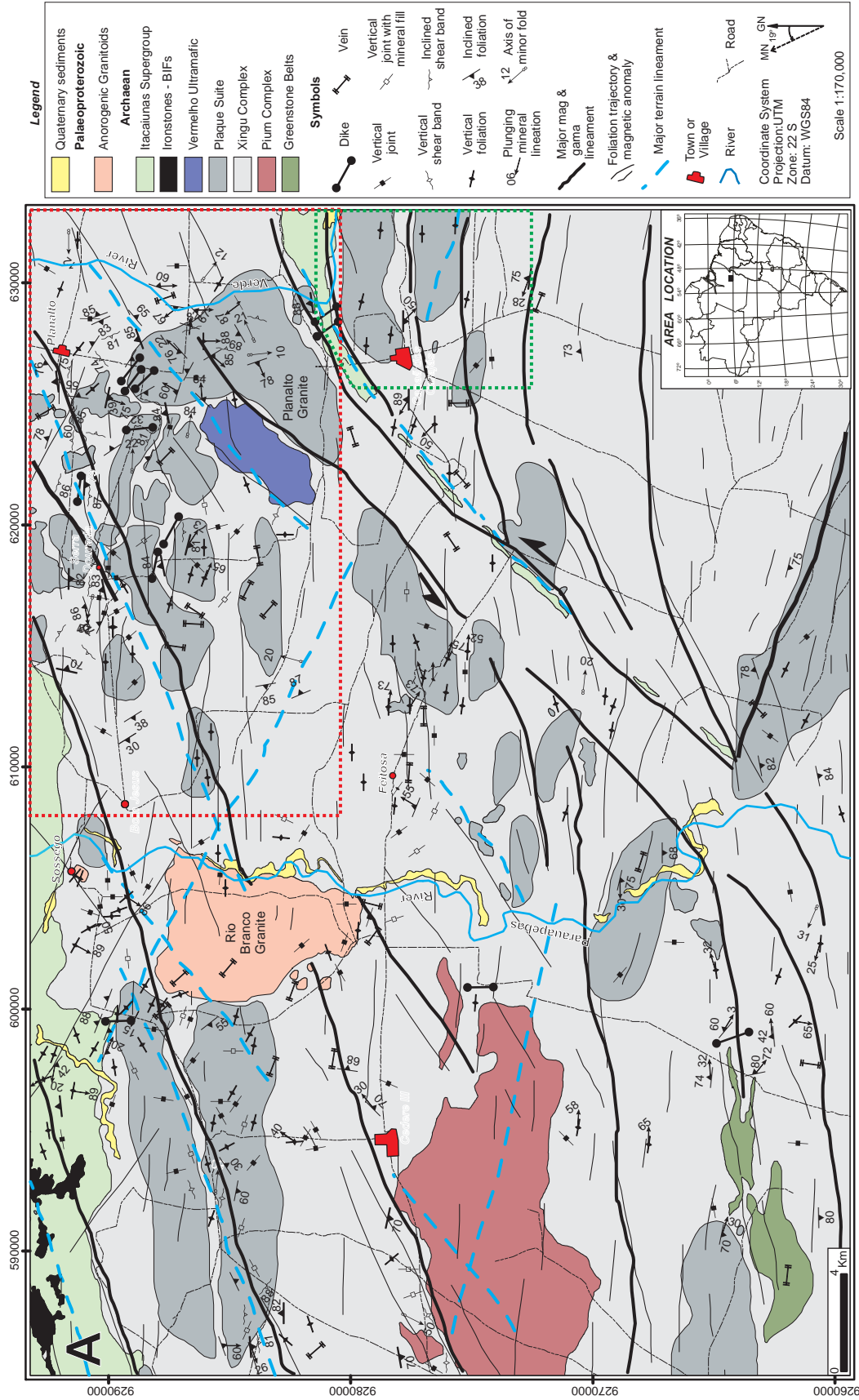
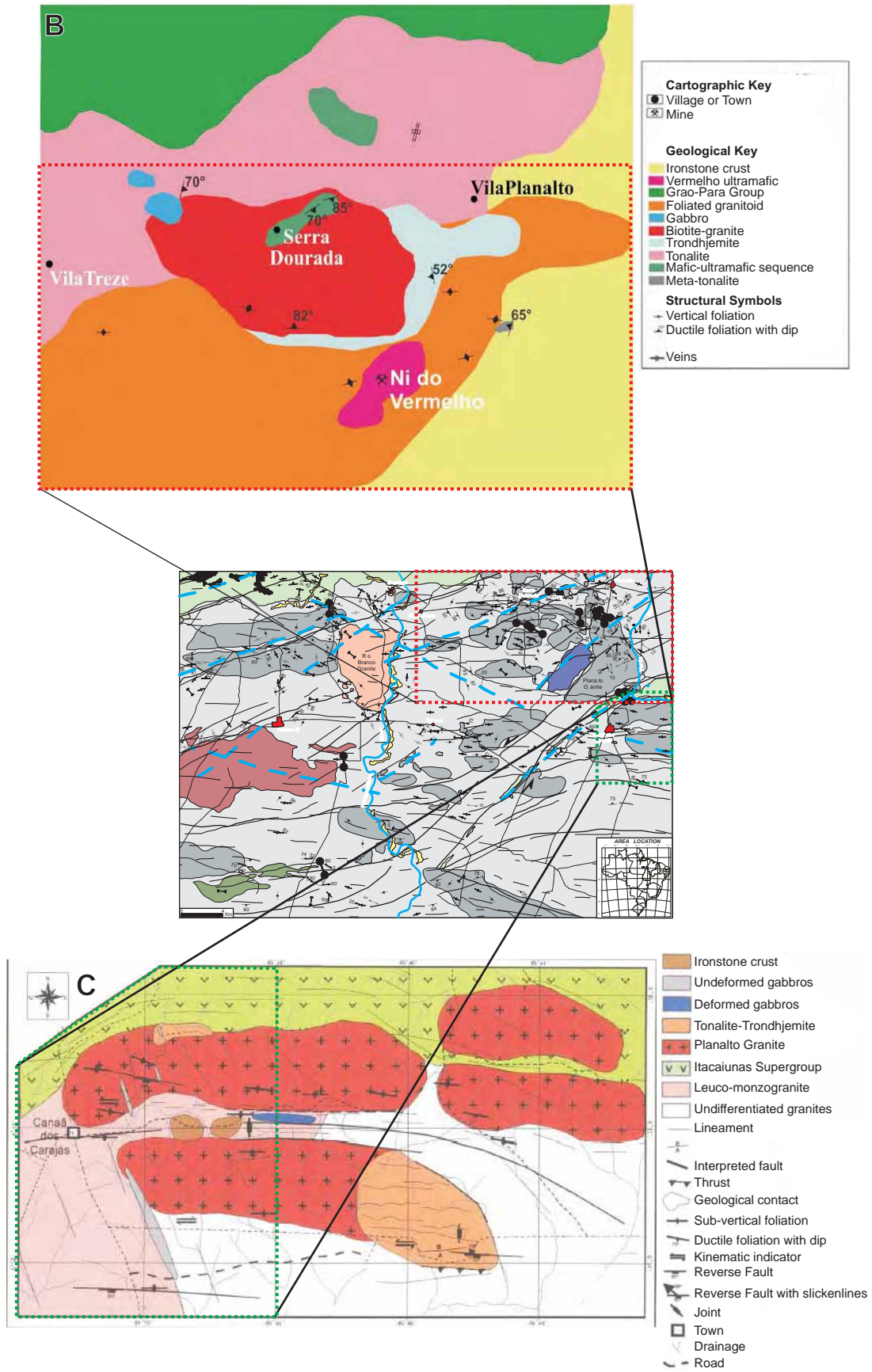


Figure 4.3 - A - Geological map of the studied area. Geological units compiled and modified from Bizzi 2002 and Gomes 2003. The dotted rectangles indicate the study areas of Gomes, 2003 (green) and Souza, 2007 (red).



Chapter 4

Supergroup	Group / Formation	Intrusive Rocks	Lithology	Age (Ga)	Method	Author				
A - Carajás Terrane										
Proterozoic Anorogenic Granites		Cigano Granite	Granite	1.883 ± 3	ZR U-Pb	Machado et al. (1991)				
		Carajás Granite	Granite	1.880 ± 2	ZR U-Pb	Machado et al. (1991)				
		Carajás Granite	Granite	1.820 ± 49	ZR U-Pb	Olszewski et al (1989)				
		Pojuca Granite	Granite	1.874 ± 2	ZR U-Pb	Machado et al. (1991)				
		Breves Granite	Episyenite	1.880 ± 9	ZR SHRIMP II	Tallarico et al. (2004)				
		Breves Granite	Granite	1.878 ± 8	ZR SHRIMP II	Tallarico et al. (2004)				
		Young Salobo Gran.	Syenite	1.88 ± 80	W-R Rb-Sr	Cordani (1981)				
		Águas Claras	gabro	2.645 ± 12	ZR Pb-Pb	Dias et al. (1996)				
	Cover Assemblage	Itacaiunas Group	Grão-Pará	volcanic sill	2.751 ± 4	ZR Pb-leach	Krymsky et al. (2002)			
			Grão-Pará	Rhyodacite	2.759 ± 2	ZR U-Pb	Machado et al. (1991)			
			Grão-Pará	Mylonitised Metarhyolite	2.757 ± 7	ZR SHRIMP	Trendall et al (1998)			
			Grão-Pará	Rhyolite	2.758 ± 39	ZR U-Pb	Macambira & Lafon (1995)			
			Grão-Pará	Rhyolite	2.757 ± 18	ZR Pb-Pb	Macambira et al. (1996)			
			Igarape Pojuca	Aphibolite	2.732 ± 2	ZR U-Pb	Machado et al. (1991)			
			Igarape Pojuca	Garnet-Biotite-Schist	2.668 ± 60	WR Sm-Nd	Lindenmayer et al. (2001)			
			Igarape Pojuca	mafic intrusive rocks	2.705 ± 2	ZR Pb-Pb	Galarza et al. (2002b)			
			Igarape Pojuca	Meta Gabro/ Andesite	2.757 ± 81	WR Sm-Nd	Pimentel et al. (2003)			
			Igarape Salobo	Rhyolite	2.740 ± ?	ZR U-Pb	Wirth et al. (1986)			
			Igarape Salobo	Aphibolite	2.761 ± 3	ZR U-Pb	Machado et al. (1991)			
			Igarape Salobo	Gneiss	2.851 ± 4	ZR U-Pb	Machado et al. (1991)			
Igarape Salobo			BIF	2.551 ± 2	Mi U-Pb	Machado et al. (1991)				
Ultramafic			Igarape Bahia	Basic granophyre	2.577 ± 144	WR Rb-Sr	Ferreira Filho (1985)			
				metapyroclastic	2.747 ± 1	ZR Pb-Pb	Galarza et al. (2002)			
	Meta volcanic/pyroclastic	2.759 ± 24		WR Sm-Nd	Santos (2002)					
	Metavolcanic	2.748 ± 34		ZR SHRIMP	Tallarico et al. (2005)					
	Metavolcanic	2.624 ± 8		ZR SHRIMP	Tallarico et al. (2005)					
	Luanga Complx.	Anorthosite		2.763 ± 6	ZR U-Pb	Machado et al. (1991)				
	Archean Syn-tectonic Granites	Itacaiunas Granite		Granitoid	2.560 ± 37	ZR Pb-Pb	Souza et al. (1996)			
				Granitoid	2.525 ± 38	ZR Pb-Pb	Souza et al. (1996)			
				Old Salobo Granite	Granitoid	2.573 ± 2	ZR U-Pb	Machado et al. (1991)		
				Geladinho Granite	Granitoid	2.688 ± 11	ZR Pb-Pb	Barbosa et al. (2001)		
Estrela Granite			Granitoid	2.527 ± 68	WR Rb-Sr	Barros et al. (1992)				
Basement Assemblage	Pium Complex	hornblenda sienogranite	2.763 ± 7	ZR Pb-Pb	Barros et al. (2001)					
		Xingu Complex	Granitic Leucossoma	2.859 ± 2	ZR U-Pb	Machado et al. (1991)				
		Xingu Complex	Felsic Gneiss	2.851 ± 4	ZR U-Pb	Machado et al. (1991)				
		Xingu Complex	Aphibolite	2.519 ± 5	TI U-Pb	Machado et al. (1991)				
		Pium Complex	Granulite	3.050 ± 114	WR Pb-Pb	Rodrigues et al. (1992)				
		Pium Complex	Enderbite Protolith	3.002 ± 14	ZR SHRIMP	Pidgeon et al. (2000)				
		Pium Complex	Granulite	2.859 ± 9	ZR SHRIMP	Pidgeon et al. (2000)				
B - Transitional Domain										
Archean Syn-tectonic Granites	Rio Maria Granod.	Plaque Suite	Granitoid	2.729 ± 29	ZR Pb-Pb	Avelar et al. (1999)				
		Plaque Suite	Granitoid	2.736 ± 24	ZR Pb-Pb	Avelar et al. (1999)				
		Planalto Granite	Granitoid	2.747 ± 2	ZR Pb-Pb	Huhn et al. (1999)				
		Cristalino Diorite	Diorite	2.738 ± 6	ZR Pb-Pb	Huhn et al. (1999)				
		Serra do Rabo Gran.	Granitoid	2.743 ± 1	ZR U-Pb	Sardinha et al. (2002)				
		Undifferentiated	Granitoid	2.765 ± 39	ZR Pb-Pb	Sardinha et al. (2004)				
Basement Units	Xingu Complex	Granitoid	2.850 ± 17	ZR Pb-Pb	Avelar et al. (1999)					
		Gneiss	2.972 ± 16	ZR Pb-Pb	Avelar et al. (1999)					
		Granitoid	2.928 ± 1	ZR Pb-Pb	Sardinha et al. (2004)					
C - Rio Maria Greenstone Terrane										
Proterozoic Anorogenic Granites	Rio Maria Granod.	Musa Granite	Granitoid	1.883 +5/-2	ZR U-Pb	Machado et al. (1991)				
		Jamon Granite	Granitoid	1.885 ± 32	ZR Pb-Pb	Dall'Agnol et al. (1999)				
		Jamon Granite	Granitoid	1.601±42	WR Rb-Sr	Dall'Agnol et al. (1984)				
		Marajoara Granite	Granitoid	1.724 ± 50	WR Rb-Sr	Macambira (1992)				
		Redenção Granite	Granite	1.870 ± 68	WR Pb-Pb	Barbosa et al. (1995)				
		Calc-alkaline	Rio Maria Granod.	Granodiorite	2.874 +9/-10	ZR U-Pb	Macambira (1992)			
				Granodiorite	2.874 ± 10	ZR U-Pb	Macambira & Lancelot (1996)			
				Quartz-Diorite	2.878 ± 4	ZR Pb-Pb	Dall'Agnol et al. (1999)			
				Diorite	2.880 ± 4	ZR Pb-Pb	Rolando & Macambira (2003)			
				Água Fria Trondhjemite	banded trondhjemite	2.864 ± 21	ZR Pb-Pb	Leite et al. (2004)		
				Mogno Trondhjemite	Granitoid	2.871 ± ?	TI U-Pb	Pimentel & Machado (1994)		
				Mogno Trondhjemite	Granitoid	2.87	TI U-Pb	Dall'Agnol et al. (1998)		
				Granitoids	Rio Maria Granod.	Parazonia Tonalite	Granitoid	2.858	TI U-Pb	Pimentel & Machado (1994)
						Cumaru Granodiorite	Granitoid	2.817 ± 4	ZR Pb-Pb	Lafon et al. (1994)
						Mata Surrao Granite	Leucogranite	2.871 ± 7	ZR Pb-Pb	Althoff et al. (2000)
		Mata Surrao Granite	Monzogranite			2.881 ± 2	ZR Pb-Pb	Rolando & Macambira (2003)		
		Mata Surrao Granite	Monzogranite			2.875 ± 11	ZR Pb-Pb	Rolando & Macambira (2003)		
		Guaranta Granite	Leucogranite			2.93	ZR Pb-Pb	Althoff et al. (2000)		
		Xinguara Granite	Granitoid			2.87	ZR Pb-Pb	Dall'Agnol et al. (1998)		
		Xinguara Granite	Leucogranite			2.865 ± 1	ZR Pb-Pb	Leite (2001)		
Xinguara Granite	Leucogranite	2.875	ZR Pb-Pb			Rolando & Macambira (2002)				
Greenstone Belts	Andorinhas Supergroup	Inaja Group	Metabasalt			2.988 ± 4	ZR U-Pb	Rolando & Macambira (2003)		
		Lagoa Seca Grp.	Metagraywakes	2.971 ± 18	ZR U-Pb	Macambira (1992)				
		Lagoa Seca Grp.	Felsic Metavolcanic	2.979 ± 5	ZR U-Pb	Pimentel & Machado (1994)				
		Identidade Grp.	Metadacite	2.944 ± 88	WR Pb-Pb	Souza (1994)				
		Tucumã Grp.	Metabasalt	2.868 ± 8	ZR Pb-Pb	Avelar et al. (1999)				
		Ultramafic	Serra Azul Complex	peridotite	2.970 ± 7	ZR U-Pb	Pimentel & Machado (1994)			
				TTG Granitoids	Caracol Ton.	Tonalite	2.936 ± 3	ZR Pb-Pb	Leite et al. (2004)	
						Tonalite	2.942 ± 2	ZR Pb-Pb	Leite et al. (2004)	
						Arco Verde Ton.	Tonalite	2.957 +25/-21	ZR U-Pb	Macambira (1992)
				Arco Verde Ton.	Tonalite	2.96	ZR U-Pb	Dall'Agnol et al. (1998)		
Arco Verde Ton.	Tonalite			2.981 ± 8	ZR Pb-Pb	Rolando & Macambira (2003)				

Table 4.1 Compilation of isotopic ages for rocks in the Carajás, Transitional (or Canaã dos Carajás region) and Rio Maria Granite Greenstone domains. The isotopic ages generally date the time of crystallization of the rocks. Transitional and Rio Maria Granite Greenstone domains.

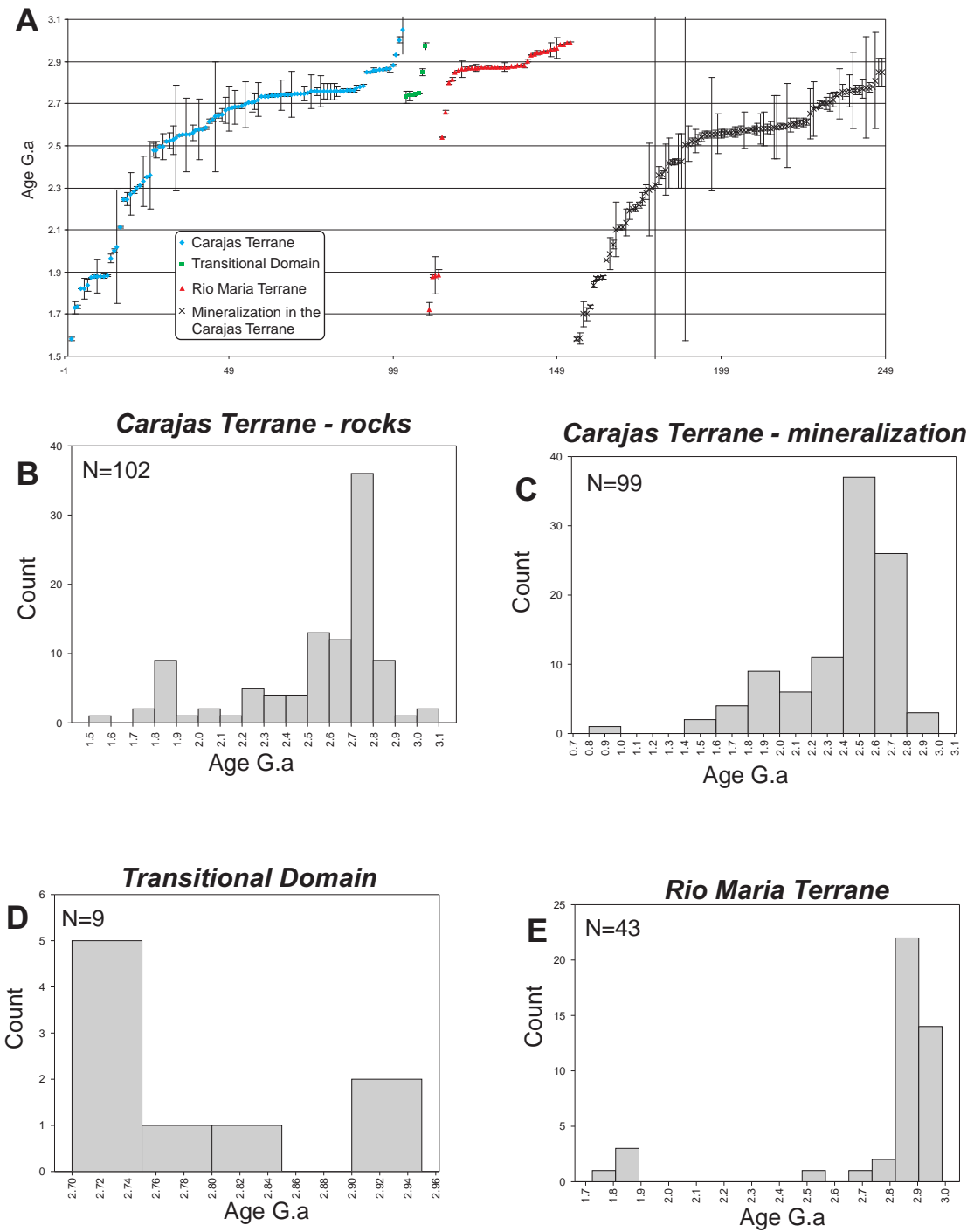


Figure 4.4 Graphic representation of the isotopic ages presented in Table 01. **A** Plot of the isotopic ages sorted by age and grouped into: Carajás Terrane, Transitional Domain, Rio Maria Terrane and Mineralization in the Carajás Terrane. **B** Age histogram of isotopic ages for granitic and volcano sedimentary rocks seen in the plot A. **C** Histogram for ages of mineralization from the Carajás block. **D** Distribution of U/Pb zircon ages in juvenile continental crust. Abundance is proportional to areal distribution of juvenile age provinces scaled from an equal area projection of the continents (Condie, 1998)

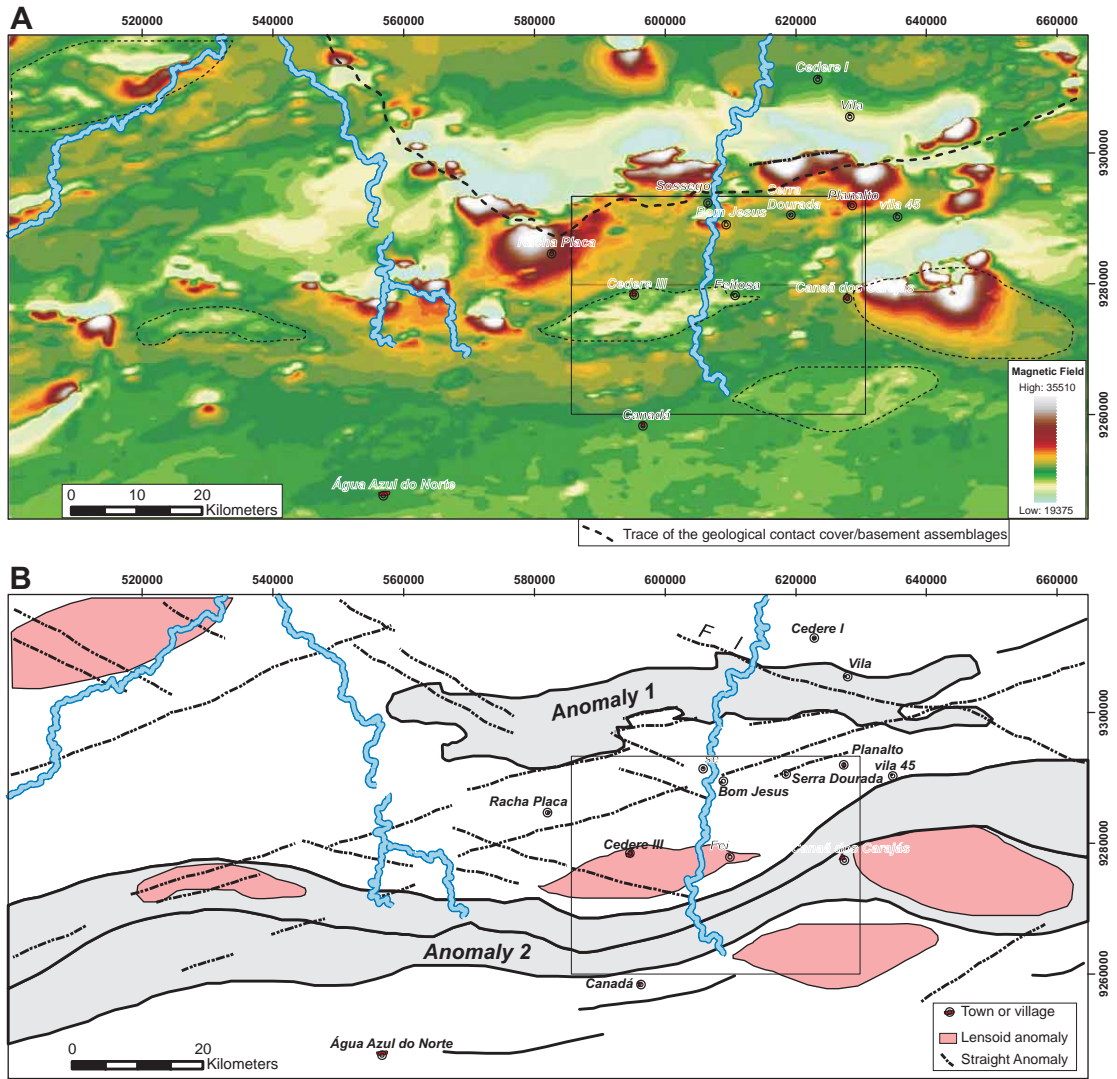


Figure 4.5 *A* Map of interpolated magnetic field by Inverse Distance Weighted method; and **B** Major interpreted magnetic anomalies. Grey polygons represent prominent long and continuous anomalies, while lensoid pink anomalies coincide with granitoids. The dashed lines correspond to discrete and straight linear anomalies likely to be produced by shear or fault zones. The rectangle indicates the limits of the map in Fig. 4.3 A

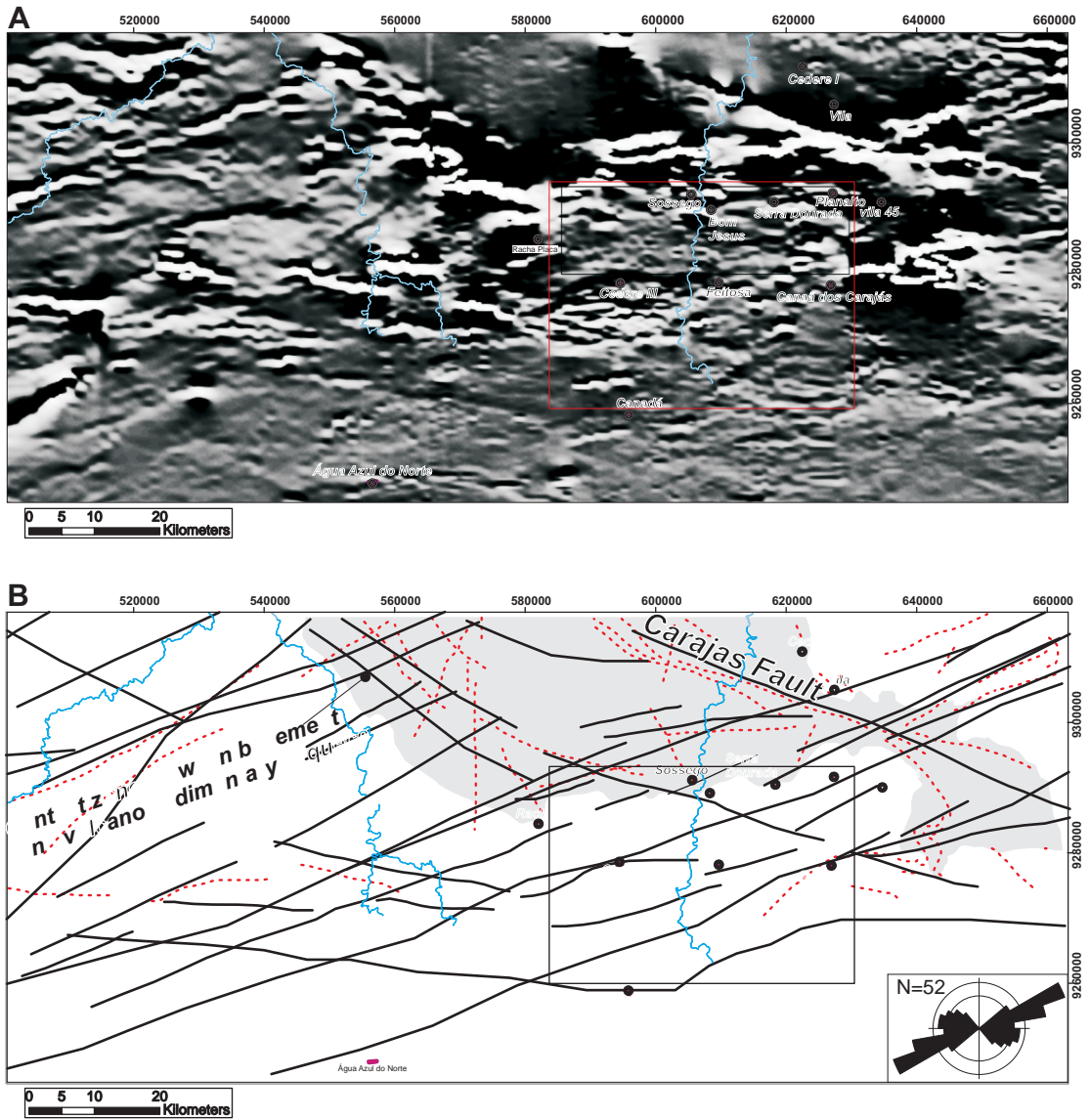


Figure 4.6 *A* Map of the hill shaded magnetic field with illumination source inclined at 30° from 20° Az. *B* Interpreted magnetic lineaments (solid black lines). The grey region corresponds to the volcano sedimentary assemblage and the red dashed lines indicate the main topographic lineaments. The rectangle indicates the limits of the map in Fig. 4.3 A

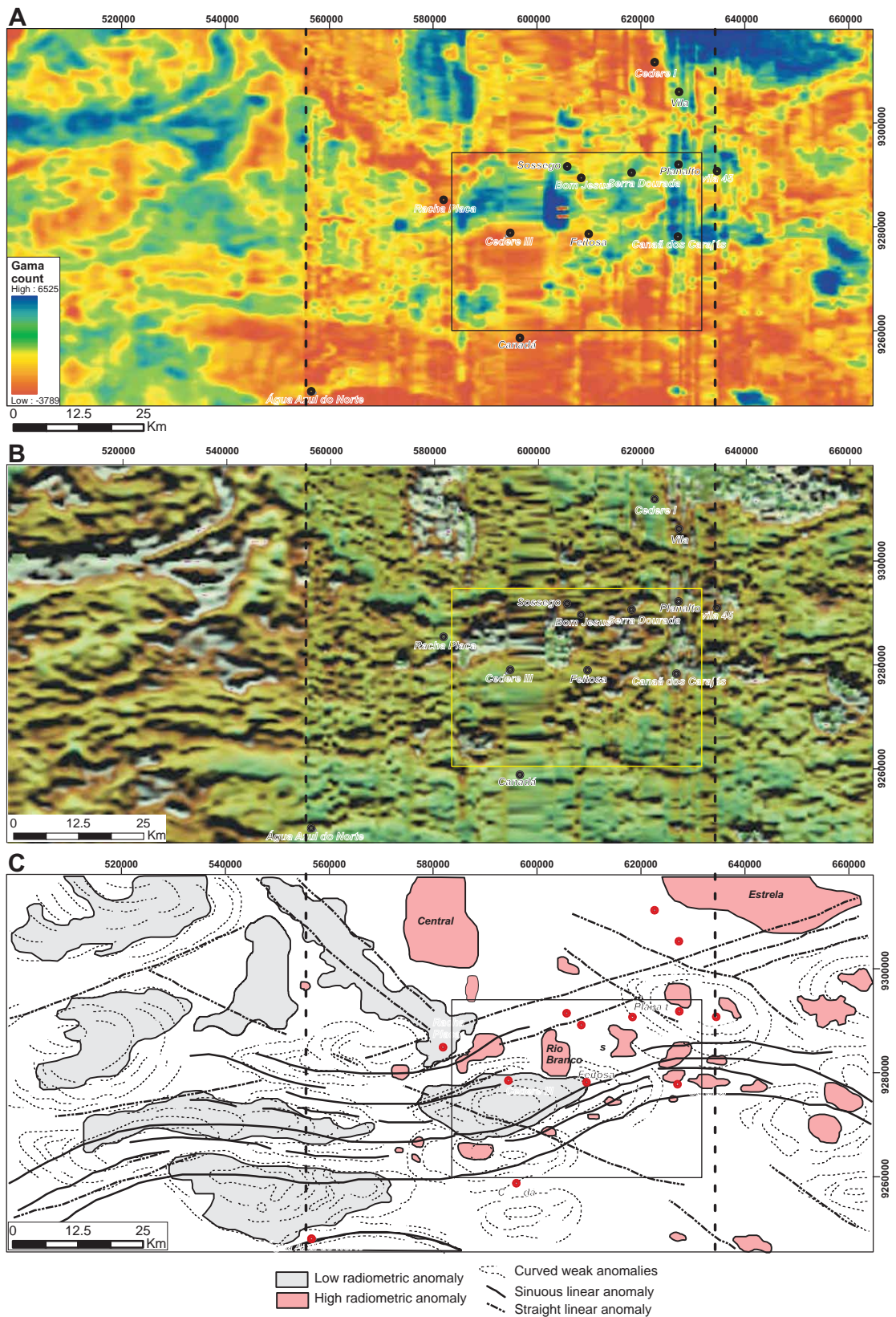


Figure 4.7 *A* Airborne gamma spectrometric map for (U K Th) channels, interpolated by Inverse Distance Weighted method. The red and blue colours correspond to lowest and highest radiometric values respectively. *B* Coloured hillshade image of the interpolated radiometric data. *C* Interpreted radiometric anomalies (see text for description). The rectangle indicates the limits of the map in Fig. 4.3 A

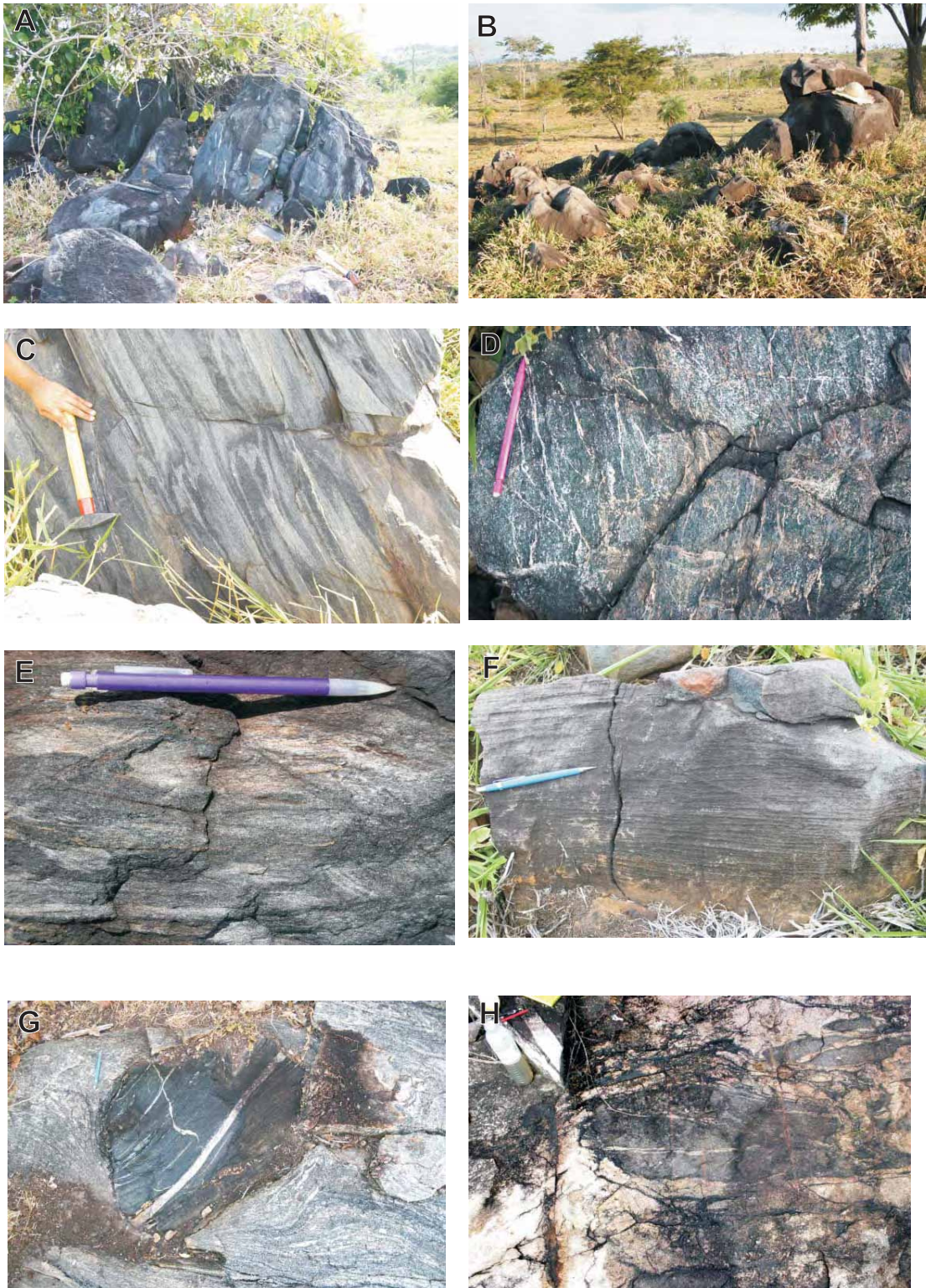


Figure 4.8 General aspects of the older basic rocks observed in the study area. **A** and **B**, typical boulders of amphibolite and basalt. **C** In situ steeply dipping, banded amphibolite. **D** Coarse grained, hornblende rich amphibolite cross cut by quartz veinlets. **E** Detail of the banded amphibolite, clear portions are feldspar rich. **F** Detail of basalt containing sub parallel veins of chlorite+epidote tens of millimetres. **G** and **H** Sub rounded and lens shaped amphibolite xenoliths in granitic gneisses. Note the presence of fabrics in the xenoliths.



Figure 4.9 General aspects of the granitic gneisses from the Xingu Complex in the study area. **A** and **B** Typical gneiss outcrops, as boulders or flat lying outcrops. **C** and **D** Examples of the coarse gneiss variety; note the textural magmatic appearance. **E** and **F** General and close up view of fine grained gneiss, with markedly straight foliation or lenses produced by shearing, and **G** Remobilised k feldspar rich segregation within fine grained gneiss.



Figure 4.10 Examples of mylonites from relatively wide (A) and narrow (B) shear zones. C, D and E Fine, medium and coarse varieties of mylonite. Note the variations in porphyroclasts and matrix size and in the matrix porphyroclast ratios. F Relatively rare *k* feldspar porphyroclasts in coarse grained mylonite.



Figure 4.11 Field photographs exemplifying some of the varieties of granitoids observed in the study area. **A i** and **ii** an outcrop and a closer view of a syenogranite and **iii** albitized portion of a syenogranite. **B** and **C** Flat outcrops of tonalites with its respective close up photos. **D** Magmatic contact between tonalite and syenogranite, in detail an elongated mafic xenolith oriented parallel to the magmatic foliation.



Figure 4.11 (cont) *E* Road cut outcrop of isotropic granite with enclosed microgranite, the detail photo shows the sharp contact between the coarse isotropic granite and the fine grained microgranite. *F* Small outcrop of a granodiorite and detail photo the general granular texture of the rock that also contains mafic lens shaped xenolith. *G* and *H* Isotropic and sheared varieties of tonalities, note the discrete shear zones in the outcrop at *H*.



Figure 4.12 Examples of outcropping dykes and close up photos. **A** and **B** Isotropic and medium grained basaltic dikes. **C** Basaltic dyke cross cut by two sets of chlorite and epidote veinlets or shear bands. **D** Dioritic dyke with markedly pink colour and larger feldspar crystals floating in a fine grained matrix. The dashed lines in **B**, **C** and **D** indicate the approximate boundary of the dykes.

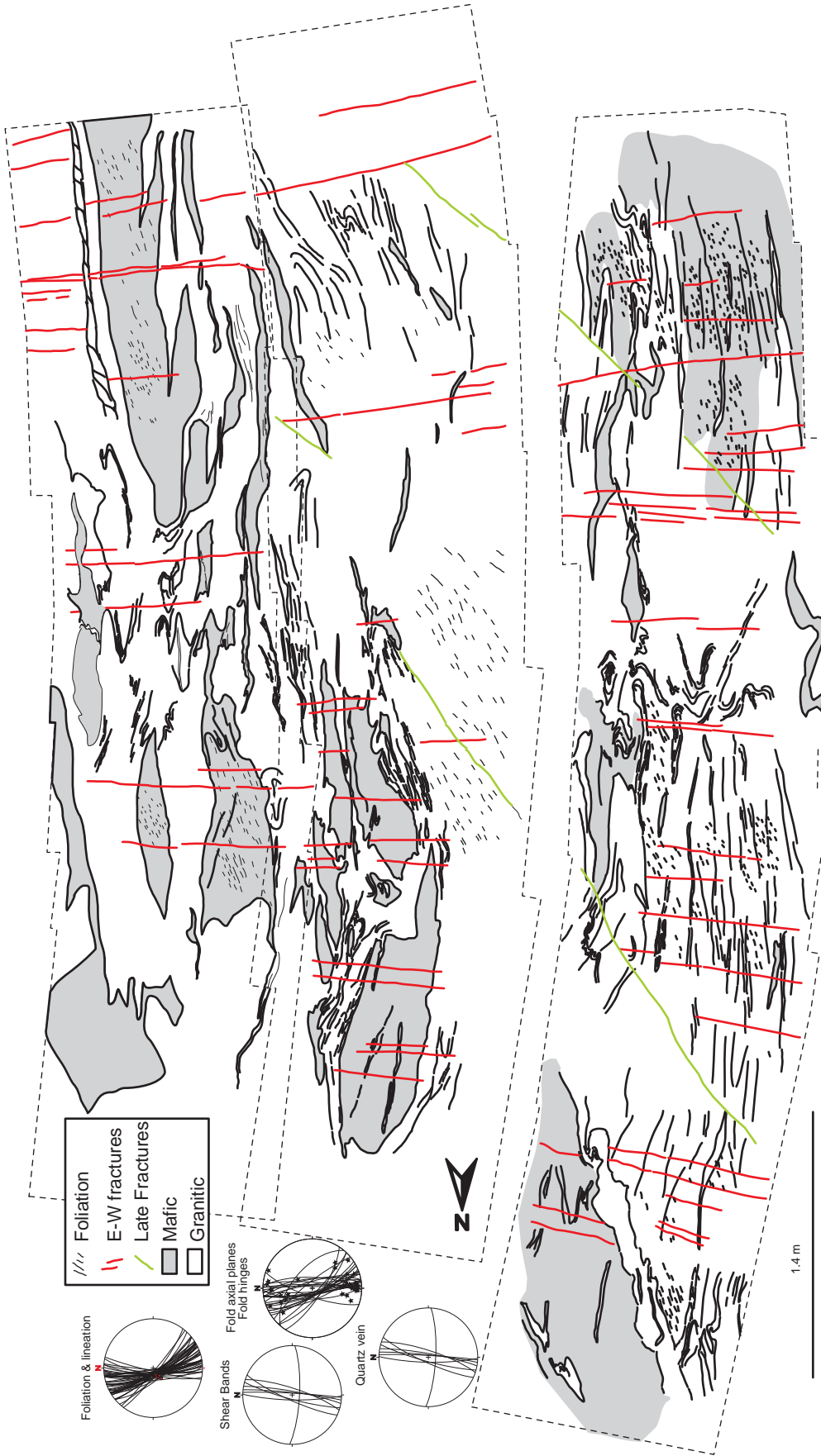


Figure 4.13 - Plan view map of an outcrop displaying complex magmatic contacts between more mafic (grey) and felsic granitic portions. Structures are oriented under a general N-S trend as seen for the foliation, shear bands, fold hinges and axial planes.

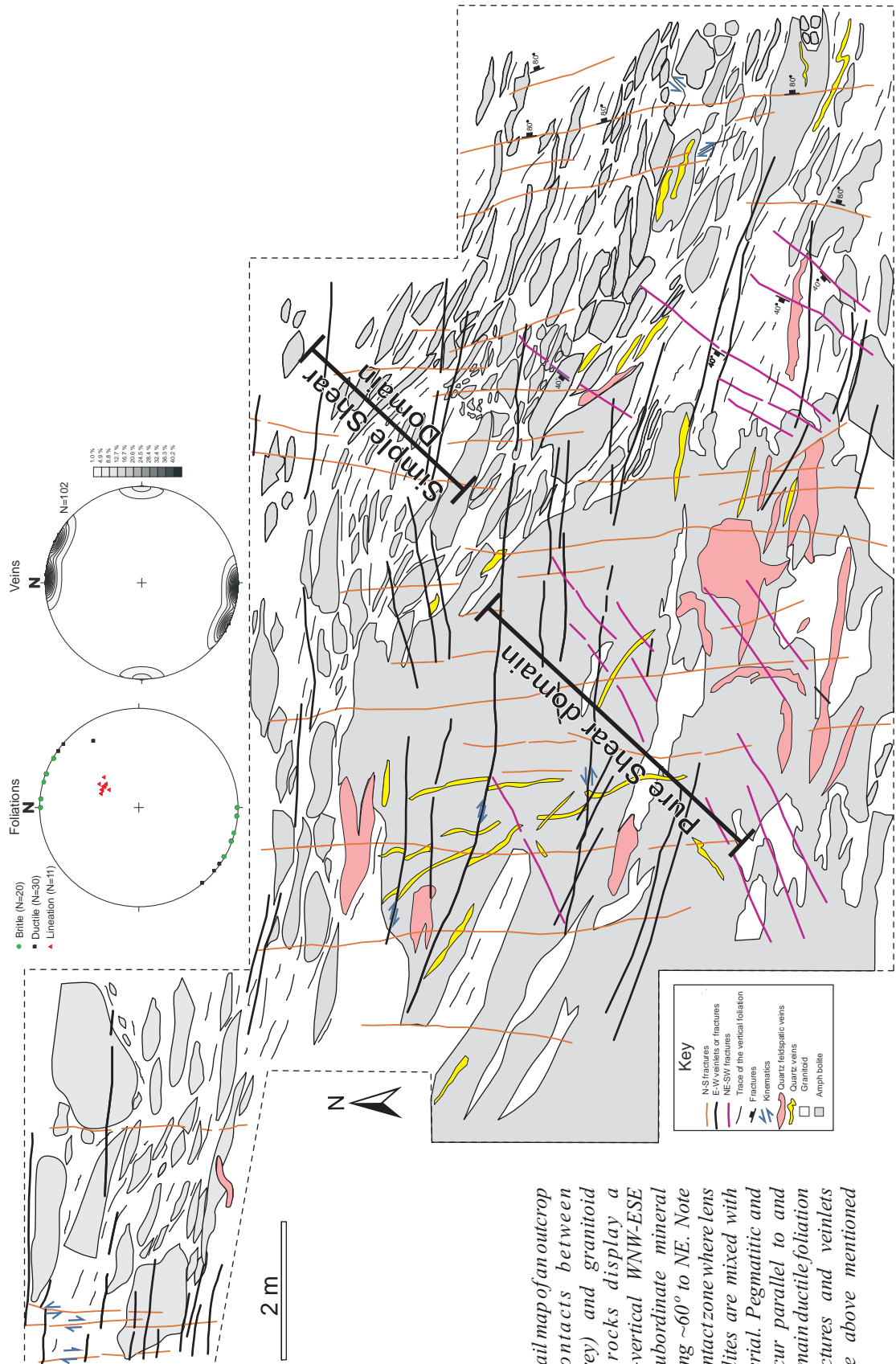


Figure 4.14 - Detail map of an outcrop showing a contacts between amphibolite (grey) and granitoid (white). The rocks display a widespread sub-vertical WNW-ESE foliation and subordinate mineral lineations plunging ~60° to NE. Note the WNW-ESE contact zone where lens shaped amphibolites are mixed with the granitic material. Pegmatitic and quartz veins occur parallel to and cross-cutting the main ductile foliation trend. Late fractures and veinlets cross-cut all the above mentioned features.

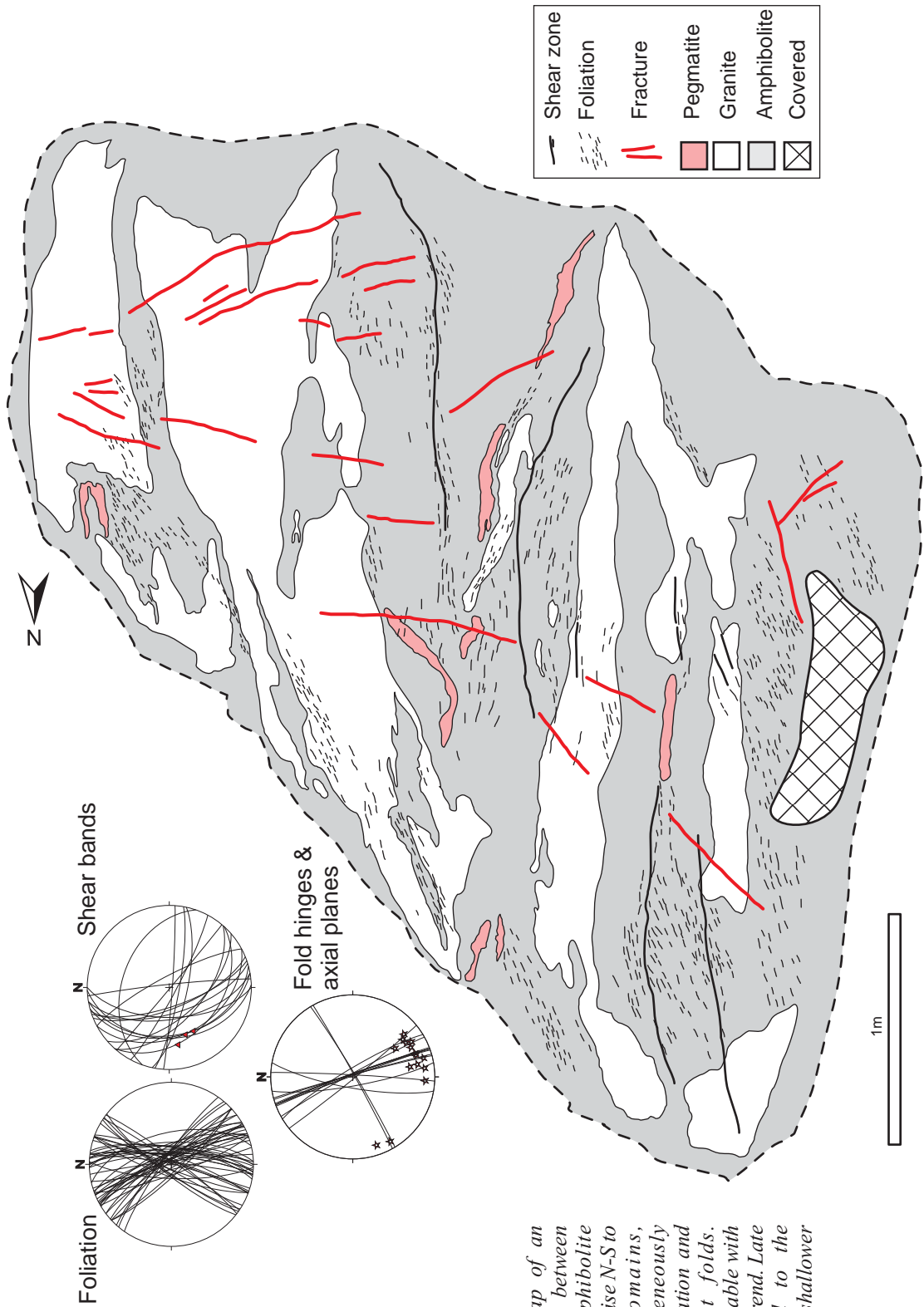


Figure 4.15 - Detailed map of an outcrop displaying contacts between granite (white) and amphibolite (grey). The granitoids comprise N-S to NNW-SSE oriented domains, associated with heterogeneously developed, sub-vertical foliation and centimetre-scale upright folds. Pegmatite veins are conformable with the main observed foliation trend. Late shear bands are parallel to the foliation, but with average shallower dip values.

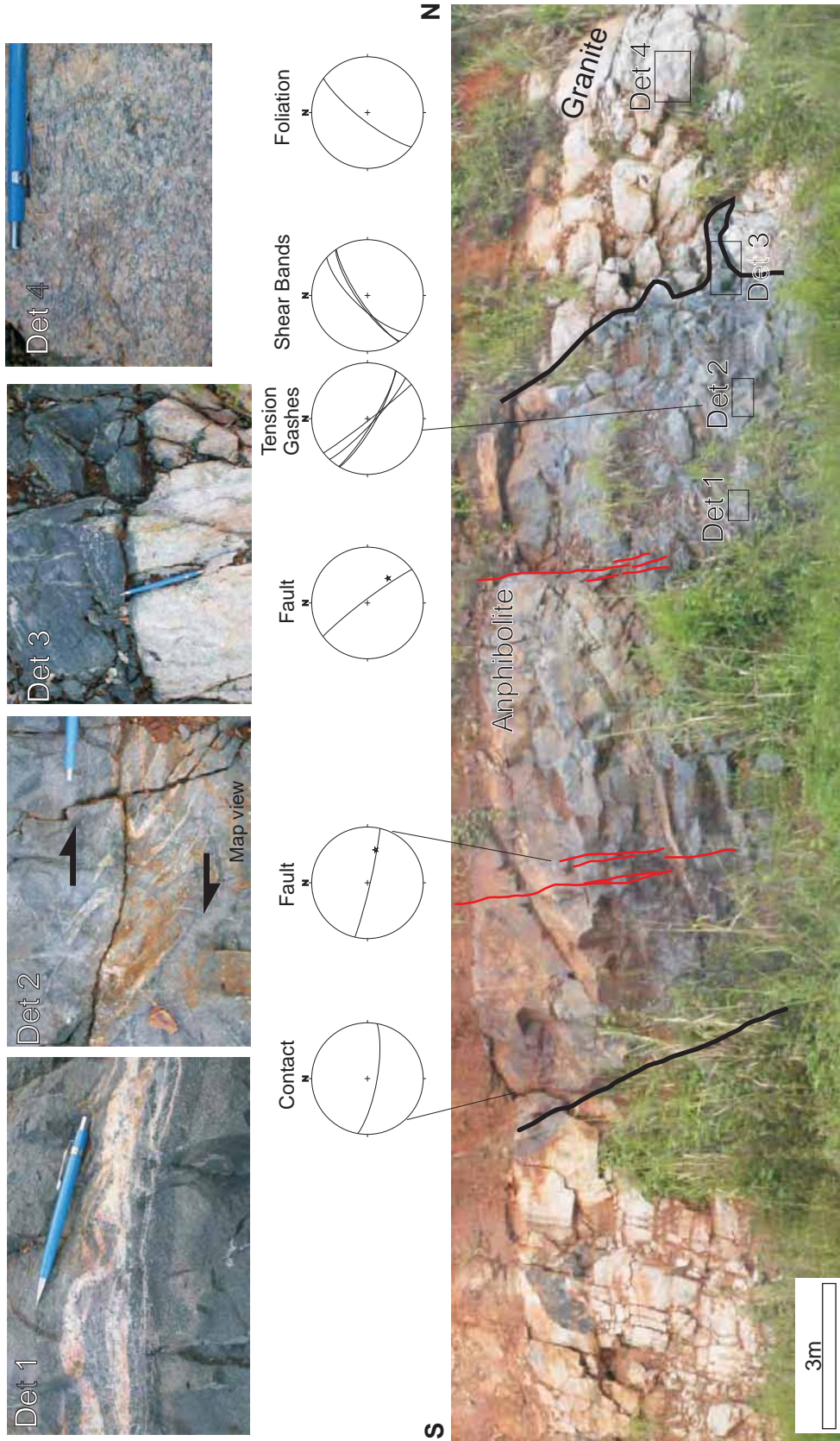


Figure 4.16 - Amphibolite body tectonically emplaced into a granitic body. The contact planes are sharp as show in **Det. 3** and represented by surfaces trending **WNW-ESE**, dipping steeply **SSW**. The host granitoid shows a weak and heterogeneously developed foliation (see **Det. 4**). Mineralized shear bands (**Det. 1**) and tension gashes (**Det. 2**) are evidence of shearing in the amphibolite body. Late sub-vertical fractures (red) and oblique faults cross-cut the previously mentioned lithologies.



Figure 4.17 Detailed photographs of tectonic contacts between granitoid and amphibolite (A) and volcanic mafic (B). In A, the banded amphibolite seems to accommodate most of the deformation while the granitoid displays only discrete faults. In B, a sheared boundary (15 cm wide) separates granite from volcanics and oblique structures in the volcanic portion suggest sinistral kinematics.

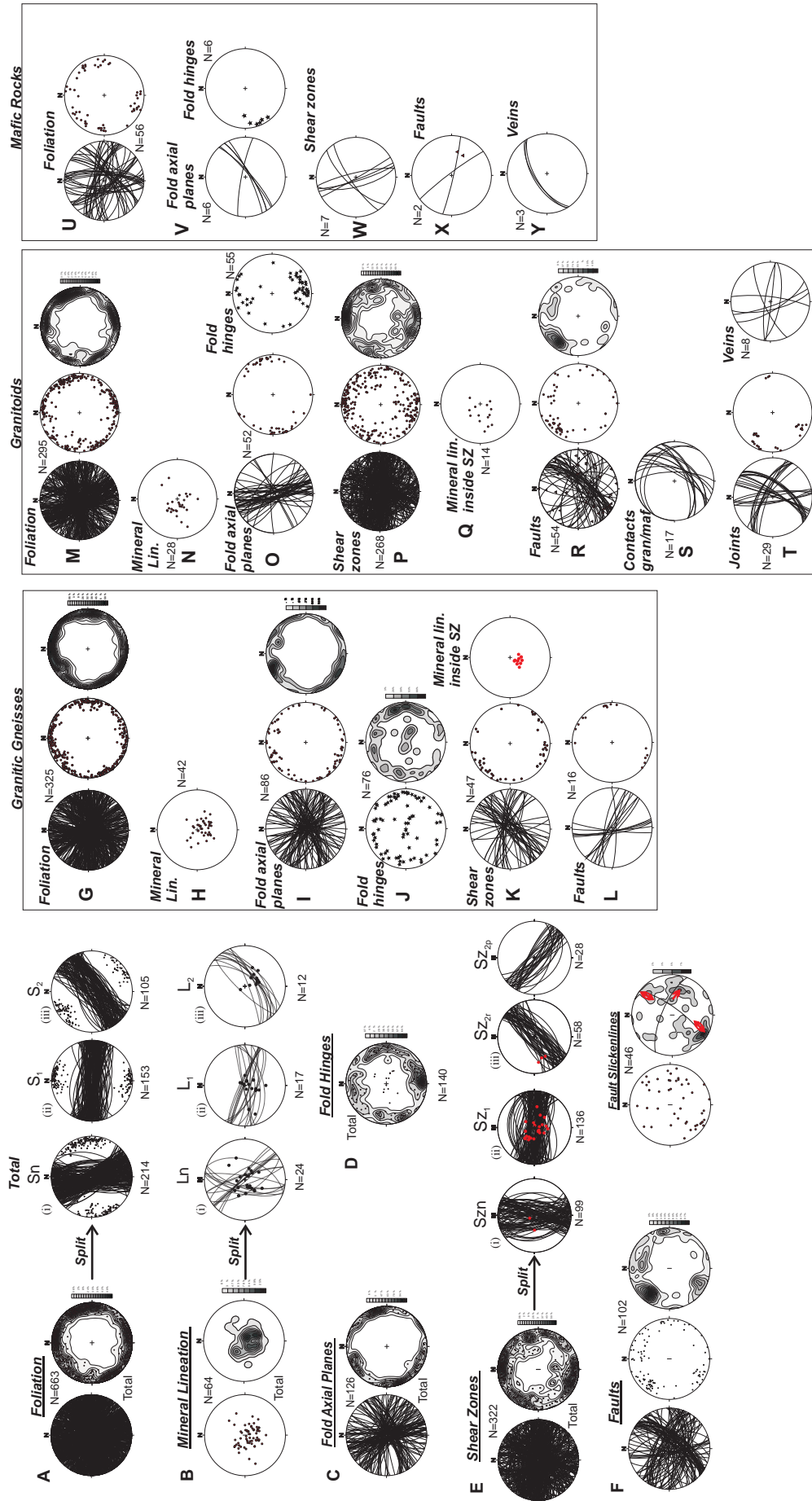


Figure 4.18 - Stereographic diagrams for the recorded structural features in the studied area. All data was plotted in lower hemisphere, equal area stereographic projection (Lambert projection; Schmidt net). **A, B, C, D** and **E** show stereonets for total measurements and complementary diagrams for data grouped by main statistic trends (Sn, S₁ and S₂). In **A**, the dots in the stereonets represent poles to the foliation planes. In **B**, the stereonets grouped according to the main observed trends, display dots for mineral lineation and the respective representation of the foliation plane containing the lineation. In **E**, the stereonets for shear bands separated by main trend show red dots representing mineral lineation.

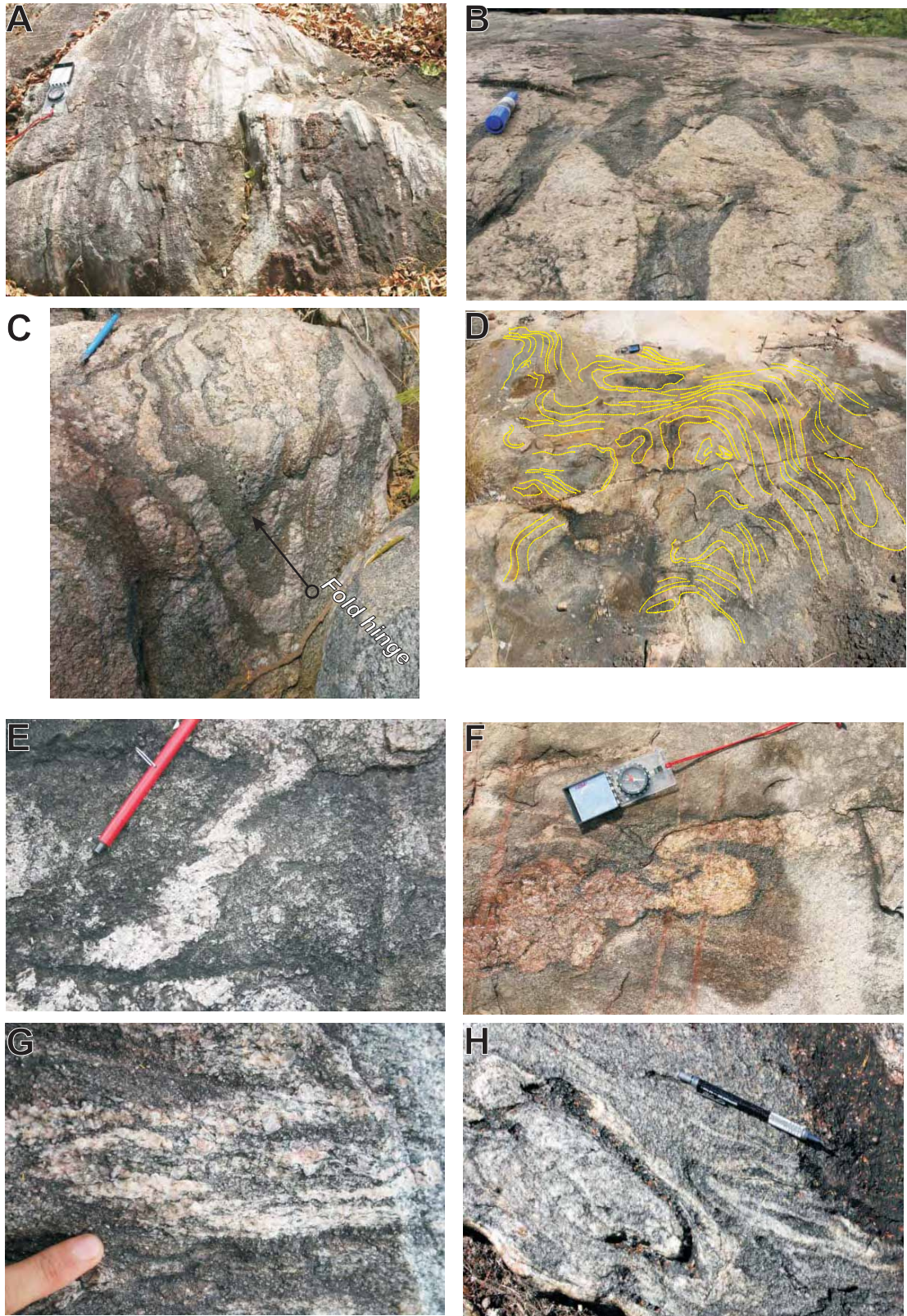


Figure 4.19 - Photos showing the different types of folds observed in the study region. **A, B, C** are examples of upright folds observed in granitic gneisses with fold hinges and axial planes trending N S. **D** Disharmonic folds in granitoid. **E-F** Display "S" shaped pygmatic folds of granitic veins in granitoids. **G-H** Centimetre scale sheath folds evidenced by the development of eye structures. Sheath folds are all steeply plunging.



Figure 4.19 (cont) - I, J, K, L Examples of transposed folds in granitic gneisses. Fold hinges and axial planes are generally sub vertical trending E W or WNW ESE. **M-N** Photos showing in plan view “drag” folds formed adjacent to discrete shear zones. **O-P** Examples of folded gneissic banding with asymmetric geometries.



Figure 4.20 – Outcrop of granitic gneiss displaying disharmonic folds (S_n) transposed by NE-SW shear zones. Note the labeled intrafolial and drag folds associated with the shear zones.



Figure 4.22 - Photographic examples of the different styles of ductile foliation observed in granitoids. *A* and *B* show typical symmetrical foliation marked by elongated ribbons of quartz. *C-D* Display asymmetric foliation characterized by the sigmoidal geometry of quartz ribbons. *E* Weak foliation outlined by elongate clusters of hornblende. *F, G, H* Show samples of relatively coarse granitoids with weakly developed foliations.

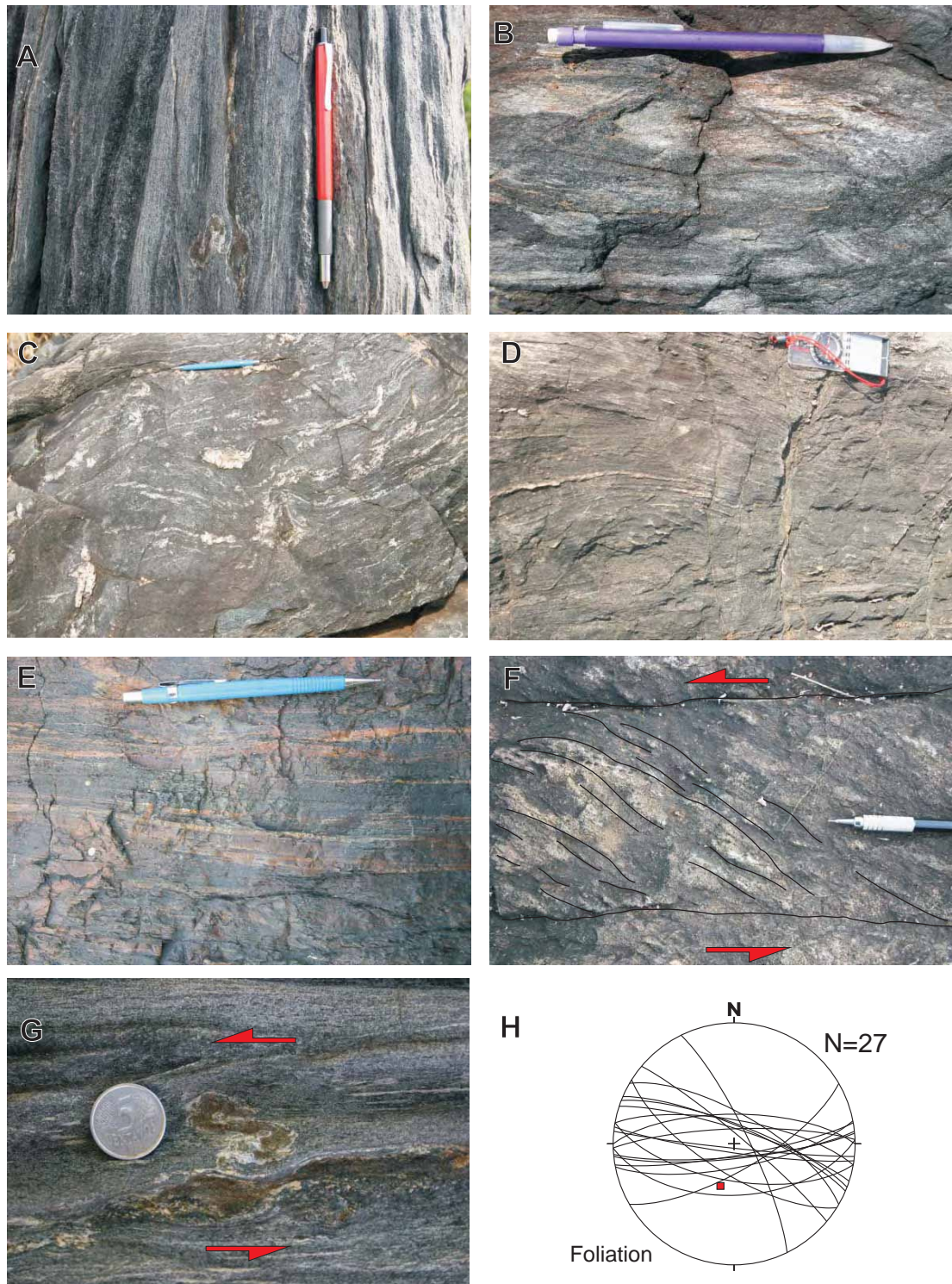


Figure 4.23 - Ductile planar fabrics observed in amphibolites. **A-B** Show the compositional banding present in amphibolites, with dark and white coloured bands representing the amphibole and feldspar rich domains, respectively. **C** compositional banding in amphibolite folded at centimetre scale. **D** gently wavy compositional banding in amphibolite. **E** straight and sharp compositional banding. **F** foliation showing S C geometry indicative of sinistral kinematics. **G** “S” shaped porphyroclast enveloped in the compositional banding and suggestive of sinistral kinematics. **H** stereonet for mean foliation planes measured in amphibolites.



Figure 4.24 - Representative examples of mineral lineations in the studied region. **A- B** Show mineral lineations in granitoids. **C** Mineral lineation in sub vertical foliation plane in banded amphibolite. **D-E** Display a wider and detailed view of "L" tectonites in granitoids, note the "cigar" shaped quartz grains in both pictures.

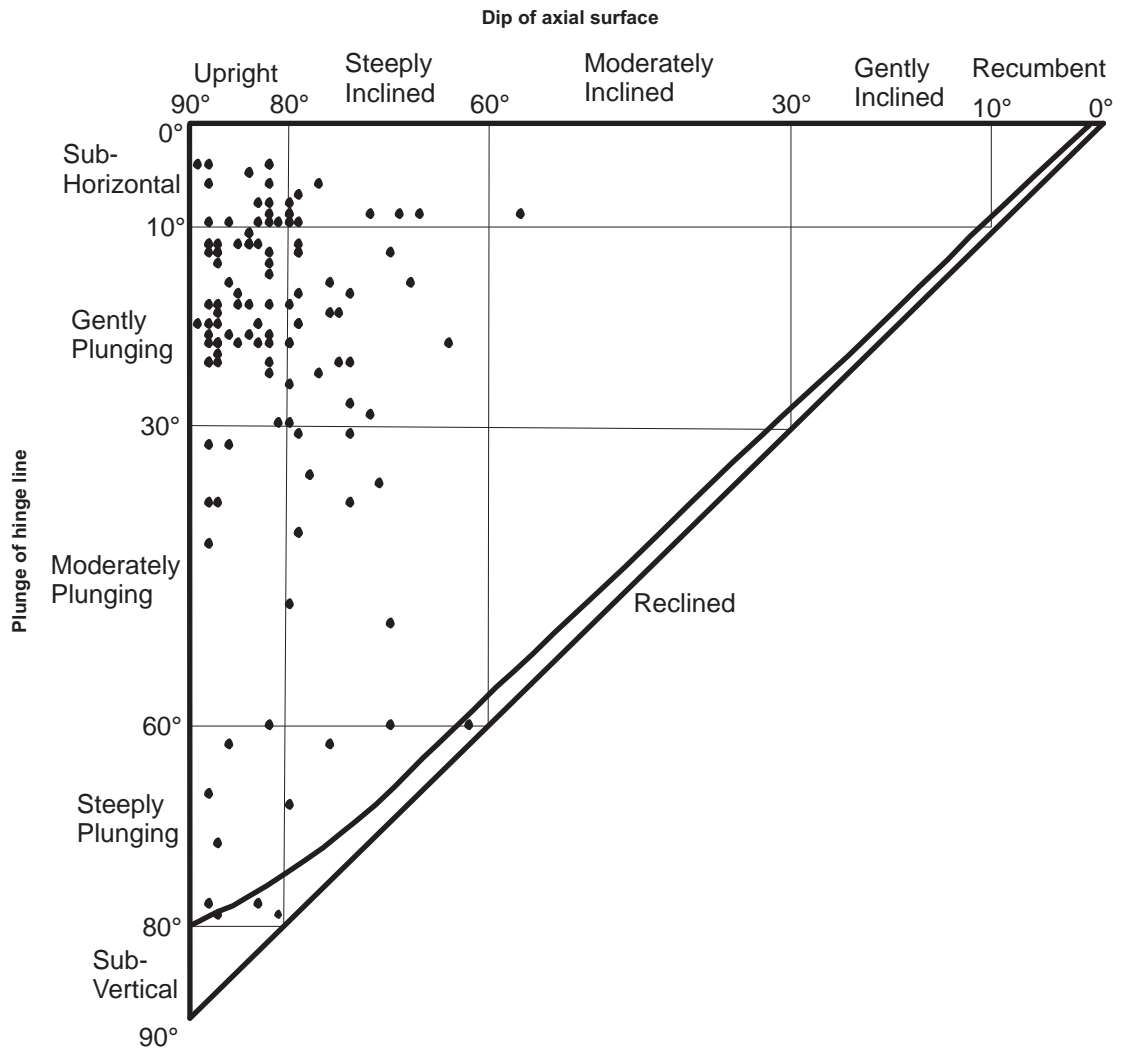


Figure 4.25 - Classification of the folds observed in the gneisses using the Fleuty Diagram. The classification is based on: the dip of the axial surface (x axis) plotted against the plunge of the hinge line (y axis).

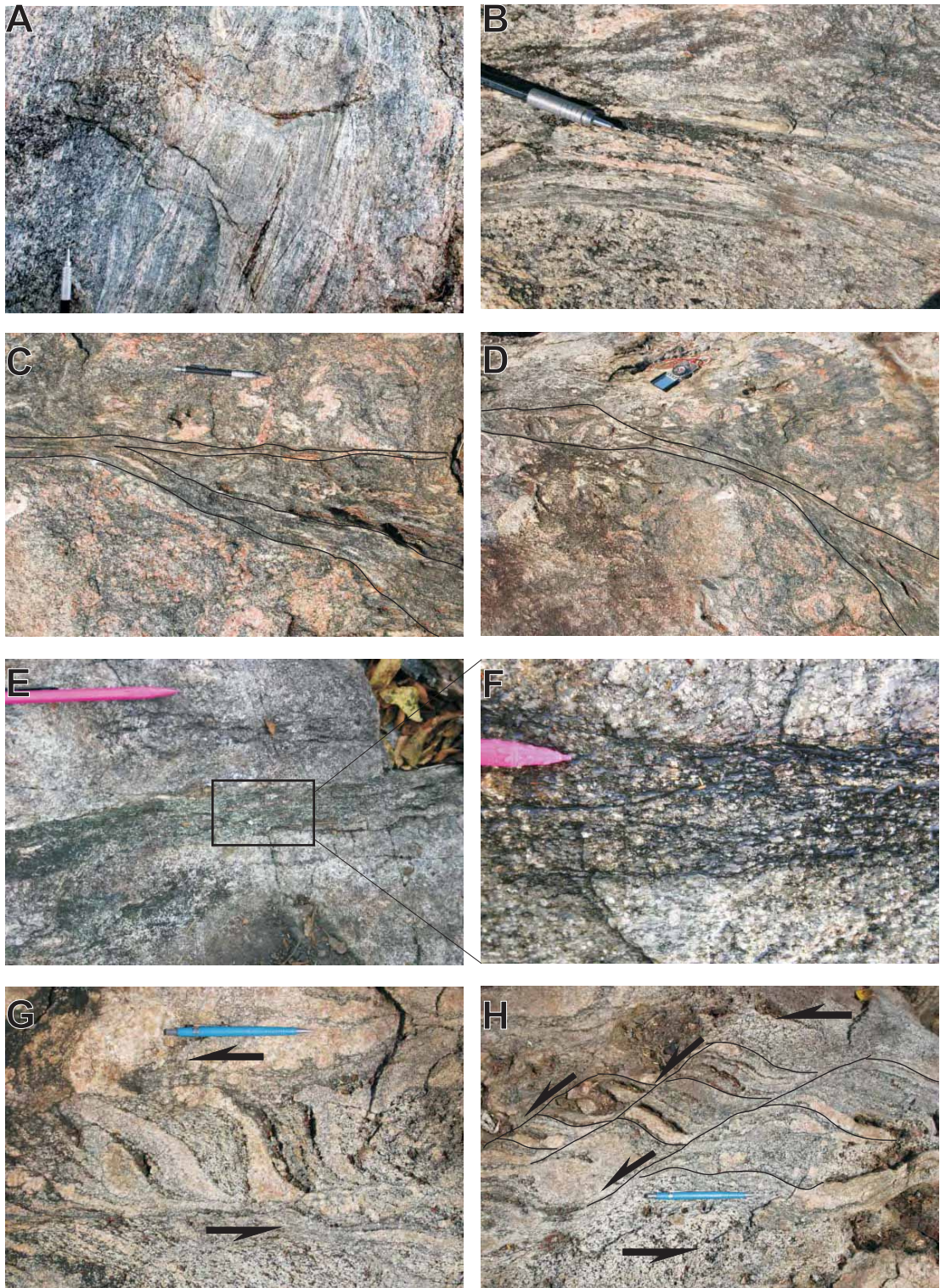


Figure 4.26 - Representative examples of shear zone geometries and their characteristics. **A-B** Show aspects of the internal fabric of a planar shear zone. Note the straight geometry of the foliation. **C-D** Show examples of curvilinear shear zones, the shear zones walls and internal fabric are wavy and occasionally anastomosing. **E-F** Show the intensely reduced grain size and strong mineral alignment forming a disjunctive foliation in shear zones. **G-H** Show sigmoidal S C fabrics formed by sinistral shear zones offsetting and displacing the early gneissic banding.

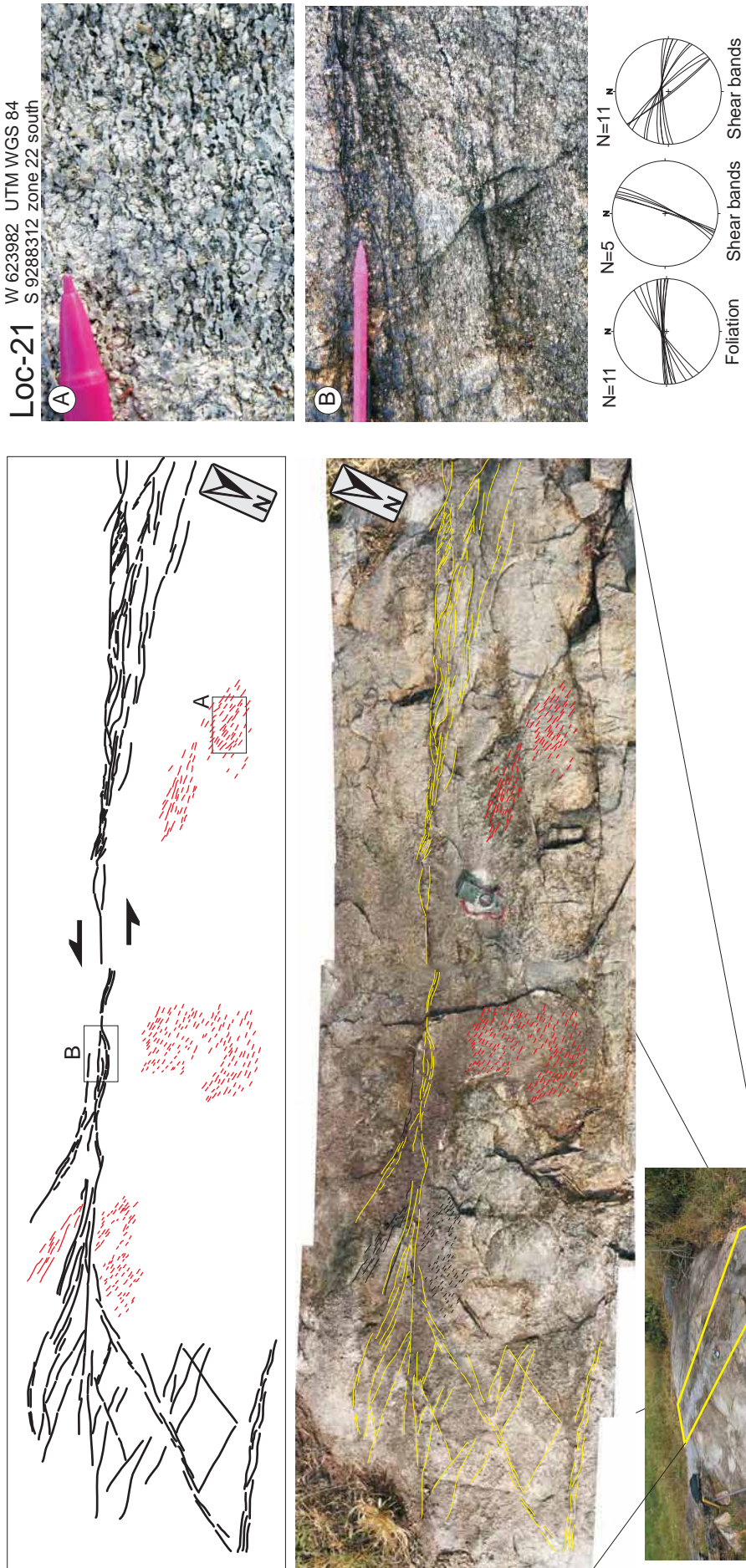


Figure 4.27 - Photo-mosaic and schematic diagram of an isinistral shear zone in foliated granitoid. The long axis of the shear zone is *WNW-ESE* oriented, with several *NE-SW* and *E-W* branches projected from the main structure. The granitoid shows a ductile foliation (see photo A) with a mean *E-W* orientation. The interior of the shear zone is marked by a relatively fine grained planar fabric as shown in photo B.

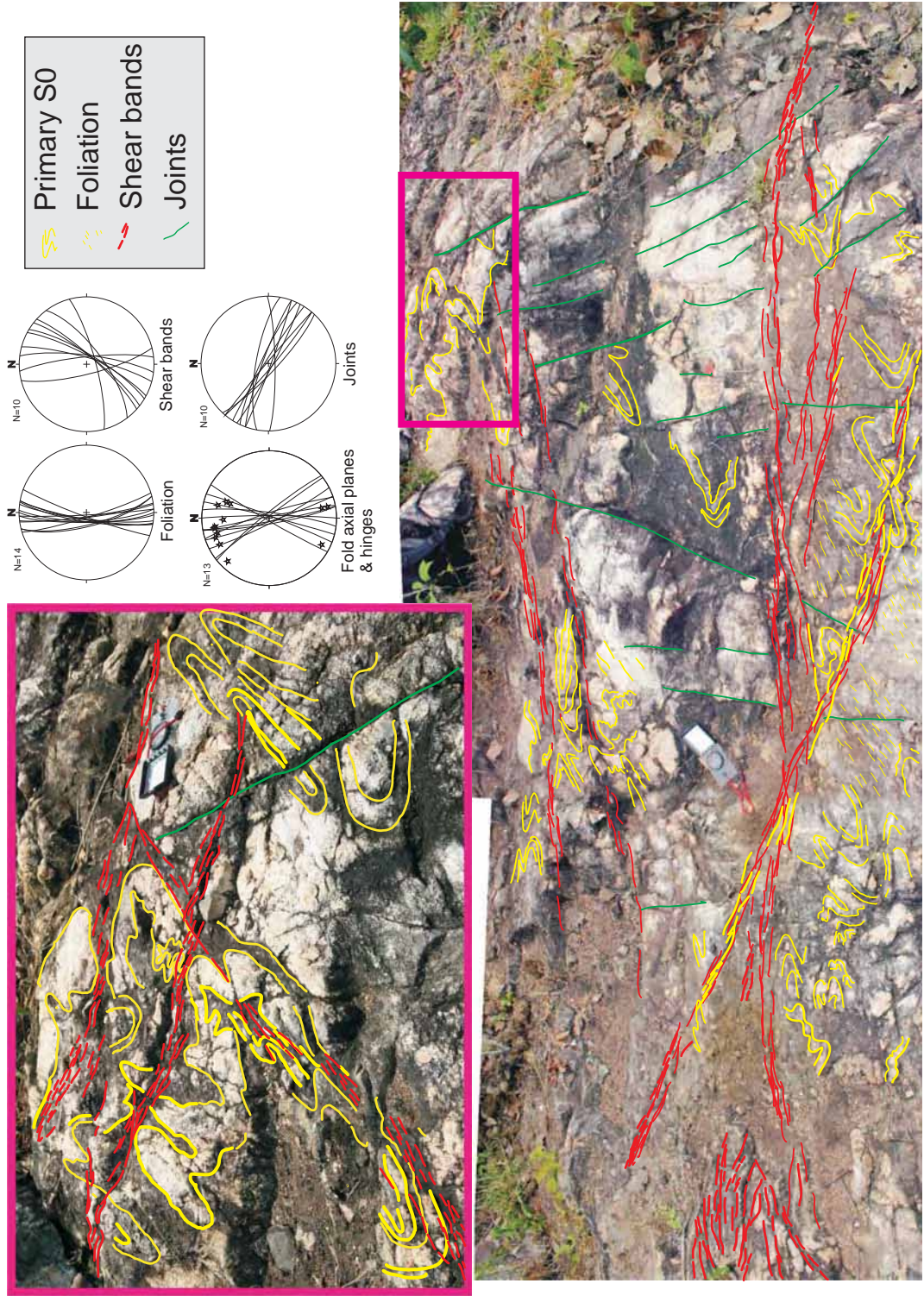


Figure 4.28 - Outcrop of a gneissic granitoid exhibiting the primary (S₀) gneissic banding (yellow lines), disrupted by NE-SW ductile shear zones (red lines). Late NW-SE brittle fractures (green lines) crosscut the early ductile structures.

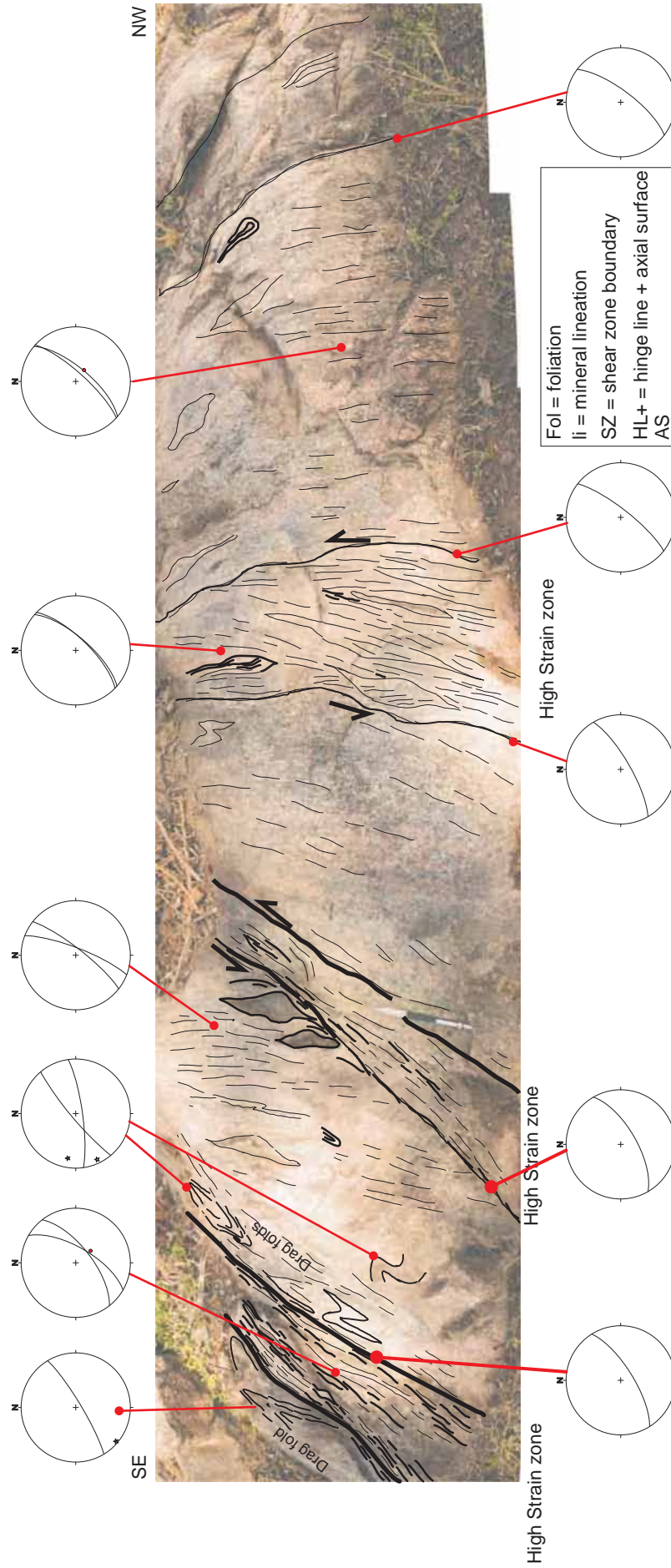


Figure 4.29 - Outcrop of an alkali-granite crosscut by NE-SW trending shear zones. Strain is intensely concentrated along the shear zones that locally form “drag” folds. Note the presence of sigmoidal lenses and the narrow spacing of the foliation within the shear zones.

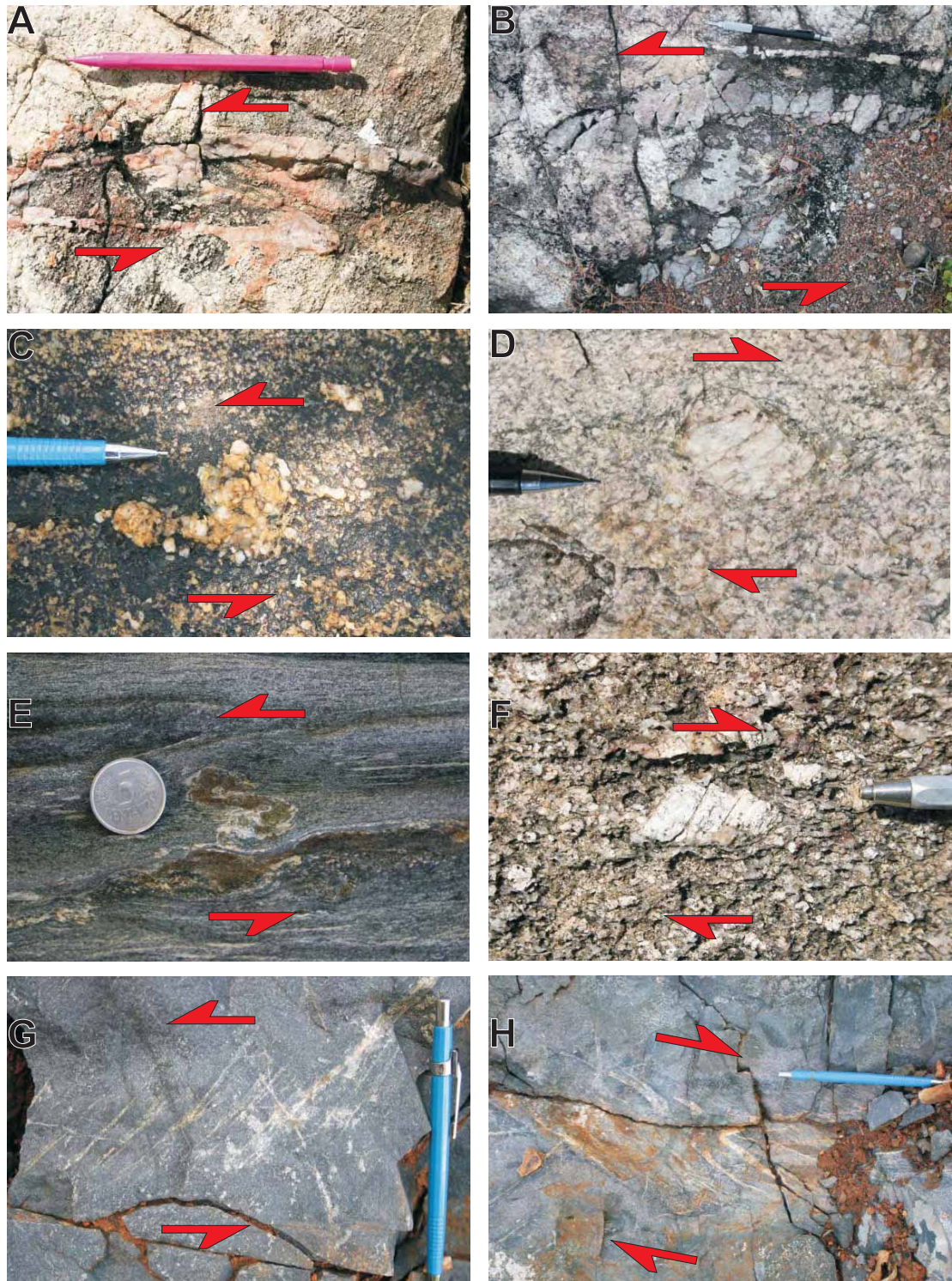


Figure 4.30 - Selected examples of sense of shear indicators. **A-B** "S" shaped folded veins suggesting sinistral kinematics. **C,D,E, F** Examples of 4 distinct geometries of propylitic clasts wrapped by foliation, indicating dextral and sinistral kinematics. **G,H** Show "en echelon" veins and tension gashes formed under semi brittle regime indicating sinistral and dextral sense of shear respectively.

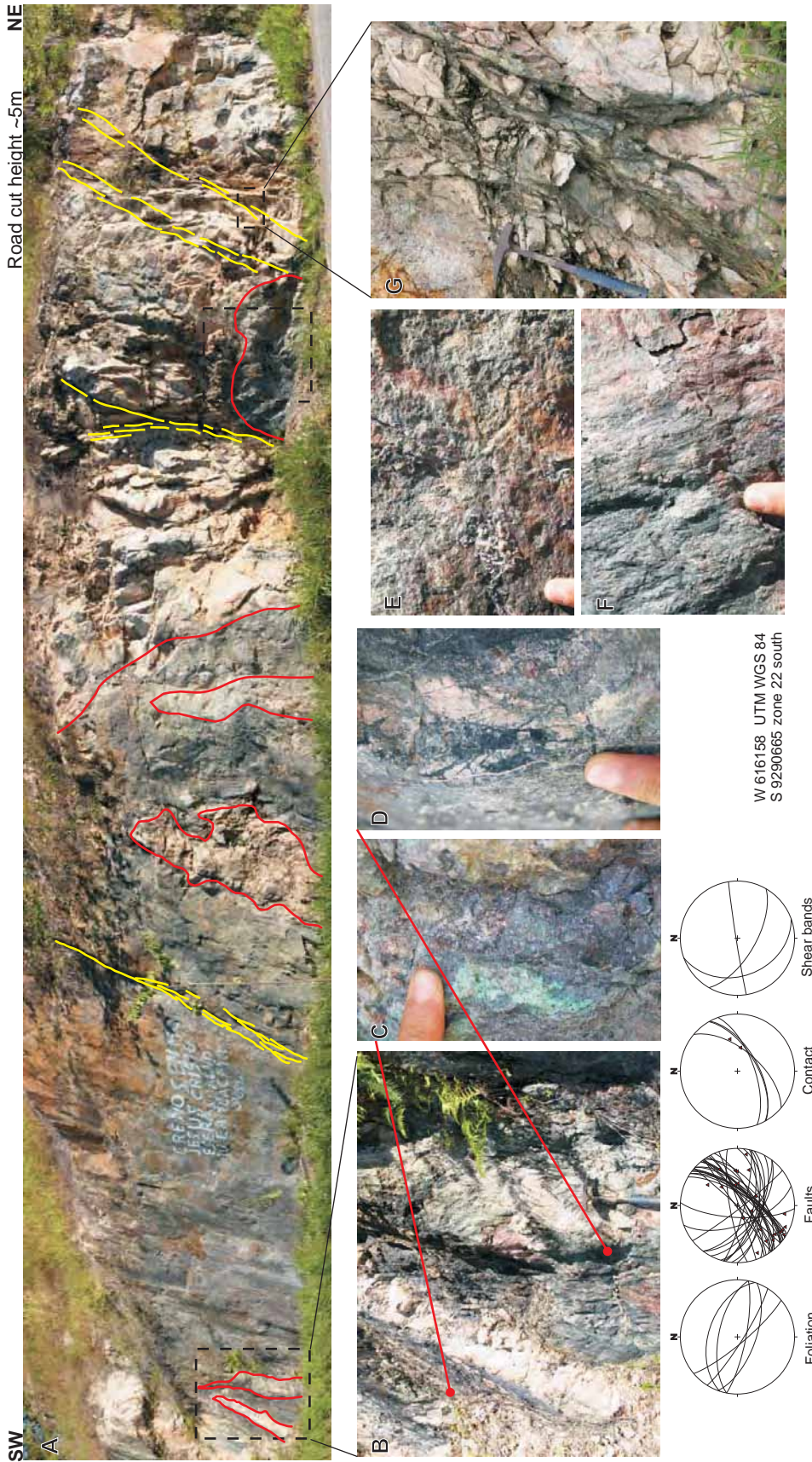


Figure 4.31 - The best example of a likely fault zone exposed in the study region. A Road-cut outcrop where the dark coloured cataclastic rocks correspond to fault related rocks domains with sub-vertical lenses of relict granitoids. B Detail showing the contact between the fault rocks (black) and a granitoid lenses (white-pinkish). C-D Close-up pictures of the fault rocks; note the cataclastic texture in both images. E-F Examples of sub-horizontal and sub-vertical fault slickenlines. G A relatively narrow (~10 cm wide) and discrete fault zone with intense comminution and chloritization in the fault core (note the green colour along the fault zone).



Figure 4.32 - Selected examples of discrete faults producing centimetre-scale displacements. **A** Quartz veinlet in amphibolite displaced by a set of parallel faults. **B** Lozenge shaped feldspar porphyroclast in granite mylonite cross cut by sinistral fault. **C-D** Sinistral fault displacing shear zones in granitoid; **E** gneissic compositional banding offset by apparently dextral fault.

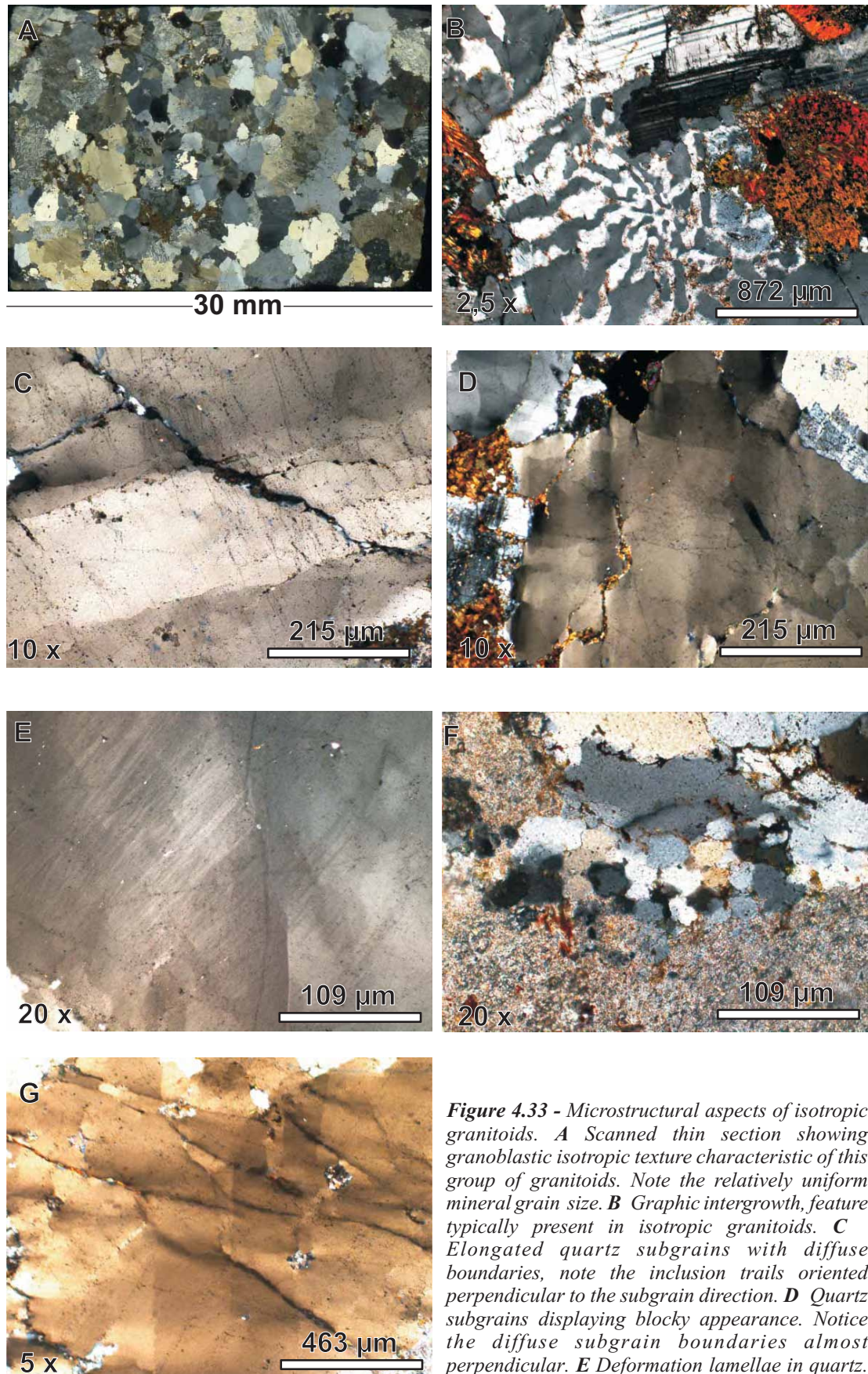


Figure 4.33 - Microstructural aspects of isotropic granitoids. *A* Scanned thin section showing granoblastic isotropic texture characteristic of this group of granitoids. Note the relatively uniform mineral grain size. *B* Graphic intergrowth, feature typically present in isotropic granitoids. *C* Elongated quartz subgrains with diffuse boundaries, note the inclusion trails oriented perpendicular to the subgrain direction. *D* Quartz subgrains displaying blocky appearance. Notice the diffuse subgrain boundaries almost perpendicular. *E* Deformation lamellae in quartz. *F* Localized recrystallized quartz; note the reduced size of the new grains compared to the surrounding grains. *G* Zones of strain accumulation (highlighted in black) in a large quartz grain.

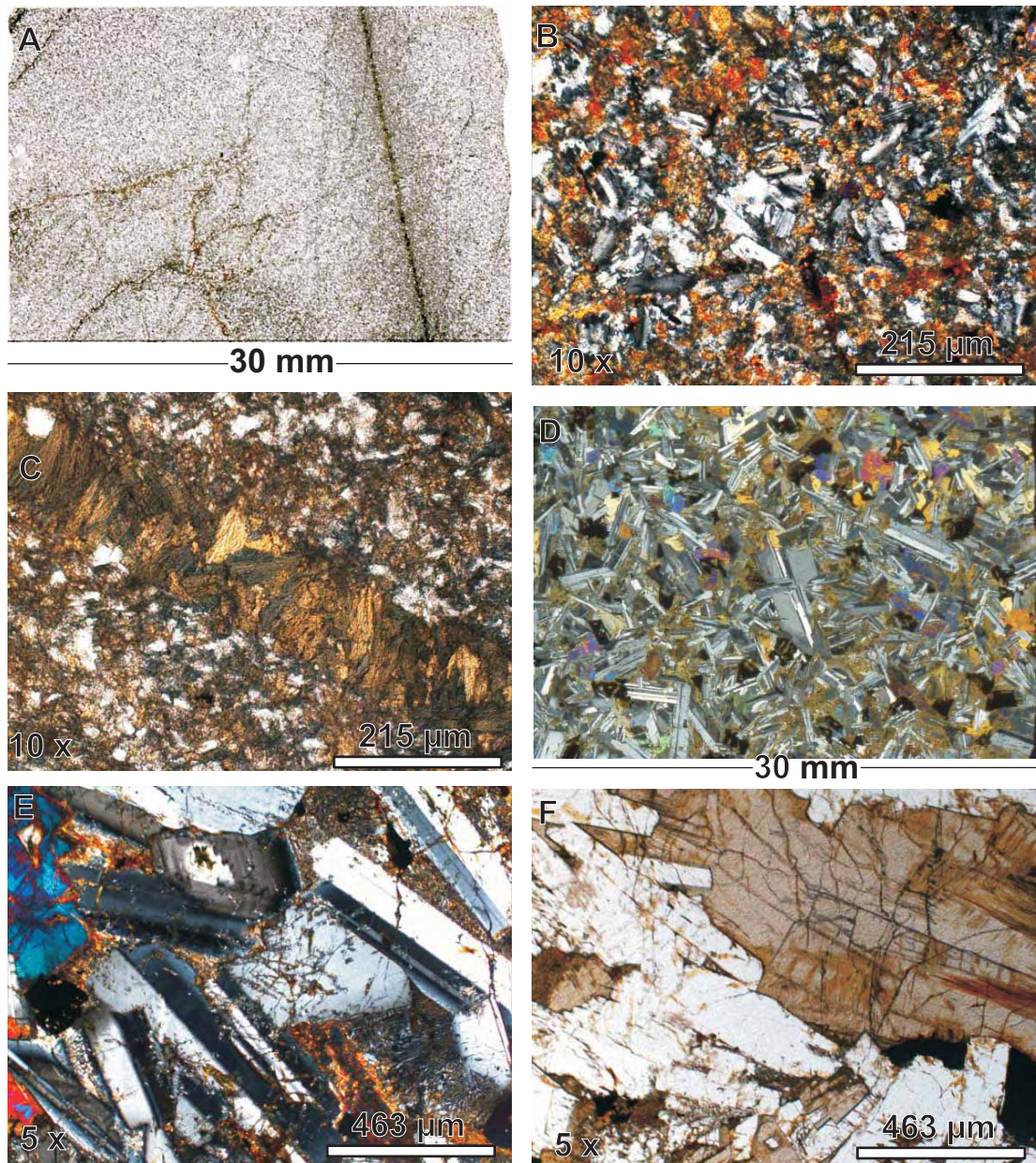


Figure 4.34 - General microstructural aspects of basalts (A,B,C) and gabbros (D,E,F). *A* Basalt scanned thin section showing the very fine texture of the rock cross cut by few chlorite veinlets. *B* Typical aspect of basalt under the microscope, displaying lozenge shaped plagioclase crystals with tapering ends. *C* Detailed image showing the geometry of the chlorite crystals forming the veinlet seen in A. Notice the crystal growth perpendicular to the veins walls. *D* Scanned thin section of gabbro exhibiting coarse, inequant granular texture, characterized by laths of plagioclase subophitically enclosed by pyroxene. *E* Feldspar typical appearance: tabular, with zoning, minor alteration and fracturing. *F* Mineral fracturing concentrated in a pyroxene crystal.

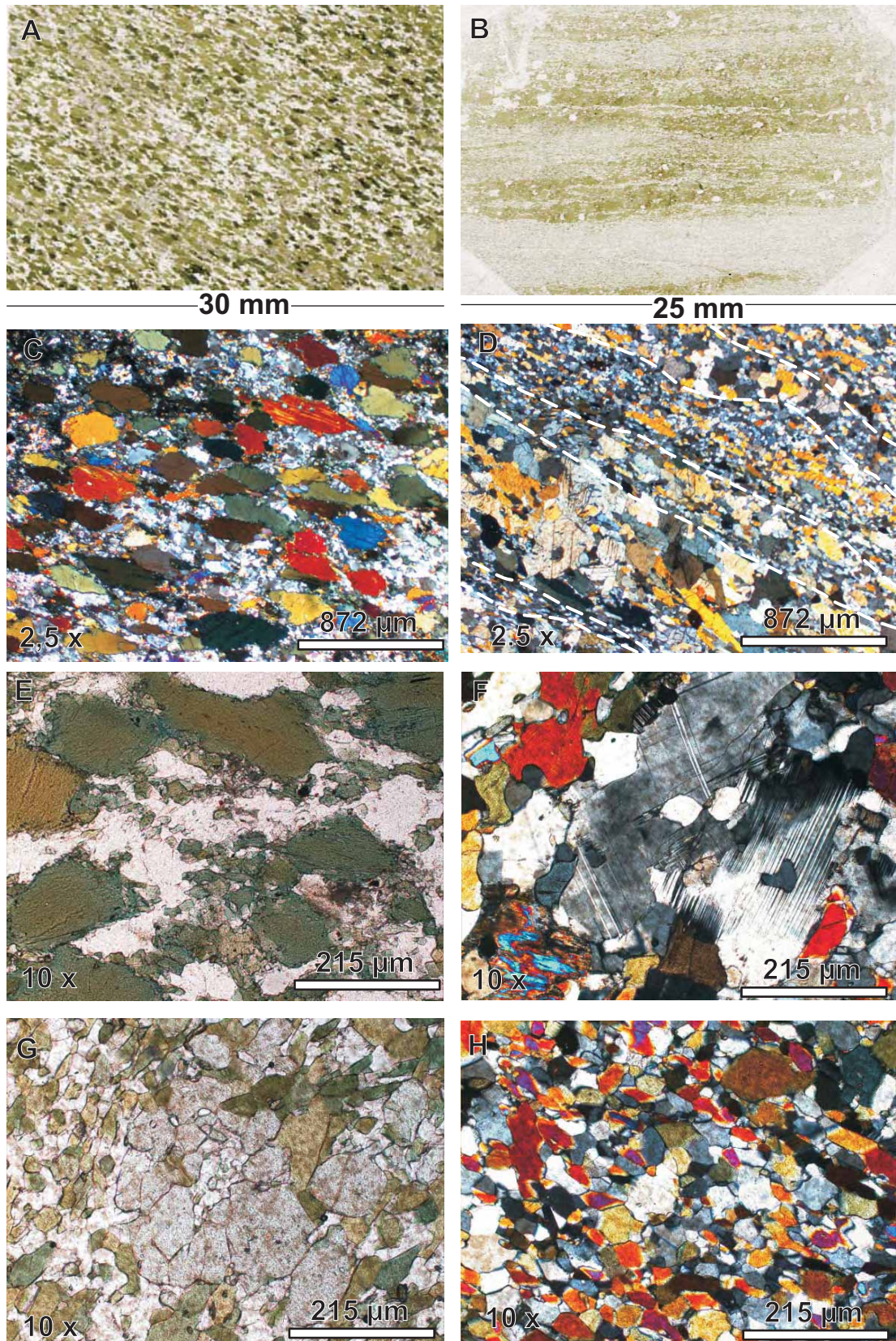


Figure 4.35 Representative examples of microstructural aspects observed in amphibolites. **A B** Thin sections displaying continuous foliation and compositional banding in amphibolites. **C** Grain shape preferred orientation of hornblende in amphibolite with continuous foliation. **D** Microphotograph of the alternating compositional banding. Note the striking difference in grain size for each layer. **E** Larger hornblende crystals surrounded by smaller grains apparently formed by mechanical fragmentation. **F** Typical appearance of feldspars in amphibolites, showing sharp and lobate boundaries, undulose extinction and stress induced glide twins; **G** Pristine pyroxene grains showing straight and sharp boundaries; **H** Polygonal mineral aggregate with straight and sharp boundaries, formed of quartz feldspar and hornblende.

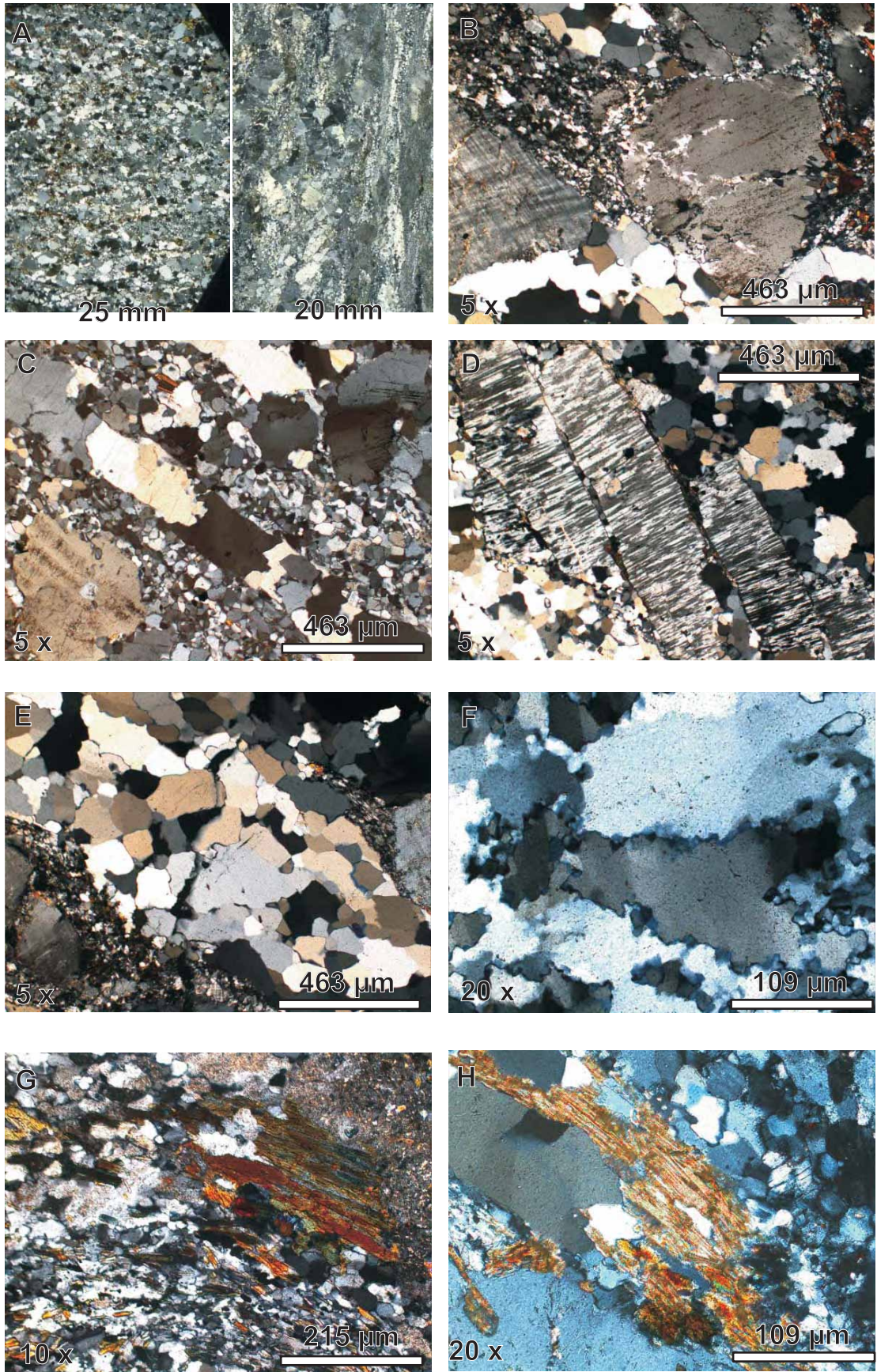


Figure 4.36 - Microstructural aspects of deformed granitoids. **A** Scanned slides showing the general appearance of a weakly (to the left) and a strongly foliated (to the right) granitoid. **B** Relict feldspar porphyroclasts and its recrystallized portions. Note thin zones of very finely recrystallized feldspar in the sub rounded grain approximately in the centre of the image. **C** Foliation defined by layered domains formed of fine recrystallized feldspar and elongated quartz crystals. **D** Feldspar forming “book shelf” feature caused by fracturing of a larger grain. The geometry of the “book shelf” array also indicates counter clock wise rotation. **E** Strain free recrystallized quartz grains composing a mosaic in a lens parallel to the foliation. Note the sharp, straight grain boundaries. **F** Partially recrystallized flattened quartz, grain boundaries are serrated and subgrains with undulose extinction of the crystals. **G** Hornblende crystal elongated parallel to the foliation and surrounded by recrystallized feldspar. Minuscule acicular fragments of hornblende are present on the bottom left of the image. **H** Elongated biotite crystals with no deformation or fracturing, the long and straight boundary of the crystal seems to control the shape of the adjacent quartz crystal.

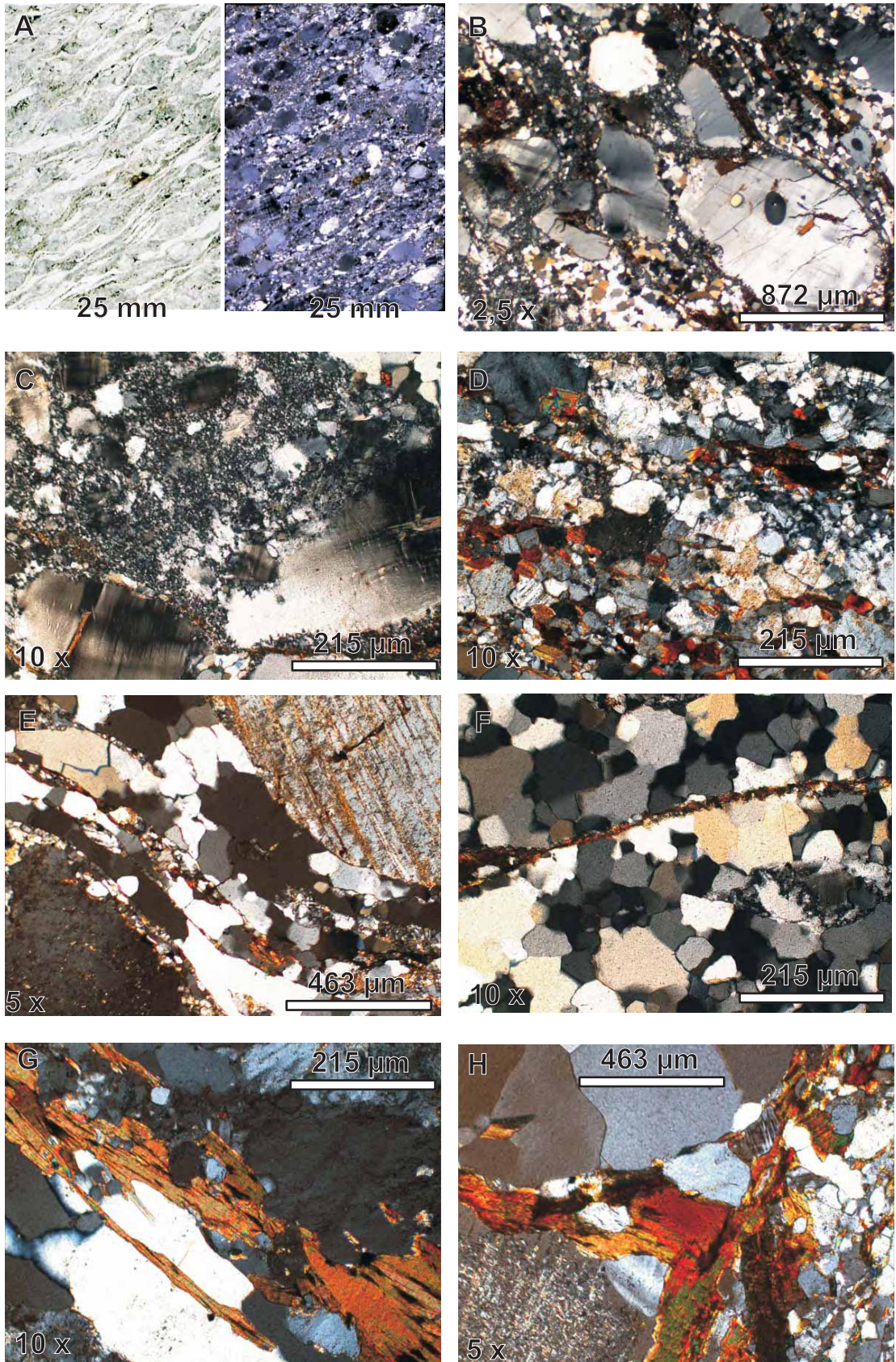


Figure 4.37- Typical microstructural aspects of mylonites. **A** Scanned slide of a mylonite sample under natural and polarized light showing the general texture of the mylonitic foliation. **B** Inequant feldspar porphyroclasts with augen and sub rounded shapes immerse in a fine grained matrix of recrystallized quartz and feldspar; note the strong undulose extinction and strain induced twins in some of the clasts. **C** feldspar porphyroclasts and very fine grained recrystallized domains, deformational features in porphyroclasts include undulose extinction, stress induced twins and perthites. The recrystallized domain is almost pure fine grained feldspar. **D** Matrix of mixed, recrystallized feldspar, quartz and biotite. **E** Quartz foliae developed between two feldspar porphyroclasts, note the slightly preferred elongation of quartz grains parallel to the foliation and a thin layer of recrystallized feldspar and biotite separating the individual folia. **F** Mosaic of recrystallized quartz displaying sharp and straight boundaries suggestive of grain boundary area reduction. **G** Fine flakes of tabular biotite showing preferred orientation parallel to the mylonitic foliation. **H** Biotite crystals forming a symmetrical “tail” of a feldspar porphyroclast.

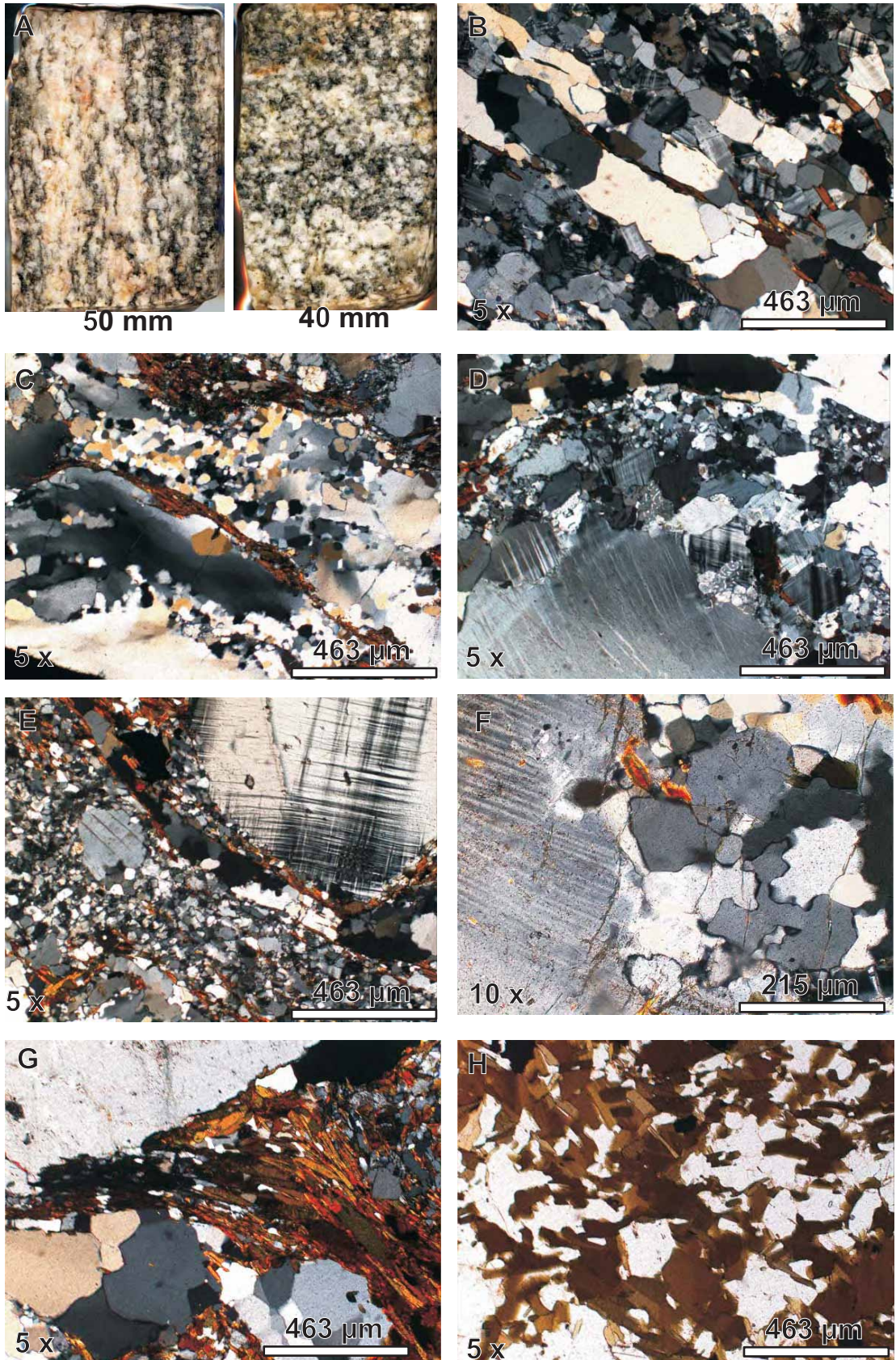


Figure 4.38 - A Scanned slides of ortho gneisses showing their distinctive compositional banding, the sample on the left displays mylonitic fabric. **B** Straight quartz ribbons composing the planar fabric together with smaller recrystallized feldspar; quartz grains are strain free with sharp and straight boundaries. **C** Microphotograph showing two flattened domains comprising totally and partially recrystallized quartz. The small recrystallized grains show gently curved or irregular boundaries while the non recrystallized domain displays strong undulose extinction and elongated subgrains. **D** A larger feldspar porphyroclast at the bottom of the image, surrounded by smaller feldspar crystals. Deformation features include: intense undulose extinction, perthites and stress induced tapering twins and myrmekites. **E** Mantled K feldspar porphyroclast with bended tapering twins, in contact with a band of smaller unimodal grains of recrystallized feldspar. **F** Boundary between a plagioclase porphyroclast and a mantle of recrystallized feldspar; note the sharp lobate grain boundary in the recrystallized feldspar crystals. **G** Cluster of tabular elongated biotite crystals defining a mica rich folia. This is the typical mode of occurrence of this mineral. **H** Anhedral to subhedral biotite grains filling interstitial spaces between quartz and feldspar crystals, the less common way of occurrence for biotite and probably a relict magmatic texture.

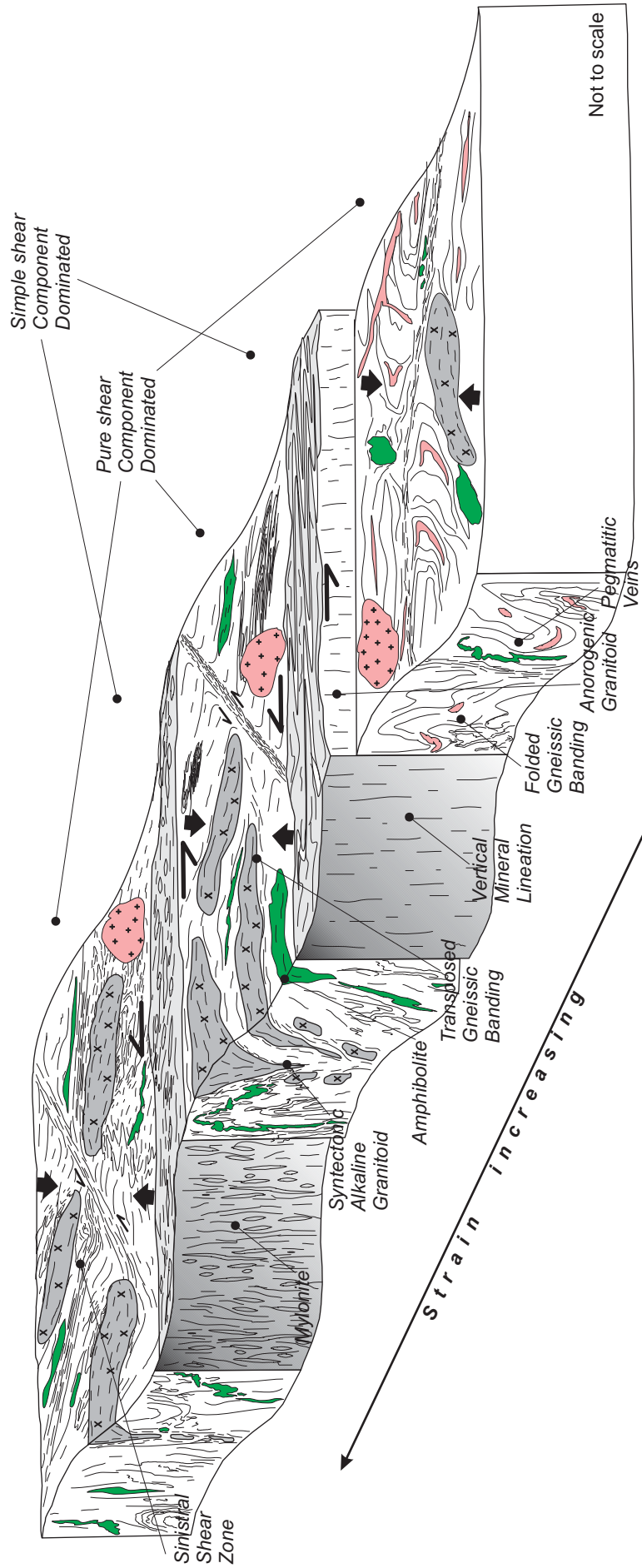


Figure 4.39 - Cartoon representing the heterogeneous sinistral transpression model applied to the study area. Portions in grey are simple shear-dominated zones and the white blocks represent pure shear-dominated regions. Bulk strain intensity increases from the bottom to the upper part of the diagram.

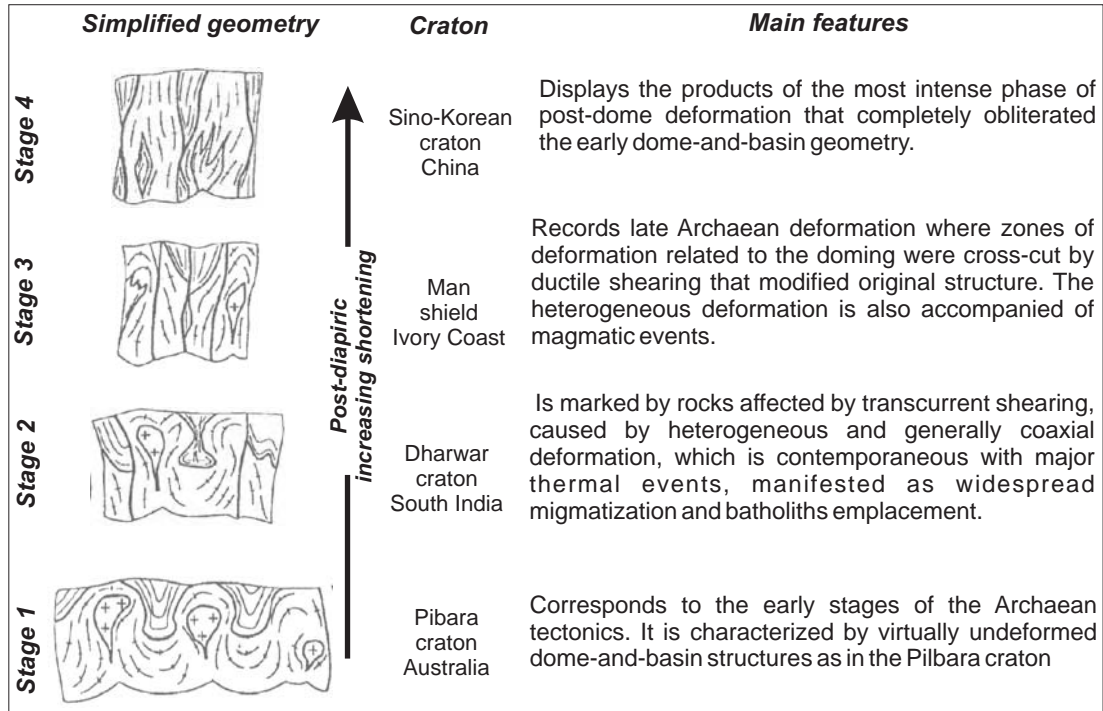


Figure 4.40 - Stages of evolution of the Archaean crust, interpreted on the basis of field evidence from China, India and Ivory Coast (modified from Choukroune et al., 1995). The diagram presents the main representative stages of deformation recognized in Archaean terranes from the least to the most deformed member.

Chapter 5

The role of tectonic structures in the development of Archaean IOCG deposits: examples from the Sossego and Sequeirinho deposits, Carajás, Brazil

5.1 Introduction

The following statement gives an insight into what drives studies into one of the most challenging research topics in economic geology: “*It is quite possible that examples of what have so far been called IOCG (iron oxide-copper-gold) deposits will ultimately prove to be products of several fundamentally different processes and/or environments*” (Williams et al. 2005). The combination of multiple IOCG deposits into a single class is complicated by their unusually wide variations in age, size, mineralogy, geochemical signatures, host rock lithologies and tectonic setting (Hitzman et al. 1992; Haynes 2000). The size and grade of the larger examples, together with their geological diversity has drawn considerable attention from exploration companies and academic researchers in the last decade (Pollard 2006). Despite the increasing number of deposits classified under this category, detailed geological studies have mainly been focused on the largest examples such as the Salobo, Ernest Henry, Olympic Dam, Candelaria-Punta del Cobre, Manto Verde and Raul-Condestable deposits.

IOCG deposits are recognized in all continents, ranging in age of formation from the Late Archaean to the Early Tertiary; a majority have an age between 2.55 and 1.5 Ga. Tectonically, they are considered to have formed in intracratonic or continental margin environments and, in many cases, show spatial and temporal controls associated with extensional tectonics (Hitzman et al. 1992). The sources of the hydrothermal mineralizing fluids are controversial, and are thought to result from either magmatic (Pollard 2001; Sillitoe 2003; Mark et al. 2005) or non-magmatic (Barton 2000; Haynes 2000) processes. In the former case, this deduction is based upon the temporal and spatial association between magmatic intrusions, the fluids that formed the Cu-Au mineralization and regional alteration patterns (Barton 1996; Oliver et al. 2004).

The Carajás Terrane region hosts Precambrian Cu-Au deposits with resources larger than 100 million tonnes of ore. Examples include the Igarapé Bahia-Alemão, Cristalino, Sossego, 118 (or 118 Target) and the world class Salobo deposits. Research on these deposits has generally focussed on petrological, metallogenic, geochemical and geochronological aspects, with structural characteristics and possible controls being very poorly documented in most cases. This chapter describes the structural framework of the Sossego and Sequeirinho mines and surroundings by investigating the structural controls on their mineralization. An improved understanding of the processes, controls and styles of the Archaean IOCG examples will help to reduce the degree of uncertainty when comparing the setting of these deposits to those formed by modern plate tectonic processes during the Phanerozoic.

5.2 Tectonic Setting

The Carajás geochronological province (Santos et al. 2000; Tassinari et al. 2004) lies in the southern portion of the Amazon Craton, part of the Brazil Central Shield (**Fig. 5.1 A**). The province is bounded to the east by the N-S-trending Neoproterozoic Araguaia Fold Belt (Moura 1993) and to the west by the Iriri-Xingu geochronological domain. To the north, it is covered by Palaeozoic and Cenozoic sediments of the Amazon Basin (Pinheiro et al. 1997a), and lies at the eastern margin of one of the globally recognized A-type granitoid provinces (Dall'Agnol et al. 2005).

Carajás represents an important metallogenic province with several base-metal deposits and it also contains some of the oldest and best preserved sequences of Archaean-Proterozoic rocks in the craton (Galarza et al. 2007).

5.3 Regional Geology of the Carajás Terrane

5.3.1 Lithostratigraphy

The Carajás geochronological province was formed and stabilized during the Archaean and was later affected by extensive Palaeoproterozoic magmatism characterized by the intrusion of anorogenic granitoids, together with mafic and felsic dykes (Pidgeon et al. 2000). It is divided into two major tectonic domains (**Fig. 5.1 B**): the *Rio Maria Granite–Greenstone Terrane* (3.05 to 2.86 Ga) to the south, and the *Carajás Terrane* (2.76 to 2.55 Ga) to the north (DOCEGEO 1988; Machado

et al. 1991; Macambira et al. 1995; Dall'Agnol et al. 1997). Both domains have distinctive lithological, tectonic, stratigraphic and geochronological characteristics and yet their boundary remains rather poorly defined (Galarza et al. 2007). It should be noted that the Carajás Terrane is also variously referred to in the literature as the 'Carajás Ridge' 'Carajás Mineral Province' and 'Itacaiúnas Belt'.

The oldest rocks in the Carajás geochronological province are located in the Rio Maria Granite Greenstone Terrane (Macambira et al. 1995) and include: the Arco Verde Tonalite, the Caracol Tonalite, the Rio Maria Granodiorite, the Mogno Trondhjemite, the Xinguara and Mata Surrão Granites and a series of greenstone-belt sequences (see **Fig. 5.1 B**).

The Carajás Terrane located to the north (**Fig. 5.2**) comprises two main Archaean and Proterozoic domains separated according to their tectonostratigraphic characteristics and ages (Araújo et al. 1991; Pinheiro 1997). The older *Basement Assemblage* (ca 3.0-2.86 Ga) contains orthogneisses of the Pium Complex that were originally intruded into tonalitic gneisses, granodiorites and migmatites of the Xingu Complex; all rocks are granulite–upper amphibolite facies (see **Table 5.1 for ages**). Sub-vertical, WNW-ESE-trending mylonitic fabrics were formed coeval with the development of the broad Itacaiúnas Shear Belt and experienced several episodes of reactivation (Pinheiro et al. 1997b; Pinheiro et al. 1997a; Holdsworth et al. 2000).

Lower grade supracrustal volcano-sedimentary sequences make up the younger *Cover Assemblage* (Pinheiro 1997) that in this study is considered to include the Grão-Pará, Igarapé Salobo and Igarapé Pojuca Groups given their comparable ages (ca 2.7 Ga; see **Table 5.1**). These units show a range of deformation states and metamorphic grades from virtually undeformed greenschist facies in the region adjacent to the Carajás Fault, to intensely sheared, amphibolite-granulite facies in the

Cinzento Strike-Slip System (DOCEGEO 1988; Lindenmayer et al. 1991; Pinheiro et al. 1997a). The Cover Assemblage is overlain by a clastic sequence of shallow-water marine to fluvial deposits of the Águas Claras Formation. Dating of a gabbroic sill (ca 2.65 Ga) constrains the minimum age of the formation (see **Table 5.1**). (Pinheiro et al. 1997a; Holdsworth et al. 2000) considered the Águas Claras Formation as part of the *Cover Assemblage* but in this thesis, the formation is considered as an independent unit for not displaying evidence of metamorphism.

Syn-tectonic Archaean, alkaline granitoids and diorites of the Plaque Suite together with the Estrela, Planalto and Serra do Rabo granites (on average ca 2.75 Ga) are intruded into both Basement and Cover assemblages. These units are typically elongate parallel to the strike of the regional WNW-ESE foliation (Holdsworth et al. 2000; Barbosa et al. 2001; Sardinha et al. 2006).

A much younger suite of Paleoproterozoic plutons (ca 1.88 Ga) intrude most of the rocks of basement and low-grade volcano-sedimentary sequences in the Carajás Terrane, including the Águas Clara Formation (e.g. Cigano, Carajás Central and Rio Branco granites) area and Rio Maria granite-greenstone Terrane (e.g. Musa, Jamon and Banach granites) (Machado et al. 1991; Dall'Agnol et al. 1999). They are generally non-foliated, monzogarnitic-syenogranitic, coarse to medium grained, massive, and highly discordant showing sharp contacts with, and angular inclusions of the Archaean country rocks (Ramo et al. 2002; Dall'Agnol et al. 2005).

5.3.2 Structure

The Carajás and Cinzento strike-slip systems (**Fig. 5.2**) are the most prominent structures within the Carajás Terrane. These fault systems display at least three episodes of brittle-ductile strike-slip reactivation at low metamorphic grades, after the development of the precursor regional amphibolites facies ductile shear zone. They form a generally E-W trending set of discontinuous, sigmoidal, anastomosing lineaments approximately 200 km long with a collective maximum width of 80 km. The geometry of these fault zones appears to be strongly controlled by the orientation of earlier shear zone fabrics in the basement. A later set of N-S to NNE-SSW fault lineaments cross-cut the main sigmoidal structures (Pinheiro et al. 1997a; Holdsworth et al. 2000). The complex tectonic history of the Carajás Terrane, dominated by transpressional and transtensional events, is summarized in **Table 5.2**.

5.3.3 Metamorphism

High grade (granulite-upper amphibolite facies) metamorphic rocks are present in the basement units, the Pium and Xingu complexes. The supracrustal sequences of the Cover Assemblage record a range of metamorphic grades, from virtually unmetamorphosed through to greenschist-amphibolite facies. Collectively, these grades imply that regional metamorphic temperatures rarely exceeded 700°C (Lindenmayer 1990).

Hydrothermal submarine metamorphism has been documented in some parts of the Cover Assemblage (Grão Pará and Igarapé Bahia Groups) prior to the regional

metamorphic events. This produced variable amounts of decalcified plagioclase, epidote, chlorite, tremolite-actinolite, white mica, quartz and carbonate (Villas et al. 2001).

The Grão-Pará and Igarapé Salobo Groups are affected by low grade greenschist and amphibolite-granulite facies regional metamorphism respectively (DOCEGEO 1988; Olszewski et al. 1989).

Two specific styles of contact metamorphism related to the intrusion of younger granite plutons overprinting the submarine and regional metamorphic assemblages have been documented: (a) anthophyllite-cordierite-rich rocks developed in the metavolcanics of the Igarapé Pojuca Group (Winter 1995); and (b) pyroxene-hornfels and albite-hornblende-hornfels facies rocks developed at temperatures of 600-650 °C in the thermal aureole of the Estrela Granite (Barros 1997).

5.4 The Sossego Deposit

The southern boundary of the Carajás Terrane, hosts three major Precambrian IOCG deposits: Cristalino, Sossego/Sequeirinho and 118 or Target 118 shown in **Fig. 5.2**. Sossego is hosted in the granite-gneissic basement, while the others are hosted in the volcano-sedimentary rocks of the Cover Assemblage. Thus, the Sossego deposit gives an opportunity to study and characterize the mineralization style and controls in basement rocks.

The following sections include a summary of the previous studies carried out at Sossego, comprising: geology, geochronology, hydrothermal alteration and

temperature & sources of the fluids. This information is then followed by a new study of the macro- and micro-structural aspects of the Sossego and Sequeirinho orebodies.

5.4.1 History

The Sossego Cu-Au deposit is located in the area known as *Serra do Rabo* in the south of the Carajás region (see **Fig. 5.1** and **Fig. 5.2**). In 1984, during the gold rush decade, gold was initially discovered in streams and later in Sossego Hill by prospectors sampling alluvium and oxidized portions of the deposit in 1990. The area was acquired by MSS (*Mineração Serra do Sossego*) in 1998, who initiated studies to determine and evaluate the size and grade of the deposit. In 2002, the first Cu mine opened in Carajás, with the development the nearby Sequeirinho orebody, with total reserves of 245 Mt with an average grade 1.1% Cu and 0.28 g/t Au (Lancaster et al. 2000).

5.4.2 Geology

The Sossego deposit comprises two main orebodies, Sequeirinho and Sossego that are extended and linked laterally by minor orebodies ‘Pista’, ‘Baiano’ and ‘Curral’ (**Fig. 5.3**). The Sequeirinho and Sossego bodies hold 85% and 15% of the bulk copper reserves, respectively (Villas et al. 2005).

The mineralized bodies are located close to the southern contact zone between the volcano-sedimentary rocks of the Grão-Pará Group and the tonalitic to

trondhjemite gneisses and migmatites of the Xingu Complex (Monteiro et al. 2005; Moraes 2005). Detailed mapping shows that the deposit is located 1.6 km south of the inferred contact, enclosed completely within rocks of the granitic basement terrain. (Sardinha et al. 2004) suggest that the granitic gneisses and syn-tectonic granitoids in the Serra do Rabo area and around Canaã Village represent independent igneous bodies with intrusion ages ranging between 2.9 and 2.7 Ga.

In detail, the host rocks of the deposit include: various granites *sensu lato* (**Fig. 5.4 A, B, C, D and E**), granophyres (**Fig. 5.4 E**), gabbros (**Fig. 5.4 F and G**), felsic and mafic volcanics (**Fig. 5.4 L, M, N, O**), hydrothermally altered rocks (**Fig. 5.4 H and J**), breccias (**Fig. 5.4 I**) and dykes (**Fig. 5.4 N and O**), with varying degrees and styles of deformation and hydrothermal alteration (Lancaster et al. 2000; Neves 2007).

The granites are mostly quartz-bearing and dioritic-granodioritic comprising grey, medium to fine grained rocks (**Fig. 5.4 C, D and E**). They are typically altered with an isotropic or mylonitic fabric with subordinate porphyritic varieties (e.g. **Fig. 5.4 A and B**). Mineralogically they comprise albite, quartz, k-feldspar, hastingsite, actinolite, with accessory epidote, chlorite, allanite and hematite (Villas et al. 2005).

The granophyric granite or granophyre is dark grey, with a fine-grained quartzofeldspathic groundmass containing blue quartz, microcline and plagioclase phenocrysts (e.g. **Fig. 5.4 E and O**). Micrographic intergrowths of K-feldspar and quartz are characteristic (Carvalho et al. 2005; Monteiro et al. 2008).

Felsic metavolcanic rocks (e.g. **Fig. 5.4 L and M**) are grey, fine grained, dacitic and carry feldspar phenocrysts set in a microcrystalline matrix of quartz and albite. They are often mylonitised and enclose green metamorphosed ultramafic

lenses made of serpentine, olivine, disseminated chromite/magnetite and talc (Monteiro et al. 2008).

The early granites are cross-cut by two distinct intrusive sequences (Carvalho et al. 2005; Villas et al. 2005): (1) early altered, medium-coarse grained gabbroic bodies displaying sub-ophitic textures, comprising plagioclase, pyroxene and hornblende (e.g. **Fig. 5.4 F** and **G**); and (2) late, brown rhyolite/dacite dykes with a marked porphyritic texture characterized by phenocrysts of plagioclase set in a fine matrix of K-feldspar and quartz (e.g. **Fig. 5.4 O**).

Hydrothermalites include: (1) metasomatic magnetite bearing rocks (**Fig. 5.5 A**) with coarse grained magnetite (>50%) and subordinate chalcopyrite-epidote-actinolite-apatite-albite-chlorite; and (2) massive ore bodies (**Fig. 5.5 C**) consisting of sulphides (chalcopyrite>>>siegenite+pyrite), magnetite, (F-Cl) apatite, chlorite, actinolite-Cl-K-Fe-hastingsite, Cl-biotite and quartz (Neves 2007).

The Cu mineralization in the Sossego and Sequeirinho orebodies is represented by breccias and stockwork domains. The breccias are texturally characterized by sub-rounded (Sequeirinho, **Fig. 5.5 B** and **C**) to angular (Sossego **Fig. 5.4 I** and **Fig. 5.5 F, G**) fragments of altered wall-rock. Clasts size varies from a few millimetres to 10 centimetres. The matrix is composed of chalcopyrite-magnetite-actinolite-epidote-chlorite-quartz in the Sequeirinho body. In the Sossego body an early magnetite-actinolite-calcite-apatite assemblage is post-dated by a later pyrite-chalcopyrite-chlorite-quartz-epidote-muscovite assemblage (Carvalho et al. 2005; Monteiro et al. 2005; Villas et al. 2005). The stockwork domains comprise millimetre to centimetre wide veins containing sulphide (+chalcopyrite and \pm pyrite), actinolite, magnetite and calcite (e.g. **Fig. 5.5 D, E** and **G**).

5.4.3 Hydrothermal Alteration

Host rocks and mineralized bodies display evidence of varied and locally intense hydrothermal activity characterized by at least six well-developed hydrothermal mineral assemblages within and surrounding the deposit (Villas et al. 2005; Monteiro et al. 2008). Hydrothermal episodes are mainly represented by sodic, sodic-calcic, potassic and mineralizing assemblages forming zones of pervasive alteration and/or vein stockwork arrays. **Table 5.3** summarizes mineral parageneses and occurrence of the main types of alteration for the Sequeirinho-Pista-Baiano and Sossego-Curral orebodies from (Carvalho et al. 2005; Monteiro et al. 2005; Villas et al. 2005; Monteiro et al. 2008).

5.4.4 Fluids Sources and Temperature

Previous studies of the hydrothermal fluids in the Sossego deposit support the hypothesis that deeply-sourced mantle/metamorphic/magmatic-derived fluids were mixed with surface meteoric water or basinal brines e.g. (Marschik et al. 2003a). (Chiaradia et al. 2006) determined elemental ratios for Cl/Br (800–1,500), $\delta^{37}\text{Cl}$ isotope (+0.2 to +2.1‰) and Sr values that indicate mixing of a mantle-derived magmatic fluid with basinal brines. Positive $\delta^{37}\text{Cl}$ values may result from a higher mantle chlorine contribution or from fractionation during the hydrothermal process, before mixing with the basinal brines. (Neves 2007) used $\delta^{13}\text{C}_{\text{PDB}}$ values (-6,65 to -4,66) for calcite to indicate a homogeneous, probably mantle-derived source. Values

of $\delta^{18}\text{O}_{\text{fluid}}$ from calcite (-7.24 to -5.17‰ and +1.14‰ to +3.21‰ at 150° and 350°C) indicate active participation of meteoric water in the Sossego hydrothermal system. However, higher values (+9.79‰ at 250°C and +12.77‰ at 350°C) also suggest a magmatic or metamorphic water signature. (Monteiro et al. 2008) propose that the massive magnetite bodies were formed by $\delta^{18}\text{O}$ which was enriched ($6.9\pm 0.9\%$) from deep-seated, formational/metamorphic fluids, possibly with a magmatic contribution. Sodic-calcic ($6.0\pm 0.8\%$, at $500\pm 25^\circ\text{C}$), and regional sodic alteration ($3.6\pm 0.6\%$, at $450\pm 50^\circ\text{C}$) reflect decreasing $\delta^{18}\text{O}_{\text{H}_2\text{O}}$ values, which suggests mixing with ^{18}O depleted, externally derived meteoric or basinal fluids.

5.4.5 Geochronology

(Marschik et al. 2003b) obtained a minimum alteration age (2.2-2.3 Ga) for the hydrothermal system using $^{40}\text{Ar}/^{39}\text{Ar}$ dating of amphibole from the ore. Neves (Neves) analyzed Pb-Pb in chalcopyrite and Sm-Nd (whole-rock) from the main mineralized zones to obtain ages of $2,530\pm 25$, $2,608\pm 25$ and $2,578\pm 29$ (Sm-Nd) Ma in Sequeirinho; and 1.585 ± 28 Ma (Pb-Pb) in Sossego. The Archaean ages of 2.6-2.5 Ga were interpreted as the time when the mineralization occurred, and is in good agreement with the timing of major regional tectonic events dated at 2.6 Ga (Machado et al. 1991; Holdsworth et al. 2000). The Mesoproterozoic age of 1.5 Ga was not considered to be geologically significant for the deposit, although it could be related to the granitic intrusion event of 1.5 Ga recognized in the Gameleira deposit (deposit location in **Fig. 5.2**) (Lindenmayer et al. 2001).

5.5 Field Logistics and Methods

The field data presented in this chapter comprise geological and structural observations from both outcrops and drill-cores, collected during 140 days of field work. The studied localities include the Sossego and Sequeirinho mine pits and a nearby relatively small outcrop of isotropic granite (see **Fig. 5.6**). The areas surrounding the mines are covered by vegetation developed in soil cover, 13 to 30 m thick. The studied mine benches form a series of vertical sections with excellent exposure of rocks and structures. However, only the benches with clear access and free of debris and landslide risk, were studied. The cores selected for study were the most continuous, complete and displaying intact orientation marks.

The issues that potentially affected the data collection in the mines include: (a) restricted access to some of the mine benches; and (b) difficulty in observing the rocks and structures in detail where the benches were covered by a consolidated layer of dust or where there was the risk of rock fall. Additionally, unclear cross-cutting relations and sense of kinematics for faults, represent major problems in constraining fault temporal relations.

Four main data collection methods were used during the present study: (1) lineament analysis; (2) field data acquisition; (3) breccia clast analysis; and (4) microstructural analysis.

An interpretation and analysis of lineaments using a Digital Elevation Model (DEM) and map of magnetic field anomalies was used to define the large-scale characteristics of the structural framework. Airborne magnetic surveys were interpreted at two scales: 1:300,000 for survey 1 (**Fig. 5.7**; 2,653 km²) and 1:35,000 for survey 2 (**Fig. 5.8**; 52 km²). Both surveys consist of N-S flight lines with a

spacing and frequency of sampling at 1km/70m and 250m/1m, respectively. Magnetic measurements were taken in a time-domain with an accuracy of 1nT. The DEM with a 90 m resolution was interpreted at the same scale as survey 1. Lineaments were picked and analysed in a GIS environment using ArcMap® version 9.1.

Structural field mapping was carried out along the mine benches using the digital mapping system developed at Durham University by the Reactivation Research Group known as GAVA - *Geospatial Acquisition Visualisation and Analysis* (McCaffrey et al. 2005; Wilson et al. 2005). Structural data locations and attributes were recorded using a mobile GIS platform (see (Edmondo 2002) based on a system using a DGPS and Tablet PC as described by (Clegg et al. 2006). GPS positions for the structural measurements were post-processed enabling a sub-metre spatial accuracy for the mapped elements. Photographic sections of the mapped benches were compiled by merging a sequence of photos covering the studied interval into a single scene onto which structural observations were then sketched and annotated. The number and total length of sections per mine were: Sossego= 15 (998m), Sequeirinho= 29 (1160m).

Five oriented drill cores were examined to constrain the three dimensional characteristics of structures in the Sossego-Sequeirinho orebodies. Structural orientation data were recorded in 683 metres of core logs. Tectonic fabrics and related hydrothermal features were catalogued using close-up photographs.

Optical microstructural analyses were carried out using 49 thin sections of samples taken from mine benches and drill-cores and were interpreted using standard approaches and techniques (Hirth et al. 1992; Snoke et al. 1998; Tullis 2002;

Passchier et al. 2005). These data were used to characterize the dominant deformation mechanisms.

Clasts size and textural analysis of breccias were carried out using the methods and procedures presented by various authors (Jebrak 1997; Heilbronner et al. 2006; Mort et al. 2008). Nine breccia samples, including barren and mineralized types, were photographed at a high resolution. Clasts were first manually digitized and then imported into the UTHSCSA Image Tool software where particle geometrical properties were computed. These data were finally plotted as X-Y diagrams for comparison and analysis

5.6 Lineament Analysis

The regional structural framework for the Sossego-Sequeirinho Deposit and its surroundings was developed by analysis of topographic and magnetic lineaments at 1:170,000 (**Fig. 5.7**) as outlined below:

- E-W-trending long (7-22 km) and short (3 km) traces correspond to the most evident magnetic anomalies in the area; these are hardly represented on the DEM at this scale. The longer traces seem to coincide to the large iron orebodies present in the *Serra do Rabo* region and adjacent to the Carajás Fault. The shorter lineaments are mainly located in the central and southern portions of the granitic basement terrain.
- NE-SW lineaments, formed by longer topographic and some shorter magnetic lineaments, stretch across the centre of the area. These correspond

to low magnetic value zones that seem to cross-cut E-W lineaments. Notably, the Sossego and Sequeirinho orebodies sit into one of these traces.

- NW-SE lineaments were picked on both the DEM and magnetic surveys. The longest observed magnetic anomaly correlates with a deep valley following the surface trace of the Carajás Fault. This lineament set appears to cross-cut the other sets.

A finer scale (1:35,000), magnetic survey 2 (**Fig. 5.8**) displays pronounced 0.5 to 4 km long anomalies while on the DEM, topographic lineaments are poorly visualized. The Sossego and Sequeirinho deposits show a close spatial proximity to a prominent 3.5 km long, WNW-ESE anomaly (white-gray shades). In this survey, two sets of lineaments were visually identified:

- WNW-ESE lineaments are characterized by relatively short and slightly wavy segments that show local deflection to the E-W. These lineaments configure an important 9 km long structural corridor that hosts the main anomaly where the deposits are located. Additionally, the Sossego orebody lies close to the intersection of the E-W and NE-SW sets.
- NE-SW lineaments are relatively straight and long segments that define a 3km wide zone that extends across the area, deflecting the main WNW-ESE anomaly towards the SW in an apparently left-lateral fashion. The Sequeirinho orebody lies within this deflected anomaly that marks the intersection between the WNW-ESE and NE-SW lineaments.

Analysis of the geological contacts in the area of the deposits indicates that the lithological distribution is controlled by the major tectonic structures (see geological map from MSS/VALE and the traced geological boundaries in **Fig. 5.9**). Geometrically, contacts form WNW-ESE straight lines that separate elongated, sub-parallel domains of granitic, gabbroic and metavolcanic rocks. NE-SW traces intercept and displace WNW-ESE contacts causing apparently sinistral offsets of 100m up to 850m towards the SW. The Sequeirinho corridor (see **Fig. 5.9 C**) is an important feature in the area. It is 130m wide and accommodates seemingly left-lateral offsets of approximately 800m.

5.6.1 Regional Structural Framework – summary and implications of lineament analysis

In the region of the Sossego-Sequeirinho deposits, four sets of lineaments have been obtained from interpretations of DEM, magnetic surveys and geological maps. Short *E-W* lineaments seem to correspond to the previously described early ductile fabric in the granite-gneiss basement (Pinheiro 1997; Holdsworth et al. 2000). The major lineaments in this orientation correspond to the southern contact separating basement from the Grão-Para Group in the Rabo Ridge area, where iron ore deposits are located (see **Fig. 5.2** and **Fig. 5.7**). The contact may be influenced by the earlier *E-W* ductile fabric and this tectonic discontinuity probably results from the inversion stage of the Grão-Para basin when significant vertical displacements were accommodated by reverse faults across much of the area.

WNW-ESE lineaments are interpreted to represent subtle directional variations of the early *E-W* ductile fabric. These two sets are found in most of the

granitic rocks in the area older than 1.8 Ga., as widespread foliation or locally as narrow ductile shear zones. They are normally associated with minor, well defined magnetic anomalies distinct from those generated by iron-ore bodies.

NW-SE lineaments detected in the magnetic survey at 1:170,000 scale correspond to the Carajás Fault. This is a well-defined structure that has been described in several of the previous studies of the area e.g. (Pinheiro et al. 1997a; Holdsworth et al. 2000; Rosière et al. 2006). The fault trace appears to be closely associated with larger E-W lineaments, implying that the fault perhaps nucleated from a major E-W discontinuity in a latter stage of tectonic inversion.

NE-SW lineaments are expressed in the magnetic surveys and geological maps. They define linear features that intercept and deflect the E-W and WNW-ESE lineaments towards SW suggesting a regional sinistral kinematic framework. At the deposit scale, NE-SW lineaments played an important role in controlling the geometry of the Sequeirinho orebody, which is aligned with one of these regional linear features (see the association between lineament and mineralization in **Fig. 5.8 B** and **Fig. 5.9 C**).

The regional setting of the Sossego-Sequeirinho deposits seems to be similar to other described examples of mineral deposits hosted along regional scale lineaments, on lineament intersections or associated with linear magnetic anomalies (Odriscoll 1986; Kutina 1999; Hildenbrand et al. 2000; Reynolds 2000; Gay 2003). It further illustrates that regional scale lineaments can be used to identify high permeability conduits for pulsed discharges of crustal metamorphic or magmatic hydrothermal fluids as proposed by (Kerrick 1986b; Kerrich 1986a) and many others. This has important implications for present and future mineral exploration in the Amazon Craton, by highlighting areas of potential mineral occurrence in regions

that are covered by thick soil cover and dense vegetation. In the future, examining regional scale lineaments identified on remote sensing and aerogeophysics products can aid preliminary exploration surveys.

5.7 Structures and Mineralization Controls

This section presents the results of geological and structural observations from the Sossego and Sequeirinho mines, and some of their drill cores. The description of the results starts from the general (at mine bench scale) and ends with the more detailed aspects (at drill core scale).

5.7.1 Sossego orebody

The Sossego orebody is hosted in syn-tectonic tonalite and granophyre granitoids (see geological map in **Fig. 5.10**). These are fine-to-medium grained, generally isotropic and locally foliated showing varied degrees of hydrothermal alteration (e.g. **Fig. 5.38 D and E**). Schematically, the orebody comprises a concentric, sub-circular sequence of approximately 500m in diameter. The inner part of the sequence includes a sub-vertical breccia body that holds the bulk of the ore. The breccia shows multi-sized, mainly angular and subordinate sub-rounded fragments set in a matrix of sulphide and pulverized rock. The breccia body is surrounded by a stockwork domain, characterized by a multi-directional network of sub-vertical to gentle dipping sulphide veins, which forms the disseminated mineralization.

5.7.1.1 Foliation

Foliation development is heterogeneous in the granitic exposures of the mine and spatially associated with shear zones. Additionally, detailed observations from the drill cores FG-9 and FG-14 (see their location in **Fig. 5.10**) allowed the foliation to be classed as continuous, smooth, spaced and parallel according to Paschier & Trouw, 2005 (see foliation photos in **Fig. 5.12 A** and **Fig. 5.39 A, C and D**). Structural attitudes of foliation recorded within the mine (see map in **Fig. 5.10**), display a slightly heterogeneous pattern on stereonet (**Fig. 5.11 A**), with a strong 115°-120° striking trend dipping on average 55° to the NNE, and a subordinate trend oriented 090°-130° with dips of 78° to the S-SW.

The attitude of the foliation on drill-cores appears to agree with those observed in the mine. The core *FG-9* (**Fig. 5.28**) cross-cuts mainly biotite schists, which show a prominent NE-SW foliation dipping moderately-to-steeply to the NE or steeply SW (**Fig. 5.29 A**). Foliation attitude is relatively constant although strike gradually swings clockwise vertically from 120° to 140° down the logged interval. On the other hand, core *FG-14* (**Fig. 5.30**) in granitic rocks, shows foliation with strong variations in strikes and dips along the core. The stereonet for foliation (**Fig. 5.31 A**) shows a diffuse pattern, with a subtle preferred orientation with a NW-SE trend and moderate dips to the NE and SW. Mineral lineations were not observed in the foliated rocks in either the mine or drill-cores. Collectively, the rocks in the Sossego orebody show heterogeneous foliation, associated with shear zones. Foliation trends dominantly NW-SE, dipping moderately to the NE. The directional

variation of the foliation can be possibly explained by: (1) its anastomosing nature; and/or (2) the occurrence of multimodal shear zones.

5.7.1.2 Ductile Shear Zones

These structures were observed mainly in the stockwork domain of the mine, being absent in the central breccia domain (see **Fig. 5.10**). Shear zones are, on average, 30-50cm wide, not often exceeding 1m and show sharp contacts with the surrounding rocks (see field examples in **Fig. 5.12**). These zones are marked by a strong foliation often defined by alternating felsic and mafic millimetre wide bands occasionally enveloping porphyroclasts in the granite (**Fig. 5.12 A**); and homogeneous, gently wavy, darker and very thin bands for the zones within the granophyre (**Fig. 5.12 B**). Sulphides are often found in the ductile shear zones, disseminated in the foliation or as small pods formed of sulphide+quartz±carbonate (see detail in **Fig. 5.12 B**). Further, drill-core observations in *FG-9* and *FG-14* showed that in addition to the wider examples (e.g. **Fig. 5.12** and **Fig. 5.39 A, C, D**), shear zones also occur as widespread, few centimetre-wide structures (e.g. **Fig. 5.42 A, B D, F**) marked by sharp boundaries and a prominent planar fabric.

Structural attitudes of shear zones are fairly heterogeneous (see stereonet in **Fig. 5.11 B**). However, density contours on stereonet indicate a dominance of NW-SE trends with moderate to steep dips to the NE. Other statistically relevant trends are defined by: NE-SW, NNW and E-W strikes, with moderate to steep dips (**Fig.**

5.11 B). Shear zones observed in drill-cores show consistent orientations in core *FG-9* (**Fig. 5.28**), trending: (1) NW-SE with moderate dips to the NE; and (2) NE-SW dipping moderate-to-steeply towards the NW and SE (see stereonet in **Fig. 5.29 E**). On the other hand, shear zones in core *FG-14* (**Fig. 5.30**), display multi-directional orientations (see stereonet in **Fig. 5.31 C**). Mineral lineations were absent in the shear zones observed in the mine and drill-cores.

Shear zones recorded in the mine outcrops and on drill-cores, agree in their main characteristics (e.g. fabric style, geometry and orientation). The prominent variation in orientation is suggestive of a multimodal array of the shear zones. However, the lack of favourable exposures did not permit their temporal relations to be constrained. Additionally, foliation and shear zones appear to be coeval structures because of their spatial coexistence and similar orientations (e.g. the prominent NW-SE trend observed for both types of structures). Finally, shear zones and associated foliation, mark domains of concentrated ductile strain that bound zones of relatively isotropic rocks. On the basis of the available evidence and the fact that shear zones show similar fabric (discusses in the microstructural section), the most plausible explanation is that they are all broadly the same age. But in the absence of mutual cross-cutting relationship this can not be proven conclusively.

5.7.1.3 Faults

In the area of the Sossego orebody, two types of faults were documented, based on their geometry:

- *Type 1* faults are the most abundant and comprise discrete, narrow fault zones 3-5 cm wide, geometrically represented by a single, continuous segment or minor irregular interlinked traces that show small offsets (see examples in **Fig. 5.13**). Very thin seams of dark grey, clay-rich fault gouge are present along individual fault planes with occasional presence of carbonate in veins. Fault boundaries are sharp, and are mostly characterized by the presence of a polished fault surface that commonly preserves slickenlines.

- *Type 2* faults are represented by wider fault zones (0.5 - 8m), characterized by parallel sets of relatively continuous fault planes, separated by a very fine, dark and incohesive material that bounds fragmented lenses of granitic protolith (see examples in **Fig. 5.14**). The fine and incohesive material appears to correspond to a fault gouge, formed of an intensely comminuted quartz-clay rich material composed of visible quartz fragments immersed in a very fine, foliated dark matrix. Protolith fragments are normally fractured and altered, occurring as elongate, sub-angular lenses oriented sub-parallel to the fault planes. Observed fault zones show considerable variations in the volumetric ratios of gouge/protolith lenses, with protolith lenses generally dominating.

Faults are clustered and homogeneously distributed along the logged intervals of the drill cores *FG-9* (**Fig. 5.28**) and *FG-14* (**Fig. 5.30**), respectively. Fault surfaces form discrete, few millimetre wide and relatively straight planes (see examples in **Fig. 5.47 B, C, E**), which show displacements of up to 20 mm.

Fragmented rock material, texturally similar to those described for *type 2* faults, was occasionally present in the studied drill-cores. However, the material had very limited use for geological description because of its intense degree of disaggregation and fine grain size.

Faults mapped in the mine display multi-directional attitudes (e.g. see map in **Fig. 5.10** and stereonets in **Fig. 5.11 C**), but N-S and E-W trending faults, with moderate-to-steep dips (60° - 80°) seems to be the statistically dominant trends based on density contours on stereonets. Additionally, the N-S trending faults were the longest and widest observed within the mine. Fault attitudes from drill-cores agree with those recorded in the mine (e.g. compare stereonets in **Fig 5.11 C**, **Fig. 5.29 B** and **Fig. 5.31 B**). Fault displacements were not estimated within the mine because of the absence of displacement markers in the exposed sections.

Approximately 70% of the fault planes at Sossego contain slickenlines, but the stereonet for all their measurements (**Fig. 5.11 C**) shows a scattered pattern that is difficult to interpret. The analysis of slickenlines and fault planes sorted by spatial sectors within the mine (**Fig. 5.11 F**) shows two types of domains containing: (1) single oriented fault planes with slickenlines indicative of dominant strike-slip and subordinated oblique slip faults (**Fig. 3.11 I, II, VI**); and (2) multiply oriented fault planes with fault sets showing either distinct kinematics (**Fig. 5.11 F III and V**), or displaying slickenlines oriented approximately at the fault intersections (**Fig. 5.11 F IV and VII**), which indicates contemporaneous fault slip. Further, the contemporaneous character of the faults in the mine is also supported by the preferential occurrence of slickenlines in fault plane intersection observed in drill cores (see **Fig. 5.29 C** and **Fig. 5.31 E**).

5.7.1.4 Veins

Veins are widespread at Sossego (see map in **Fig. 5.10**). They show a broad range of thicknesses varying from few millimetres (see various examples in **Fig. 5.45**) up to 3 m (**Fig. 5.18 A**), with tabular geometries (**Fig. 5.15 A**), sharp and straight contacts with the wall rocks. Subordinately, some veins display slightly curved shapes (**Fig. 5.17 A**), branching geometries (**Fig. 5.15 B**) and stockwork arrays (see examples in **Fig. 5.16** and **Fig. 5.46 B, C, D**). In the mine, veins show good vertical continuity, normally observed from top to bottom of the 8 m high benches, extending in some cases up to 40 metres. Sulphide veins are generally thicker and therefore more obvious within the mine, while barren veins are thinner and are better observed in drill-core samples.

Veins can be grouped into three main classes based on their mineral assemblage, geometry and the nature of their contact with the host rocks:

1 – *Tensile* veins (**Fig. 5.15** and **Fig. 5.45 F, H, G**) correspond to relatively thin structures that are generally mono-mineralic, showing an ultra-sharp contact with the host rocks and occasionally forming stock-work arrays (**Fig. 5.16**). Tensile veins, millimetre to centimetre thick, also often form stockwork arrays observed in drill cores (see **Fig. 5.46 B, C, D**).

2 – *Composite* veins are characterized by at least two mineral phases that in Sossego typically include sulphides and calcite (**Fig. 5.17** and **Fig. 5.45 A, C, D**). Vein margins often show evidence of shearing and have a distinctive fine-dark material developed on its walls, very similar to the gouge associated with *type 2 faults*. Additionally, slickenlines were often observed in few of the vein walls,

evidencing a possible genetic link between the development of this type of vein and faults.

3 – *Breccia veins* are generally much thicker than the other two vein types observed in the mine (see examples in **Fig. 5.18**). They are easily distinguished by the presence of rock fragments surrounded by a matrix consisting of pulverized rock and hydrothermal mineral phases (i.e. pyrite, chalcopyrite, calcite and \pm magnetite). At drill-core scale, breccia-veins comprise zones, 3 to 5 cm wide, of intensely fragmented rocks, cemented by at least two phases of hydrothermal minerals (e.g. **Fig. 5.43 A,B,F**) of apparently different ages (i.e. variable amounts of sulphides, carbonate, actinolite and magnetite). Evidence of fluid-fragment and fragment-fragment interactions are indicated by: (1) the presence of thin reaction rims in a number of breccia clasts (e.g. **Fig. 5.43 F**); and (2) the well rounded nature of some clasts (e.g. **Fig. 5.43 A**), indicative of wearing or abrasion. Finally, clasts in breccia veins show textural differences including varied clasts sizes and degrees of roundness/angularity. These aspects will be discussed in detail later in the present Chapter.

The bulk of sulphide veins were recorded in the mine benches. Stereonets for their spatial attitudes (**Fig. 5.11 D**) highlight the statistical dominance of the trends: E-W, NNE-SSW and NE-SW with typical steep dips. Non-sulphide veins, mainly recorded in the drill-cores FG-9 and FG-14, show polymodal directions in the stereonet containing total measurements (see **Fig. 5.11 E**). Individually compared, barren veins in drill-cores display distinct directional patterns. Core *FG-09* shows veins trending (i) NE-SW with steep dips to the SE; (ii) NE-SW with moderate dips to the NW; and (iii) NW-SE dipping moderately to the NE and SW (see stereonet in **Fig. 5.29 D**). Veins in core *FG-14* follow the dominant trend NNW-SSE, dipping

moderately to the SW and steeply to the NE (see stereonet in **Fig. 5.31 D**). In summary, sulphide and barren veins have different structural attitudes with generally steeper dips observed in the sulphide types.

Sulphide veins are heterogeneously distributed in the mine, forming clusters of poly-directional domains (**Fig. 5.10**). Neither map nor field evidence suggests a spatially or lithologically controlled distribution in the major trends of sulphide veins. Conversely, the relatively thinner barren veins from drill-cores show distinct trends amongst themselves and in relation to the sulphide veins. These differences can be explained by distinct ages of formation for the two vein types.

5.7.2 Interpretations of the structures at Sossego

The structural framework in Sossego, comprises an interlinked array of heterogeneously distributed, sub-vertical and poly-directional structures (e.g. foliations, shear zones, faults and veins), with a relatively good correlation between some of the principal structural trends identified (compare the stereonets in **Fig. 5.11**). Mineralization is focussed in a central, vertical pipe-like breccia body enveloped by a stock-work of veins.

Foliation and ductile shear zones striking WNW-ESE with moderate dips to the NE seem to have formed initially, possibly contemporaneously. Faults, veins and shear bands were later formed under brittle-ductile conditions and show mutual cross-cutting relationships in the rare localities where temporal relations were preserved.

Tensile and sheared veins are typically sub-vertical with subordinate sub-horizontal examples. There are no clear crosscutting relationships between flat and steeply-dipping fault veins which suggests a broad contemporaneity of the vein sets and a cyclic developmental sequence (Sibson et al. 1988). Episodic vein opening is indicated by the occurrence of different mineral phases within the veins suggesting that the hydrothermal fluid compositions may have changed through time. Displacement magnitudes along faults and shear zones were generally not estimated due to the absence of stratigraphic markers, and lack of evidence for displacement senses on a majority of faults, shear zones or veins. However, most of these structures display evidence of intense fluid influx and/or fluid flow indicated by the precipitation of hydrothermal minerals (e.g. chlorite, epidote, calcite, sulphides) within or around the structures and severe mineral alteration in the wall rocks. These observations indicate that faults, veins and shear zones played important roles as conduits of substantial fluid discharges in the hydrothermal system. These features are very similar to those described for fault-controlled vein systems by other authors (Newhouse 1940; Ray 1954; Peters 1993; Brown et al. 1996). In general, such vein systems are referred to as undulating, tabular to pipe-like bodies composed of intact and brecciated vein minerals, and slices of hydrothermally altered wall rocks. Veins widths typically vary from mm to more than 10 m in some deposits, with overall pinch and swell geometries seen in cross-section.

(Sibson 1996; Sibson 2000b) acknowledged the importance of low-displacement faults and interconnected fractures as conduits for fluid flow stating that: “...while it is clear that fault-fracture networks form the principal avenues for large volume fluid flow in many areas, it is also notable that the hosting structures are generally not large displacement features”. Fluid circulation during faulting

processes can be linked to the seismic cycle (Schulz et al. 1998; Scholz 2002), increasing fluid pressures and reducing fault strength e.g. (Sibson 1994; Sibson 2000a). Additionally, the presence of implosion breccias, made up of country rock fragments, resulting from sudden pressurization and depressurization processes that occur during distributed flow are also indicative of repetitive deformation characteristic of the seismic cycle (Scholz 2002).

Dip-slip, strike-slip, and oblique faults are present at Sossego. However, temporal relations between fault trends are not easily constrained because cross-cutting relations are either poorly exposed or unclear. In general, however, it seems most likely based on the existing field evidence that the various orientations of faults show mutual cross-cutting relationships suggesting that the faults are broadly contemporaneous features.

5.7.3 Sequeirinho Orebody

Sequeirinho is the largest orebody in the area, exposed in an elliptical, NE-SW open pit mine, approximately 1,270m long and 585m wide (see **Fig. 5.6**). The Sequeirinho mine is located 1300 metres to the west of the Sossego mine, and comprises the following geological domains (see map in **Fig. 5.19**):

1- Syn-tectonic tonalitic leucogranites, hosting minor lens-shaped bodies of gabbro, and hydrothermal epidote and actinolite are the dominant lithologies in the southern half of the mine. The granitoids form isotropic domains (see examples in **Fig. 5.5 D**

and **Fig. 5.38 A, B, C, F**) bounded by portions of foliated rocks related to shear zones (see examples in **Fig. 5.5 A, B** and **Fig. 5.39 B, E, F, G, H**).

2- The northern or upper portion of the mine comprises a domain of mafic rocks represented by metabasalts and sheared felsic metavolcanics, granophyre and minor lenses of gabbro and hydrothermal magnetite and actinolite bodies. The metabasalts occurs as subordinate, isotropic domains sandwiched by dominant, intensely foliated metavolcanics represented by quartz-biotite schists (see examples in **Fig. 5.5 K** and **Fig. 5.40**). The granophyre domain is isotropic and intensely cross-cut by faults.

3- The central part of the mine includes a major NE-SW shear zone that hosts the bulk of the mineralization in Sequeirinho, which is composed of sulphide breccias containing actinolite and magnetite fragments, surrounded by chalcopyrite matrix (e.g. **Fig. 5.6 C**). Minor disseminated sulphide mineralization occurs outside the breccia domain (examples in **Fig. 5.6 A, B, D**).

The geometric aspects, styles and orientations of the structures in the mentioned lithological domains, are presented in the following sections.

5.7.3.1 Foliation

At Sequeirinho, foliation is prominent in the quartz-biotite schists and granitoids exposed in the NW and SE flanks of the mine, respectively (**Fig. 5.19**). Distinctive characteristics were observed in foliation from these lithological domains. Where the biotite schists display a pronounced foliation, it can be morphologically classified as

continuous, smooth and parallel (Passchier et al. 2005). The schistosity is characterized by fine to very-fine, millimetre wide alternating bands of biotite and quartz with occasional, but considerable occurrences of quartz seams parallel to the foliation (**Fig. 5.20**). Symmetric boudins of metavolcanics 13-35 cm long are locally present, with parallel internal and external foliation and pressure shadows formed of quartz, actinolite and occasionally sulphide aggregates (**Fig. 5.21**). The slightly higher quartz content observed in the boudins provides a mechanical contrast with the surrounding biotite rich rocks, perhaps explaining their presence. No asymmetric shear-sense indicators were observed.

The drill-cores *FG-5* and *FG-20* (see location on **Fig. 5.19**) intersect the biotite schists characterized by a fine to very fine, typically straight foliation with minor porphyroclasts and occasional quartz-rich levels (see examples in **Fig. 5.40 A** and **B**). Evidence of hydrothermal activity is relatively limited in the schists, corresponding to zones or haloes of alteration parallel to the foliation (e.g. **Fig. 5.40C** and **D**). Albitization (e.g. **Fig. 5.40 C** and **D**), potassic alteration (e.g. **Fig. 5.40 E**) and sulphide deposition (e.g. **Fig. 5.41 F** and **I**) are commonly observed. Localized brecciation (e.g. **Fig. 5.40 E**) within the hydrothermal pathways indicates the development of high fluid overpressures.

Biotite rich boudins (~ 3 cm wide) separated by quartz pressure shadows were observed in the cores (e.g. **Fig. 5.41 A** and **B**). They are relatively smaller than the examples from the mine benches, but show matching geometry and style. Finally, quartz veins, 1.5 cm or less thick, are folded to various degrees within the schists. Fold styles include parasitic (**Fig. 5.41 C**); asymmetric with short limb to long limb geometries (**Fig. 5.41 D**); isoclinal to tight, with a wavelength of 2-3 cm (**Fig. 5.41 E** and **F**). In high strain zones, the quartz veins are parallel to the foliation

with hinges separated from limbs (**Fig. 5.41 H and I**). The varied degrees of deformation observed in quartz, suggests that strain was heterogeneously accumulated in the schists.

Foliation in the granitic rocks is spatially associated with WNW-ESE shear zones that show gradational contacts with virtually undeformed granitoids. The shear zones comprise mylonites that form 1 to 6 m wide intervals in drill cores (see drill core examples in **Fig. 5.39 E, F, G, H**). These foliated intervals in drill core FG-15 (**Fig. 5.32**) display a dominant NE-SW foliation dipping steeply to NE (**Fig. 5.33 A**). The mylonitic fabric is characterized by straight (**Fig. 5.22 A and Fig. 5.39 H**), wavy (**Fig. 5.22 B, C, D, F and Fig. 5.39 E and G**) or anastomosing/sigmoidal (**Fig. 5.22 E and Fig. 5.39 F**) features defined by elongated mineral aggregates that wrap around porphyroclasts or lenses of relatively more rigid material. Additionally, mylonites often show compositional banding characterized by a prominent and continuous planar fabric. Hydrothermal alteration is widespread in mylonites, including: sodic (**Fig. 5.22 D, F**); sodic-calcic (**Fig. 5.22 A, B, C, E**); chloritic (**Fig. 5.39 E, F, H**); and potassic (**Fig. 5.39 E, G**) alteration. The mineral alteration in mylonites by hydrothermal fluids suggests that the intense strain accumulation in shear zones was associated with the throughput of large volumes of fluids. Finally, weak mineral lineations, defined by preferred linear alignments of mafic mineral grains (e.g. biotite and amphibole) are also preserved.

Collectively, the attitude of foliation recorded in the mine a drill cores, follows one principal and two subordinate trends (see stereonet in **Fig. 5.23 A**): (1) a prominent WNW-ESE-trend with steep, mostly SSW dips; (2) a NE-SW trend with moderate NW dip values; and (3) NNW-SSE trends with mean moderate dips to the WSW. Mineral lineations show mostly vertical to steep plunges towards the ESE.

The association of steep to sub-vertical foliations and mineral lineations, suggests a near horizontal compressional component connected with a sub-vertical stretching direction. The foliation trends measured in drill cores, agree with the attitudes in the mine and include: (1) *FG-20* cross-cutting schists, displaying a strong E-W trend with moderate to steep dips toward the N and S (**Fig. 5.37 A**); and (2) *FG-5* and *FG-15* intercept schists and granitoids respectively, and show prominent NE-SW foliation with NW moderate dips (see stereonets in **Fig. 5.33 A** and **Fig. 5.35 A**). Furthermore, the *FG-5* core also shows a NNW-SSE foliation dipping moderately W.

The foliation defines two main spatial domains in the mine: (1) a marginal domain, located in the NW and SE flanks of the mine, where the steeply dipping WNW-ESE foliation prevails; and (2) a central domain characterized by NE-SW foliation with moderate dips to the NW. The NNW-SSE trend only occurs locally, and it is not important at the orebody scale. Note, however, that, the central part of the mine displays relatively fewer structural measurements because the mining operations were concentrated in this area at the time fieldwork was carried out.

5.7.3.2 Shear Zones

Shear zones at the mine scale comprise major structures associated with the foliated domains, previously described. Two notable examples of these structures recognized in Sequeirinho include:

- (1) a WNW-ESE sub-vertical shear zone, 8 up to 40 meters wide that extends from the SE to the NW flanks of the mine, and produced mylonites and

biotite schists in the domains of granitoids and felsic metavolcanics, respectively. The spatial relationship between the steep dipping to sub-vertical foliation and mineral lineation indicates dominantly vertical displacements.

- (2) a NE-SW shear zone with moderate dips to the NW coincides with the long axis of the mine and with the position of the mineralized zone. Map scale observations (e.g. **Fig. 5.9 C**) show that the NE-SW shear zone offsets the regional WNW-ESE trend with apparent sinistral kinematics. Outcrop scale evidence for cross-cutting relationships was often unclear, but NE-SW foliations linked to the larger shear zone was observed in a number of localities.

Shear zones in drill cores comprise discrete and relatively thin bands, of few millimetres up to 5 cm wide, showing tabular (**Fig. 5.42 C**) or gently curved (**Fig. 5.42 E, G**) geometries. They represent compartments of accumulated shear strain in sharp contact with the wall rocks. Further, shear zones display hydrothermal mineralization (e.g. quartz, sulphide, k-feldspar), suggesting the presence of fluids during ductile shearing. Total shear zone structural measurements show a fairly scattered pattern on the stereonet (see **Fig. 5.23 E**). However, the structural attitudes sorted by drill-cores *FG-5* (**Fig. 5.35 D**), *FG-15* (**Fig. 5.33 C**) and *FG-20* (**Fig. 5.37 C**) indicate that the shear zones trend NE-SW with NW and SE moderate to steep dips, and NW-SE with moderate to steep dips to the NE and SW. The relative ages of the two sets of shear zones remain unclear because exposures of cross-cutting relationships are not preserved. However, they are most likely to be the same age based on microstructural evidence that indicates common fabric styles and

deformation conditions for the studied shear zones samples (later described in the microstructural section).

5.7.3.3 Faults

Faults and fault zones are abundant in schists, granophyre and granitoid domains in the Sequeirinho orebody. They are distinguished from blast-generated fractures by good continuity and lateral and vertical persistence along the mine benches. Fault displacements at outcrop scale were not calculated or estimated given the general absence of offset stratigraphic markers in the mapped sections. Faults and fault zones were grouped into two types:

Type 1 comprises discrete fault zones that may occur as individual surfaces (**Fig. 5.24 A**) or parallel sets of faults forming continuous zones tens of centimetres up to 3m wide (**Fig. 5.24 B**). This fault type is normally present in the biotite schist domain and tends to occur parallel to the foliation in these rocks. Type 1 fault planes exhibit fairly straight planes (**Fig. 5.24 C**), but gently curved surfaces with broad wavelength also occur (**Fig. 5.24 D**). Fault gouges or fragmented fault rock materials are rare.

Type 2 faults (see examples in **Fig. 5.25** and **Fig. 5.26**) are characterized by the presence of fragmented materials within the fault planes including altered and fractured lenses of wall-rock (e.g. **Fig. 5.25 A, C, D**), and fault gouge in variable quantities (see **Fig. 5.25 B** and **Fig. 5.26**) often showing an internal planar fabric or presence of hydrothermal mineral phases (see **Fig. 5.26 B, C, D**). Fault boundaries are sharp, straight or irregular, forming zones on average 20cm wide, ranging from 4 cm up to a maximum of 2 m wide.

The intensely friable fault gouge forms brown-reddish and minor green varieties (**Fig. 5.26 B, C, D**). They are mainly composed of phyllosilicates, clay minerals and very small lithic fragments, forming a fine anastomosing fabric oriented generally parallel or oblique to the associated fault plane (**Fig. 5.26 B, C, D**). Principal and subordinate fracture surfaces are present in the fault gouge domains, rarely displaying slip lineations indicative of the shear direction. The subordinate fractures can be either parallel or oblique to the cataclasite layers, but the principal surfaces are typically planar, continuous and often separate fault gouge layers of different colours (e.g. **Fig. 5.26 D**). Narrow fault zones also preserve fault gouge as thin (1 to 2 cm) layers smeared along the fault plane (**Fig. 5.25 B**). In broad fault zones (**Fig. 5.26 A**), fractured lenses of wall-rock and calcite bands were observed intercalated with fault gouge layers.

Drill cores *FG-5* and *FG-20*, show faults with characteristics compatible with those described in the mine outcrops. *Type 1* faults comprise narrow, well-defined planes showing small displacements of markers (1 mm up to 4 cm). Fault planes are discrete, cohesive and often filled with hydrothermal minerals (see **Fig. 5.47 A, D, F**). Strain is restricted to the immediate region of the fault plane with no evidence for the development of damage zones. Significant fluid flow along the fault planes is indicated by the presence of narrow alteration haloes. *Type 2* faults show up in the drill cores as relatively long intervals of intensely fragmented material with similar properties to those observed in these faults in mine exposures.

Total faults attitudes (see stereonets in **Fig. 5.23 B**) show three major trends cited in order of statistical weight (**Fig. 5.23 B**): (1) E-W to WNW-ESE, dipping mainly steeply south; (2) NW-SE with steep dips both to the NE and SW; and (3) NE-SW dipping moderately to the SE and, to a lesser extent NW. Steep N-S faults

are also present in the area, but are relatively uncommon. The fault trends WNW-ESE and NE-SW agree with the foliation trends, suggesting that at least some of the faults may have formed along pre-existing “weak” planes. The temporal relations between faults is not well constrained.

Slickenlines formed by elongate aggregates of clay minerals, quartz, chlorite, epidote or calcite are present in approximately 25% of the measured fault planes. Stereonets for the total number of fault slickenlines (**Fig. 5.23 C**) shows a scattered pattern, limiting interpretations. However, fault planes and slickenlines sorted by their location within the mine (see stereonets I to X in **Fig. 5.23 F**), show multi-oriented fault planes with many of the slickenlines oriented close to fault intersections (see stereonets I, II and X **Fig. 5.23 F**), which suggests that faults slipped contemporaneously. Further, the overall attitude of the slickenlines indicates an oblique and strike-slip character for the faults.

5.7.3.4 Veins

Veins at Sequeirinho were observed and measured in drill-cores and range from few millimetres up to 10 cm in width. Cross-cutting relations were not observed, compromising the definition of veins on the basis of their relative ages. Vein fillings typically comprise the hydrothermal minerals quartz (**Fig. 5.45 B, G**), sulphide (**Fig. 5.45 H**) and actinolite (**Fig. 45 E**) with contrasting composition and texture from the adjacent host rocks. Locally, interconnected veins form stockwork arrays, but these were only observed in the drill cores (see **Fig. 5.46 A, E, F**). The interconnected network of veins and veinlets facilitates the percolation of hydrothermal fluids, promoting alteration of the wall-rocks.

The total vein attitudes from drill cores *FG-15* (**Fig. 5.33 B**) and *FG-20* (**Fig. 5.37 D**) show a diffuse pattern on the stereonet (see **Fig. 5.23 D**). However, directional trends appear better when veins attitudes are sorted by individual core. So in *FG-15* (see **Fig. 5.33 B**) the following orientations are observed - NE-SW striking, dipping steeply to the NW; NNW-SSE striking, dipping moderately to the E and W; and E-W striking, with moderate dips to the S. In *FG-20* core (see **Fig. 5.37 D**) the main orientations are - N-S striking, with moderate dips to the W; NW-SE strikes, dipping steeply to the NW, and NE-SW striking, dipping steeply to the SE.

Minor breccia veins were observed in the drill core *FG-20*. They comprise zones, tens of centimetres wide, containing typically angular fragments of varied sizes cemented by hydrothermal mineral matrix: actinolite (**Fig. 5.43 C**), carbonate (**Fig. 5.43 D**) and quartz (**Fig. 5.43 E**). These features are highly localized and do not seem to play a major role in the structural framework of the deposit.

5.7.4 Interpretations of the structures at Sequeirinho

Sequeirinho corresponds to an “S” shaped orebody (see **Fig. 5.9 C** and **Fig. 5.19**) where: (1) the ends are hosted by schists and granitoids with sub-vertical WNW-ESE foliation; whilst (2) the central part linking the “S” tips, comprises mineralized breccias developed in a NE-SW shear or fault zone dipping moderately to NW. Thus the early WNW-ESW ductile fabric is offset by a sinistral NE-SW fault zone where the main sulphide breccia body is centred.

The early foliation is accompanied by a down-dip mineral lineation, suggesting that these structures record the action of near horizontal compressional

component, linked to a vertical stretching component. Foliation is restricted to mylonitic zones that mark domains of intense strain accumulation, intercalated with relatively undeformed domains. The alternating and interlayered character of the mylonitic and undeformed zones suggests that strain was partitioned into the mylonitic zones.

The biotite schists seem to represent localized sheared products of adjacent isotropic metavolcanic mafic rocks. This hypothesis is supported by: (1) the gradual development of foliation, moving from an isotropic domain of felsic volcanics into a foliated domain over a small region; (2) microscopic mineralogical and textural observations indicating similarities between the mafic metavolcanics and biotite schists; and (3) cross-cutting quartz veins in the mafic rocks are observed in the schists to be sub-parallel to and folded within the schistosity or forming boudins and sigmoidal lenses.

The main fault sets in the mine include the following trends: WNW-ESE; NE-SW; NW-SE; and N-S. Most are steeply dipping. The WNW-ESE trend coincides with the regional foliation (e.g. compare the statistical contours corresponding to the WNW-ESE trend in stereonet **A** and **B** in **Fig. 5.23**), suggesting that the early ductile fabric controlled the orientation and development of these faults. NE-SW faults are easily seen at map scales and show anticlockwise kinematics when displacing the regional foliation (the best example of these faults in **Fig 5.9 C**). The NW-SE fault set relative age is estimated to be younger than WNW-ESE and NE-SW and older than N-S fault sets. Finally, the N-S trending faults are the youngest identified and are typically associated with late tabular diabase dykes regionally, although these are relatively rare in the mine itself.

Type one faults, characterized by discrete narrow slip surfaces, are interpreted as having been produced by a short-lived movement history, under low regimes of pore fluid pressure at shallow crustal depths. Hence these faults generally lack significant breccias, cataclasites, gouge and hydrous mineral assemblages. By contrast, *type two* faults, with their associated fault rocks (i.e. cataclasites, ultramylonites) and hydrothermal minerals, are indicative of longer lived fault activity possibly associated with seismic slip. (Sibson 1977) suggests that continuous slip on principal slip surfaces is associated with various wear processes that produce layers of breccia, cataclasites and gouge bounded by tabular zones of damaged rocks. Indeed, the structural characteristics of the elements observed on faults containing cataclasites at Sequeirinho are comparable with those from the exhumed Punchbowl fault in the San Andreas System (Chester et al. 1998). Their observations on cataclasites led them to suggest that fault cores accommodated nearly all of the shear displacement leading here to the development of ultracataclasites along principal slip surfaces. They proposed that the localization of displacement along principal slip surfaces associated with zones of less cohesive ultracataclasites is consistent with seismic slip. It is possible that fault weakening in such cases may have been triggered by mechanisms such as thermal pressurization of pore fluids (Sibson 1973; Lachenbruch 1980). This takes place in fluid-saturated rocks when shear heating produced during seismic faulting causes sudden, highly localised increases in pore fluid volume leading to pressurization of the fluid and local reduction in effective stress and dynamic weakening.

Fault slickensides associated with multiple fault planes, and oriented close to the faults intersections indicate that many of the faults slipped contemporaneously. The hypothesis agrees with (Nietosamaniego et al. 1995) and (NietoSamaniego et al.

1997), who proposed that multiple fault patterns can be formed during one or more deformation phases with or without rotation of the principal stresses in the continental crust. They assume that old rocks from structurally complex zones contain multiple faults or planes of weakness formed during tectonic events that affected the rocks during the geological past. Further, due kinematic interactions, a fault pattern formed during a single deformation event of sliding on pre-existing planes has no restrictions regarding symmetry, number of slickenlines sets, number of faults nor orientation of the faults.

Finally, a more detailed fault analysis is limited by the lack senses of motion and displacement indicators. Fault planes are typically covered by a “wax” formed of hydrothermal minerals, rock fragments and clay. Whilst the direction of shear is often evident, the sense of motion is more rarely preserved. Offset markers were generally absent in the mapped benches of the mine.

5.7.5 Rio Branco Granite

The Rio Branco Granite is considered to be part the 1.88 Ga. suite of anorogenic granites described elsewhere in the Carajás Terrane, e.g. (Dall'Agnol et al. 2005). The structures in the granite were studied to be compared with those observed in the older rocks that host the Sossego and Sequeirinho orebodies.

The studied outcrops of the granite are located 3.8 km away from the Sequeirinho mine. They comprise a salmon-pink, medium- to coarse-grained isotropic granite, composed of plagioclase, quartz and minor amounts of biotite. The granite is cross-cut by faults and fault zones typically 9 to 20 cm wide (see **Fig. 5.27**

A), with exception of one 2m wide zone (see **Fig. 5.27 B**). Faults show sharp contacts with the granite and comprise sets of relatively straight sub-parallel surfaces e.g. (**Fig. 5.27 B and C**), bounding wall-rock lenses (**Fig. 5.27 C**) and a dark mass of fine rock fragments and hydrothermal minerals.

The Rio Branco Granite is cross-cut by two fairly consistent sets of faults: (1) a WNW-ESE striking set, dipping on average 65° to the SSW; and (2) a NNE-SSW set, dipping 80° to the ESE (see stereonet in **Fig. 5.27 E**). The slickenlines preserved (see red dots in **Fig. 5.27 E**) associated with the fault planes, indicate mainly a strike-slip character for these structures. Faults shear sense, cross-cutting relations and displacement of the sets were not determined.

Hydrothermal activity along fault planes is recorded by the development of quartz veins, plagioclase altered into clay and within the faults, the presence of hematite, calcite and malachite mineralisation along fault surfaces e.g. (**Fig. 5.27 D**).

5.7.6 Interpretation of the faults in the Rio Branco Granite

The Rio Branco granite shows a moderately dipping ($\sim 50\text{-}60^\circ$), WNW-ESE-trending set and a steeply dipping ($\sim 80\text{-}90^\circ$) NNE-SSW-trending set, that seem to be strike-slip features. These fault trends agree with the orientation of fractures and faults described in other 1.88 Ga. granitoids (e.g. Central and Cigano) in (Pinheiro 1997).

The WNW-ESE faults show orientation comparable with the regional scale strike-slip Carajás and Cinzento faults (see **Fig. 5.2**). This fault set also agrees in direction with numerous surface lineaments highlighted within the volcano-

sedimentary cover sequence in Carajás (lineaments in **Fig. 5.2**). (Pinheiro et al. 1997a; Holdsworth et al. 2000) proposed that a regional sinistral transpression with brittle character, nucleated the Carajás and Cinzento strike-slip systems at ca. 2.6 Ga. The 1.88 Ga isotropic granitoids are older than the Carajás Fault and the therefore the presence of WNW-ESE trending faults in the Rio Branco Granite suggests that these structures were possibly formed by reactivation of pre-existing structures with the same orientation. These faults seem to also control the regional distribution of the volcano-sedimentary cover sequence in Carajás.

The observed NNE-SSW trending faults are comparable with N-S faults previously described in the Carajás Terrane, e.g. (Costa et al. 1997; Veneziani et al. 2004) and are linked to the breakup of Pangea in the Early-Cretaceous, 130-120 Ma (Windley 1995), which subjected the Amazon Craton to extensional regimes. During that time, several N-S graben were formed, that locally preserve Paleozoic rocks notably at the eastern margin of the craton (Costa et al. 1997; Schobbenhaus et al. 2003).

5.8 Breccia Classification and Characterization

Fault breccias from the Sossego and Sequeirinho orebodies were classified using the schemes proposed by (Woodcock et al. 2008) and (Mort et al. 2008) (see **Fig. 5.49 B**). These authors suggest the terminology *crackle*, *mosaic* and *chaotic* for fault related breccias. This classification has the advantage of being non-genetic and uses clasts size as the primary criterion to classify a fault breccia. It assumes that the rock

has at least 30 % of its volume formed by “large” clasts, where fragments are greater than 2 mm in diameter (i.e. that the rock is a breccia (Sibson 1977).

Barren and mineralized breccias were studied using image analysis software (UTHSCSA ImageTool 3.0) to determine the geometrical parameters (see **Table 5.4**) of their fragments. The studied samples are generally representative of barren (**Fig. 5.48 B1, B8** from Sossego and **Fig. 5.48 B2, B5, B6** from Sequeirinho) and mineralized (**Fig. 5.48 B4, B9** from Sossego and **Fig. 5.48 B3, B7** from Sequeirinho) breccias as a whole in the orebodies. The analysed images were captured from outcrop (**Fig. 5.48 B1, B2**), drill core (**Fig. 5.48 B3, B7, B8, B9**) and slab (**Fig. 5.48 B4, B5, B6**) scale samples.

The breccias are generally described as cohesive, isotropic, with monomineralic or lithic fragments amalgamated by cement and/or matrix, composed of a single or several mineral phases (e.g. calcite, actinolite, biotite, pyrite, chalcopyrite, magnetite). Clasts display varied sizes and range from angular to sub-rounded morphologies. There is also evidence of rotation, evidenced by the misfit of adjacent clasts.

Breccias typically comprise large fragments (30-54%) with cement/matrix (40-63%) and a limited amount of smaller clasts (0-9%) (see **Fig. 5.49 A**). The nine analyzed samples fall into the field of chaotic breccias when plotted on the ternary diagram from (Woodcock et al. 2008) (**Fig. 5.49 B**).

5.8.1 Textural characterization

The breccia characterization carried out during the present study was based on a textural analysis of the clasts to quantify: (a) particle size distribution (PSD); and (b) fragment shapes. Particle morphological properties for each sample were quantitatively described using the parameters presented in **Table 5.4**.

Clasts size analyses were carried out using two types of measurements for fragment size: maximum clasts diameter, S (Billi et al. 2004; Hayman 2006; Mort et al. 2008), and clasts size, r , calculated as $\log \sqrt{\text{grain area}}$, (e.g. (Bjornerud 1998; Clark et al. 2003; Clark et al. 2006). Different particle size parameters were used to investigate the influence of these values on fractal dimensions.

Particle size distributions (PSD) were quantified using log-log plots of clasts size (S and r) against number of clasts (with a range of sizes) (**Fig. 5.50**). The PSD's follow a power-law distribution, indicative of a self-similar or fractal distribution of clasts sizes using both measurement criteria (i.e. S and r). Fractal dimension values D are varied and range between a maximum of 2.58 / 2.46 and a minimum of 1.17 / 1.56 for PSD plots of S and r , respectively. The D values from PSD's using S and r parameters show average difference of 0.24 (compare the values in the **F** and **G** graphs in **Fig. 5.51**), except for samples B9 and B6 that show the same D values for S and r . Breccias from the same ore-body can show considerable variations in D and no distinct pattern of fractal dimension was observed between barren and/or mineralized breccias.

5.8.2 Textural analysis

The results of an analysis of clasts geometrical attributes in 9 breccia samples are presented in **Fig. 5.51**. The data is grouped by orebody and occurrence of mineralization.

Roundness and compactness values are relatively high for breccias at Sequeirinho compared to those from Sossego. **Figure 5.51 (A & B)** illustrates the gentle increase in roundness and compactness, progressing from B1 to B7. Clasts from mineralized breccias tend, in general, to be closer to a circular shape than those from their barren counterparts.

Sossego breccias have high aspect ratios and a greater variation in clasts elongation, in particular for the barren breccias (**Fig. 5.51 C**) compared to equivalent Sequeirinho samples. These display relatively homogeneous values for both barren and mineralized members.

Angularity values are heterogeneous, ranging from 15.7 to 18 (**Fig. 5.51 D**), with three distinct data clusters at values between: 15.7-15.9 (B3/B6/B7); 16.5-17 (B2/B4/B5/B8); and 18 (B1/B9). Average clasts angularity is greater than 16.7 for Sossego and less than 16.7 for Sequeirinho. The presence of sulphide mineralization does not appear to affect clasts angularity measurements.

Graphs of clasts angularity vs. roundness and elongation vs. compactness, illustrated respectively on **Figs. 5.52 A and B**, show an inversely proportional relationship between these parameters, with the exception of samples B3 and B9. The Sequeirinho samples (B3-B6-B7) are progressively more rounded (less angular) than the Sossego samples (B9-B1), with evident clustering in the data distributions.

Additionally, an inversely proportional relationship is consistent between the values of *fractal dimension* $D(S)$ vs. *elongation* (**Fig. 5.52 C**) and *fractal dimension* $D(r)$ vs. *angularity* (**Fig. 5.52 D**), whose graphs show overall negative trends, if discarded the samples B1 for the graph (**Fig. 5.52 C**) and B1 and B9 for the graph (**Fig. 5.52 D**). Collectively, the Sequeirinho breccias tend to show more rounded/circular fragments with higher D values for their PSD, than the Sossego breccias, which display more angular/elongated fragments with lower D values. The cited relationships are important because they validate the PSD results, which in theory have $D(r)$ and $D(S)$ depending respectively on particle area, and maximum clasts diameter.

5.8.3 Interpretation of the clasts size analysis

The barren and mineralized breccias from the Sossego and Sequeirinho orebodies have been classified as chaotic breccias. According to (Mort et al. 2008; Woodcock et al. 2008), these breccia types have strongly rotated clasts, typically showing more than 20° average rotation and not preserving any geometric fit to formerly adjacent clasts.

The breccias at Sequeirinho show more rounded and less angular clasts compared to those at Sossego. Clasts concentration values for breccias from both orebodies range between 40% and 60%. The fractal dimension D values calculated from the particle size distribution of breccias range from 1.17 up to 2.58. Sossego breccias have smaller D values than those from Sequeirinho. Finally, the presence of Cu mineralization appears to show no direct influence on the geometrical properties of the breccias clasts.

The textural analysis results generally agree with those presented by (Mort et al. 2008) for chaotic breccias. Values of clasts roundness and compactness indicate that the clasts are generally sub-rounded whilst the relatively low clasts concentration results attest to the dilatant character of the studied breccias. Clasts angularity is inversely proportional to roundness, which is theoretically predicted (Lin 1999; Storti et al. 2007). Angularity has been shown to be more sensitive to small changes in particle shape so it is thought to be more suitable than roundness for studying fault rocks with subtle variations in clasts shape (Storti et al. 2007).

Angularity values decrease and roundness values increase from Sossego to Sequeirinho. The change in particle shape suggests that the breccias were formed by distinct fragmentation mechanisms (Storti et al. 2007). Angular particles (*Sossego*) are thought to be formed mainly by sliding, cracking, fragmentation and dilatation, whilst more rounded clasts (*Sequeirinho*) likely formed due to rolling-attrition mechanisms during shearing (Mair et al. 2002; Guo et al. 2004; Anthony et al. 2005).

The calculated fractal D values for the Sossego and Sequeirinho breccias (1.17-2.58) are consistent with published data on grain size analysis of natural and experimental fault rocks (e.g. see Table 1 in (Keulen et al. 2007)). Fractal D -values are related to specific fragmentation processes that operate in fault zones (Blenkinsop 1991). Therefore, the variation of D values, lower at Sossego and higher at Sequeirinho, indicate that the Sequeirinho breccias are more evolved/sheared as they have experienced more intense shearing with rolling and attrition. Systematic increases in D -value from immature to mature cataclastic rocks have also been observed by several other authors (Marone et al. 1989; Hattori et al. 1999; Billi et al. 2004).

The fractal dimension values (D) calculated for clasts size distribution in terms of area (r) diverges from those of clasts maximum diameter (S). Both size parameters have been used in studies on grain size distributions in fault rocks. If the difference in fractal dimension values presented here is related to way in which particle size has been measured, then future work on this topic will need to use a standard method for calculating fractal dimension for fault rocks in order to avoid biased or inappropriate comparisons.

5.9 Microstructures

Qualitative observations of the microstructural fabrics and deformation mechanisms were conducted to estimate temperatures and metamorphic conditions during the main deformation events and the geological evolution of the area. The rocks analysed in the following section comprise a mix of samples from the mine outcrops and drill cores that are representative as a whole of the geological units and fault rocks described in the orebodies.

5.9.1 Sequeirinho

In the *Sequeirinho Mine* four main categories of deformed rocks and associated structural features were identified:

Old weakly deformed granitoids are generally located in sections of the mine away from the major shear zones. They consist typically of a granular mixture of

coarse subhedral quartz and altered feldspar crystals (see examples in **Fig. 5.53 A, B, C**). Feldspar grains are generally larger than quartz and commonly show widespread alteration to fine grained white mica and clay minerals, which gives feldspar the dark “dirty” appearance under the microscope. Apart from the alteration, feldspar grains are fairly well preserved displaying weak to moderate undulose extinction, strain-induced twin lamellae (**Fig. 5.53 D**) at some grain margins and localized grain size reduction due to brittle fracturing and cataclasis (**Fig. 5.53 D**). Quartz crystals have anhedral to subhedral forms, prominent undulose extinction that outlines elongated subgrains (**Fig. 5.53 C, E**) and chessboard features in few grains. Grain boundaries are straight and sharp or commonly serrated or interdigitated, indicating strain induced grain boundary migration recrystallization (**Fig. 5.53 F**). Locally, grain boundaries display dynamically recrystallized fine grained quartz (**Fig. 5.53 F**) by subgrain rotation recrystallization (SGRR). Ferromagnesian minerals are accessories or are absent in the observed samples.

Foliated granitoids mark the transition from weakly deformed granitoids to mylonites. Progressive and heterogeneous flattening of quartz grains from subhedral (**Fig. 5.54 A**) to elongate quartz ribbons (**Fig. 5.54 C**), with an aspect ratio of 0.125, defines a foliation ranging from weak to strong depending on the strain intensity (see the increase in strain from **Fig. 5.54 A** to **C**). The occasional presence of preferentially oriented fine-grained biotite or a hydrothermal aggregate of white mica+epidote further strengthens this foliation. Feldspars are strongly altered to sericite (note the dark dirty patches in the microphotographs under polarised light), limiting detailed microstructural observations in this mineral. No evidence of magmatic foliations was observed in any of the studied samples.

Quartz grains in the initial stages of flattening (**Fig. 5.54 A**) tend to develop a relatively symmetrical augen shape with the co-existence of partially or totally dynamically recrystallized mineral aggregates. Remaining crystals show strong undulose extinction with elongate or polygonal subgrain boundaries, typically mantled by finer grained subgrains indicating SGRR (note the quartz domains in **Fig. 5.54 A**, under crossed nicols). Lobate and straight grain boundaries on the newly formed quartz crystals indicate some grain boundary migration recrystallization (GBMR) and late recovery. Progressive flattening and recrystallization throughout the sample, of newly formed quartz grains by GBMR promotes an almost exclusive occurrence of newly formed quartz grains by GBMR as elongated aggregates with preferred orientation that characterizes aggregate shape preferred orientation (ASPO) (note the recrystallized quartz domains in **Fig. 5.54 B** and **C** under crossed nicols). Insertion of a sensitive tint plate reveals random and strong lattice preferred orientation (LPO) for the grains aggregates from the samples in **Fig. 5.54 B** and **C** respectively.

Granitic mylonites comprise highly strained deformed granitoids in the Sequeirinho mine. The anastomosing foliation is relatively continuous and composed of aligned aggregates of medium to fine grained recrystallized minerals. It wraps around porphyroclasts or lenses of “strong” minerals (**Fig. 5.55 A**). The main mineral assemblage is composed of quartz, K-feldspar, plagioclase and amphibole. Retrogression products are common, with abundant chlorite and alteration of feldspar to sericite.

Dynamic recrystallization is pervasive, indicated by intense grain size reduction. Quartz is almost totally recrystallized into narrow and elongate lenses or

ribbons of uniform grain size polygonal aggregates suggesting SGRR (**Fig. 5.55 B**). Grain boundaries are commonly straight with limited interlobate contacts. A few large relict grains, weakly or moderately flattened, are preserved within the recrystallized portions. They show notably undulose extinction, subgrains and enclosed recrystallized regions. A moderate to strong LPO is evident. Aligned quartz aggregates define a strong ASPO, but shape preferred orientation (SPO) and grain shape preferred orientation (GSPO) are generally absent.

Feldspars occur as fine or very fine recrystallized aggregates or larger fractured grains. The aggregates show uniform grain size distribution, forming elongated clusters or lenses that normally wrap around “rigid” grains (**Fig. 5.55 C**). Fractured grains have a variety of grain sizes and shapes, patchy undulose extinction and internal shear bands that develop aligned aggregates of very fine recrystallized grains.

Amphibole occurs as fractured grains aggregates with varied grain sizes and orientations, normally surrounding larger relict grains (**Fig. 5.55 D**). Relict grains show some degree of fracturing with gentle bending or kinking of cleavage planes. They often display a texture similar to mantle and core, but it is fact effect of fracturing and not crystal plasticity.

Porphyroclasts are mainly composed of K-feldspar and plagioclase, with smaller proportions of quartz, amphibole and with mineral aggregates (feldspar+amphibole+quartz) forming well defined pressure shadows. Clasts shapes vary from elliptical to sub-rounded, with poorly developed asymmetric tails (**Fig. 5.55 E**). Feldspar clasts generally display a thin mantle of very fine recrystallized grains, moderate sweeping undulose extinction (**Fig. 5.55 F**) and strain induced twinning lamellae on the grain borders.

Biotite schists show a banded aspect, dark colour, relatively high mica content (see scanned thin sections in **Fig. 5.56 A, B** and **Fig. 5.57 A, B**) and marked tendency to break along foliation planes. They were classified as schists based on field observations (see field photos in **Fig. 5.20** and drill core examples in **Fig. 5.40**). However, examined under the microscope, the rocks reveal a prominent mylonitic foliation characterized by a fine grained matrix, strongly developed planar foliation, presence of lenses and layers of elongated mineral aggregates and porphyroclasts.

The schist protolith is an isotropic rock composed of strain-free sub-angular to sub-rounded quartz and k-feldspar crystals set in an aggregate of randomly oriented fine-grained biotite crystals (see scanned thin section and microphotography in **Fig. 5.58 A** and **B** respectively). This rock type corresponds to isotropic felsic metavolcanic rocks (see their distribution in **Fig. 5.19**) that are preserved in regions where the ductile deformation that formed the schists is low. In these protolith rocks, plagioclase, amphibole and chlorite veins cross-cut the rock (**Fig. 5.58 C, D, E, F**). Veins are typically massive with diffuse (**Fig. 5.58 C**) or sharp (**Fig. 5.58 E**) boundaries, and range in width from a few millimetres up to 2.5 cm. They suggest an axial growth process which generated blocky (**Fig. 5.58 F**) and elongate (actinolite crystals in **Fig. 5.58 D**) crystals either perpendicular or oblique to the vein walls.

The mylonites are typically fine (**Fig. 5.56 C, E**) to very fine (**Fig. 5.56 D, F**) grained, showing a well developed ductile fabric. The fabric is composed of alternating biotite-rich and quartz-feldspathic layers, with a high degree of mineral preferred orientation (**Fig. 5.56 E, F**). Variations in the quartz-biotite ratio within these layers controls the overall composition (see the difference between **Figs. 5.56 C** and **D**). Chlorite and epidote occur locally as products of secondary retrogression.

The observed foliation is typically continuous and parallel, wrapping around porphyroclasts and lenses. It varies locally, defining a weak sinistral S-C fabric.

Very-fine grained layers or bands are formed from a matrix of dynamically recrystallized biotite, quartz and K-feldspar that constitute a micro mosaic of mica crystals with a strong preferred alignment and unimodal grain-size distribution (e.g. **Fig. 5.56 F**). Mica grain size is proportional to its relative abundance, with the larger crystals associated with biotite-rich domains. Biotite commonly occurs between K-feldspar and quartz grain margins or inside the grains, indicating grain boundary pinning and secondary grain growth. Aggregate shape preferred orientations (ASPO) are defined by quartz or feldspar forming lenses elongated parallel to the main layering (e.g. **Fig. 5.59 A, B, C**). Quartz lenses show random, weak-to-moderate LPO (**Fig. 5.59 A**).

Thin quartz lenses, ribbons or “fish” typically display strong sweeping undulose extinction, subgrain development (**Figs. 5.59 B**) and newly formed grains (**Figs. 5.59 C**), indicating that during deformation SGRR and GBMR were active. Feldspar occurs as domains of fractured grains (see domino fracture feature in **Fig. 5.59 D**) or relict porphyroclasts. Fractured feldspars also form domains shaped as seams or lenses composed of finely fractured k-feldspar and plagioclase, showing homogeneous grain size distributions. Relict feldspar porphyroclasts sit in the matrix of recrystallized fine-grained quartz, feldspar and biotite. These relict porphyroclasts have a sub-rounded to slightly elongated shapes (**Fig. 5.59 E, F**). They do not show recrystallization and intracrystalline tensile fractures are often present. Tailing is absent or when observed, is poorly developed with unclear asymmetry.

Biotite schist domains contain deformed veins that vary from 1.5cm up to 5 cm in thickness and normally show a coarser grain size compared to the wall rocks.

The main minerals present are: quartz and K-feldspar, biotite and amphibole. Epidote, chlorite, and white mica are present as secondary alteration products. Veins can be subdivided into two groups based on their microstructures: (1) boudinaged (**Fig. 5.57 A**), displaying augen-shaped fragments composed of generally coarse grained mineral aggregates of quartz, feldspar, biotite and amphibole; or (2) sheared (**Fig. 5.57 B**), dominantly composed of quartz and subordinate feldspar. Boudinaged veins show minerals relatively well preserved in the centre of the veins, with recrystallized portions restricted to high strain zones localized in their outer margins. Quartz grains from the inner portions are virtually undeformed with patchy undulose extinction, limited subgrain boundaries and deformation bands (see contrasting quartz grains in **Fig. 5.57 C**). Grain boundaries are sharp and serrated. Recrystallized quartz has very similar microscopic features in both vein types: fine to very fine, dynamically recrystallized, elongated grains that form an oblique foliation indicative of sinistral shear sense (**Fig. 5.57 D, E**). Deformation in quartz grains from the veins is characterized by SGRR mechanisms. Recrystallized grains exhibit a relatively uniform grain size and strong LPO (**Fig. 5.57 F**). Feldspar grains show varied grain sizes and shapes from subhedral to sub-rounded. Intracrystalline fractures and shear bands are common deformational features, whilst some crystals seem to have experienced sub-grain rotation processes. Deformation in biotite is mainly represented by kinking and, in amphibole, by intracrystalline fracturing.

Veins, faults and hydrothermal features at Sequeirinho, record fluid activity associated with mineral deposition and hydrothermal alteration. This section summarises the microstructural aspects of these structures in order to assess the relationships between fluids and deformation.

Veins and *veinlets* are commonly found in the host rocks at Sequeirinho. Selected examples are presented in **Table 5.5**. They range in width from a few millimetres up to 10 centimetres. They typically comprise sets of sub-parallel and continuous master veins with subordinate anastomosing stockwork arrays and branching veins. Vein boundaries are either diffuse or sharp with irregular/regular shapes.

The veins are typically composed of: chlorite, epidote, amphibole, plagioclase, quartz, magnetite, Cu-sulphide or calcite. Commonly at least two mineral phases are deposited in layers within the cavity, but monomineralic veins also occur (**Fig. 5.60 A, B**). Massive and fibrous veins occur in roughly equal proportions. Massive veins are composed of blocky, elongate crystals oriented normal to the vein walls (**Fig. 5.60 C**). Fibrous veins are mainly formed of chlorite and amphibole with mineral fibres oblique or sub-parallel to vein walls (**Fig. 5.60 D**). Fibrous infills are also present in composite veins, generally forming the inner portion of the cavity when associated with quartz and plagioclase.

Most of veins show an internal structure characterized by layering or zoning that comprises either: (1) monomineralic grain size zoning with fine grains in the outer and coarse grains in the inner portions of the vein; or (2) two mineral phases forming/developing blocky, fibrous or blocky-fibrous layering. Solid (mineral) and fluid inclusions are widespread in quartz and feldspar grains. These occur as parallel discontinuous bands or random clusters together with subordinate wall rock fragments.

The degree of deformation and recrystallization in the veins is variable with the presence of both recrystallized and undeformed/preserved phases of the same mineral. Other than calcite and chlorite, most mineral phases show evidence for

either crystal plastic or brittle deformation (**Fig. 5.60 E**). Folded veins are rare and were only widely developed in the biotite schist domain (**Fig. 5.60 F**). Veins are normally cross-cut by faults, fractures and other veins.

Faults invariably show mineral precipitation onto the fault surface. They are distinguished from veins and mineral filled fractures by the presence of slip surfaces, comminuted wall-rock fragments or offset markers.

The geometry of single faults is characterized by a well defined, relatively smooth, straight slip surface varying in thickness from narrow discrete planes to wider fault zones. Narrow single fault planes are 1-2 mm wide, varying in width along their length. The fault planes are composed of a dark brownish cryptocrystalline material, perhaps iron oxide-stained, precipitated minerals or wall rock fragments in varied sizes and elongate euhedral to sub-rounded shapes (**Fig. 5.61 A, B**). Displacement observed along these faults ranges up to 20 mm.

Fault zones comprises parallel sets of slip surfaces with secondary, obliquely oriented fault branches projecting off the main slip surfaces (**Fig. 5.61 C, D**). Comminuted wall-rock fragments with varying shapes and sizes occur within the zones and are totally or partially altered into chlorite, epidote or sericite (**Fig. 5.61 E**). Fine to very-fine sub-rounded fragments occur along the master slip surfaces (**Fig. 5.61 F**). First and second order faults are effectively interconnected, leading to the development of a crude foliation within the fault zone.

Chlorite, iron oxide and epidote are the main mineral phases associated with faults and fault zones. These minerals are precipitated along the structures, filling open spaces or forming alteration haloes. Chlorite occurs as fibrous elongated grains,

oriented parallel or oblique to the fault planes. Epidote occurs as a granular mass normally mixed with chlorite in varied proportions.

5.9.2 Sossego

For the Sossego orebody, microstructural observations were made for the host rock, its deformed equivalents and in mineralized veins.

Granophyre granite is the dominant lithology in the mine (see macroscopic examples in **Fig. 5.4 E** and **Fig. 5.38 E**). It is a coarse-grained isotropic granitoid formed of K-feldspar, quartz, plagioclase and minor amounts of opaque oxide minerals. Intense micrographic and radiating intergrowths of quartz and K-feldspar are the distinguishing textural features of this rock (**Fig. 5.62 A**).

Quartz shows little evidence of dynamic recrystallization. Instead, it shows lobate grain boundaries and uniform extinction. Sub-grains are rare. Feldspars show no undulose extinction and when deformed develops fine grained aggregates of fractured grains. Very fine fibrous chlorite and subordinate sulphides are deposited along a pervasive network of late micro fractures.

Mylonites and *ultramylonites* are products of localized shear zone development within the granophyre granite. Mylonites typically show an anastomosing continuous foliated matrix that wraps around augen-shaped feldspar fragments, occasionally forming S-C fabrics. In localized mica-rich portions, foliation is straight, and eventually forms S-C' fabric (**Fig. 5.62 B**). The matrix is commonly composed of medium-fine grained recrystallized quartz, biotite and feldspars – the latter severely altered to sericite, clay minerals and minor epidote.

Quartz is dynamically recrystallized forming porphyroclasts and elongated lenses or ribbons (**Fig. 5.62 C**), which are strongly flattened, totally or partially recrystallized indicating SGRR. New grains form polygonal aggregates with a unimodal grain size and limited examples of oblique foliation. Subgrain domains show strong undulose extinction with either elongate or subhedral grain shapes.

Quartz clasts have sharp boundaries with the matrix and are represented by: (1) “fish” objects with irregular/sweeping undulose extinction (**Fig. 5.62 D**); (2) mantled clasts with an undulose core and a mantle of sub-grains and/or newly formed polygonal grains (**Fig. 5.62 E**); and (3) sigmoids of subgrains and new grains (**Fig. 5.62 F**). Rare feldspar relicts occur as naked clasts being invariably saussuritized. The main SPO is defined by aligned quartz ribbons forming the foliation. An LPO is present in domains where subgrains and new grains coexist. Subgrain rotation and grain boundary migration are the dominant operative deformation mechanisms. The studied samples do not show consistent shear senses.

Ultramytonites are characterized by well defined millimetre-scale bands (**Fig. 5.63 A**) formed of a fine matrix (<30 μm) containing varied proportions of quartz, K-feldspar, plagioclase, and chlorite. Sub-rounded relicts of quartz, feldspars and sulphide, form porphyroclasts within the matrix (**Fig. 5.63 B, C**). The matrix typically shows alternating felsic/mafic rich bands of fine grains that possess no marked SPO or LPO. Foliation is straight with the localized development of anastomosing fabrics. It is marked by elongated chlorite and sulphide grains (**Fig. 5.63 D**). Quartz is dynamically recrystallized occurring as clusters or ribbons of polygonal new grains or subgrains formed by SGRR. Feldspars are intensely saussuritized and display reduced grain size by fracturing. Porphyroclasts can be

naked or occur as winged σ -type mantled clasts. GSPO and LPO are absent.

Mineralized and barren veins are widespread at Sossego and can be classed as shear or tensile features. Their mineral assemblages comprise: calcite, quartz, chalcopyrite, magnetite, albite, k-feldspar, chlorite, \pm biotite, \pm white mica

Vein walls typically show a 5 mm or less wide hydrothermal chlorite or biotite halo associated with intense microfracturing and subordinate veining. Thinner vein branches are commonly projected from the master fracture into the wall-rocks. Sheared boundaries characterise veins initiated by non-coaxial extension (**Fig. 5.64 A**). They are typically a few millimetres wide, fine grained, comprising micas, quartz and k-feldspar and subordinate sulphide that forms aggregates oblique to the vein walls. The majority of these veins show an abrupt change from the sheared fabric to a granular isotropic texture.

Tensile veins have no apparent fabric and show a granular texture with heterogeneous grain size distribution (**Fig. 5.64 B**). Internal zoning is common and characterized by stratified domains, sub-parallel to the vein walls with distinct grain sizes and mineralogical characteristics. In the centre of the veins, minerals are subhedral/euhedral with sharp straight boundaries. Towards vein walls, crystals show interlocked, lobate or sub-rounded boundaries.

Deformation within the veins is relatively limited, mostly accommodated within sheared domains. Quartz shows uniform undulose extinction, deformation lamellae and several trails of fluid and solid inclusions. Subgrains can be present, but are generally rare. Calcite typically displays large grains with sulphide inclusions, serrated boundaries and tabular thick twins. Strain is manifested by the development

of locally curved twins, irregular undulose extinction and subordinate recrystallized grains. K-feldspar occurs in a variety of grain sizes and shapes from sub-rounded to euhedral. The crystals are fractured and have corroded boundaries when in contact with calcite. Undulose extinction, when present, is weak.

5.9.3 Interpretation of the microstructural observations

5.9.3.1 Ductile Features

A summary of the ductile microstructural features and estimated temperatures of each of the dislocation creep regimes proposed by (Hirth et al. 1992) is presented in **Table 5.6**.

The little deformed and weakly deformed wall-rock domains comprise isotropic granites and metavolcanics at Sequeirinho and granophyre at Sossego. Generally these rocks show little evidence of crystal plastic deformation, although weakly developed Regime 1 dislocation creep characteristics were identified in a few samples.

The mylonites and ultramylonites at Sossego show microstructural features compatible with Regime 2. At Sequeirinho, similar mylonitic fault rocks and foliated granitoids were interpreted to have deformed at conditions compatible with the transition between Regime 2 and Regime 3.

The microstructural observations from quartz indicate that deformation occurred under the following conditions: ~300-400°C (lower to middle greenschist facies) in Sossego; and ~400-500°C (middle to upper greenschist facies) in Sequeirinho. Additionally, the minor presence of recrystallized feldspar at

Sequeirinho is consistent with temperatures that possibly exceeded 500°C in this orebody, since crystal plastic deformation of feldspar generally occurs at higher temperatures compared to quartz (Tullis et al. 1985; Bell et al. 1989).

These temperature estimated agree well with results presented by (Monteiro et al. 2008) who suggest temperatures using oxygen isotope partitioning data between mineral pairs as > 500°C for Sequeirinho and ~460°C for Sossego.

The coeval occurrence of microstructural features from Regime 2 and Regime 3 at Sequeirinho is possibly related to the presence of fluid. (Hirth et al. 1992) and; (Tullis 2002) demonstrate that the transition from Regime 2 to Regime 3 can occur due to the addition of trace amounts of water, since dislocation creep flow strengths depend on water fugacity. Widespread evidence of fluid activity in the studied samples is marked by: (a) the pervasive alteration of feldspars and micas; and (b) the precipitation of sulphides and magnetite along the mylonitic foliation. These observations make it very likely that the ductile deformational processes were intimately influenced by the presence of fluids.

5.9.3.2 Kinematic Indicators & Porphyroclasts

Oblique foliations and mineral fish indicate an overall sinistral shear sense for the mylonites. These features are considered to be reliable shear sense indicators (Passchier et al. 2005), but they are not observed in all the studied samples. The presence of σ -type porphyroclasts indicates that the shear flow regime favoured relatively high recrystallization rates at low shear–strain rates (Passchier 1986).

Porphyroclasts display both sinistral and dextral shear senses with approximately 60:40 relative proportion. This ambiguous character may not be useful to determine the overall shear sense, but can give insights into the operative shear regime. (Simpson et al. 1993) demonstrated that in shear zones with a component of both pure and simple shear, porphyroclasts may rotate in directions opposite to that of the bulk flow regime. In summary, microstructural observations on mylonites indicate an overall sinistral shear sense with dextral components, which are consistent with transpression.

5.9.3.3 Brittle Features

Shear zones, veins and faults are ubiquitous in both deposits. These structures record important hydrothermal activity under brittle-ductile conditions and play a major role in controlling the genesis and architecture of the mineral deposits.

Observations on mineral filling highlighted mono and poly- mineralic veins. Massive, monomineralic veins are interpreted to have formed by a relatively simple growth history with a single phase of vein opening and sealing. The second group includes veins with multiple mineral fillings, which are interpreted as having opened episodically with associated temporal changes in fluid composition. Elongate crystals, fibrous mineral fills, the development of wall rock inclusion bands and fluid inclusions trails are indicative of crack–seal mechanisms similar to those described by several authors (e.g. (Ramsay 1980; Cox et al. 1983; Ramsay et al. 1987). Such models generally consider the repetition of a sequence of events to form a vein, involving: (1) crack opening, driven by fluid pressure increase; (2) fluids percolating along extension fractures with further precipitation of new crystalline materials onto

the fracture walls; (3) crack sealing leading to build up of tectonic stresses until the critical failure stress is reached causing a new failure; and (4) the new vein forms inside the earlier one splitting it into two parts, or forms along one of the vein-wall contacts. Vein sealing continues until there is wall to wall cohesion. This cycle is repeated and may form wide veins made up of numerous composite microveins, which appears to work well for the veins at Sossego.

5.9.3.4 Veins and temperature

Minimum estimated temperature conditions during vein formation were constrained using indirect evidence. Some of the observed veins are composed of fibrous aggregates and were interpreted as formed by crack-seal mechanisms. According to (Ramsay 1980), crack-seal veins are formed during deformation where temperature and pressure conditions were below upper greenschist facies. They also state that fibrous forms of crystal infills in veins are unstable at temperatures higher than 350°C. Therefore, this can be interpreted as the maximum temperature for the formation of crack-seal fibrous veins. Additionally, (Passchier et al. 2005) suggest that twin geometries in calcite are one of the most promising temperature gauges to be used. Calcite twins from veins at Sossego were classified as Type II (tabular thick twins) following the standard geothermometry classification (Burkhard 1993; Ferrill et al. 2004). These “thick twin” types indicate temperatures greater than 170°C and less than 250°C. This constrains the minimum and maximum temperatures for this late-stage phase of hydrothermal mineralization.

The greenschist facies minerals (i.e., epidote, chlorite, calcite) are generally found within high temperature veins estimated to have formed at 400°C to 600°C by (Monteiro et al. 2005).

5.9.3.5 Faults & Fault Zones

Fault zones are characterized by slip surfaces often associated with phyllosilicate-rich planar fabrics and the presence of comminuted wall rock fragments mixed with hydrothermal minerals. Microstructural observations on fault zones provide evidence for cataclastic deformation coupled with hydrothermal fluid influx. Cataclasis is defined as deformation involving repeated brittle fracturing of grains operated by sliding and rotation of the fragments past each other and further fragmentation of these into smaller particles (Sibson 1977; Passchier et al. 2005). This process is restricted to shallow levels in the crust (<10km) generally at relatively low temperatures and higher strain rates (Sibson 1977; Evans 1988). Heterogeneous degrees of fragmentation were observed in the fault zones, marked by variations in clasts average size and roundness. Hydrothermal minerals are ubiquitous within the faults. Epidote and chlorite were the main mineral phases identified along slip surfaces, filling open spaces and replacing altered minerals (especially feldspars).

Dilatancy associated with brittle deformation allows fluid influx, and fluids are crucially important to fault behaviour (Snoke et al. 1998). They may promote fault weakening by: (1) reducing the effective stress (Miller et al. 1997); (2) causing stress corrosion around crack tips (Kerrick 1986a); or (3) causing reaction of the finely comminuted material with water to form weaker mineral phases (Mitra 1978). Syn-tectonic growth of epidote, chlorite and alteration of feldspars into fine grained

aggregates of epidote and micas are evidence of channelized fluid flow possibly facilitated by a pervasive fracture network (Jefferies et al. 2006). The fluids are interpreted to be related to the earthquake cycle on faults; during inter-seismic periods precipitation causes decreasing permeability and increasing fluid pressure, leading eventually to rupture, which then increases the permeability and decreases the fluid pressure (Sibson 1990; Snoke et al. 1998). These cyclic processes described as seismic pumping and fault valve behaviour (Sibson 1990) are particularly likely to occur towards the base of the seismogenic zone along high angle reverse faults, where metamorphic fluids develop a high fluid pressure due to the low permeability cap produced at the brittle-plastic transition (Etheridge et al. 1983). This setting is consistent with the observed sinistral transpressional tectonic regime associated with the development of the Sequeirinho and Sossego mineral deposits.

5.10 Tectonic Interpretation

The sequence of the major geological events in the study area is described based on the multi-scale structural data herein presented, and the previously published geochronological data.

The basement in the area comprises reworked granite-gneisses dated at 3.0 to 2.9 Ga. These rocks represent products of early Precambrian tectonics and are not exposed in the studied mines. The forming processes of these rocks are unclear, but appear to be comparable to the vertical tectonics processes (i.e. diapirism) described in the adjacent Rio Maria Granite Greenstone Terrane to the south.

The metavolcanics and schists present in the north of the mines may represent tectonised fragments of the volcano-sedimentary sequences of the Grão Para Group, which lie nearby. These rocks were deposited in an intracratonic basin formed at 2.8-2.7 Ga. The regional extensional regime that formed the basin, led to the emplacement of 2.7 Ga. granitoids (e.g. Estrela, Planalto, Serra do Rabo and Plaque Suite), that are dominant in the mines and host the bulk of the copper mineralization. Both metavolcanics and granitoids can be considered as the potential sources for the metals deposited during mineralization.

Tectonic inversion of the basin initiated at about 2.7 Ga, lasting up to 2.6 Ga. The basin inversion involved a regional phase of sinistral transpression controlled by a general NNE-directed oblique shortening with angle of relative shortening (α) of approximately 20° Az relative to the geographic north (see **Fig. 5.65**). Shortening produced a pervasive sub-vertical ductile fabric with 15° swing from E-W to WNW-ESE trending foliation (see stereonets in **Fig. 5.15 A** and **Fig. 5.23 A** and field photos in **Figure 5.20** and **Fig. 5.22 A and F**). The steeply plunging mineral lineation associated with the steep foliation, indicates that the principal shortening and extensional axes were approximately oriented near the horizontal and vertical positions respectively. Shear criteria observed in mylonites is consistent with sinistral transpression. Transpression was accompanied by metamorphism with conditions compatible with lower-to-middle (~ 300 - 400°C) and middle-to-upper (~ 400 - 500°C) greenschist facies.

As deformation progressed, it is proposed that the rocks locally reached their limit of mechanical plasticity promoting nucleation and propagation of NE-SW sinistral brittle-ductile shear zones and faults (e.g. **Fig. 5.65**). These structures are

evident in the aeromagnetic survey and at map scales curving and dragging early WNW-ESE structures (e.g. **Fig. 5.8 B** and **Fig. 5.9 B and C**).

At 1.8 Ga granitic plutons were intruded the basement domain during a later region phase of crustal extension. The Rio Branco Granite, adjacent to Sequeirinho belongs to this generation of granitoids. Despite the lack of isotopic dating, this granite shares petrological, textural and structural characteristics with other 1.8 Ga. anorogenic granites recognised in the region (e.g. Cigano and Central granites).

Mineralization appears to have formed at during the late stages or shortly after the 2.7-2.6 Ga transpressional event. Published isotopic ages constrain the time of mineralization between 2.6 and 2.5 Ga e.g. (Neves 2007) in Sequeirinho, under rheological conditions compatible with semi-brittle and brittle regimes. The mineralization at Sossego, compatible with dominantly brittle rheological conditions, was dated at ~1.5 Ga by (Neves 2007). The age has limited genetic significance because is not comparable with other ages obtained for copper mineralization in the region. Collectively, the copper mineralization in Sossego and Sequeirinho is probably linked to the major thermo-tectonic event at 2.7-2.6 Ga., when the interplay between deformation-metamorphism-magmatism provided the source metals, transporting fluids and the structures where the mineralization was hosted.

5.11 Fragmentation Mechanisms

Based on clasts shape analysis and fractal D -values, breccia bodies can be separated according to the intensity of their experienced shearing:

- low shearing breccias (*Sossego*): relatively high clasts angularity and smaller D -values are characteristic of immature explosion breccias. These correspond to the early products of fragmentation dominated by particles fracturing and cracking that generate coarse and angular fragments.

- high shearing breccias (*Sequeirinho*): rounded fragments with low angularity and higher D -values are typical of more mature breccias. They represent a further, later stage of particle fragmentation, dominated by wear and attrition when particles interact by rolling, sliding and rotation during subsequent slip along a fault zone (Blenkinsop 1991; Hattori et al. 1999; Keulen et al. 2007). Interestingly, the decrease in particle angularity can help promote a continuous reduction in friction during fault displacement, possibly favouring fault weakening processes (Mora et al. 1999) and reactivation.

Despite the differences in their degree of fragmentation, the breccia bodies share some characteristics with important implications for their genetic interpretations. Firstly, geological observations suggest that the brecciation process was repeated (seismogenic??). This assumption is reinforced by the presence of multiple variants of breccias that represent different products of brecciation cycles. Secondly, the presence of alteration halos in the clasts is evidence that breccia fragments experienced transport in the presence of chemically reactive fluid phases. These interpretations permit speculation that the breccias were formed by single rapid events related to the quick release or increase of fluid overpressure. This is

consistent with the suggestion that breccia formation is at least partially controlled by cyclic variations in shear stress during the seismic cycle, and by fluctuations in fluid pressure, which are associated with deformation-induced changes in fault permeability during fault-valve behaviour.

5.12 Implications for exploration

The Sossego and Sequeirinho orebodies are important examples of medium to large IOCG deposits. These deposits, together with the Salobo, Cristalino and Target 118 deposits confirm the potential of the Carajás area for future prospects of this class and suggest that the Amazon Craton needs to be considered for further exploration of Archaean-Proterozoic IOCG deposits.

Soil geochemistry and geophysics have been the most used and successful exploration methods applied in the search for IOCG deposits in Carajás. Geophysics has proved to be a robust tool for prospecting these types of deposit, playing important roles in the location of large discoveries in Finland, Australia, Africa and Canada, especially the use of magnetometry. However, despite several examples of IOCG deposits around the world displaying close spatial association with major structures (i.e. faults or shear zones), structural criteria still seem to be viewed as being of secondary importance in the strategy of exploration campaigns. This is clearly inappropriate since it is widely accepted that major mineralised hydrothermal systems develop sufficient connectivity to create networks that link fluid source rocks to favourable sites for ore deposition (Jiang et al. 1997; Cox 1999). Relatively well-connected faults thus have the potential to form long-distance fluid

channelways and ore deposition may occur at specific structural sites such as terminal fault branches, fault offsets/jogs, faults in particular orientations, and smaller faults connecting larger faults (Stephens et al. 2004).

The data presented on this work agrees with other examples in the literature showing that the structural-tectonic framework represents one of the key elements in controlling the formation major mineralized IOCG systems. It is therefore suggested that the search and identification of crustal scale structures should become part of the exploratory strategy. These structures have the potential to act as fluid pathways, and parts of the system can act as traps of hydrothermal fluids at both regional and local scales. In summary, for exploration on the basement terrain of the Carajás Region it is recommended that careful observations should be focused on magnetic anomalies corresponding to NE-SW sinistral structures and, in particular on their intersections with the WNW-ESE regional trend.

5.13 Conclusions

The integration of data at map, mesoscopic and micro scales and its interpretation permits to the following conclusions to be made:

The deposits sit in the basement domain of the Canaã dos Carajás region including 2.9 Ga. Archaean gneisses intruded by 2.7 Ga syntectonic granitoids. These rocks display a widespread sub-vertical WNW-ESE ductile fabric formed at amphibolite facies.

The structural framework of the area consists of regionally developed WNW-ESE structures (foliations and shear zones) offset by NE-SW sinistral faults observed

at magnetic surveys and geological maps. The Sequeirinho orebody is hosted along a NE-SW sinistral fault, associated with positive magnetic anomaly whilst the Sossego orebody does not show obvious link to a major structure or prominent magnetic anomaly.

The main phase of deformation and mineralization took place at 2.7-2.6 Ga. under a region regime of sinistral transpression. Strain was heterogeneously accommodated defining low strain domains separated by high strain, mylonitic shear zones showing gradual boundaries. The transpressional deformation produced a ubiquitous sub-vertical foliation and locally developed steep mineral lineation; sinistral shear criteria are dominant. Microstructural observations of quartz and feldspar indicate that the sinistral transpressive deformation at Sossego and Sequeirinho initially took place under low-to-middle (300-400°C) and middle-to-upper (400-500°C) greenschist facies, respectively. The relatively high-temperature fabrics were then overprinted by a late brittle-ductile structures and veins containing the main copper mineralization and lower-temperature minerals interpreted to be formed at between 170 up to 250°C.

Hydrothermal fluid flow was ubiquitous in both thermal regimes, intimately associated with high strain zones and nucleation/development of structures. Fluid circulation caused intense mineral alteration (particularly of feldspars) and precipitation of new minerals, some of them weak. What may have promoted fault weakening, possibly facilitating later fault reactivation. The evidence of temporal changes in fluid composition and the presence of ultracataclasites in some faults can be indicative of episodic fault slip triggered by fluid overpressure e.g. fault valve behaviour.

The Sossego ore body comprises a sub-vertical pipe-like feature with an inner breccia body surrounded by a stockwork array of sulphide veins faults and shear zones (**Fig. 5.65**). By contrast, the Sequeirinho deposit is formed by a sub-vertical, NE-SW tabular breccia body hosted along a fault (**Fig. 5.65**).

Both orebodies record intense hydrothermal activity with varied mineral alteration assemblages developed along faulted and sheared domains. Faults and shear zones acted as fluid pathways facilitating episodic fluid flow that formed the sulphide mineralization and caused pervasive alteration on the host rocks.

The studied breccia bodies show distinct textural characteristics and fractal D values. Sossego comprises immature breccias formed by fracturing and cracking assisted by highly pressurized fluids that produced coarse and angular fragments. Sequeirinho contains mature breccias formed by processes dominated by wear and attrition of particles consistent with episodic slip along a fault zone.

The intrusion of granitoids and subsequent metamorphism during sinistral transpression were the potential sources for the fluids that promoted widespread hydrothermal alteration and formed the mineralization when mixed with surficial fluids. The late emplacement of the 1.8 Ga. anorogenic granites may also have caused further fluid circulation that promoted some remobilization of mineralization.

Ultimately, the presented findings suggest that the rocks in the area of the mines record deformational processes that initially took place under the viscous regime (>15km), represented by mylonites and ultramylonites. Progressive exhumation, possibly synchronous with regional transpressional thickening led to conditions compatible with the frictional-viscous regime and intense fluid activity,

with mineralisation. Finally “dry” fractures and faults were later formed under a frictional regime.

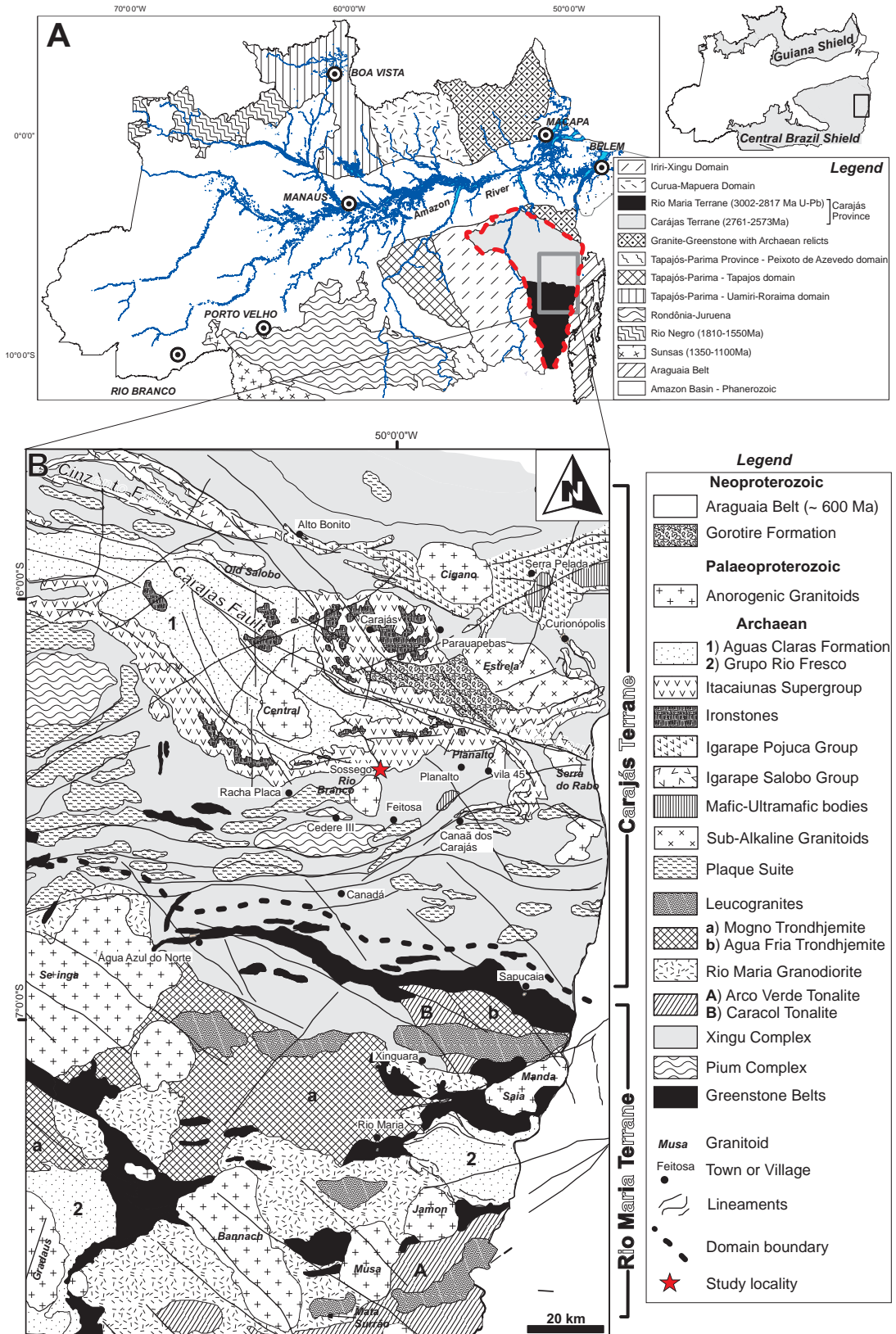


Figure 5.1 *A* The Amazon Craton and its geochronological provinces according to Santos, 2000; the highlighted red dashed polygon indicates the limits of the Carajás geochronological Province. *B* Geological map of parts of the Carajás and Rio Maria Terranes with the location of the Sossogo deposit (star).

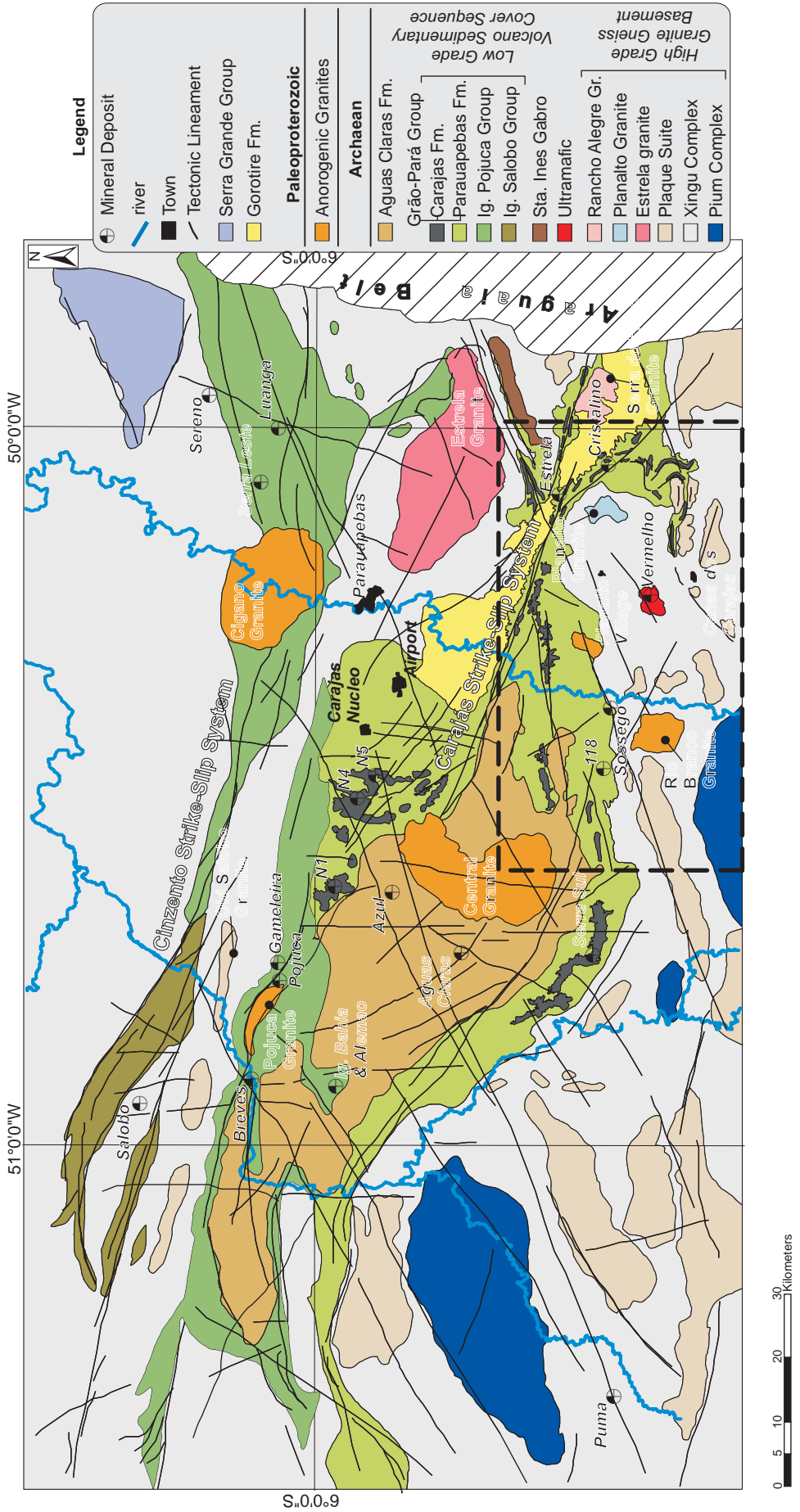


Figure 5.2 - Geological map of the Itacatiúas Belt and its main tectonic features, lithologic domains, and ore deposits. The studied Sossego deposit is located near to the Rio Branco Granite at the southeastern portion of the map. The dashed line indicates the location of the magnetic survey and lineaments presented in Fig. 5.7

Supergroup	Group / Formation	Intrusive Rocks	Lithology	Age (Ga)	Method	Author		
Proterozoic Anorogenic Granites	[]	Cigano Granite	Granite	1.883 ± 3	ZR U-Pb	Machado et al. (1991)		
		Carajás Granite	Granite	1.880 ± 2	ZR U-Pb	Machado et al. (1991)		
		Carajás Granite	Granite	1.820 ± 49	ZR U-Pb	Oliszewski et al. (1989)		
		Pojuca Granite	Granite	1.874 ± 2	ZR U-Pb	Machado et al. (1991)		
		Breves Granite	Episyenite	1.880 ± 9	ZR SHRIMP II	Tallarico et al. (2004)		
		Breves Granite	Granite	1.878 ± 8	ZR SHRIMP II	Tallarico et al. (2004)		
		Young Salobo Gran.	Syenite	1.88 ± 80	W-R Rb-Sr	Cordani (1981)		
		Águas Claras	Gabbro	2.645 ± 12	ZR Pb-Pb	Dias et al. (1996)		
		Grão-Pará	volcanic sill	2.751 ± 4	ZR Pb-leach	Krymsky et al. (2002)		
		Grão-Pará	Rhyodacite	2.759 ± 2	ZR U-Pb	Machado et al. (1991)		
Cover Assemblage	[]	Mylonitised Metarhyolite	Rhyolite	2.757 ± 7	ZR SHRIMP	Trendall et al. (1998)		
			Rhyolite	2.758 ± 39	ZR U-Pb	Macambira & Lafon (1995)		
		Rhyolite	Rhyolite	2.757 ± 18	ZR Pb-Pb	Macambira et al. (1996)		
			Aphibolite	2.732 ± 2	ZR U-Pb	Machado et al. (1991)		
		Garnet-Biotite-Schist	Garnet-Biotite-Schist	2.668 ± 60	WR Sm-Nd	Lindenmayer et al. (2001)		
			mafic intrusive rocks	2.705 ± 2	ZR Pb-Pb	Galarza et al. (2002b)		
		Meta Gabbro/Andesite	Meta Gabbro/Andesite	2.757 ± 81	WR Sm-Nd	Pimentel et al. (2003)		
			Rhyolite	2.740 ± ?	ZR U-Pb	Wirth et al. (1986)		
		Itacaiunas Group	[]	Aphibolite	Aphibolite	2.761 ± 3	ZR U-Pb	Machado et al. (1991)
				Gneiss	Gneiss	2.851 ± 4	ZR U-Pb	Machado et al. (1991)
BIF	BIF			2.551 ± 2	MI U-Pb	Machado et al. (1991)		
Basic granophyre	Basic granophyre			2.577 ± 144	WR Rb-Sr	Ferreira Filho (1985)		
	metapyroclastic			2.747 ± 1	ZR Pb-Pb	Galarza et al. (2002)		
Meta volcanic/pyroclastic	Meta volcanic/pyroclastic			2.759 ± 24	WR Sm-Nd	Santos (2002)		
	Metavolcanic			2.748 ± 34	ZR SHRIMP	Tallarico et al. (2005)		
Metavolcanic	Metavolcanic			2.624 ± 8	ZR SHRIMP	Tallarico et al. (2005)		
	Anorthosite			2.763 ± 6	ZR U-Pb	Machado et al. (1991)		
Ultamafic	[]			Luanga Complx.	Granitoid	2.560 ± 37	ZR Pb-Pb	Souza et al. (1996)
		Itacaiunas Granite	Granitoid	2.525 ± 38	ZR Pb-Pb	Souza et al. (1996)		
		Itacaiunas Granite	Granitoid	2.573 ± 2	ZR U-Pb	Machado et al. (1991)		
		Gelaadinho Granite	Gelaadinho Granite	2.688 ± 11	ZR Pb-Pb	Barbosa et al. (2001)		
			Estrela Granite	2.527 ± 68	WR Rb-Sr	Barros et al. (1992)		
		Estrela Granite	Estrela Granite	2.763 ± 7	ZR Pb-Pb	Barros et al. (2001)		
			Serra do Rabo Granite	2.743 ± 1	ZR U-Pb	Sardinha et al. (2002)		
		Planalto Granite	Planalto Granite	2.747 ± 2	ZR Pb-Pb	Huhn et al. (1999)		
			Granitic Leucosome	2.859 ± 2	ZR U-Pb	Machado et al. (1991)		
		Basement Assemblage	[]	Felsic Gneiss	Felsic Gneiss	2.851 ± 4	ZR U-Pb	Machado et al. (1991)
Amphibolite	2.519 ± 5				TI U-Pb	Machado et al. (1991)		
Granulite	Granulite			3.050 ± 114	WR Pb-Pb	Rodrigues et al. (1992)		
	Enderbite Protolith			3.002 ± 14	ZR SHRIMP	Pidgeon et al. (2000)		
Granulite	Granulite			2.859 ± 9	ZR SHRIMP	Pidgeon et al. (2000)		
Xingu Complex	[]			Xingu Complex				
				Xingu Complex				
				Xingu Complex				
				Xingu Complex				
Plum Complex	[]	Plum Complex						
		Plum Complex						

Table 1 – Collection of key isotopic ages for the rocks at the Carajás Terrane, grouped into basement and cover assemblages, Archean and Proterozoic granites. The isotopic ages generally date the time of crystallization of the rocks.

Chapter 5

Age (Ga)	Event	Kinematics
Present day	Reactivation of fault system recorded by recent small-scale seismicity	Uncertain
0.24-0.15	Brittle reactivation of fault systems during opening of the South Atlantic in the Mesozoic	Extension
1.92-1.88	Intrusion of granite plutons and dyke swarms Weak tectonic inversion by fault reactivation with moderate to strong Brittle-ductile deformation of the rocks adjacent to the Carajás Fault	Extension or transtension Sinistral transpression (sinistral strike-slip faults, reverse faults, folding)
2.6-2.5	Emplacement of granitic intrusions, e.g. Old Salobo Development and further brittle reactivation of the Carajás and Cinzento strike-slip systems. Intrusion of sills and dykes and formation of the Carajás Fault	Dextral transtension (small dextral strike-slip on E-W and NW-SE faults)
2.8-2.7	Volcanism and deposition of the Grão-Para; Igarapé Salobo, Igarapé Bahia and Igarapé Pojuca Groups , with the later deformed and metamorphosed under very-low to medium temperature conditions Emplacement of syntectonic granitoids, e.g. Estrela, Plaque Suite, Planalto Formation of the Itacaiunas Shear Belt by high temperature ductile deformation affecting the basement rocks	Sinistral transpression Sinistral transpression Sinistral transpression
3.1-2.9	Formation of the tonalitic gneisses of the Xingu Complex and Pium	

Table 2 Summary of the main tectonic events, their age intervals, products and kinematics recorded in the Carajás Region. After Pinheiro and Holdsworth 1997 and Holdsworth and Pinheiro, 2000.

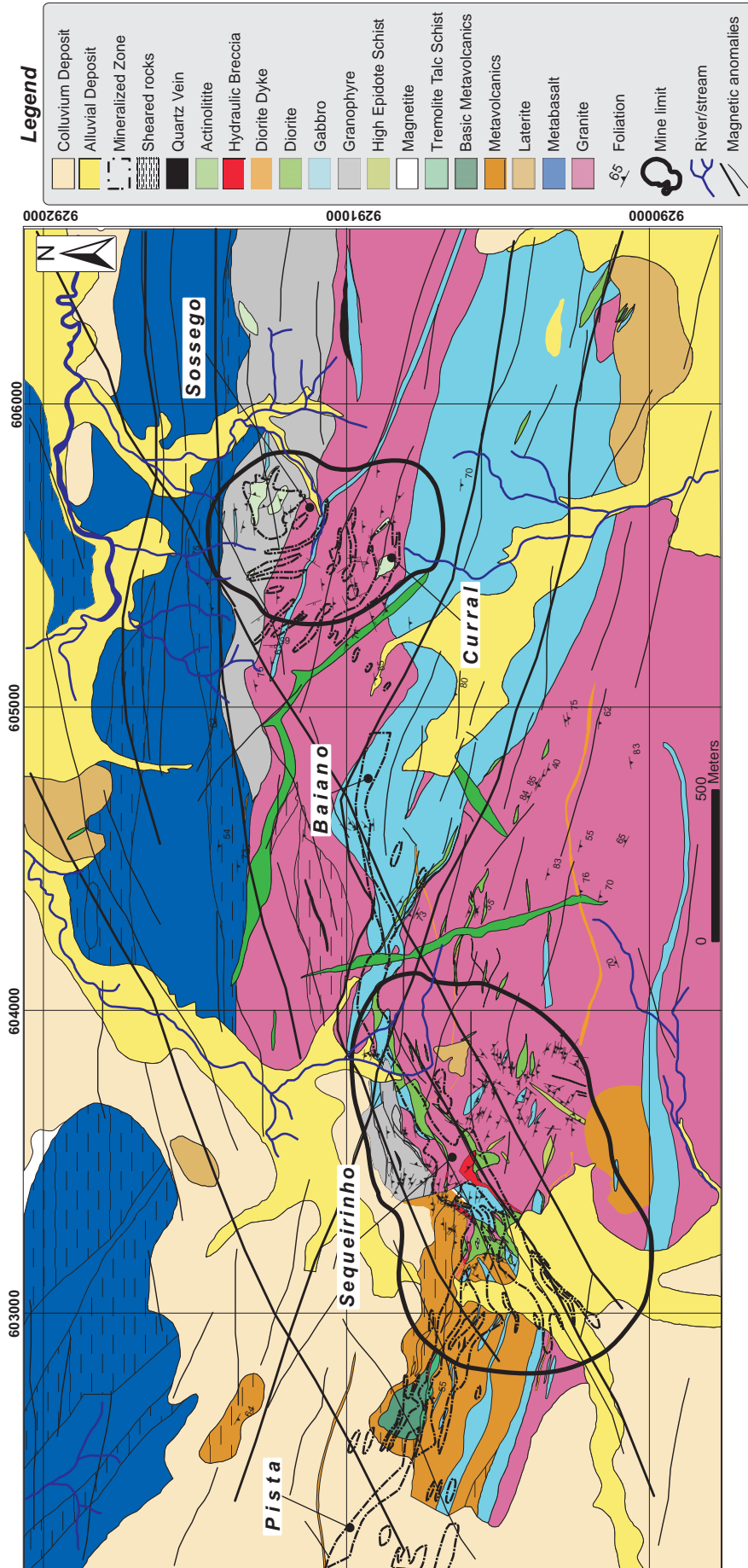


Figure 5.3 - Detailed geological map of the area hosting the studied deposits (Sossego and Sequeirinho) and satellite orebodies (Pista, Baiano and Curral). Cartographic coordinates UTM, Zone 22South, Datum WGS84. Modified from CVRD/MSS.

Sossego Deposit - Rock types

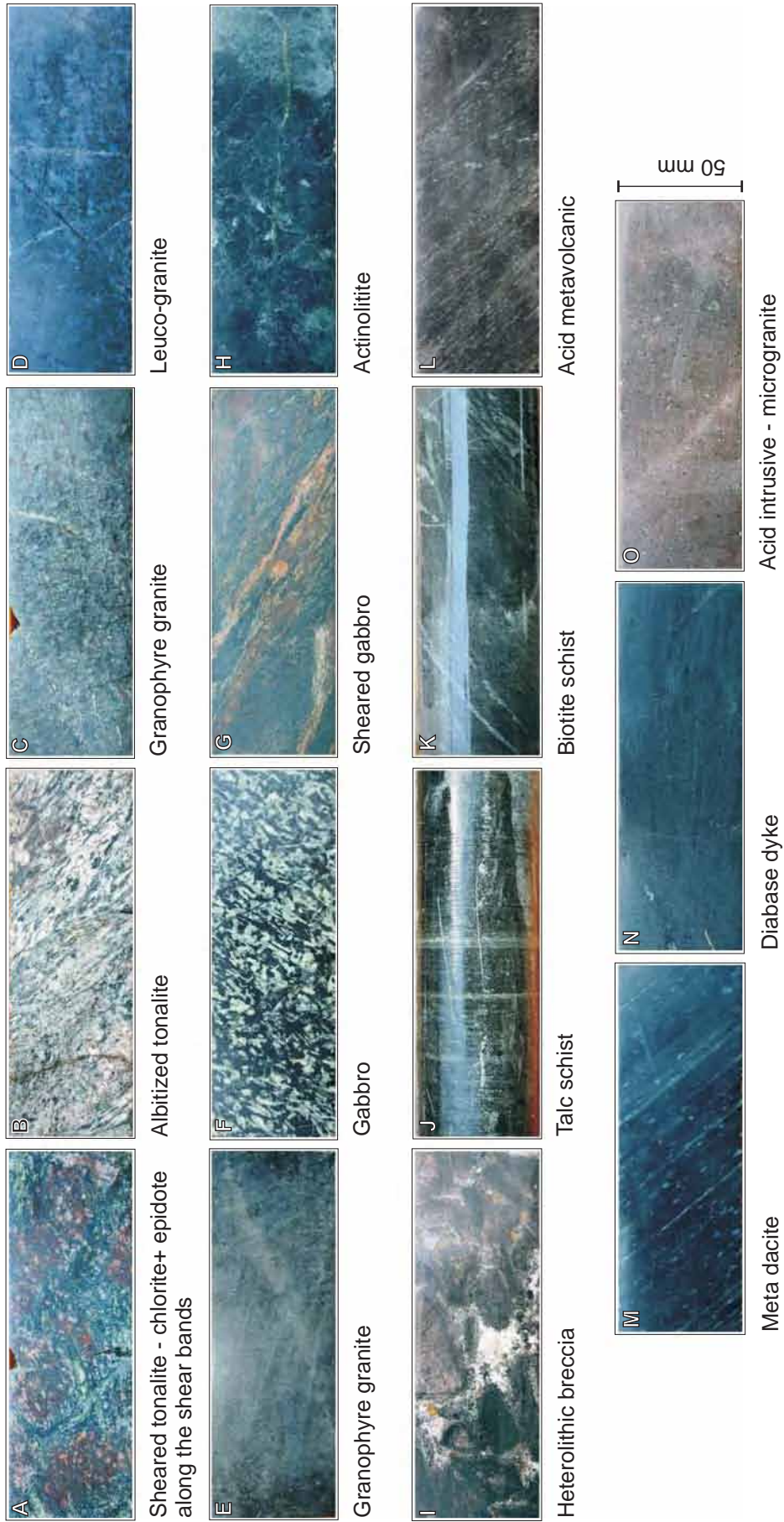


Figure 5.4 - Photographic composition of representative samples from the main types of wall-rocks present in the deposits. These photos correspond to the lithological units on the geological map from fig. 04. Approximated width of drill-core = 50 mm.

Sossego Deposit - Mineralization Styles

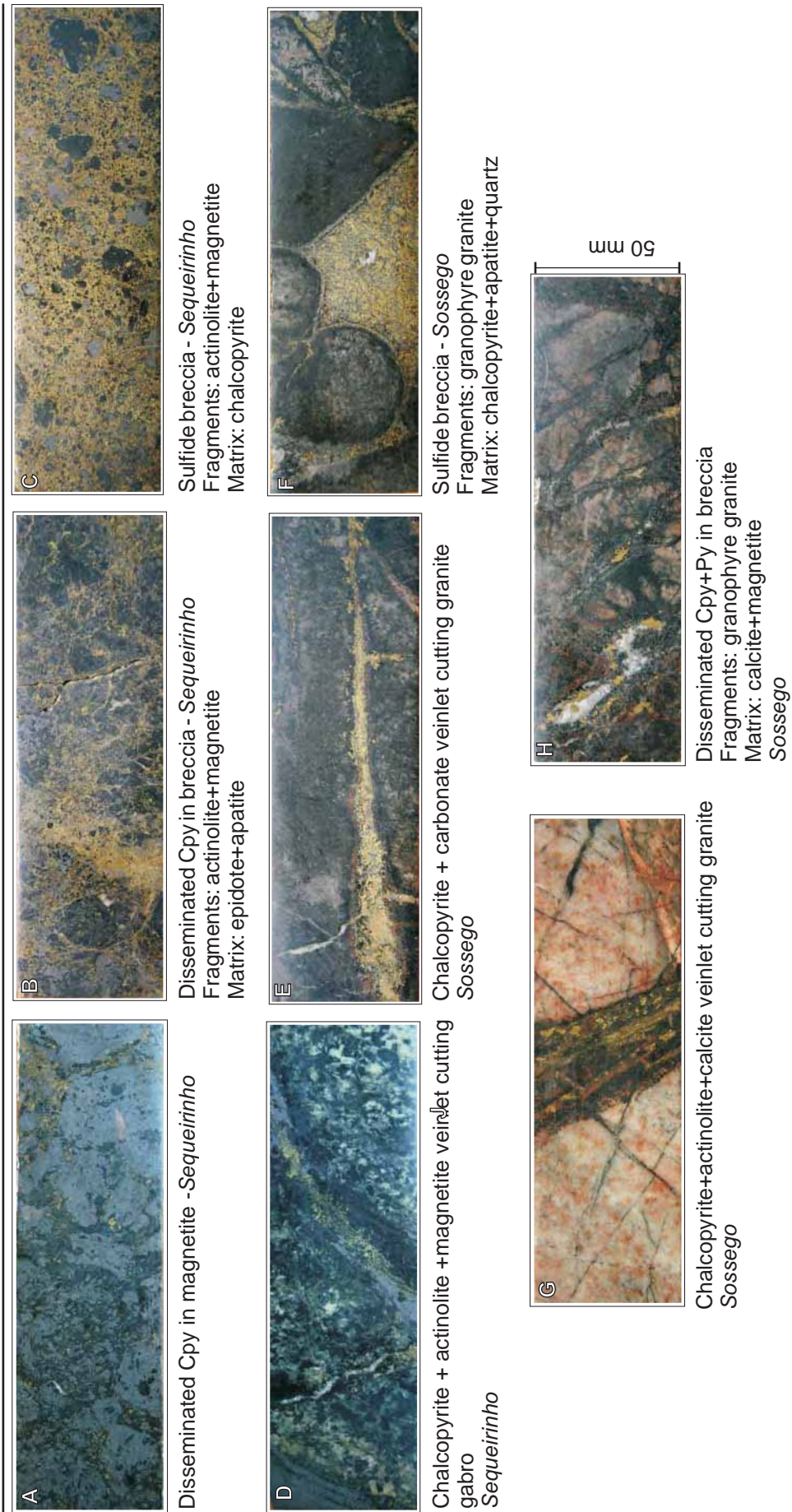
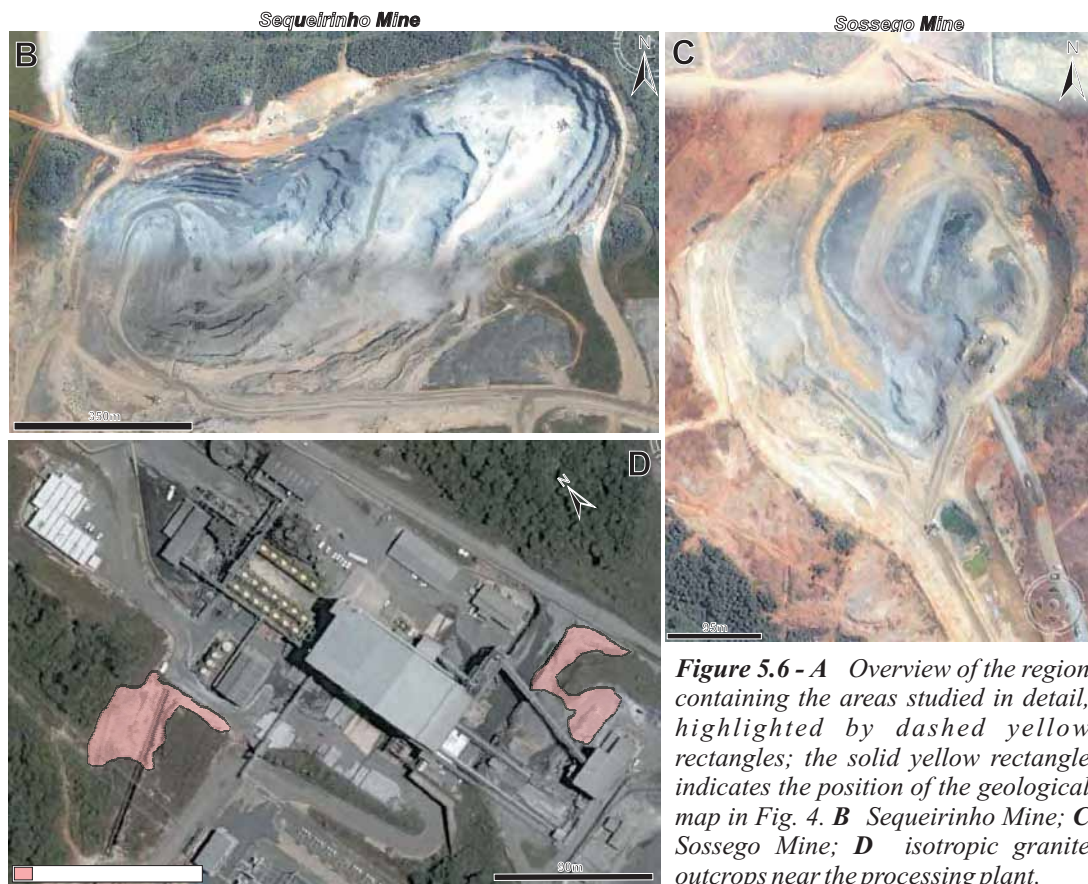


Figure 5.5 - Photographic chart showing the main types of massive and disseminated sulphide mineralization intercepted by drill-cores from Sossego and Sequeirinho.



	<i>Hydrothermal Assemblage</i>	<i>Generalities</i>	
<i>Sequeirinho-Pista-Baiano</i>	Sodic Alteration	Albite+tourmaline+scapolite+hematite+epidote (veins)	Generally pervasive alteration with restricted occurrence of albite veinlets
	Silicification Epidotization	Quartz+epidote	Epidote filling fractures-veins
	Sodic-Calcic Alteration	Albite+hastingsite+actinolite; Accessories:magnetite+calcite+epidote+quartz+titanite	regional character; fracture controlled; cuts and replaces the sodic alteration assemblage; best developed in gabbroic rocks; also represented by massive bodies of actinolite and magnetite cross-cut by late epidote veins
	Apatite- Iron oxide formation	Actinolite+magnetite+apatite	_____
	Potassic Alteration	K-feldspar, Cl-biotite, quartz, magnetite subordinated allanite, thorianite, chalcopyrite; Pista: biotite±hastingsite-tourmaline-scapolite	overprints sodic and sodic-calcic assemblages; forms hydrothermal haloes around mineralized zones poorly developed at Sequeirinho; best developed at Pista
	Chloritization Carbonatization	Albite+calcite+chlorite Accessories: rutile+pyrophanite+perovskite	Spatially associated with potassic assemblage, generally in metavolcanics of Pista
<i>Sossego-Curral</i>	Mineralization	(I) early: actinolite/ferroactinolite+Cl-Apatite+magnetite (II) late: epidote+chlorite+quartz+calcite+chalcopyrite+pyrite+siegenite+millerite	Breccia body displaying two distinct assemblages forming the breccia matrix;late mineralized assemblage strongly replace and alterate the early assemblage
	Sodic Alteration	Albite as veinlets and massive albitite	Intensively overprinted by potassic alteration
	Silicification Epidotization	Quartz+albite+epidote	_____
	Potassic Alteration	K-feldspar+Cl-biotite+quartz±magnetite	Occurs as veins when away and pervasive close the mineralized zones; is the best developed alteration assemblage
	Chloritization Carbonatization	Chlorite+calcite±quartz±titanite±rutile±magnetite	Characterized by veinlets and replacement zones adjacent to the potassic alteration
Mineralization	(I) early: magnetite-actinolite-apatite-calcite (II) main: calcite-chlorite-epidote-quartz-pyrite-chalcopyrite±gold±siegenite±millerite (III) late: calcite-quartz-chlorite-actinolite	Mineralized breccia bodies and veins show three characteristic mineral assemblages produced by distinct episodes	

Table 3 - General summary of mineral parageneses and modes of occurrence of the main types of hydrothermal alteration recognized in the Sequeirinho Pista Baiano and Sossego Curral orebodies. Table summarized from Carvalho et al., 2005; Villas et al., 2005 ; and Monteiro et al., 2008.

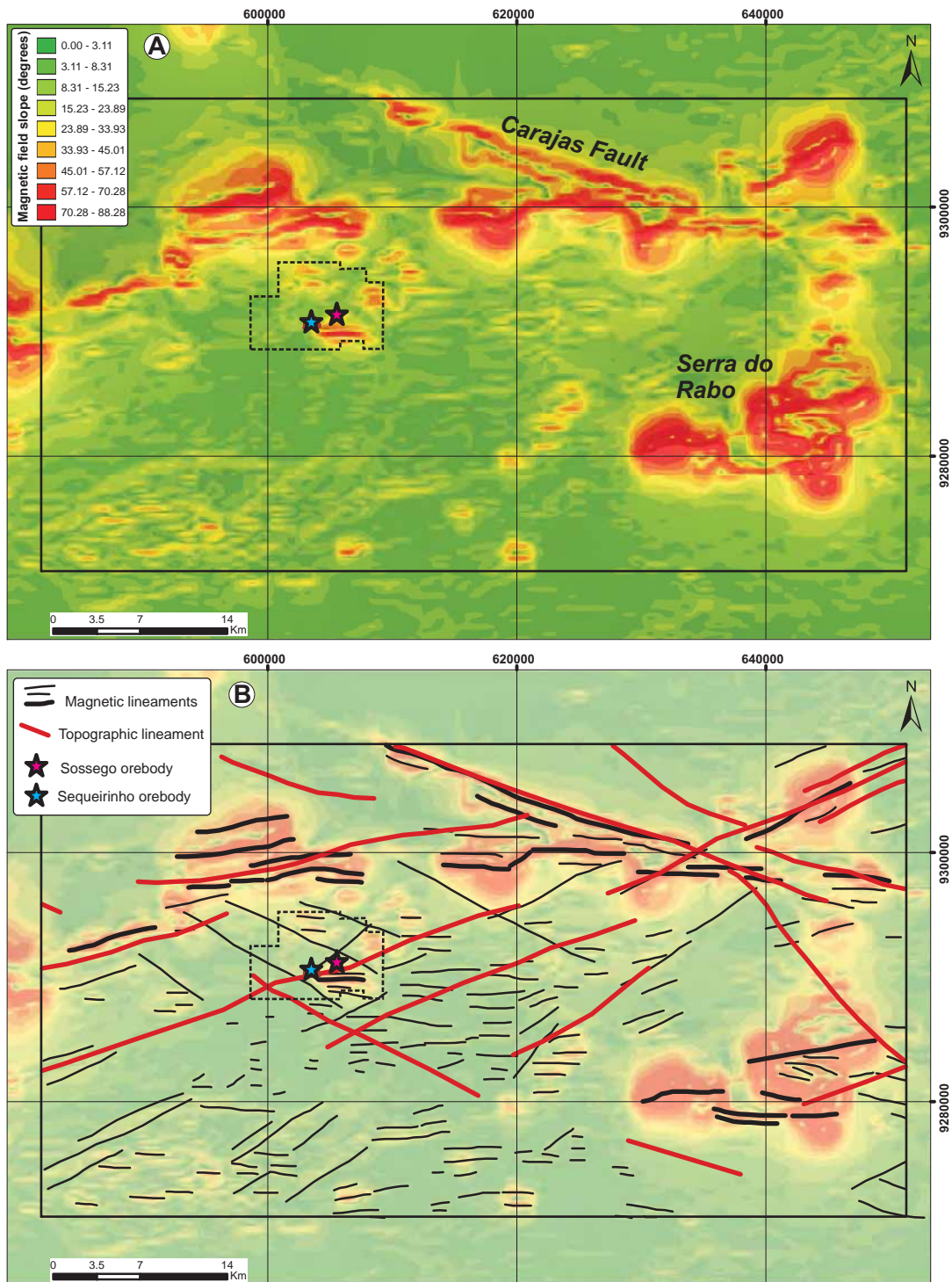


Figure 5.7 - Magnetic survey and interpreted lineaments picked at 1:170.000. **A** aeromagnetic survey (IGRF total intensity) with 1 km spacing between the flight lines; the anomalies represent the steepness of the magnetic field in the area. **B** Interpreted magnetic lineaments (black) and topographic lineaments picked from digital elevation model (red). Stars represent the Sossego and Sequeirinho orebodies respectively. Coordinate grid: UTM zone 22 south datum WGS89. The dashed polygon indicates the location of the finer scale survey presented in Fig. 8.

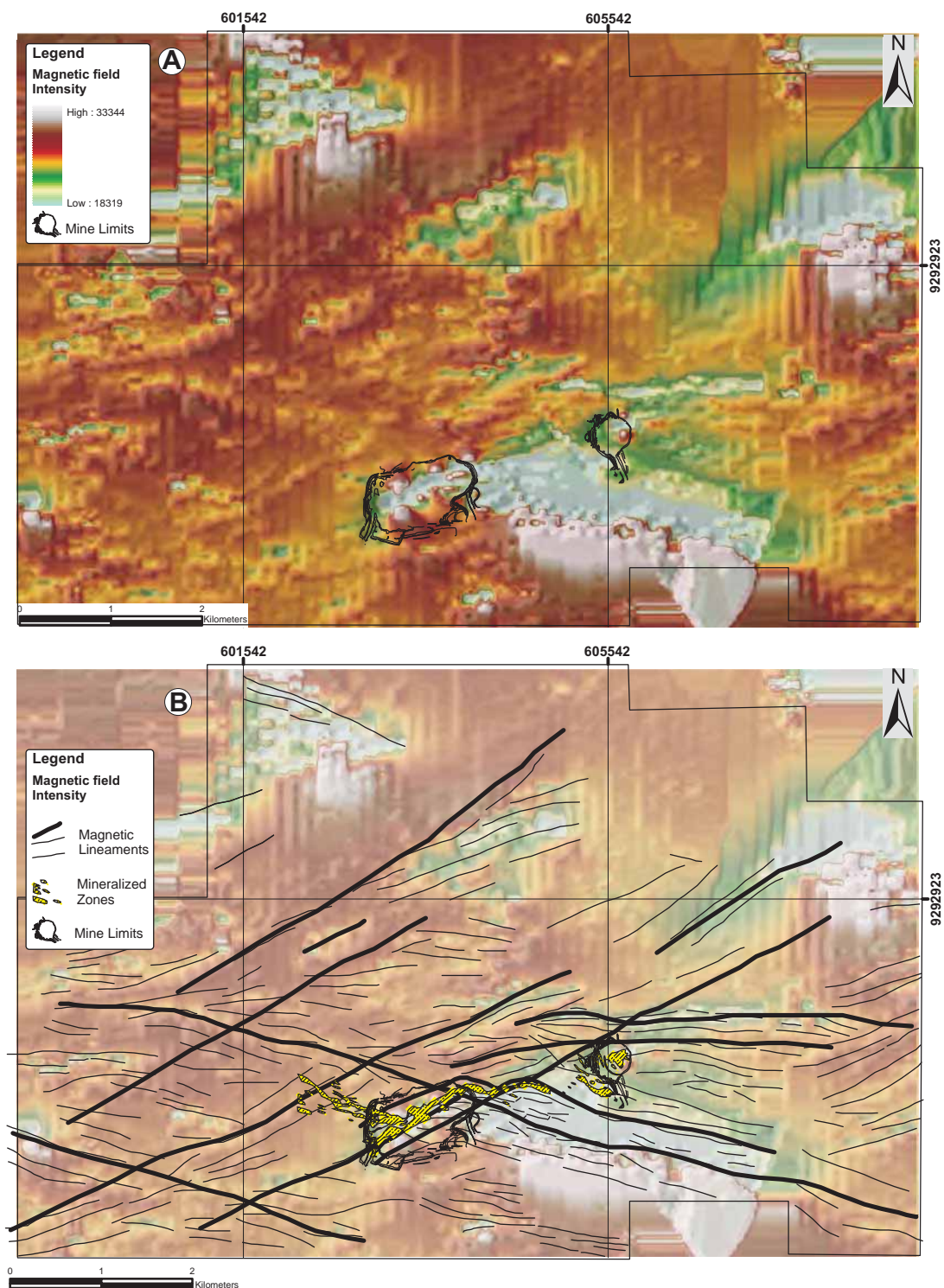


Figure 5.8 Magnetic survey and interpreted lineaments picked at 1:35,000. **A** aeromagnetic survey (IGRF total intensity) with flight lines spaced 250m; magnetic intensity represented in nT. **B** Interpreted magnetic lineaments and projected mineralized zones. The location of the Sossego and Sequeirinho orebodies is indicated but the outer limits of the mines. Coordinate grid: UTM zone 22 south datum WGS84.

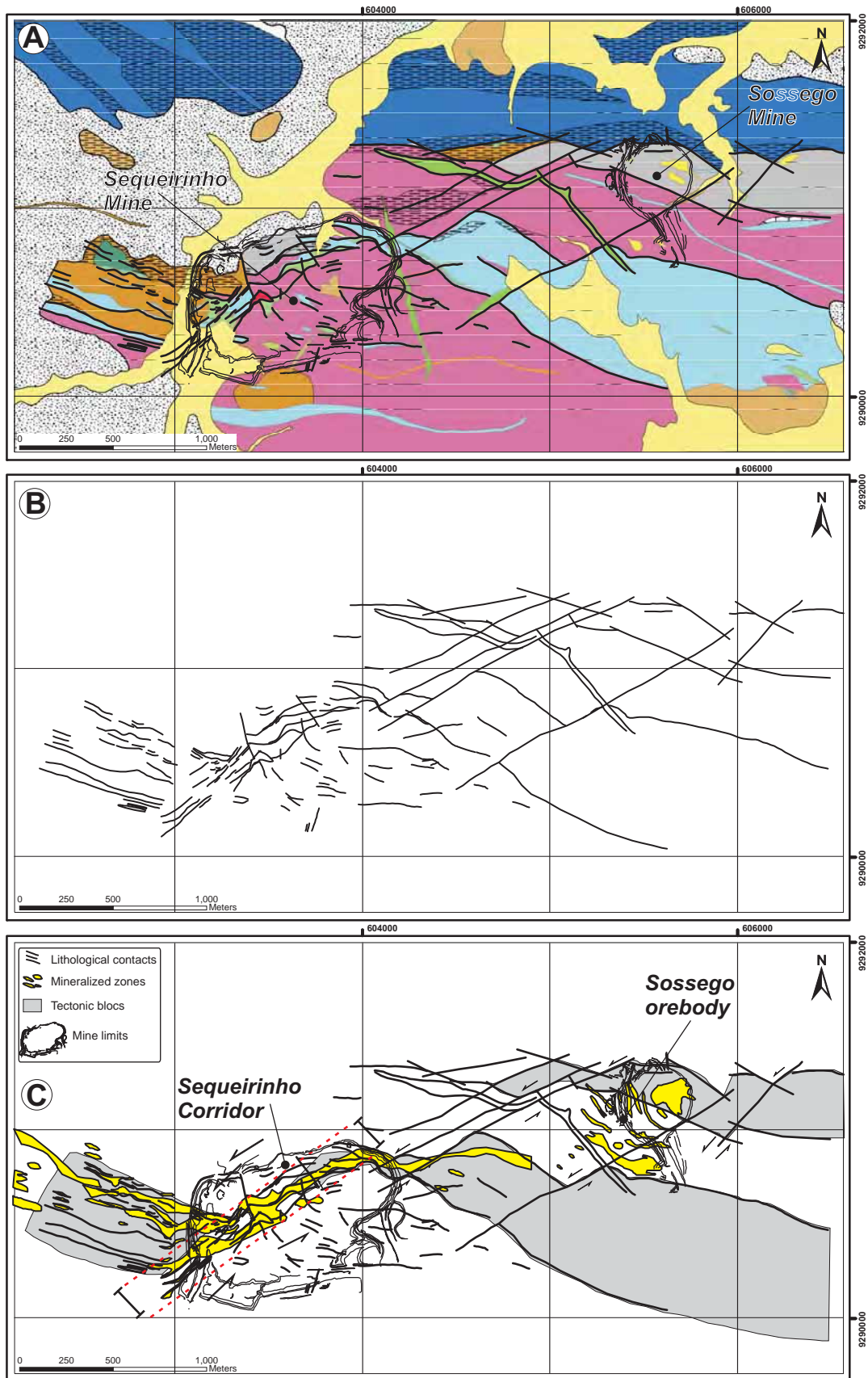


Figure 5.9 Analysis of geological contacts at map scale. **A** geological map of the area containing the Sossego and Sequeirinho deposits with lithological contacts delineated by black lines (the colour key is the same as Fig. 5.3); **B** Lineaments corresponding to lithological contacts only; **C** Kinematic interpretation of lithological lineaments displaying projected mineralized zones and major deformed blocks in grey.

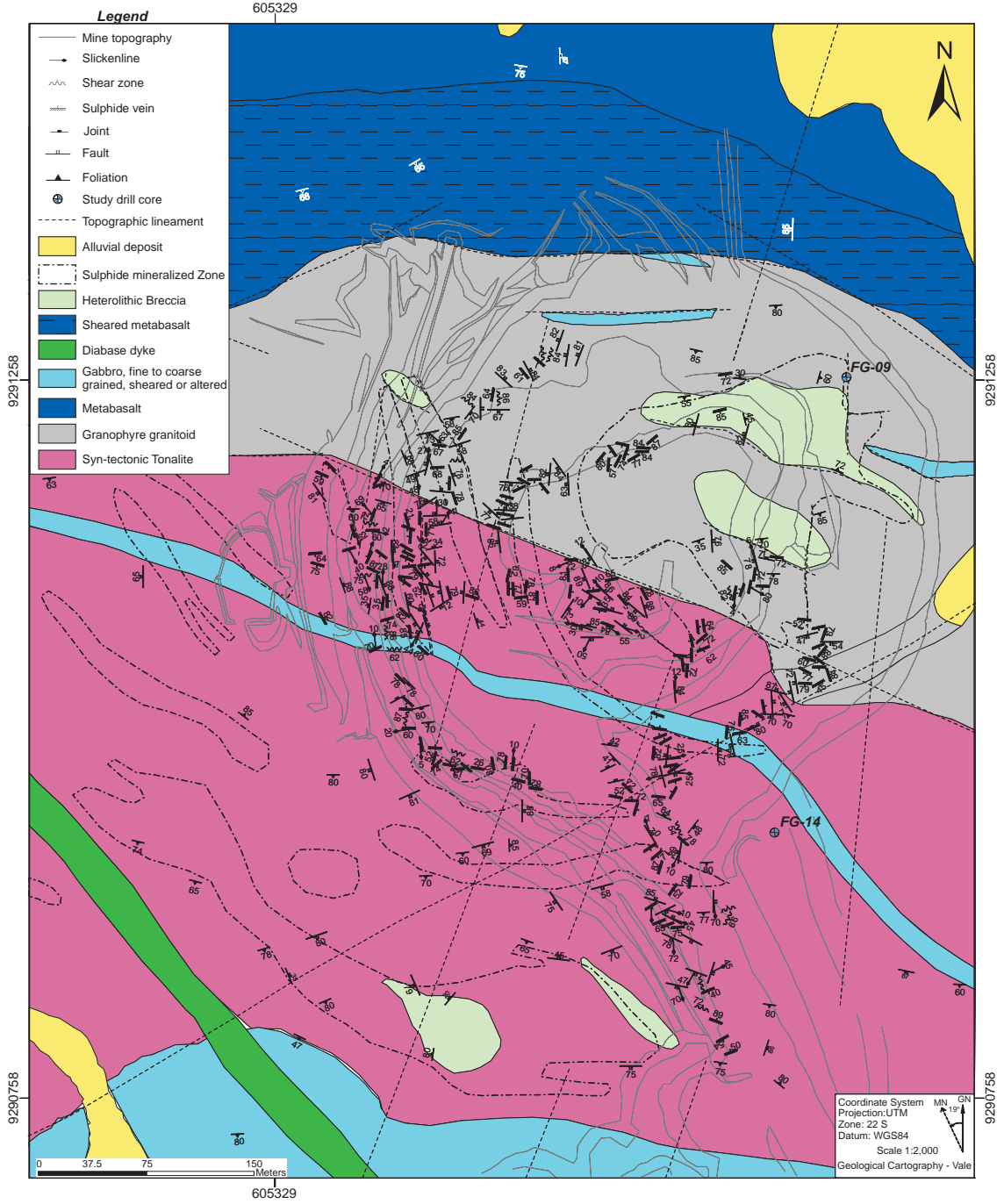
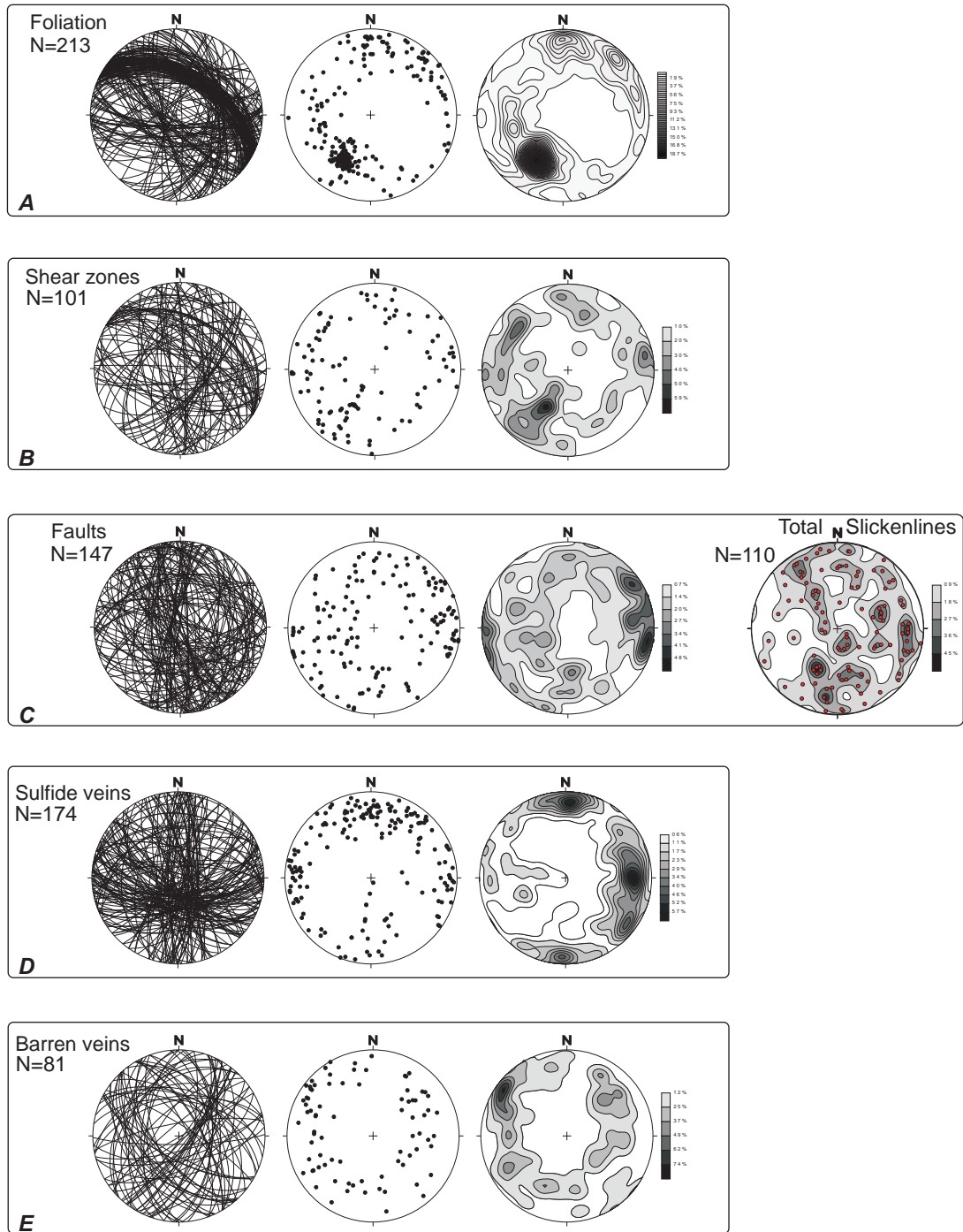


Figure 5.10 Geological map of the Sossego orebody. The mine topography, limits of the mineralized zones and lithologies are MSS/VALE mapping products. The structural symbols correspond to the mapped structures during fieldwork in the mine. FG 9 and 14 indicate the location of the logged drill cores



*Figure 5.11 - Stereographic projection diagrams presented as planes, poles of planes and density contours of poles for mapped structures in the Sossego mine: **A** foliation; **B** shear zones; **C** faults and faults slickenlines; **D** sulphide veins; and **E** barren veins. Data is represented in equal area plots, projected in the lower hemisphere.*

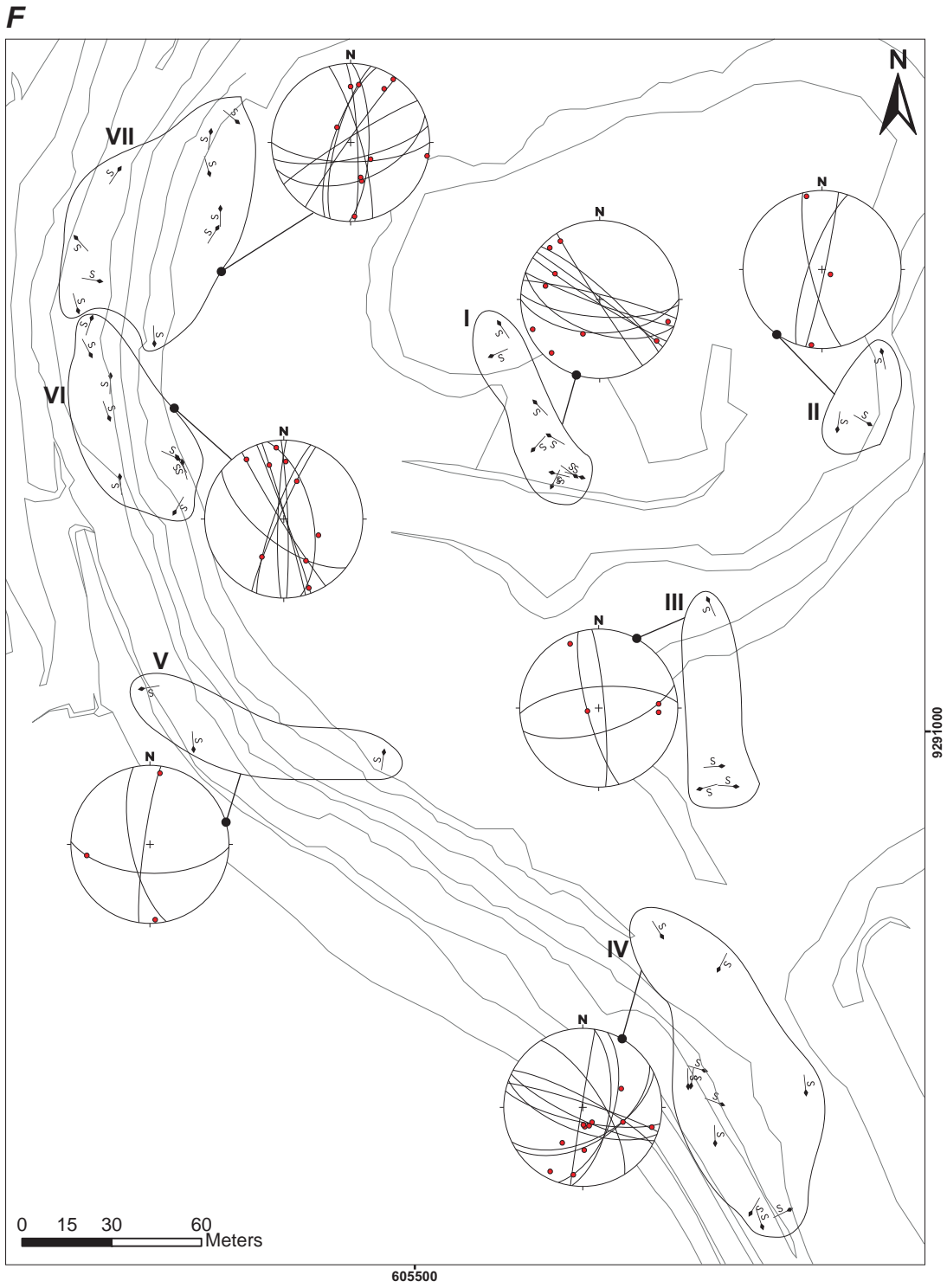


Figure 5.11 cont. - F stereonet for fault slickenlines and fault planes sorted by their spatial location in the Sossego mine. Data is represented in equal area plots, projected in the lower hemisphere.

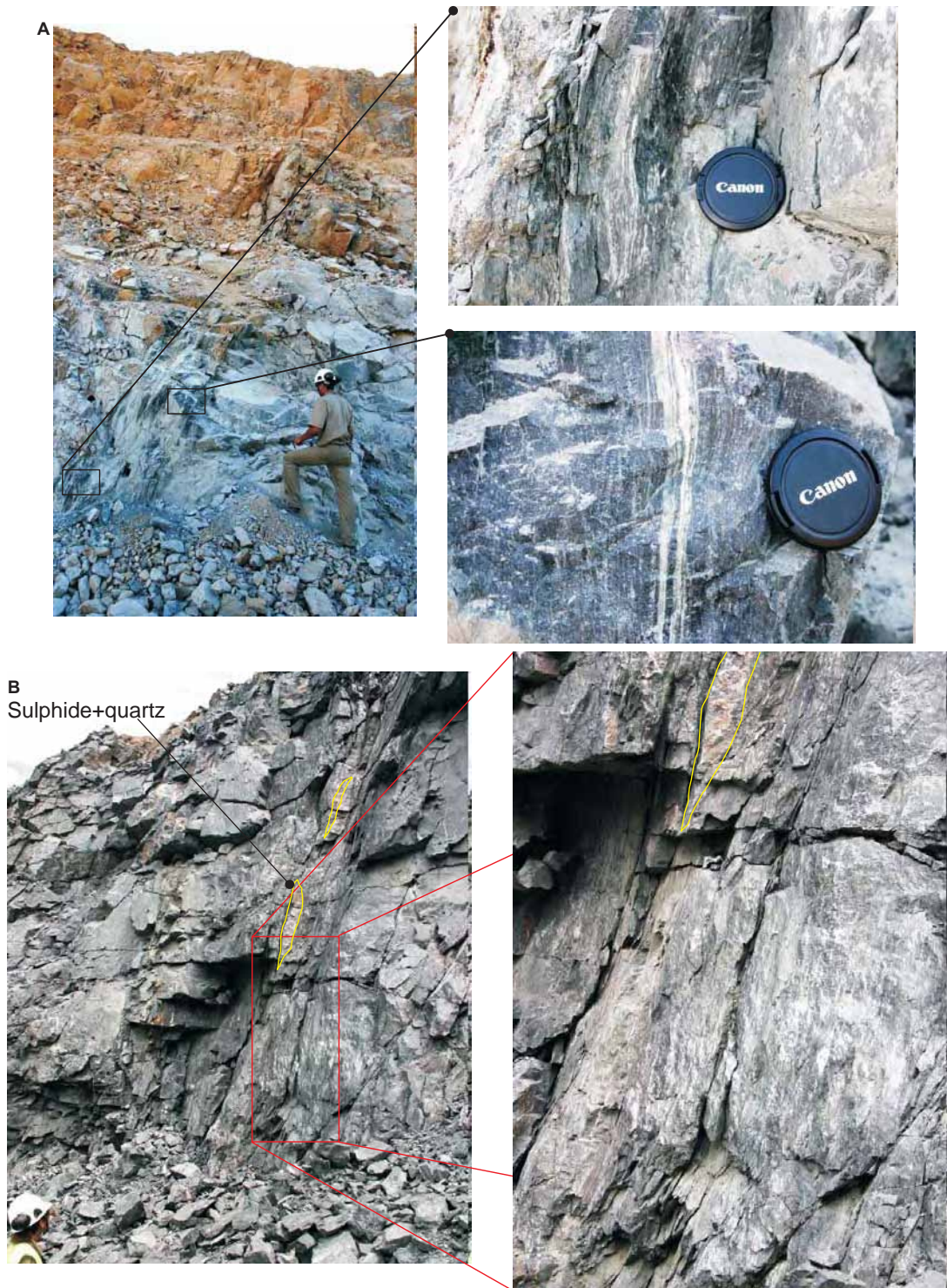


Figure 5.12 - Shear zones at Sossego. **A** banded type shear zone and in detail, a close view of the straight banding and a sigmoidal feature. **B** steep dipping shear zone showing elongated mineralized "pods" of sulphide+quartz.

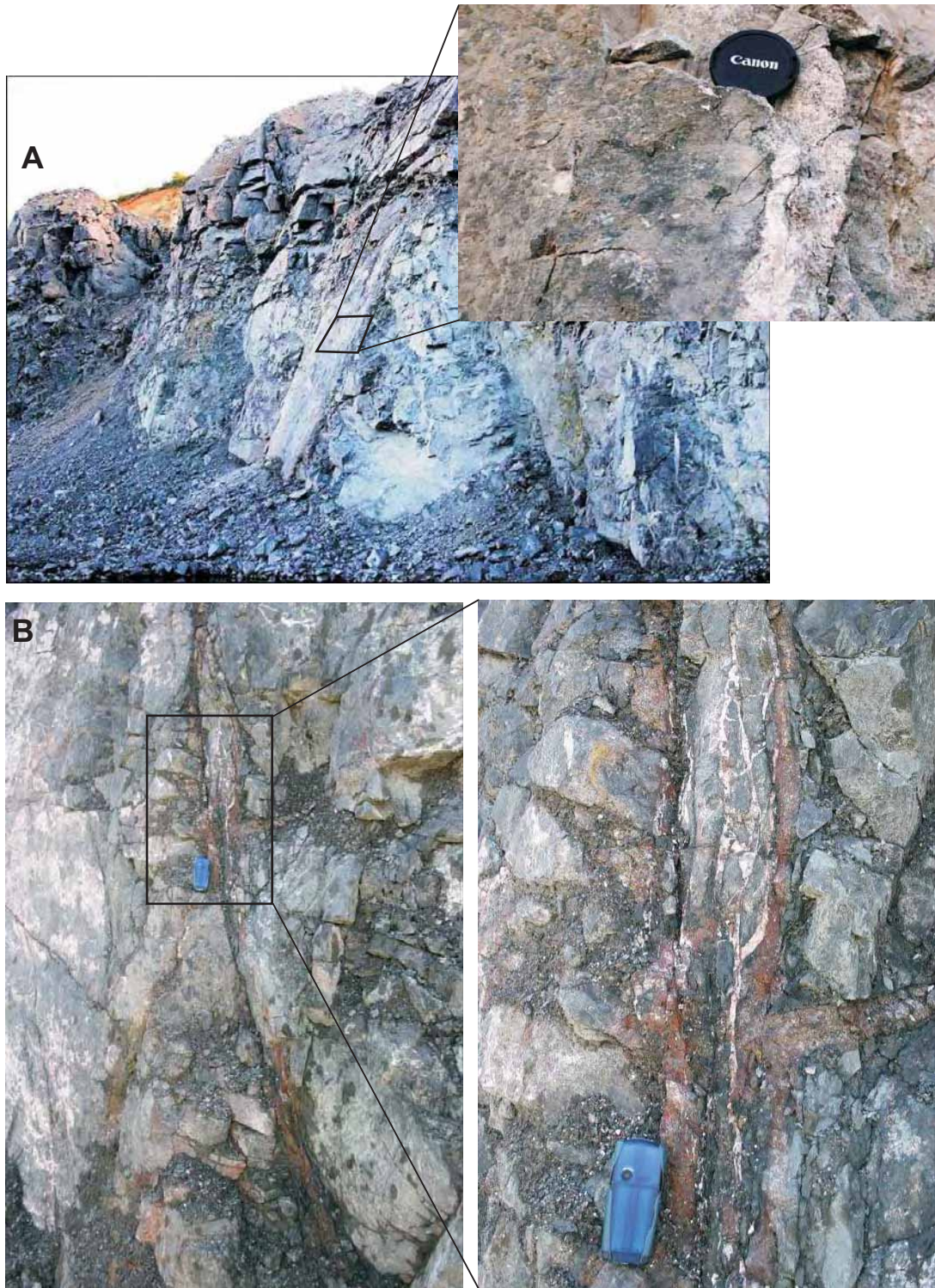


Figure 5.13 - Type 1 faults at Sossego. **A** moderately dipping discrete and straight fault plane; in detail: (i) subhorizontal fault striae indicating directional fault motion and (ii) the white material is a thin cataclasite layer. **B** a gently curved fault plane showing fragmented material cemented by calcite into the fault plane.

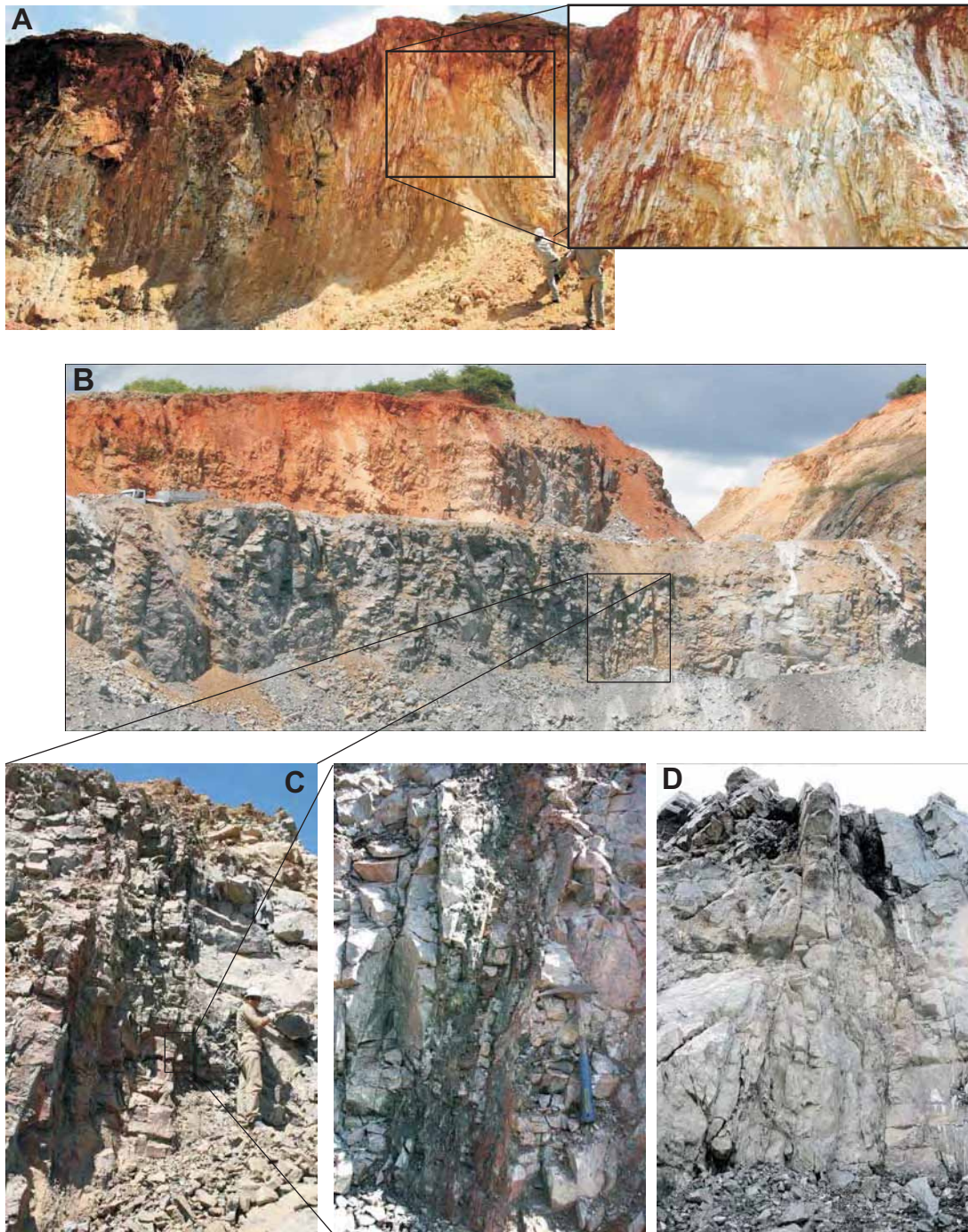


Figure 5.14 - Type 2 faults at Sossego. **A** relatively wide sub vertical fault zone on the weathered profile; note the prominent banded aspect of red and white altered bands see detail photo. **B** overview of a steep dipping fault zone in “fresh” rock; **C** closer view of the fault in B displaying evident “striped” pattern comprising alternating domains of less fractured and intensely fragmented friable material (in detail) composed of clay minerals and rock chips; **D** another example of fault zone characterized by parallel sets of high strain fault strands separated by relatively less or undeformed domains of angular fragments.

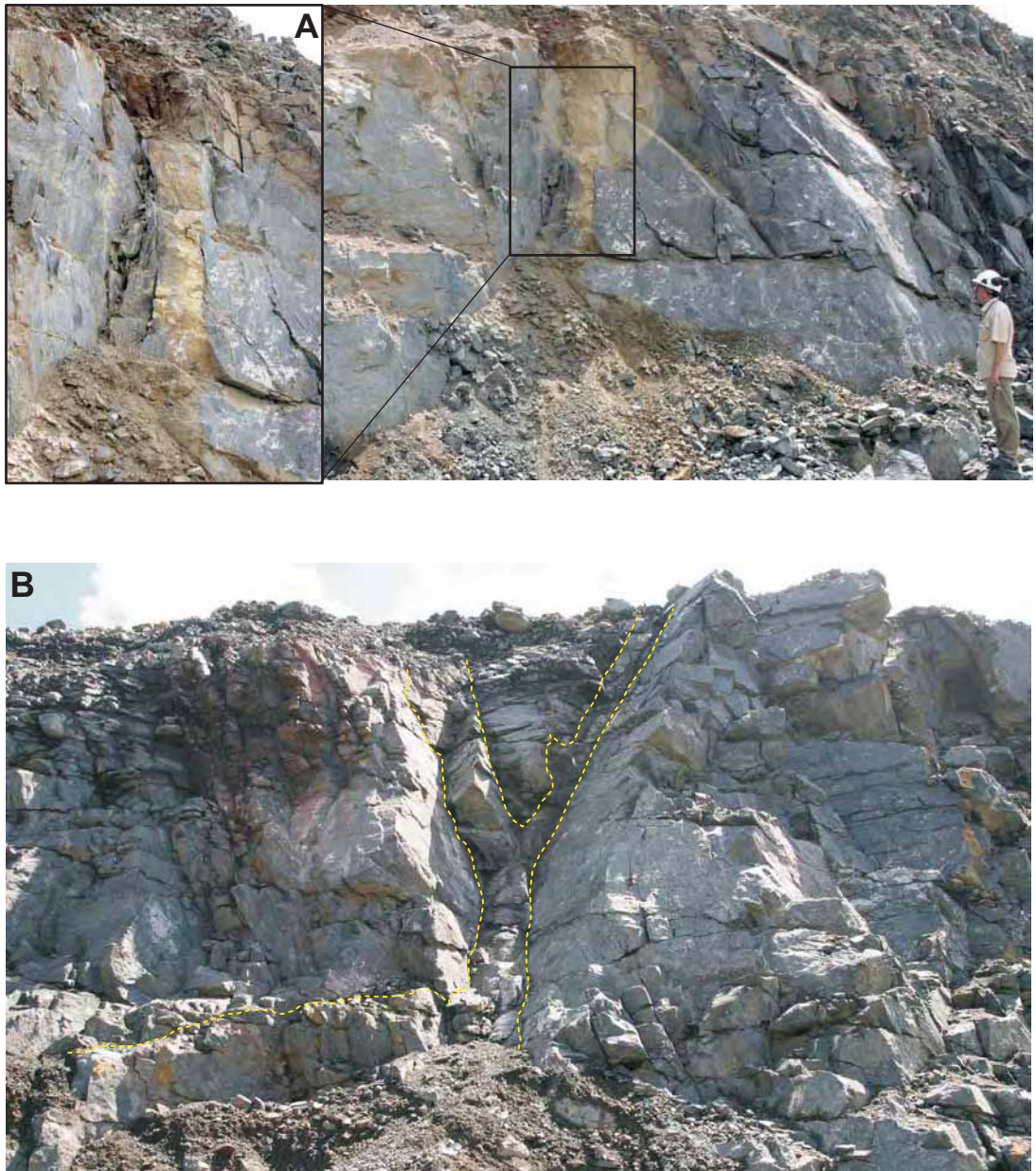


Figure 5.15 - Extension veins at Sossego. **A** typical single tabular vein filled with massive sulphide, note the straight vein walls; **B** branching sulphide vein with “Y” geometry, bench height= 6m.

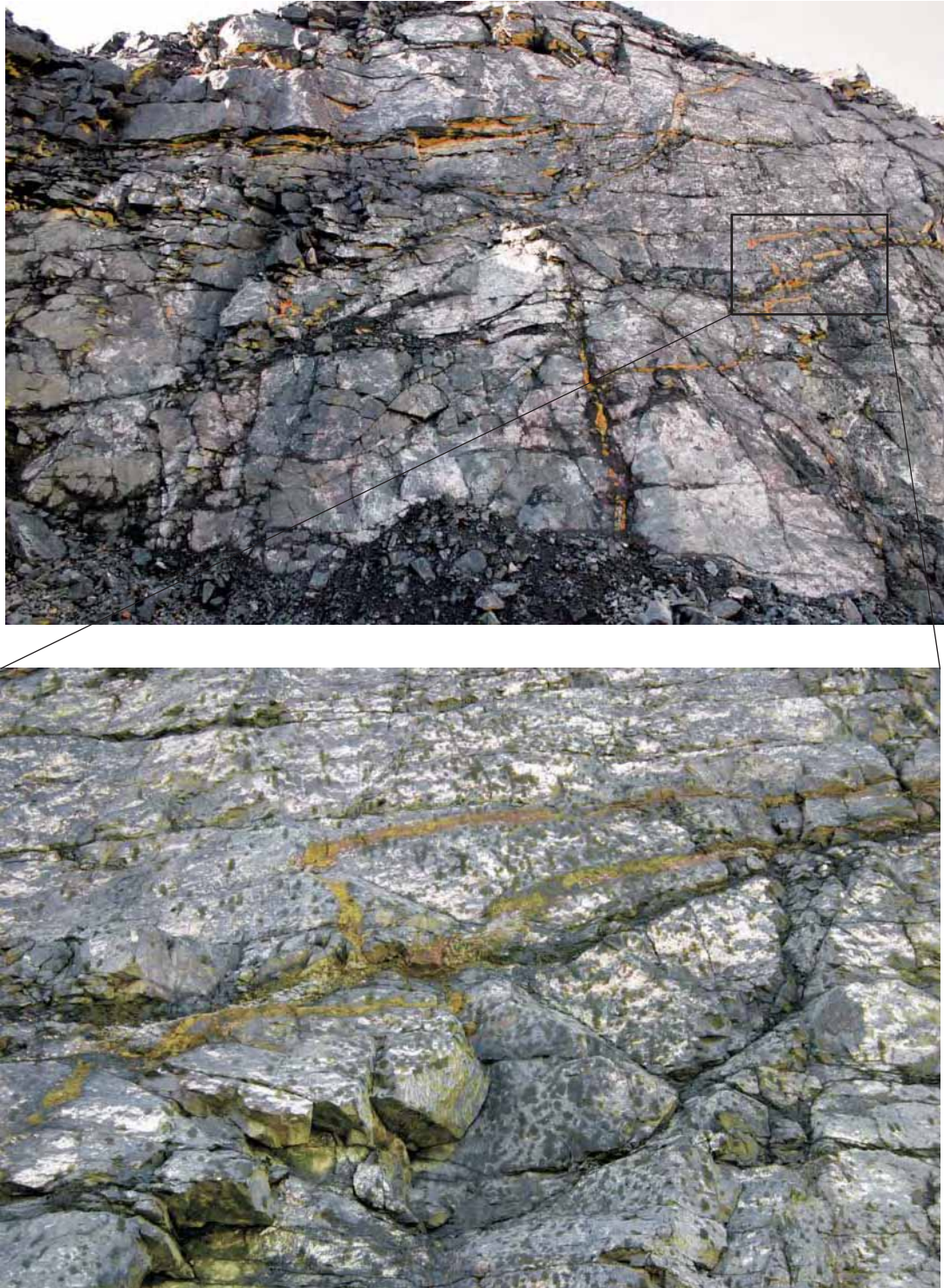


Figure 5.16 - Sulphide and magnetite veins forming a well connected stockwork array. Note the random orientation of the veins ranging from sub horizontal to sub vertical position. Stockwork veins show both curved and straight angular geometry (in detail).



Figure 5.17 - Sheared veins at Sossego. *A* zoned vein showing sulphides+quartz in the outer part and calcite±actinolite forming the inner fill. Note the presence of fine incohesive material along the vein walls; *B* & *C* examples of relatively narrow mono mineralic sheared veins.

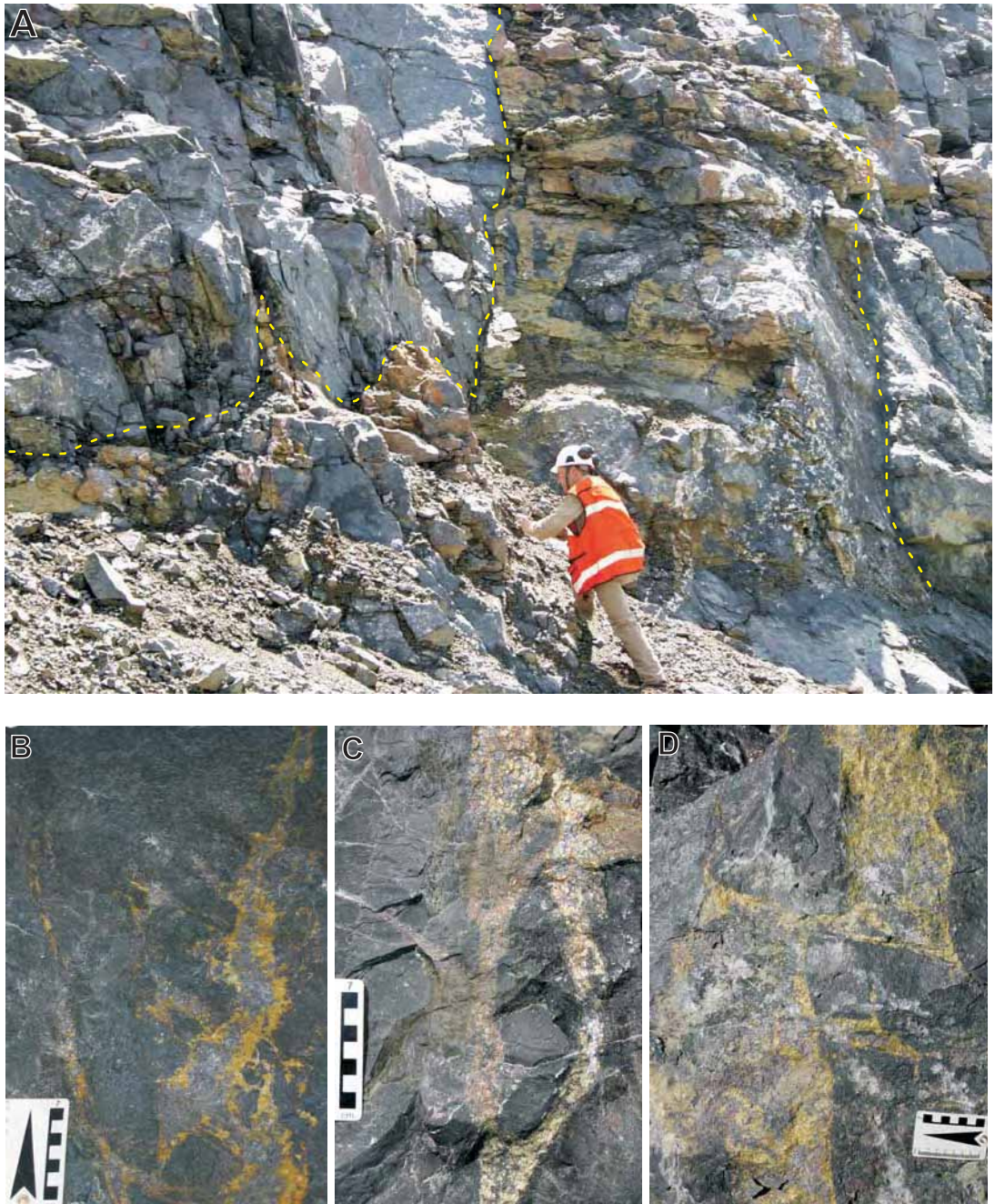


Figure 5.18 - Examples of mineralized breccia veins at Sossego. **A** robust sub vertical tabular breccia vein, note the large angular fragments within the vein and calcite white patches; **B** curvy tip of a composite vein showing chalcopyrite in the outer and an unidentified mineral in the inner portion of the vein that also contains sub rounded fragments; **C** relatively narrow branch of vein containing an elongated fragment approximately 10cm long; **D** breccia vein apparently offset by shear band.

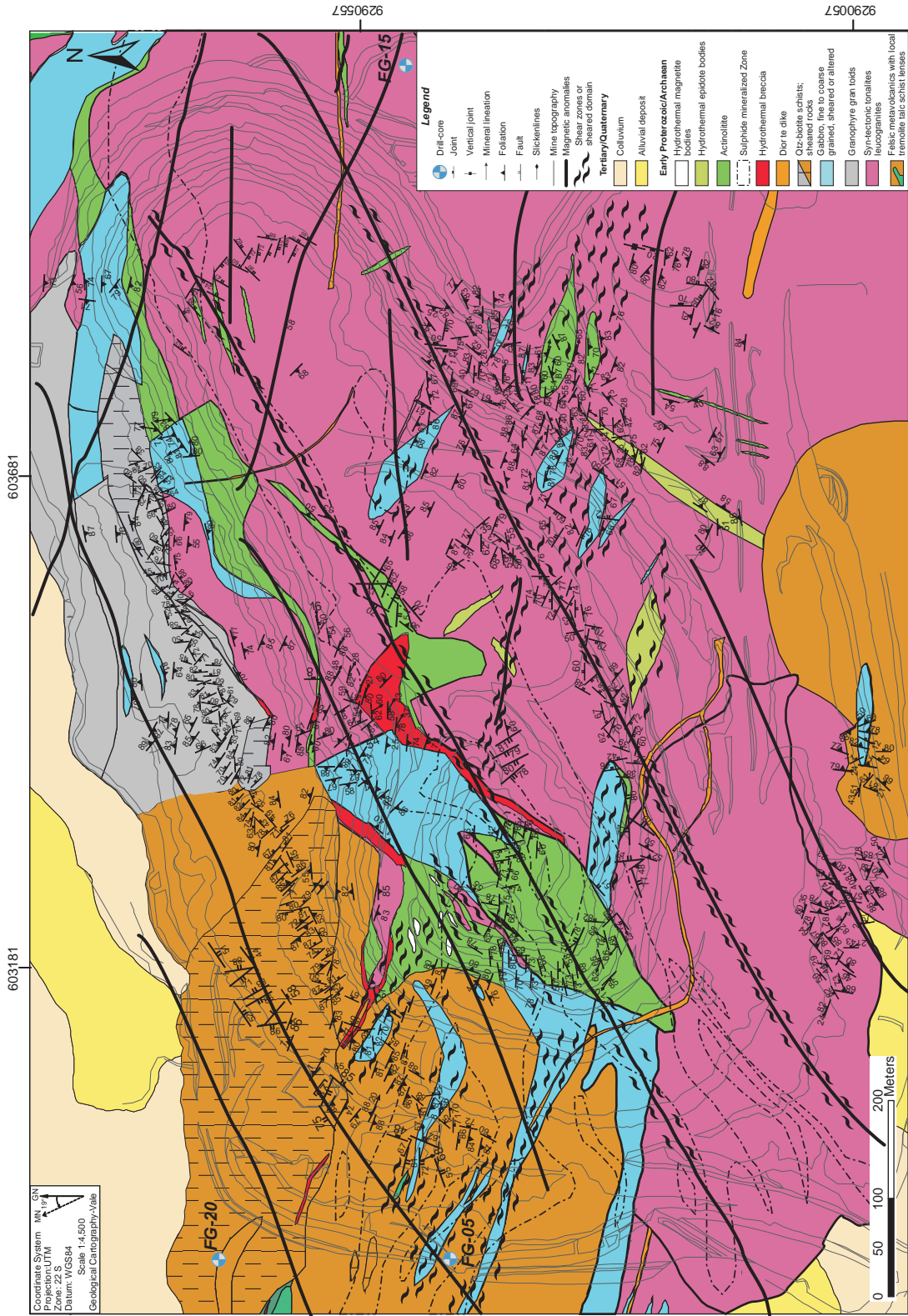


Figure 5.19 - Overview of the Sequeirinho mine and indication of the granitic, schists domains and an approximated position of the main mineralized zone. Black line on the geological map indicates the orientation of the vertical cross-section.

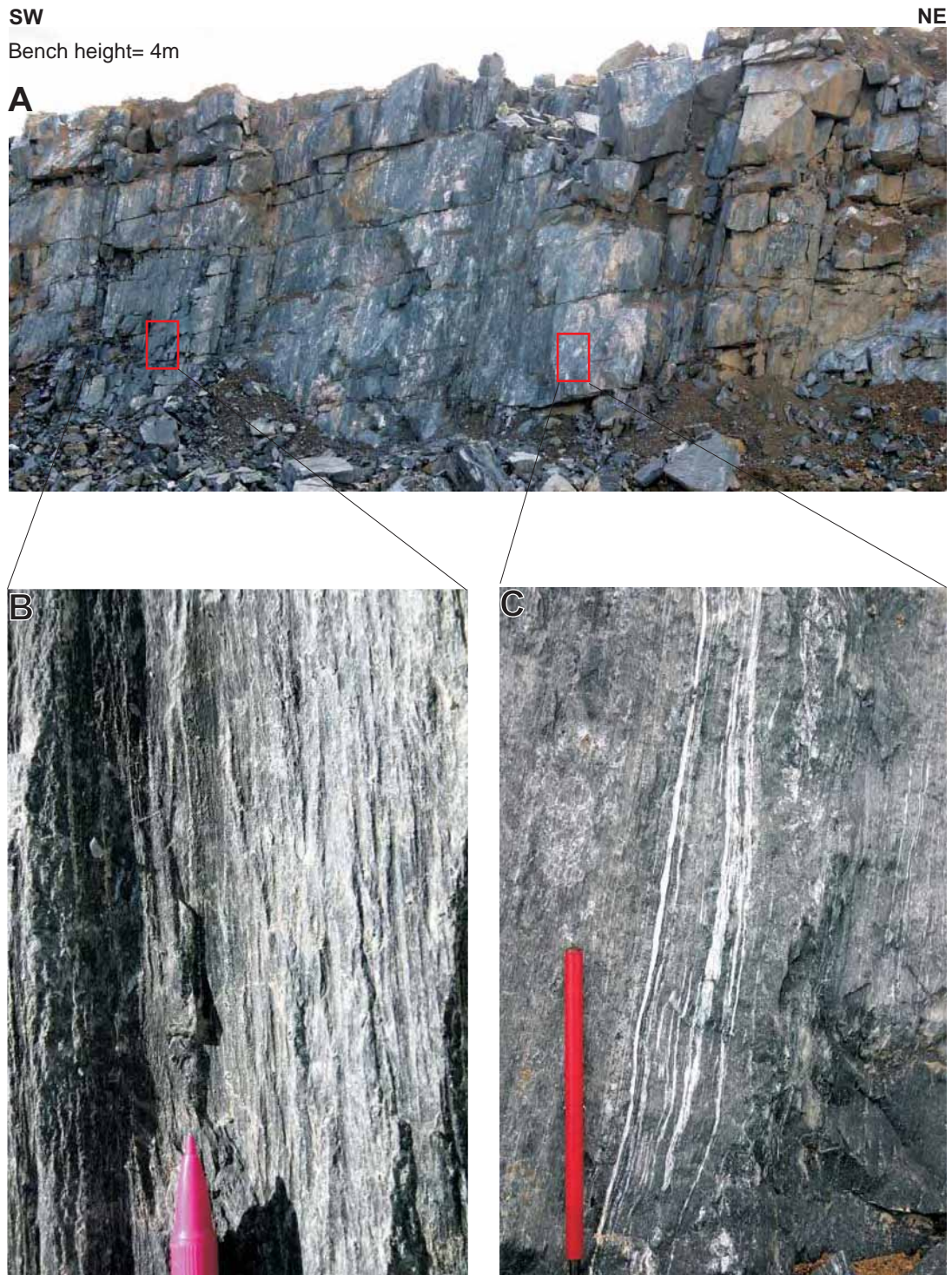


Figure 5.20 - Examples of foliation at Sequeirinho within the schists domain. **A** typical appearance of the prominent sub vertical schistosity observed in the mine benches; **B & C** detailed views of the foliation aspects: fine to very fine, straight and continuous prominent fabric, locally showing alternating bands.



Figure 5.21 - Symmetric boudins wrapped by foliation in the schist domain at Sequeirinho. In detail quartz+biotite pressure shadows occasionally present at the boudins neck. Note the absence of foliation inside the boudins.



Figure 5.22 - Selection of the most representative planar fabrics typically found in sheared granitic domains at Sequeirinho. **A** red plane represents the sub vertical foliation and arrow indicates the position of the mineral lineation; **B** & **C** general and detailed aspects of mylonitic foliation showing its anastomosing character and rigid porphyroclasts and lenses; **D** & **E** also show prominent anastomosing foliation associated with albite and epidote rich alteration, note the limited presence of porphyroclasts; **F** a relatively weak foliation in the boundaries of a sheared domain.

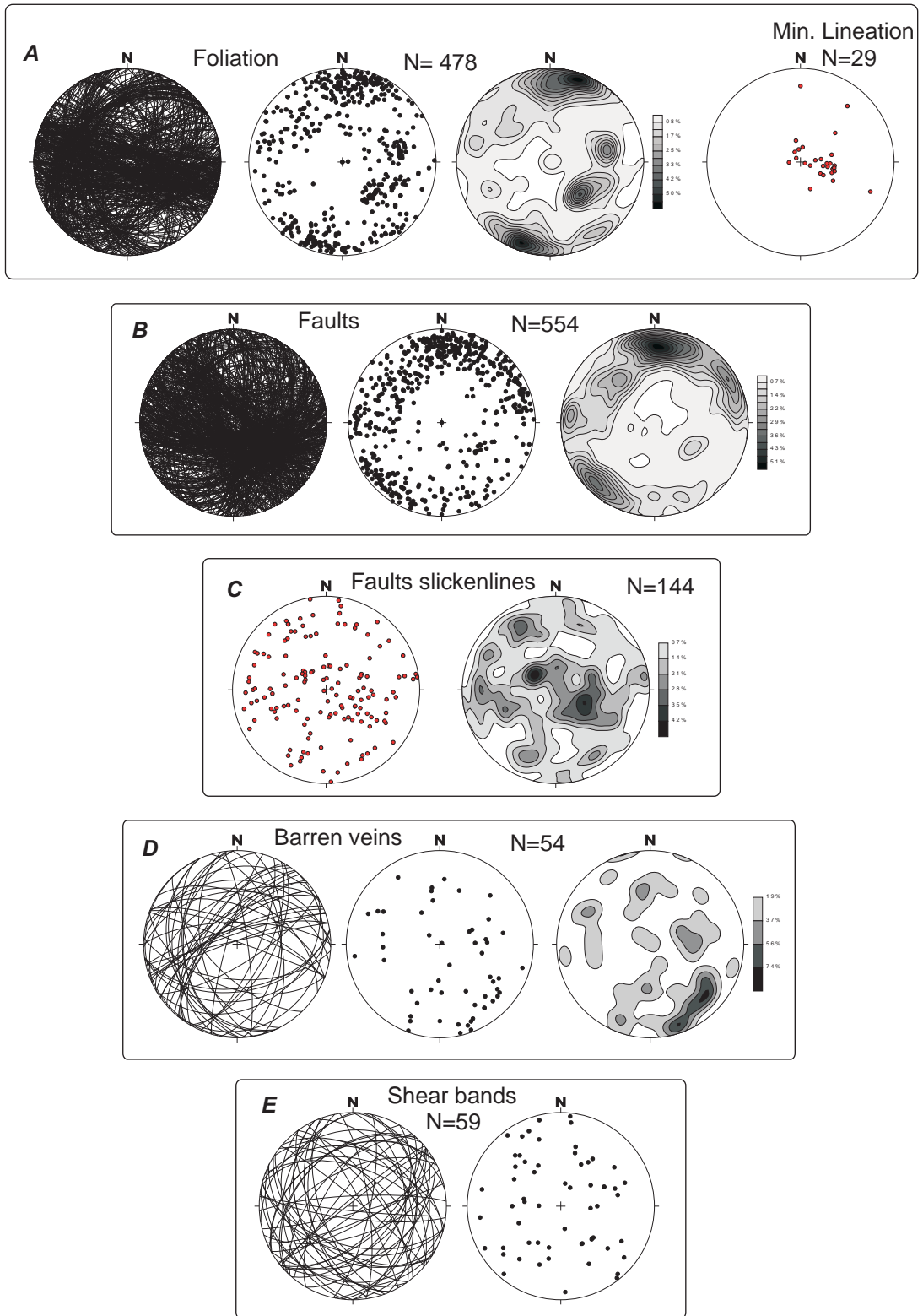


Figure 5.23 - Diagrams of stereographic projection diagrams presented as planes, poles of planes and density contours of poles for mapped structures at the Sequeirinho mine: **A** foliation and mineral lination; **B** fault planes and zones; **C** faults slickenlines; **D** barren veins; and **E** shear bands. Data is represented in equal area plots, projected in the lower hemisphere.

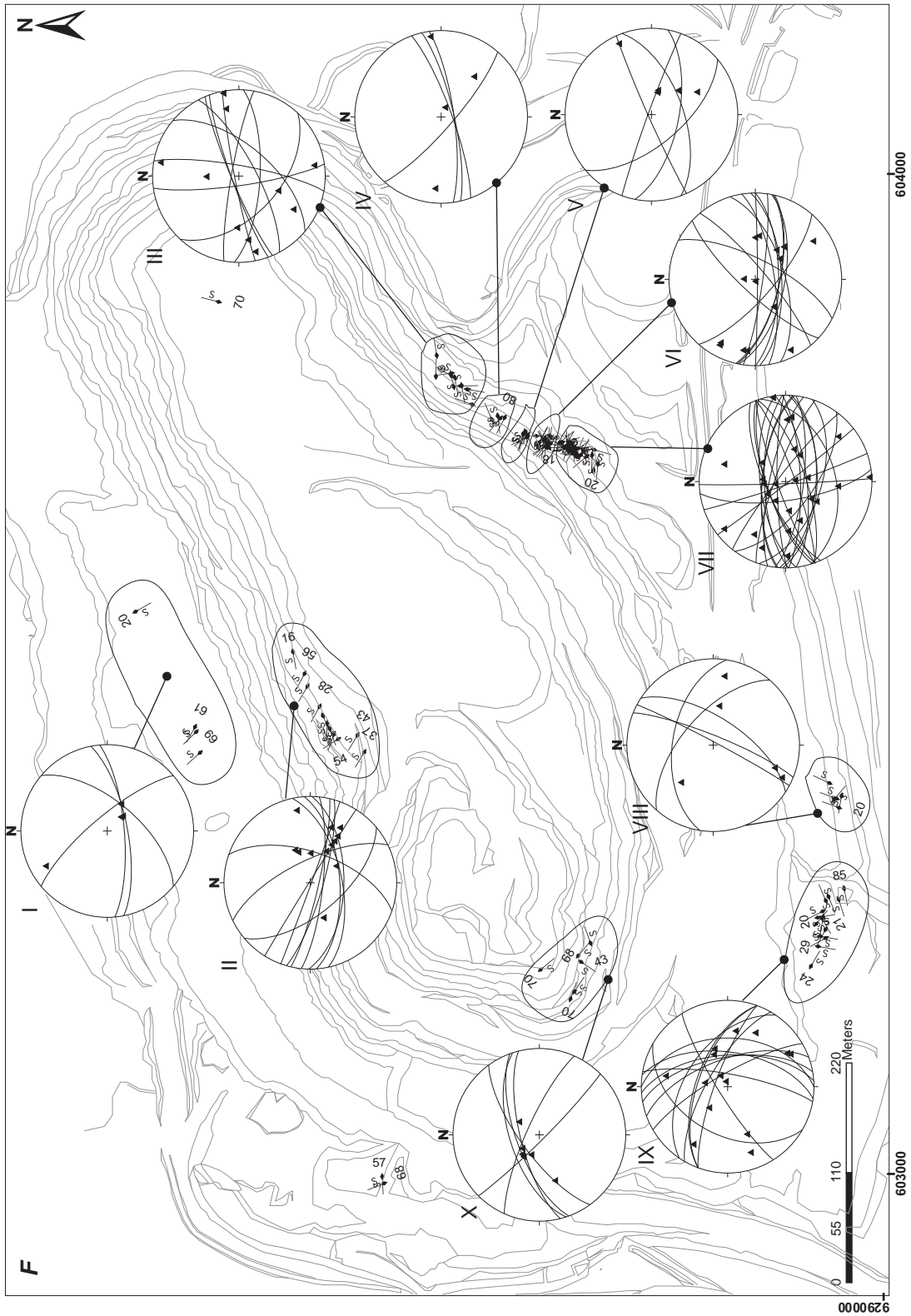


Figure 5.23 cont - F Stereonets for fault slickenlines and fault planes sorted by their spatial location in the Sequeirinho Mine. Data is represented in equal area plots, projected in the lower hemisphere (black triangles = slickenlines).

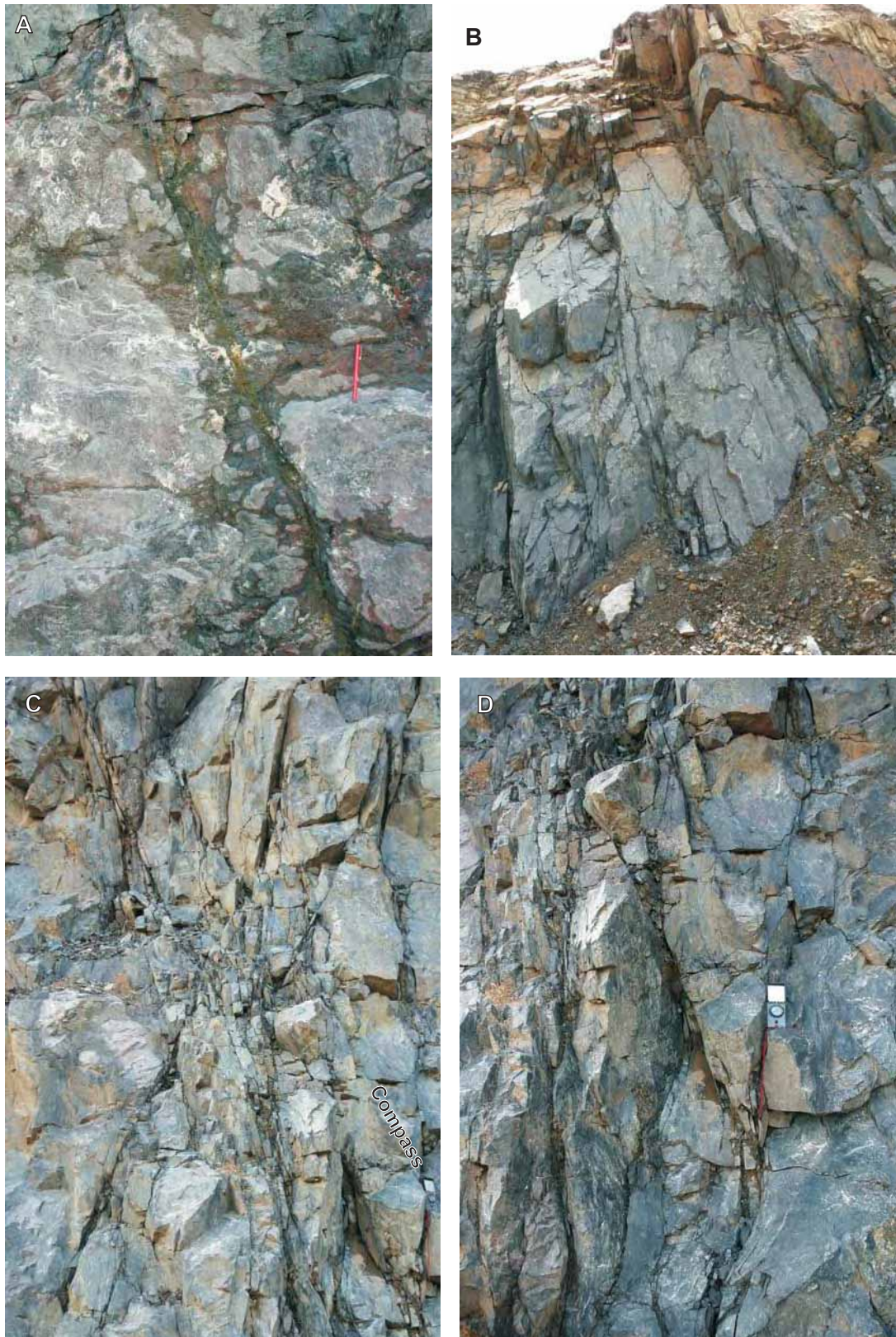


Figure 5.24 - Type 1 faults at Sequeirinho. **A** discrete and straight fault plane in metavolcanic rock; **B** sub parallel set of sub vertical faults develop in biotite schist, bench height = 4m; **C** conjugated “dry” faults containing lozenge shaped fragments along the fault planes; **D** set of “dry” sub vertical faults with prominently curved planes.

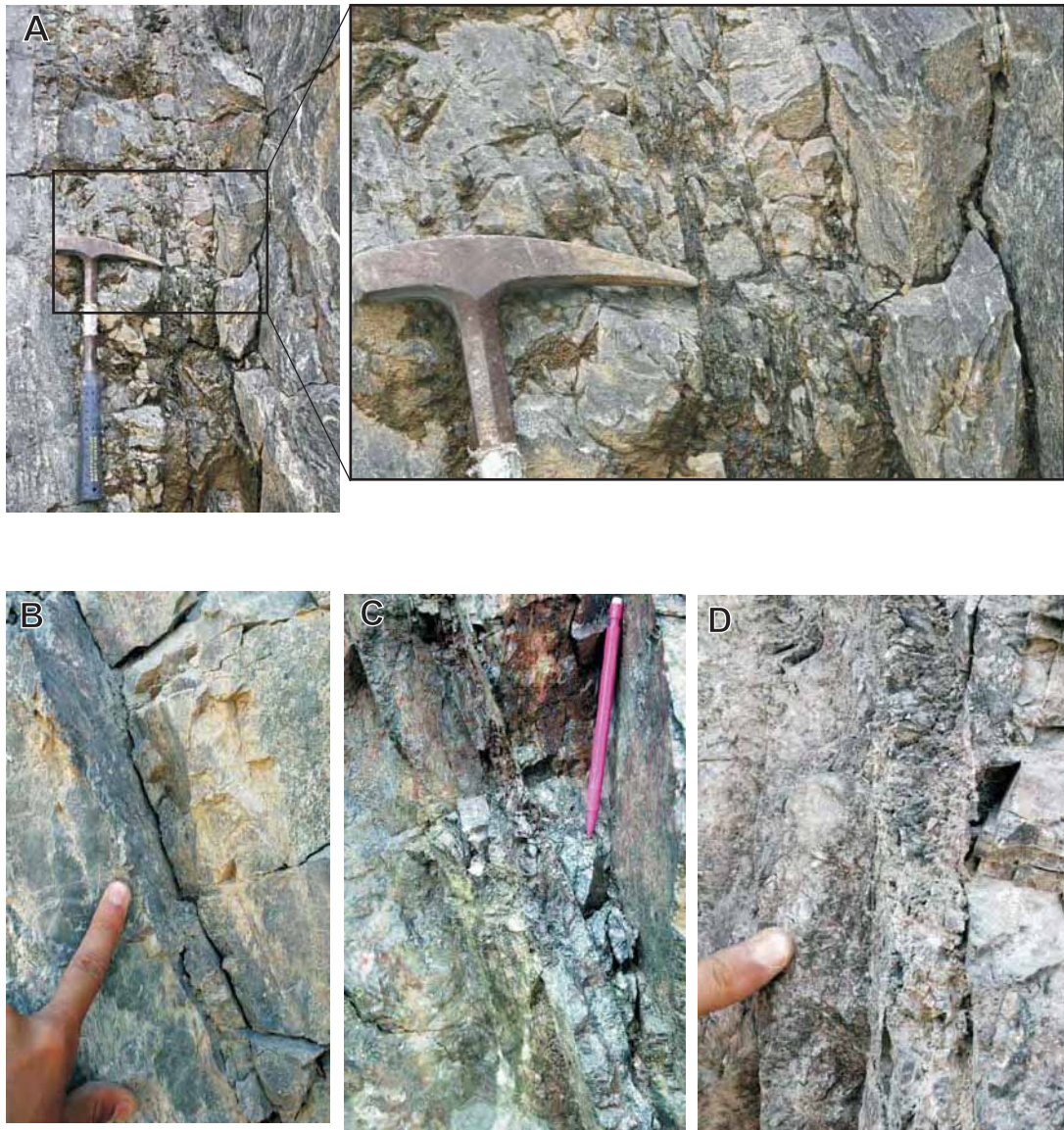


Figure 5.25 - Some examples of the Type 2 faults at Sequeirinho. **A** sub vertical fault zone displaying fragmented material within the fault plane, in the close up photo is possible to identify coarse and angular fragments immerse in a very fine dark mass of extremely fine friable material; **B** discrete fault plane showing a thin layer of very fine and dark material smeared onto the fault plane, tiny chips of quartz are visible within the fine material; **C & D** layered intensely fractured material on the fault planes bounded by well defined surface (slip?), chloritization in C and precipitation of calcite in D are evidence of fluids activity during or post faulting.

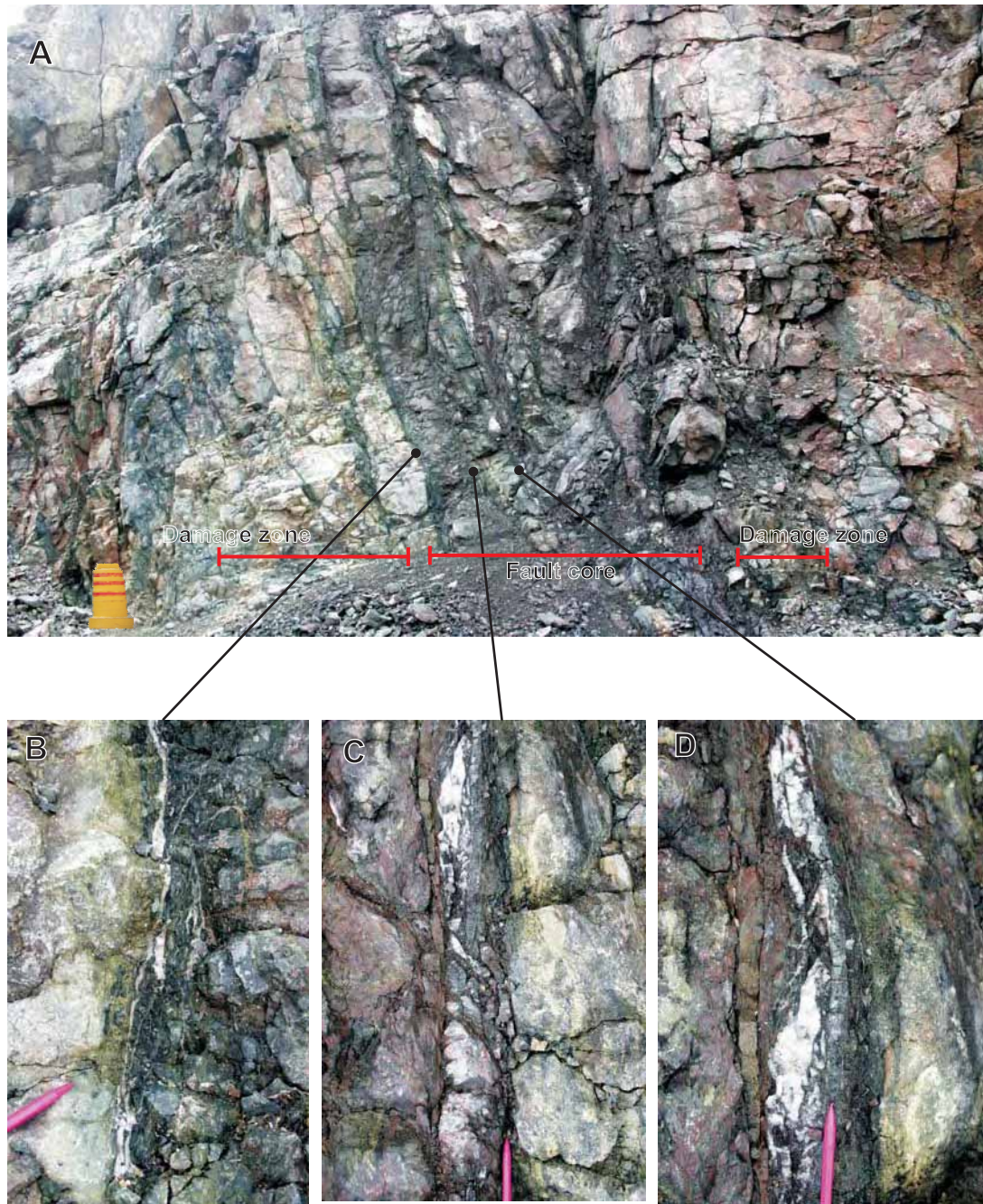


Figure 5.26 - Wide fault zone in the granitic domain at Sequeirinho. **A** outcrop wide photo shows the general features of the fault zone including: dark fault core containing ultracataclasites intercalated with wall rock fragments and asymmetric damage zones characterized by faults and fractures cross cutting intensely altered granitic rocks. Note the apparent decrease in faults/fractures density from the core towards the damage zones. The red brownish patches in the fault core are hematite stained ultracataclasites; **C D E** detailed photos of the features observed in the fault core: in **B** the sharp contact between ultracataclasite and altered granite; **C & D** well defined slip surfaces separating different cataclasites layers (note different colours) and also making the limits between ultracataclasites and lenses or layers of rock fragments. Late calcite is present along the lenses or surfaces.

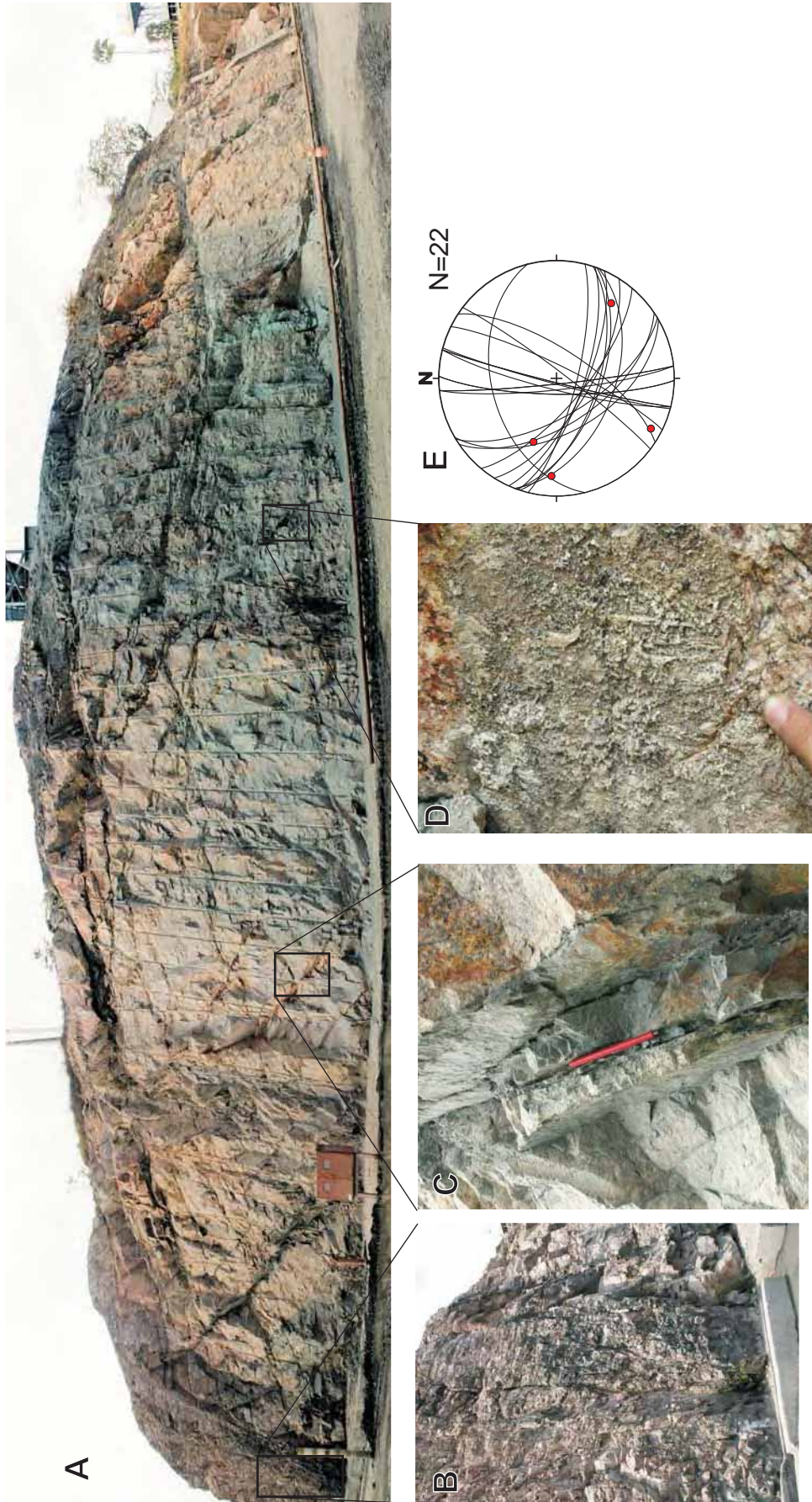


Figure 5.27 - *A* panorama of one of the outcropping parts of the Rio Branco granite cross-cut by several faults with moderate dips; **B** example of “dry” fault from the N-S set, the fault zone comprises severely fractured angular fragments; **C** a typical fault from the WNW-ESE set with relatively smooth and straight fault planes containing cohesive cataclasis cemented by very fine dark hydrothermal mineral; **D** fibrous and granular quartz formed onto the fault plane evidencing the presence of siliceous fluids and extensional stresses; **E** stereonets for fault planes and poles of planes indicating the main N-S and WNW-ESE fault sets cross-cutting the granite.

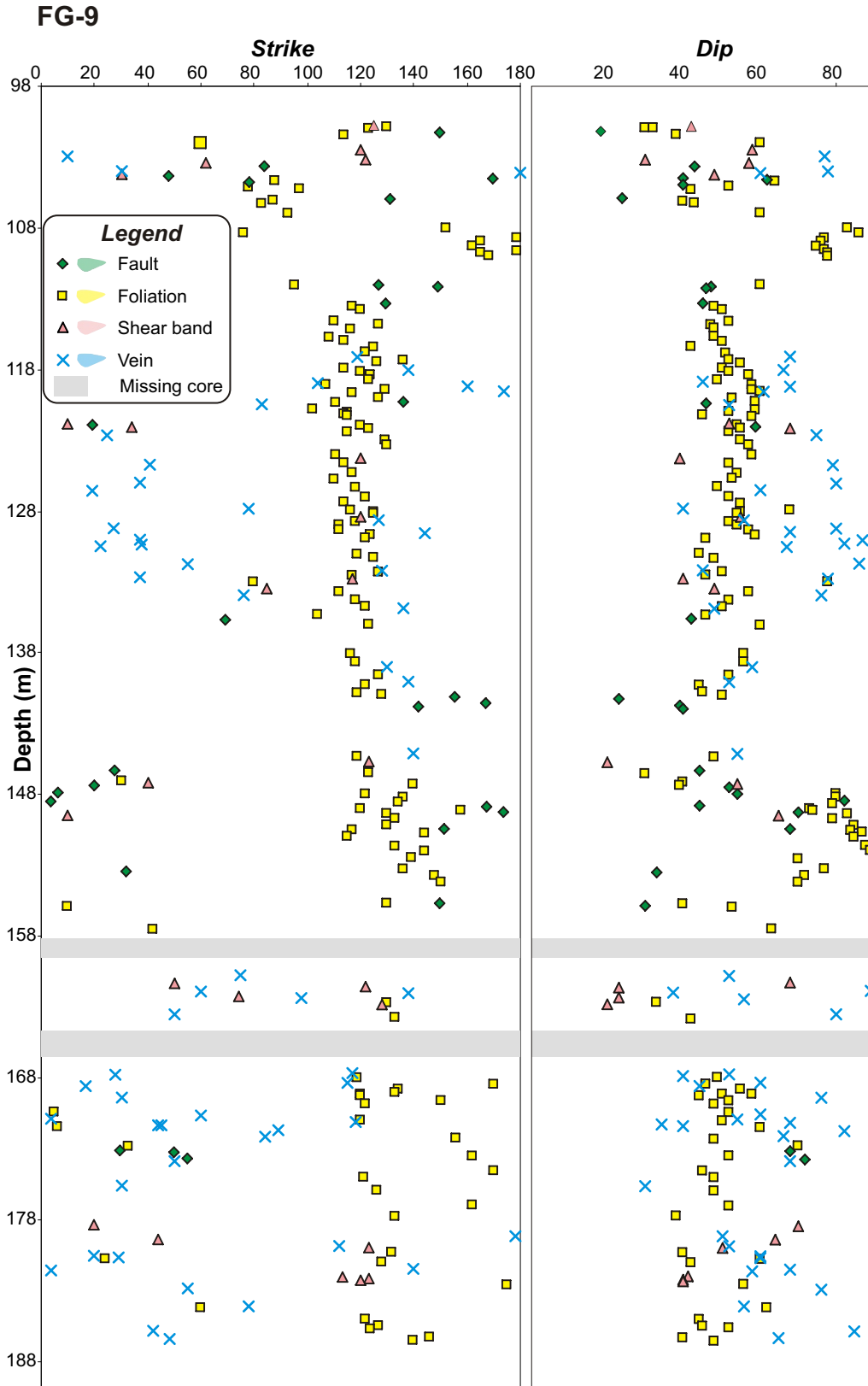


Figure 5.28 - Graphic representation of *strikes* and *dips* of structural elements logged along the core **FG-9**.

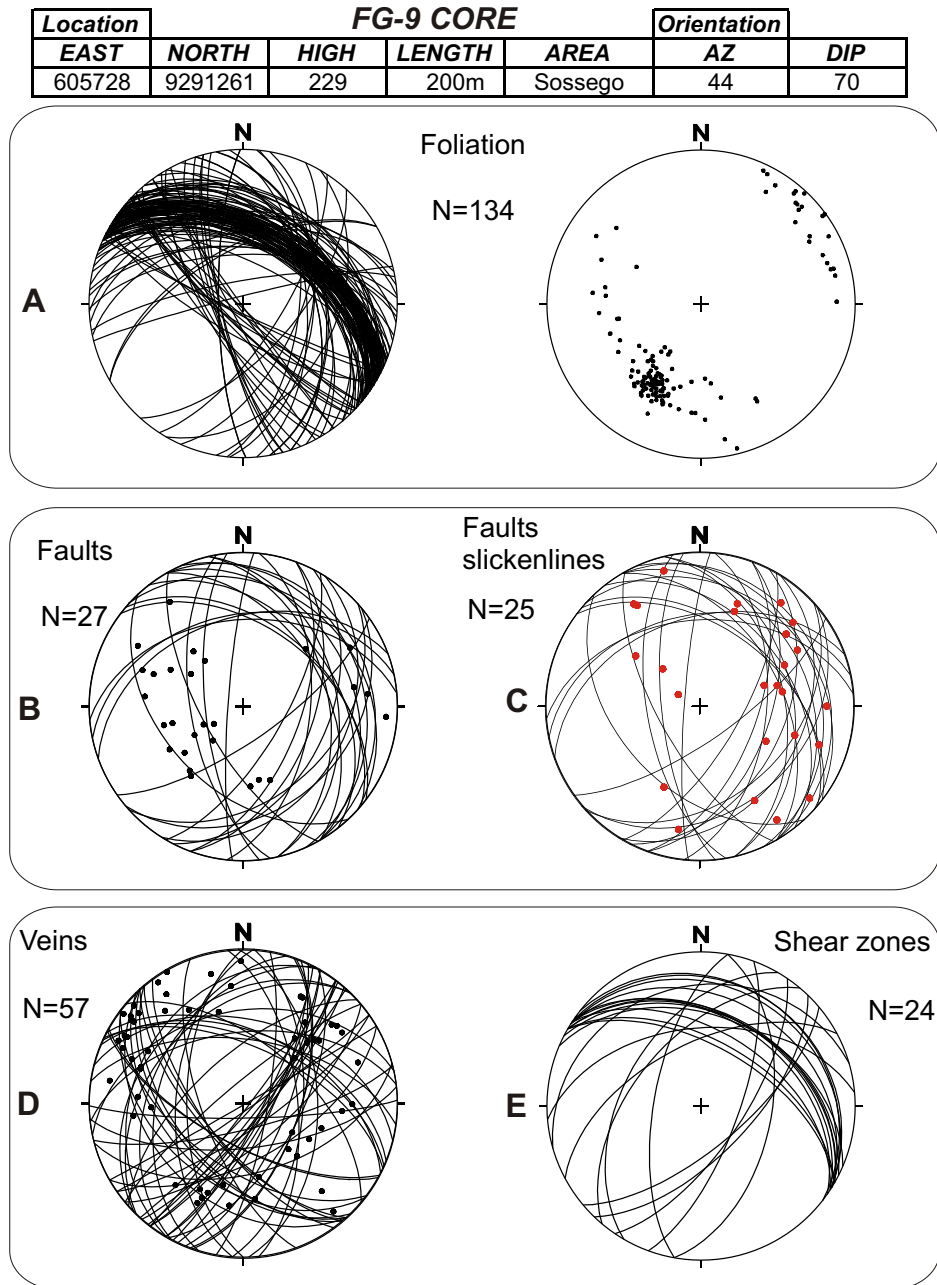


Figure 5.29 - Total stereonet for structures logged along the core **FG-9**. **A** planes and poles for planes of foliation; **B** faults and poles for fault planes; **C** faults slickenlines (red dots) and fault planes; **D** non sulphide veins and respective poles for planes; **E** shear zones planes . The data is represented in equal area plots, projected in the lower hemisphere.

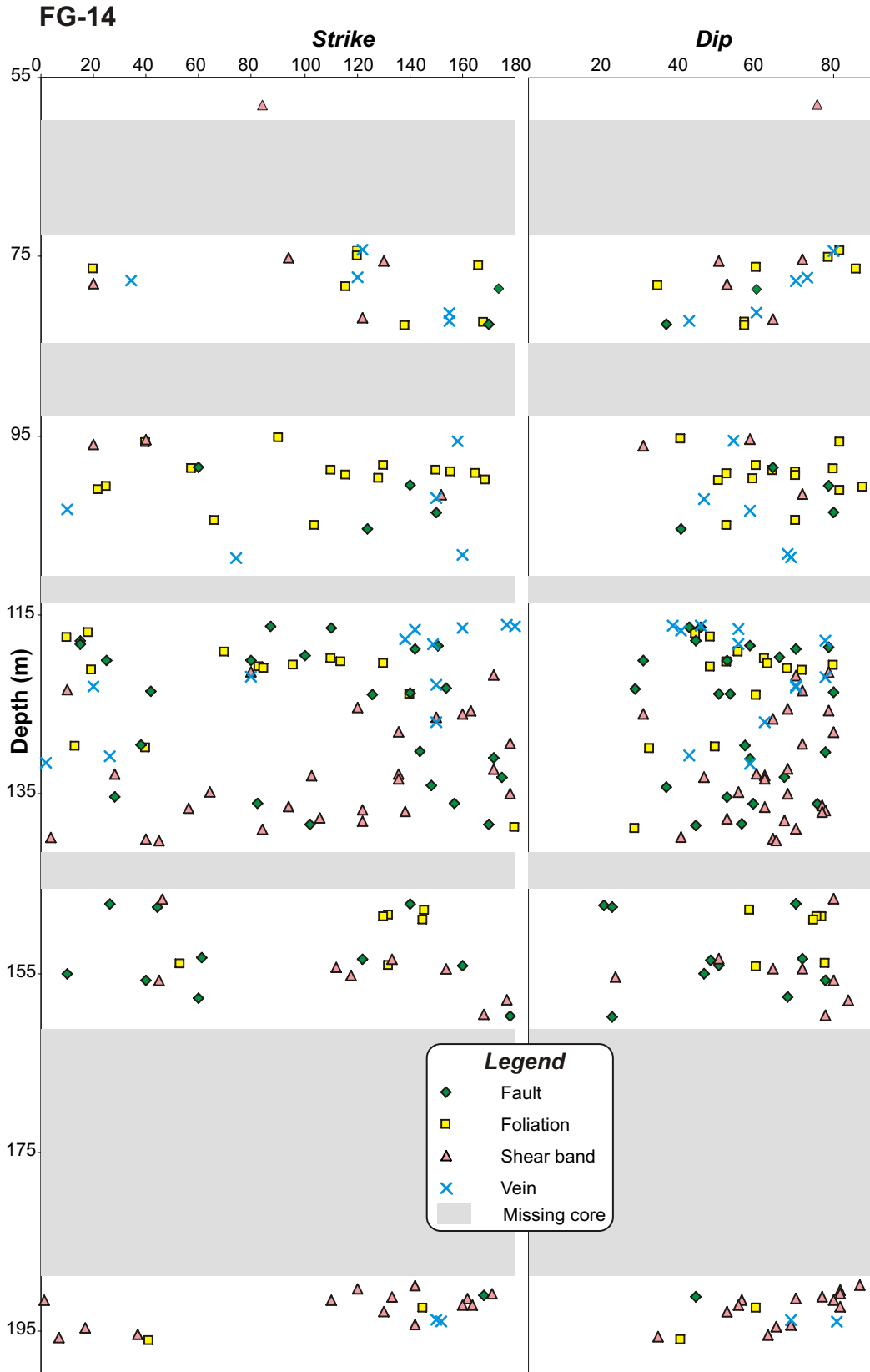


Figure 5.30 - Graphic representation of *strikes* and *dips* of structural elements logged along the core FG-14.

Location					FG-14 CORE			Orientation	
EAST	NORTH	HIGH	LENGTH	AREA	AZ	DIP			
605678	9290943	225	200m	Sossego	135	65			

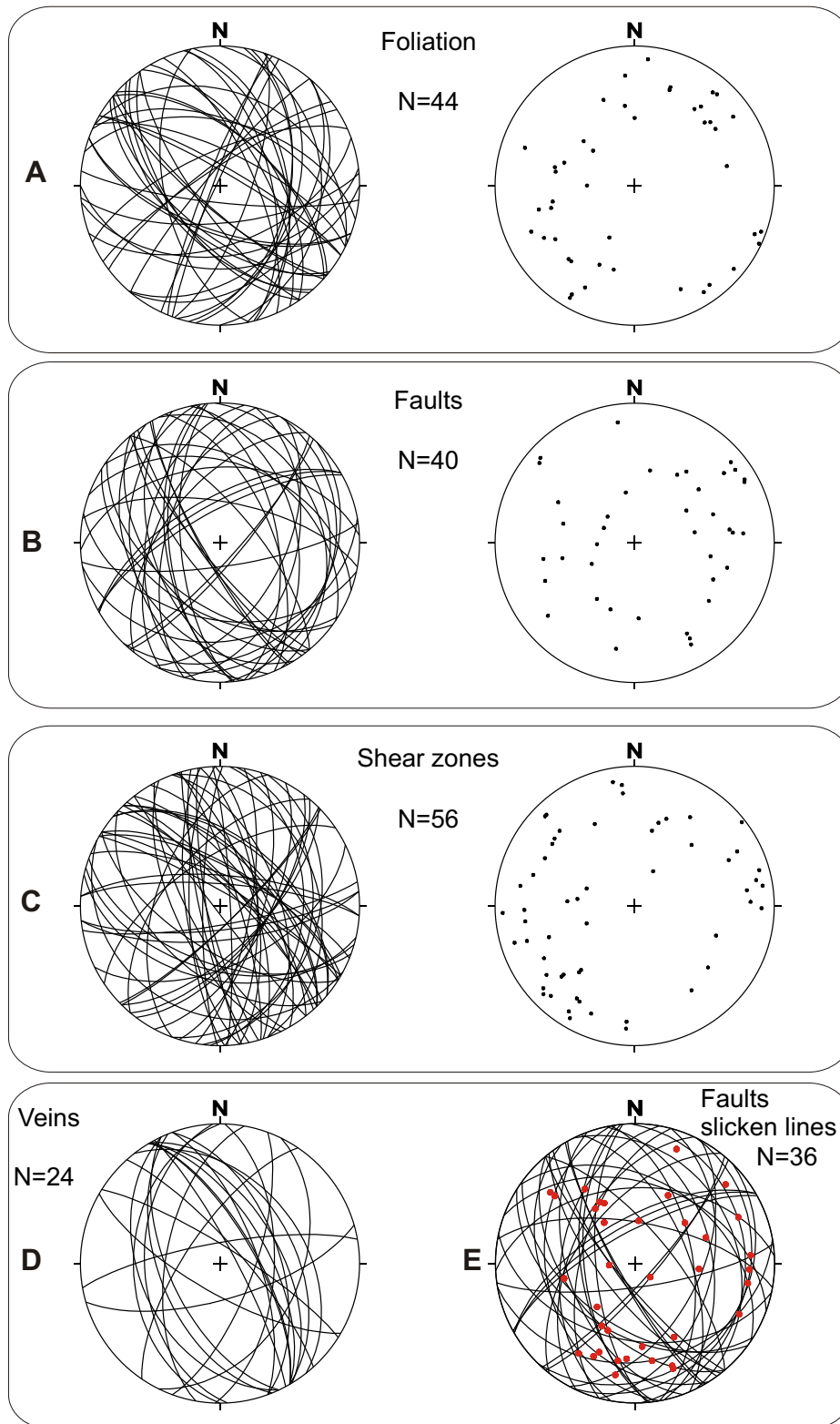
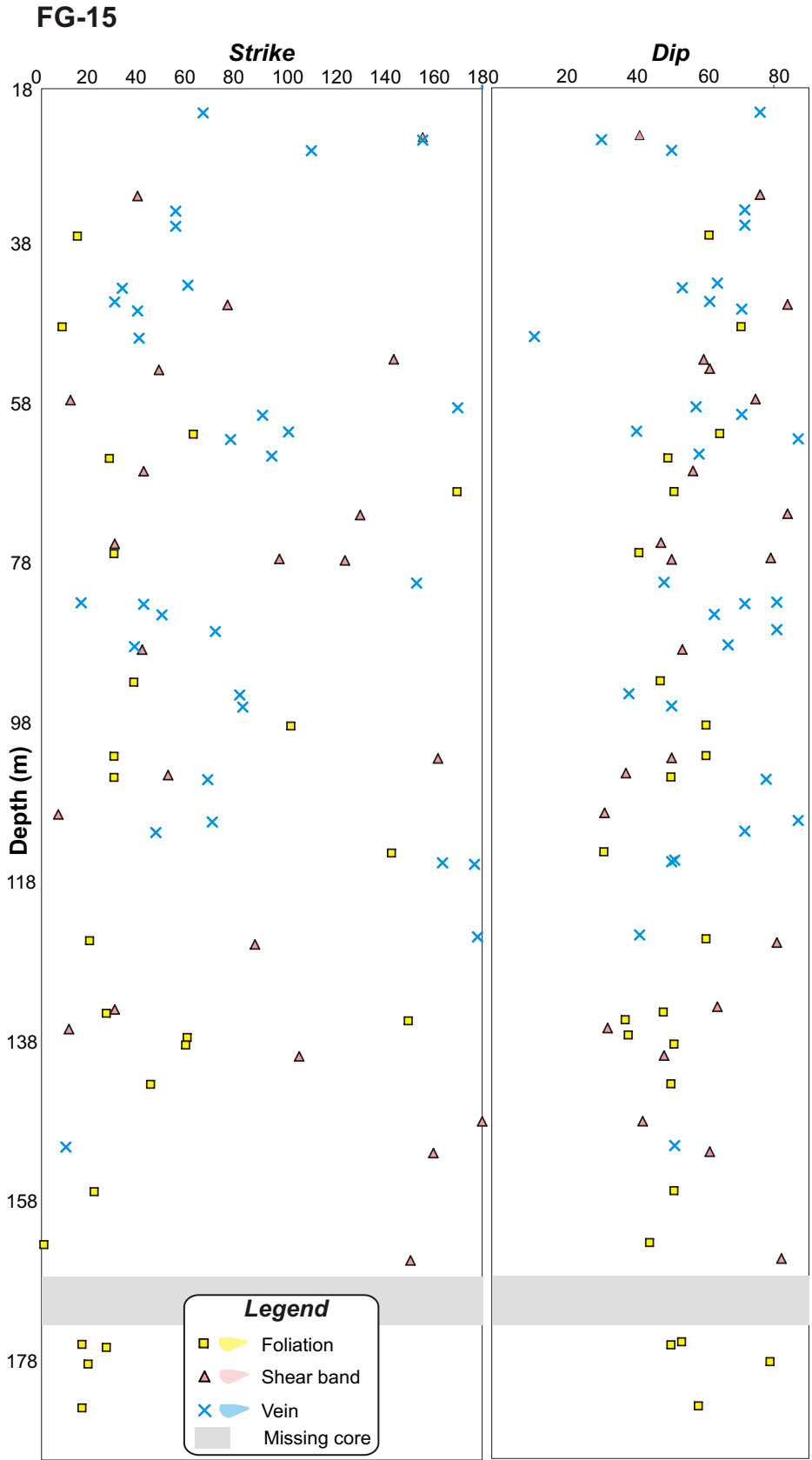


Figure 5.31 - Total stereonet for structures logged along the core **FG-14**. **A** foliation planes and poles for planes; **B** fault planes and respective poles to planes; **C** shear zones and poles for the respective planes; **D** veins; **E** fault slickenlines and respective fault planes . The data is represented in equal area plots, projected in the lower hemisphere.



*Figure 5.32 - Graphic representation of **strikes** and **dips** of structural elements logged along the core **FG-15**.*

Location					FG-15 CORE		Orientation	
EAST	NORTH	HIGH	LENGTH	AREA	AZ	DIP		
604160	9290558	254	314m	Sequeirinho	180	65		

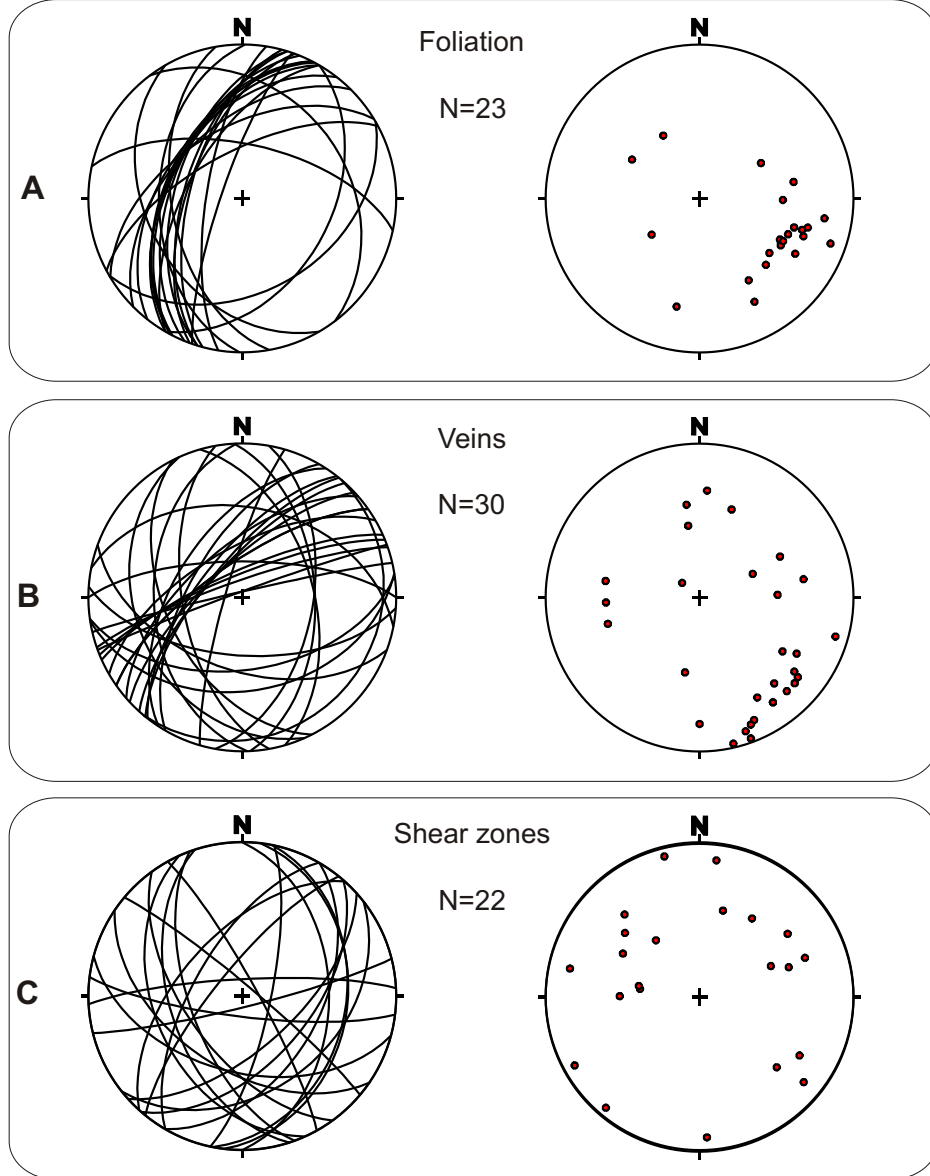


Figure 5.33 - Total stereonet for structures logged along the core **FG-15**. **A** foliation and poles for foliation planes; **B** veins and poles for veins planes; **C** shear zones and poles for their respective planes. The data is represented in equal area plots, projected in the lower hemisphere.

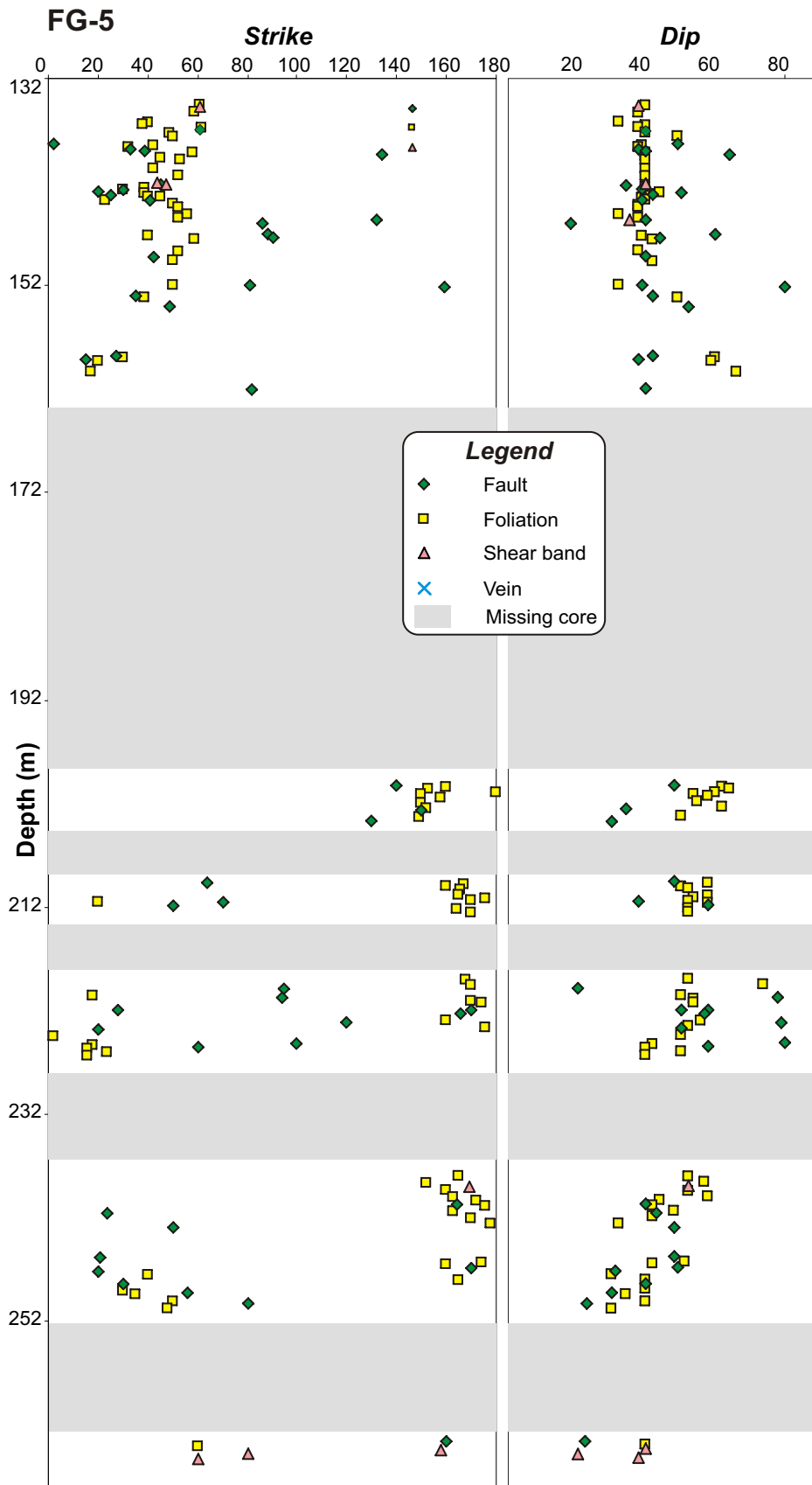


Figure 5.34 - Graphic representation of *strikes* and *dips* of structural elements logged along the core FG-5.

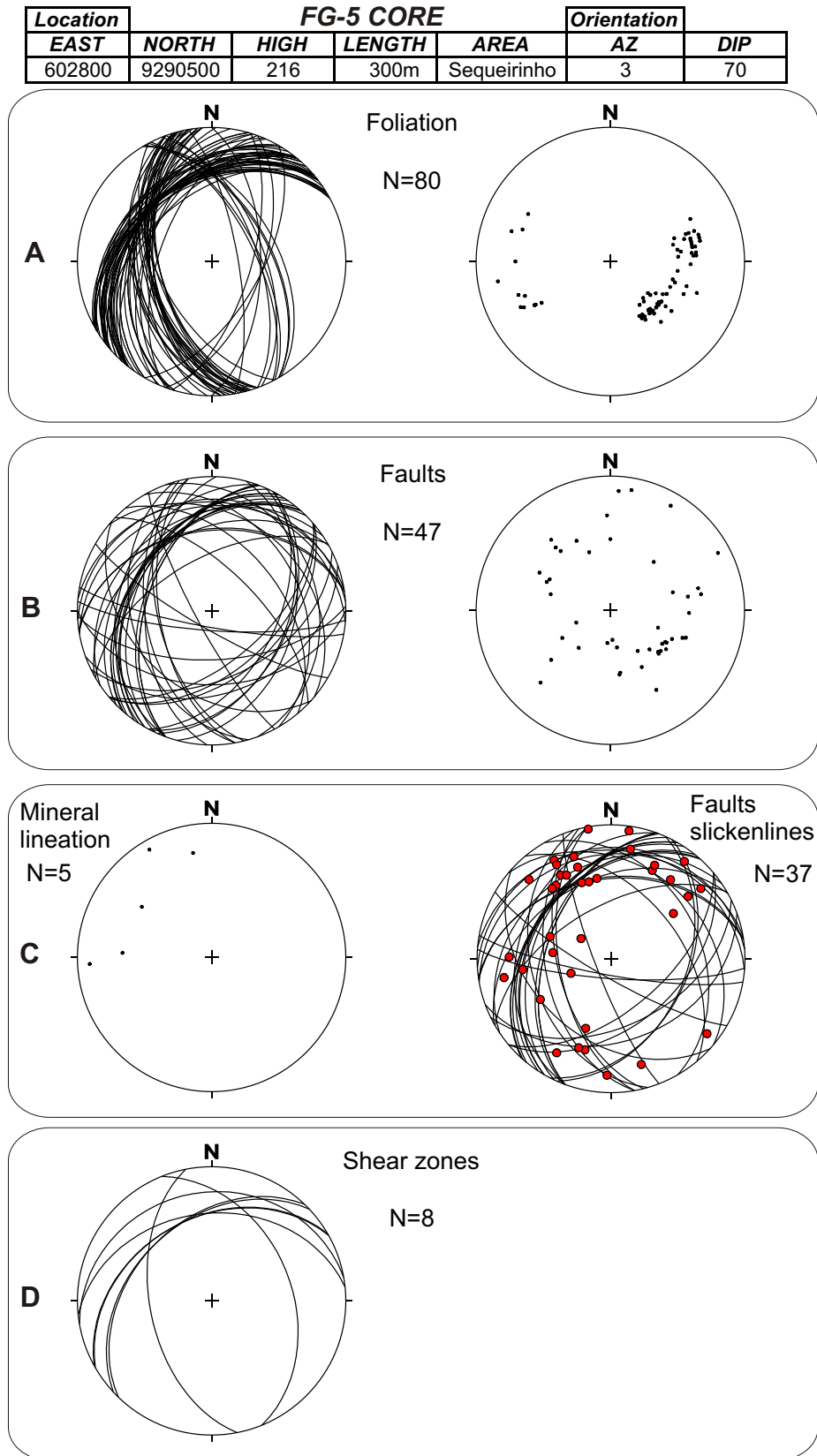
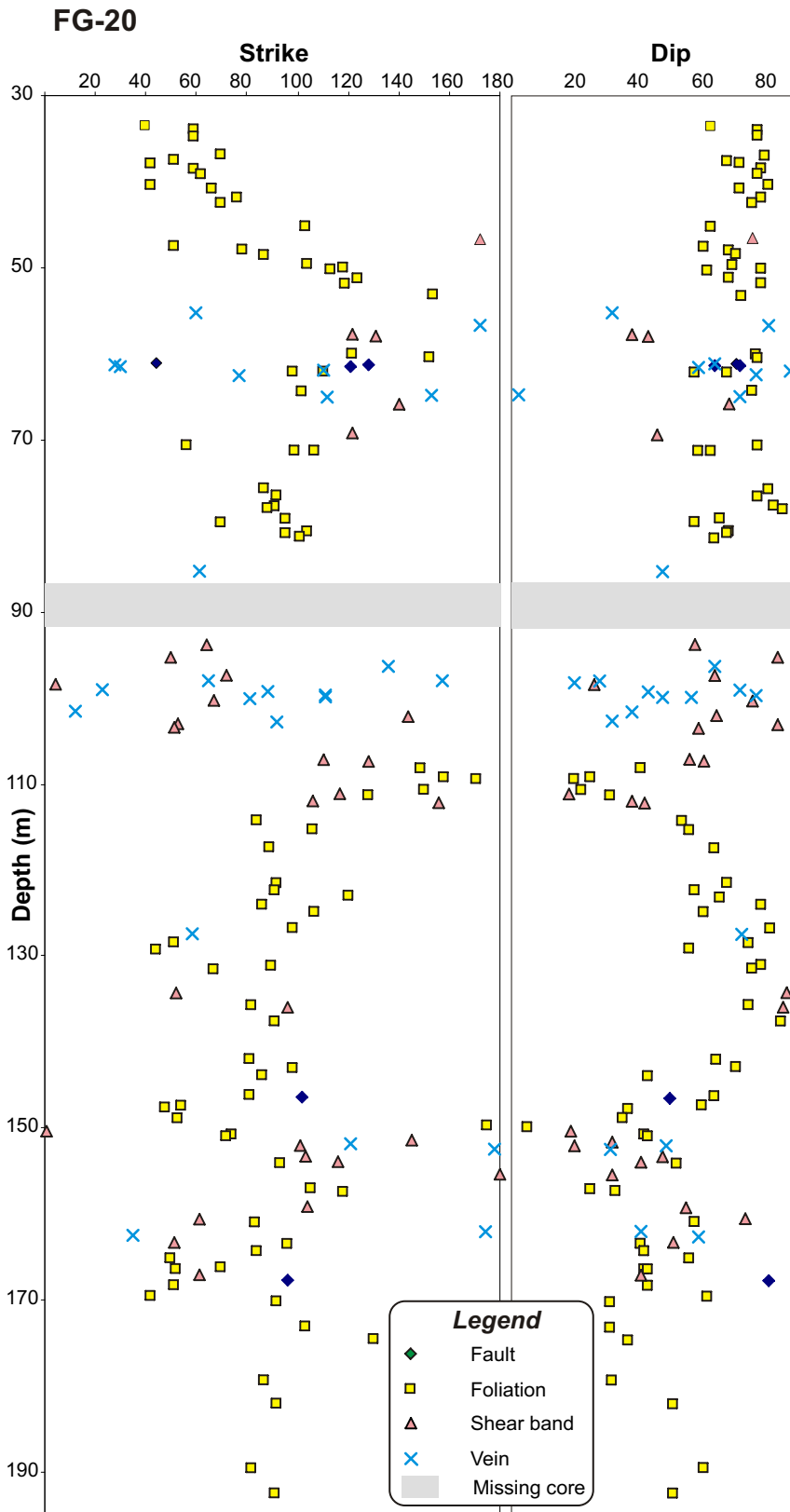


Figure 5.35 - Total stereonet for structures logged along the core FG-5. **A** foliation planes and poles to planes ; **B** fault planes and respective poles to the planes; **C** mineral lineation and fault slickenlines represented with their respective fault planes; **D** shear zones. The data is represented in equal area plots, projected in the lower hemisphere.



*Figure 5.36 - Graphic representation of **strikes** and **dips** of structural elements logged along the core FG-20.*

Location					Orientation		
EAST	NORTH	HIGH	LENGTH	AREA	AZ	DIP	
602799	9290755	217	200m	Sequeirinho	270	65	

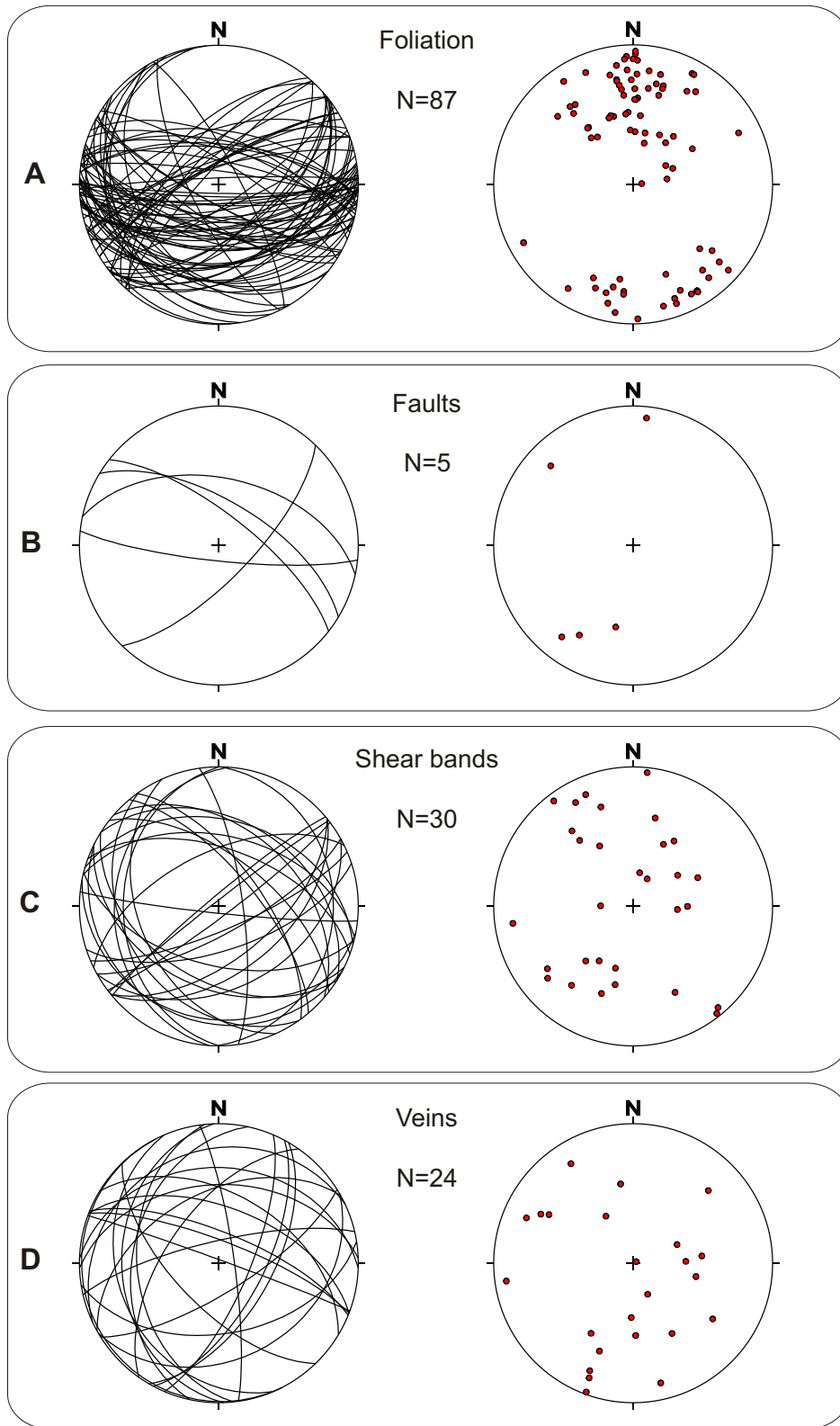


Figure 5.37 - Total stereonets displaying planes and poles to planes of the structures logged along the core FG-20. **A** foliation; **B** faults; **C** shear bands; **D** veins. The data is represented in equal area plots, projected in the lower hemisphere.

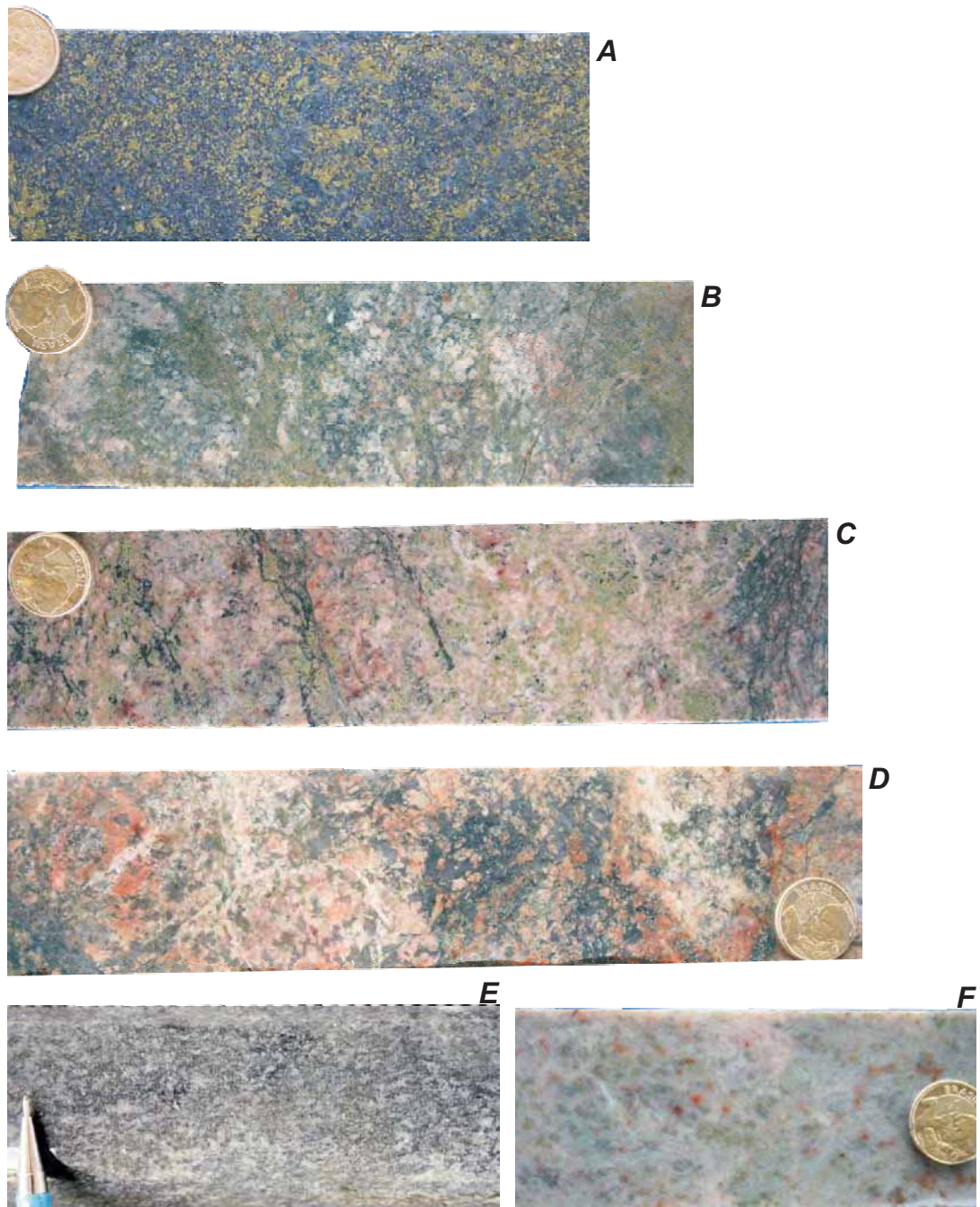
Isotropic Granites

Figure 5.38 - Core samples of isotropic granites with some examples of locally representative alteration assemblages. **A** granitoid showing sulphide (chalcopyrite) mineralization; **B** albitized granitoid overprinted by epidote; **C** granitoid displaying three generations of hydrothermal minerals k feldspar (pink) albite (white) epidote (green); **D** granitoid showing potassic alteration partially overprinted by albitization; **E** unaltered granophyre; **F** totally albitized granitoid. Samples from Sossego (D, E) and Sequeirinho (A, B, C, F) orebodies.

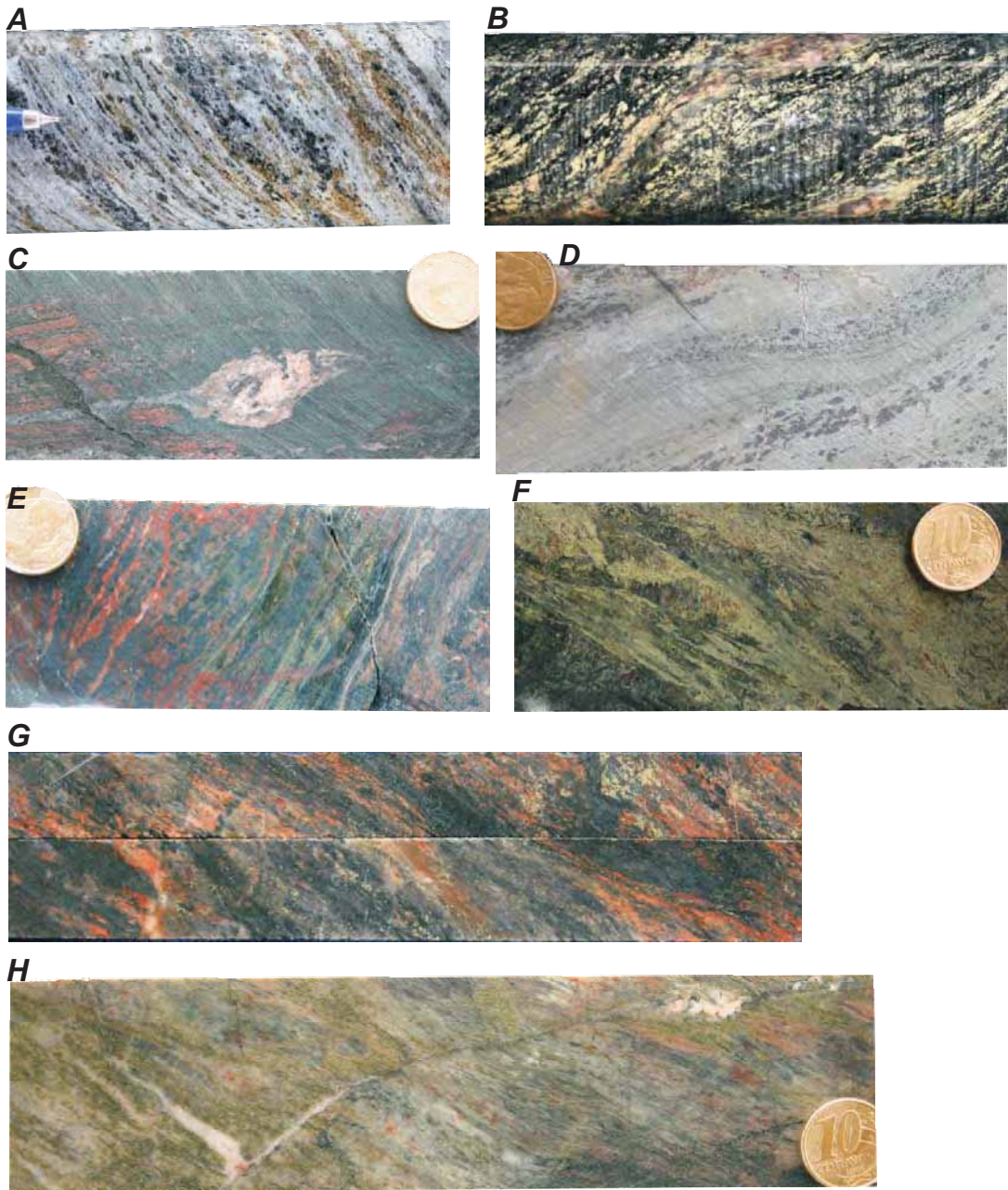
Mylonites

Figure 5.39 - Selected samples of representative types of mylonites developed in granitic rocks. Foliation varies from relatively straight to gently anastomosing, typically enveloping porphyroclasts or lenses. The mylonitic fabric can be found as: (i) “coarse” characterized by mineral fragments or lenses and porphyroclasts; or (ii) fine, composed of narrow layers or ribbons of alternating minerals. Dominant mineral assemblage includes: **A** albite; **B** actinolite+chlorite; **C** albite porphyroclast and some *k* feldspar; **D** actinolite+magnetite; **E** *k* feldspar+quartz+chlorite; **F** epidote; **G** *k* feldspar+actinolite; **H** albite+chlorite. Samples from Sossego (A, B, C, D) and Sequeirinho (E, F, G, H) orebodies.

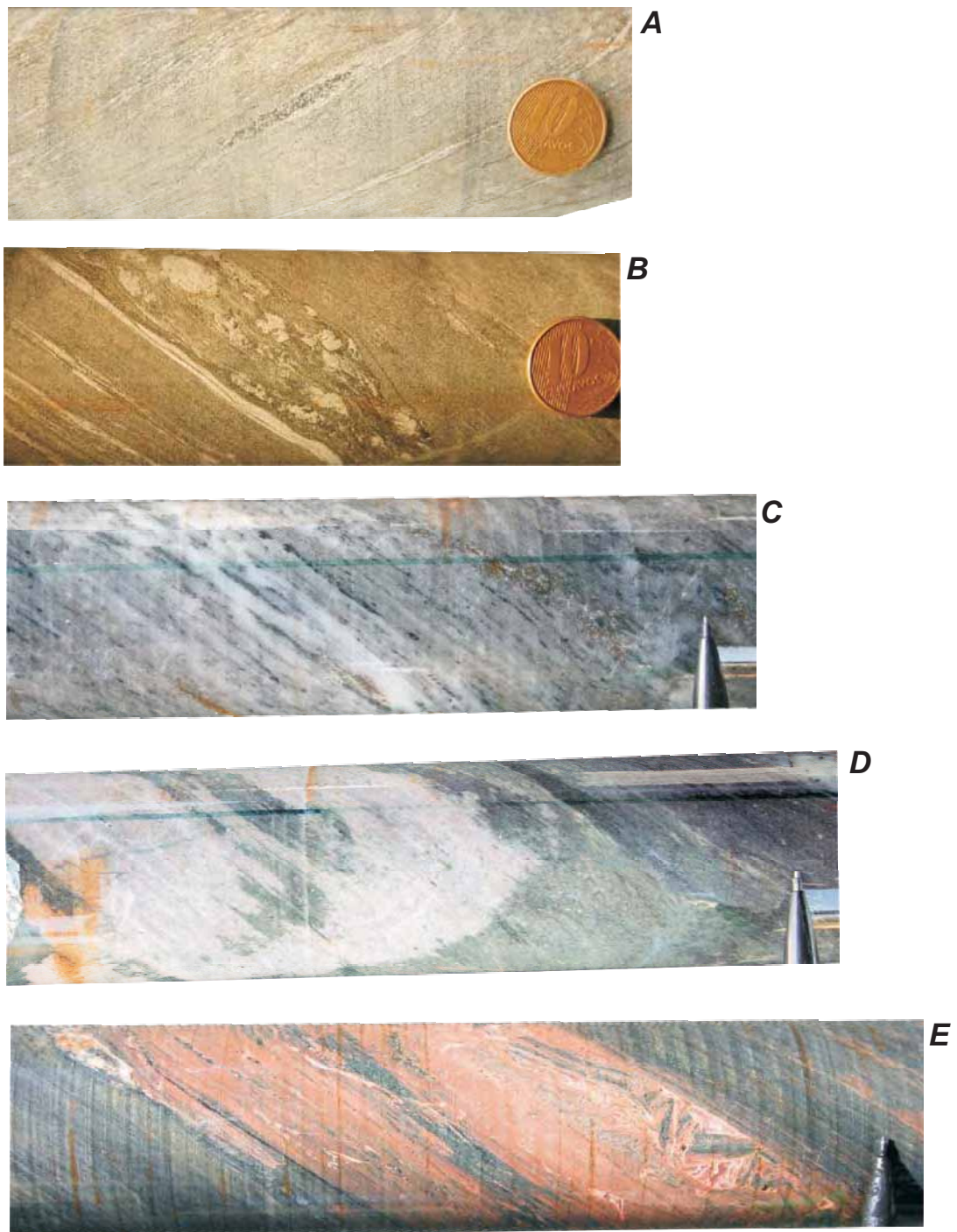
Schists

Figure 5.40 - Representative biotite schist samples from Sequeirinho. These rocks are characterized by their prominent fine to very fine foliation. Hydrothermal alteration is represented by fluid pathways marked by silicification, albitization and discrete brecciation. **A** schist with alternating very thin bands of quartz and biotite; **B** coarser schist comprising mylonitic level with prominent quartz porphyroclasts; **C** intensely albitized schist with preserved ductile fabric; **D** partially albitized schist, the patchy altered domains mark the sites of fluid rock interaction; **E** schist with zone of intense potassic alteration and localized brecciation, evidencing elevated pressures in the fluid pathways.

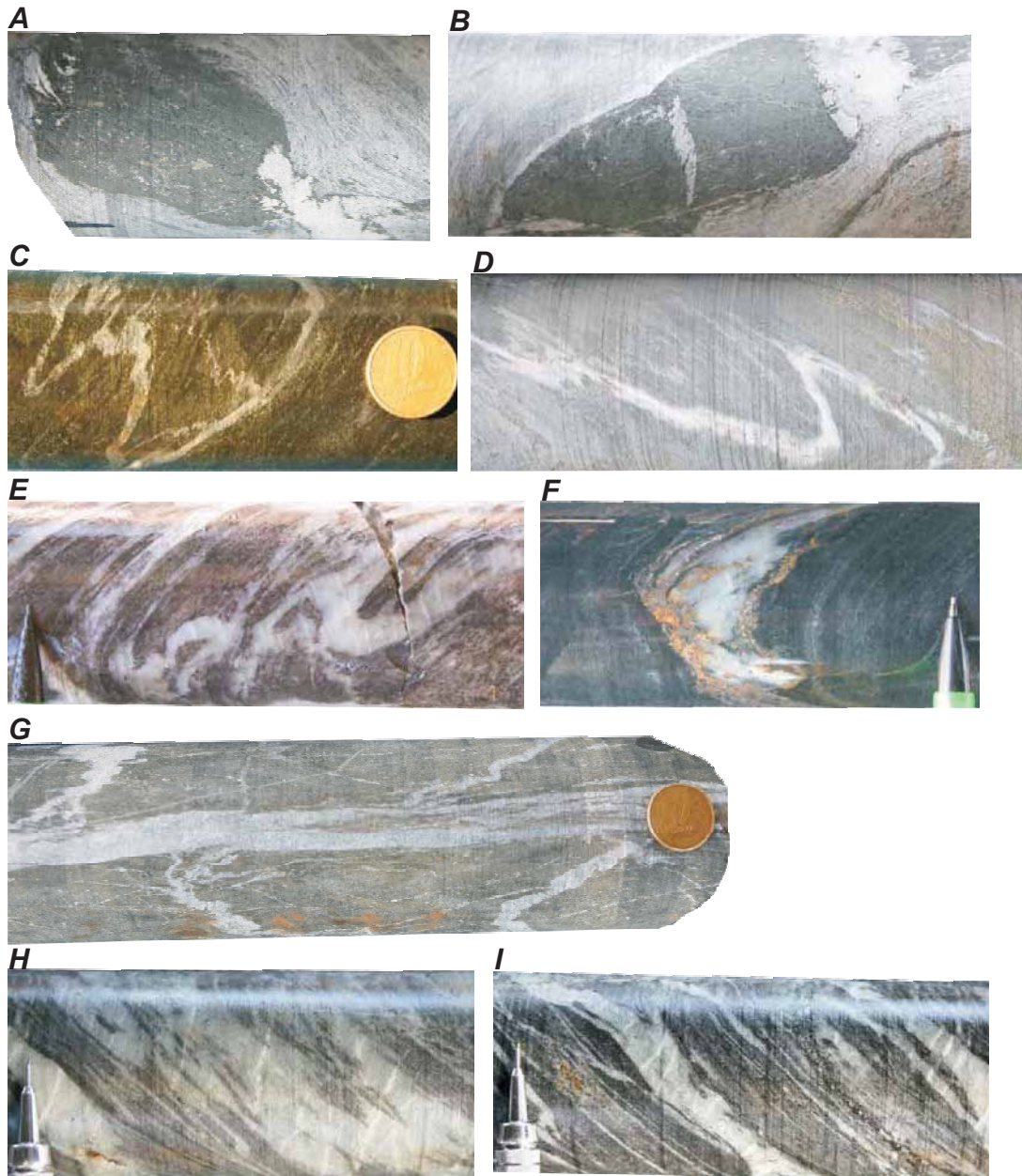
Boundins and deformed veins

Figure 5.41 Boudins and deformed veins in ultramylonites from the shists domain at Sequeirinho. The two photos on the top show slightly asymmetric boudins with quartz pressure shadows along the boudin necks. Note the absence of foliation inside the boudins. Folded quartz veins are ordered from top to bottom displaying strain increase. Observe the occurrence of sulphide mineralization associated with these veins and transposed folded veins on the photos at the bottom of the page. **A** and **B** show biotite rich boudins surrounded by quartz rich schist; **C** quartz vein forming a parasitic fold; **D** quartz vein forming a asymmetric fold; **E** isoclinal folded quartz vein; **F** quartz and sulphide tight fold; **G** secondary folded quartz veins projected from a central unfolded vein; **H** and **I** folded quartz veins displaying their hinges distended from the fold limbs.

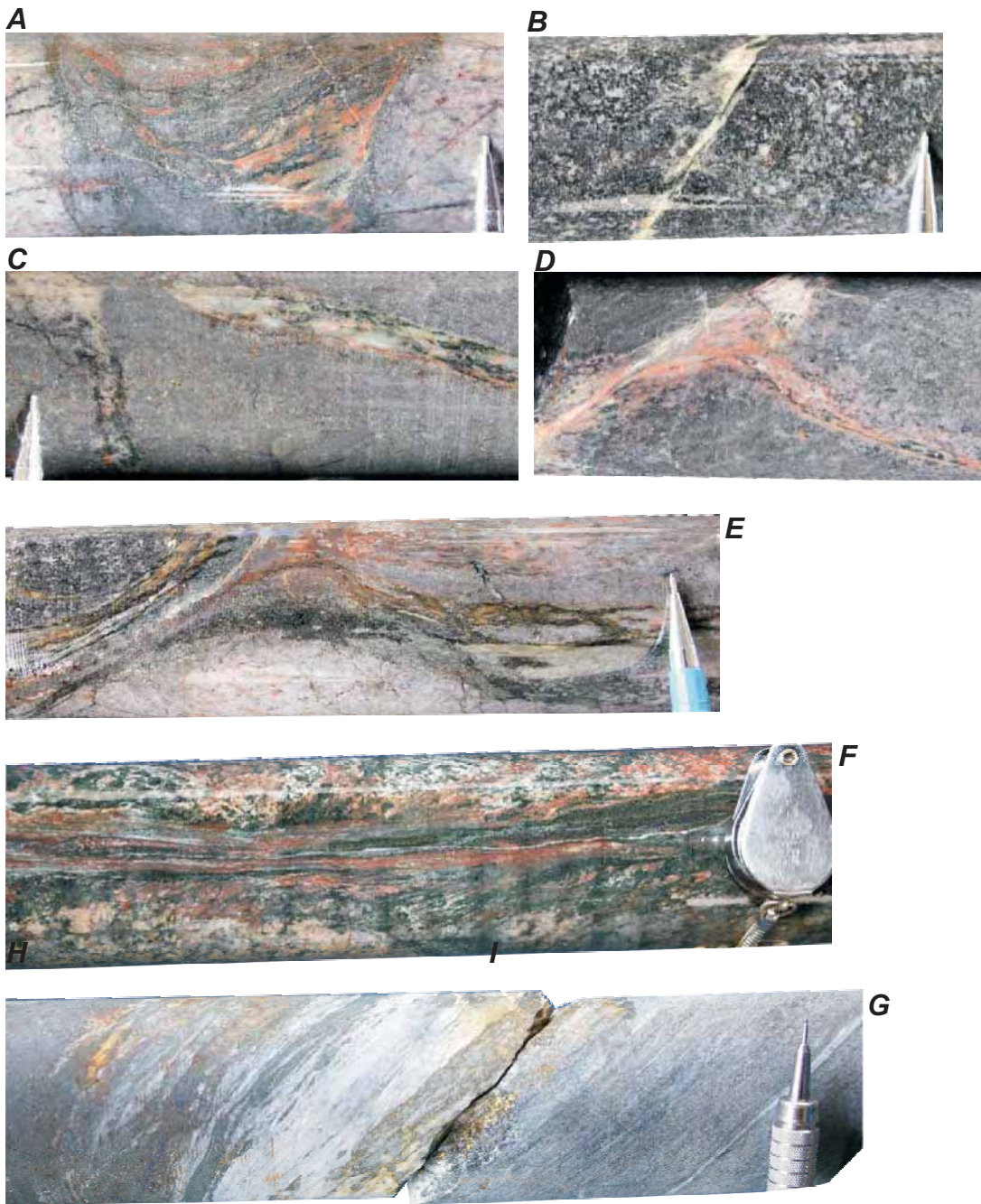
Shear zones

Figure 5.42 - Shear bands or zones developed in granite, granophyre and schist. Photos show the main characteristics of these zones observed in all the studied domains of the mines. They are normally narrow but may be up to 4 cm wide. Their geometry varies from straight to curved or anastomosing. Sharp boundaries, internal foliation and hydrothermal alteration are notably observed in these structures. Samples from Sossego (A, B, D, F) and Sequeirinho (C, E, G) orebodies.

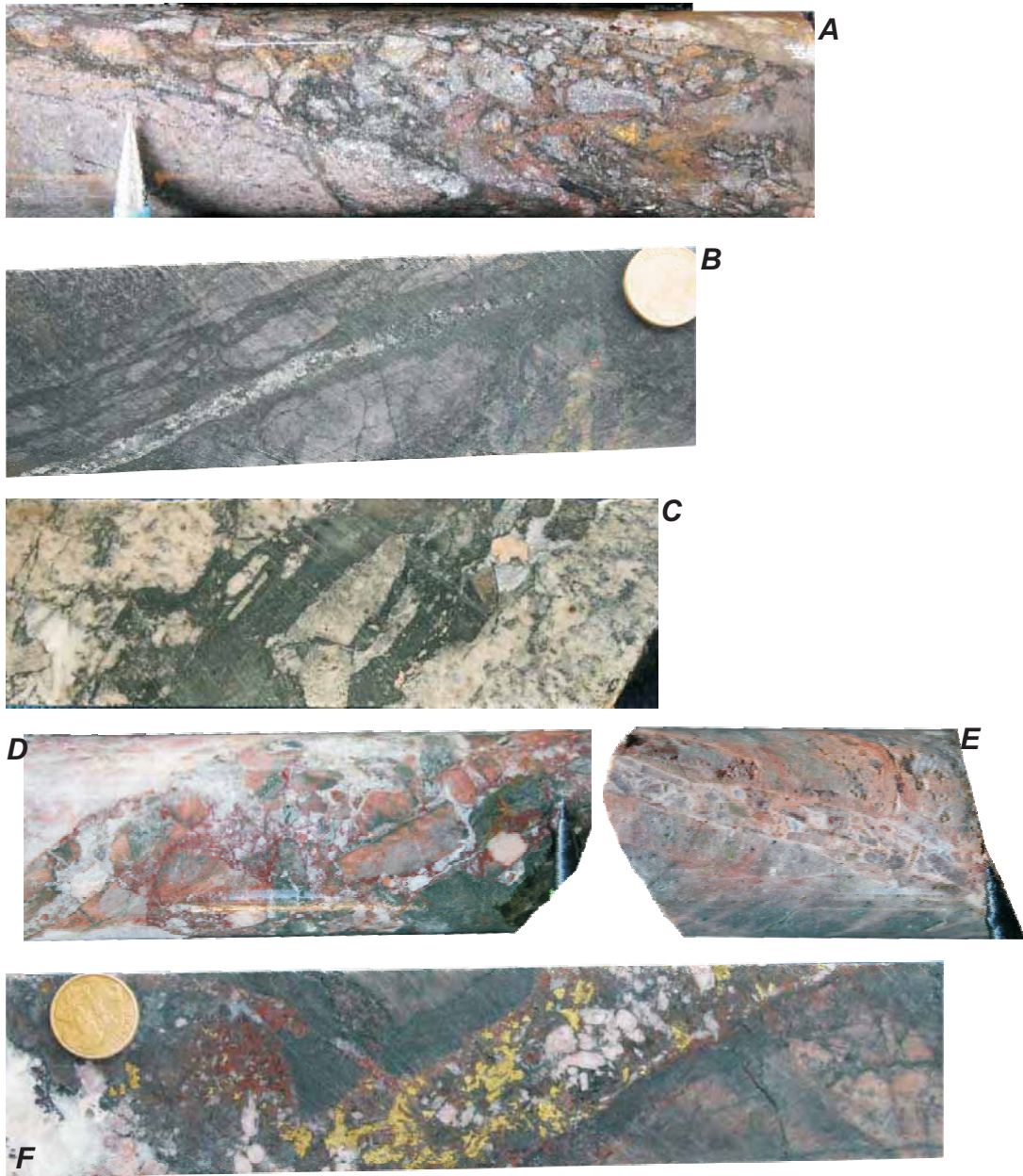
Breccia Veins

Figure 5.43 - Photo collection of breccia veins and its key aspects. These features main characteristics are: sharp boundaries with the wall rock and the presence of rock fragments generally cemented by hydrothermal minerals. The three photos on the top show examples of “sheared” breccia veins. Their distinctive features are either the presence of sheared boundaries or imbricated fragments indicating flow. The photos on the bottom correspond to the mosaic type breccia veins with relatively angular fragments with no evidence of rotation or motion. Breccia veins from: **Sossego A** breccia showing sub rounded fragments cemented by pulverized rock and minor sulphide; **B** breccia composed of elongated, sub angular and imbricated fragments; **F** breccia showing reaction rings in fragments cemented by hydrothermal sulphide and carbonate and **Sequeirinho C, D, E**.

Breccias

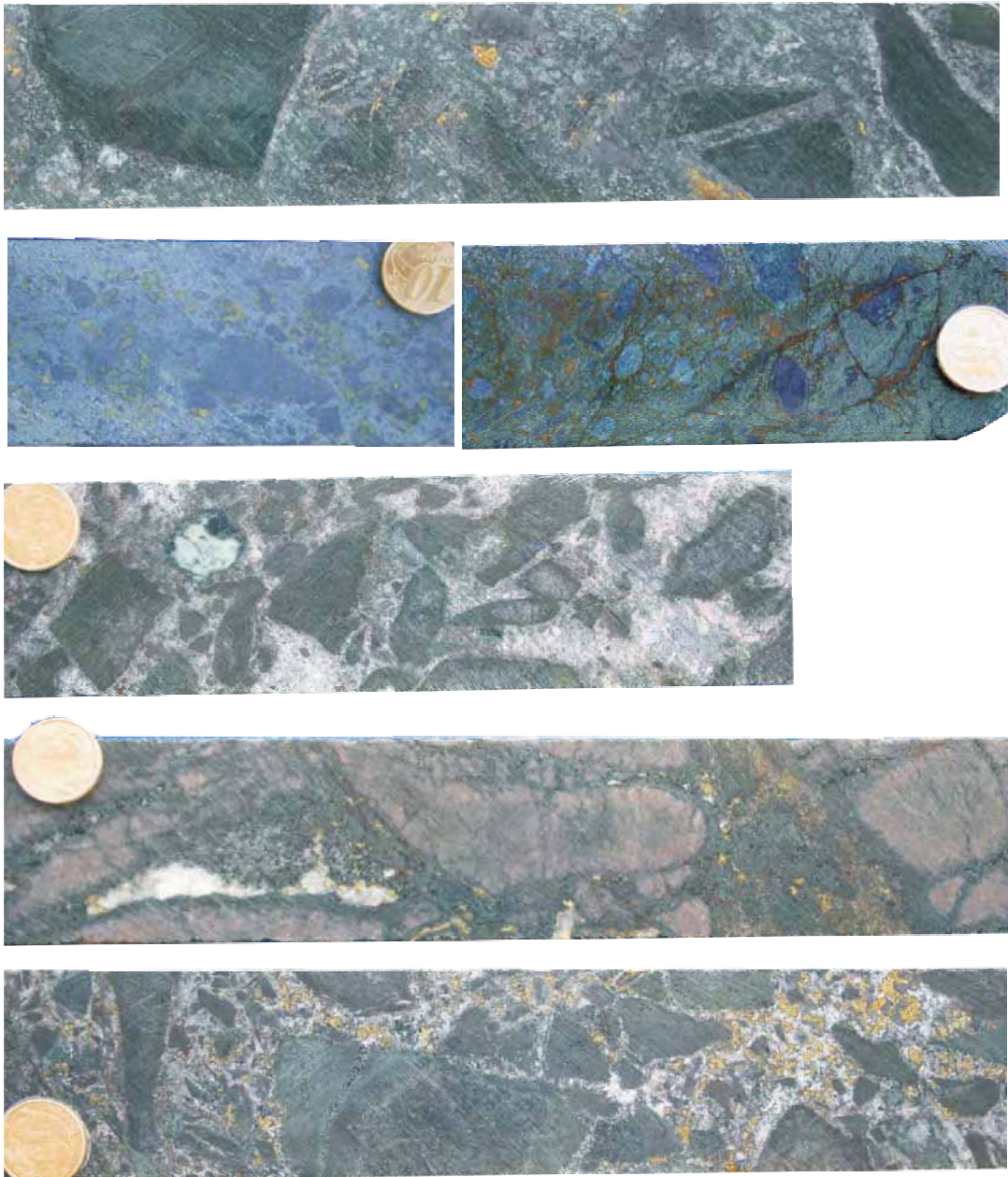


Figure 5.44 - Mineralized and barren breccias from Sossego and Sequeirinho. These rocks main characteristics are: varied fragment sizes ranging from few millimetres up to tens of centimetres; and fragments shape varying from angular to sub rounded. Some samples show fragments with reaction haloes indicating highly reactive fluids.

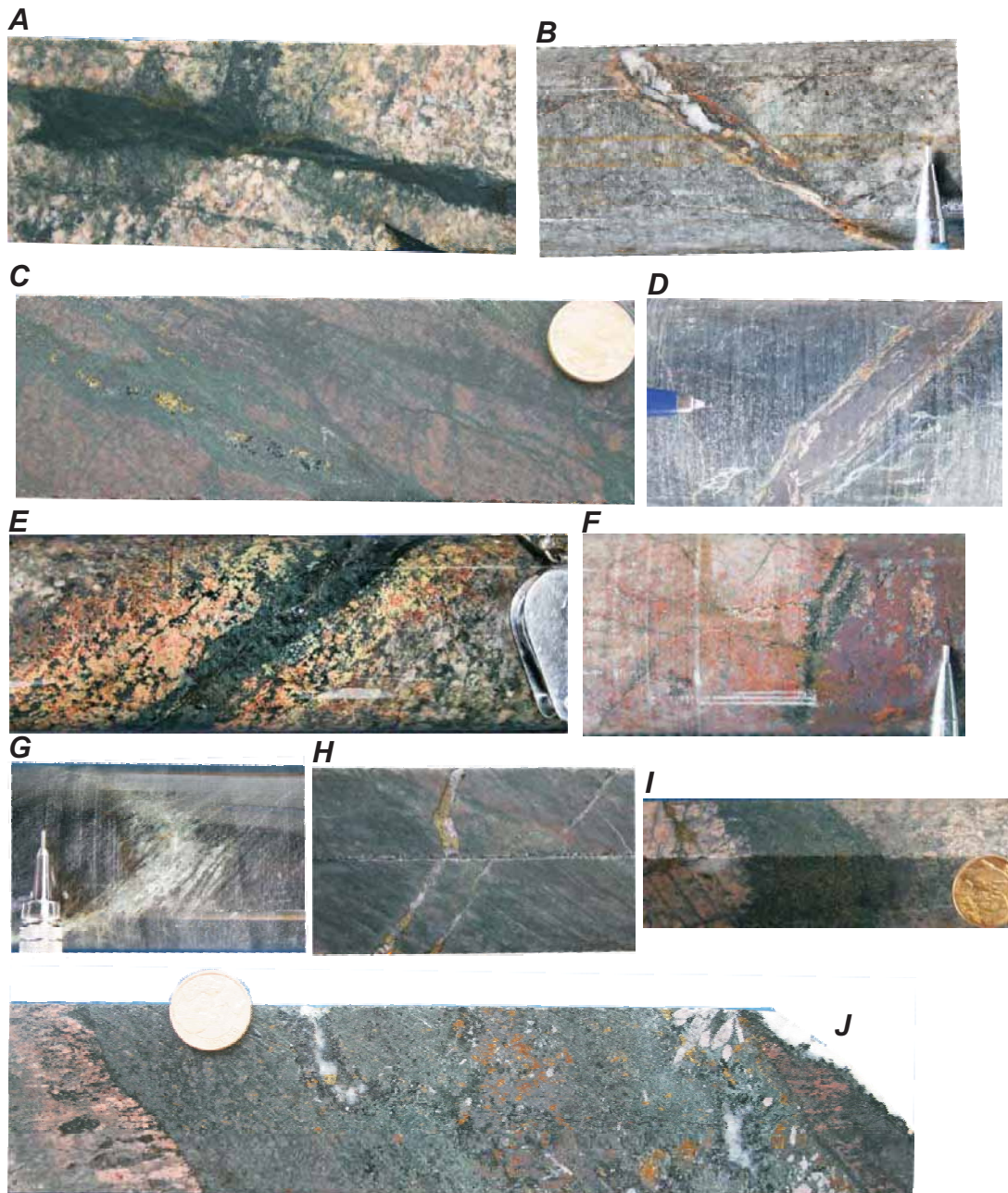
Veins

Figure 5.45 - Representative samples of extensional and sheared veins from Sossego and Sequeirinho. The two upper rows show sheared veins (note sheared walls) and the three rows at the bottom display simple extensional types. Sheared veins formed of: **A** actinolite and minor sulphide; **B** quartz and minor actinolite; **C** actinolite and minor sulphide; **D** magnetite and minor calcite. Extensional veins composed of: **E** actinolite; **F** magnetite; **G** quartz; **H** chalcopyrite + quartz; **I** Actinolite; **J** magnetite and minor sulphide. Samples from Sossego (**A**, **C**, **D**, **F**, **I** and **J**) and Sequeirinho (**B**, **E**, **G** and **H**).

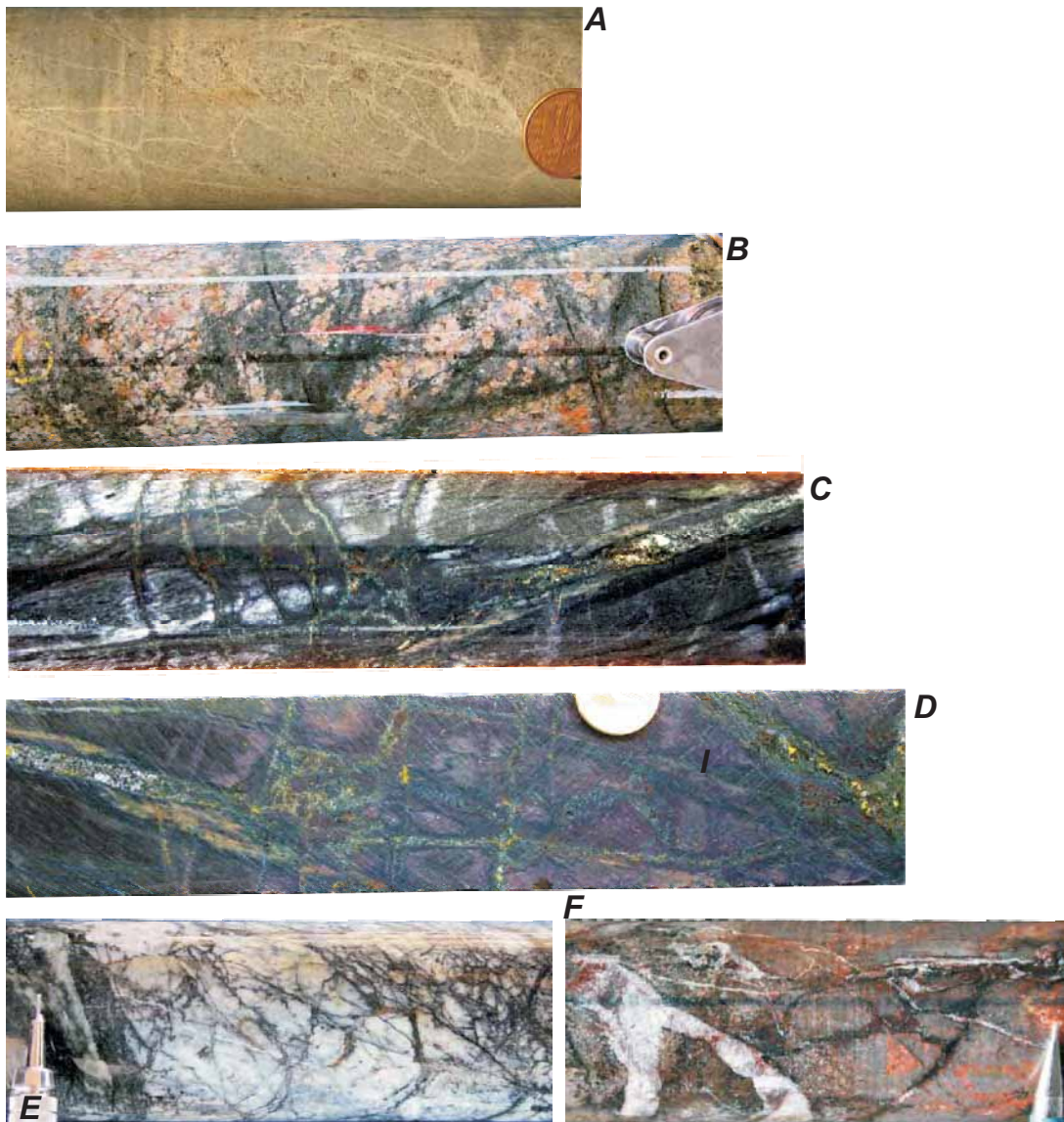
Stockwork

Figure 5.46 - Typical aspects of stockwork domains formed by thin interconnect veins or veinlets. The network of veins indicate favourable conditions for fluid percolation and/or flow evidenced by alteration of vein walls and precipitation of minerals along the veins. The selected samples from Sossego are filled with actinolite (**B**), chalcopyrite (**C**), and sulphide + epidote (**D**); while in Sequeirinho, the veinlets comprise epidote (**A**), actinolite (**E**) and calcite/actinolite (**F**).

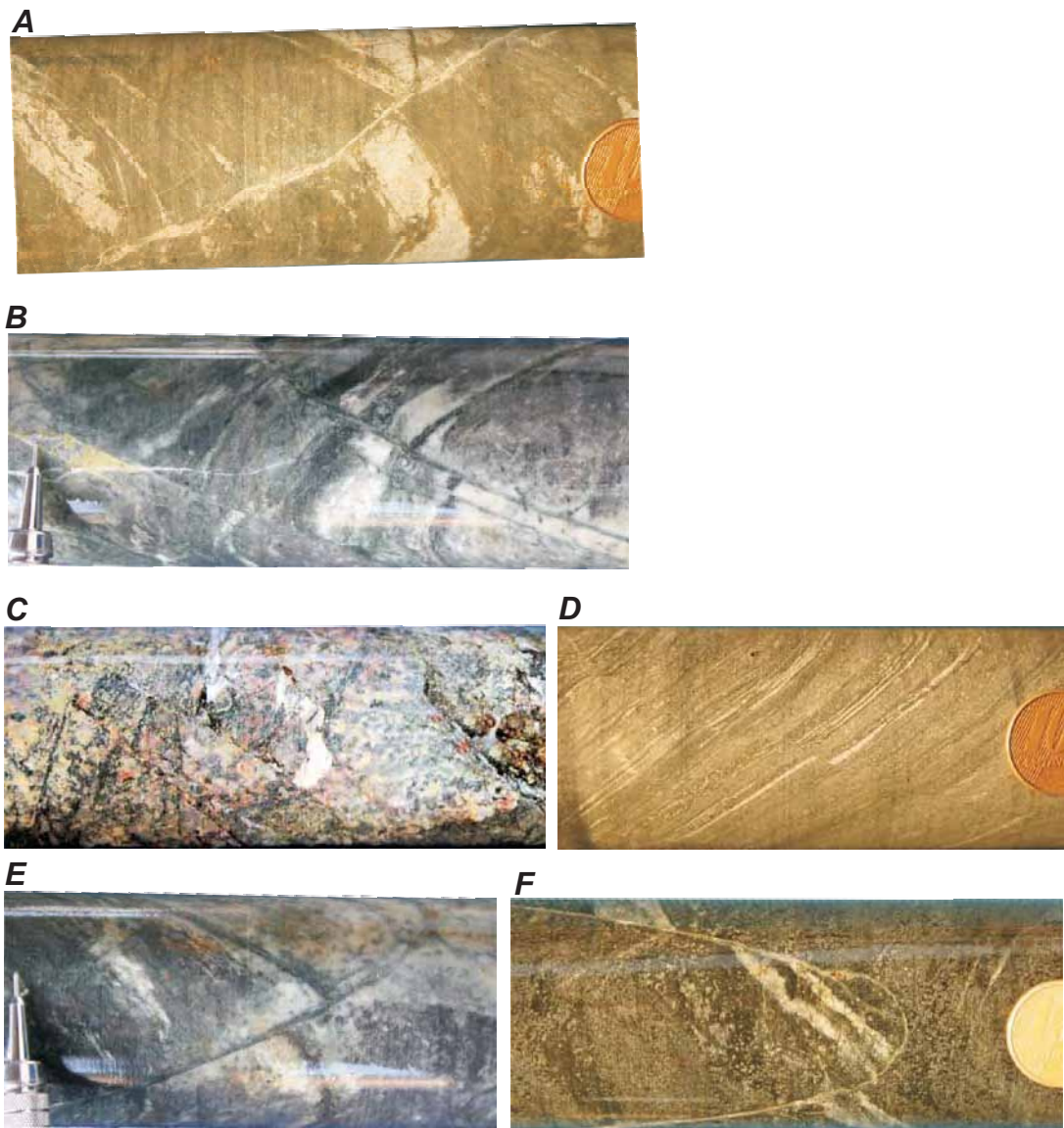
Faults

Figure 5.47 - Examples of discrete fault planes in drill cores and its marking characteristics: (1) straight and narrow fault planes commonly filled with very fine hydrothermal minerals; and small order of fault displacements. Samples from the Sossego (B, C, E) and Sequeirinho (A, D, F) orebodies.

<i>Analysed Parameters</i>	<i>Description</i>	<i>Equation</i>
<i>clast roundness</i>	Describes the smoothness of the particle edge, ranging between 0 and 1. The greater the value, the rounder the object. If the ratio is equal to 1, the object is circular. As the ratio decreases from 1, the object departs from a circular shape (Baxes 1994)	$4 \pi \frac{AREA}{perimeter^2}$
<i>clast concentration</i>	Expressed as a percentage of the total area of the sample, including matrix and cement, in relation to the summed area of the clasts in the 2D surface (Mort & Woodcock 2008)	
<i>clast elongation or aspect-ratio</i>	The ratio of the length of the clast major axis to the length of the minor axis. For an elongation of 1, the object is roughly circular or square. As the ratio increases from 1, the object becomes more elongated (Baxes 1994)	
<i>clast compactness</i>	The ratio of the Feret diameter to the object's length ranging between 0 and 1. At 1, the object is roughly circular. As the ratio decreases from 1, the object becomes less circular	$\frac{\sqrt{\frac{4 \cdot AREA}{\pi}}^{Feret \text{ diameter}}}{MAJOR \text{ AXIS LENGTH}}$
<i>clast angularity</i>	Angularity value is 16 in a square and 13.8 in a hexagon. Increasing the number of sides causes an asymptotic decrease of the value that eventually tends to 12.6 (4π) in a circle (Storti et al. 2007)	$\frac{perimeter^2}{clast \text{ AREA}}$
<i>fractal dimension</i>	Where the fractal dimension of clast size D is characterized by the slope of the best-fit line onto a log-log plot of the clast size distribution (Turcotte 1986)	

Table 5.4 - Summary of the six analysed parameters for fragments from barren and mineralized breccias from Sossogo and Sequeirinho.

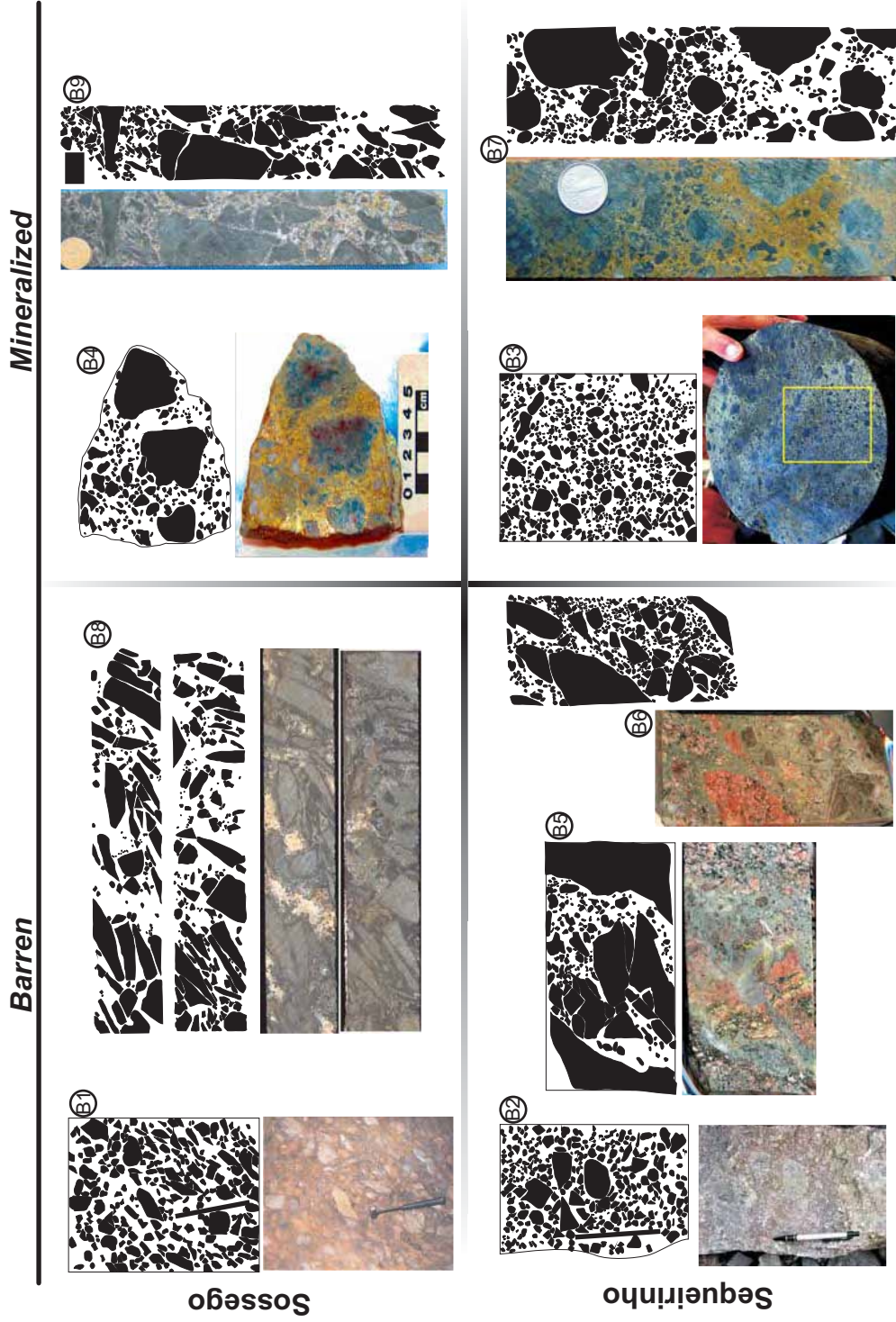


Figure 5.48 - Chart displaying the nine analysed breccia samples and their respective photographs and maps of digitized fragments. Samples are grouped according to their orebody of origin and separated into barren and mineralized.

A

Sample	number of clasts	clasts > 2mm %	clasts 0.1-2mm %	cement-matrix (<0.1mm) %
B1	251	41	0	59
B2	305	43	0	57
B3	707	30.1	6.2	63.7
B4	214	44.3	1.7	54
B5	190	54.8	3.3	41.9
B6	499	50.1	9.6	40.3
B7	441	54.6	2.5	42.9
B8	358	47	0.5	52.5
B9	255	54.9	0.5	44.6

B

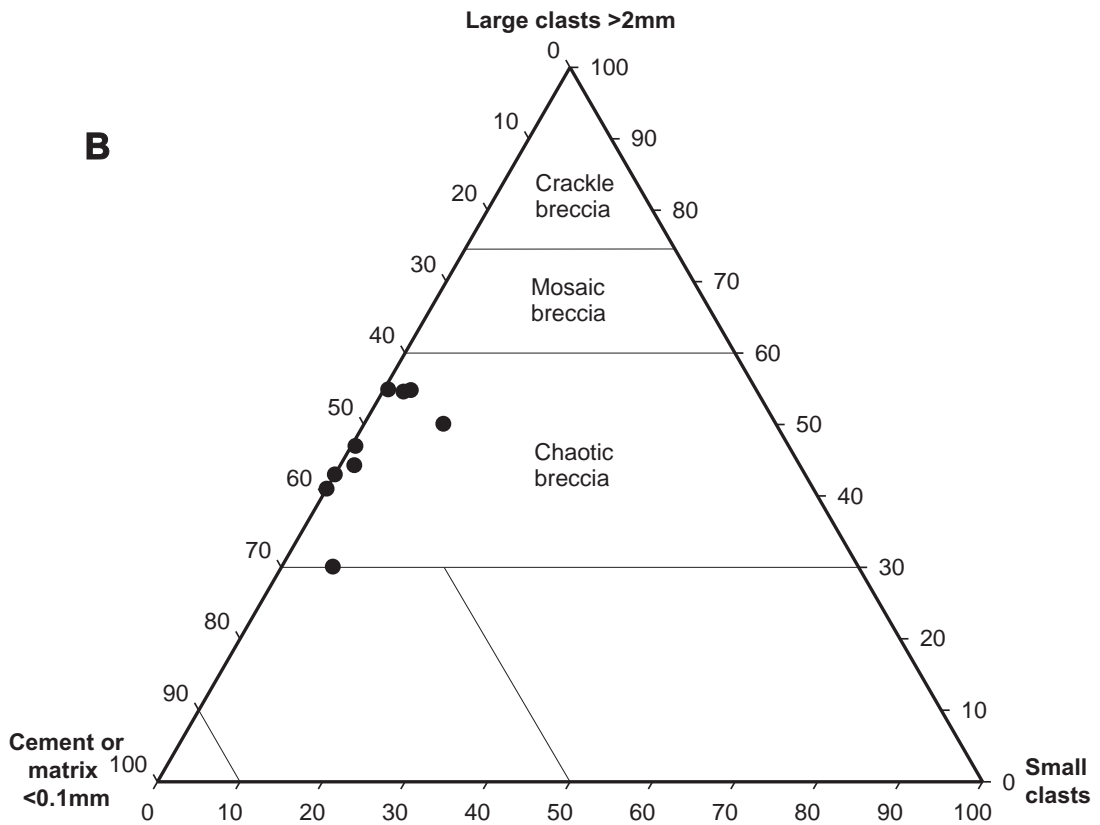


Figure 5.49 - A table showing the number of measured clasts, the three clast size divisions used to classify the breccias and the respective percentage of the number of clasts per sample; **B** ternary diagram from Woodcock & Mort (2008), the triangle vertexes correspond to large clasts, small clasts and cement/matrix. The black dots plotted into the “chaotic breccia” field correspond to the studied breccias from Sossego and Sequeirinho.

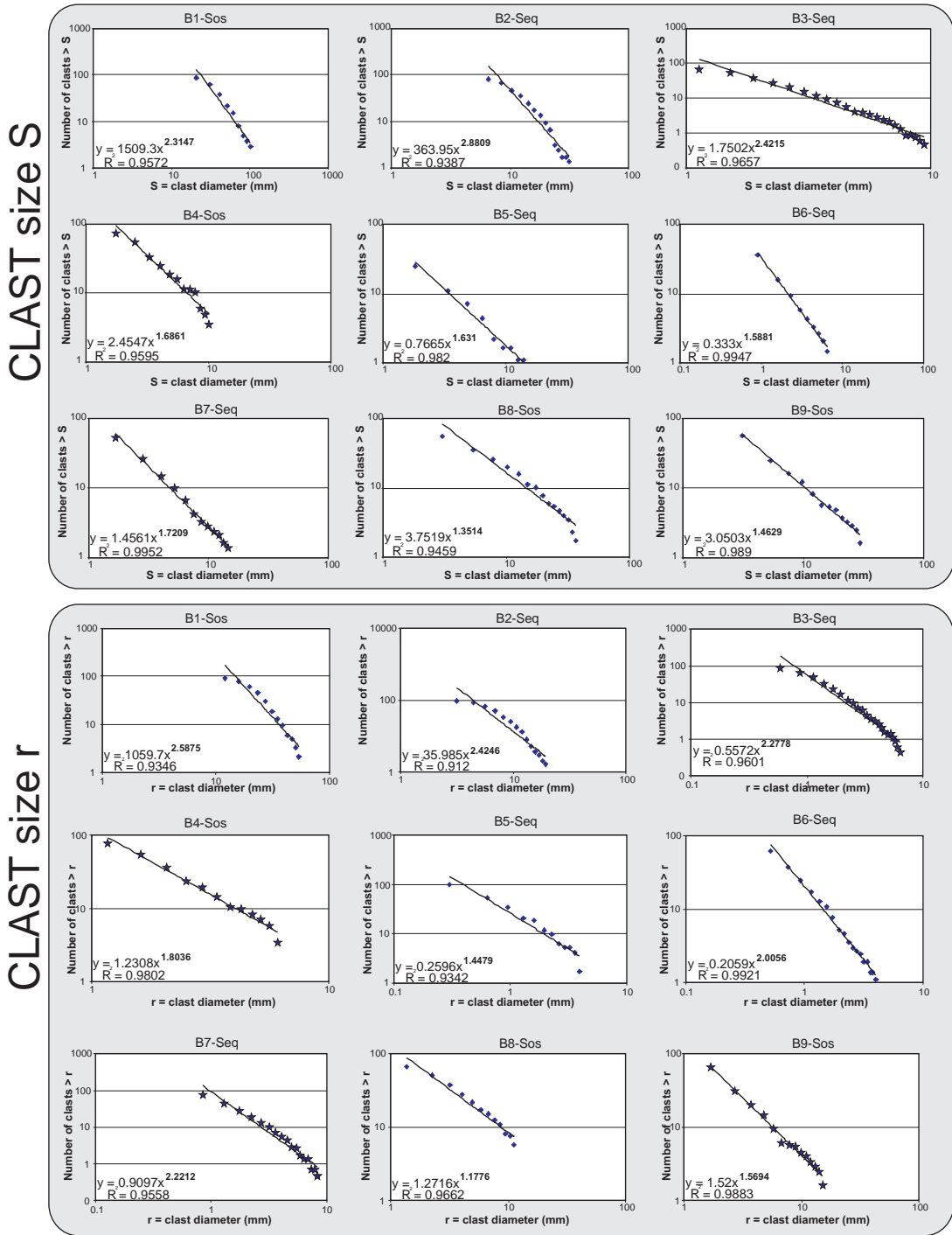


Figure 5.50 - Log log plots of clast size against their cumulative frequency. The graphs are grouped according to the size parameter used (S or r). Stars and squares represent mineralized and barren breccias respectively. The R squared value indicates how well the data fit the model of a straight line. The closer this value is to 1.0, the better the fit of the data to the linear model. The y value represents the equation of the best fit line and the negative exponent D (in bold) measures the slope of this line.

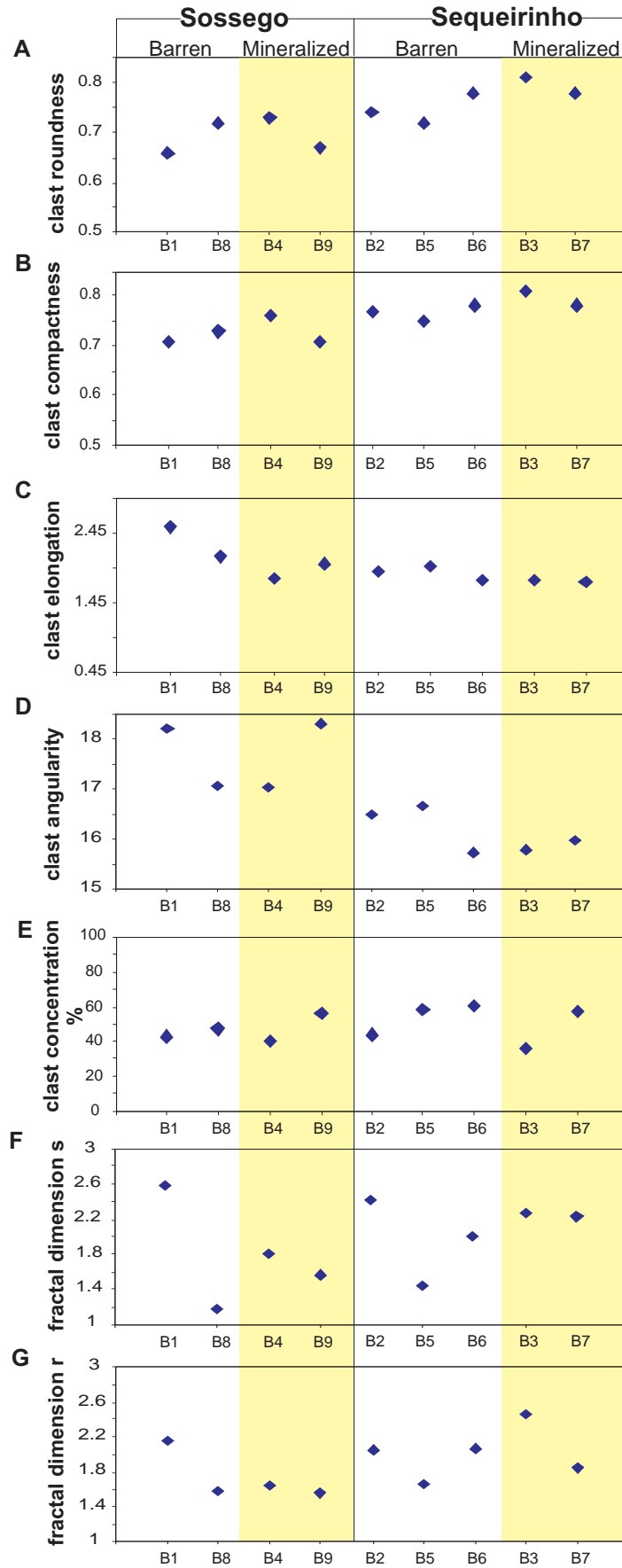
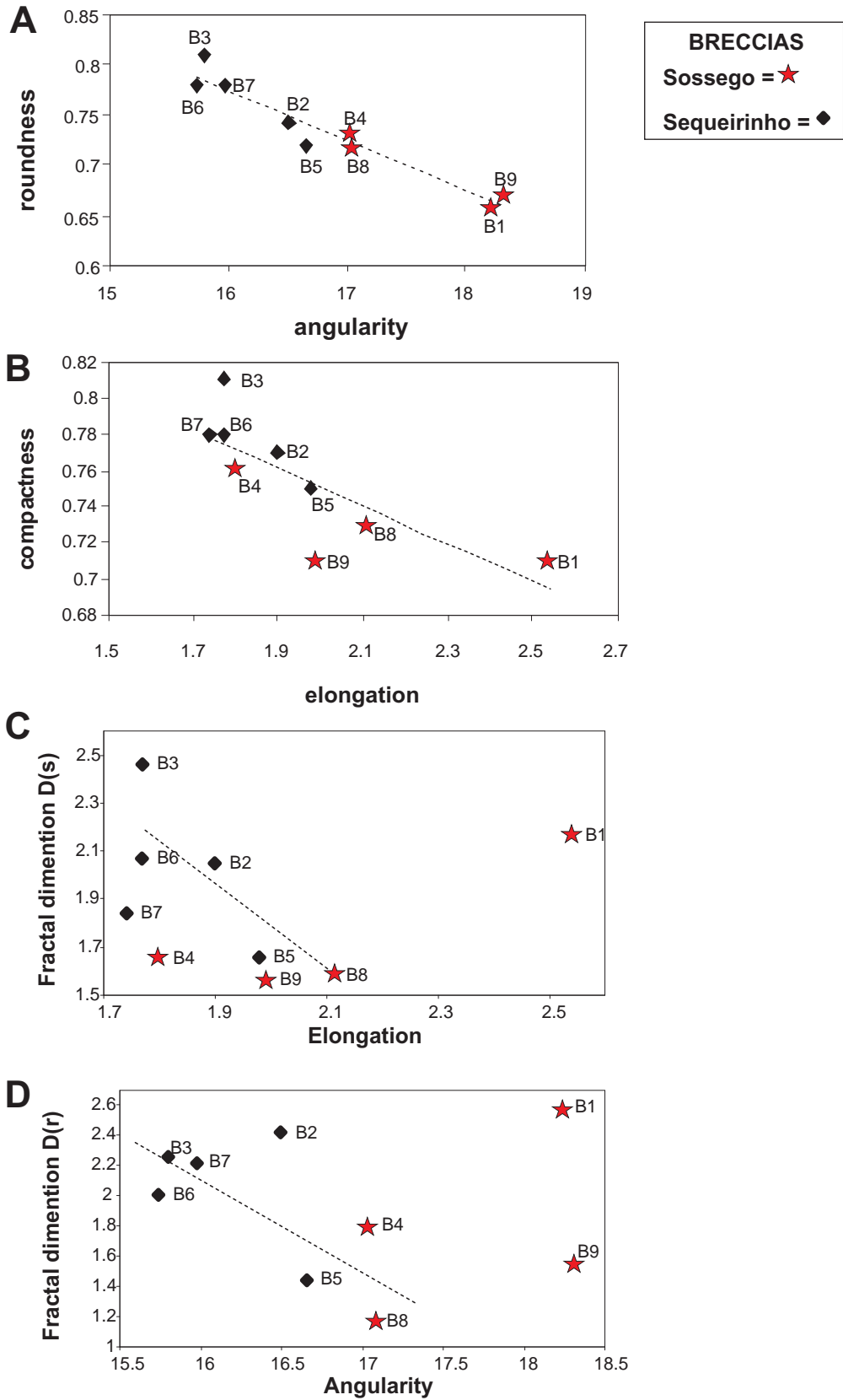


Figure 5.51 - Graphic representation of the analyzed textural parameters of breccia fragments. The samples are grouped by orebody of origin and the presence of Cu mineralization.



*Figure 5.52 - X & Y plots indicating a negative relation between the clasts shape parameters: **A** roundness vs angularity; **B** compactness vs elongation; **C** fractal dimension $D(S)$ vs. elongation; and **D** - fractal dimension $D(r)$ vs. Angularity. Studied breccia samples from Sossego and Sequeirinho are plotted in the graphs as stars and squares respectively.*

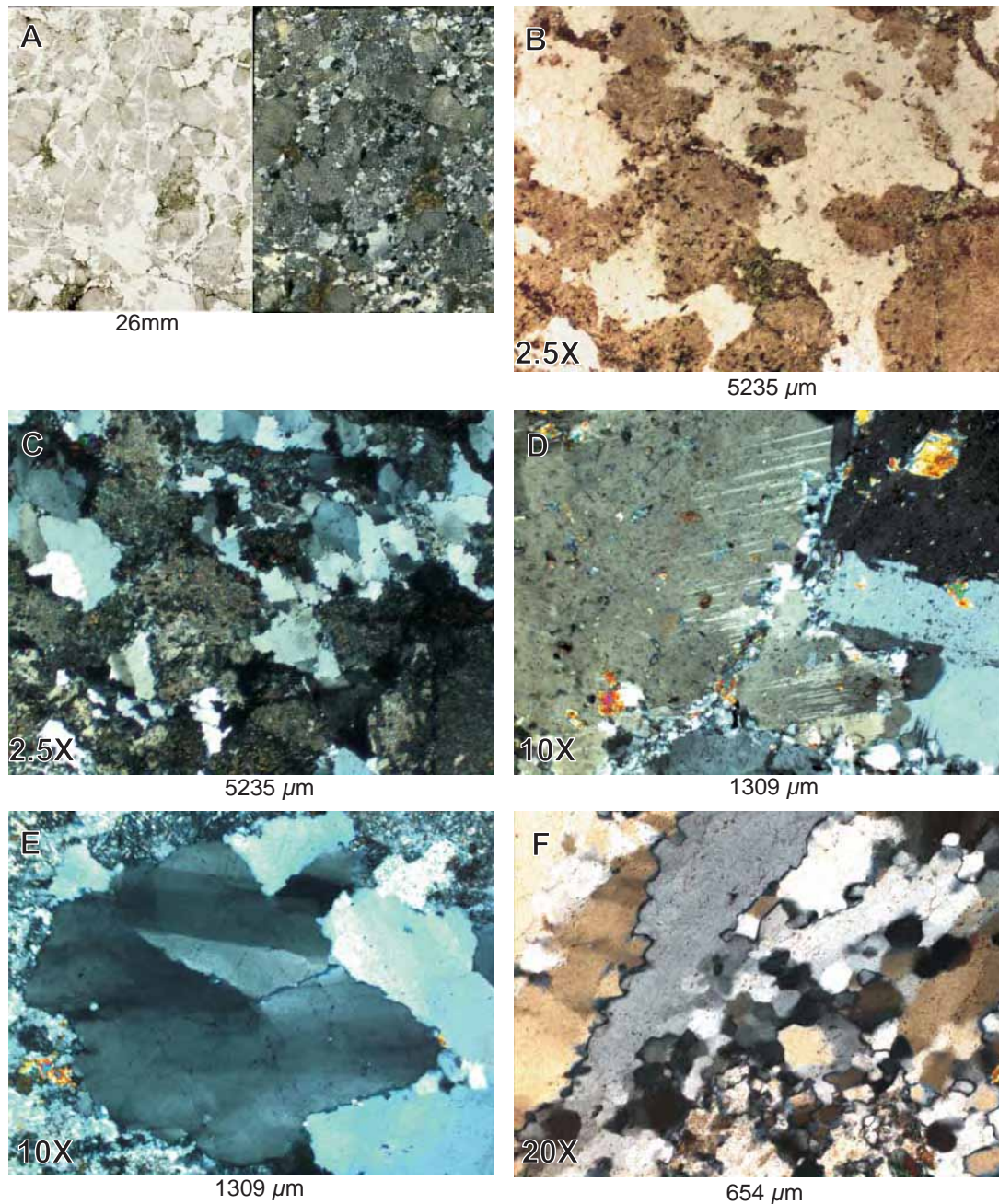


Figure 5.53 - *A* coarse granular aspect of anisotropic granite in thin section under natural and polarized lights. *B* and *C* in natural light, anhedral quartz (clear) and altered feldspar (dark) aggregates; in polarized light these minerals show interlocking contacts with no visible recrystallized crystals. *D* strain induced twins in feldspar crystals; note the finely fragmented material along the major crystals. *E* relatively large quartz crystals with undulose extinction, elongated subgrains and curvy serrated boundaries. *F* localized recrystallized small quartz subgrains and large grains with strain induced interdigitated boundaries.

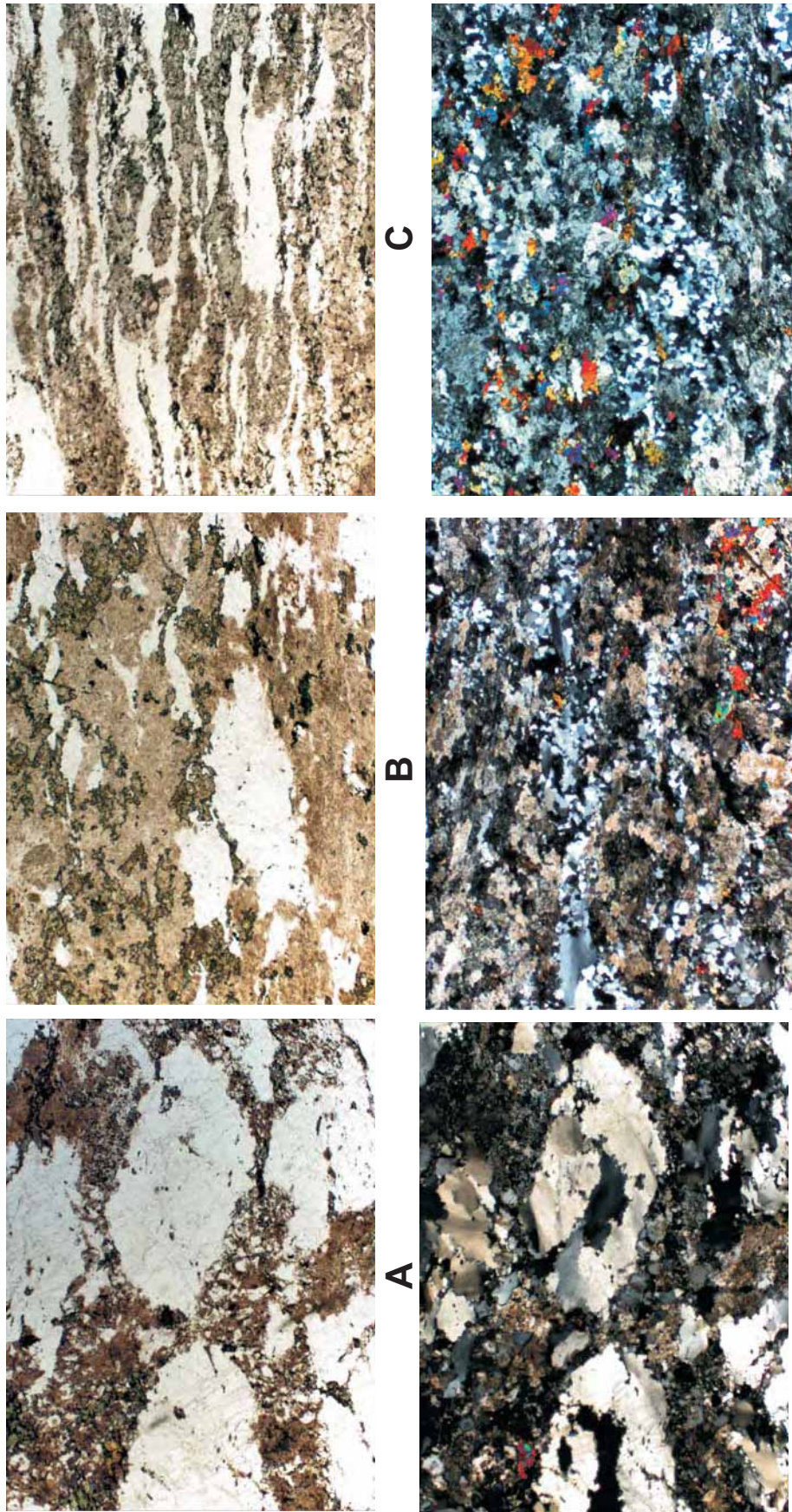


Figure 5.54 - sequence of photos showing varieties of foliated granitoids displaying progressive increase of strain and recrystallization from left-to-right. The initial stages of deformation (photos on the left) are marked by augen shaped quartz aggregates with undulose extinction and limited recrystallization. The increase of strain rates promotes progressive development of ductile fabric characterized by flattening and recrystallization of quartz aggregates together with strong preferred orientation of micas (photos on the right).

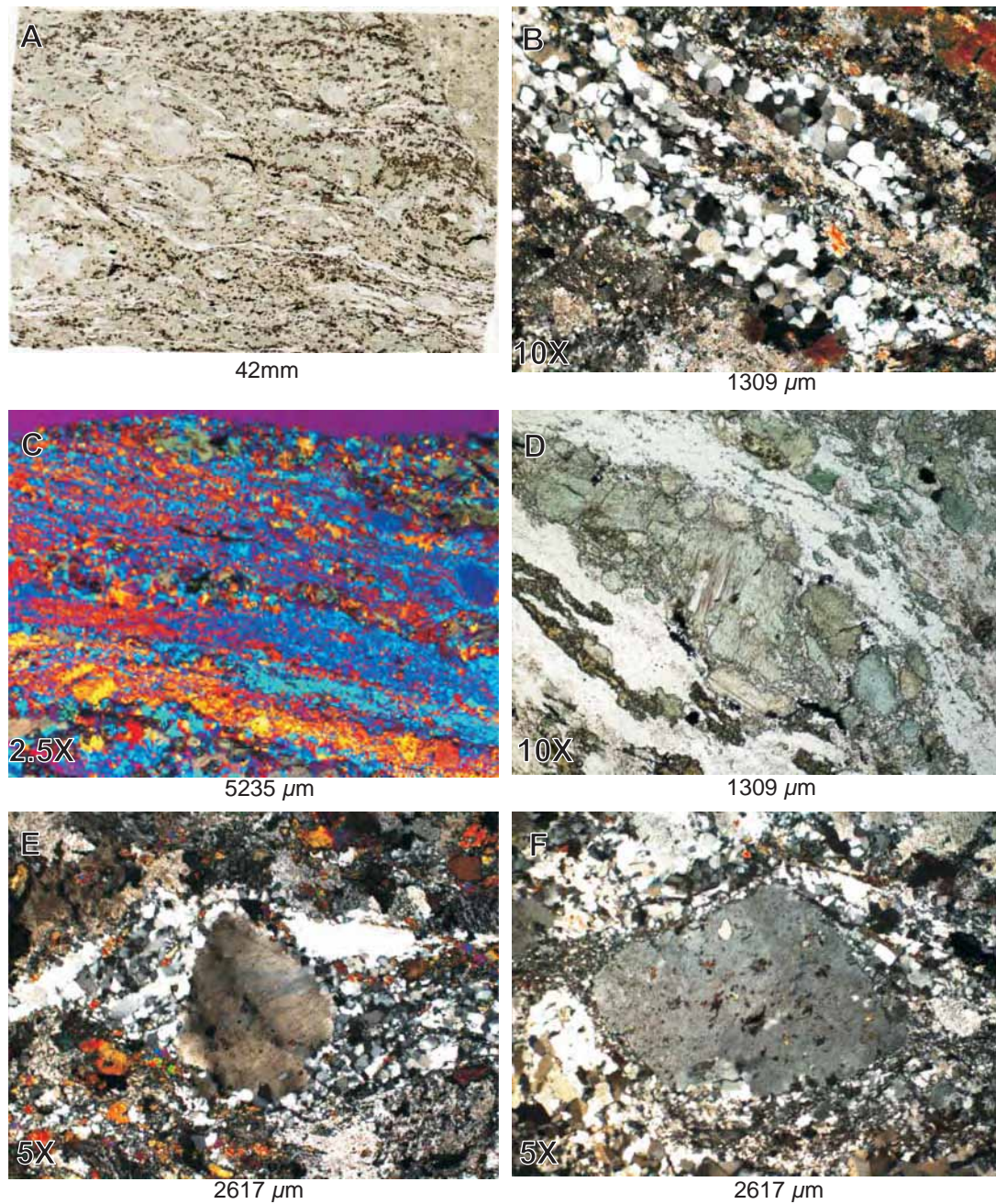


Figure 5.55 *A* thin section image from a mylonite from Sequeirinho and its marked wavy foliation wrapping around porphyroclasts. **B** quartz ribbons formed of equidimensional crystals composing a mosaic of polygonal recrystallized grains indicating subgrain rotation recrystallization. **C** fine grained aggregates of recrystallized feldspar forming bands with moderate LPO. **D** actinolite porphyroclast consisting of aggregates of small fragments and preserved larger crystals, crystallization is dominated by fracturing. **E** sub rounded quartz porphyroclast with internal subgrains and tiny inclusion trails, dynamically recrystallized quartz wraps around it forming gently asymmetric tails. **F** sub angular undeformed feldspar porphyroclast mantled by very fine recrystallized feldspar aggregate.

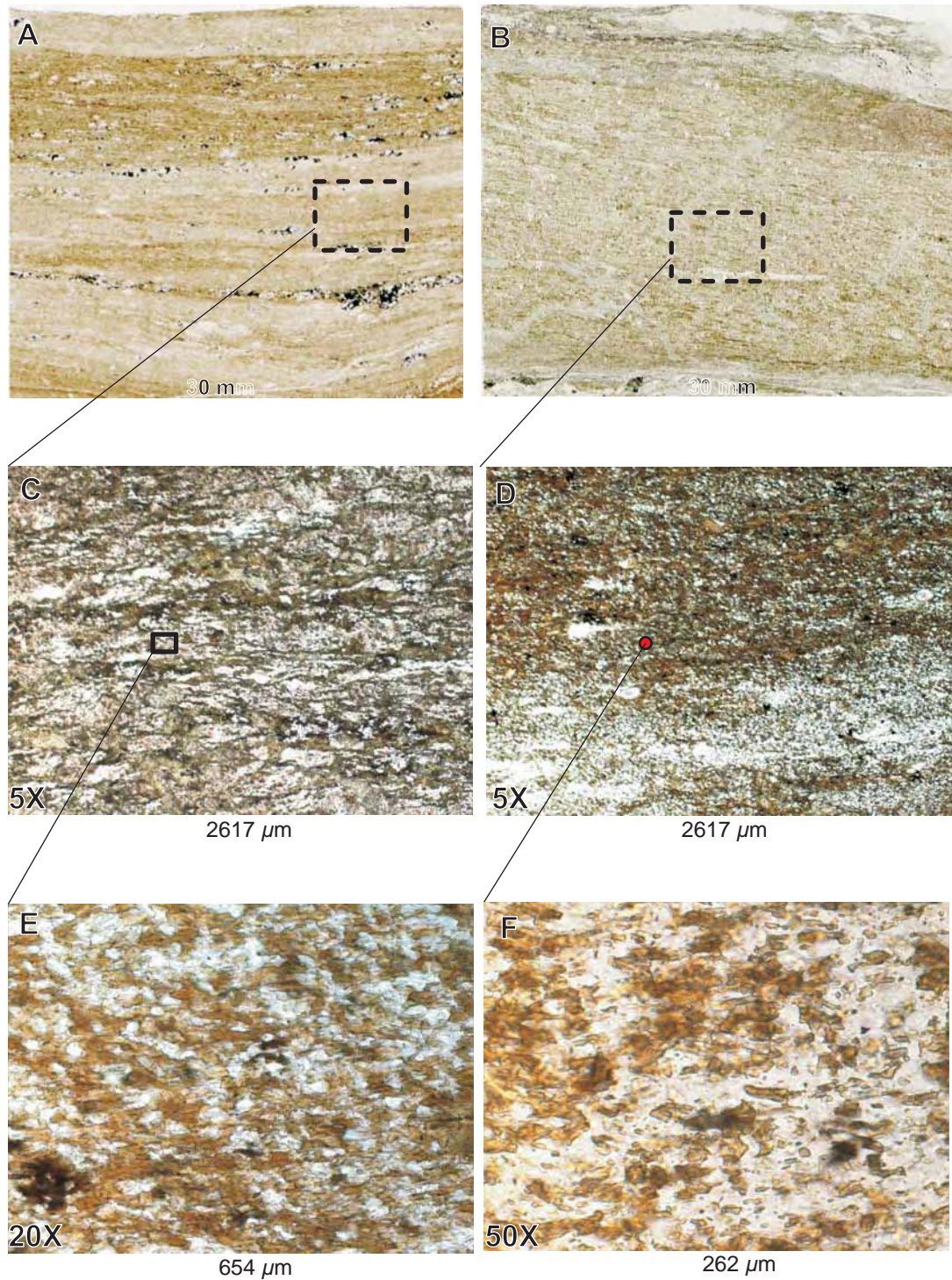


Figure 5.56 - Microscopic aspects of ultramylonites also described as schists. *A* and *B* scanned thin sections and the general finely banded aspect of these rocks. *C* and *D* five times magnification displaying examples of sharp and diffuse contact between the banding in the ultramylonites; note the elongated quartz rich domains and marked orientation of biotite. *E* and *F* high magnification, highlighting extremely fine biotite crystals and its intense degree of orientation.

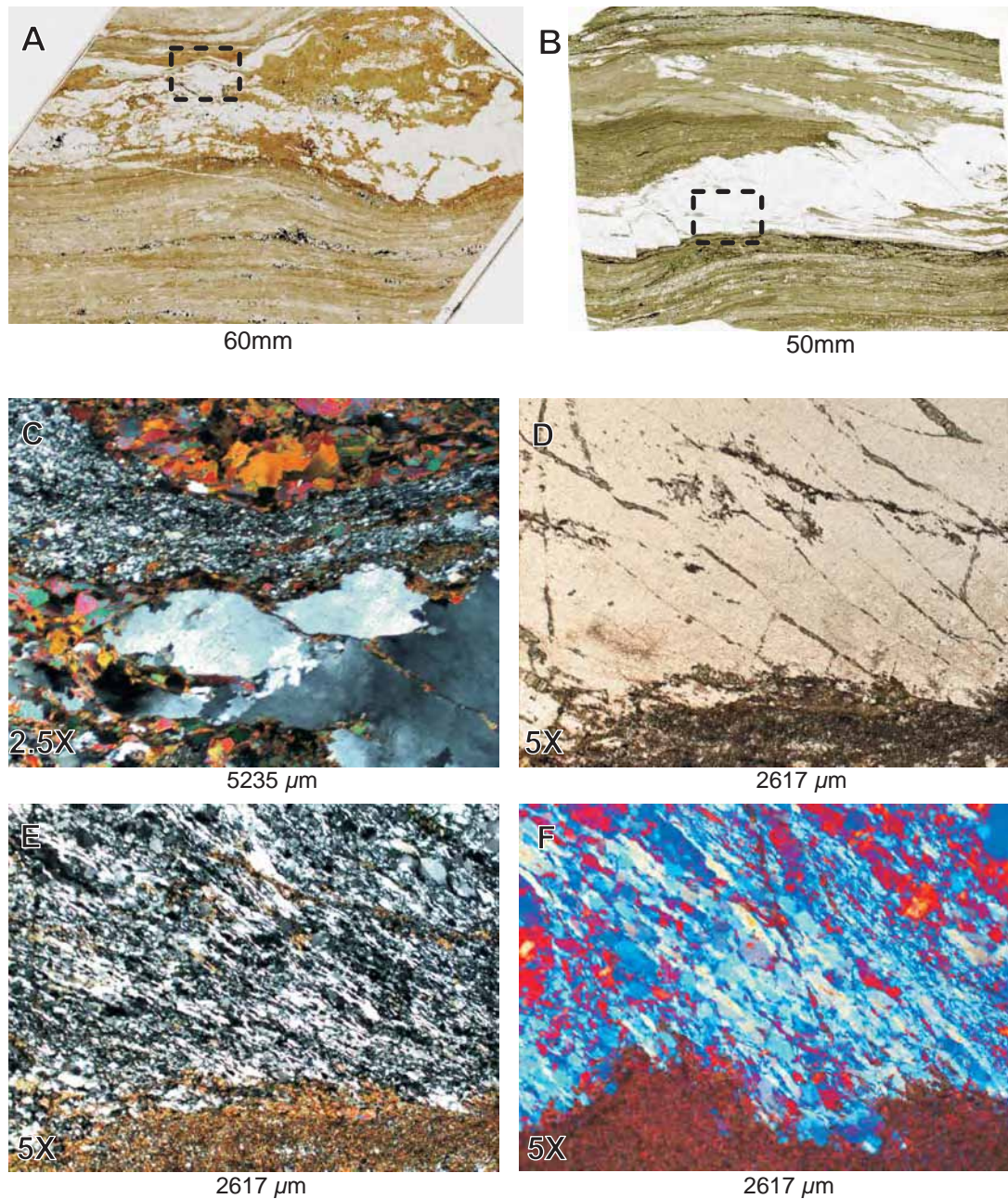


Figure 5.57 - *A, B* scanned thin sections containing boudinaged and sheared quartz veins respectively. *C* microphotography from the detail in *A* showing the internal portion of a boudinaged vein; coexisting dynamically recrystallized (subgrain rotation) and undeformed quartz evidencing strain partitioning. *D, E* microphotography from the detail in *B*, presenting in natural and polarised light the sharp boundary of a sheared vein in ultramylonite. Quartz is dynamically recrystallized (subgrain rotation) into elongated subgrains oblique to the vein walls. *F* dynamically recrystallized quartz displaying strong LPO.

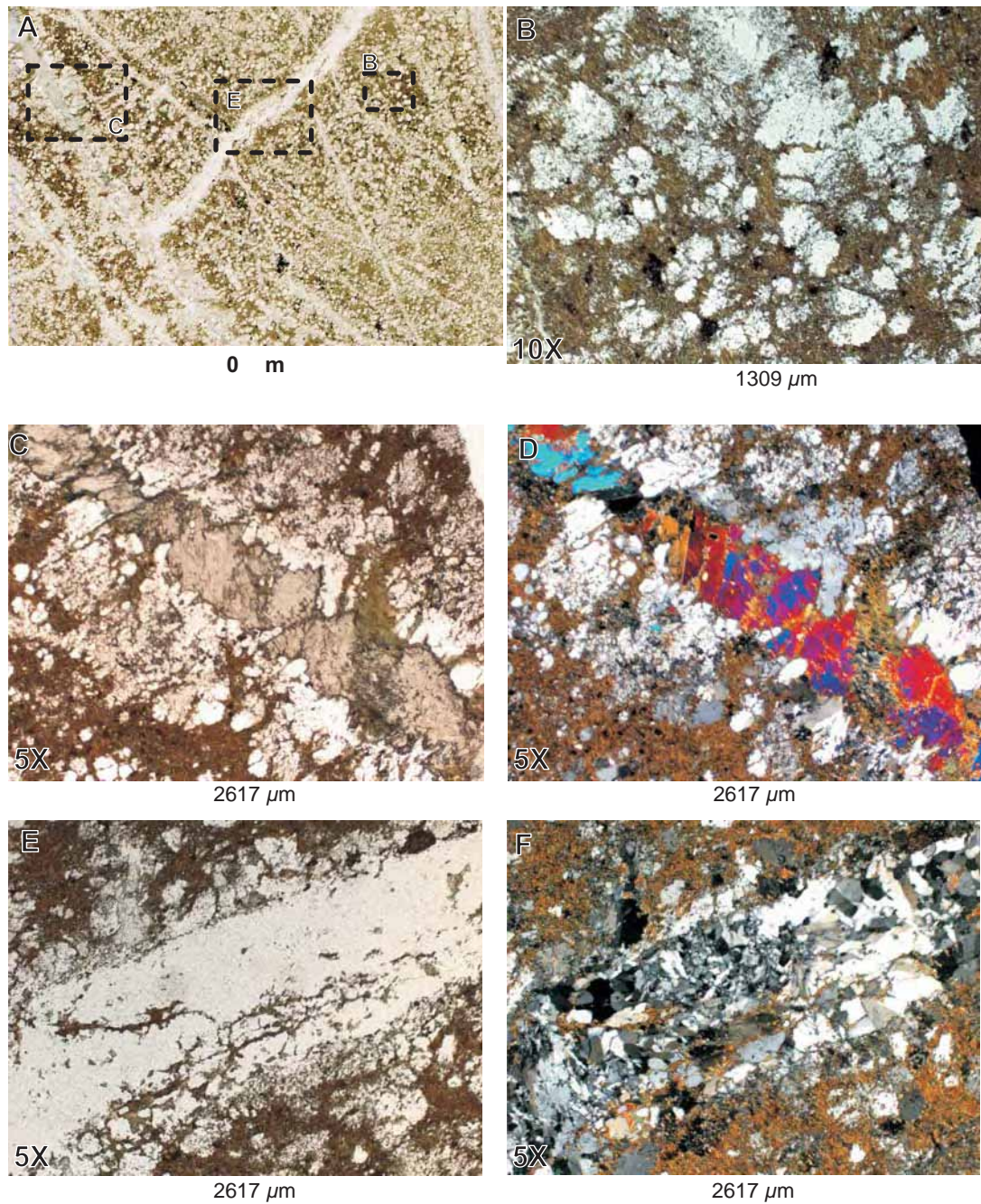


Figure 5.58 - *A* scanned thin section showing the general microscopic texture of the metavolcanic acid rock type, note the intense presence of veins and shear bands; **B** anhedral quartz and k feldspar crystals immerse in a fine to very fine green biotite rich matrix; **C** and **D** composite micro vein showing feldspar on the external portion and actinolite crystals in the inner part, perpendicular to the vein walls. **E** and **F** solid inclusion trails in quartz feldspar veins evidencing episodic vein opening.

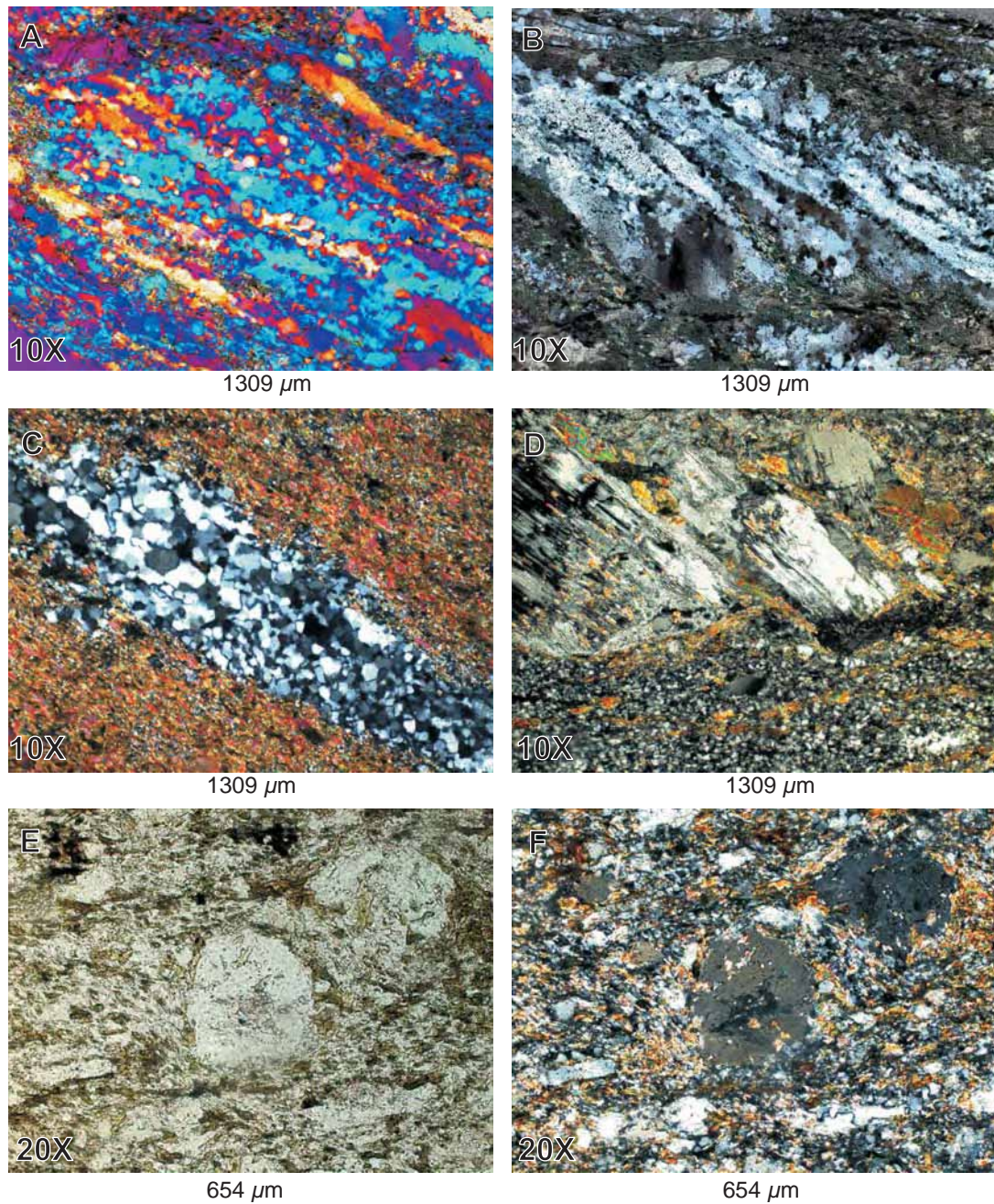


Figure 5.59 - Detail of microstructures in ultramylonites. **A** recrystallized quartz lenses displaying random LPO; **B** quartz fish with sweeping undulose extinction and **C** totally dynamically recrystallized grains forming quartz lens; **D** plagioclase porphyroclasts deformed as a domino like segmentation; **E,F** sub rounded and augen shapes of quartz porphyroclasts enveloped by the foliation and containing mineral inclusions.

sample	mineralogy	vein filling	vein boundary	crystal shape	growth/filling event	type	deformed	internal structure	inclusions	median line
SQ-8-5	plagioclase+epidote	massive	sharp irregular	blocky equidimensional	single-gradual	extension	no	no	no	no
FG-15-170	amphibole	massive	sharp smooth	blocky	single	extension	fracturing and recrystallization of grains; vein displacement	no	no	no
FG-15-150	amphibole+epidote									
SQ-6-DT-3	epidote	massive	sharp irregular	blocky	single-gradual	extension	displaced by late faults	fine grains on the borders; coarse grains in the center	wall rock fragments	no
SQ-10-DT-12	chlorite	fibrous	sharp irregular+smooth	fibrous	periodic	shear	displaced by late faults	fibers parallel to the vein walls, locally oblique or perpendicular	very fine opaque spheres aligned parallel to the chlorite fibers; wall rock fragments	no
SQ-10-DT-16	feldspar	massive	sharp smooth	blocky equidimensional	single & periodic	extension	locally displaced by faults	absent in some veins; composite vein with qtz on the walls and feldspar in the center; crystals are randomly oriented	several micro inclusions; few fragments from wall rock; inclusions are parallel to grain growth	no
SQ-10-DT-16	qtz+carbonate	massive	sharp smooth	blocky-varied grain size	single & periodic	extension + shear	no	composite veins with qtz on the walls and calcite in the center; growth domains with crystals parallel, oblique or perpendicular to the walls	discontinuous parallel inclusion banding	no
FG-15-168	amphibole+chlorite	fibrous	fuzzy	elongated fibers	periodic	shear	internally deformed crystals; fractured or bent	composite veins with amphibole in the outer border and chlorite in the center	few wall rock inclusions	no
FG-15-158	epidote	massive	sharp irregular	blocky - medium/fine	periodic	extension+shear	cross-cut by other deformation bands and faults	internal layering parallel to the vein walls characterized by quartz fragments content	several wall rock fragments with diverse size and shapes; presence of discontinuous fragments banding	no
FG-15-104	amphibole+magnetite	massive	sharp irregular	blocky equidimensional	single-gradual	extension with localized shear along the boundaries	intracrystalline deformation by recrystallization and localized fractures and def. bands recrystallized in the vein boundaries	no	several randomly spaced magnetite inclusions within amphibole grains	no
SQ-6-DT-1	epidote+sulphide+chlorite+amphibole	massive	fuzzy	blocky-varied grain size	periodic	fault - shear	intense grain size reduction by faulting and fracturing	mineral aligned parallel to the vein walls and slip surfaces	no	no
FG-20-106	amphibole+quartz	fibrous+massive	fuzzy	quartz-blocky/elongated; amphibole-fibrous	periodic	extension & shear	amphibole locally recrystallized; ondulose quartz	composite vein with quartz crystallized in the vein boundaries and amphibole in the center	ultra fine biotite in quartz	no
FG-20-106	feldspar	massive	sharp irregular	blocky	periodic	extension	no	feldspar grains occur in two ways defining domains within the vein: blocky and elongated grains	very fine biotite inclusions configuring discontinuous inclusions banding	no

Table 5 - description of veins properties and characteristics for selected representative samples.

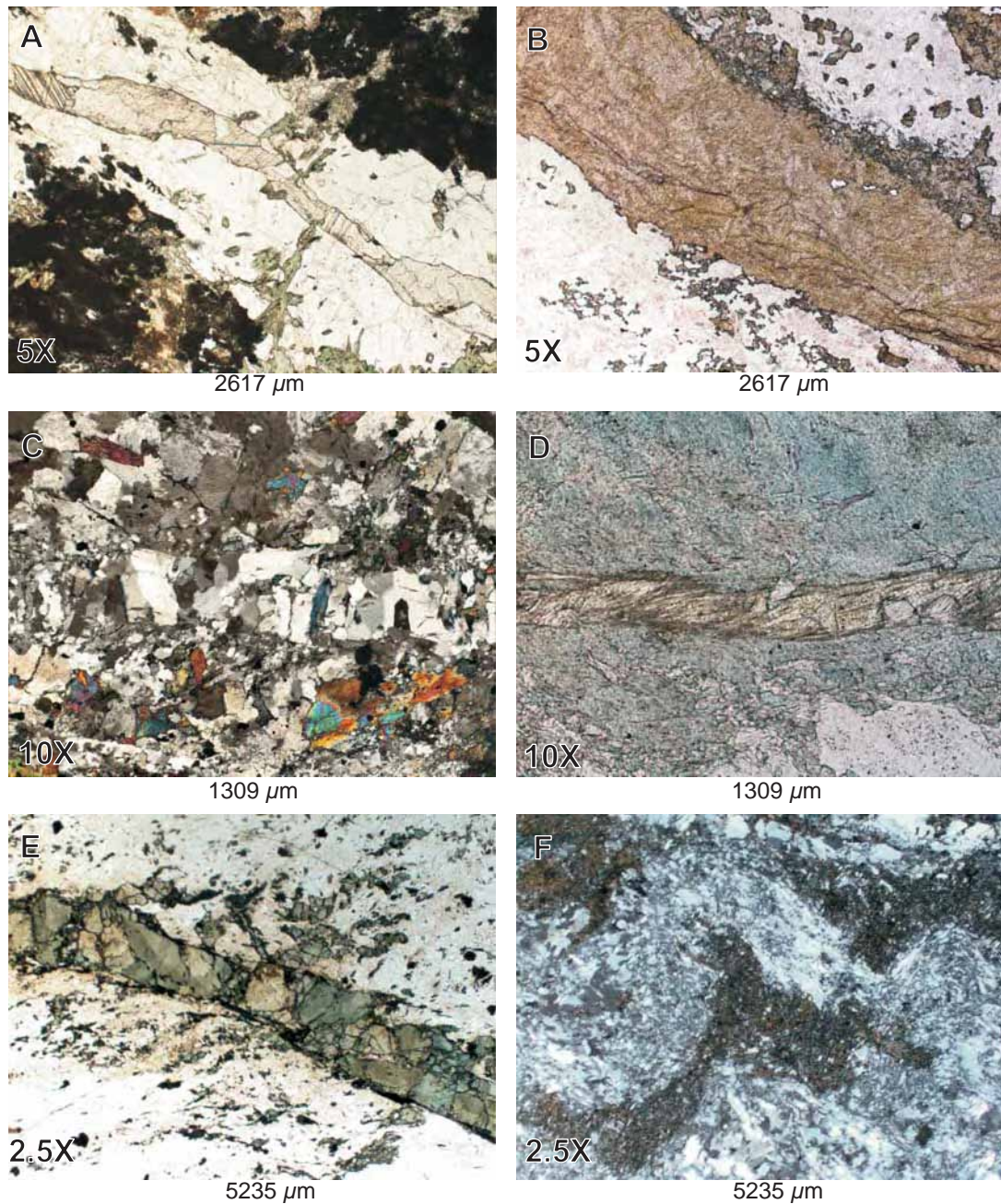


Figure 5.60 - *A* composite vein formed of calcite in the inner and quartz with mica inclusions in the outer portion of the vein, suggesting at least to opening episodes. *B* monomineralic very fine epidote vein, the internal structures seem to be fractures. *C* blocky quartz veins showing crystal growth perpendicular to the vein walls and tiny inclusion trails parallel to the vein. *D* fibrous chlorite vein with fibres position indicating vein opening direction oblique to its walls. *E* actinolite vein showing fracturing limited to the internal part of the vein. *F* asymmetric folded vein composed of fine dynamically recrystallized quartz.

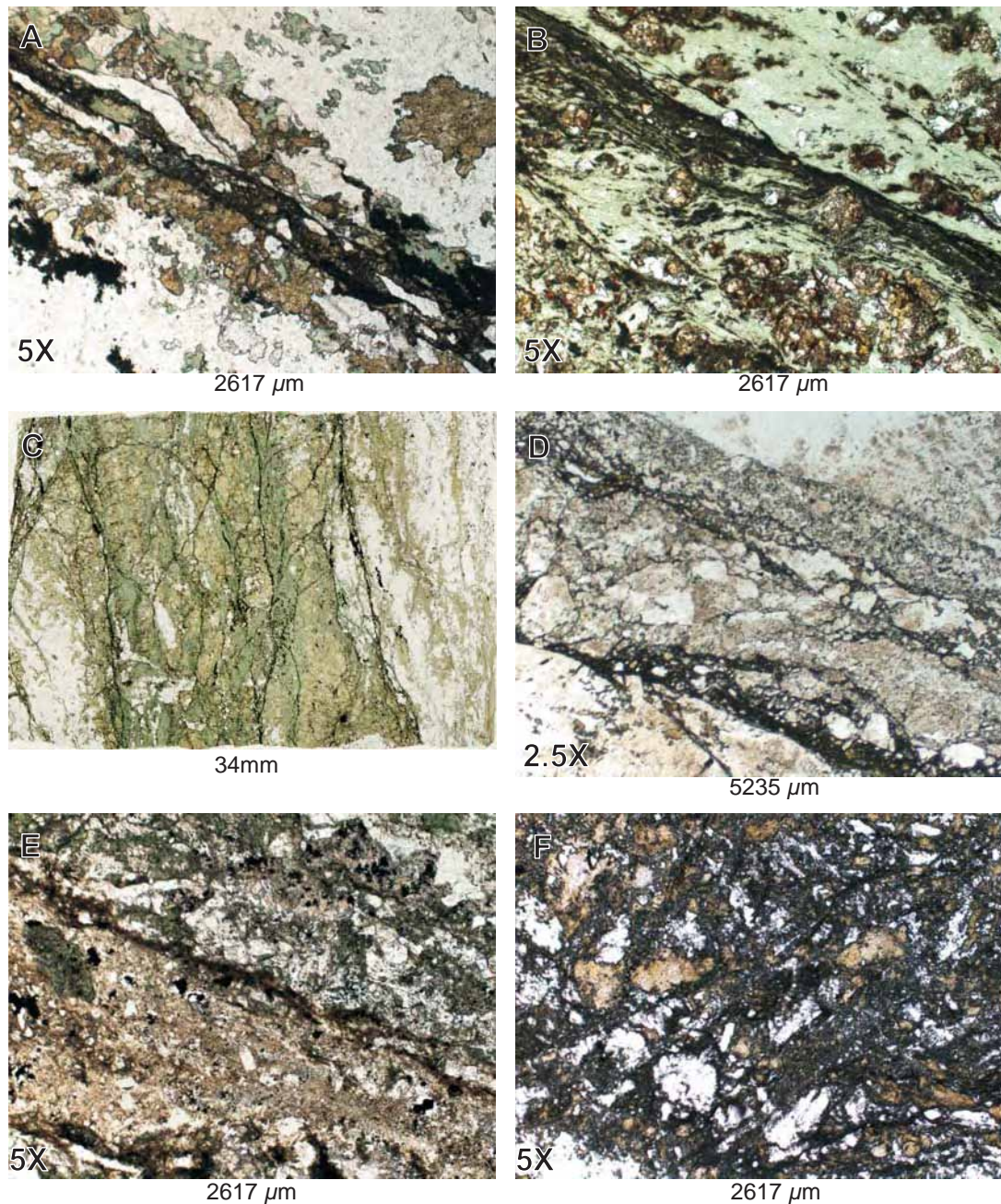


Figure 5.61 - *A* discrete fault plane with sharp boundaries and comprising elongated, imbricated fragments immerse in brown cryptocrystalline material. Epidote along the fault external boundary is product of alteration (hydrothermal?). *B* fault plane in intensely chloritized rock showing well defined slip surface and sub rounded fragments slightly porphyroclasts like mixed with ultra fine dark brown matrix. Epidote replaces feldspars. *C* chloritized fault zone defined by sub parallel faults (vertical structures on photo) linked by oblique secondary fault strands, forming an interconnected network of faults and micro cracks. *D* fault zone characterized by main parallel slip surfaces (filled with ultra fine dark material) bounding domains of intensely fractured and altered fragments showing a great range in sizes and shapes. *E* few randomly oriented angular fragments mixed with fine and very fine fault products (material in between the two dark lines on photo) contrasting with minerals sizes and shapes outside the fault zone. *F* characteristic aspects of the material associated with fault zones: varied grain sizes and shapes, randomly oriented and notably associated with the amorphous fine and dark matrix. The clear minerals are quartz and brownish, altered feldspar. The dark lines are fault strands (slip surfaces?).

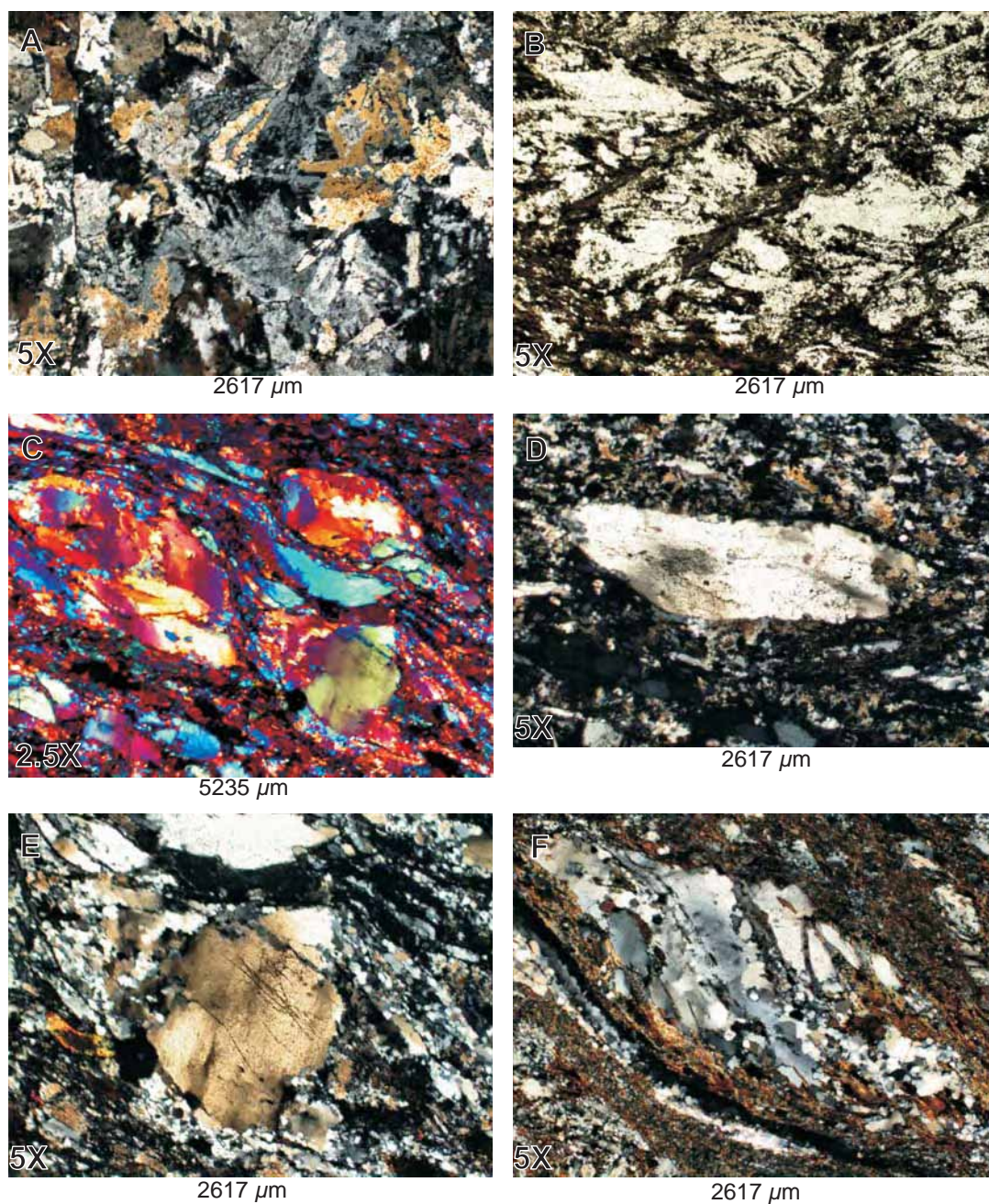


Figure 5.62 *A* micrographic radiate intergrowth of quartz and *k* feldspar, the distinguishing feature of granophyre granite at Sossego. *B* locally developed *S C'* fabric on mica rich member of mylonites at Sossego. *C* flattened quartz porphyroclasts with strong undulose extinction and subgrains. *D* quartz "fish" with irregular/sweeping undulose extinction. *E* quartz porphyroclast displaying core with irregular undulose extinction mantled by dynamically recrystallized quartz aggregates. *F* sigmoidal quartz lens showing oblique internal structures characterized by parallel elongated domains of recrystallized aggregates and "undeformed" quartz.

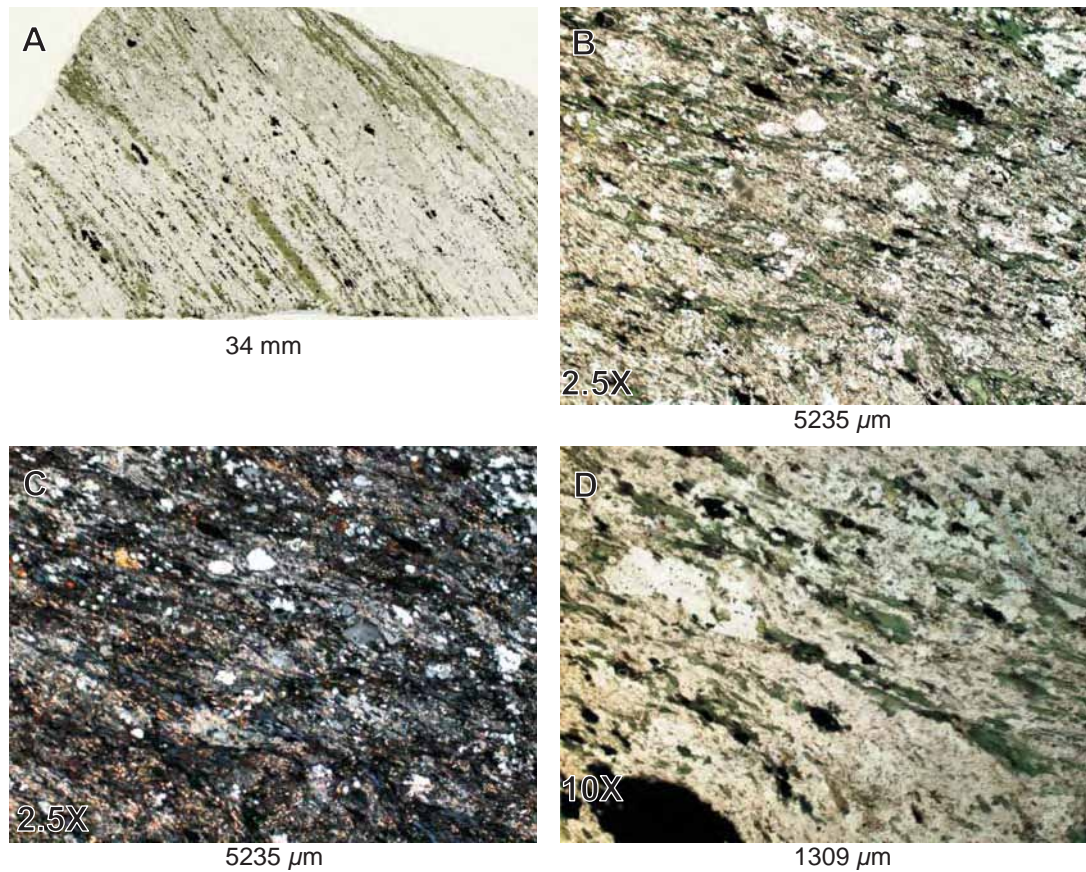


Figure 5.63 - *A* scanned thin section of ultramylonite exhibiting fine to very fine grain sizes and prominent foliation defined by millimetre to sub millimetre wide bands. *B* and *C* image in natural and polarized lights of the general features characterizing ultramylonites from Sossego: relatively straight and continuous foliation comprising alternating quartz+feldspar and mica rich bands; presence of very small quartz, altered feldspar and sulphide porphyroclasts. *D* grain shape preferred orientation characterized by elongated quartz and sulphides (black). Note the perfectly aligned long and fine mica grains.

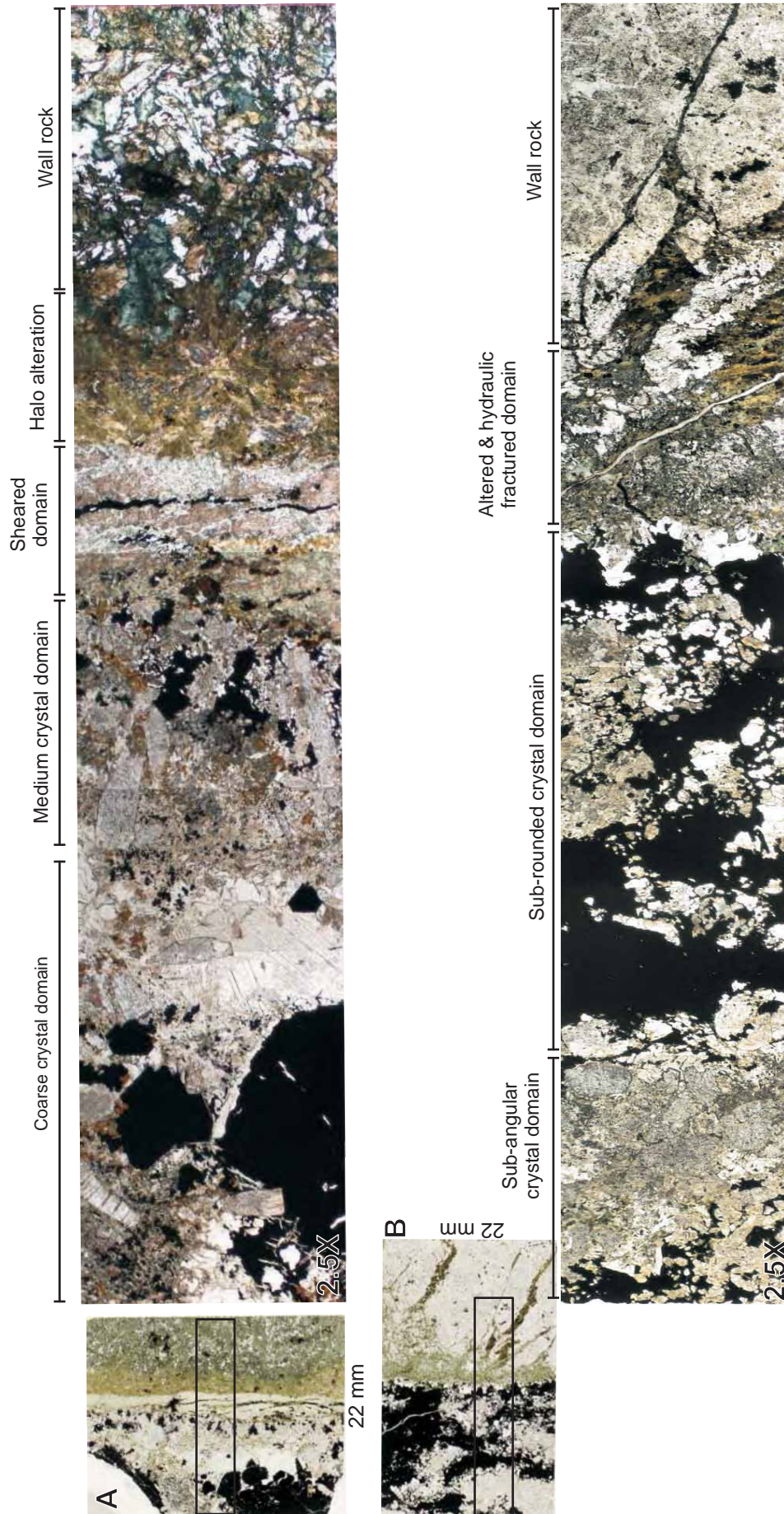


Figure 5.64 - Scanned thin sections and photo-panorama across the veins and wall-rock indicated by the rectangle on the thin section's photo. **A** sheared type vein marked by sharp sheared boundary that divides altered wall-rock to the right and medium and coarse size crystals domains to the left. The transition from medium to coarse domains seems to be drawn by a diffuse zone of fine crystals. **B** extension type vein with secondary veinlets penetrating the wall rock to the right and two internal domains divided according to crystal geometry.

Facies	Temp.	General Features	Quartz	Feldspar
Sub-greenschist	250-300°C	Progressive deformation tends to produce phylionites. Micas tend to develop cracks on cleavage planes and kink bands boundaries	is more resistant to fracturing and so only limited crystal plasticity	Plagioclase and K-feldspar are pervasively fractured and altered to muscovite, due to fluid access
Lower to middle greenschist	300-400°C	Deformation tends to be heterogeneous, resulting in highly localized ductile shear zones. Micas undergo easy glide but also some cataclasis	Depending on the strain rate quartz may deform heterogeneously, with strong undulose extinction and very small recrystallized grains (regime 1); or they may be homogeneously flattened with subgrains and recrystallized grains of the same size (regime 2)	At low strains grain-scale fractures develop, reducing grain size and allowing fluid access promoting breakdown reactions with further deformation. These reactions together with progressive strain promote feldspar weak behaviour
Middle to upper greenschist	400-500°C	Progressive strain leads to highly localized ductile shear zones. Micas are the weakest phase and undergo easy glide and some cataclasis	Is weak and deforms by regime 2 or 3 dislocation creep, depending of strain rate and fluids	Develop grain-scale fractures at low strain. Plagioclase develops deformation and kink bands with very fine albite recrystallized grains along clast margins. K-feldspar may develop myrmekite and flame perthite on high stress boundaries. High strain rates lead to strain weakening and localization
Upper greenschist to lower amphibolite	500-600°C	Progressive deformation results in SC mylonites and ultramylonites. At higher strain SC mylonites develop when mica, quartz and new feldspar grains wrap around feldspar porphyroclasts. At very high strain ultramylonites are formed, with small feldspar porphyroclasts set in a fine-grained foliated matrix	Is completely recrystallized even at low strain with strong LPO; possible optically visible subgrains, indicative of regime 3 dislocation creep	Commonly develop grain scale fractures. Myrmekite on k-feldspar may recrystallized to fine grains of quartz and plagioclase, and the boundaries of plagioclase porphyroclasts tend to be serrated, with very small new grains
Lower to middle amphibolite	600-650°C	Progressive strain promotes retrograde reactions, and result in SC or banded mylonites. At high strain recrystallized quartz, plagioclase and k-feldspar all appear to have strong LPO suggesting that all phases deformed by dislocation creep	Is completely recrystallized to relatively coarse size, also containing small smaller subgrains	At moderate strain plagioclase is partially recrystallized with smaller grain size than quartz. Myrmekite of k-feldspar porphyroclasts recrystallizes into fine grained aggregates of quartz and plagioclase

Table 6 - Correlation between microstructures produced in quartz and feldspars, metamorphic facies and deformation temperatures. Adapted from Tullis, 2002.

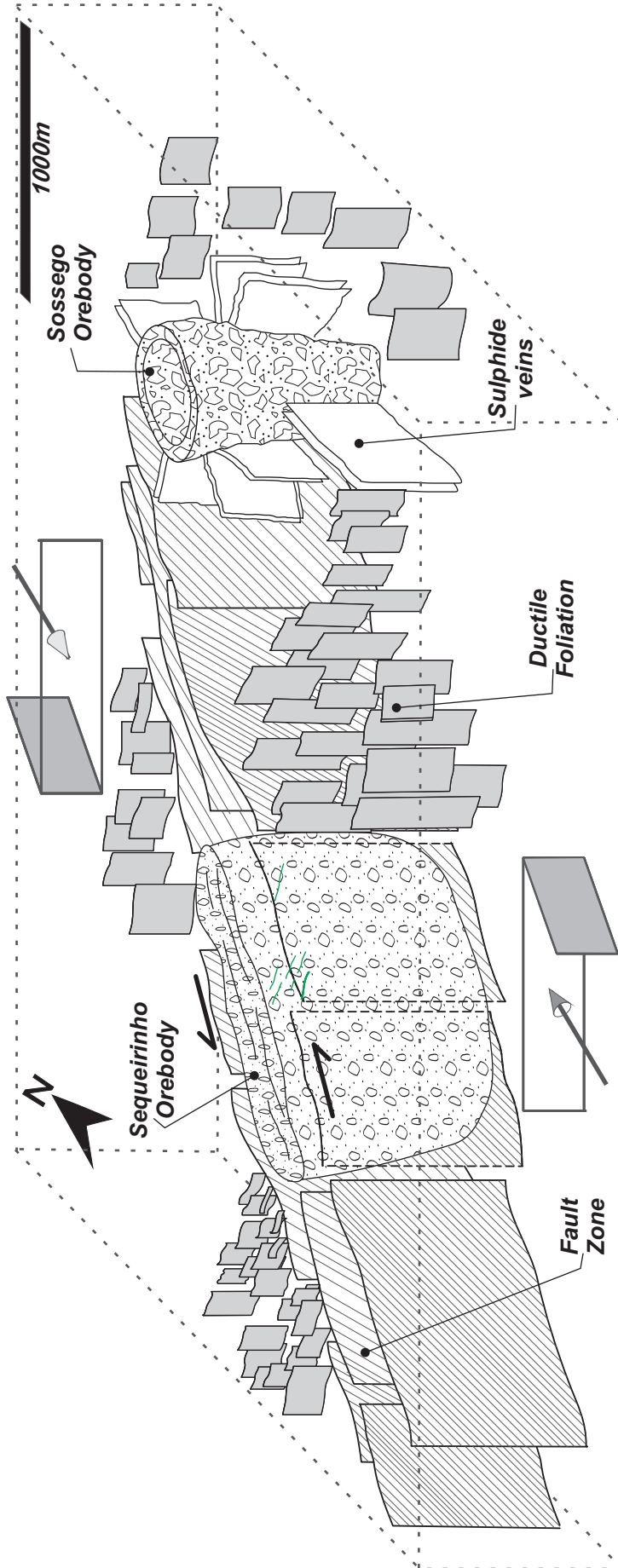


Figure 5.65 -Schematic representation of the structural framework in the area comprising the Sossego and Sequeirinho IOCG deposits. The geometries of the orebodies and prominent structures are highlighted..

Chapter 6

Conclusions summary and suggestions for future work

This section presents a summary of the major findings and conclusions from chapters 3, 4 and 5. These are concerned with: regional geological issues and the lineament analysis; the geological and structural character and history of the Canaã dos Carajás region; and finally the structural styles and controls on the mineralization of the Sossego and Sequeirinho IOCG Deposits. Finally, a brief discussion on broader regional issues and a discussion of possible future work are presented.

6.1 – Regional Lineaments

- The main sets of lineaments identified in the Carajás Terrane have the following orientations: WNW-ESE to E-W, NE-SW, NW-SE and N-S. - Overall, the volcano-sedimentary Cover Assemblage domain displays higher lineament densities with a dominance of short NW-SE traces, while the granitic-gneissic Basement Assemblage has a much lower lineament density with a number of prominent, long NE-SW traces.

- The contacts between the Basement and Cover assemblages (such as those around the Salobo and Serra Sul deposits) coincide with long and continuous WNW-ESE lineaments that change locally into E-W traces.

- The large-scale NE-SW lineaments, most prominent in the granitic basement, appear to interrupt the lateral continuity of the WNW-ESE trending outcrops of the Cover Assemblage. This is consistent with the suggestion that these NE-SW lineaments are faults formed late in the geological history.
- Zones of higher lineament density also coincide with domains containing numerous lineament intersections, particularly those produced by the mutual intersection of the WNW-ESE and NE-SW lineaments sets.
- The geology does not appear to control the spatial distributions of the lineaments, i.e. the lineament sets occur in all geological units in the Carajás Terrane. However, geology does influence lineament frequencies, which are higher in the units forming the Cover Assemblage compared to the Basement Assemblage.
- Mineral occurrences and deposits in the Carajás Terrane form clusters spatially associated with: (i) domains of higher lineament density; and (ii) areas where major WNW-ESE and NE-SW lineaments intersect. Clearly, then, there is a spatial relationship between major lineaments and the occurrence of mineral deposits.

6.2 – The Canaã dos Carajás region

- The regional macro-structures in the area, delineated by magnetic and gamma spectrometric surveys show: (i) a prominent broadly E-W trending, continuous and sinuous anomaly that may correspond to a regional scale shear zone or set of shear zones; and (ii) consistent late sets of NE-SW-trending, and subordinate NW-SE-trending magnetic lineaments that possibly represent major brittle faults.

- The Canaã dos Carajás region comprises Archaean TTG gneisses, lens shaped amphibolite bodies, 2.7 Ga. syn-tectonic alkali granitoids and 1.88 Ga. isotropic granites. These rocks display a localized early N-S fabric developed in the granitic gneisses and amphibolites, overprinted by widespread heterogeneous, anastomosing WNW-ESE and NE-SW foliation sets related to later, steeply dipping ductile shear zones. The latter regional foliation is associated with steep-to-moderately plunging mineral lineations, consistent with a near vertical orientation for the stretching axis of finite strain.

- The ductile fabric is locally folded, with fold axial planes and hinges at low angles to or sub-parallel with the trend of ductile shear zones and regional foliation. The early folded gneissic banding forms upright folds with tight to isoclinal limbs, sub-vertical to steep dipping NNW-SSE axial surfaces and shallowly plunging hinge lines. Minor disharmonic folds also occur in the early gneisses. The widespread transposed fabric displays intrafolial and asymmetric “drag folds” typically oriented subparallel to the (transposed) foliation. Collectively, these folds have sub-vertical axial surfaces trending WNW-ESE and NE-SW combined with mainly gently plunging hinge lines. Lastly, ptygmatic and sheath folds occur locally in pegmatitic and migmatitic gneisses.

- The nature and geometry of the planar and linear fabrics are compatible with a bulk pure-shear dominated transpression with partitioning of strain intensity with shortening and extensional directions oriented at approximately near horizontal ($\sim 020^\circ$ Az) and near vertical respectively.

- Later brittle structures are ubiquitous in the geological units of the Canaã dos Carajás Region. Outcrop-scale discrete fault planes, moderately-to-steeply dipping, show apparent displacements ranging from few millimetres up to 10 cm and

comprise sets that broadly agree with the major ductile trends: E-W and WNW-ESE, NE-SW and NW-SE. Quartz, albite and actinolite veins are common in granitoids and mafic rocks, occurring either as “S” and “Z” geometry tension gash arrays or as tabular veins, with both broadly following fault trends.

- Microstructures in quartz and feldspar show that the basement rocks experienced deformation at metamorphic conditions compatible with middle to upper amphibolite facies (~650-700°C), later overprinted by relatively low temperature deformation at middle to upper greenschist facies conditions (~400-500°C).

- The Archaean rocks in the Canaã dos Carajás region represent part of an original granite-greenstone terrane that has undergone substantial reworking during a late sinistral transpressional deformation. The reworking took place at c.a. 2.7 Ga during and was coeval with syn-tectonic sub-alkaline magmatism.

- The granitic-gneissic basement comprises intensely deformed rocks uplifted from the lower-to-middle crust, initially deformed under high amphibolite facies conditions and later affected by localised, deformation along discrete shear zones at greenschist facies conditions.

- Faults, fault zones and veins formed during late brittle events and record widespread hydrothermal alteration and localized evidence of copper mineralization. A number of these structures correspond to major magnetic and topographic lineaments, confirming that the lineaments and their associated mineral deposits have a spatial correlation.

6.3 – The IOCG Sossego and Sequeirinho Deposits

- The structural framework of the deposits comprises regionally developed WNW-ESE structures (foliations and shear zones) offset by NE-SW sinistral faults most clearly seen in magnetic surveys and geological maps. The Sequeirinho orebody is hosted along a NE-SW sinistral fault, associated with a positive magnetic anomaly, whilst the Sossego orebody does not show any obvious link to a major structure or prominent magnetic anomaly.
- The Sossego deposit comprises a sub-circular, vertical, pipe-like orebody with a central breccia body surrounded by a stockwork array of sulphide veins, faults and shear zones. The deposit displays early, heterogeneous and apparently contemporaneous WNW-ESE trending foliation and shear zones, overprinted by mutually cross-cutting, polymodal, sub-vertical to gently dipping faults, veins and shear bands. Tensile and shear veins show single or composite mineral fillings consistent with episodic vein opening, with a progressive change in hydrothermal fluid composition during time. Faults and shear zones generally contain hydrothermal minerals suggesting intense fluid influx and/or fluid flow. The mutually cross-cutting dip-slip, strike-slip, and oblique-slip nature of the faults suggest that they were broadly contemporaneous.
- The Sequeirinho orebody is significantly different. It comprises an “S” shaped orebody whose tips are hosted by sub-vertical WNW-ESE-trending sheared and foliated granitoids and schists. These are linked by a NE-SW sinistral fault zone containing mineralized breccias.
- The granitoids and schists in Sequeirinho show prominent mylonitic zones intercalated with relatively undeformed domains, suggestive of strain intensity

partitioning. The steeply-dipping to sub-vertical WNW-ESE mylonitic foliation is accompanied by a down-dip mineral lineation, indicating a near horizontal compressional component, linked to a vertical stretching component that acted to form these structures.

- Rocks in Sequeirinho display multiple, steeply-dipping fault sets that include: WNW-ESE, NE-SW, NW-SE and N-S trends. The WNW-ESE trending faults clearly had their nucleation and development controlled by the pre-existing weakness planes parallel to the early ductile foliation. NE-SW faults cross-cut and displace the regional foliation in map view (see **Fig. 5.9** in Chapter 5). The precise ages of the NW-SE fault set is unclear, but the N-S trending faults are clearly the youngest identified and are typically associated with late tabular diabase dykes regionally.

- Fault slickenlines associated with multiple fault planes are often oriented close to the fault intersections indicating that many of the differently oriented faults may slipped contemporaneously.

- In the Sequeirinho body, two distinct types of faults are recognised: i) discrete narrow fault planes that are thought to have been produced by a short-lived movement history, under low regimes of pore fluid pressure at shallow crustal depths; and ii) larger fault zones with well-developed fault rocks (i.e. cataclasites, ultramylonites) and hydrothermal mineral assemblages, that are thought to represent structures with long lived fault activity possibly associated with seismic slip.

- Particle size and shape analyses for barren and mineralized breccias fragments indicate that: (i) the Sossego breccias show relatively high clast angularity and smaller *D*-values, characteristic of immature explosion breccias, compatible with fragmentation processes dominated by particles fracturing and cracking that generate

coarse and angular fragments; and (ii) the Sequeirinho breccias display rounded fragments with low angularity and higher *D*-values, typical of mature breccias whose particle fragmentation was dominated by wear and attrition when particles interact by rolling, sliding and rotation during subsequent slip along a fault zone.

- Microstructural observations of quartz and feldspar indicate that the sinistral transpressive deformation at Sossego and Sequeirinho initially took place under low-to-middle (300-400°C) and middle-to-upper (400-500°C) greenschist facies, respectively. These relatively high-temperature fabrics were then overprinted by later brittle-ductile structures and veins containing lower-temperature minerals interpreted to be formed at between 170-250°C.

- Microveins include: (i) massive and monomineralic types formed by a relatively simple growth history with a single phase of vein opening and sealing; and (ii) polymineralic veins showing multiple mineral fillings, elongate crystals, fibrous mineral fills, wall rock inclusion bands and fluid inclusions trails. The latter set show evidence of crack–seal mechanisms and temporal changes in fluid composition through time.

- The geometry of calcite twins in microveins and major composite ore veins suggests temperature formations ranging from 170°C up to 250°C.

- Brittle fault rocks under the microscope revealed heterogeneous degrees of fragmentation and indicative textures of repeated brittle fracturing (cataclasis) accompanied by intense hydrothermal fluid influx.

- The rocks in the area of the mines record deformational processes that initially took place under the viscous regime (>15km), represented by mylonites and ultramylonites. Progressive exhumation, possibly synchronous with regional

transpressional thickening led to conditions compatible with the frictional-viscous transition with intense fluid activity, with mineralisation.

6.4 - Timing of the major crust forming events and global implications

The isotopic ages available for the Carajás Geochronological Province (see Tables 2.3 and 2.4 in chapter 2) can be used to indicate the timing of crystallization and mineralization for the rocks and mineralization within this region. Histograms for these groups of ages (see **Fig. 6.1 A and B**) highlight peaks at 1.88 Ga and 2.7 Ga, corresponding to major periods of continental crust formation in this craton. Importantly, these ages coincide with two peaks of inferred crustal generation from a range of additional studies worldwide (see **Fig. 6.1 C**) (Condie 1998; Condie 2000; Parman 2007; Pearson et al. 2007). They suggest that the formation of Earth's continental crust was mainly controlled by large-scale mantle melting events at 1.9, 2.7 and 3.3 Ga, caused by pulses of mantle depletion. This proposed mechanism implies that the formation of the continental crust was episodic and punctuated by large, potentially global, melting events. These periods of pulsing enhanced crustal generation, termed 'super events' by (Condie 1998), can be linked to the formation of granite–greenstone terranes recognized in cratons worldwide. The Carajás Terrane records two of the three major super events of global continental crust formation; the 2.7 Ga syntectonic granitoids (e.g. Plaque Suite, Estrela, Serra do Rabo) and 1.88 Ga. a-type anorogenic granitoids.

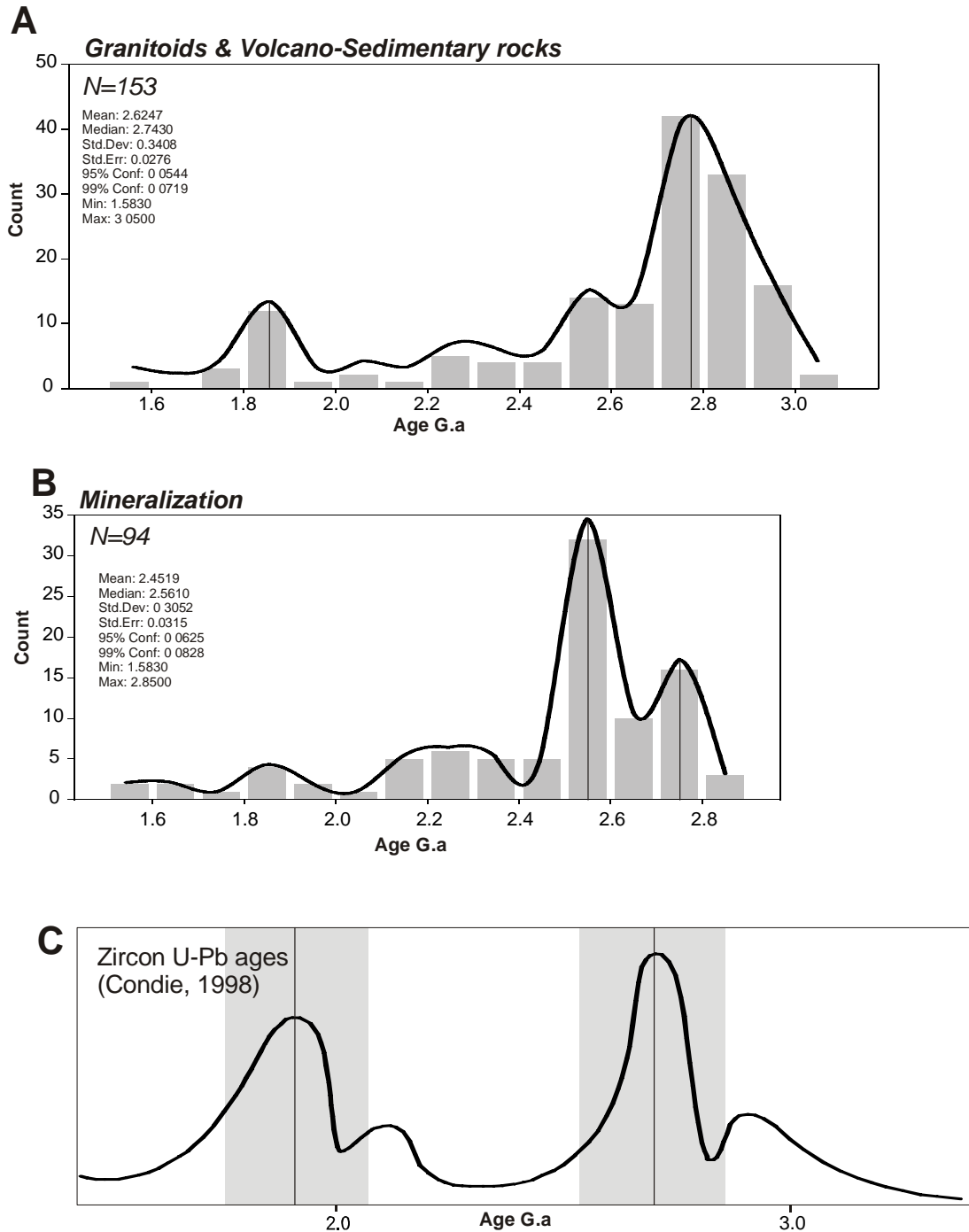


Figure 6.1 – A - age histogram of isotopic ages representing the crystallization time of granitic-gneissic and volcano-sedimentary rocks in the region of Carajás, Canaã dos Carajás and Rio Maria (ages sources in table 2.3 – Chapter 2). B - Histogram for ages of mineralization from the Carajás Terrane (ages sources in table 2.4 – Chapter 2). C - Distribution of U/Pb zircon ages in juvenile global continental crust. Abundance is proportional to areal distribution of juvenile age provinces scaled from an equal-area projection of the continents (Condie, 1998).

6.5 - Regional Issues

The study region of Canaã dos Carajás represents a boundary zone separating the Carajás and Rio Maria Granite Greenstone Terranes, which exhibit distinct structural styles and varied ages.

The Canaã dos Carajás area and nearby Sossego and Sequeirinho deposits indicate that the region comprises an intensely reworked granite-gneiss terrane deformed by pure-shear dominated, sinistral transpression. The deformation was highly heterogeneous and mainly localized along and adjacent to shear zones. The intervening less deformed “islands” of gneisses and amphibolites show fabric orientations similar to that described for the basement in the Rio Maria granite greenstone terrane (described in Chapter 4). This evidence suggests that the rocks in the Canaã area represent highly deformed, reworked parts of the granite-greenstone sequence seen in the Rio Maria Terrane. This implies that: (i) the current location of the Carajás-Rio Maria Granite Greenstone Terranes boundary sits in Canaã dos Carajás town; and (ii) calls into question the current accepted division of the Amazon Craton into the tectonic-geochronological Terranes of Carajás and Rio Maria Granite Greenstone, a proposal that is mostly made using geochemical and isotopical data.

6.5 Future work

This section presents suggestions for future research topics that may contribute to resolve two key geological issues remaining in the region: (i) the subsurface geometry-architecture of the Carajás geochronological province and (ii) the absolute ages of the faults and fabrics in the granite-gneiss basement.

- *Regional Geophysics*

Despite the available regional-scale magnetic, gamma radiometric and minor gravimetric datasets, the 3D crustal architecture of the Carajás Geochronological Province remains poorly understood. The acquisition of seismic data could provide an initial step to building a subsurface model that would enable an improved understanding of the spatial configuration of the geological domains and structures.

Onshore seismic surveys have successfully delineated the crustal architecture of poly-deformed Archaean and Proterozoic provinces elsewhere in the world, e.g. the Yilgarn Craton-Australia (Dentith et al. 2000; Goleby et al. 2006), North China Craton (Tian et al. 2009) and the Skellefte Proterozoic District-Sweedden (Malehmir et al. 2006). The principles and methods used in the mentioned examples could be applied in seismic transects across the Rio Maria Granite Greenstone Terrane, the Canaã dos Carajás region and the Carajás Terrane to better elucidate the sub-surface anatomy and crustal scale structures in the craton.

Examples of the potential information that seismic data obtained across the Carajás and other provinces of the Amazon Craton could provide are:

- P and S wave data to indicate velocity variations within and across the craton that may correspond to province and terrane boundaries.
- deep seismic reflection data to detect the depth of the Moho discontinuity and image crustal scale geometric features. One disadvantage here might be that many of the tectonic structures are steeply dipping or sub-vertical and may not then be clearly imaged by seismic reflection methods.
- seismic refraction data to indicate variations in crustal thickness, density and geometric constraints on crustal architecture.

- Dating of fabrics and faults

In Chapters 4 and 5 a widespread regional ductile fabric in the granitic basement, normally associated with shear zones trending in three directions (WNW-ESE, N-S and NE-SW) was described. The WNW-ESE fabric is present within syn-tectonic granitoids and is interpreted therefore to have formed at 2.7 Ga. However, there are no constraints on the relative ages of the other two fabric sets and exposures showing cross-cutting relationships are rarely found. Therefore, the ages of these fabrics and associated shear zones remain open to debate. More recent studies based on $^{39}\text{Ar}/^{40}\text{Ar}$ dating of individual minerals have successfully dated deformation phases in the ductile fabrics from greenschist-to-amphibolite facies shear zones e.g.: white mica (Alexandrov et al. 2002; Challandes et al. 2003), hornblende (Barreiro et al. 2006), and tourmaline (Bea et al. 2009). Future studies utilizing these analytical techniques can potentially answer the questions: (1) what are the absolute ages of the fabric sets observed in the region? (2) are the ductile fabric sets contemporaneous or

formed by distinct tectono-metamorphic events? and (3) in case of distinct ages for the fabrics, what regional events formed the fabrics?

The relative ages of the faults are also not well constrained in the study region. The poly-directional fault sets often show uncertain or ambiguous cross-cutting relations and absolute ages for faults are absent. Age constraints for the faults sets and perhaps for different stages of fault slip may be inferred through detailed structural mapping in key outcrops with good exposure, combined with the dating of fault rock materials, e.g. using $^{40}\text{Ar}/^{39}\text{Ar}$ dating of illite in fault gouges; (Solum et al. 2007; Haines et al. 2008).

Appendix

Digital geological mapping with tablet PC and PDA: A comparison

P. Clegg^{a,*}, L. Bruciatelli^b, F. Domingos^a, R.R. Jones^{c,d},
M. De Donatis^b, R.W. Wilson^a

^aDepartment of Earth Sciences, University of Durham, DH1 3LE, UK

^bLaboratory of Information Technology for Earth and Environmental Sciences, Università degli Studi di Urbino,
Campus Scientifico Loc. Crocicchia, 61029 Urbino, Italy

^cGeospatial Research Ltd., Department of Earth Sciences, University of Durham, DH1 3LE, UK

^de Science Research Institute, University of Durham, DH1 3LE, UK

Received 24 October 2005; received in revised form 23 February 2006; accepted 16 March 2006

Abstract

Both the hardware and software available for digital geological mapping (DGM) have advanced considerably in recent years. Mobile computers have become cheaper, lighter, faster and more power efficient. Global Positioning Systems (GPS) have become cheaper, smaller and more accurate, and software specifically designed for geological mapping has become available. These advances have now reached a stage where it is effective to replace traditional paper based mapping techniques with those employing DGM methodologies. This paper attempts to assess and evaluate two currently available DGM systems for geological outcrop mapping: one based on a Personal Digital Assistant (PDA) running ESRI “ArcPad”, and the second based on a Tablet PC running “Map IT” software. Evaluation was based on field assessment during mapping of a well exposed coastal section of deformed Carboniferous and Permian rocks at N. Tynemouth in NE England. Prior to the field assessment, several key criteria were identified as essential attributes of an effective DGM system. These criteria were used as the basis for the assessment and evaluation process. Our findings suggest that the main concerns presented by sceptics opposed to DGM have largely been resolved.

In general, DGM systems using a Tablet PC were found to be most suitable for a wide range of geological data collection tasks, including detailed outcrop mapping. In contrast, systems based on a PDA, due to small screen and limited processing power, were best suited for more basic mapping and simple data collection tasks. In addition, PDA based systems can be particularly advantageous for mapping projects in remote regions, in situations where there is a limited power supply or where total weight of equipment is an important consideration.

© 2006 Elsevier Ltd. All rights reserved.

Keywords: Digital geological mapping; Tablet PC; PDA; GIS; GPS

1. Introduction

Digital geological mapping (DGM) is the process of mapping and collecting geological data using some form of portable computer and Global

*Corresponding author. Tel.: +44 (0) 1913342338;
fax: +44 (0) 1913342301.

E-mail address: p.clegg@durham.ac.uk (P. Clegg).

Positioning System (GPS), rather than a traditional approach based on notebook and paper map. Digital mapping is rapidly becoming accepted and established as a valuable tool for geoscientists.

Over the past years there have been numerous papers discussing the methodology, software development, applications and the merits of DGM (e.g. Struik et al., 1991; Brodaric, 1997; Briner et al., 1999; Brimhall and Vanegas, 2001; Maerten et al., 2001; Edmondo, 2002; McCaffrey et al., 2003; Jones et al., 2004; Wilson et al., 2005; McCaffrey et al., 2005). These papers document the ongoing technological development, which has allowed relatively unwieldy computer equipment available to the early digital pioneers to be replaced by lightweight and user-friendly DGM systems. Most modern users favour a DGM setup based around either a palm-sized Personal Digital Assistant (PDA) or a larger Tablet PC. In this paper, we examine and assess the particular merits of these two types of DGM system. In addition, we briefly summarize the evolution and current status of DGM, and consider some of the more general issues that remain unresolved in digital mapping.

2. Overview of DGM

In recent years, technological advances and innovations in portable computing, GPS, and mobile Geographical Information Systems (GIS) software have permitted geoscientists to undertake digital data capture and mapping in the field. This process has been referred to as “born digital mapping” (Fitzgibbon, 1997) or primary digital mapping (McCaffrey et al., 2005), and is the main focus of this paper. Primary digital mapping contrasts with other digital tasks such as transcribing field data into spreadsheets or databases, and reproduction of field maps with cartographic or graphic software; these are post-fieldwork tasks related to secondary digitizing (McCaffrey et al., 2005).

Digital field acquisition has been used by surveyors and workers in the utility industries since the late 1980s to input data or to correct, modify, or create maps directly in the field. Generally the data collected by these user groups, although often varied, is in a relatively simple format, and can be input into a handheld computer relatively easily by an operator with limited computing skills using standard software containing simple data collection forms. In contrast, geological field mapping is an

iterative process of observation, reasoning, and interpretation, which is strongly influenced by the geoscientist’s prior knowledge, experience and expertise (Jones et al., 2004). In the field the geoscientist uses a combination of processes and scientific tools to gather the rich data provided by the field environment. These include; recording direct observations, collection of field samples, measurement of bedding and structure, field sketching, photography and mapping. This process therefore requires a more flexible approach and a broader range of recording media than that used to record basic types of utility data mentioned above. This level of flexibility is already met by traditional paper-based mapping methodologies, so geologists will need to be convinced of the added value offered by digital mapping over traditional methods before they are likely to adopt the new methods.

3. Advantages of DGM

DGM is not simply a direct replacement for traditional paper-based mapping methods; importantly, it gives the geoscientist the enhanced ability to collect geospatially georeferenced field data that can be analysed and visualized in ways that are impossible or very difficult to achieve using traditional techniques (McCaffrey et al., 2005). Pioneers of DGM (e.g. Struik et al., 1991; Brodaric, 1997; Briner et al., 1999; Kramer, 2000; Brimhall and Vanegas, 2001; Edmondo, 2002; McCaffrey et al., 2003; Jones et al., 2004; Wilson et al., 2005; McCaffrey et al., 2005) have discussed the many advantages offered by DGM over traditional methods, which include:

- GPS allows all data and their attributes to be geospatially referenced in x,y,z , space, i.e. latitude, longitude and elevation, (although data added freehand by drawing with the stylus will generally lack altitude values).
- There is a streamlined workflow from data collection to final map production without the need for disparate and separate data processing.
- Data derived using other geophysical and geographical systems can be easily integrated e.g. satellite imagery, gravity and magnetic surveys, geochemical sampling, Digital Elevation Models (DEM) etc.
- Data management and storage capability are enhanced.

- There is greater accessibility to data for a wider audience through data archives.
- A wider range of analytical techniques including 3D analysis, spatial analysis etc. can be applied.
- Accuracy and precision of GPS positional data can be tested and quantified. This is not the case in traditional mapping, where this possible source of error is largely ignored.
- Cost savings can be gained by reduction in the need for time-consuming data conversion and handling.

Despite these numerous advantages many field geologists are still reluctant to try the new technology, preferring instead to continue to use the old tried and tested methods of paper-based field mapping. For example, in a survey of twenty nine geological survey organizations in Europe, all utilized secondary digitization for data storage and the production of maps, however only two were actively investigating the use of primary digital data acquisition during geological mapping (Jackson and Asch, 2002). Consequently, field geoscientists practising traditional methods of mapping and interpretation of the complex geological structure and history of the Earth, do not yet derive appreciable benefit from the digital and information technological advances and innovations that have been made in other related fields of science (Brimhall et al., 2002). Of the reasons often given for a particular geoscientists' reluctance to embrace DGM, three main themes commonly arise: (1) cost and reliability of equipment; (2) time required to learn the new techniques required for DGM and (3) the complex nature of the mapping process and the flexibility required by any methodology.

4. Requirements of a DGM system

The technology involved in traditional field mapping is cheap, well-proven, flexible, has a familiar user interface, and is highly reliable. Geological mapping is a time consuming and often expensive process. Therefore, any DGM system not only has to be as efficient as traditional methods, but also in addition has to offer distinct advantages over them. An important definition here is "Fit for purpose" i.e. will the chosen DGM system perform the tasks required of it efficiently, accurately and consistently throughout the range of environmental conditions met during mapping e.g. extreme cold and heat, high humidity, very wet or dry? Prior to

field assessment we identified several key criteria that we felt were critical to a well-designed DGM system regardless of its intended purpose (Table 1).

4.1. Assessment criteria

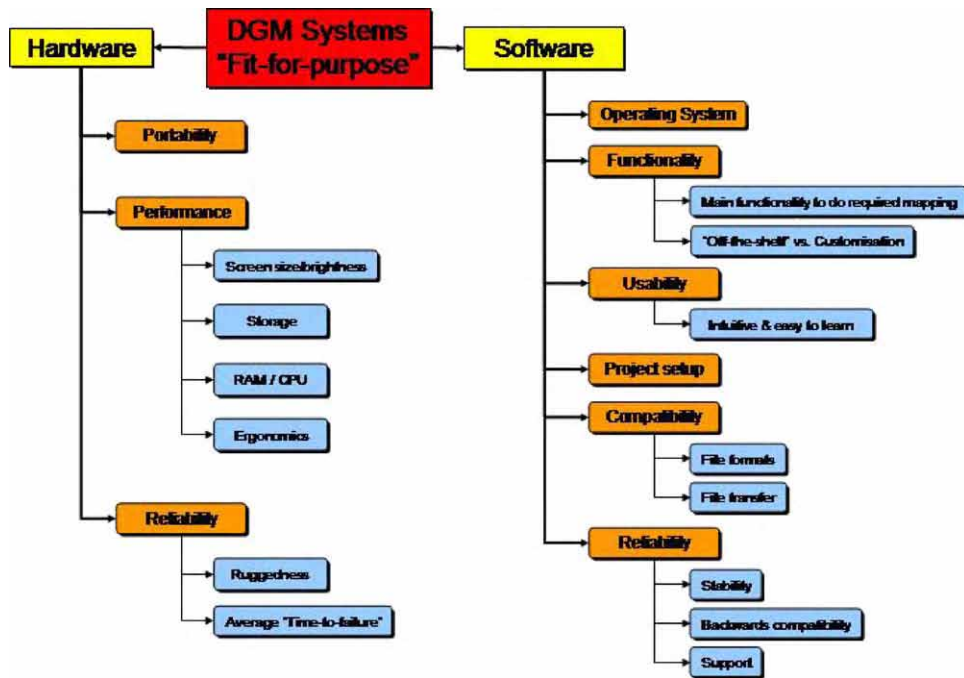
4.1.1. Hardware

- *Portability*: the portability of a DGM system is an important issue and not only concerns issues of weight and size, but is also related to ergonomics i.e. how comfortable the system is to carry and hold in use. The location of any individual mapping project can vary enormously from roadside cuttings where weight of the system is not an issue to extremely remote settings where all equipment must be carried by hand. In addition, peripheral equipment such as extra batteries, chargers etc. need to be taken into account.
- *Performance*: this covers aspects of screen size and brightness, storage capacity, RAM and CPU size/speed and the general ergonomics of each system. Of vital importance is that the screen should be clearly visible in bright sunlight. Transreflective screens are the most effective; these are relatively common in modern PDAs, but less so in Tablet PCs.
- *Reliability*: this concerns the ruggedness of each system and its suitability to carry out its task in a variety of environmental conditions e.g. rain, cold, heat and dust. Also under this heading is the average "time-to-failure" i.e. how long will the system (or its components) last under normal operating conditions?

4.1.2. Software

- *Operating system*: the operating system (OS) ultimately dictates which digital mapping software can be used. Some manufacturers provide different versions of their software for different operating systems whilst others only produce software for a single OS.
- *Functionality*: This criterion concerns two specific issues: firstly does the software require any setting-up or customization before even basic mapping can be carried out i.e. is it "out-of-the-box" ready? Secondly, does the software contain an appropriate range of tools and functions to carry out the required mapping, and can it be customized to the users specifications?

Table 1
Critical criterion for the design of a ‘Fit for purpose’ digital geological mapping system



- *Usability*: this can be a subjective issue and depends largely on the user’s familiarity with Graphical User Interfaces, and in particular, previous experience with desktop GIS software. However, a well designed, clear interface will enable the user to utilize the software for maximum efficiency as quickly as possible and will also encourage them to continue to use the system.
- *Project set up*: the pre-fieldwork setup of any DGM project is critical and is typically a much more involved process than the preparation required for traditional paper-based mapping. Base maps, aerial photographs, satellite images etc. need to be scanned or downloaded. Scanned raster images must be georeferenced, shapefiles (or equivalent geographical objects) need to be created and data collection forms produced. The ability to be able to define levels of user control within a project at set up is highly desirable. This allows a project manager to establish a clearly defined set of forms, base cartography and symbols etc. that will be used by any particular group.
- *Compatibility*: DGM systems need to be able to import and export files from and to a wide

variety of other applications which employ numerous different file formats e.g. ESRI shapefile, ArcInfo, MapInfo MIF, DXF, TIFF, JPG, GIF, MrSID. The range of file formats supported and/or the ease of conversion is a key issue.

- *Reliability*: issues of reliability are critical for any system that will be used in remote settings or to collect data that is not easily re-collected. Crashes in software lead to delays in progress, reduced confidence in the system and particularly important, possible data loss. “Backwards compatibility” (the ability of a system to open files generated with earlier versions of the software) is also an important consideration, particularly where archive data is more than a few years old. The level of support offered by a software manufacturer to its client is also important.

In general, good DGM systems:

- need to be reliable, rugged and not significantly bulkier than a field notebook and mapping board;

- should be fit for purpose and priced accordingly; i.e. a system designed for reconnaissance mapping at a scale of 1:250 000 need not be coupled to an expensive differential GPS capable of sub-metre precision;
- have a simple and logical visual interface in order to make the transition from traditional paper-based mapping to DGM easier;
- should require little prior knowledge of computer skills from the operator (with current students and recently qualified geoscience graduates this requirement is becoming less important because of their general high level of IT expertise);
- should be adaptable enough to allow users to easily configure the software to their particular requirements whilst in the field without the need for computer programming skills.

5. DGM hardware and software

Currently, many DGM systems belong to one of two types: those built around a Personal Digital Assistant (PDA), and those built around a Tablet PC. The systems shown in Table 2 are just a small selection of the many different PDAs and Tablet PCs available on the market, and simply represent those with which we have direct experience. The main focus of this paper is to review the pros and cons of both these types of DGM systems by focussing on two in particular (Table 3). The first is a PDA-based system comprising Trimble Recon PDA, a GPS, and ArcPad mapping software (Fig. 1a). The second system comprises an Xplore iX104R rugged Tablet PC, Haicom HI-204S GPS and MapITTM software (Fig. 1b). We will also look briefly at the Trimble GeoXT, which is an integrated PDA and GPS receiver system (Fig. 1c).

5.1. GPS choice and testing

The GPS is an important and integral component in any digital mapping system and the choice currently available is large. However, the GPS is only required to provide positional information, which is then displayed via the DGM software. Therefore, more advanced features offered by some GPS models, such as colour screens, ability to store and display map data etc. are not required. What is important is that the choice of a particular GPS is determined by the mapping task to be undertaken

and the levels of accuracy and precision required. Table 4 of McCaffrey et al. (2005), provides precision and accuracy information for a range of GPS units including the Garmin Geko 201 and the Trimble GeoXT.

5.2. Accuracy and precision

Although many users assume that GPS receivers give exact positions, it is important to understand that there is some amount of uncertainty, or error, inherent in these positions. Several factors contribute to this error including satellite clock drift, atmospheric conditions, measurement noise, and multipath (i.e. reflection of the signal off buildings etc. before being received by the GPS). Additionally, vertical accuracy (elevation) for GPS measurements is generally one and a half to three times worse than horizontal accuracy.

5.3. Differential GPS, WAAS and Egnos

The accuracy of GPS receivers can be improved by using differential correction (“differential GPS”, DGPS), to reduce some of the error. DGPS involves using a GPS base station, located at a known position, to calculate corrections for each satellite. The corrections can be derived by comparing the known location of the base station to the apparent location measured using GPS. This can increase the accuracy of the autonomous GPS position (i.e. one without differential corrections) from 5 to 10 m down to less than 1 m, depending on the system used.

There are two approaches to DGPS: real-time and post-processing. Post-processing corrections are stored on a disk and then applied to the field data after data collection is complete. Real-time corrections are broadcasted from the base station to the field GPS receiver almost instantly, so that you can begin to work with the more accurate GPS positions immediately. There are various sources of real-time DGPS signals, including Coastal beacons; Wide Area Augmentation System (WAAS, North America), and European Geostationary Navigation Overlay System (EGNOS, Europe only). The Geko 201 and Haicom HI-204S are capable of receiving real-time differential corrections using WAAS and EGNOS, while the GeoXT can utilize both real-time correction using WAAS, EGNOS and beacon data, as well as permitting differential corrections via post-processing software.

Table 2
Some of the available digital mapping core devices grouped into PDA or tablet PC platform and their main features

System	Example	Type	Cost (approx.)	Weight incl. batteries (kg)	Battery life (manufactures data) (h)	Pros	Cons
PDA	HP iPAQ H3950	Standard windows pocket PC 2003 PDA	£350	0.185	4	Light and portable. Daylight readable screen.	Small screen size. Speed. Not ruggedised ^a . Short battery life.
	Trimble recon	Ruggedised PDA	£1200	0.49	8	Light and portable. Daylight readable screen. Ruggedised.	Expensive. Small screen size. Speed.
	Trimble GEOXT	Ruggedised, integrated PDA & GPS	£3500	0.72	8	Light & portable. Daylight readable screen. Ruggedised. Integrated GPS (no cables).	Expensive. Small screen size. Speed.
Tablet PC	Acer TravelMate C110 Tablet PC	Note book/tablet PC hybrid	£1200	1.4	0	Relatively cheap. Light weight. Large screen. Full PC specs.	Screen not visible in daylight conditions. Not ruggedised. Short battery life.
	HP Compaq tc1100 Tablet PC	Standard tablet, with detachable keyboard	£1600	1.4 ^b	3 ^c	Large screen. Daylight visible. Full PC specs.	Not ruggedised. Short battery life.
	Xplore iX104	Ruggedised tablet	£2700	2	6 ^c	Ruggedised. Large screen. Daylight visible. Full PC specs.	Expensive.

Costs are approximate and are likely to change by time of publication.

^aA rugged case is available.

^b1.8 kg with detachable keyboard.

^cDepends on operating system, power management and applications in use.

Table 3
Technical specifications of the DGM systems compared in the present work.

Features	Rugged PDA and GPS	Tablet PC and GPS receiver unit	“All in one” handheld
Hardware	Trimble Recon	Xplore iX104R	Trimble GeoXT
Processor	40 MHz Intel PXA255 XScale	866 MHz Intel Pentium III M	206 MHz Intel Strong ARM SA-1110
Physical memory	64 MB RAM	512 MB RAM	32 MB RAM
Display	240 × 320 pixel full outdoor colour display, with backlight	10.4" XGA TFT colour (1024 × 768)	240 × 320 pixel full outdoor colour display, with backlight
Battery	Removable internal lithium-ion (all day)	48 MB shared RAM	Internal lithium-ion (all day)
Storage	128 MB internal flash disk and 2 user changeable compact flash slots	Internal Li-ion (up to 6 h ^a operation)	512 MB internal flash disk
Weight	0.49 kg with battery	2 kg with standard battery	0.72 kg with battery (including antenna)
Dimensions	16.5 × 9.5 × 4.5 cm	28.4 × 20.9 × 4 cm	21.5 × 9 × 7.7 cm
Chassis/caising	Rugged water-resistant, shock-resistant, and dustproof (MIL-STD-810F)	Rugged magnesium, Patented industrial bumper system, sealed and protected from the environment (MIL-STD-810F)	Rugged water-resistant, shock-resistant, and dustproof Wind-driven rain and dust-resistant as per IP 55 specifications
User Interface	TFT touch screen, 10 hardware control keys	Hi-Resolution active screen; 8 key backlit keypad—tablet pc keys and programmable; 5 way navigation joystick	Anti glare touch screen; 2 hardware control keys; 4 programmable permanent touch buttons;
Communications	USB, DE9(M) RS-232 serial port	Wireless radio bay; 1 × USB; 1 × IEEE 1394; LAN (RJ-45); 1x mic/spk; 15-pin D-SUB connector for external VGA monitor	USB connectivity via support module, serial communications via optional DE9 serial clip adapter; integrated Bluetooth for wireless connectivity
Operational system	Windows Pocket PC 2003	Windows XP Professional Tablet PC Edition	Windows CE 3.0
GPS receiver	Garmin Geko 201	Hicom HI-204S GPS	Trimble
Channels	12	12	12
Integrated real time Protocol	WAAS/EGNOS NMEA-0183, Garmin, Garmin DGPS, RTCM	WAAS/EGNOS NMEA-0183 (GGA, GSA, GSV, RMC, VTG, GLL)	WAAS/Egnos & Beacon ^b NMEA (GGA, VTG, GLL, GSA, GSV, RMC) and TSIP (Trimble Standard Interface Protocol)
Update rate	1 Hz	1 Hz	1 Hz
Weight	88 g without batteries (2 × AAA)	120 g	N/A (integrated)
Accuracy	5–25 m (standard); 2–5 m (DGPS)	5–25 m (standard); 1–5 m (DGPS)	Sub metre (real-time DGPS)
Acquisition time	warm 15 s; cold 45 s	hot 8 s; warm 40 s; cold 50 s	No autonomous data given
Mapping Software	ArcPad 6.03	MapIt Version 1.3 (now 2.0 is available)	30 s (typical)
Price	Trimble Recon £1200 Garmin Geko £90 PDA-GPS cable £25 ArcPad 6.03 £75 (educational) ArcPad £450 + vat (non educational) ArcGIS 9 £1495 + vat (non educational) ArcStudio £1495 + vat (non educational) ArcGIS £100 + vat (educational) ArcPad Studio £250 + vat (educational)	Xplore iX104R US\$ 2723 = £1540 (Sept 05) Hicom HI-204S GPS receiver £70 Map IT £1050, £750	Trimble GeoXT £3150 ArcPad 6.03 £75 (educational) ArcPad £450 + vat (non educational) ArcGIS 9 £1495 + vat (non educational) ArcStudio £1495 + vat (non educational) ArcGIS £100 + vat (educational per year) ArcPad Studio £250 + vat (educational)
Total cost of system	£1810–£4833	£2360	£3645–£6960

^aBattery life is dependent upon operating system, power management and applications in use. All prices are approximate and likely to change by time of publication.

^bOptional extra.



Fig. 1. PDA and tablet PC systems compared: (a) Trimble Recon PDA running ArcPad software with Garmin Geko 201 GPS; (b) Xplore tablet PC running Map IT software with Hicom HI 204S GPS receiver and (c) Trimble GeoXT integrated PDA and GPS receiver running ArcPad software.

5.4. Testing accuracy and precision

Accuracy is the closeness of a measurement to the actual value of the measured quantity, whereas precision is the repeatability of a particular measurement method. It is possible to be accurate and not precise, and vice versa (Fig. 2). The precision or error in a GPS position may be estimated by repeated observations at the same location over a given length of time (McCaffrey et al., 2005). Accuracy can be determined by making observations on a known survey point (e.g. <http://users.erols.com/dlwilson/gps.htm>). Wilson (2006) has tested the accuracy of a variety of GPS units including the Garmin Geko 201 and Trimble GeoXT GPS (the Haicom HI-204S was unavailable at the time of testing). For the test the position of a known surveyed location was recorded daily over a fifty day period. Fig. 3 provides the results for the Geko 201 and GeoXT. The accuracy observed for the Geko and GeoXT is sufficient for a wide range of typical field-mapping scales e.g. 1:250,000–1:5000.

Table 3 summarises the manufacturers' specifications of all the GPS units evaluated. Predictably, the more expensive GeoXT is more accurate than the Geko, however, this difference is marginal and would generally not be noticeable when mapping at scales greater than 1:10,000. Although the Haicom HI-204S was not tested, the manufacture's accuracy figures imply that it should have a similar accuracy than that of the Geko and should therefore be suitable across a similar range of mapping scales.

5.5. DGM system 1

5.5.1. Hardware

This DGM system is based around the Trimble Recon PDA (Fig. 1a, Table 3). The Recon is a ruggedised PDA, and is water, dust, and shock-proofed to military standards (MIL-STD-810F). The battery is user changeable, and provides the PDA with approximately 8 h of operation in normal conditions. The unit is bright yellow, which gives it high visibility, and has black rubber bumpers on each end that provide protection and cover the battery and compact flash slots. The PDA was connected to a Garmin Geko 201 via a serial/Garmin cable, which provided a lightweight, accurate, digital mapping system.

5.5.2. Software

The mapping software installed on the PDA is ArcPad, part of the ESRI suite of GIS products.

Table 4
Summarized evaluation of the DGM systems assessed in the present work

		Pros	Cons
Hardware	Xplore Tablet	Large data storage capacity. Processing power.	Relatively heavy. The supplied case is poorly designed for field mapping purposes.
		Large screen size.	Battery life (4.5 h ave.) requires additional batteries to be carried.
		Full PC specs.	Screen needs dedicated digital pen loss could be disastrous.
Hardware	Trimble Recon PDA	Light weight.	Small screen size requires lots of scrolling.
		Portable.	Generally slow processor speeds long refresh times for displays containing large raster images.
		8 h + battery life.	Needs PC and Active Sync to upload/download data.
Software	MapIT	Fully specced GIS e.g. georeferencing, spatial analysis, coordinate conversion etc.	Polyline data cannot be added manually when using GPS (continuous streaming time or distance only this has been rectified in v2).
		Designed for digital pen input including direct drawing onto map/photographs. Fully field editable projects. Easy Note function is extremely useful. Automatic correlation of digital images with geographical object.	Polygon data cannot be entered using GPS (this has been rectified in v2).
Software	ArcPad	Easy user interface particularly to those familiar with ArcGIS. Part of the ArcGIS suite. Full customization with ArcStudio (e.g. data entry forms, toolbars etc.) Wide range of scripts, applets & third party plugins available.	Some operations are difficult to locate & help files are limited. Needs ArcGIS for full capability. Needs ArcStudio for full customization. Requires a high level of IT skill for customization.

This GIS mapping application is designed specifically for PDAs and integrates almost seamlessly with ESRI's desktop GIS application ArcGIS as a front-end data-capture solution. It cannot be considered as a standalone mapping software as it needs to be used in conjunction with ArcGIS and ArcPad Studio to provide the full range of GIS functionality. ArcPad Studio is a separate software development package for building custom ArcPad applications.

5.6. DGM system 2

5.6.1. Hardware

This system is based around the Xplore iX104R (Fig. 1b, Table 3). Like the Recon this Tablet PC conforms to MIL-STD-810F standards for water, dust, and shock resistance. Battery life is specified at approximately 8 h; although in our experience under normal mapping conditions with the GPS connected the average battery life is 4.5 h. The GPS receiver

used in this system is a Haicom HI-204S, which is WAAS/EGNOS enabled and has a specified accuracy of 1–5 m (DGPS) (Table 3). The GPS draws its power from the tablet via the USB port.

5.6.2. Software

The mapping software installed on the iX104R tablet is Map ITTM. This is a bespoke DGM software application which has been developed in collaboration with Terra Nova (De Donatis and Bruciatelli, 2006). Unlike ArcPad, Map ITTM is a fully functioning, stand-alone GIS mapping package with all the functionality and capability of a desktop GIS such as ArcGIS. It has been designed specifically for the Tablet PC and thus makes full use of the “digital pen”.

5.7. Trimble GeoXT

The GeoXT is an integrated GPS and PDA unit ruggedised to IP54 standards of water, dust and

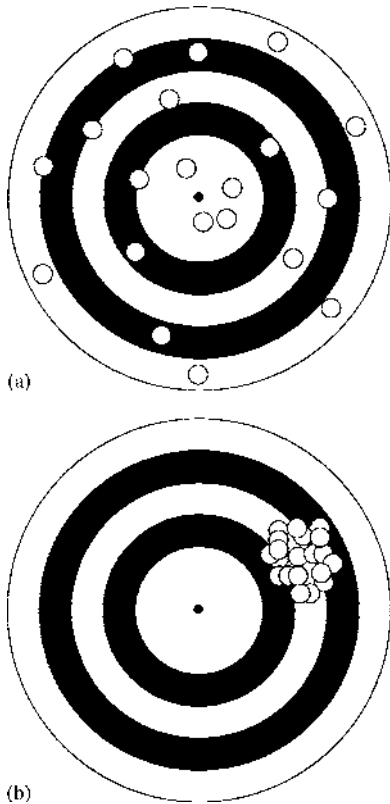


Fig. 2. Accuracy versus precision: (a) GPS positions relative to true location (centre of target) show high accuracy and low precision and (b) GPS positions relative to the true position show high precision, but low accuracy.

shock resistance (Fig. 1c, Table 3). Autonomous positions have an accuracy of 1–3.5 m, while DGPS accuracies of <1 m are achievable (Table 3). In addition, an external beacon receiver (“Beacon-on-a-Belt” or “BoB”) can be attached which will provide correction data that can be post-processed to achieve an accuracy of 10–20 cm. This requires the installation of GPSCorrect™ software on the GeoXT and post-processing of the data using Pathfinder Office™ on a PC. If these levels of accuracy and portability are required this is an excellent system. However, it is a relatively costly alternative (Table 3) and the speed of the processor is slower than that of the Recon. This can cause

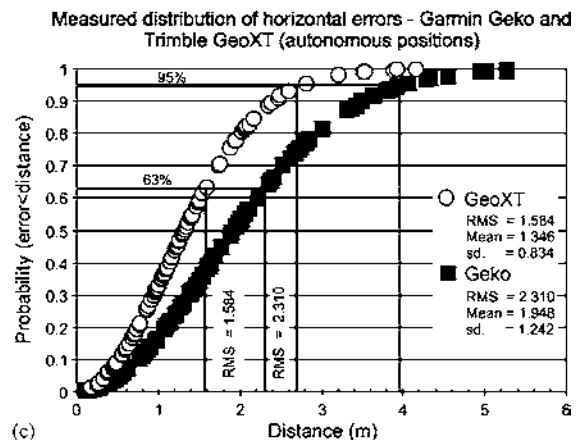
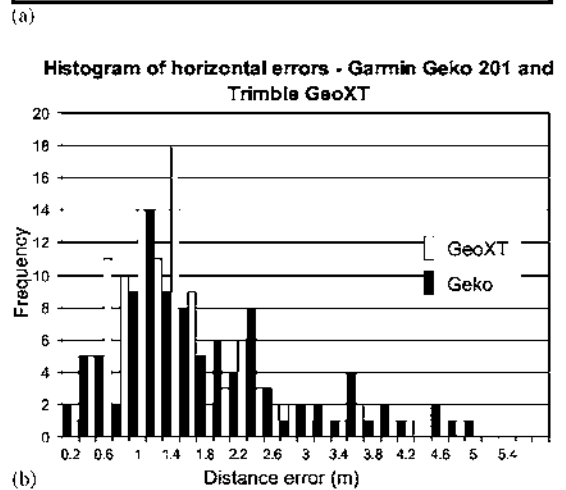
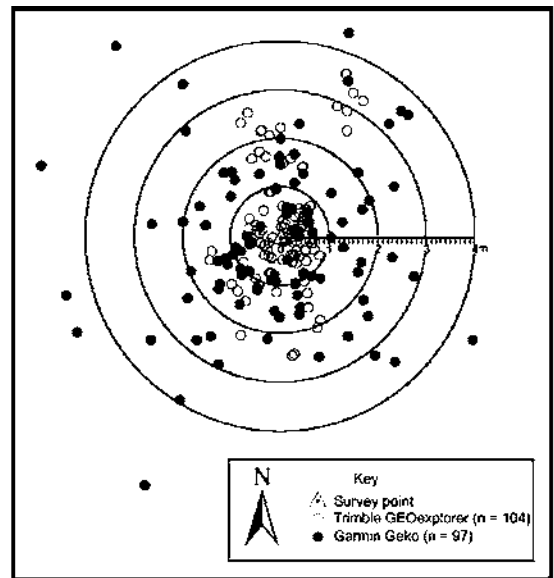


Fig. 3. Accuracy plots for the Garmin Geko and Trimble GeoXT: (a) plan view of recorded GPS positions relative to a known point collected over a fifty day period, (b) histogram showing horizontal errors in metres of GeoXT and Geko GPS positions and (c) probability vs. distance plot for GeoXT and Geko GPS positions.

quite long delays while the screen updates, especially when mapping onto raster images such as base maps or aerial photographs. In this respect, it is probably more suited to simple data collection tasks where accurate GPS positioning is required rather than a full DGM project.

6. Field assessment

We tested the suitability of each system using the criteria given in Table 1 by mapping a section of well-exposed outcrops of deformed Permian and Carboniferous sedimentary rocks at N. Tynemouth on the coast of NE England, near to Newcastle (Fig. 4a–c). Here, the outcrops offer a sequence of easily identified, distinctive lithological units which are deformed by a number of different structures (e.g. faults, folds and fractures), which we felt would serve as a suitable test of system performance, and provide us with the necessary user-experience and personal impression of each system. The findings of the field assessment are presented below and summarized in Table 4.

6.1. Hardware

- *Portability*: The extra external and internal protection required to meet the MIL-STD-810F standards have added both weight and bulk to both units when compared to more conventional PDAs and tablets (Table 2). Despite this, both are well-designed and relatively easy to carry in the field. The relatively small size of the Recon allows it to be stowed easily when not required or when both hands are needed on difficult terrain. The iX104R tablet is by necessity larger and heavier than the Recon. The carrying system provided by the manufacturer, though adequate, is not particularly well suited to outdoor work, and is not well designed for mapping, where the user may make regular measurements and often needs both hands free for security on steep ground.
- *Performance*: The two systems are vastly different where it comes to performance. The iX104R tablet is a fully specified PC, which can be purchased in a variety of configurations depending on the available budget and or the requirements of the user. The Recon, although relatively well specified for a PDA, lacks the processing power, memory and storage capacity compared to the iX104R. This becomes apparent when

attempting to view large files such as aerial/satellite images and raster maps. The iX104R handles these with ease whilst the Recon may take several minutes to initially display an image, and redraw times are slow. This, coupled with the small screen size of the Recon can be very frustrating for the user while waiting for data to load and display during scrolling of the screen. The large, bright screen of the iX104R is comfortable to use and feels more like mapping onto a traditional paper field map. The buttons on both the Recon and the iX104R are well laid out and can be used while wearing gloves. One important issue concerns the use of the digital pen for operating the iX104R. The screen on this particular model is not touch sensitive but uses a special digital pen. Without this, the system is useless, thus the loss of the pen can be catastrophic. With this in mind it is important that a spare pen or pens are carried. In contrast the Recon uses a touch sensitive screen that can be operated by any pointed object (e.g. a pencil).

- *Reliability*: Potential problems with hardware reliability are often cited by those promoting the continued use of traditional geological mapping. Both systems are built to MIL-STD-810F standards and should therefore be suitable for all, but the most extreme conditions. In our test both performed perfectly in typical British spring conditions of rain and wind. The longer-term reliability of each system could not be tested in the short duration of our test period, although both systems are over a year old and have not suffered failure in any of their components.

6.2. Software

- *Operating system*: Map IT and ArcPad are designed to be used with Windows operating systems. Specifically, Map IT runs on Windows XP whilst ArcPad runs on Windows XP and Pocket PC/Windows CE. Neither can be used directly with Macintosh or Linux. An advantage with ArcPad is that although it is specifically designed to run on a PDA it will also run on any PC running Windows XP or XP Tablet. This is a consideration if a combination of PDA's and Tablet PC's will be used during a mapping project.
- *Functionality*: Map IT is a fully functional stand-alone GIS and offers all of the tools available in

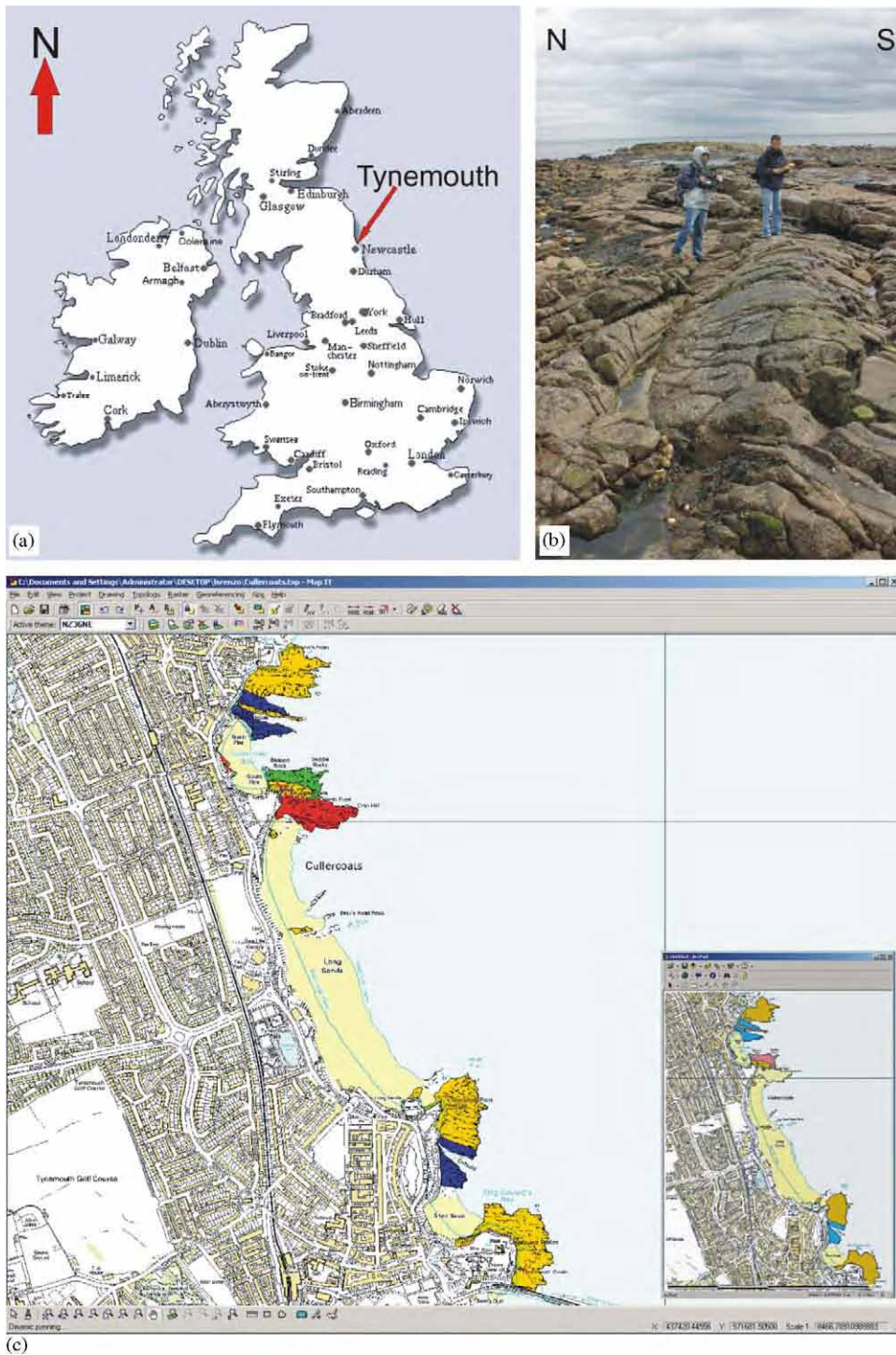


Fig. 4. (a) Map of UK with location of Tynemouth arrowed, (b) inset photograph showing the general appearance of the foreshore outcrops mapped and (c) screen shot of the area mapped displayed using Map IT and the Xplore tablet PC. Inset bottom right shows equivalent area viewed on the Recon PDA running ArcPad.

other desktop GIS such as ArcGIS. In addition Map IT has been specifically designed for *geological* mapping. Therefore it is ready to use “straight-from-the-box” for DGM purposes. Map IT offers the user two levels of operation. The first as a *manager* where all the characteristics and parameters of a project can be set up, and the second as a *surveyor* who physically carries out the mapping. The surveyor works within the bounds of the project interface prepared by the manager. This can provide a simplified user interface for novices or a specific set of data collection tasks, symbology etc. for group use. ArcPad on the other hand is a generic mapping package and requires a degree of customization to optimize it for geological mapping. Although there is a limited degree of customization available within ArcPad itself, to fully manage and customize a geological mapping project requires the additional resources provided by ArcGIS and ArcPad Studio at a considerable cost (Table 3). From this point of view ArcPad is less “straight-from-the-box” ready than Map IT. However, for the advanced user, the combination of ArcPad and ArcPad

Studio allows a high level of customization to be undertaken to create a highly tailored mapping system.

Both ArcPad and Map IT allow the user to create point, polyline, and polygon data either manually or using the GPS. For polylines and polygon data GPS vertices can be added individually or in a continuous streaming mode. Both mapping packages allow feature editing in the field. ArcPad supports a limited degree of feature editing; points and vertices on polyline and polygon features cannot be dragged to new locations, but can only be moved to a new position by entering the x,y,z values of the new position or by the using the current GPS position. Feature attributes e.g. strike and dip etc. can be edited quickly and simply within the appropriate features attribute table. As would be expected from a fully functional GIS Map IT allows full editing. The use of specific feature symbology is an important issue when mapping. It is possible to define and use specific feature symbols within Map IT and ArcPad, however, a number of problems occurred where symbols failed to be correctly shown in ArcPad. User defined forms for the rapid

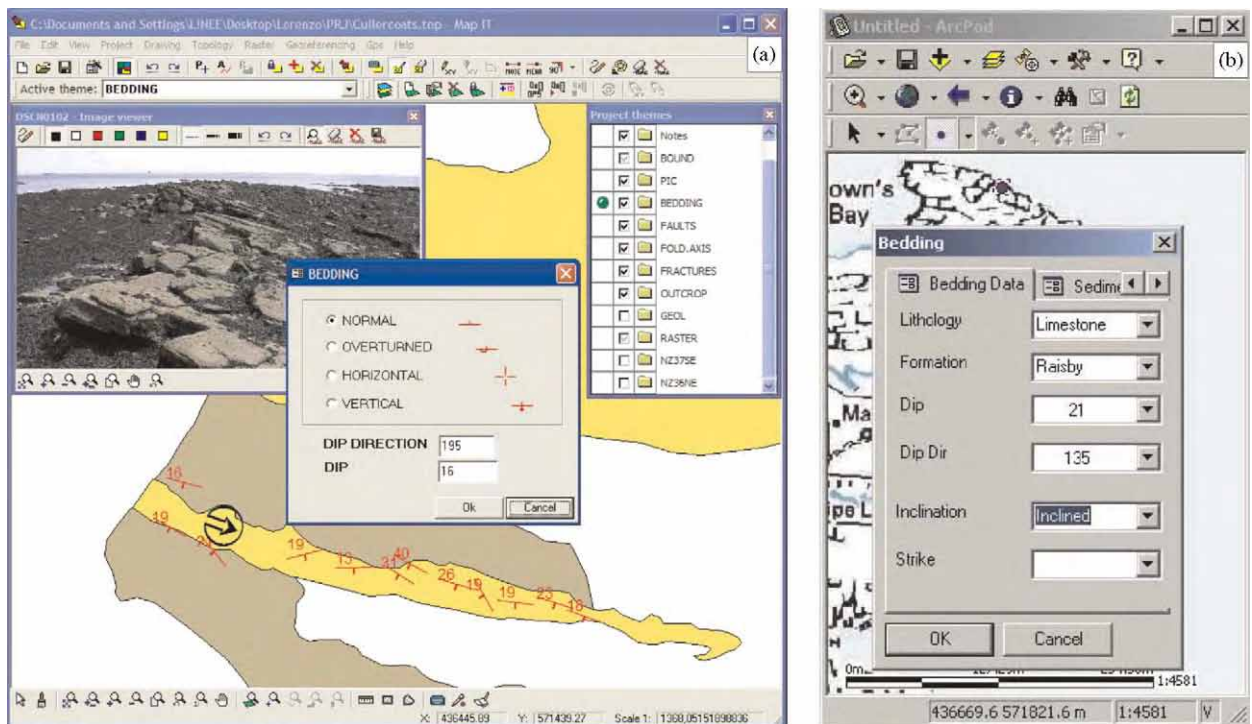


Fig. 5. Screen shots of (a) Map IT and (b) ArcPad showing general layout of working area and customized forms used for recording feature attribute data.

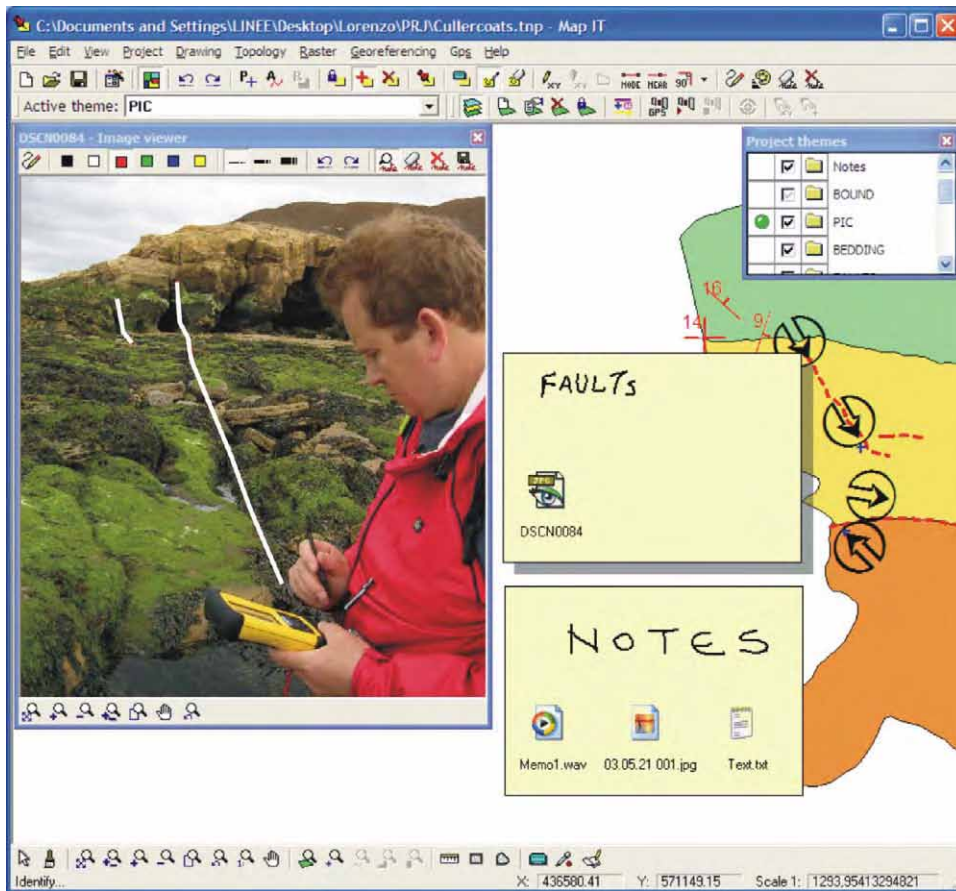


Fig. 6. Screen shot of the “Easy Note” resource available in Map IT. Two “Easy Notes” labelled “faults” and “notes” have been linked to the recorded feature. The note labelled “faults” contains a .jpg image file (shown on the left). This image has been annotated to show two faults (highlighted). The note labelled “notes” contains a video .wav file, a .jpg file and a text file. All are fully georeferenced within the project.

recording of feature attribute data can be created in both packages (Fig. 5).

Several innovative features within Map IT allow the user to map in a more traditional way than is possible with ArcPad. Easy-Note is a georeferenced, electronic version of a Post IT note. The geologist can create an Easy-Note at any time during mapping (Fig. 6). Any type of file can be attached to the note using “drag and drop”. Digital photographs of outcrop features etc. can be annotated using the digital pen. The software uses the time and date stamp from the exif file of each image to synchronize it with the GPS location at the time the image was taken, and thus georeferences the image. Sketches and annotations using the digital pen can be made on any other raster data within the mapping project. Whilst it is possible to perform similar tasks within ArcPad, there are no dedicated tools for these tasks and the limitations

imposed by the storage capacity and screen size of the PDA make this a more difficult operation.

- *Usability:* Map IT and ArcPad both use an icon-based system for most commonly used functions and thus will be familiar to the majority of users. The Map IT user interface is generally well set out although the large number of buttons on the screen may be daunting for new users. However, it is designed to be used with a digital pen without the need to open menus or use a keyboard, and toolbars can be hidden as required. The digital pen also allows the user to write and draw as they would on a conventional paper map or notebook. ArcPad on the other hand, due to the reduced screen area compared with the Tablet PC, has fewer buttons, but utilizes drop-down menus. Toolbars can be edited to show those buttons, which are most

frequently used, and can be hidden when not needed. Although the ArcPad interface is generally good, some functions can be difficult to find, and the installed help files are very limited.

- **Project setup:** This is a crucial stage in any digital mapping campaign. As a stand-alone GIS package the advantage of Map IT is that the entire project set up, management and final map production is undertaken in a single application. ArcPad requires that the greater part of the project set up and management is undertaken in ArcGIS, with additional customization carried out using ArcPad Studio. All the required project files are then transferred to the PDA to run within ArcPad for data collection. Once mapping is complete the files are then transferred back to ArcGIS for display, analysis and map production. This is quite a cumbersome process and can lead to errors during transfer, such as overwriting newer files with older ones. The full GIS capability of Map IT also allows the user to add additional material to a project without needing to return to base e.g. non-georeferenced raster images can be georeferenced in the field and added as a new layer in a project, something which is not straightforward within ArcPad.
- **Compatibility:** Map IT supports a wide range of vector and raster formats including: ESRI shapefile, UNGENERATE, ArcInfo, AutoCad, DWG/DXF, MapInfo, NTFcadastral, Tiff, BMP, JPG, GIF, PNG, MrSID and ECW. ArcPad on the other hand is much more limited in the file formats it supports. ESRI shapefiles are the only vector data format that is supported, while raster files are limited to JPG, MrSID, BMP and CADRG. File formats that are not directly supported by ArcPad must be converted into usable formats by the wide range of tools available in ArcGIS. This reliance on conversion within ArcGIS places severe limitations on which data can be added to an ArcPad project whilst in the field.
- **Reliability:** During the test both ArcPad and Map IT performed well, with no crashes of the software. However, ArcPad has a tendency to “hang” occasionally. This appears to be due more to the limitations of the memory in the PDA rather than a problem with the stability of ArcPad. On such occasions it is necessary to perform a “soft” reset on the PDA. Although not an issue directly related to the reliability of the software, those involved in digital mapping

should save their data regularly. In the case of ArcPad running on a PDA, data should ideally be saved to non-volatile memory so it is protected in case of power failure. On some PDA's (not the Recon) the default folder for the ArcPad software is not non-volatile. In these cases, battery failure will lead to loss of the ArcPad software, which will need to be re-installed. Another important component when looking at reliability is the support and backup package offered by the manufacturer. ArcPad and the associated suite of Arc products are produced by ESRI. They provide a wide range of support services including user forums, discussion groups, software updates and online training for many of their packages. This provides the user with a vast resource, although at times it can prove time consuming to locate the required information. Map IT on the other hand lies at the opposite end of the support spectrum. As a new and small company it is possible that any problems or questions are likely to be answered more quickly. In addition the greater likelihood of direct contact with users may provide an enhanced environment for software development and evolution.

7. Conclusions

From a broad general perspective based on the critical criteria listed in Table 1 both the systems assessed in this paper performed extremely well and dispel many of the issues raised by DGM sceptics. The Recon PDA and Xplore iX104R tablet are well built, rugged and easy to operate. Map IT and ArcPad are well designed, generally stable and offer the user a broad range of mapping tools and functions. However, for the specific purpose of outcrop (“green-line”) mapping, the combination of iX104R tablet and Map IT was found to be the most suitable and most capable DGM system of the two. The iX104 tablet with Map IT software provides the geoscientist with a mapping experience, which most closely matches that provided by traditional paper-based mapping. The “Easy Note” facility and the ability to annotate photographs, draw sketches and make handwritten notes which are all georeferenced is not only extremely useful, but importantly provides the user with a familiar environment within which they can make the transition from paper to digital mapping.

Additionally, the greater processing power and storage capacity of the tablet allows the user to store and carry large volumes of supplementary data in the field, where it can be consulted as required. The functionality, usability and flexibility provided by Map IT combined with the processing and storage capacity of the Tablet PC allows the iterative process of observation and interpretation crucial to good geological field mapping to be followed in DGM methodologies.

Despite the fact that the Recon/ArcPad system was at times frustratingly slow, and the smaller screen required much scrolling to see the whole map, it was still possible to use the system for outcrop mapping, albeit in a less flexible manner than when using the tablet. The lightweight and compact size proved particularly beneficial when moving on difficult ground, as the unit can be easily slipped into a pocket or carrying pouch. Therefore, although the PDA-based system can be used for outcrop mapping, it is generally more suited to relatively simple mapping tasks such as sampling surveys. Where portability is critical (e.g. very remote areas where equipment must be carried in), the lightweight and small size of the PDA-based system may outweigh the limitations mentioned above.

From a software point of view, although the out-of-the-box usability of Map IT is superior to that of ArcPad, by using ArcPad Studio it is possible to develop fully customized mapping packages designed for specific user groups and tasks. This provides the user with a highly flexible development package that possibly makes it more suitable for large organizations where there are a broad range of tasks to be undertaken and dedicated IT development staff are available.

One critical factor, which may be the greatest influence on choice for some users is cost. Both the systems assessed are relatively expensive (Tables 2 and 3). It is possible to use cheaper hardware options (Table 2), particularly PDA's, but it should be remembered that these cheaper options are not designed nor intended to be used in hostile environments. The cost of the equipment has to be carefully weighed against the often much larger cost of repeating fieldwork due to equipment that has failed because of the rigors of fieldwork.

Although there is a general trend for consumer electronics to become progressively cheaper, this does not necessarily apply to more specialised equipment. While laptops, PDAs and Tablet PCs

have all dropped in price over recent years, ruggedised systems remain expensive. In addition, upgrades in performance are relatively slow to reach the market when compared with un-ruggedised off-the-shelf systems. Nevertheless, developments in computer technology advance at a rapid pace. What was considered to be state-of-the-art can quite quickly become ordinary or obsolete. What was once very expensive, becomes increasingly less so as newer models are introduced. Therefore, the information and conclusions presented here are just a snapshot in the continuing development of DGM technology.

Acknowledgements

We would like to thank the reviewers for their helpful comments and suggestions. Ken McCaffrey, Bob Holdsworth, Jonathan Imber & Steve Smith are thanked for their assistance, help and thoughtful discussions during the preparation of this Paper. P. Clegg was supported by NERC Follow-on Fund (NE/C506964/1) R.W. Wilson was supported by NERC Ocean Margins Link project NER/T/S/2000/01018 and tied studentship NER/S/S/2001/06740.

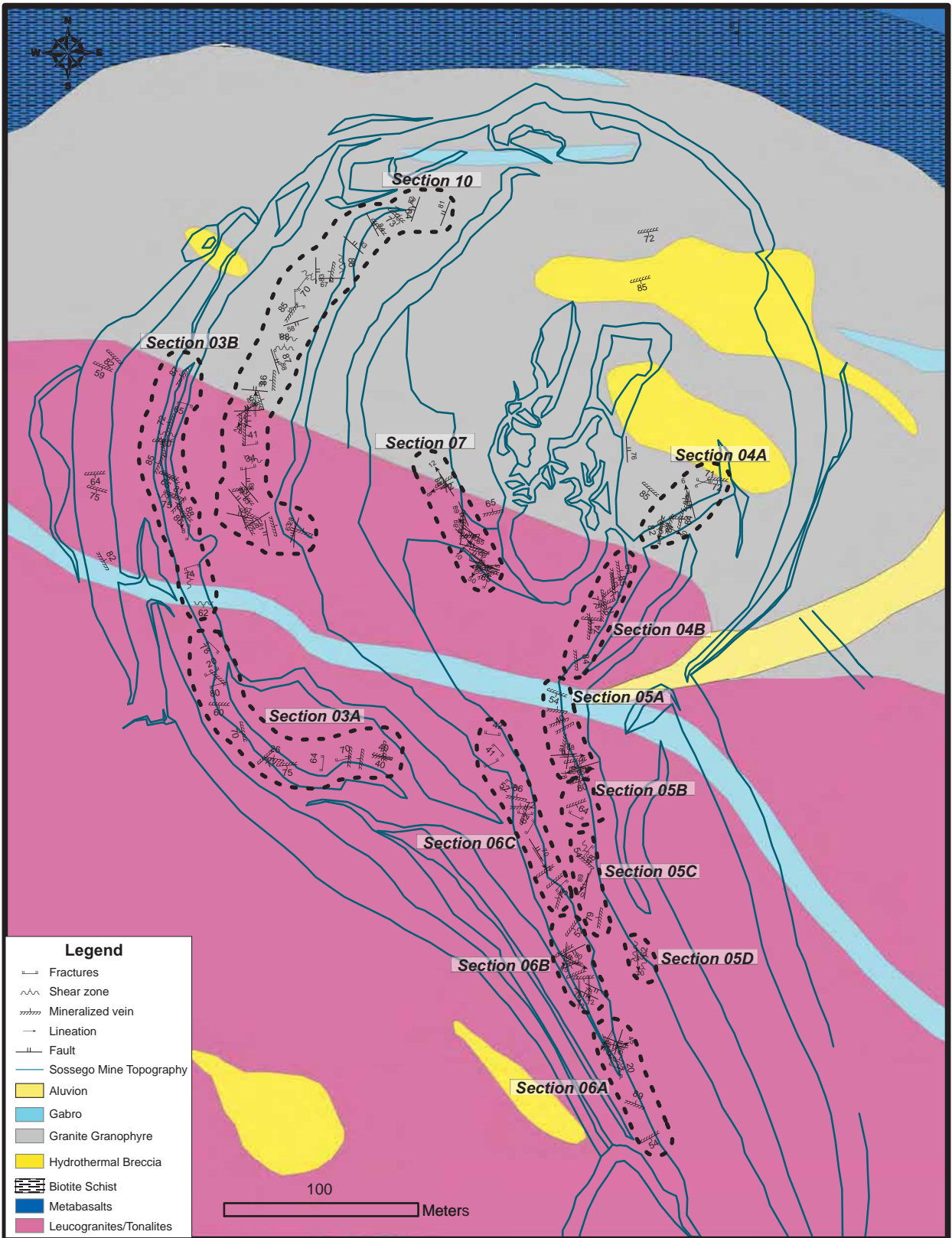
Fabio Domingos is funded by CAPES.

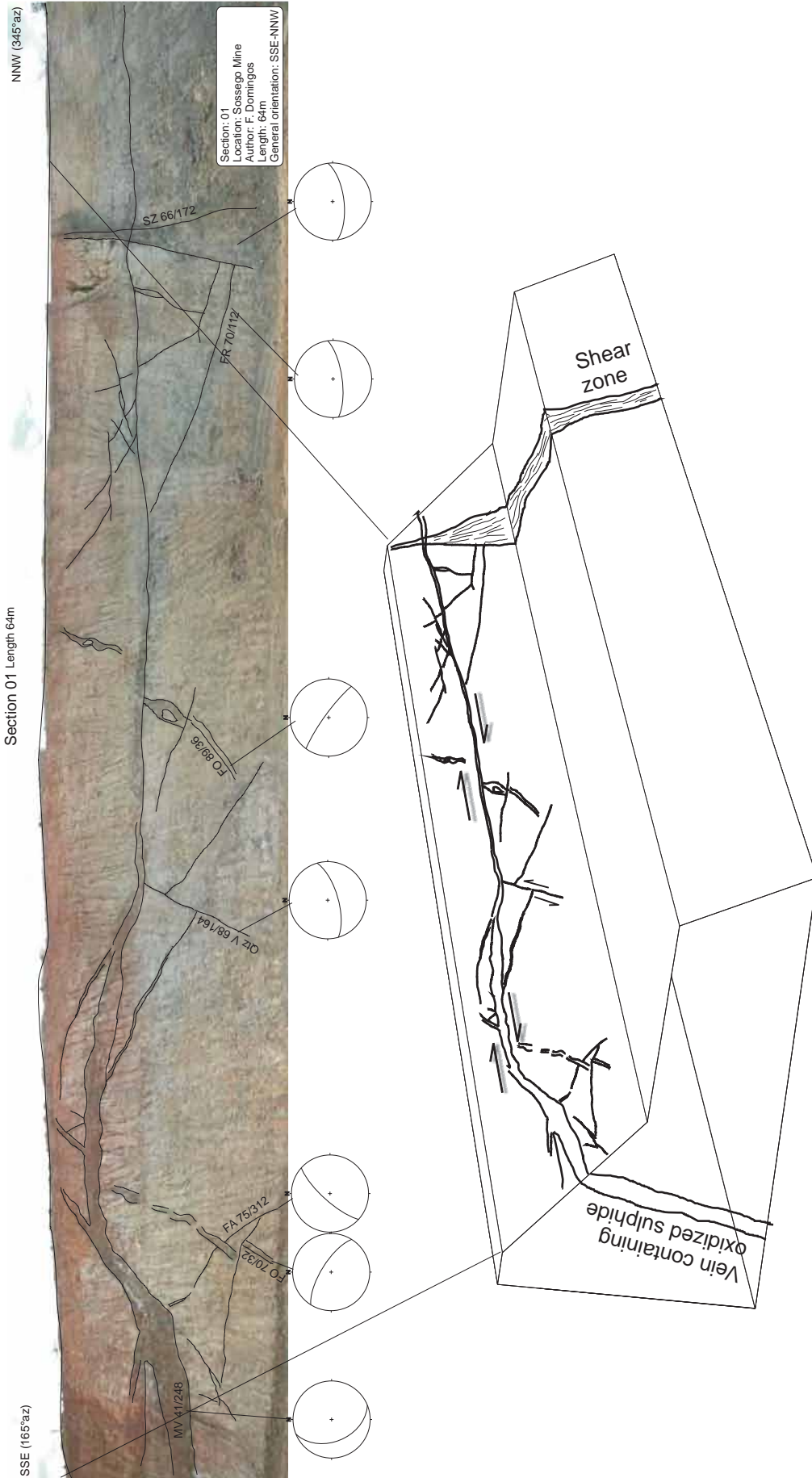
References

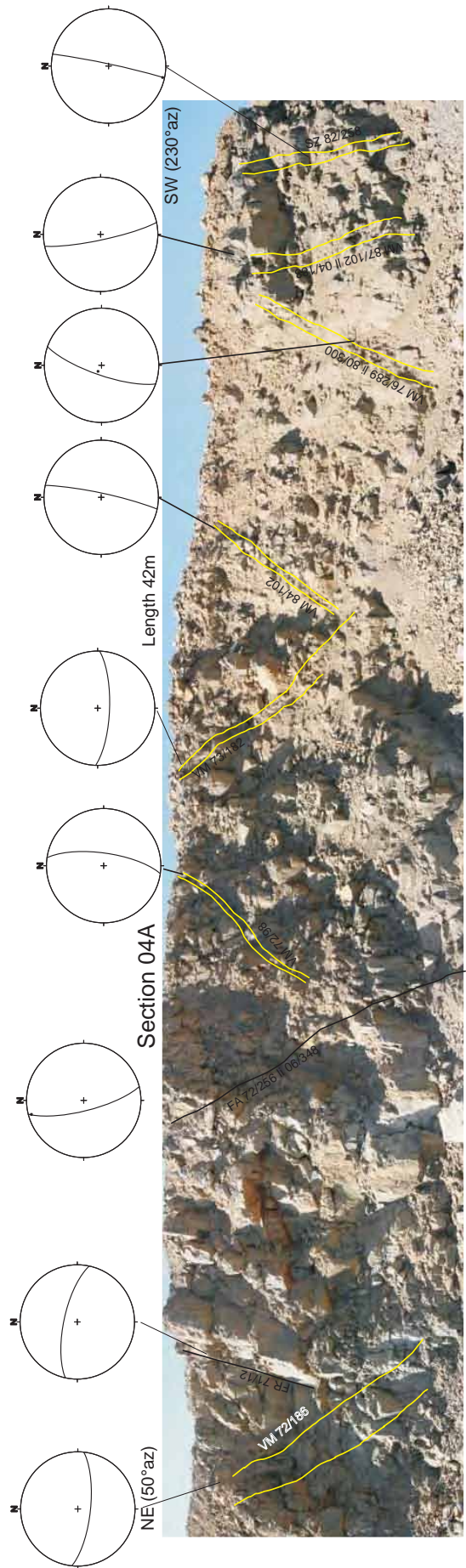
- Brimhall, G.H., Vanegas, A., 2001. Removing science workflow barriers to adoption of digital geological mapping by using the GeoMapper universal program and visual user interface: In: Soller, D.R. (Ed.), *Digital Mapping Techniques '01 Workshop Proceedings*: U.S. Geological Survey Open File Report 01 223, pp. 103–114, http://pubs.usgs.gov/of/2001/of01_223/brimhall.html.
- Brimhall, G.H., Vanegas, A., Lerch, D., 2002. GeoMapper program for paperless field mapping with seamless map production in ESRI ArcMap and GeoLogger for drill hole data capture: applications in geology, astronomy, environmental remediation, and raised relief models. In: Soller, D.R. (Ed.), *Digital Mapping Techniques '02 Workshop Proceedings* U.S. Geological Survey Open File Report 02 370, http://pubs.usgs.gov/of/2002/of02_370/brimhall.html.
- Briner, A.P., Kronenberg, H., Mazurek, M., Horn, H., Engi, M., Peters, T., 1999. FieldBook and GeoDatabase tools for field data acquisition and analysis. *Computers & Geosciences* 25, 1101–1111.
- Brodaric, B., 1997. Field data capture and manipulation using GSC FIELDLOG v3.0. In: Soller, D.R. (Ed.), *Proceedings of a workshop on Digital Mapping Techniques: Methods for Geologic Map Capture, Management and Publication*. US Geological Survey, Open File Report, pp. 77–81.

- De Donatis, M., Bruciatelli, L., 2006. MAP IT: the GIS software for field mapping with a tablet PC. *Computers & Geosciences* 32 (5), 673–680.
- Edmondo, G.P., 2002. Digital geologic field mapping using ArcPad. In: Soller, D.R. (Ed.), *Digital Mapping Techniques '02 Workshop Proceedings*. U.S. Geological Survey Open File Report 02 370, http://pubs.usgs.gov/of/2002/of02_370/edmondo.html.
- Fitzgibbon, T., 1997. Buck Rogers, field geologist: 21st Century electronic wizardry for mapping and field data collection. Geological Society of America Continuing Education Course, Annual Meeting, Salt Lake City, UT.
- Jackson, I., Asch, K., 2002. The status of digital geological mapping in Europe: the results of a census of the digital mapping coverage, approaches and standards of 29 European geological survey organizations in the year 2000. *Computers & Geosciences* 28, 783–788.
- Jones, R.R., McCaffrey, K.J.W., Wilson, R.W., Holdsworth, R.E., 2004. Digital field acquisition: towards increased quantification of uncertainty during geological mapping. In: Curtis, A., Wood, R. (Eds.), *Geological Prior Information*, vol. 239. Geological Society of London, Special Publication, pp. 43–56.
- Kramer, J.H., 2000. Digital mapping systems for field data. In: Soller, D.R. (Ed.), *Digital Mapping Techniques '00 Workshop Proceedings*. U.S. Geological Survey Open File Report 00 325, pp. 13–19, http://pubs.usgs.gov/openfile/of00_325/kramer.html.
- McCaffrey, K.J.W., Holdsworth, R.E., Clegg, P., Jones, R.R., Wilson, R., 2003. Using digital mapping tools and 3 D visualization to improve undergraduate fieldwork. *Planet Special Edition* 5, 34–36.
- McCaffrey, K.J.W., Jones, R.R., Holdsworth, R.E., Wilson, R.W., Clegg, P., Imber, J., Holliman, N., Trinks, I., 2005. Unlocking the spatial dimension: digital technologies and the future of geoscience fieldwork. *Journal of the Geological Society, London* 162, 927–938.
- Maerten, L., Pollard, D.D., Maerten, F., 2001. Digital mapping of three dimensional structures of chimney rock. *Journal of Structural Geology* 23, 585–592.
- Struik, L.C., Atrens, A., Haynes, A., 1991. Handheld computer as a field notebook, and its integration with the Ontario Geological Survey's "Fieldlog" Program. In: *Current Research, Part A, Cordillera and Pacific Margin*. Geological Survey of Canada, Paper No. 91 01A, pp. 279–284.
- Wilson, R.W., 2006. Digital fault mapping and spatial attributes of basement influenced oblique extension in passive margin settings. Ph.D. Dissertation, University of Durham, Durham, England.
- Wilson, R.W., McCaffrey, K.J.W., Jones, R.R., Clegg, P., Holdsworth, R.E., 2005. Digital mapping of Lofoten's faults. *Geoscientist* 15, 2.

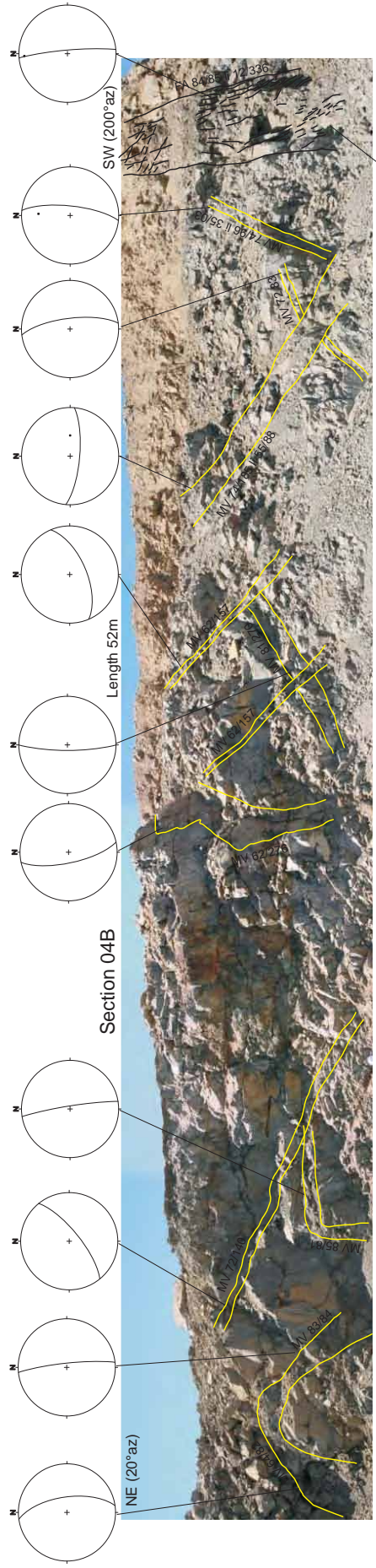
Sossego Mine and location of the photographic sections







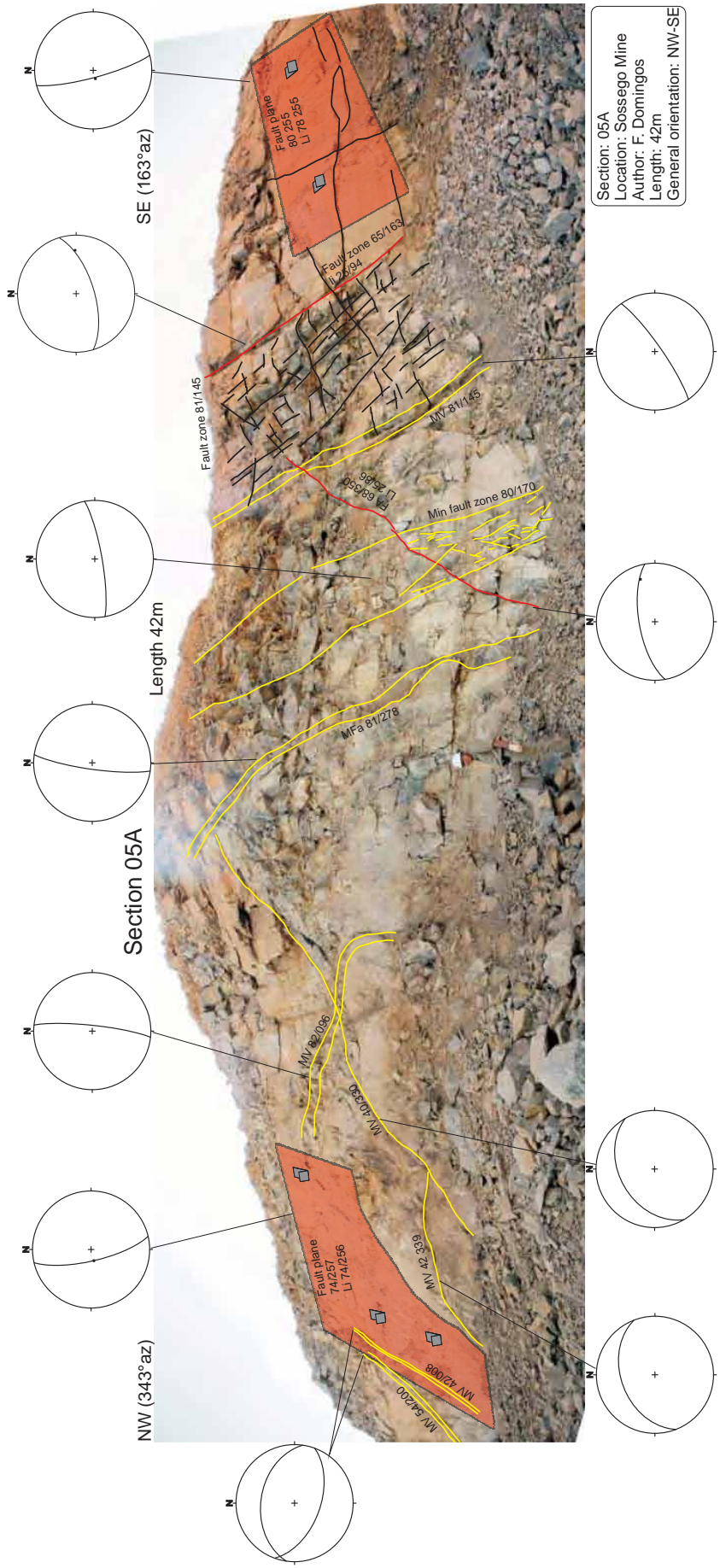
Section: 04A
 Location: Sossego Mine
 Author: F. Domingos
 Length: 42m
 General orientation: NE-SW



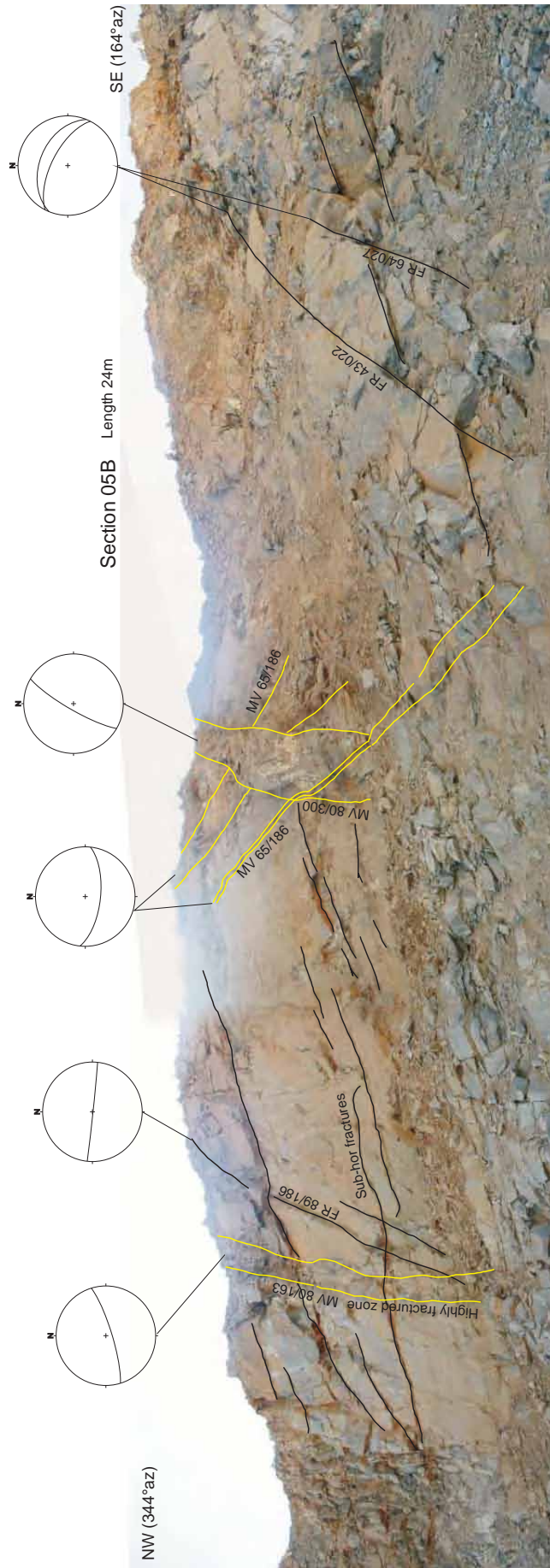
Section 04B

Section: 04B
 Location: Sossego Mine
 Author: F. Domingos
 Length: 52m
 General orientation: NE-SW

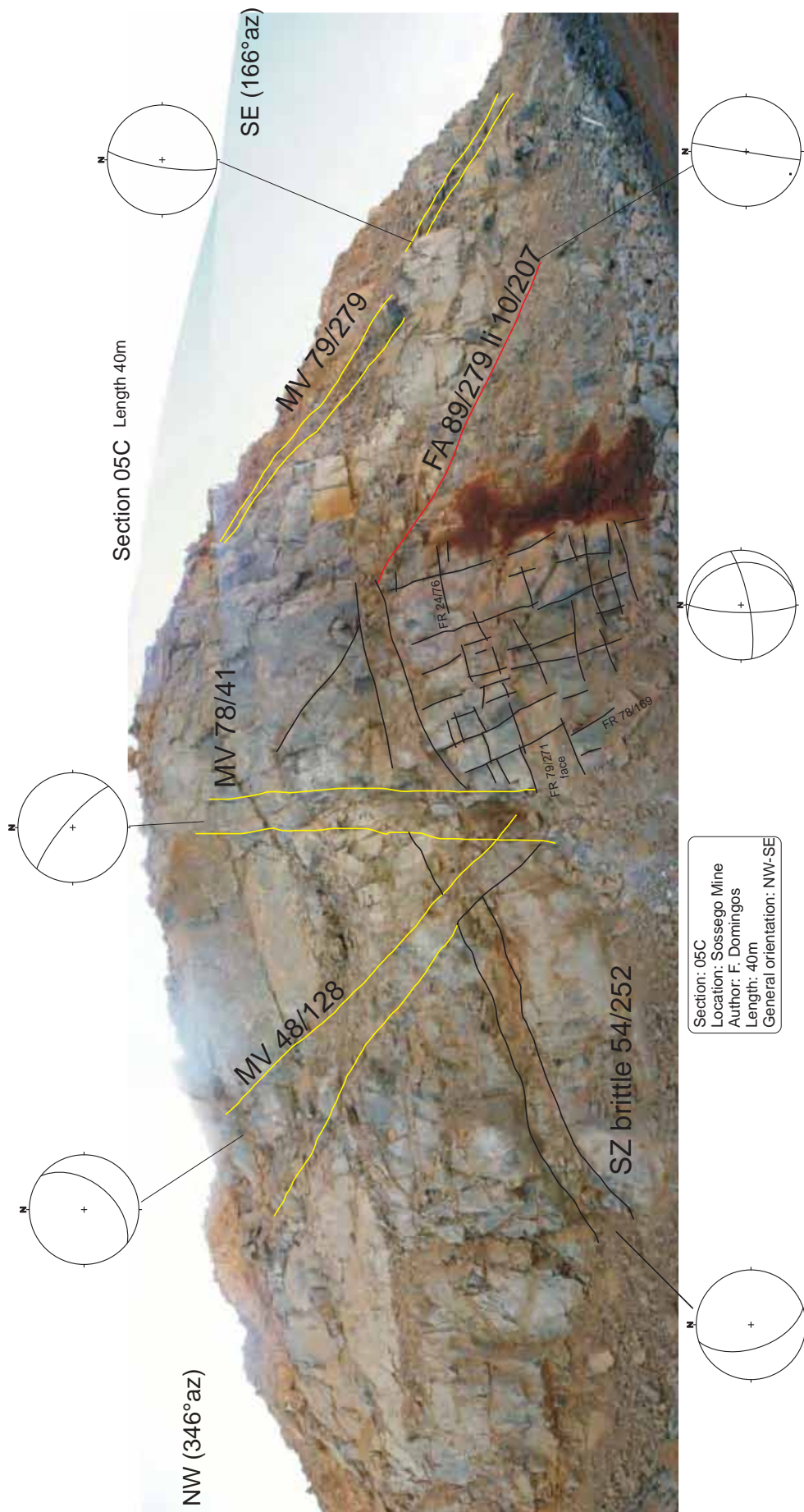
Sinistral strike-slip fault



Section: 05A
 Location: Sossego Mine
 Author: F. Domingos
 Length: 42m
 General orientation: NW-SE

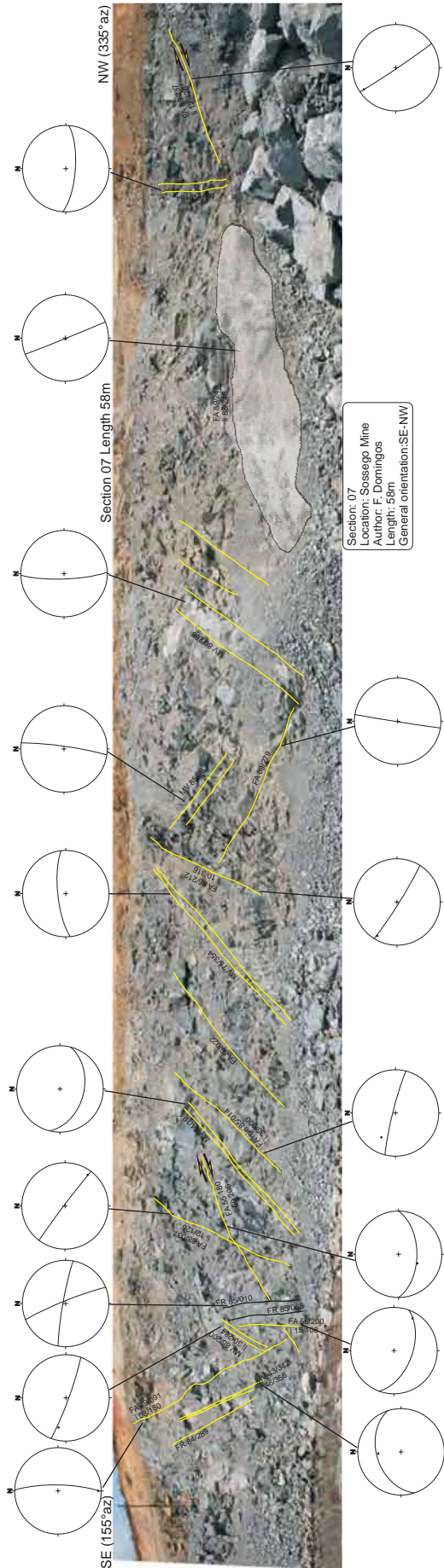


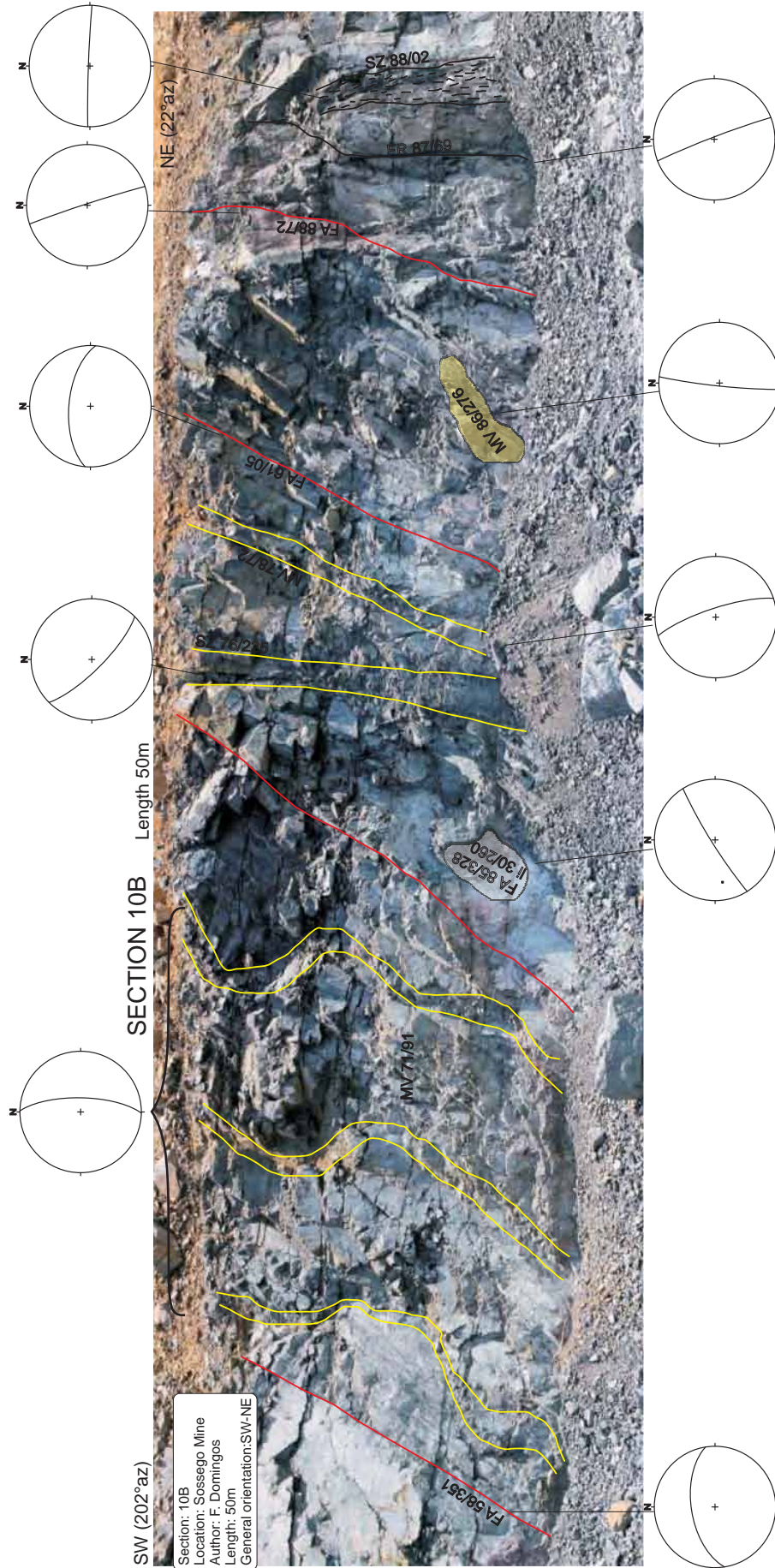
Section: 05B
 Location: Sossego Mine
 Author: F. Domingos
 Length: 24m
 General orientation: NW-SE

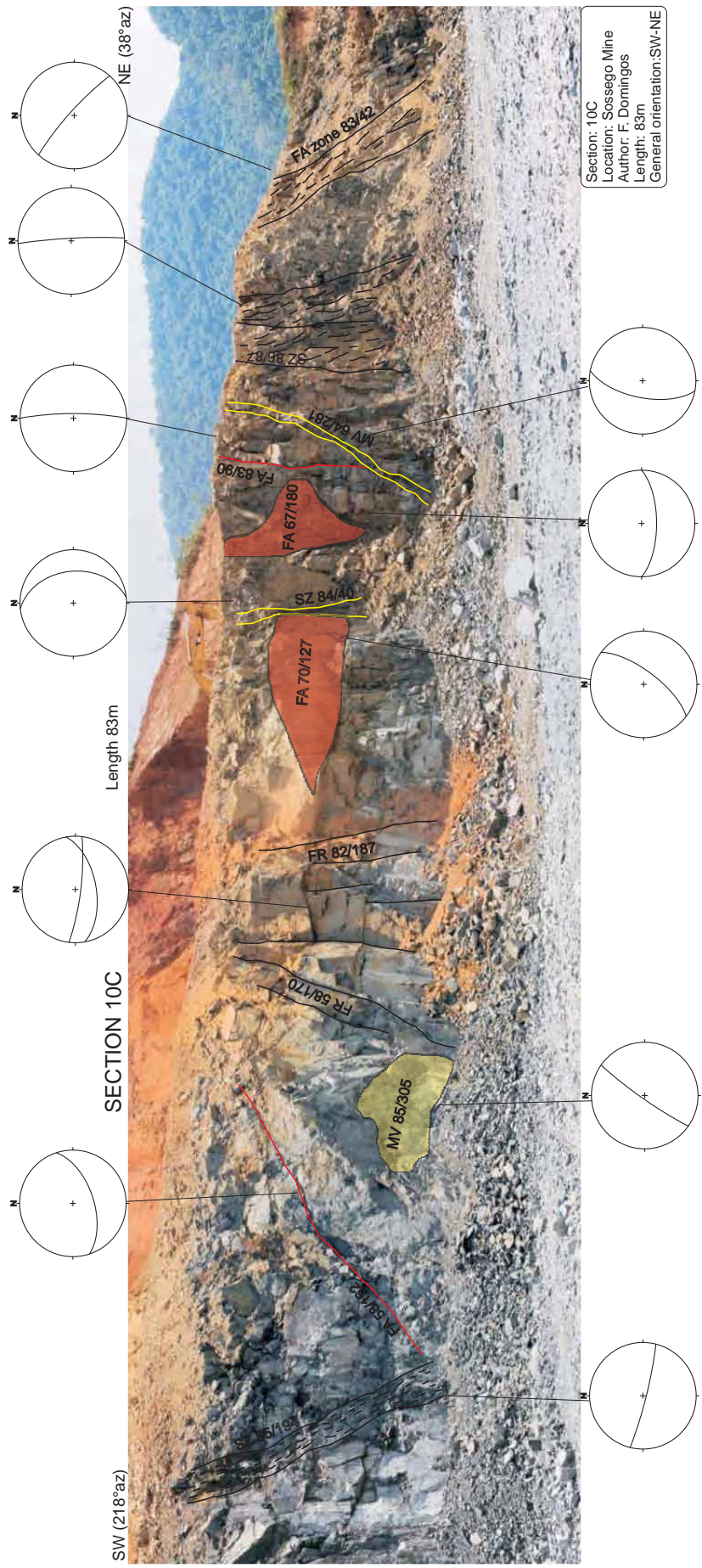




Section: 06C
 Mine: Casapago Mine
 Area: F. Drawings
 Length: 95m
 General orientation: SE-NW



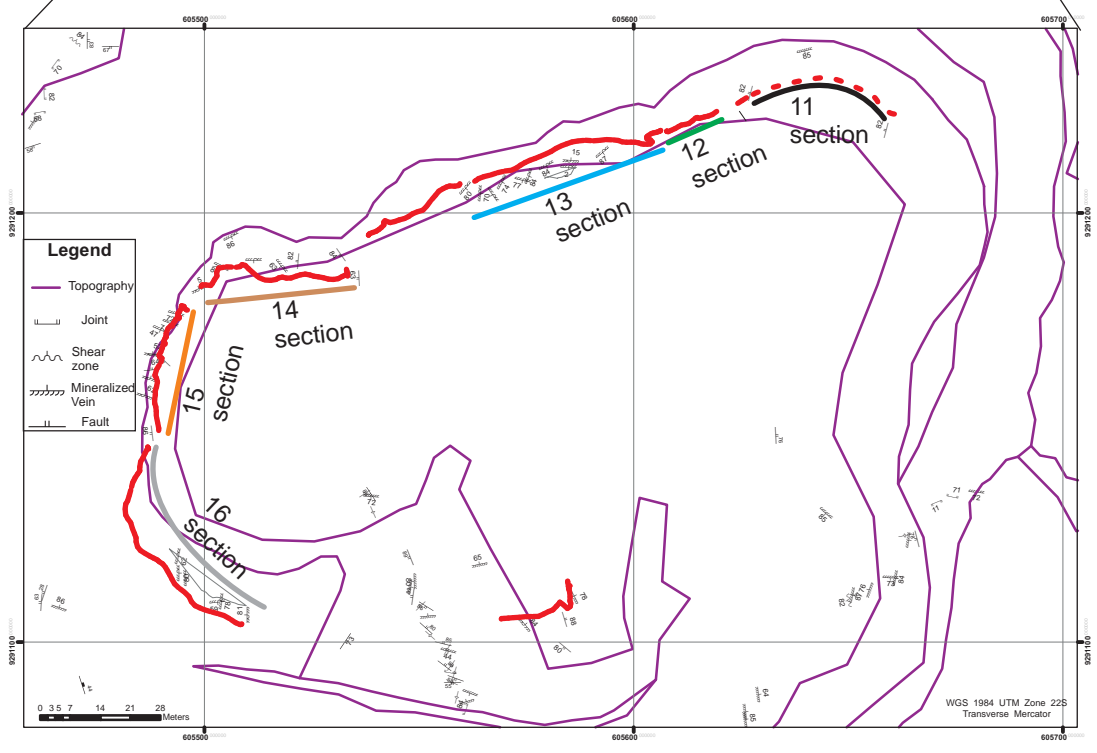
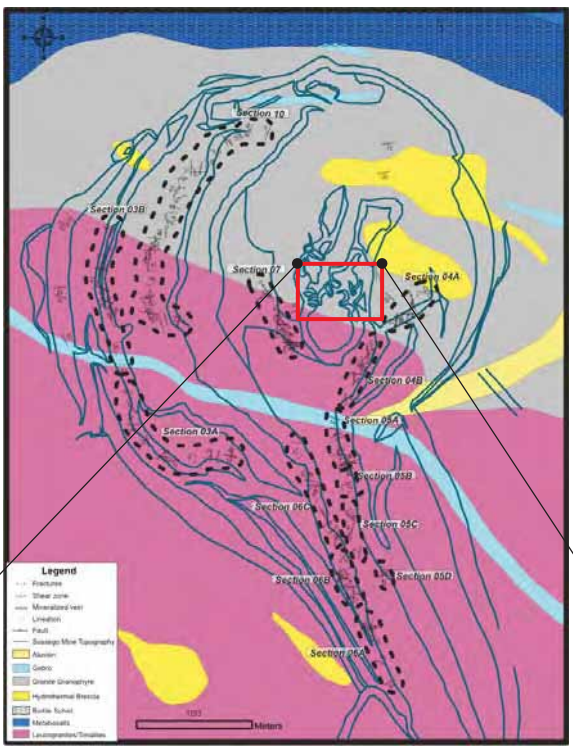




Section: 10C
 Location: Sossego Mine
 Author: F. Domingos
 Length: 83m
 General orientation: SW-NE



Section: 10D
 Location: Sossego Mine
 Author: F. Domingos
 Length: 50m
 General orientation: SW-NE



SECTION 11 - Central ore-shoot - sulphide breccia

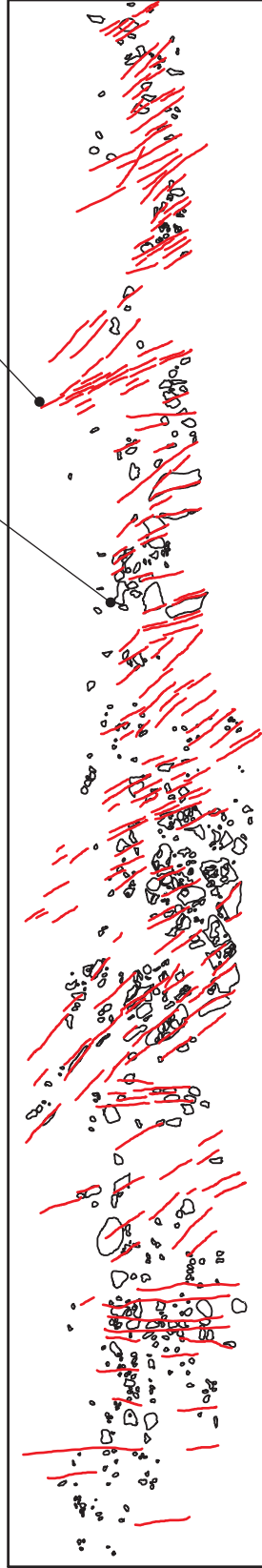
W

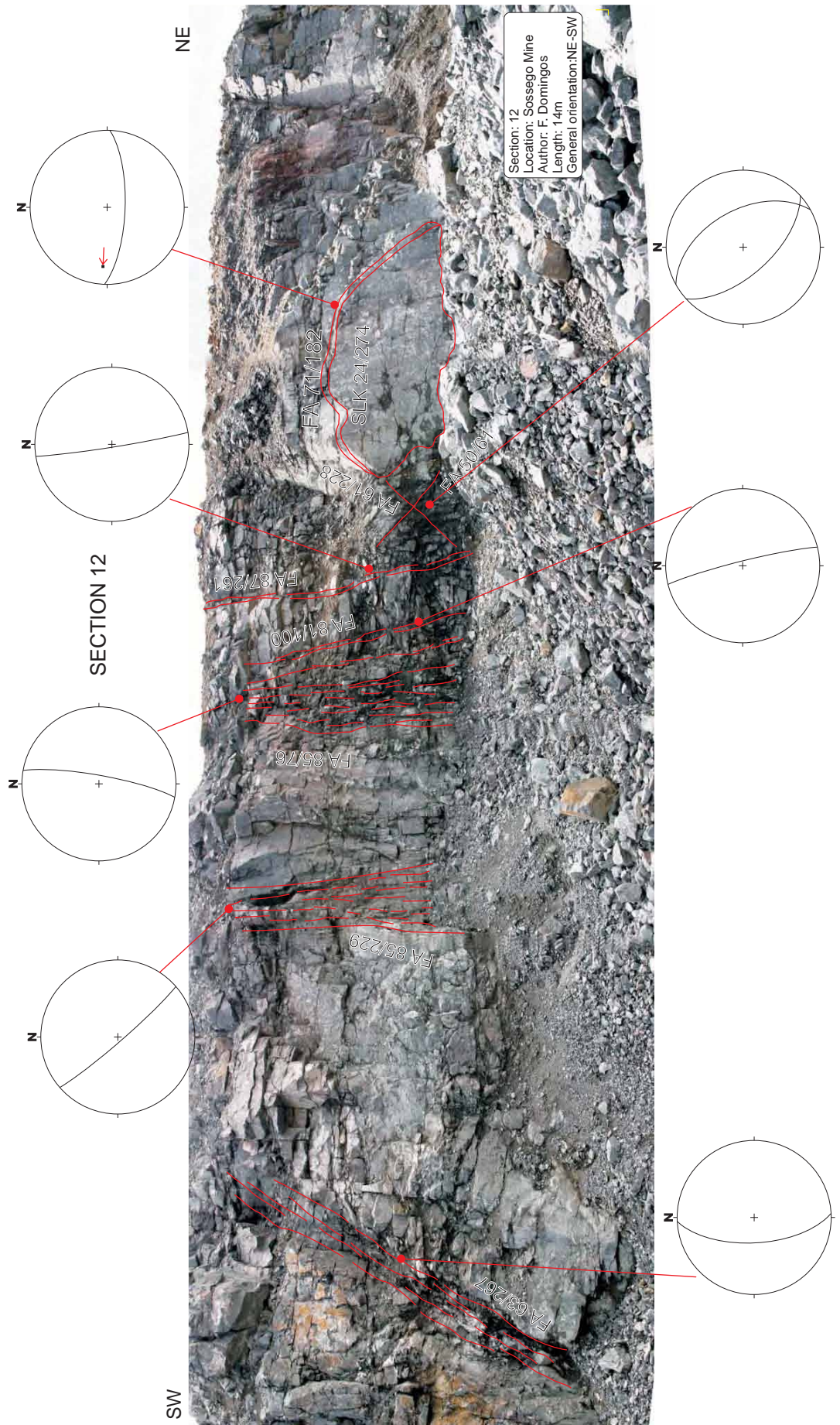


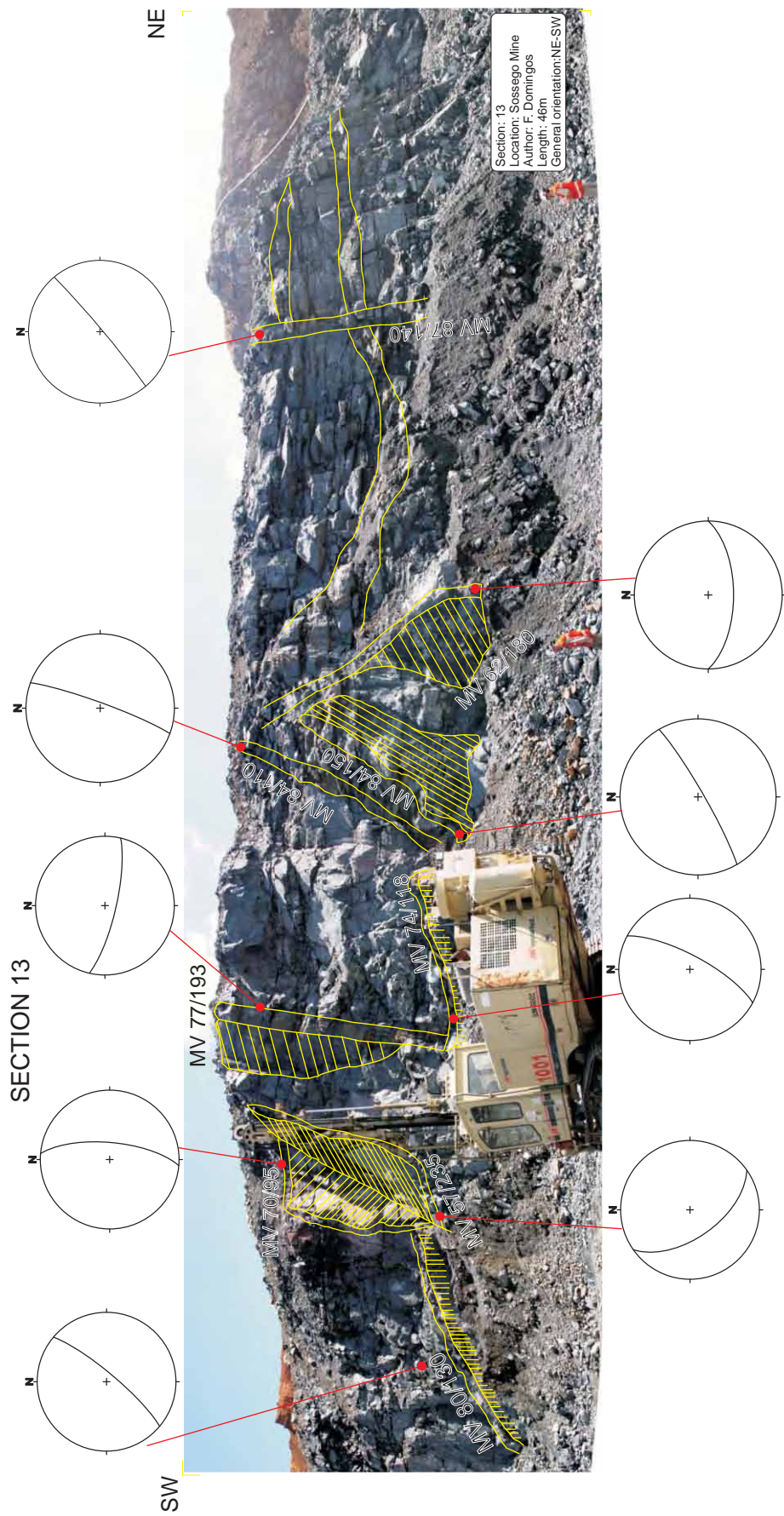
Section: 11
Location: Sossego Mine
Author: F. Domingos
Length: 34m
General orientation: E-W

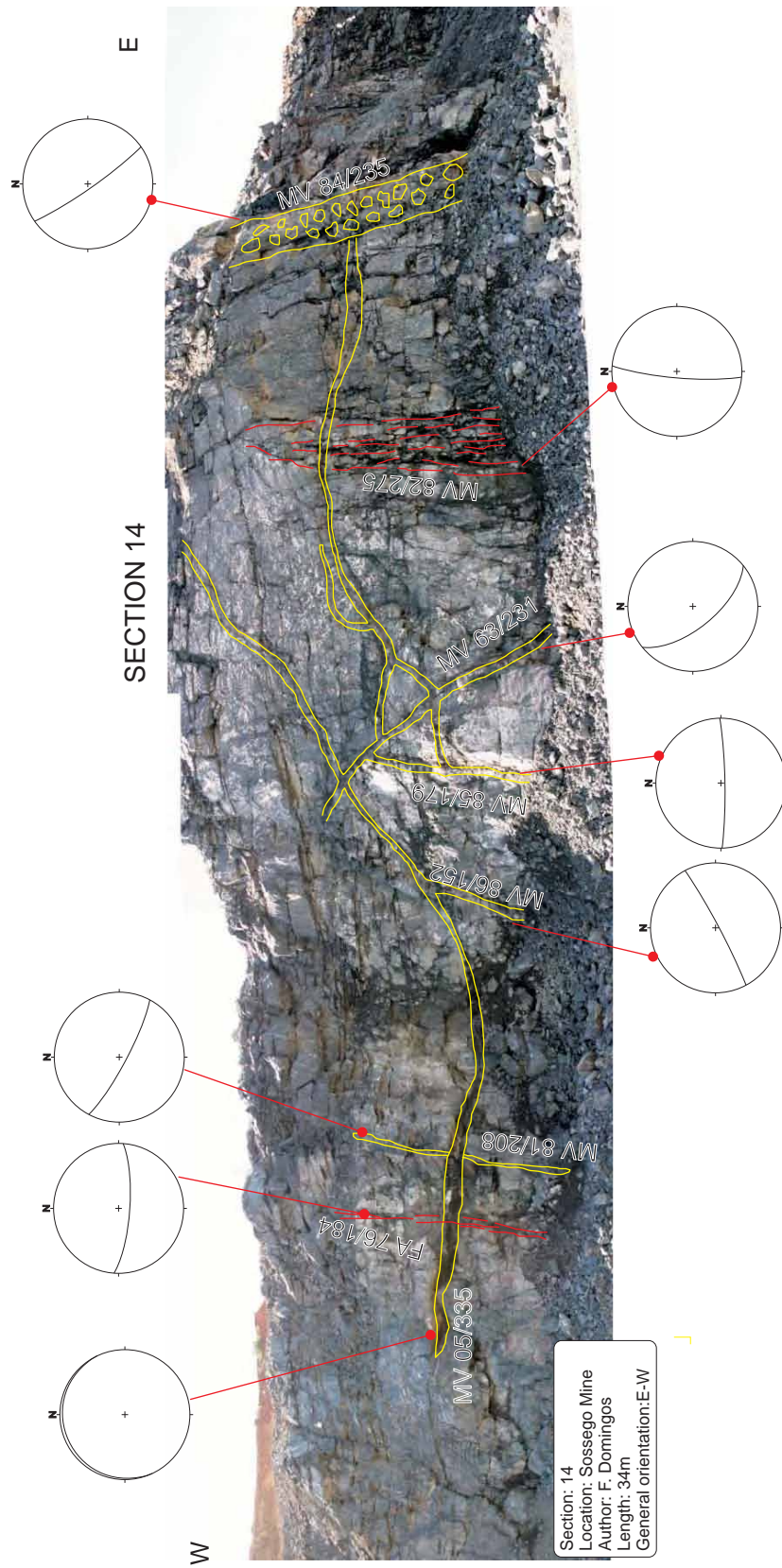
Breccia clasts

Fault planes



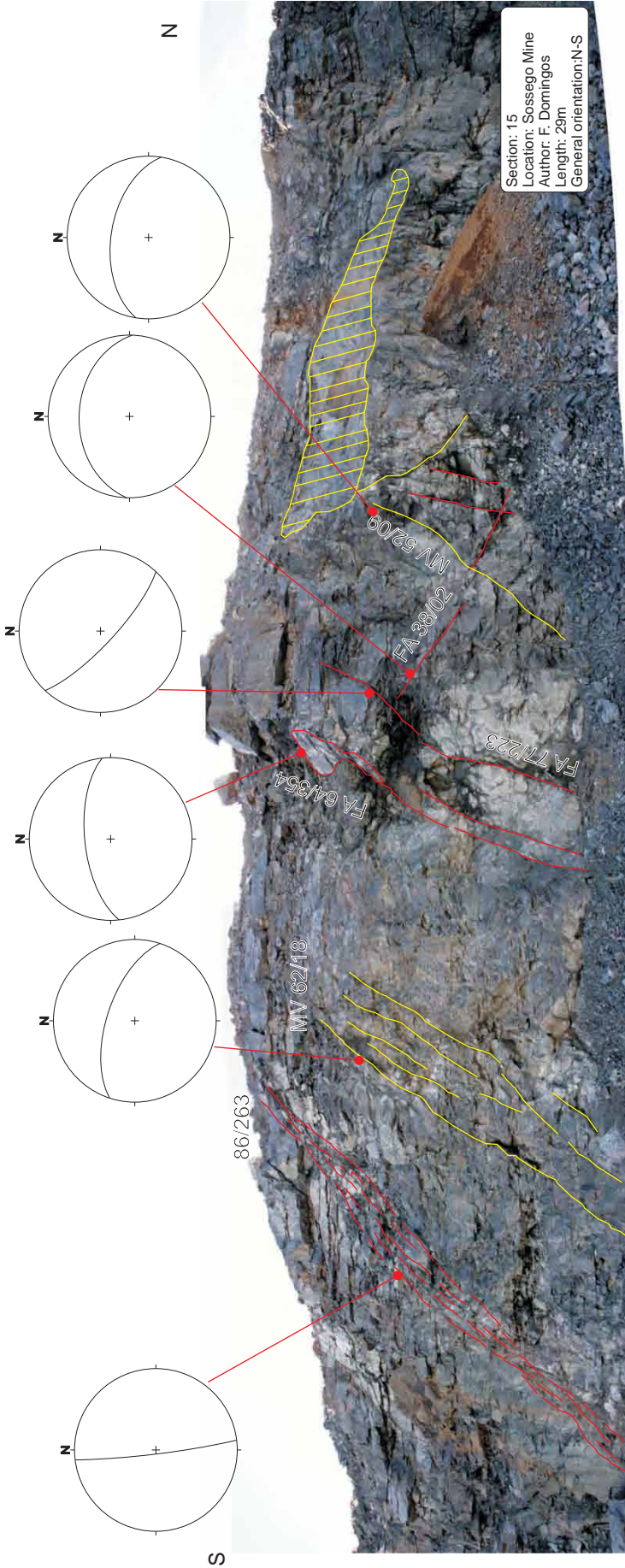




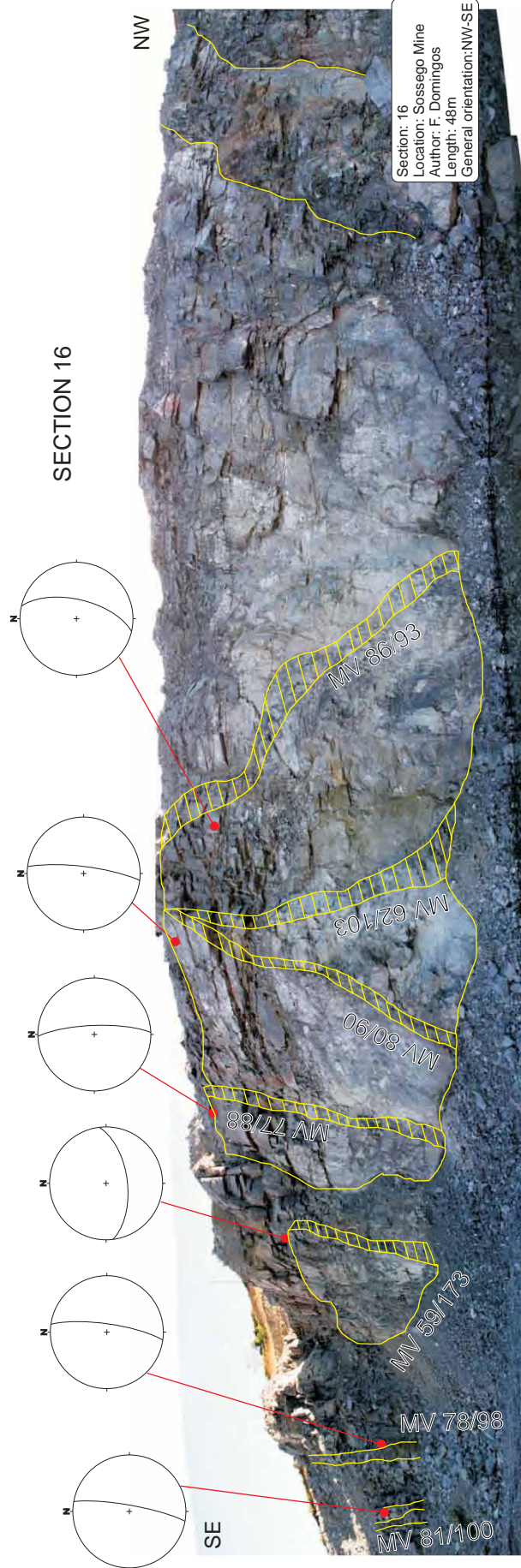


Section: 14
 Location: Sossego Mine
 Author: F. Domingos
 Length: 34m
 General orientation: E-W

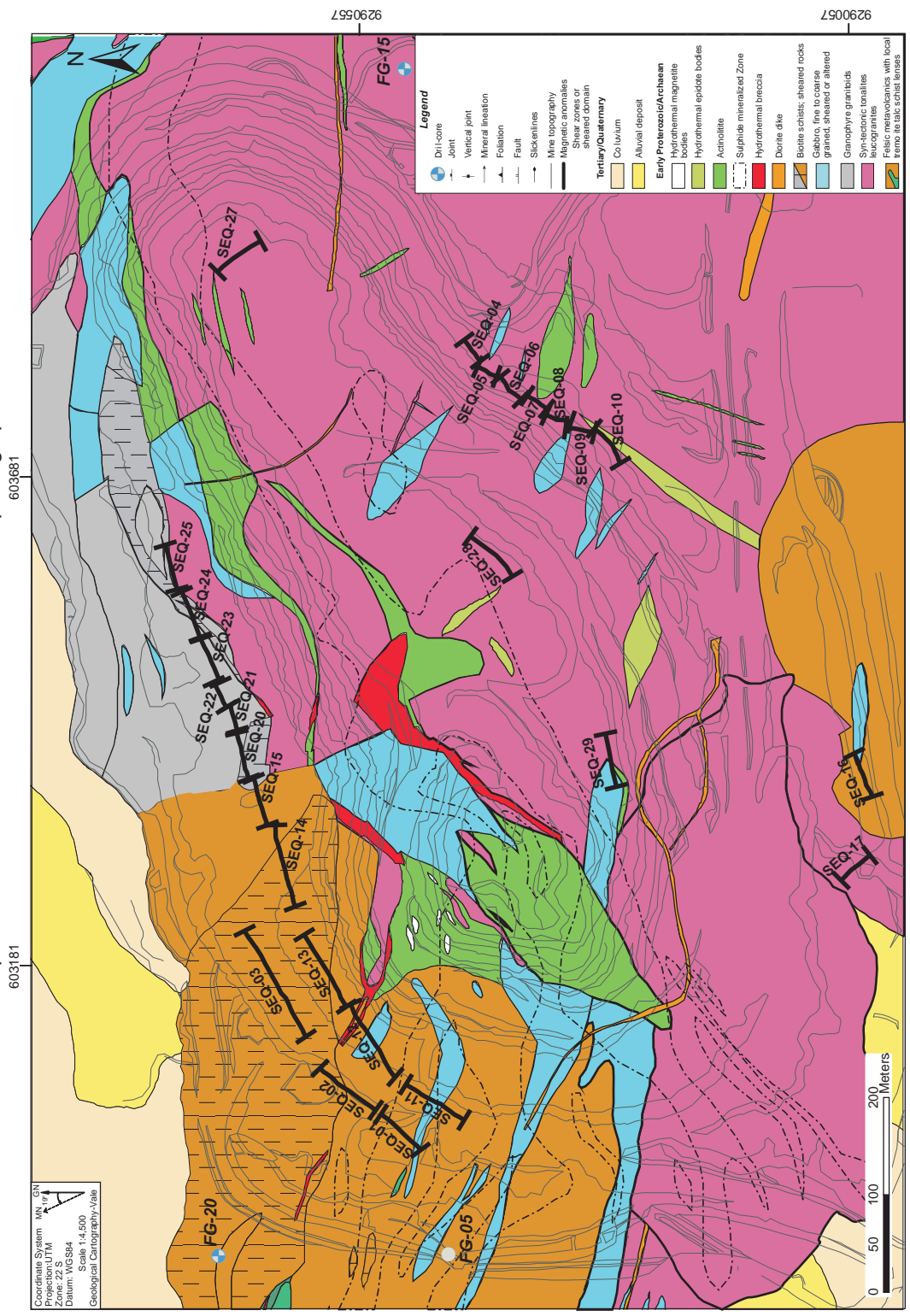
SECTION 15



Section: 15
Location: Sossego Mine
Author: F. Domingos
Length: 29m
General orientation: N-S



Sequeirinho Mine and the location of the studied phototaphic sections



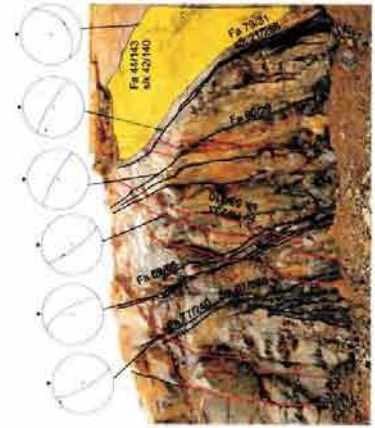
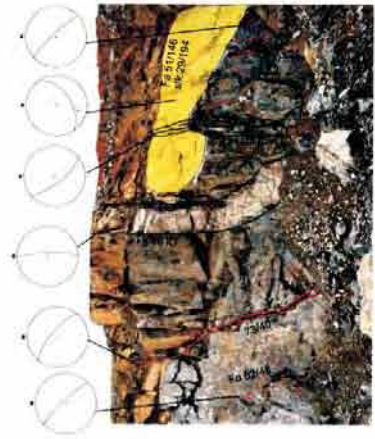
9290557

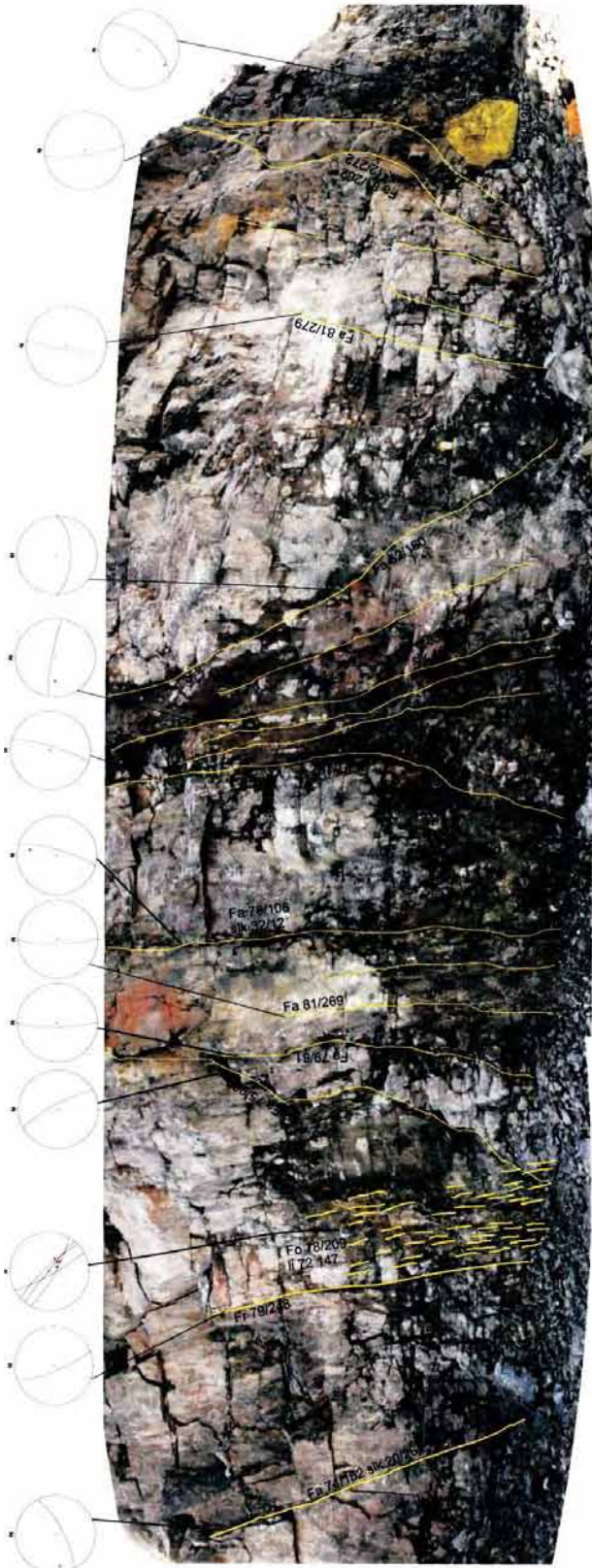
9290057

SEQ-02

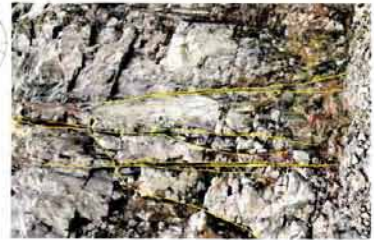


SEQ-03

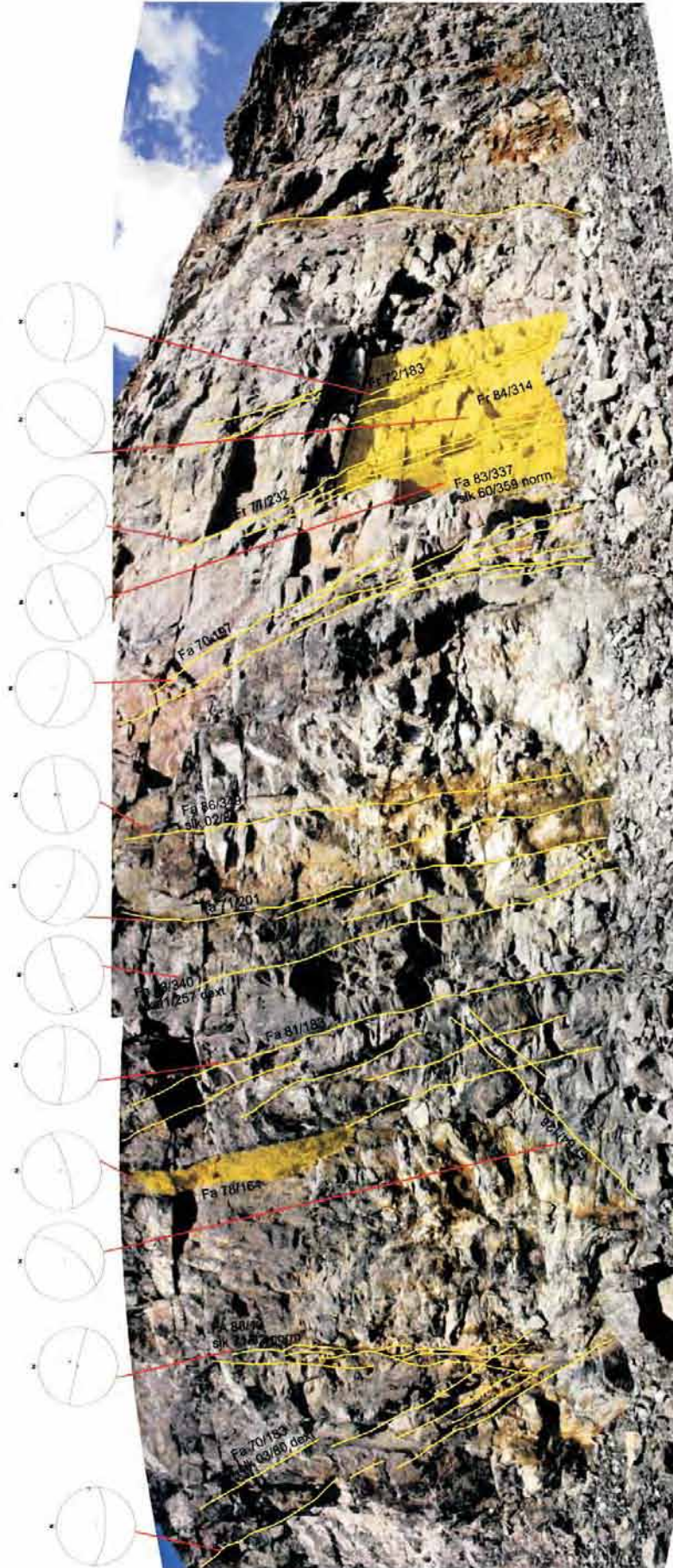


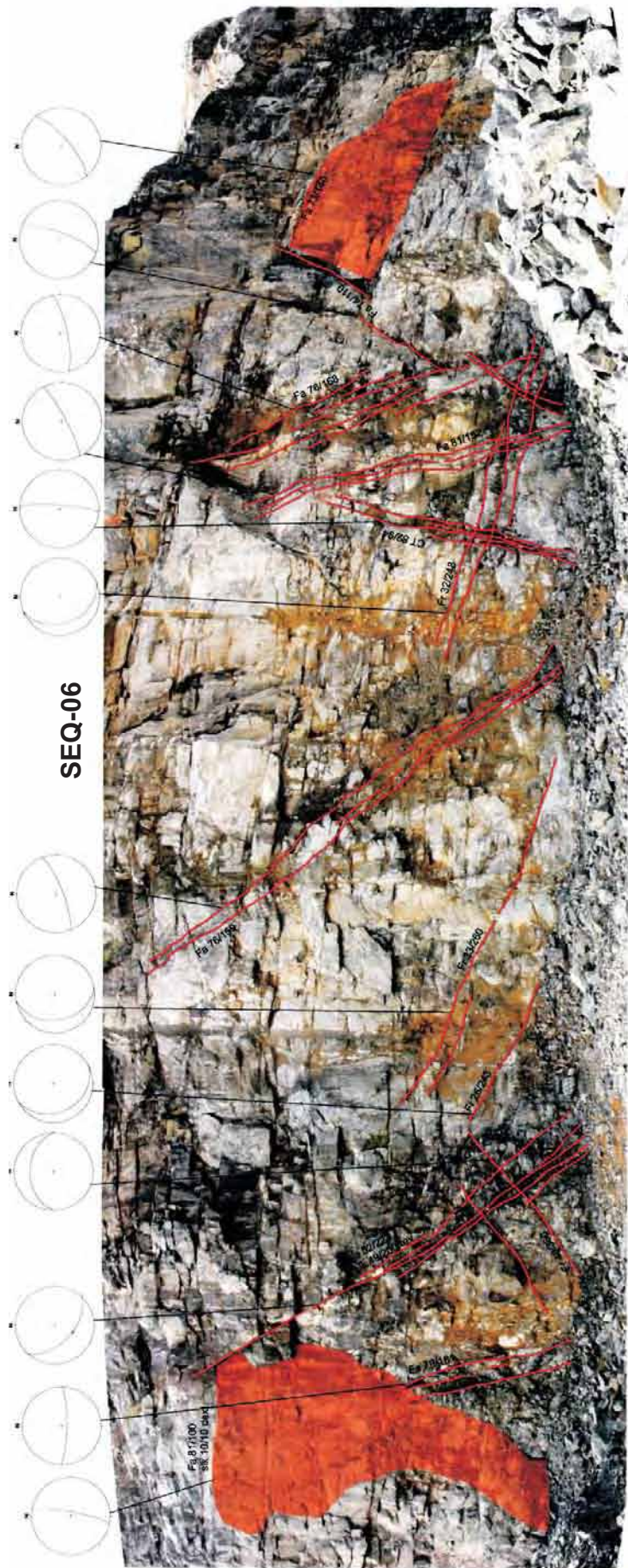


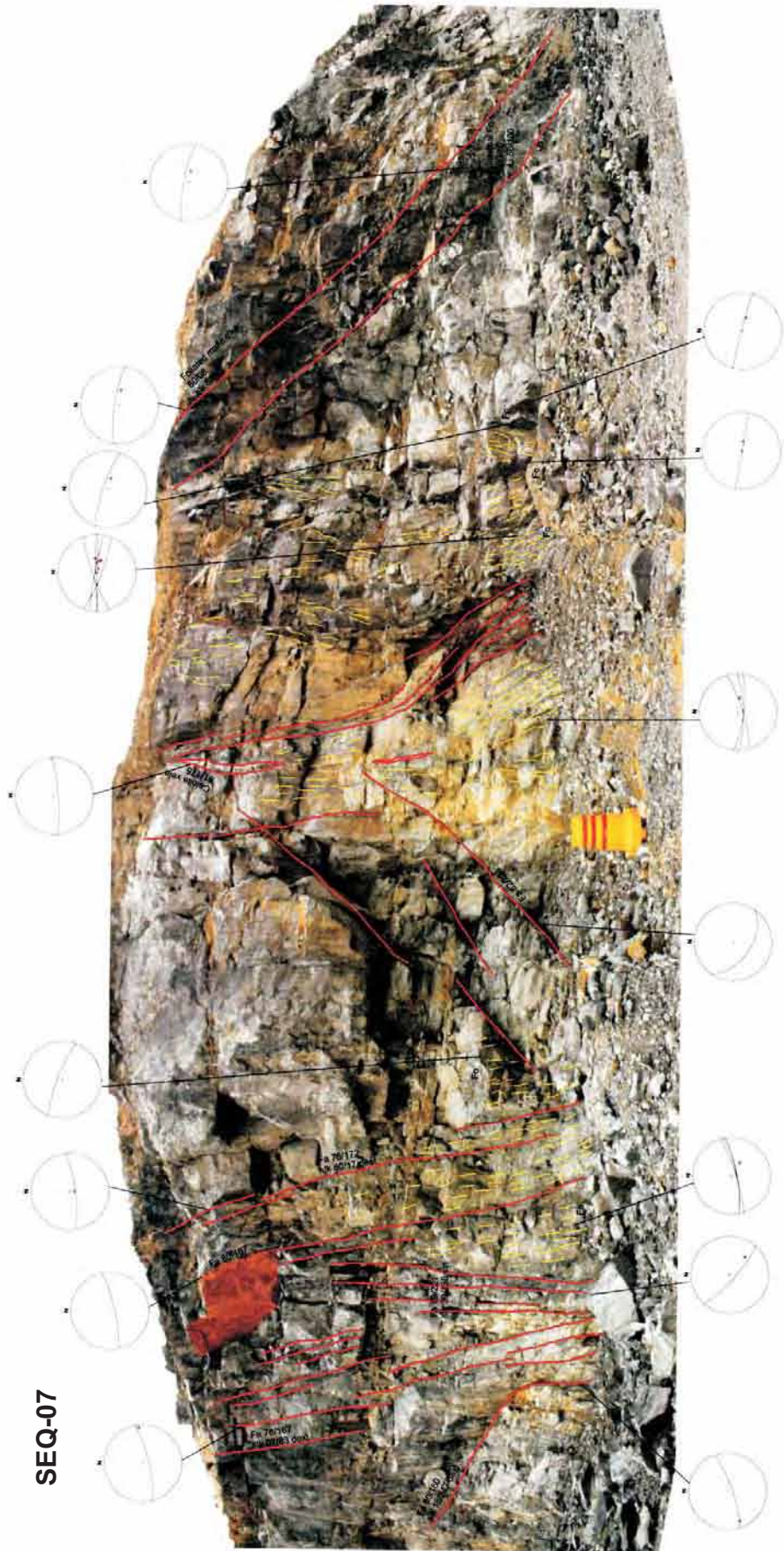
SEQ-04



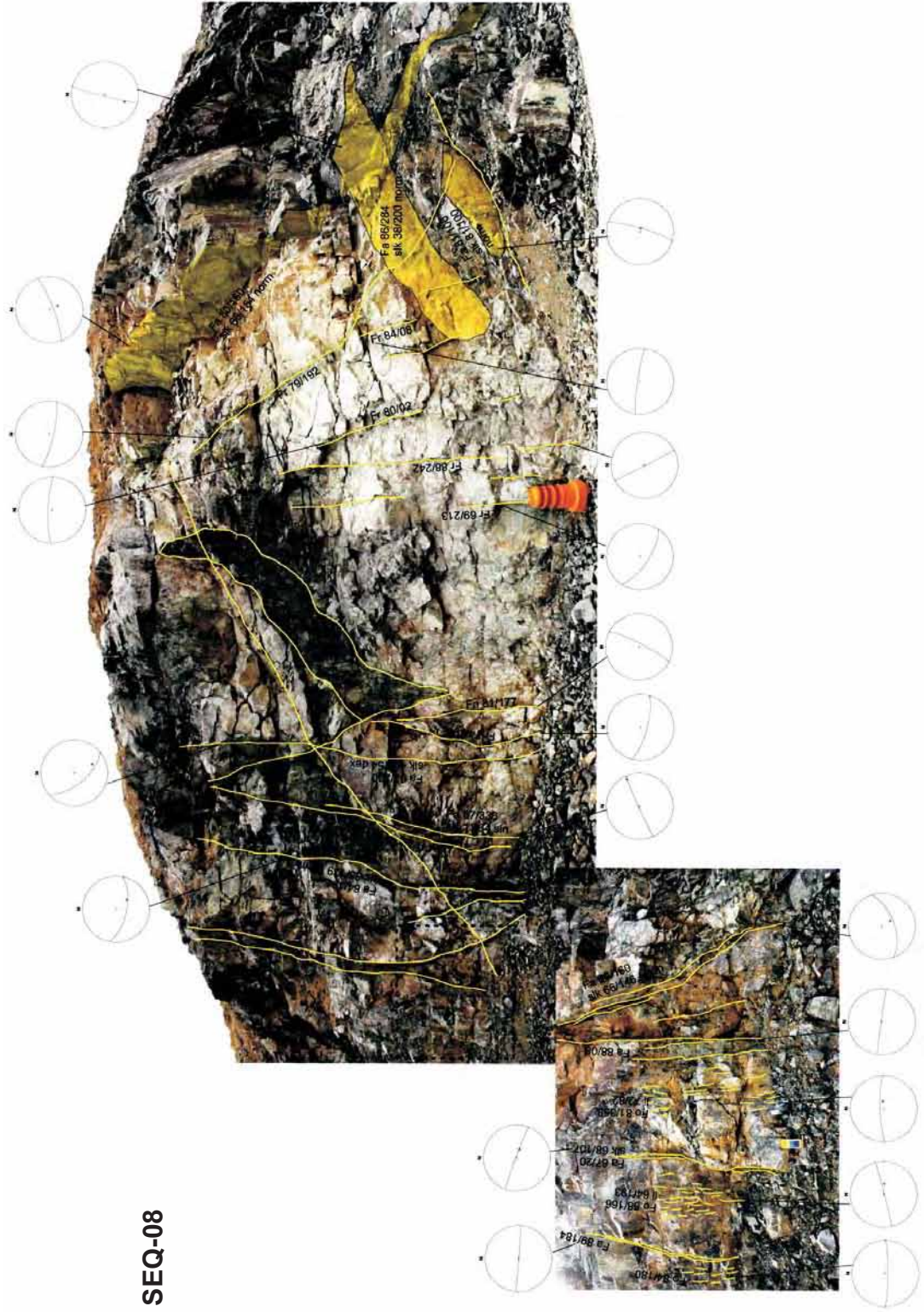
SEQ-05



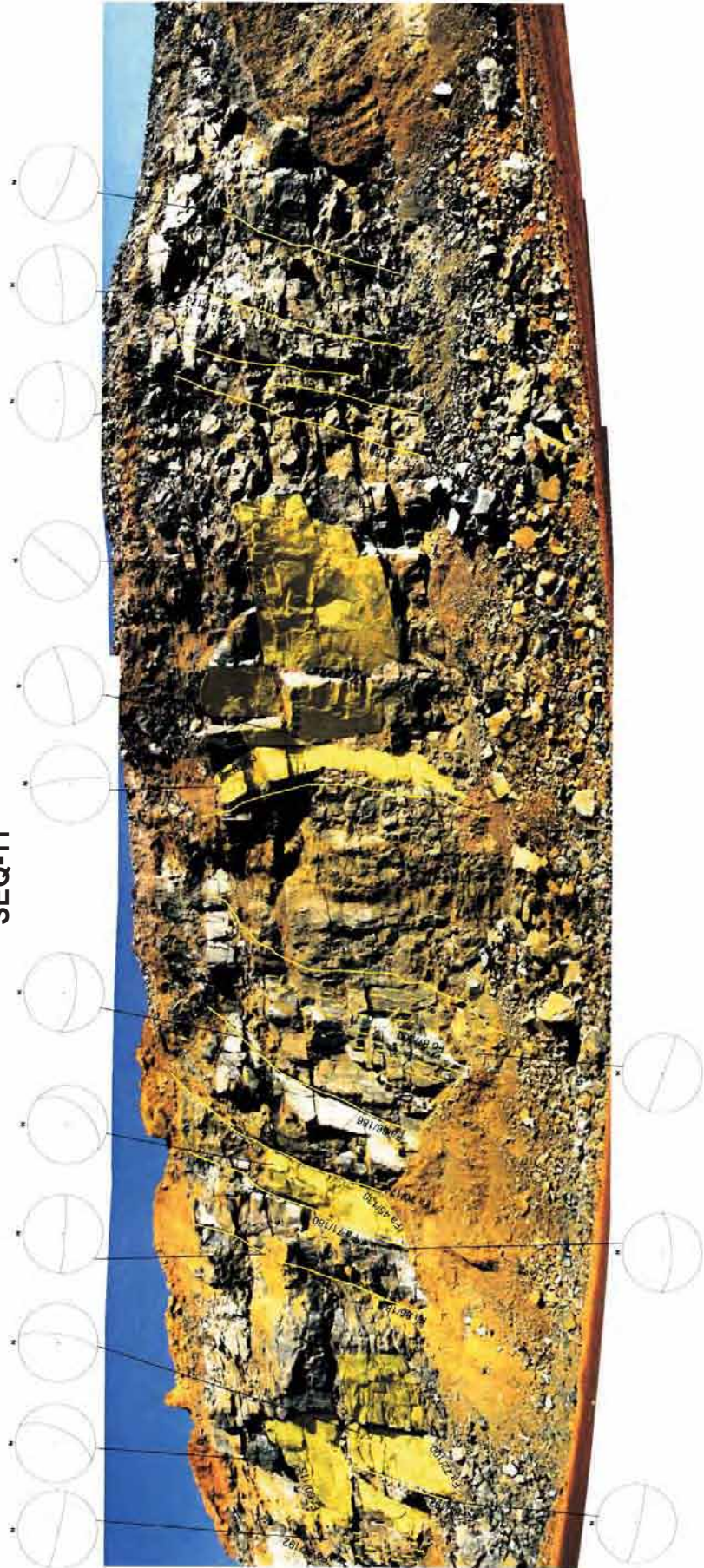




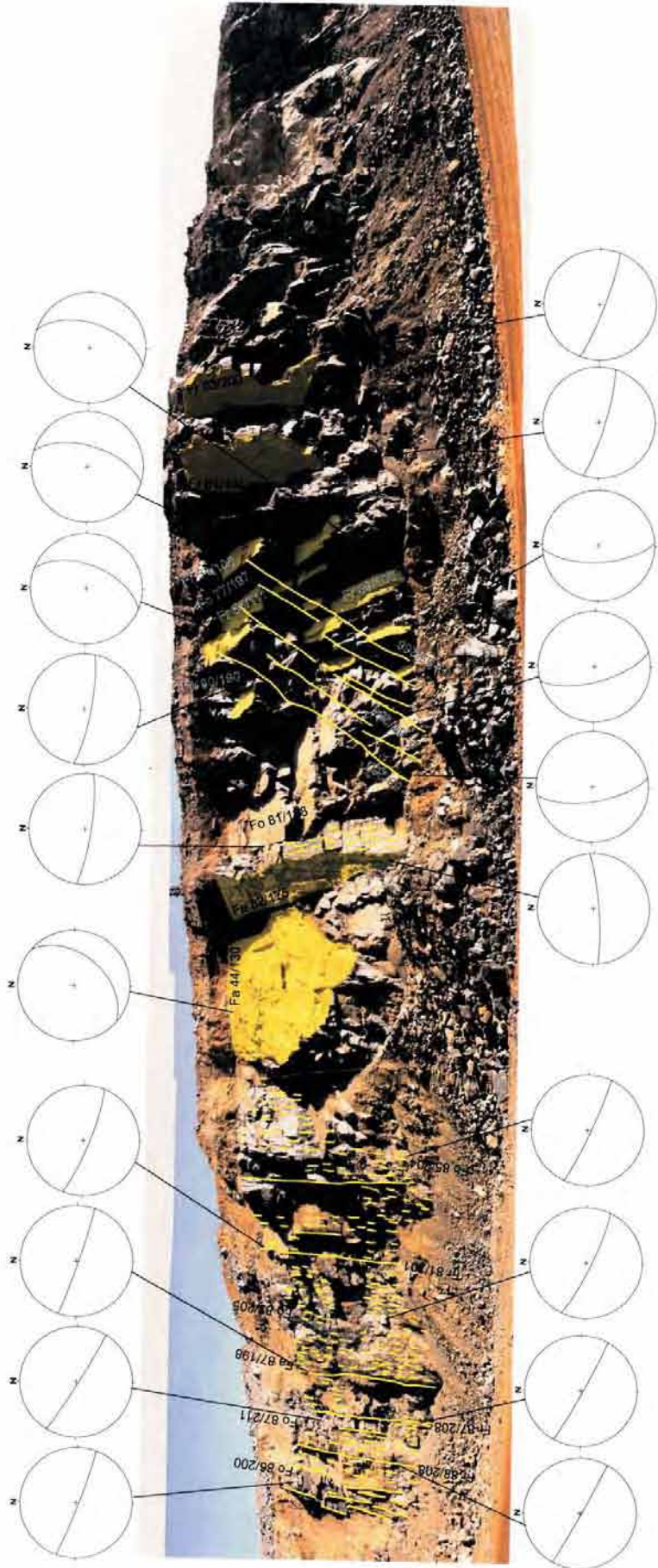
SEQ-08



SEQ-11



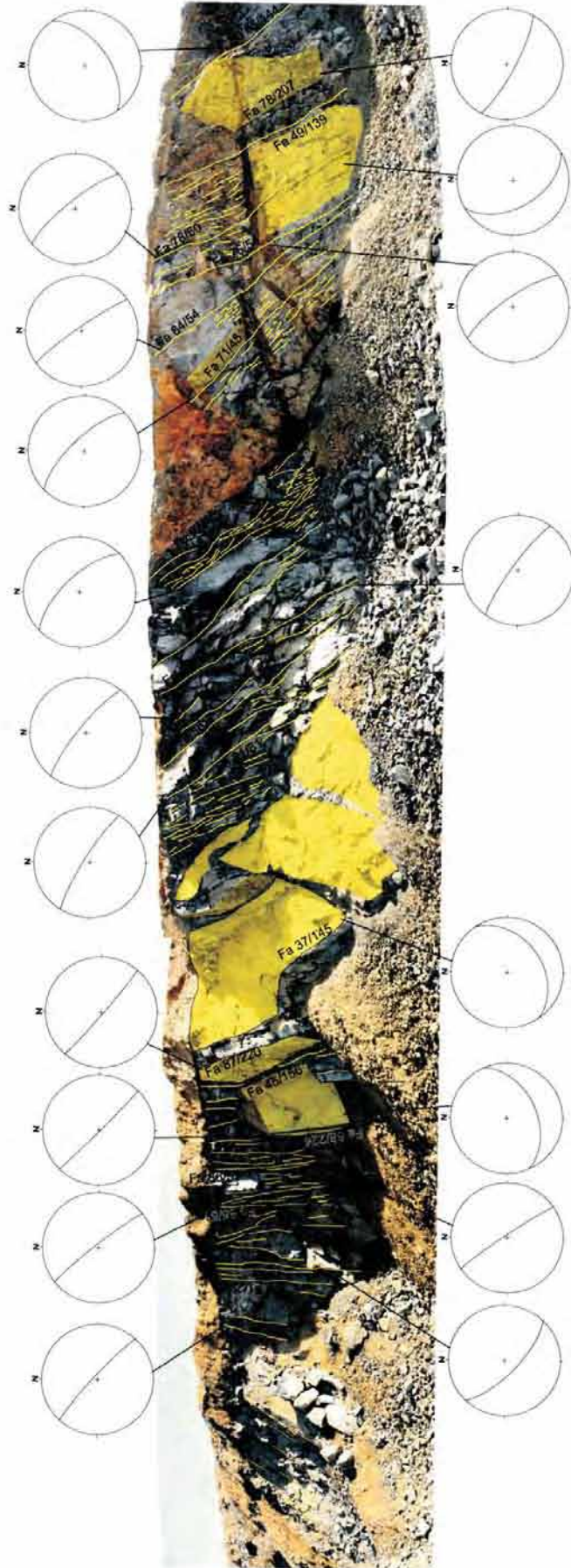
SEQ-12



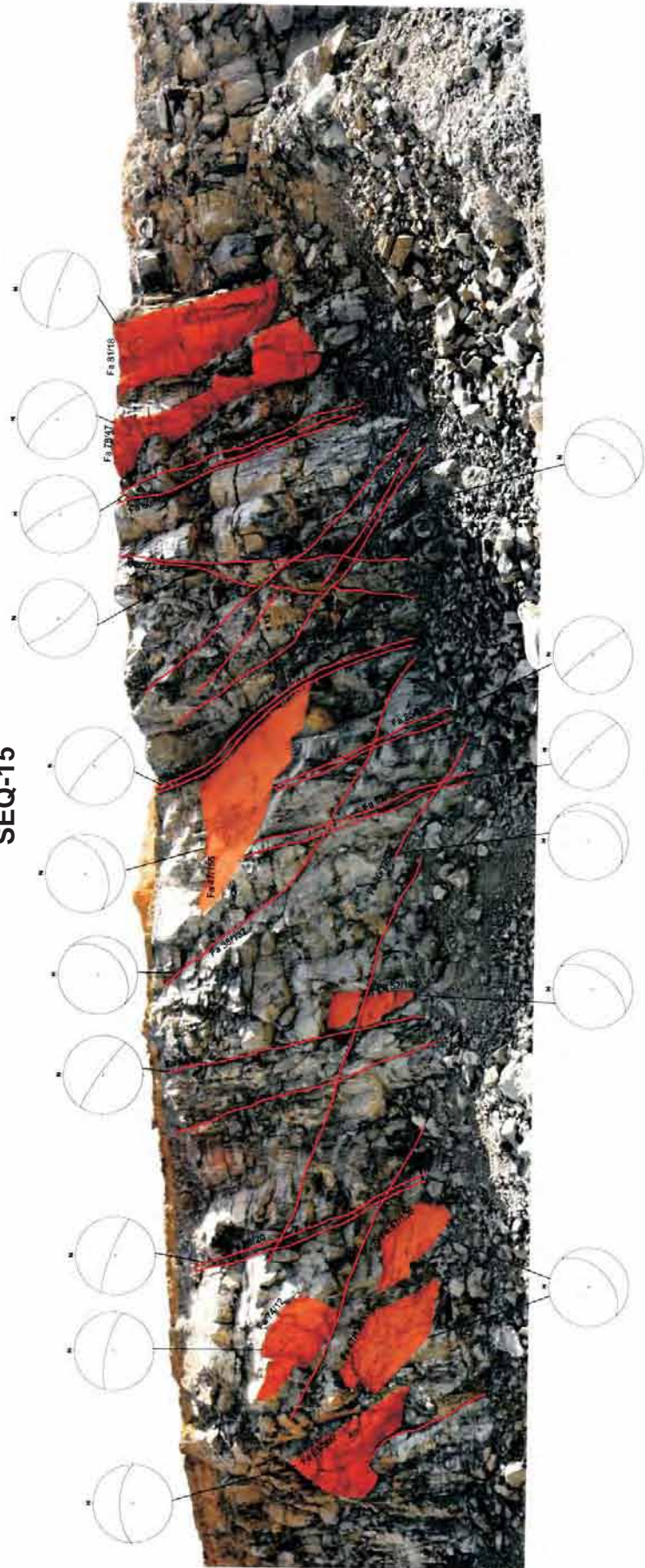
SEQ-13



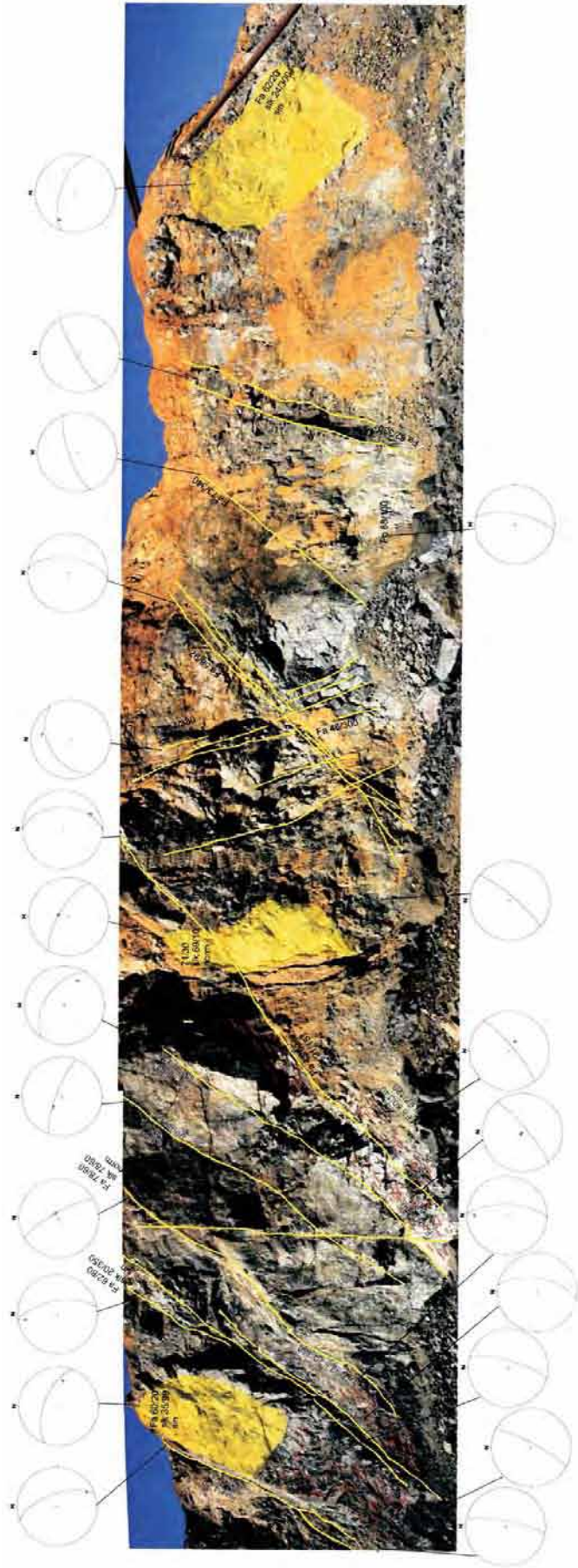
SEQ-14



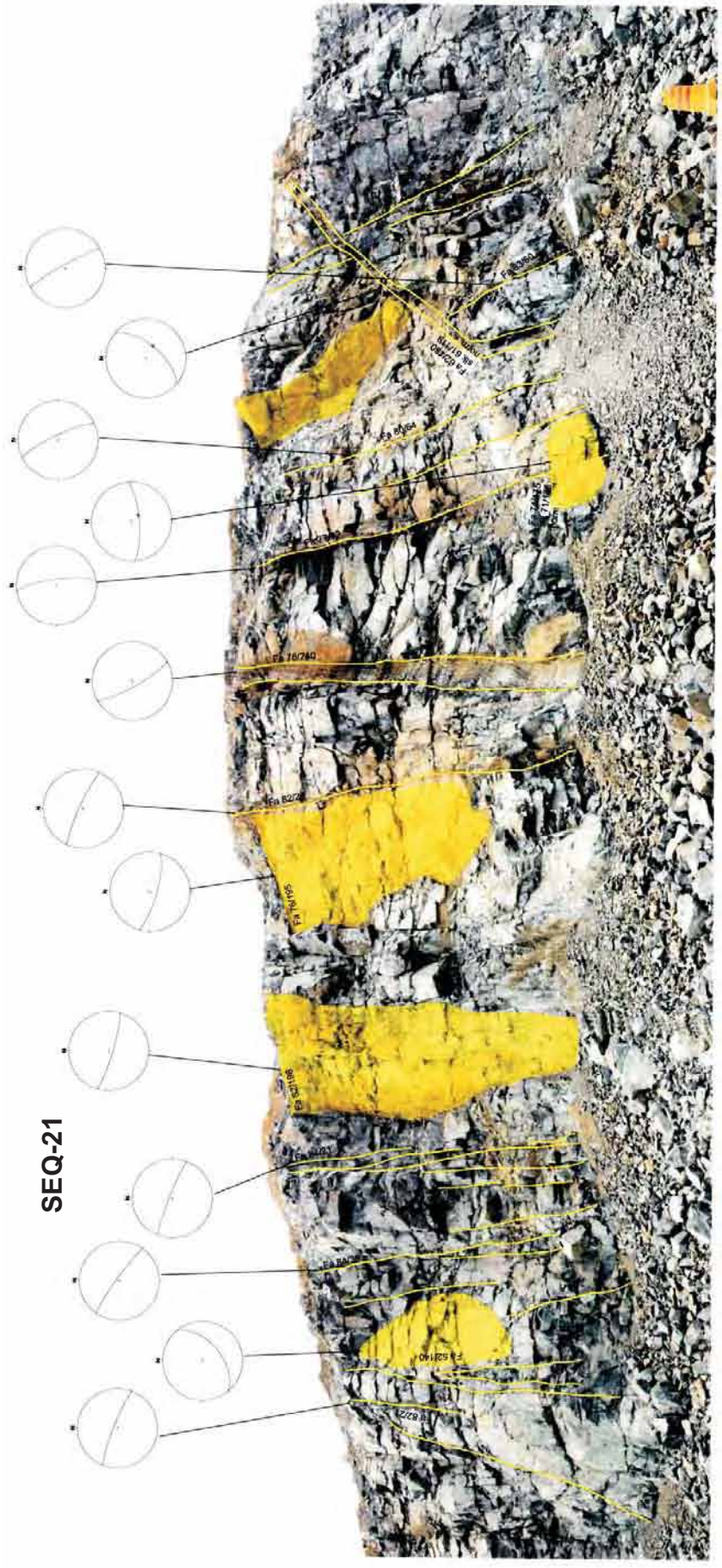
SEQ-15



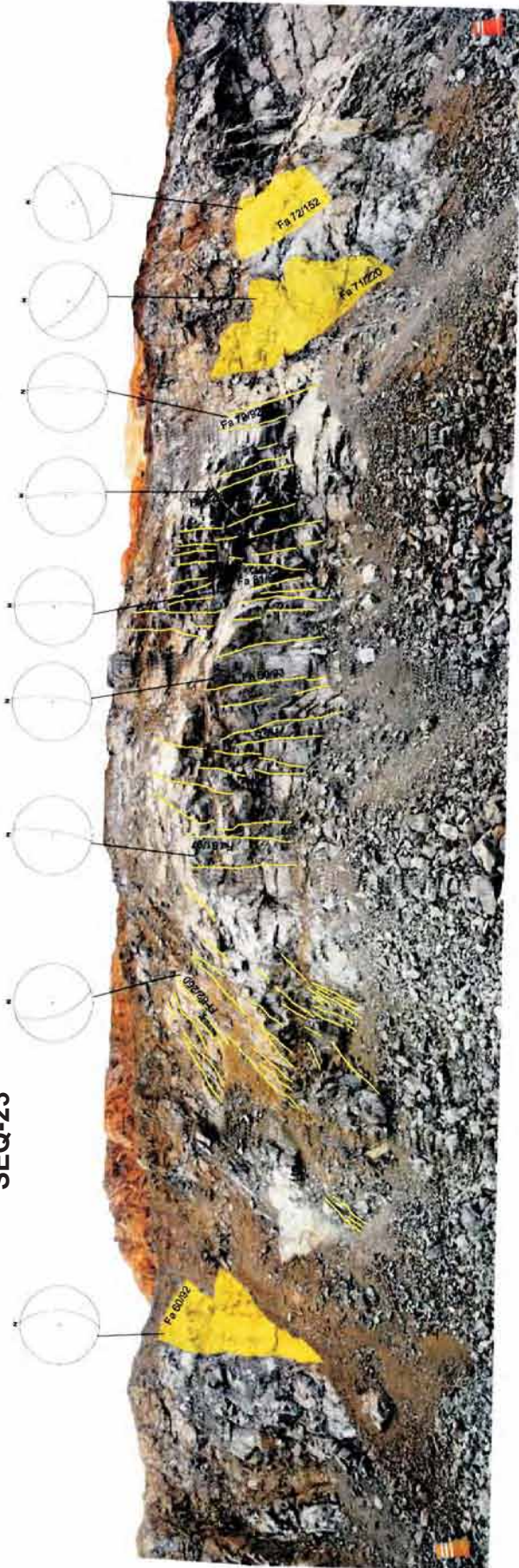
SEQ-18







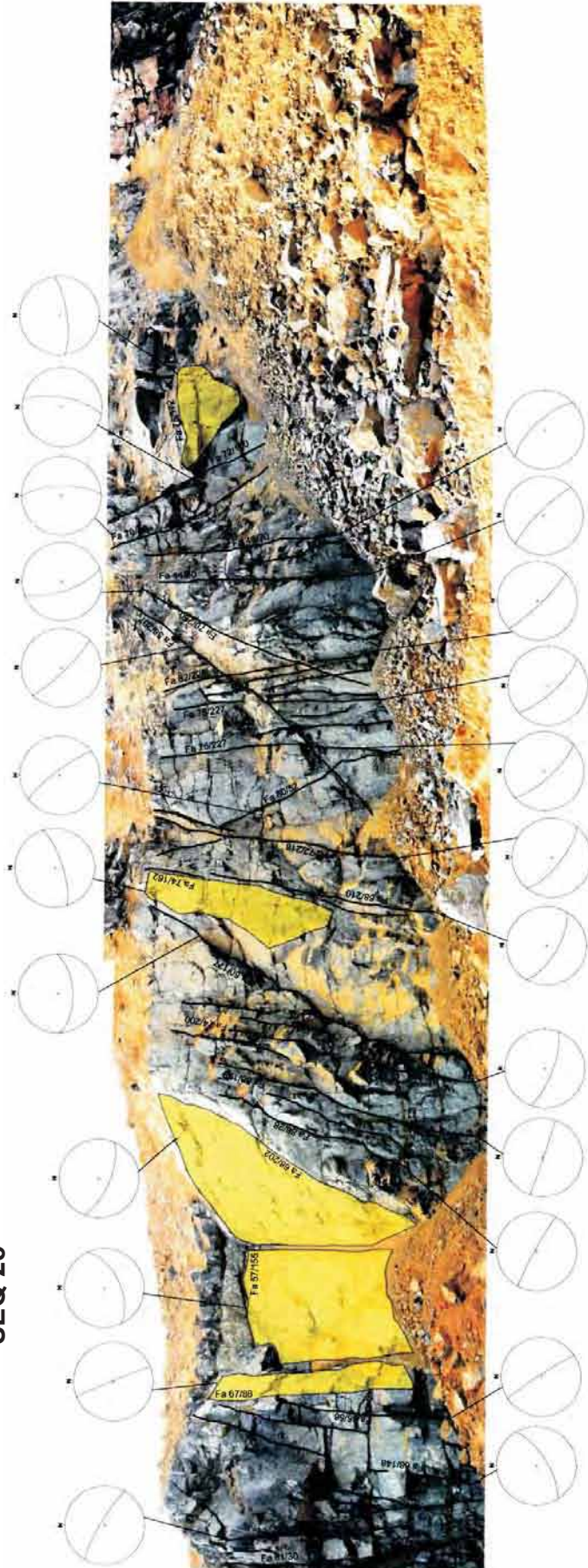
SEQ-23



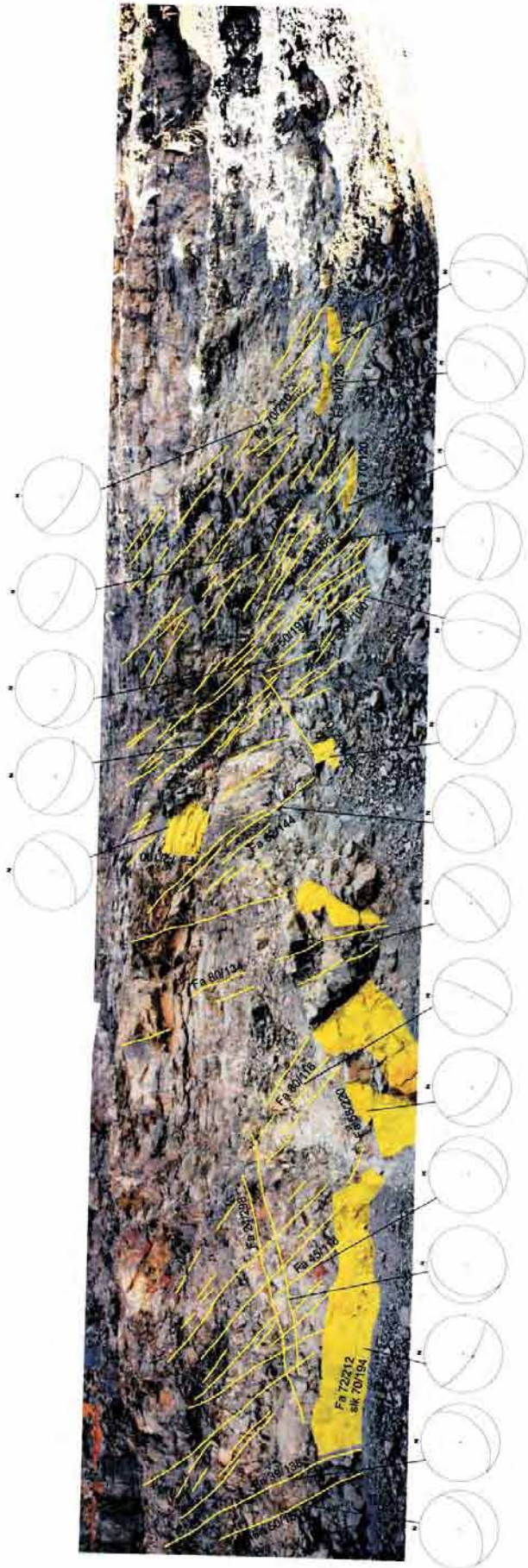
SEQ-24



SEQ-25



SEQ-27



SEQ-28





References

- Airo, M. L. and K. Loukola-Ruskeeniemi (2004). "Characterization of sulfide deposits by airborne magnetic and gamma-ray responses in eastern Finland." Ore Geology Reviews **24**(1-2): 67-84.
- Alexandrov, P., G. Ruffet, et al. (2002). "Muscovite recrystallization and saddle-shaped Ar-40/Ar-39 age spectra: Example from the Blond granite (Massif Central, France)." Geochimica Et Cosmochimica Acta **66**(10): 1793-1807.
- Allek, K. and M. Hamoudi (2008). "Regional-scale aeromagnetic survey of the south-west of Algeria: A tool for area selection for diamond exploration." Journal of African Earth Sciences **50**(2-4): 67-78.
- Almeida, F. F. M. (1976). "The system of continental rifts bordering the Santos Basin, Brazil." Anais da Academia Brasileira de Ciencias, Rio de Janeiro **48**: 15-26.
- Almeida, F. F. M., Y. Hasui, et al. (1981). "Brazilian structural provinces: An introduction." Earth-Science Reviews **17**(1-2): 1-29.
- Almeida, F. F. M., B. B. D. Neves, et al. (2000). "The origin and evolution of the South American Platform." Earth-Science Reviews **50**(1-2): 77-111.
- Almeida, F. F. M. d. and Y. Hasui (1984). O Pré-Cambriano do Brasil. São Paulo, Editora Blücher.
- Almeida, F. M. M. (1967). Origem e Evolução da Plataforma Brasileira. Rio de Janeiro, Divisão de Geologia e Mineração - DNPM.
- Almeida, J. A. C. and R. Dall'Agnol (2007). "Petrologia magnética do granito anorogênico Bannach, terreno granito-greenstone de Rio Maria, Pará." Revista Brasileira de Geociências **37**: 17-36.
- Almeida, R. C. C. (1980). Contribuição à petrologia do granito central da serra dos Carajás. . Curso de Pós-Graduação em Geologia e Geoquímica, Centro de Geociências. Belém, Universidade Federal do Pará. **Masters**: 84.
- Altenberger, U. and S. Wilhelm (2000). "Ductile deformation of K-feldspar in dry eclogite facies shear zones in the Bergen Arcs, Norway." Tectonophysics **320**(2): 107-121.
- Althoff, F., P. Barbey, et al. (2000). "2.8-3.0 Ga plutonism and deformation in the SE Amazonian craton: the Archaean granitoids of Marajoara (Carajas Mineral Province, Brazil)." Precambrian Research **104**(3-4): 187-206.
- Althoff, F. J., P. Barbey, et al. (1993). The Archaean evolution of a crustal segment over 100 Ma: the Amazonian craton. VII EUG, Strasbourg.
- Althoff, F. J., P. Barbey, et al. (1998). La croissance du craton sud-amazonien (région de Rio Maria, Brésil). Réunion des Sciences de la Terre, Brest, Soc. Géol. Fr.

- Amaral, G. (1974). Geologia Pré-Cambriana da região Amazônica. Instituto de Geociências. São Paulo, Universidade de São Paulo. **PhD**: 212.
- Amaral, G. and M. Halpern (1975). K/Ar and Rb/Sr age studies on the extensive Precambrian Volcanism of the Brazilian Amazon region. Conferencia Geologica Interguiana, Belém, DNPM.
- Anderson, W. L., R. C. Dyer, et al. (1974). Ocorrências de manganês na bacia do Rio Itacaiúnas, centro-leste do Estado do Pará. XXVIII Congresso Brasileiro de Geologia, Porto Alegre, SBG.
- Anthony, J. L. and C. Marone (2005). "Influence of particle characteristics on granular friction." Journal of Geophysical Research-Solid Earth **110**(B8).
- Araújo, O. J. B. and R. G. N. Maia (1991). Programa de levantamentos geológicos básicos do Brasil. Folha SB 22-Z-A. Serra dos Carajás, Estado do Pará. Projeto Especial Mapas de Recursos Minerais de Solo e de Vegetação para a área do Projeto Grande Carajás: Subprojeto Recursos Minerais. Brasília, CPRM: 164.
- Araújo, O. J. B., R. G. N. Maia, et al. (1988). A megaestruturação arqueana da Folha Serra dos Carajás. VII Congresso Latino-Americano de Geologia, Belém, SBG.
- Austin, J. R. and T. G. Blenkinsop (2008). "The Cloncurry Lineament: Geophysical and geological evidence for a deep crustal structure in the Eastern Succession of the Mount Isa Inlier." Precambrian Research **163**(1-2): 50-68.
- Avelar, V. G. (1996). Geocronologia Pb–Pb por evaporação em monocristal de zircão, do magmatismo da região de Tucumã, SE do Estado do Pará, Amazônia Oriental. Curso de Pós-Graduação em Geologia e Geoquímica. Belém, Universidade Federal do Pará. **MSc. thesis**: 149.
- Avelar, V. G., J. M. Lafon, et al. (1999). "O magmatismo arqueano da região de Tucumã, Província Mineral de Carajás, Amazônia Oriental, Brasil: novos dados geocronológicos." Revista Brasileira de Geociências **29**: 453-460.
- Baas, J. H. (2000). "EZ-ROSE: a computer program for equal-area circular histograms and statistical analysis of two-dimensional vectorial data." Computers & Geosciences **26**(2): 153-166.
- Barbosa, A. A., J. M. Lafon, et al. (1995). "Geocronologia Rb–Sr e Pb–Pb do Granito Redenção, SE do Pará: implicações para a evolução do magmatismo proterozóico da região de Redenção." Boletim do Museu Paraense Emílio Goeldi. Ciências da Terra **7**: 147–164.
- Barbosa, J. P. O., C. E. M. Barros, et al. (2001). Geologia e Geocronologia do Stock Granítico Geladinho, região de Parauapebas, Província Mineral de Carajás. VII SIMPÓSIO DE GEOLOGIA DA AMAZONIA, Belém, SBG.
- Barbosa, O., J. R. d. A. Ramo, et al. (1966). Geologia estratigráfica, estrutural e econômica da área do "Projeto Araguaia". Monografia. Rio de Janeiro, DGM: 94.
- Barreiro, J. G., J. R. Wijbrans, et al. (2006). "Ar-40/Ar-39 laserprobe dating of mylonitic fabrics in a polyorogenic terrane of NW Iberia." Journal of the Geological Society **163**: 61-73.

- Barros, C. E. d. M., R. Dall'Agnol, et al. (1997). "Geochemistry of the Estrela Granite Complex, Carajás region, Brazil: an example of an Archaean A-type granitoid." Journal of South American Earth Sciences **10**: 321-330.
- Barros, C. E. M. (1991). Evolução petrológica e estrutural do Gnaiss Estrela, Curionópolis, PA. Curso de Pós-Graduação em Geologia e Geoquímica. Belém, Universidade Federal do Pará. **MSc. thesis**: 134.
- Barros, C. E. M. (1997). Pétrologie et structure du Complexe Granitique Estrela (2.5 Ga) et de son encaissant métavolcano-sédimentaire (Province Métallifère de Carajás, Brésil). Nancy I/CRPG. Nancy, Université Henri Poincaré. **PhD Thesis**: 316.
- Barros, C. E. M., P. Barbey, et al. (2001). "Role of magma pressure, tectonic stress and crystallization progress in the emplacement of syntectonic granites. The A-type Estrela Granite Complex (Carajas Mineral Province, Brazil)." Tectonophysics **343**(1-2): 93-109.
- Barton, M. D. a. J., D. A. (1996). "An evaporitic-source model for igneous-related Fe-oxide(-REE-Cu-Au-U) mineralization." Geology **24**: 259-262.
- Barton, M. D. a. J., D. A. (2000). Alternative brine sources for Fe-oxide(-Cu-Au) systems: Implications for hydrothermal alteration and metals. Hydrothermal iron oxide copper-gold and related deposits a global perspective. T. M. Porter. Glenside, South Australia, Australian Mineral Foundation: 43-60.
- Basei, M. A. S. (1974). Estudo geocronológico do magmatismo da Amazônia. XXVIII Congresso Brasileiro de Geologia, Porto Alegre.
- Bea, F., A. Pesquera, et al. (2009). "Tourmaline Ar-40/Ar-39 chronology of tourmaline-rich rocks from Central Iberia dates the main Variscan deformation phases." Geologica Acta **7**(4): 399-412.
- Bedard, J. H., P. Brouillette, et al. (2003). "Archaean cratonization and deformation in the northern Superior Province, Canada: an evaluation of plate tectonic versus vertical tectonic models." Precambrian Research **127**(1-3): 61-87.
- Beisiegel, V. d. R. (1982). Distrito Ferrífero da Serra dos Carajás. I Simpósio de Geologia da Amazônia. Belém, SBG: 21-46.
- Beisiegel, V. d. R., A. L. Bernardelli, et al. (1973). "Geologia e recursos minerais da Serra dos Carajás." Revista Brasileira de Geociências **3**: 215-242.
- Beisiegel, V. d. R. and N. F. Farias (1978). Ocorrência de Cobre na Serra dos Carajás. XXX Congresso Brasileiro de Geologia, Recife.
- Bell, T. H. and S. E. Johnson (1989). "The Role of Deformation Partitioning in the Deformation and Recrystallization of Plagioclase and K-Feldspar in the Woodroffe Thrust Mylonite Zone, Central Australia." Journal of Metamorphic Geology **7**(2): 151-168.
- Bernardelli, A. L., E. M. Meirelles, et al. (1982). Província Mineral de Carajás. I Simpósio de Geologia da Amazônia, Belém, SBG.

- Bickle, M. J., L. F. Bettenay, et al. (1980). "Horizontal Tectonic Interaction of an Archean Gneiss Belt and Greenstones, Pilbara Block, Western-Australia." Geology **8**(11): 525-529.
- Billi, A. and F. Storti (2004). "Fractal distribution of particle size in carbonate cataclastic rocks from the core of a regional strike-slip fault zone." Tectonophysics **384**(1-4): 115-128.
- Bizzi, L. A., C. Schobbenhaus, et al. (2002). Geologia, Tectônica e Recursos Minerais do Brasil: Sistemas de Informações Geográficas – SIG e Mapas na escala 1:2 500 000. Brasília-DF, Companhia de Pesquisa e Recursos Minerais - CPRM.
- Bjornerud, M. G. (1998). "Superimposed deformation in seconds: breccias from the impact structure at Kentland, Indiana (USA)." Tectonophysics **290**(3-4): 259-269.
- Blenkinsop, T. G. (1991). "Cataclasis and Processes of Particle-Size Reduction." Pure and Applied Geophysics **136**(1): 59-86.
- Bonham-Carter, G. F. (1985). "Statistical association of gold occurrences with Landsat derived lineaments, Timmins-Kirkland lake area, Ontario." Canadian Journal of Remote Sensing **11**(2): 195-210.
- Bonnet, E., O. Bour, et al. (2001). "Scaling of fracture systems in geological media." Reviews of Geophysics **39**(3): 347-383.
- Boucher, R. K. (1997). Lineament tectonic data, south Australia with a focus on the cooper basin, Department of Mines and Energy Resources South Australia 75.
- Bouhallier, H., P. Choukroune, et al. (1993). "Diapirism, Bulk Homogeneous Shortening and Transcurrent Shearing in the Archean Dharwar Craton - the Holenarsipur Area, Southern India." Precambrian Research **63**(1-2): 43-58.
- Brown, S. R. and R. L. Bruhn (1996). "Formation of voids and veins during faulting." Journal of Structural Geology **18**(5): 657-671.
- Burkhard, M. (1993). "Calcite Twins, Their Geometry, Appearance and Significance as Stress-Strain Markers and Indicators of Tectonic Regime - a Review." Journal of Structural Geology **15**(3-5): 351-368.
- Carneiro, C. d. C., A. P. Crosta, et al. (2006). "Fusão de imagens altimétricas e aeromagnetométricas como ferramenta de interpretação geológica, exemplo da Província Mineral de Carajás (PA)." Revista Brasileira de Geofísica **24**(2): 11.
- Carvalho, E. R., R. P. Xavier, et al. (2005). Geology and hydrothermal alteration of the Sossego iron oxide–copper–gold deposit, Carajás Mineral Province, Brazil. I Simpósio Brasileiro de Metalogenia. Gramado-RS-Brazil, SBG.
- Casas, A. M., D. Gapais, et al. (2001). "Analogue models of transpressive systems." Journal of Structural Geology **23**(5): 733-743.
- Challandes, N., D. Marquer, et al. (2003). "Dating the evolution of C-S micro structures: a combined Ar-40/Ar-39 step-heating and UV laserprobe analysis of the Alpine Roffna shear zone." Chemical Geology **197**(1-4): 3-19.

- Chardon, D., P. Choukroune, et al. (1996). "Strain patterns, decollement and incipient sagducted greenstone terrains in the Archaean Dharwar craton (south India)." Journal of Structural Geology **18**(8): 991-&.
- Chardon, D., J. J. Peucat, et al. (2002). "Archean granite-greenstone tectonics at Kolar (South India): Interplay of diapirism and bulk inhomogeneous contraction during juvenile magmatic accretion." Tectonics **21**(3): -.
- Chen, S. F., J. W. Libby, et al. (2001). "Geometry and kinematics of large arcuate structures formed by impingement of rigid granitoids into greenstone belts during progressive shortening." Geology **29**(3): 283-286.
- Chen, S. F., J. W. Libby, et al. (2004). "Kinematic nature and origin of regional-scale ductile shear zones in the central Yilgarn Craton, Western Australia." Tectonophysics **394**(3-4): 139-153.
- Chernicoff, C. J. and C. R. Nash (2002). "Geological interpretation of Landsat TM imagery and aeromagnetic survey data, northern Precordillera region, Argentina." Journal of South American Earth Sciences **14**(8): 813-820.
- Chester, F. M. and J. S. Chester (1998). "Ultracataclasite structure and friction processes of the Punchbowl fault, San Andreas system, California." Tectonophysics **295**(1-2): 199-221.
- Chiaradia, M., D. Banks, et al. (2006). "Origin of fluids in iron oxide-copper-gold deposits: constraints from delta Cl-37, Sr-87/Sr-86(i) and Cl/Br." Mineralium Deposita **41**(6): 565-573.
- Choukroune, P., H. Bouhallier, et al. (1995). "Soft lithosphere during periods of Archaean crustal growth or crustal reworking." Geological Society, London, Special Publications **95**(1): 67-86.
- Clark, C. and P. James (2003). "Hydrothermal brecciation due to fluid pressure fluctuations: examples from the Olary Domain, South Australia." Tectonophysics **366**(3-4): 187-206.
- Clark, C., A. S. Mumm, et al. (2006). "A coupled micro- and macrostructural approach to the analysis of fluid induced brecciation, Curnamona Province, South Australia." Journal of Structural Geology **28**(5): 745-761.
- Clark, C. D. and C. Wilson (1994). "Spatial-Analysis of Lineaments." Computers & Geosciences **20**(7-8): 1237-1258.
- Clegg, P., L. Bruciatelli, et al. (2006). "Digital geological mapping with tablet PC and PDA: A comparison." Computers & Geosciences **32**(10): 1682-1698.
- Collins, W. J. and M. J. Van Kranendonk (1999). "Model for the development of kyanite during partial convective overturn of Archean granite-greenstone terranes: the Pilbara Craton, Australia." Journal of Metamorphic Geology **17**(2): 145-156.
- Condie, K. C. (1981). Archean greenstone belts. Amsterdam, Elsevier Scientific Pub. Co.
- Condie, K. C. (1998). "Episodic continental growth and supercontinents: a mantle avalanche connection?" Earth and Planetary Science Letters **163**(1-4): 97-108.

- Condie, K. C. (2000). "Episodic continental growth models: afterthoughts and extensions." Tectonophysics **322**(1-2): 153-162.
- Cordani, U. G. (1979). "Concept of Tectonic Province and Application for South-America." Anais Da Academia Brasileira De Ciencias **51**(4): 775-776.
- Cordani, U. G. and B. B. Brito Neves (1982). "The geologic evolution of South America during the Archean and Early Proterozoic." Revista Brasileira de Geociencias **12**(1): 10.
- Cordani, U. G., K. Sato, et al. (2000). Crustal evolution of the South American platform. Tectonic Evolution of South America **31** International Geological Congress. U. G. M. Cordani, E.J; Thomaz Filho, A.; and Campos, D.A. Rio de Janeiro: 856.
- Cordani, U. G., W. Teixeira, et al. (1988). "The Growth of the Brazilian Shield." Episodes **11**(3): 163-167.
- Cortes, A. L., A. Maestro, et al. (1998). "Lineaments and fracturing in the Neogene rocks of the Almazan basin, northern Spain." Geological Magazine **135**(2): 255-268.
- Costa, J. B. S., O. J. B. Araújo, et al. (1995). "Província Mineral de Carajás: Aspectos tectono-estruturais, estratigráficos e geocronológicos." Bol. Mus. Para. Emílio Goeldi, série Ciências da Terra(7): 199-235.
- Costa, J. B. S. and Y. Hasui (1991). O quadro geral da evolução tectônica da Amazônia. III Simpósio Nacional de Estudos Tectônicos, Rio Claro, UNESP-SBG.
- Costa, J. B. S. and Y. Hasui (1992). "Aspectos fundamentais do Proterozóico Médio da Amazônia Brasileira." Revista Brasileira de Geociencias **22**(4): 487-492.
- Costa, J. B. S. and Y. Hasui (1997). Evolução geológica da Amazônia. Contribuição à Geologia da Amazônia. M. L. Costa and R. S. Angélica. Belém, SBG/FINEP: 15-90.
- Cox, S. F. (1999). "Deformational controls on the dynamics of fluid flow in mesothermal gold systems." Geological Society, London, Special Publications **155**(1): 123-140.
- Cox, S. F. and M. A. Etheridge (1983). "Crack-Seal Fiber Growth Mechanisms and Their Significance in the Development of Oriented Layer Silicate Microstructures." Tectonophysics **92**(1-3): 147-170.
- Cunha, B. C. C. d., D. B. d. Santos, et al. (1984). Contribuição ao estudo da estratigrafia da região dos Gradaus, com ênfase no Grupo Rio Fresco. XXXIII Congresso Brasileiro de Geologia, Rio de Janeiro, SBG.
- CVRD/CMM (1972). Distrito ferrífero da Serra dos Carajás. XXVI Congresso Brasileiro de Geologia. S. B. d. Geologia. Belem-PA. **2**: 78-80.
- Dall'Agnol, R., O. T. Rämö, et al. (1999). "Petrology of the anorogenic, oxidised Jamon and Musa granites, Amazonian craton: implications for the genesis of Proterozoic A-type granites." Lithos(46): 431-462.
- Dall'Agnol, R., Z. S. Souza, et al. (1997). General aspects of the granitogenesis of the Carajás metallogenic province. Second International Symposium on Granites and Associated

Mineralizations, Salvador-Brazil, Companhia Baiana de Pesquisa Mineral, Superintendência de Geologia e Recursos Minerais

- Dall'Agnol, R., N. P. Teixeira, et al. (2005). "Petrogenesis of the Paleoproterozoic rapakivi A-type granites of the Archean Carajas metallogenic province, Brazil." Lithos **80**(1-4): 101-129.
- Dall'Agnol, R. (1982). Estudo comparativo de alguns maciços graníticos pós-Transamazônico da Amazônia Oriental. XXXII Congresso Brasileiro de Geologia, Salvador, SBG.
- Dall'Agnol, R., J. M. Lafon, et al. (1994). "Proterozoic Anorogenic Magmatism in the Central Amazonian Province, Amazonian Craton - Geochronological, Petrological and Geochemical Aspects." Mineralogy and Petrology **50**(1-3): 113-138.
- Dall'Agnol, R., M. A. Oliveira, et al. (2006). Archean and Paleoproterozoic granitoids of the Carajás metallogenic province, eastern Amazonian craton. Symposium on Magmatism, Crustal Evolution, and Metallogenesis of the Amazonian Craton. R. Dall'Agnol, L. T. Rosa-Costa and E. L. Klein. Belem, PA, Brazil, PRONEX-UFPA/SBG-NO. **Abstracts Volume and Field Trips Guide**: 99-150.
- Dawers, N. H., M. H. Anders, et al. (1993). "Growth of Normal Faults - Displacement-Length Scaling." Geology **21**(12): 1107-1110.
- De Donatis, M. and L. Brucciatelli (2006). "MAP IT: The GIS software for field mapping with tablet pc." Computers & Geosciences **32**(5): 673-680.
- de Oliveira, M. A., R. Dall'Agnol, et al. (2009). "Mesoarchean sanukitoid rocks of the Rio Maria Granite-Greenstone Terrane, Amazonian craton, Brazil." Journal of South American Earth Sciences **27**(2-3): 146-160.
- Debeglia, N., G. Martelet, et al. (2006). "Semi-automated structural analysis of high resolution magnetic and gamma-ray spectrometry airborne surveys." Journal of Applied Geophysics **58**(1): 13-28.
- Dentith, M. C., V. F. Dent, et al. (2000). "Deep crustal structure in the southwestern Yilgarn Craton, Western Australia." Tectonophysics **325**(3-4): 227-255.
- Dentith, M. C., A. Trench, et al. (1993). "Geophysical Exploration for Archean Gold - a Case-Study from the Southern Cross Greenstone-Belt, Western-Australia." Journal of Applied Geophysics **30**(3): 175-186.
- Dias, G. S., M. J. B. Macambira, et al. (1996). Datação de zircões de Sill de metagabro: Comprovação da idade arqueana da Formação Águas Claras, Carajás, Pará. V Simpósio de Geologia da Amazônia, Belém-Brazil, Sociedade Brasileira de Geologia.
- DOCEGEO (1981). Jazidas Salobo 3A e 4A, relatório de pesquisa-texto. Projeto Cobre Carajás. Belém.
- DOCEGEO (1988). Província Mineral de Carajás. Litoestratigrafia e principais depósitos minerais. XXXV Congresso Brasileiro de Geologia, Belém, CVRD-SBG.

- Domingos, F. H. G. (2004). Geometria, cinemática e história tectônica das rochas da Serra Norte, Carajás-PA. Curso de Pós-Graduação em Geologia e Geoquímica. Belém, Universidade Federal do Pará. **MSc. thesis**: 119.
- Edmondo, G. P. (2002). Digital Geologic Field Mapping Using Arcpad. Digital Mapping Techniques '02 - Workshop Proceedings U.S.G.S. Open-File Report 02-370, <http://pubs.usgs.gov/of/2002/of02-370/edmondo.html>.
- Etheridge, M. A., V. J. Wall, et al. (1983). "The Role of the Fluid Phase during Regional Metamorphism and Deformation." Journal of Metamorphic Geology **1**(3): 205-226.
- Evans, J. P. (1988). "Deformation Mechanisms in Granitic-Rocks at Shallow Crustal Levels." Journal of Structural Geology **10**(5): 437-443.
- Ferguson, E. W., M. Z. Picard, et al. (1997). Lineament map of area 3 of the New Hampshire bedrock aquifer assessment, eastern New Hampshire, U.S. Geological Survey.
- Ferrill, D. A., A. P. Morris, et al. (2004). "Calcite twin morphology: a low-temperature deformation geothermometer." Journal of Structural Geology **26**(8): 1521-1529.
- Figueiras, A. J. M. and R. N. N. Villas (1984). Estudo petrológico e sedimentológico da sequência clástica (pós Grupo Grão-Pará) da Serra dos Carajás, Estado do Pará. XXXIII Congresso Brasileiro de Geologia, Rio de Janeiro, SBG.
- Fossen, H., B. Tikoff, et al. (1994). "Strain Modeling of Transpressional and Transtensional Deformation." Norsk Geologisk Tidsskrift **74**(3): 134-145.
- Gabrielsen, R. H., A. Braathen, et al. (2002). "Tectonic lineaments of Norway." Norwegian Journal of Geology **82**(3): 153-174.
- Galarza, M. A., M. J. B. Macambira, et al. (2007). "Dating and isotopic characteristics (Pb and S) of the Fe oxide-Cu-Au-U-REE Igarapé Bahia ore deposit, Carajás mineral province, Pará state, Brazil." Journal of South American Earth Sciences **in press**.
- Gay, J. S. P. (2003). The use of regional, but detailed, aeromagnetic data to define the Precambrian basement fault pattern, the plumbing system for mineral concentrations in the lithosphere. Deep structure of the Earth and concentration of metals in the lithosphere: A geodynamic approach. International workshop. P. T. Taylor and J. Kutina. Reston, Virginia, Schweizerbart, Stuttgart, Germany: 226.
- Gibbs, A. K. and K. R. Wirth (1990). Geologic setting of the Serra dos Carajás iron deposits, Brazil. Ancient Banded Iron Formation Regional Presentations. J. J. Chauvel, C. A. Yuqi, E. M. El Shazly et al. Athens-Greece, Theophrastus Publications: 83-102.
- Gibbs, A. K., K. R. Wirth, et al. (1986). "Age and composition of the Grão Pará Group volcanics, Serra dos Carajás." Revista Brasileira de Geociências **16**: 201-211.
- Girardi, V. A. V., A. Ferrario, et al. (2006). "A comparison of selected Precambrian Brazilian chromitites: Chromite, PGE-PGM, and Re/Os as parental source indicators." Journal of South American Earth Sciences **20**(4): 303-313.

- Goleby, B. R., R. S. Blewett, et al. (2006). "An integrated multi-scale 3D seismic model of the Archaean Yilgarn Craton, Australia." Tectonophysics **420**(1-2): 75-90.
- Gomes, A. C. B. (2003). Geologia, petrografia e geoquímica dos granitóides de Canaã dos Carajás, SE do Estado do Pará. Curso de Pós Graduação em Geologia e Geoquímica. Belém, Universidade Federal do Pará. **Master**: 164.
- Gomes, A. C. B. and R. Dall'Agnol (2007). "Nova associação tonalítica-trondjemítica neoarqueana na região de Canaã dos Carajás: TTGS com altos conteúdos de Ti, Zr e Y." Revista Brasileira de Geociências **37**(1): 12.
- Gomes, C. B., U. G. Cordani, et al. (1975). "Radiometric ages from the Serra dos Carajas Area, Northern Brazil." Geological Society of America Bulletin(86): 939-942.
- Goodwin, L. B. and B. Tikoff (2002). "Competency contrast, kinematics, and the development of foliations and lineations in the crust." Journal of Structural Geology **24**(6-7): 1065-1085.
- Guo, Y. G. and J. K. Morgan (2004). "Influence of normal stress and grain shape on granular friction: Results of discrete element simulations." Journal of Geophysical Research-Solid Earth **109**(B12).
- Haines, S. H. and B. A. van der Pluijm (2008). "Clay quantification and Ar-Ar dating of synthetic and natural gouge: Application to the Miocene Sierra Mazatan detachment fault, Sonora, Mexico." Journal of Structural Geology **30**(4): 525-538.
- Hamilton, W. B. (1998). "Archean magmatism and deformation were not products of plate tectonics." Precambrian Research **91**(1-2): 143-179.
- Hanmer, S. K. (1982). "Microstructure and Geochemistry of Plagioclase and Microcline in Naturally Deformed Granite." Journal of Structural Geology **4**(2): 197-214.
- Harrys, J. (1991). "Mapping of regional structure of Nova Scotia using remotely sensed imagery: Implications for regional tectonics and gold exploration." Canadian Journal of Remote Sensing **17**(2): 122-136.
- Hasui, Y., N. L. E. Haralyi, et al. (1992). "Megaestruturação pré-cambriana do território brasileiro baseada em dados geofísicos e geológicos." Revista Brasileira de Geociências **07**.
- Hasui, Y., N. L. E. Haralyi, et al. (1984). Elementos geofísicos e geológicos da região amazônica: subsídios para o modelo geotectônico. II SYMPOSIUM AMAZONICO. Manaus, DNPM.
- Hattori, I. and H. Yamamoto (1999). "Rock fragmentation and particle size in crushed zones by faulting." Journal of Geology **107**(2): 209-222.
- Hayman, N. W. (2006). "Shallow crustal fault rocks from the Black Mountain detachments, Death Valley, CA." Journal of Structural Geology **28**(10): 1767-1784.
- Haynes, D. W. (2000). Iron oxide copper-gold deposits: their position in the ore deposit spectrum and modes of origin Hydrothermal Iron Oxide Copper-Gold & Related Deposits: A Global Perspective. T. M. Porter. Adelaide, PGC Publishing. **1**: 71-90.

- Heilbronner, R. and N. Keulen (2006). "Grain size and grain shape analysis of fault rocks." Tectonophysics **427**(1-4): 199-216.
- Hein, F. J. (1999). "Mixed ("multi") fractal analysis of Granite Wash fields/pools and structural lineaments, Peace River Arch area, northwestern Alberta, Canada: A potential approach for use in hydrocarbon exploration." Bulletin of Canadian Petroleum Geology **47**(4): 556-572.
- Henriksen, H. and A. Braathen (2006). "Effects of fracture lineaments and in-situ rock stresses on groundwater flow in hard rocks: a case study from Sunnfjord, western Norway." Hydrogeology Journal **14**(4): 444-461.
- Hickman, A. H. (2004). "Two contrasting granite-greenstone terranes in the Pilbara Craton, Australia: evidence for vertical and horizontal tectonic regimes prior to 2900 Ma." Precambrian Research **131**(3-4): 153-172.
- Hildenbrand, T. G., B. Berger, et al. (2000). "Regional crustal structures and their relationship to the distribution of ore deposits in the western United States, based on magnetic and gravity data." Economic Geology and the Bulletin of the Society of Economic Geologists **95**(8): 1583-1603.
- Hill, K. C., R. D. Kendrick, et al. (2002). "Copper-gold mineralisation in New Guinea: tectonics, lineaments, thermochronology and structure." Australian Journal of Earth Sciences **49**(4): 737-752.
- Hirata, W. K., J. C. Rigon, et al. (1982). Geologia regional da Província Mineral de Carajás. I Simpósio de Geologia da Amazônia, Belém, SBG.
- Hirth, G. and J. Tullis (1992). "Dislocation creep regime in quartz aggregates." Journal of Structural Geology **14**(2): 145-159.
- Hitzman, M. W., N. Oreskes, et al. (1992). "Geological Characteristics and Tectonic Setting of Proterozoic Iron-Oxide (Cu-U-Au-Ree) Deposits." Precambrian Research **58**(1-4): 241-287.
- Hofmann, A. and M. K. Timothy (2004). The Belingwe greenstone belt: ensialic or oceanic? Precambrian Ophiolites and Related Rocks. M. K. Timothy, ELSEVIER: 772.
- Holdsworth, R. E. and R. V. L. Pinheiro (2000). "The anatomy of shallow-crustal transpressional structures: insights from the Archaean Carajas fault zone, Amazon, Brazil." Journal of Structural Geology **22**(8): 1105-1123.
- Hoppe, A., C. Schobbenhaus, et al. (1987). Precambrian Iron Formation in Brasil. Precambrian Iron-Formation. P. W. W. Appel and G. LaBerge. Athens, Greece, Theophrastus Publications: 347-390 674p.
- Huhn, S. R. B., M. J. B. Macambira, et al. (1999). Geologia e geocronologia Pb/Pb do granito alcalino Arqueano Planalto, Região da Serra do Rabo, Carajás-PA. VI Simpósio de Geologia da Amazônia, Manaus, Sociedade Brasileira de Geologia.
- Huhn, S. R. B., A. B. S. Santos, et al. (1988). O terreno "granito greenstone" da região de Rio Maria-Sul do Pará. XXXV Congresso Brasileiro de Geologia, Belém, SBG.

- Hussein, H. A., S. I. Rabie, et al. (1996). "Structural interpretation of aeromagnetic data, Gabal Zubeir area, North Eastern Desert, Egypt." International Journal of Remote Sensing **17**(11): 1997-2012.
- Imon, R., T. Okudaira, et al. (2004). "Development of shape- and lattice-preferred orientations of amphibole grains during initial cataclastic deformation and subsequent deformation by dissolution-precipitation creep in amphibolites from the Ryoke metamorphic belt, SW Japan." Journal of Structural Geology **26**(5): 793-805.
- Issler, R. S. (1977). "Esboço geológico tectônico do cráton do Guaporé." Revista Brasileira de Geociências **7**(3): 177-211.
- Jayawardhana, P. M. and S. N. Sheard (2000). "The use of airborne gamma-ray spectrometry - A case study from the Mount Isa inlier, northwest Queensland, Australia." Geophysics **65**(6): 1993-2000.
- Jebrak, M. (1997). "Hydrothermal breccias in vein-type ore deposits: A review of mechanisms, morphology and size distribution." Ore Geology Reviews **12**(3): 111-134.
- Jefferies, S. P., R. E. Holdsworth, et al. (2006). "The nature and importance of phyllonite development in crustal-scale fault cores: an example from the Median Tectonic Line, Japan." Journal of Structural Geology **28**(2): 220-235.
- Jelsma, H. A., P. A. Vanderbeek, et al. (1993). "Tectonic Evolution of the Bindura-Shamva Greenstone-Belt (Northern Zimbabwe) - Progressive Deformation around Diapiric Batholiths." Journal of Structural Geology **15**(2): 163-176.
- Jiang, Z. W., N. H. S. Oliver, et al. (1997). "Numerical modeling of fault-controlled fluid flow in the genesis of tin deposits of the Malage ore field, Gejiu mining district, China." Economic Geology and the Bulletin of the Society of Economic Geologists **92**(2): 228-247.
- Kanagawa, K., H. Shimano, et al. (2008). "Mylonitic deformation of gabbro in the lower crust: A case study from the Pankenushi gabbro in the Hidaka metamorphic belt of central Hokkaido, Japan." Journal of Structural Geology **30**(9): 1150-1166.
- Kane, W. F., D. C. Peters, et al. (1996). "Remote sensing in investigation of engineered underground structures." Journal of Geotechnical Engineering **122**(8): 674-681.
- Kerrick, R. (1986a). "Fluid Infiltration into Fault Zones - Chemical, Isotopic, and Mechanical Effects." Pure and Applied Geophysics **124**(1-2): 225-268.
- Kerrick, R. (1986b). "Fluid Transport in Lineaments." Philosophical Transactions of the Royal Society of London Series a-Mathematical Physical and Engineering Sciences **317**(1539): 219-251.
- Keulen, N., R. Heilbronner, et al. (2007). "Grain size distributions of fault rocks: A comparison between experimentally and naturally deformed granitoids." Journal of Structural Geology **29**(8): 1282-1300.
- Kim, G. B., J. Y. Lee, et al. (2004). "Construction of lineament maps related to groundwater occurrence with ArcView and Avenue(TM) scripts." Computers & Geosciences **30**(9-10): 1117-1126.

- Kisters, A. F. M. and C. R. Anhaeusser (1995). "Emplacement Features of Archean Ttg Plutons Along the Southern Margin of the Barberton Greenstone-Belt, South-Africa." Precambrian Research **75**(1-2): 1-15.
- Knup, P. E. (1971). Reconhecimento Geológico na Região dos Rios Itacaiunas e Tocantins, Estado do Pará. XXV Congresso Brasileiro de Geologia, São Paulo, SBG.
- Kolb, J., A. F. M. Kisters, et al. (2000). "The origin of fluids and nature of fluid-rock interaction in mid-crustal auriferous mylonites of the Renco mine, southern Zimbabwe." Mineralium Deposita **35**(2-3): 109-125.
- Kruse, R., H. Stunitz, et al. (2001). "Dynamic recrystallization processes in plagioclase porphyroclasts." Journal of Structural Geology **23**(11): 1781-1802.
- Kutina, J. (1999). "Ore deposit controls by fracture patterns of the crust and by mantle-rooted structural discontinuities." Earth Science Frontiers (China University of Geosciences, Beijing) **6**(1): 25.
- Lab, K. L. (1992). Considerações lito-estruturais sobre o Duples Transpressivo Serra Pelada. Curso de Pós-Graduação em Geologia e Geoquímica Belém, Universidade federal do Pará. **MSc. thesis: 109.**
- Lachenbruch, A. H. (1980). "Frictional Heating, Fluid Pressure, and the Resistance to Fault Motion." Journal of Geophysical Research **85**(Nb11): 6097-6112.
- Lafon, J. M., E. Rodrigues, et al. (1994a). "Le granite Mata Surrão: un magmatisme monzogranitique contemporain des associations tonalitiques-trondhjé-mitiques-granodioritiques archéennes de la région de Rio Maria (Amazonie orientale, Brésil)." Comptes rendus de l'Académie des sciences **318**: 643-649.
- Lafon, J. M., E. Rodrigues, et al. (1994b). "The Mata-Surrao Granite - Monzogranitic Magmatism Contemporaneous with the Archean Tonalitic-Trondhjemitic-Granodioritic Magmatism of the Rio-Maria Region (Eastern Amazonia, Brazil)." Comptes Rendus De L Academie Des Sciences Serie Ii **318**(5): 643-649.
- Lalor, J. H. (1987). The Olympic Dam copper-uranium-gold-silver deposit, South Australia. 4th Circum-Pacific Energy and Mineral Resources Conference, Singapore.
- Lancaster, O. J., J. Fanton, et al. (2000). Discovery and geology of the Sossego copper-gold deposit, Carajás District, Pará State, Brazil. 31 International Geological Congress. Rio de Janeiro, Brazil, IUGS.
- Leite, A. A. S. (2001). Geoquímica, petrogênese e evolução estrutural dos granitóides arqueanos da região de Xinguara, SE do Cráton Amazônico. Centro de Geociências. Belém, Universidade Federal do Pará. **PhD thesis: 330.**
- Leite, A. A. S., F. J. Althoff, et al. (2001). Arcaço estrutural, geocronologia e petrogênese dos granitóides arqueanos de Xinguara-PA: implicações para a evolução geológica do Terreno Granito-Greenstone de Rio Maria, SE do estado do Pará. VII Simpósio de Geologia da Amazônia, Belém-Brazil, SBG.

- Leite, A. A. S., R. Dall'Agnol, et al. (2004). "Geologia e geocronologia dos granitóides arqueanos da região de Xinguara (PA) e suas implicações na evolução do terreno granito-greenstone de Rio Maria, Cráton Amazônico." Revista Brasileira de Geociências **34**(4): 447-458.
- Lima, F. D. (2002). Evolução tectônica da terminação leste da Falha Carajás, sul do Estado do Pará. Curso de Pós-Graduação em Geologia e Geoquímica. Belém, Universidade Federal do Pará. **MSc. thesis:** 96.
- Lima, F. D. and R. V. L. Pinheiro (2001). Formação Gorotire: Consideração sobre uma unidade siliciclástica particular da Serra dos Carajás-PA. Contribuição à Geologia da Amazônia. N. J. Reis and M. A. S. Monteiro. Manaus, SBG, Núcleo Norte: 205-229.
- Lin, A. M. (1999). "Roundness of clasts in pseudotachylytes and cataclastic rocks as an indicator of frictional melting." Journal of Structural Geology **21**(5): 473-478.
- Lin, S. F. (2007). "Synchronous vertical and horizontal tectonism at the late stages of archaic cratonization and implications for gold mineralization." Journal of China University of Geosciences **18**: 473-473.
- Lindenmayer, Z. G. (1981). Geologia do depósito do Salobo 3 Alfa. Belém, DOCEGEO.
- Lindenmayer, Z. G. (1990). Salobo Sequence, Carajás, Brazil: geology, geochemistry and metamorphism. Ontario, University of Western Ontario. **PhD thesis:** 406.
- Lindenmayer, Z. G. and W. S. Fyfe (1991). Metamorfismo de alta temperatura e baixa pressão no depósito de cobre do Salobo: evidência do rift continental arqueano no Cráton Amazônico. III SIMPÓSIO DE GEOLOGIA DA AMAZÔNIA, Belém-Brazil, SBG.
- Lindenmayer, Z. G. and W. S. Fyfe (1992). Comparação preliminar entre os metabasaltos dos grupos Parauapebas e Salobo da Bacia de Carajás, Estado do Pará. XXXVII Congresso Brasileiro de Geologia, São Paulo, SBG.
- Lindenmayer, Z. G. and W. S. Fyfe (1994). The Salobo Cu (Au, Ag, Mo) deposit, Serra dos Carajás, Brazil. 7th Congreso Geológico Chileno, Concepción, Universidad de Concepción.
- Lindenmayer, Z. G., M. M. Pimentel, et al. (2001). Geologia do depósito de Cu-Au do Gameleira, Serra dos Carajás, Pará. Caracterização de Depósitos Auríferos Brasileiros. H. Jost, J. A. Brod and E. T. Quieroz. Brasília, ADIMB-DNPM: 79-139.
- Mabee, S. B., K. C. Hardcastle, et al. (1994). "A method of collecting and analysing lineaments for regional-scale fractured-bedrock aquifer studies." Groundwater **32**(6): 884-894.
- Macambira, M. J. B. (1992). Chronologie U-Pb, Rb-Sr, K-Ar et croissance de la croûte continentale dans l'Amazonie du sud-est; exemple de la région de Rio Maria, Province de Carajás, Brésil. Montpellier-France, Université de Montpellier. **PhD thesis:** 212.
- Macambira, M. J. B. and J. M. Lafon (1994). Geocronologia da Província Mineral de Carajás; síntese dos dados e novos desafios. IV Simposio de Geologia da Amazonia. Belem-Pa, SBG: 3.
- Macambira, M. J. B. and J. M. Lafon (1995). "Geocronologia da Província mineral de Carajás: síntese dos dados e novos desafios." Boletim do Museu Paraense Emílio Goeldi. Ciências da Terra **7**: 263-288.

- Macambira, M. J. B., J. M. Lafon, et al. (1998). Crescimento crustal arqueano registrado em zircões de sedimentos da região de Rio Maria, Província de Carajás, Pará. XL Congresso Brasileiro de Geologia, Belo Horizonte-Brazil, SBG.
- Macambira, M. J. B. and J. Lancelot (1991). História arqueana da região de Rio Maria, SE do estado do Pará, registrada em zircões detríticos de greenstone belt e de cobertura plataformar. III Simpósio de Geologia da Amazonia, Belém-Brazil, SBG.
- Macambira, M. J. B. and J. Lancelot (1992). Idade U-Pb em zircões de metavulcânica do greenstone do Supergrupo Andorinhas; delimitante da estratigrafia arqueana de Carajás, Estado do Pará. Congresso Brasileiro de Geologia, São Paulo, SBG.
- Macambira, M. J. B., D. C. C. Silva, et al. (2003). NEW ISOTOPE EVIDENCES CONFIRMING THE EXISTENCE OF A PALEOPROTEROZOIC TERRAIN IN THE REGION AT THE NORTH OF THE CARAJAS MINERAL PROVINCE. IV South American Symposium on Isotope Geology, Salvador, CBPM.
- Machado, N., D. Lindenmayer, et al. (1988). Geocronologia U-Pb da Província Metalogenética de Carajás: resultados preliminares. VII Congresso Latino Americano de Geologia, Belém-Brazil, SBG.
- Machado, N., Z. Lindenmayer, et al. (1991). "U-Pb Geochronology of Archean Magmatism and Basement Reactivation in the Carajas Area, Amazon Shield, Brazil." Precambrian Research **49**(3-4): 329-354.
- Main, I. G., P. G. Meredith, et al. (1990). Influence of fractal flaw distributions on rock deformation in the brittle field. Deformation mechanisms, rheology and tectonics. R. J. K. a. E. H. Rutter. London, Geological Society of London. **54**: 81-96.
- Mair, K., K. M. Frye, et al. (2002). "Influence of grain characteristics on the friction of granular shear zones." Journal of Geophysical Research-Solid Earth **107**(B10).
- Malehmir, A., A. Tryggvason, et al. (2006). "Seismic imaging and potential field modelling to delineate structures hosting VHMS deposits in the Skellefte Ore District, northern Sweden." Tectonophysics **426**(3-4): 319-334.
- Marçal, M. d. S. (1991). Aspectos lito-estruturais das minas de Ferro N4E e Manganês do Azul, Serra dos Carajás (PA). Curso de Pós-Graduação em Geociências. Belém, Universidade Federal do Pará. **MSc. thesis**: 135.
- Mark, G., A. Wilde, et al. (2005). "Modeling outflow from the Ernest Henry Fe oxide Cu-Au deposit: implications for ore genesis and exploration." Journal of Geochemical Exploration **85**(1): 31-46.
- Marone, C. and C. H. Scholz (1989). "Particle-Size Distribution and Microstructures within Simulated Fault Gouge." Journal of Structural Geology **11**(7): 799-814.
- Marschik, R., R. Mathur, et al. (2005). "Late Archean Cu-Au-Mo mineralization at Gameleira and Serra Verde, Carajas mineral Province, Brazil: Constraints from Re-Os molybdenite ages." Mineralium Deposita **39**(8): 983-991.

- Marschik, R., J. E. Spangenberg, et al. (2003a). The Sossego iron oxide–Cu–Au deposit, Carajás, Brazil. Mineral exploration and sustainable development. D. E. e. al. Rotterdam, Millpress. **1**: 331–334.
- Marschik, R., J. E. Spangenberg, et al. (2003b). The Sossego iron oxide Cu-Au deposit, Carajás, Brazil. Mineral exploration and sustainable development : proceedings of the Seventh Biennial SGA Meeting. D. G. Eliopoulos, et al. Athens-Greece, Millpress, Rotterdam: 331–334.
- Mattioni, L., W. Sassi, et al. (2007). "Analogue models of basin inversion by transpression: role of structural heterogeneity." Geological Society, London, Special Publications **272**(1): 397-417.
- McCaffrey, K. J. W., R. R. Jones, et al. (2005). "Unlocking the spatial dimension: digital technologies and the future of geoscience fieldwork." Journal of the Geological Society **162**(6): 927-938.
- McCandles, G. C., W. K. Hirata, et al. (1975). Complexo ígneo ácido da região central do Pará. X Conferencia Geologia Interguianas, Belém, DNPM.
- McClay, K. R. (1991). The Mapping of Geological Structures, John Wiley and Sons Ltd.
- McLean, M. A., C. J. L. Wilson, et al. (2009). "Basement interpretations from airborne magnetic and gravity data over the Lambert Rift region of East Antarctica." Journal of Geophysical Research-Solid Earth **114**: -.
- Meireles, E. M., W. K. Hirata, et al. (1984). Geologia das folhas Carajás e Rio Verde, Província Mineral de Carajás, Estado do Pará. XXXIII Congresso Brasileiro de Geologia, Rio de Janeiro, SBG.
- Miller, S. A. and D. L. Olgaard (1997). "Modeling seismicity clustering and fault weakness due to high pore pressures." Physics and Chemistry of The Earth **22**(1-2): 43-48.
- Mirsa, K. S., V. R. Slaney, et al. (1991). "Mapping of basement and other tectonic features using Seasat and Thematic Mapper in hydrocarbon-producing areas of the western sedimentary basin of Canada." Canadian Journal of Remote Sensing **17**(2): 137-151.
- Mitra, G. (1978). "Ductile Deformation Zones and Mylonites - Mechanical Processes Involved in Deformation of Crystalline Basement Rocks." American Journal of Science **278**(8): 1057-1084.
- Montalvão, R. M. G., C. C. G. Tassinari, et al. (1984). Geocronologia dos granitóides e gnaisses das regiões do Rio Maria, Fazenda Mata Geral e Rio Itacaiúnas, Sul do Pará (Distrito Carajás-Cumaru). XXXIII Congresso Brasileiro de Geologia, Rio de Janeiro, SBG.
- Monteiro, L. V. S., R. P. Xavier, et al. (2008). "Spatial and temporal zoning of hydrothermal alteration and mineralization in the Sossego iron oxide-copper-gold deposit, Caraja's Mineral Province, Brazil: paragenesis and stable isotope constraints." Mineralium Deposita **43**(2): 129-159.
- Monteiro, L. V. S., R. P. Xavier, et al. (2005). The Sossego iron oxide-copper-gold deposit, Carajás Mineral Province, Brazil: stable isotope constraints on the genesis and hydrothermal system evolution. I Simposio Brasileiro de Metalogenia. Gramado, RS, SBG.

- Mora, P. and D. Place (1999). "The weakness of earthquake faults." Geophysical Research Letters **26**(1): 123-126.
- Moraes Rego, L. F. (1933). "Notas Geográficas e Geológicas e Geológicas Sobre o Rio Tocantins." Boletim do Museu Emílio Goeldi de História Natural e Etnografia, **9**: 272-288.
- Moraes, R. P. S. A., F. F. (2005). O controle litoestrutural da mineralização de cobre do depósito Sequeirinho, Canaa dos Carajás, PA. Simposio Brasileiro de Metalogenia. Gramado, RS, SBG, Extended Abstract - CD-ROM.
- Mort, K. and N. H. Woodcock (2008). "Quantifying fault breccia geometry: Dent Fault, NW England." Journal of Structural Geology **30**(6): 701-709.
- Mougeot, R., J. P. Respaut, et al. (1996). Isotope geochemistry constrains for Cu, Au mineralizations and evolutions of the Carajás Province (Pará, Brazil). XXXIX Congresso Brasileiro de Geologia, Salvador-Brazil, SBG.
- Moura, C. A. V. G., H. E. (1993). "Evidence of Brasiliano/Panafrican deformation in the Araguaia Belt: implication for Gondwana evolution." Revista Brasileira de Geociências **23**: 117-123.
- Neves, A. P. and A. G. Vale (1999). Programa Levantamentos Geológicos Básicos do Brasil. Folha SC.22-X-A Redenção. Estado do Pará e Tocantins. Escala 1:250.000. Brasília-Brasil, CPRM.
- Neves, M. P. (2007). Estudos isotópicos (Pb-Pb, Sm-Nd, C e O) do depósito Cu-Au do Sossego, Província Mineral de Carajás. Curso de Pós-Graduação em Geologia e Geoquímica. Belém-PA, Universidade Federal do Pará. **Msc**: 74.
- Newhouse, W. H. (1940). "Openings due to movement along a curved or irregular fault plane." Economic Geology **35**(3): 445-464.
- Nietosamaniego, A. F. and S. A. Alanizalvarez (1995). "Influence of the Structural Framework on the Origin of Multiple-Fault Patterns." Journal of Structural Geology **17**(11): 1571-1577.
- NietoSamaniego, A. F. and S. A. AlanizAlvarez (1997). "Origin and tectonic interpretation of multiple fault patterns." Tectonophysics **270**(3-4): 197-206.
- Nogueira, A. C. R. (1995). Análise faciológica e aspectos estruturais da Formação Águas Claras, Região Central da Serra dos Carajás - Pará. Curso de Pós-Graduação em Geociências. Belém-Brazil, Universidade Federal do Pará. **MSc. thesis**: 167.
- Nogueira, A. C. R. and W. Truckenbrodt (1994). "Evidências de marés e tempestades na Formação Águas Claras, Pré-Cambriano, Serra dos Carajás." Acta Geológica Leopoldensia **17**(40): 7-30.
- Nogueira, A. C. R., W. Truckenbrodt, et al. (1995). "Formação Águas Claras, Pré-Cambriano da Serra dos Carajás. Redescrição e redefinição." Boletim do Museu Paraense Emílio Goeldi, Série Ciências da Terra **7**: 177-197.
- Nunes, A. R. (2002). Análise de dados geológicos, geofísicos e de sensoriamento remoto para geração de modelos prospectivos para a região de Serra Leste, Carajás (PA). Instituto de Geociências Campinas-SP, Universidade Estadual de Campinas **Msc Thesis**: 150.

- Nyman, M. W., R. D. Law, et al. (1992). "Cataclastic Deformation Mechanism for the Development of Core-Mantle Structures in Amphibole." Geology **20**(5): 455-458.
- O'Driscoll, E. S. T. (1983). Broken Hill at the cross roads. Australasian Institute of Mining and Metallurgy, Conference series 12.
- O'Driscoll, E. S. T. (1985). "The application of lineament tectonics in the discovery of Olympic Dam Cu-Au-U deposit at Roxby Downs, South Australia." Global Tectonics and Metallogeny **3**(1): 43-57.
- Odling, N. E. (1997). "Scaling and connectivity of joint systems in sandstones from western Norway." Journal of Structural Geology **19**(10): 1257-1271.
- Odriscoll, E. S. T. (1986). "Observations of the Lineament Ore Relation." Philosophical Transactions of the Royal Society of London Series a-Mathematical Physical and Engineering Sciences **317**(1539): 195-218.
- Oliveira, J. K. M. d. (2002). Caracterização estrutural da borda sudeste do Sistema Transcorrente Carajás com ênfase nas rochas do Terreno Granítico-Gnáissico. . Curso de Pós-Graduação em Geologia e Geoquímica Belém, Universidade Federal do Pará. **MSc. thesis**.
- Oliveira, J. R., C. S. S. Neto, et al. (1994). Geologia da Folha Serra Pelada. Programa Levantamentos Geológicos Básicos do Brasil. Serra Pelada. Folha SB.22-X-C. Estado do Pará. J. R. Oliveira, C. S. S. Neto and E. J. S. Costa. Brasília, CPRM: 248.
- Oliver, N. H. S., J. S. Cleverley, et al. (2004). "Modeling the role of sodic alteration in the genesis of iron oxide-copper-gold deposits, Eastern Mount Isa block, Australia." Economic Geology **99**(6): 1145-1176.
- Olszewski, W. J., K. R. Wirth, et al. (1989). "The Age, Origin, and Tectonics of the Grao-Para Group and Associated Rocks, Serra-Dos-Carajas, Brazil - Archean Continental Volcanism and Rifting." Precambrian Research **42**(3-4): 229-254.
- Paradella, W. R., P. A. Bignelli, et al. (1997). "Airborne and spaceborne Synthetic Aperture Radar (SAR) integration with Landsat TM and gamma ray spectrometry for geological mapping in a tropical rainforest environment, the Carajas Mineral Province, Brazil." International Journal of Remote Sensing **18**(7): 1483-1501.
- Parman, S. W. (2007). "Helium isotopic evidence for episodic mantle melting and crustal growth." Nature **446**(7138): 900-903.
- Passchier, C. W. (1986). "Flow in Natural Shear Zones - the Consequences of Spinning Flow Regimes." Earth and Planetary Science Letters **77**(1): 70-80.
- Passchier, C. W., J. S. Myers, et al. (1990). Field geology of high-grade gneiss terrains. New York, Springer-Verlag.
- Passchier, C. W. and R. A. J. Trouw (2005). Microtectonics. Berlin ; New York, Springer.
- Pearson, D. G., S. W. Parman, et al. (2007). "A link between large mantle melting events and continent growth seen in osmium isotopes." Nature **449**(7159): 202-205.

- Peters, S. G. (1993). "Formation of oreshoots in mesothermal gold-quartz vein deposits: examples from Queensland, Australia." Ore Geology Reviews **8**(3-4): 277-301.
- Petri, S. and V. J. Fulfaro (1983). Geologia do Brasil. São Paulo, Editora da Universidade de São Paulo.
- Pidgeon, R. T., M. J. B. Macambira, et al. (2000). "Th-U-Pb isotopic systems and internal structures of complex zircons from an enderbite from the Plum Complex, Carajas Province, Brazil: evidence for the ages of granulite facies metamorphism and the protolith of the enderbite." Chemical Geology **166**(1-2): 159-171.
- Pimentel, M. M. and N. Machado (1994). Geocronologia U-Pb dos terrenos granito-greenstone de Rio Maria, Pará. XXXVIII Congresso Brasileiro de Geologia, São Paulo, SBG.
- Pinheiro, R. V. L. (1997). Reactivation history of the Carajás and Cinzento strike-slip systems, Amazon, Brazil. Department of Earth Sciences. Durham, University of Durham. **PhD thesis**: 407.
- Pinheiro, R. V. L. and R. E. Holdsworth (1997a). "Reactivation of Archaean strike-slip fault systems, Amazon region, Brazil." Journal of the Geological Society **154**: 99-103.
- Pinheiro, R. V. L. and R. E. Holdsworth (1997b). "The structure of the Carajas N-4 Ironstone deposit and associated rocks: relationship to Archaean strike-slip tectonics and basement reactivation in the Amazon region, Brazil." Journal of South American Earth Sciences **10**(3-4): 305-319.
- Platt, J. P. (1984). "Secondary Cleavages in Ductile Shear Zones." Journal of Structural Geology **6**(4): 439-442.
- Pollard, P. J. (2001). "Sodic(-calcic) alteration in Fe-oxide-Cu-Au districts: an origin via unmixing of magmatic H₂O-CO₂-NaCl +/- CaCl₂-KCl fluids." Mineralium Deposita **36**(1): 93-100.
- Pollard, P. J. (2006). "An intrusion-related origin for Cu-Au mineralization in iron oxide-copper-gold (IOGG) provinces." Mineralium Deposita **41**(2): 179-187.
- Pryer, L. L. (1993). "Microstructures in Feldspars from a Major Crustal Thrust Zone - the Grenville Front, Ontario, Canada." Journal of Structural Geology **15**(1): 21-36.
- Pryer, L. L. and P. Y. F. Robin (1995). "Retrograde Metamorphic Reactions in Deforming Granites and the Origin of Flame Perthite." Journal of Metamorphic Geology **13**(6): 645-658.
- Puty, C. O. F., R. C. Martins, et al. (1972). Projeto Marabá. Belém, DNPM-CPRM: 124.
- Raghavan, V., K. Wadatsumi, et al. (1993). "Automatic extraction of lineament information of satellite images using digital elevation data." Nonrenewable Resources **2**(2): 148-155.
- Ramo, O. T., R. Dall'Agnol, et al. (2002). "1.88 Ga oxidized A-type granites of the Rio Maria region, eastern Amazonian craton, Brazil: Positively anorogenic!" Journal of Geology **110**(5): 603-610.
- Ramos, J. F. d. F., C. F. Melo, et al. (1983). Mapeamento Geológico - Projeto Parauapebas. Belém, Convênio SUDAM-UFPA-FADESP: 66.

- Ramos, J. F. d. F., C. A. U. Moura, et al. (1984). Uma discussão sobre as sequências sedimentares tidas como Formação Rio Fresco, sudeste do Pará. XXXIII Congresso Brasileiro de Geologia, Rio de Janeiro, SBG.
- Ramsay, J. G. (1980). "Crack-Seal Mechanism of Rock Deformation." Nature **284**(5752): 135-139.
- Ramsay, J. G. and M. I. Huber (1987). The techniques of modern structural geology. Vol. 2, Folds and fractures. London, Academic P.
- Ray, R. G. (1954). "Geology and ore deposits of the Willow Creek mining district, Alaska." U.S. Geological Survey Bulletin **1004**: 86 p.
- Reis, F. N. and R. N. Villas (1999). O depósito de sulfetos de Cu+Au de Serra Verde, Província Mineral de Carajás: Caracterização mineralógica, rochas encaixantes e evidências de metamorfismo. VI Simpósio de Geologia da Amazônia, Manaus, SBG.
- Requia, K., H. J. Stein, et al. (2003). "Re-Os and Pb-Pb geochronology of the Archean Salobo iron oxide coppergold deposit, Carajás Mineral Province, northern Brazil." Mineralium Deposita **38**: 727-738.
- Resende, N. P. d. and A. L. d. M. Barbosa (1972). Relatório de pesquisa de minério de ferro, distrito ferrífero da Serra dos Carajás - Estado do Pará. Relatório Final de Pesquisa. Belém, AMZA.
- Reynolds, L. J. (2000). Geology of the Olympic Dam Cu-U-Au-Ag-REE deposit. Hydrothermal iron oxide copper-gold and related deposits: A global perspective. T. M. Porter. Adelaide, PGC Publishing. **1**: 93-104.
- Robin, C. M. I. and R. C. Bailey (2009). "Simultaneous generation of Archean crust and subcratonic roots by vertical tectonics." Geology **37**(6): 523-526.
- Rodrigues, E. S., J. M. Lafon, et al. (1992). Geocronologia Pb-Pb da Província Mineral de Carajás: primeiros resultados. XXXVII CONGRESSO BRASILEIRO DE GEOLOGIA, São Paulo-Brazil, SBG.
- Rolando, A. P. and M. J. B. Macambira (2003). ARCHEAN CRUST FORMATION IN INAJÁ RANGE AREA, SSE OF AMAZONIAN CRATON, BRAZIL, BASED ON ZIRCON AGES AND Nd ISOTOPES. IV South American Symposium on Isotope Geology, Salvador-Brazil, CBPM.
- Rosière, C. A., F. J. Baars, et al. (2006). "Structure and iron mineralization in the Carajas Province." Applied Earth Science **115**(4): 126-133.
- Saadi, A., M. N. Machette, et al. (2002). Map and Database of Quaternary Faults and Lineaments in Brazil. A project of the International Lithosphere Program Task Group II-2, Major Active Faults of the World, U.S. Geological Survey, Open-File Report 02-230.
- Sabins, F. F. (1987). Remote Sensing — Principles and Interpretation. New York, NY, W.H. Freeman.
- Sanderson, D. J. a. Z., X. (1999). Critical stress localization of flow associated with deformation of well-fractured rock masses, with implications for mineral deposits. Fractures, fluid flow and

- mineralization. K. J. W. McCaffrey, L. Lonergan and J. Wilkinson. London, Geological Society of London: pp.69-81.
- Santos, B. A. d. (1980). Geologia e potencial mineral da região dos Carajás. Simpósio sobre a Província Mineral da Serra dos Carajás. Rio de Janeiro, DOCEGEO: 46.
- Santos, J. O. S. (2003). Geotectonica dos Escudos das Guianas e Brasil-Central. Geologia Tectonica e Recursos Minerais do Brasil. L. A. Bizzi, C. Schobbenhaus, R. M. Vidotti and J. H. Gonçalves. Brasília, CPRM: 169-226.
- Santos, J. O. S., L. A. Hartmann, et al. (2000). "A new understanding of the provinces of the Amazon craton based on integration of field mapping and U-Pb and Sm-Nd geochronology." Gondwana Research 3(4): 453-488.
- Santos, J. O. S. and S. O. C. Loguécio (1984). A parte meridional do Cráton Amazônico (Escudo das Guianas). Geologia do Brasil. C. Schobbenhaus, D. A. Campos, G. R. Derze and H. E. Asmus. Brasília, DNPM: 93-127.
- Sardinha, A. S., C. E. D. Barros, et al. (2006). "Geology, geochemistry, and U-Pb geochronology of the Archean (2.74 Ga) Serra do Rabo granite stocks, Carajas Metallogenic Province, northern Brazil." Journal of South American Earth Sciences 20(4): 327-339.
- Sardinha, A. S., R. Dall'Agnol, et al. (2004). Geocronologia Pb-Pb e U-Pb em zircão de granitóides arqueanos da região de Canaã dos Carajás, Província Mineral de Carajás. 42 Congresso Brasileiro de Geologia. Araxa, MG, SBG.
- Sardinha, S. A. (2002). Geologia, geoquímica e geocronologia do granito Serra do Rabo, Província Mineral de Carajás. Curso de Pós-Graduação em Geologia e Geoquímica. Belém-Brazil, Universidade Federal do Pará. **MSc. thesis**: 108.
- Scanvic, J.-Y. and J.-P. Deroin (1997). Aerospatial Remote Sensing in Geology. Rotterdam, A. A. Balkema.
- Schobbenhaus, C., G. R. Derze, et al. (1984). Geologia do Brasil. Texto explicativo do mapa geológico do Brasil e da área oceânica adjacente, incluindo depósitos minerais. Brasília, DNPM.
- Schobbenhaus, C. and B. B. d. B. Neves (2003). A Geologia do Brasil na Plataforma Sul-Americana. Geologia, tectônica e recursos minerais do Brasil : texto, mapas & SIG. L. A. Bizzi, C. Schobbenhaus, R. M. Vidotti and J. H. Gonçalves. Brasília, CPRM: 5-54.
- Scholz, C. H. (1990). The mechanics of earthquakes and faulting. Cambridge, Cambridge Univ. P.
- Scholz, C. H. (2002). The Mechanics of Earthquakes and Faulting. Cambridge, Cambridge University Press.
- Schreurs, G. and B. Colletta (1998). "Analogue modelling of faulting in zones of continental transpression and transtension." Geological Society, London, Special Publications 135(1): 59-79.

- Schulz, S. E. and J. P. Evans (1998). "Spatial variability in microscopic deformation and composition of the Punchbowl fault, southern California: implications for mechanisms, fluid-rock interaction, and fault morphology." Tectonophysics **295**(1-2): 223-244.
- Segall, P. and D. D. Pollard (1983). "Joint Formation in Granitic Rock of the Sierra-Nevada." Geological Society of America Bulletin **94**(5): 563-575.
- Shackleton, R. M. (1995). "Tectonic evolution of greenstone belts." Geological Society, London, Special Publications **95**(1): 53-65.
- Sibson, R. H. (1973). "Interactions between Temperature and Pore-Fluid Pressure During Earthquake Faulting and a Mechanism for Partial or Total Stress Relief." Nature-Physical Science **243**(126): 66-68.
- Sibson, R. H. (1977). "Fault rocks and fault mechanisms." Journal of the Geological Society **133**(3): 191-213.
- Sibson, R. H. (1990). Conditions for fault-valve behaviour. Deformation mechanisms, rheology and tectonics - Geological Society Special Publications. R. J. Knipe and E. H. Rutter. London, Geological Society of London: 54.
- Sibson, R. H. (1994). "An Assessment of Field Evidence for Byerlee Friction." Pure and Applied Geophysics **142**(3-4): 645-662.
- Sibson, R. H. (1996). "Structural permeability of fluid-driven fault-fracture meshes." Journal of Structural Geology **18**(8): 1031-1042.
- Sibson, R. H. (2000a). "A brittle failure mode plot defining conditions for high-flux flow." Economic Geology and the Bulletin of the Society of Economic Geologists **95**(1): 41-47.
- Sibson, R. H. (2000b). "Fluid involvement in normal faulting." Journal of Geodynamics **29**(3-5): 469-499.
- Sibson, R. H., F. Robert, et al. (1988). "High-Angle Reverse Faults, Fluid-Pressure Cycling, and Mesothermal Gold-Quartz Deposits." Geology **16**(6): 551-555.
- Sillitoe, R. H. (2003). "Iron oxide-copper-gold deposits: an Andean view." Mineralium Deposita **38**(7): 787-812.
- Silva, G. G., M. J. C. Lima, et al. (1974). Geologia das folhas SB-22 Araguaia e parte SC-22 Tocantins. Rio de Janeiro.
- Silvennoinen, H. and E. Kozlovskaya (2007). "3D structure and physical properties of the Kuhmo Greenstone Belt (eastern Finland): Constraints from gravity modelling and seismic data and implications for the tectonic setting." Journal of Geodynamics **43**(3): 358-373.
- Silverman, B. W. (1986). Density Estimation for Statistics and Data Analysis. London, Chapman and Hall.
- Simpson, C. and D. G. Depaor (1993). "Strain and Kinematic Analysis in General Shear Zones." Journal of Structural Geology **15**(1): 1-20.

- Simpson, C. and R. P. Wirth (1989). "Evidence for Deformation-Induced K-Feldspar Replacement by Myrmekite." Journal of Metamorphic Geology **7**(2): 261-275.
- Siqueira, J. B. (1990). Organização litoestrutural do dúplex Salobo-Mirim, Serra dos Carajás, PA. Instituto de Geociências. Belém, Universidade do Pará. **MSc. thesis**: 125.
- Snoke, A. W., J. Tullis, et al. (1998). Fault-related rocks : a photographic atlas. Princeton, N.J., Princeton University Press.
- Soares, J. E. B. (2002). Geologia, petrografia e geoquímica das rochas granitóides arqueanas da região de Serra Dourada, Canaã dos Carajás-PA Programa de Pós-Graduação em Geologia e Geoquímica. Belém, Universidade Federal do Pará. **Exame de Qualificação de Doutorado**.
- Solum, J. G. and B. A. van der Pluijm (2007). "Reconstructing the Snake River-Hoback River Canyon section of the Wyoming thrust belt through direct dating of clay-rich fault rocks." Geological Society of America Special Papers **433**: 183-196.
- Souza, F. D. S. (2007). Estudo da alteração hidrotermal, com ênfase no metamorfismo sódico de rochas granitóides e máficada região de Canaã de Carajás, Província Mineral de Carajás. . Curso de Pós-Graduação em Geologia e Geoquímica. Belém, Universidade Federal do Pará. **Masters**: 195.
- Souza, S. R. B., M. J. B. Macambira, et al. (1996). Novos dados geocronológicos para os granitos deformados do Rio Itacaiúnas (Serra dos Carajás, PA); implicações estratigráficas. V SIMPÓSIO DE GEOLOGIA DA AMAZONIA, Belém, SBG.
- Souza, Z. S. d., R. Dall'Agnol, et al. (1997). "Geochemistry and petrogenesis of metavolcanic rocks from archaean greenstone belts: Rio Maria region (Southeast Pará, Brazil)." Revista Brasileira de Geociências **27**(2): 169-180.
- Souza, Z. S. d., A. Potrel, et al. (2001). "Nd, Pb and Sr isotopes in the Identidade Belt, an Archaean greenstone belt of the Rio Maria region (Carajas Province, Brazil): implications for the Archaean geodynamic evolution of the Amazonian Craton." Precambrian Research **109**(3-4): 293-315.
- Stephens, J. R., J. L. Mair, et al. (2004). "Structural and mechanical controls on intrusion-related deposits of the Tombstone Gold Belt, Yukon, Canada, with comparisons to other vein-hosted ore-deposit types." Journal of Structural Geology **26**(6-7): 1025-1041.
- Stipp, M., H. Stunitz, et al. (2002). "The eastern Tonale fault zone: a 'natural laboratory' for crystal plastic deformation of quartz over a temperature range from 250 to 700 degrees C." Journal of Structural Geology **24**(12): 1861-1884.
- Storti, F., F. Balsamo, et al. (2007). "Particle shape evolution in natural carbonate granular wear material." Terra Nova **19**(5): 344-352.
- Stünitz, H. (1993). Transition from fracturing to viscous flow in a naturally deformed metagabbro. Defects and Processes in the Solid State: Geosciences Applications. J. N. a. F. G. Boland, J.F. Amsterdam, Elsevier: 121-150.
- Suita, M. T. F. and A. A. Nilson (1988). Geologia do complexo máfico-ultrámáfico Luanga (Província de Carajás, Pará) e das unidades encaixantes. XXXV Congresso Brasileiro de Geologia, Belém, SBG.

- Suita, M. T. F. and A. A. Nilson (1991). O depósito de cromita estratiforme do complexo Luanga, província de Carajás, Pará—Aspectos geoquímicos. III Congresso Brasileiro de Geoquímica and I Congresso de Geoquímica dos Países de Língua Portuguesa, São Paulo, SBGQ.
- Suszczynki, E. (1972). A origem vulcânica do minério de ferro primário Serra dos Carajás - Estado do Pará. XXVI Congresso Brasileiro de Geologia, Belém.
- Tallarico, F. H. B., B. R. Figueiredo, et al. (2005). "Geology and SHRIMP U-Pb geochronology of the Igarape Bahia deposit, Carajas Copper-Gold belt, Brazil: An Archean (2.57 Ga) example of iron-oxide Cu-Au-(U-REE) mineralization." Economic Geology **100**(1): 7-28.
- Tassinari, C. C. G., U. G. Cordani, et al. (1996). "Geochronological Systematics on Basement Rocks from the Rio Negro–Juruena Province (Amazonian Craton) and Tectonic Implications." International Geology Review **38**: 161-175.
- Tassinari, C. C. G., W. K. Hirata, et al. (1982). "Geologic evolution of the Serra dos Carajás, Pará, Brazil." Revista Brasileira de Geociências **12**(1-3): 263-267.
- Tassinari, C. C. G. and M. J. B. Macambira (1999). "Geochronological provinces of the Amazonian Craton." Episodes **22**(3): 174-182.
- Tassinari, C. C. G. and M. J. B. Macambira (2004). Evolução tectônica do Cráton Amazônico. Geologia do Continente Sul Americano: Evolução da obra de F.F.M. de Almeida. V. Mantesso-Neto, A. Bartorelli, C. D. R. Carneiro and B. B. d. Brito Neves. São Paulo, BECA: 471–486.
- Tchalenko, J. S. (1968). "Evolution of Kink-Bands and Development of Compression Textures in Sheared Clays." Tectonophysics **6**(2): 159-174.
- Tchalenko, J. S. (1970). "Similarities between Shear Zones of Different Magnitudes." Geological Society of America Bulletin **81**(6): 1625-1640.
- Teixeira, J. B. T. and D. H. Egger (1994). "Petrology, geochemistry and tectonic setting of Archean basaltic and dioritic rocks from the N4 iron deposit, Serra dos Carajás, Pará, Brazil." Acta Geológica Leopoldensia **40**: 71–114.
- Teixeira, N. P., J. S. Bettencourt, et al. (2002). "Archean crustal sources for Paleoproterozoic tin-mineralized granites in the Carajas Province, SSE Para, Brazil: Pb-Pb geochronology and Nd isotope geochemistry." Precambrian Research **119**(1-4): 257-275.
- Teixeira, W., C. C. G. Tassinari, et al. (1989). "A Review of the Geochronology of the Amazonian Craton - Tectonic Implications." Precambrian Research **42**(3-4): 213-227.
- ten Brink, U. S., M. Rybakov, et al. (2007). "Magnetic character of a large continental transform: An aeromagnetic survey of the Dead Sea Fault." Geochemistry Geophysics Geosystems **8**: -.
- Tian, Y., D. P. Zhao, et al. (2009). "Seismic imaging of the crust and upper mantle beneath the North China Craton." Physics of the Earth and Planetary Interiors **172**(3-4): 169-182.
- Tikoff, B. and D. Greene (1997). "Stretching lineations in transpressional shear zones: An example from the Sierra Nevada Batholith, California." Journal of Structural Geology **19**(1): 29-39.

- Trendall, A. F., M. A. S. Basei, et al. (1998). "SHRIMP zircon U-Pb constraints on the age of the Carajas formation, Grao Para Group, Amazon Craton." Journal of South American Earth Sciences **11**(3): 265-277.
- Tribe, I. R. and R. S. D'Lemos (1996). "Significance of a hiatus in down-temperature fabric development within syntectonic quartz diorite complexes, Channel Islands, UK." Journal of the Geological Society **153**: 127-138.
- Tsurumi, J., H. Hosonuma, et al. (2003). "Strain localization due to a positive feedback of deformation and myrmekite-forming reaction in granite and aplite mylonites along the Hatagawa Shear Zone of NE Japan." Journal of Structural Geology **25**(4): 557-574.
- Tullis, J. (2002). "Deformation of granitic rocks: Experimental studies and natural examples." Plastic Deformation of Minerals and Rocks **51**: 51-95.
- Tullis, J., H. Stunitz, et al. (2000). Deformation microstructures in quartzo-feldspathic rocks. Stress, Structure and Strain: a volume in honour of Win D. Means. M. W. a. U. Jessell, J.L. , Journal of the Virtual Explorer. **2**.
- Tullis, J. and R. A. Yund (1985). "Dynamic Recrystallization of Feldspar - a Mechanism for Ductile Shear Zone Formation." Geology **13**(4): 238-241.
- Twiss, R. J. and E. Moores (1992). Structural geology. New York, W.H. Freeman.
- Van Kranendonk, M. J. (2004). "Archaean Tectonics 2004: A review - Preface." Precambrian Research **131**(3-4): 143-151.
- Van Kranendonk, M. J., W. J. Collins, et al. (2004). "Critical tests of vertical vs. horizontal tectonic models for the Archaean East Pilbara Granite-Greenstone Terrane, Pilbara Craton, Western Australia." Precambrian Research **131**(3-4): 173-211.
- Van Kranendonk, M. J., R. H. Smithies, et al. (2007). "Review: secular tectonic evolution of Archean continental crust: interplay between horizontal and vertical processes in the formation of the Pilbara Craton, Australia." Terra Nova **19**(1): 1-38.
- Veneziani, P., A. R. d. Santos, et al. (2004). "A evolução tectono-estratigráfica da Província Mineral de Carajás: um modelo com base em dados de sensores remotos orbitais (SAR-C RADARSAT-1, TM LANDSAT-5), aerogeo-física e dados de campo." Revista Brasileira de Geociências **34**(1): 67-78.
- Vernon, R. H. (1999). "Flame perthite in metapelitic gneisses at Cooma, SE Australia." American Mineralogist **84**(11-12): 1760-1765.
- Vernon, R. H. (2004). A practical guide to rock microstructure. Cambridge, Cambridge University Press.
- Villas, R. N., L. F. O. Lima, et al. (2005). Relações entre deformação, alteração hidrotermal e mineralização no depósito Cu-Au do Sossego, Província Mineral de Carajás. I Simpósio Brasileiro de Metalogenia. Gramado-RS, SBG.
- Villas, R. N. N. and M. D. Santos (2001). "Gold deposits of the Carajas mineral provinces: deposit types and metallogenesis." Mineralium Deposita **36**(3-4): 300-331.

- Wernick, E. (1981). "The Archean of Brazil." Earth Science Reviews **17**: 17.
- Williams, P. J., M. D. Barton, et al. (2005). "Iron oxide copper-gold deposits: geology, space-time distribution, and possible modes of origin." Economic Geology **100th Anniversary Volume**: 34.
- Wilson, R. W., K. J. W. McCaffrey, et al. (2006). "Complex fault patterns, transtension and structural segmentation of the Lofoten Ridge, Norwegian margin: Using digital mapping to link onshore and offshore geology." Tectonics **25**(4): -.
- Wilson, R. W., K. J. W. McCaffrey, et al. (2005). Digital mapping of Lofoten's faults. Geoscientist. **15**.
- Windley, B. F. (1995). The evolving continents. Chichester, John Wiley & Sons.
- Winter, C. J. (1995). Geology and base-metal mineralization associated with Archean iron-formations in the Pojuca Corpo Quatro deposit, Carajás, Brazil. Southampton, University of Southampton. **PhD Thesis**: 238p.
- Wintsch, R. P. and K. Yi (2002). "Dissolution and replacement creep: a significant deformation mechanism in mid-crustal rocks." Journal of Structural Geology **24**(6-7): 1179-1193.
- Wirth, K. R., A. K. Gibbs, et al. (1986). "U-Pb ages of zircons from the Grao-Para Group and Serras dos Carajas, Para, Brazil." Revista Brasileira de Geociências **16**(2): 195-200.
- Wirth, R. and G. Voll (1987). "Cellular Intergrowth between Quartz and Sodium-Rich Plagioclase (Myrmekite) - an Analog of Discontinuous Precipitation in Metal-Alloys." Journal of Materials Science **22**(6): 1913-1918.
- Woodall, R. (1991). WMC's Australian mineral exploration: Yesterday, today and tomorrow. Western Australian Geoscientific Technical Conference, Perth.
- Woodall, R. (1992). Empiricism and concept in successful exploration. 11th Australian Geological Convention, Ballarat, Geological Society of Australia Abstracts.
- Woodcock, N. H. and K. Mort (2008). "Classification of fault breccias and related fault rocks." Geological Magazine **145**(3): 435-440.